



Russian - Dutch Workshop
**“CATALYSIS FOR SUSTAINABLE
DEVELOPMENT”**

June 22-25, 2002

Abstracts

Novosibirsk - 2002

Boreskov Institute of Catalysis of Siberian Branch of Russian
Academy of Sciences, Russia

NIOK, The Netherlands

Scientific Council on Catalysis of Russian Academy of
Sciences, Russia

Russian-Dutch Workshop
“Catalysis For Sustainable
Development”

Novosibirsk
June 22-25, 2002

ABSTRACTS

Novosibirsk-2002

PROGRAMME SCIENTIFIC COMMITTEE

The Netherlands

A. Blik	University of Amsterdam
H. Bouma	NIOK
K.P. de Jong	Catalysis Center Utrecht
G. van Koten	NIOK
L. Lefferts	Twente University
J. A. Moulijn	Delft University of Technology
B.E. Nieuwenhuys	Leiden University
A. Stankiewicz	DSM Research
H.J. Veringa	ECN, Twente University

Russia

Z.R. Ismagilov	Boreskov Institute of Catalysis
V.B. Kazanskii	Zelinskii Institute of Organic Chemistry
V.V. Lunin	Lomonosov Moscow State University
I.I. Moiseev	Kurnakov Institute of General and Inorganic Chemistry
A.E. Shilov	Institute of Biochemical Physics
G.M. Zhidomirov	Boreskov Institute of Catalysis

ORGANIZING COMMITTEE

Co-Chairs:

Valentin N. Parmon	Boreskov Institute of Catalysis, Russia
Rutger A. van Santen	Eindhoven University of Technology, The Netherlands

Co-Vice-Chairs:

Hans Bouma	NIOK, The Netherlands
Zinfer R. Ismagilov	Boreskov Institute of Catalysis, Russia
Bernard E. Nieuwenhuys	Leiden University, The Netherlands

Workshop Secretary:

Tatiana V. Zamulina	Boreskov Institute of Catalysis, Russia
---------------------	---

Organizers express their gratitude to

NIOK, The Netherlands

**Russian Foundation for Basic Research
(RFBR), Russia**

for the financial support of the Workshop

PLENARY LECTURES

MOLECULAR MODELLING

R.A. van Santen

Schuit Institute of Catalysis, Eindhoven University of Technology, Eindhoven, The Netherlands

Introduction

A review will be presented of our recent studies of the kinetics of the hydroisomerization reaction and the mechanism of selective toluene alkylation.

The approach is an integrated one of theory and experiment.

Computational

Density Functional Theory is an excellent tool to analyse reaction intermediate structures as well as their energetics. Results will be presented of cluster as well as periodical structure calculations.

To predict adsorption isotherms and diffusion force field based Molecular Dynamics and Monte Carlo approaches are used.

Overall kinetics is simulated using kinetic Monte Carlo or conventional kinetic simulation approaches.

Experimental

Solid State C^{13} NMR is an excellent tool to analyse the siting of alkanes in zeolites with different adsorption possibilities. Al Quadrupole Coupling Constant measurements probe changes at the protonic sites when molecules interact.

Positron Emission Profiling studies using C^{11} labeled alkane molecules enable the measurements of zeolite micropore filling at reaction conditions.

Conventional catalytic measurements provide catalytic rate data as Turn Over Frequencies, apparent activation energies and reaction orders.

Discussion

An analysis of the relative importance of adsorption versus diffusion and proton activation is made for the alkane hydroisomerization reaction.

It will be shown that differences in the adsorption isotherms are the main parameter that control differences in reactivity of zeolites as long as the Al/Si ratio is lower than 0.1.

The alkylation reaction of toluene is sterically controlled. Differences in diffusivity of the product turn out not to be essential. The key geometric factor is the stability of the pre-reaction intermediate that leads to the relevant transition states.

PL-2

**LOCALIZATION OF BIVALENT TRANSITION METAL IONS IN HIGH SILICA
ZEOLITES PROBED BY LOW TEMPERATURE ADSORPTION OF MOLECULAR
HYDROGEN**

V.B. Kazansky

Zelinsky Institute of Organic Chemistry of Russian Academy of Sciences, Moscow, Russia

ZSM-5 zeolites modified with bivalent cations possess unique catalytic properties. Therefore, the study of sitting in these materials of bivalent cations is of a definite interest. Due to the low concentration of the cations and the lack of their ordering in the zeolite framework this is a difficult problem. In the present work, which was carried out in collaboration with the group of Prof. R.A. van Santen at the Eindhoven Technical University we used for this purpose H₂ adsorption at 77 K as a molecular probe. The perturbation resulting from adsorption of hydrogen was monitored by DRIFT.

Our results for HZSM-5 with the very broad Si/Al ratios in the framework modified with several weight % of Zn⁺² cations indicated appearance in the zeolites with the lower Si/Al ratios of several new adsorption sites, which only moderately perturb adsorbed H₂. They were ascribed to the exchangeable Zn⁺² ions, compensating two negatively charged adjacent aluminum occupied oxygen tetrahedra in the same five- or six- membered rings of the zeolite framework. In contrast, in the zeolites with the very high Si/Al ratios over 25, modification with zinc ions results in appearance of only one kind of adsorption sites with much stronger perturbation of adsorbed molecular hydrogen. These sites were ascribed to the Zn⁺² ions compensating more strongly separated from each other negatively charged aluminum occupied oxygen tetrahedra localized in the two adjacent rings of the zeolite framework. Adsorption of H₂ by such sites at room temperature results in the strongest perturbation of H-H stretching vibrations and in dissociative adsorption.

Comparison of molecular hydrogen perturbation by Mg⁺² and by different transition metal cations indicated that despite almost similar dimensions and equal formal positive charges, the transition metal ions perturb H-H stretching vibrations of adsorbed H₂ much stronger than the Mg⁺² cations. The perturbation decreases in the following sequence: Ni⁺² > Co⁺² > Zn⁺² > Mn⁺² > Mg⁺² in consistence with the similar decrease of the second ionization potentials of the corresponding metal atoms. This indicates that interaction of adsorbed molecular hydrogen with the transition metal ions involves some features of the covalent chemical bonding.

ELECTRON DISTRIBUTION EFFECTS IN CATALYSIS

D.C. Koningsberger

*Department of Inorganic Chemistry and Catalysis, Debye Institute, Utrecht University,
P.O. Box 80083, 3508 TB Utrecht, The Netherlands*

In homogeneous catalysis it is well known that ligands can play an important role in determining the catalytic properties of the catalytic active site. In heterogeneous catalysis catalytic active species like metal particles, metal-oxides and metal-sulfides are normally dispersed on high surface area (200 m²/g) supports. The support is generally believed to play no role in determining the catalytic properties of the supported catalytic active species. This lecture will show that just like in homogeneous catalysis the support can be considered as a ligand and that the composition of the support can determine the catalytic properties of the supported active species.

Catalytic studies demonstrate that the turnover frequency of small (10 to 15 Å) Pt metal particles dispersed in zeolite Y for Neo-pentane (hydrogenolysis) and tetralin (hydrogenation) conversion (without and with sulfur compounds in the feed) is a strong function of the composition of the support (zeolite Y). The TOF increases with increasing acidity, polarisation power of the charge compensating cations (Na⁺, H⁺, La³⁺), Si/Al ratio and the presence of extra-framework Al produced after steaming. In addition, the application of a new spectroscopic technique *Atomic XAFS* reveals that also the electron distribution of the supported Pt metal particles is influenced by the composition of the support. This suggests that the support-induced change in catalytic behavior is directly related to the change in electron distribution of the Pt metal particles.

A new analysis method of the X-ray absorption near edge structure of carbon supported Pt particles in solution shows that the electron distribution of the Pt particles can also be influenced by the pH of the solvent.

These results lead to a more general model in which the medium surrounding the catalytic active site influences the electron distribution and therefore the catalytic properties of the active site.

CATALYTIC METHODS OF ENERGY PRODUCTION FROM RENEWABLE SOURCES AND MATERIALS

V. N. Parmon

*Boreskov Institute of Catalysis SB RAS, Novosibirsk 630090, Russia
E-mail: parmon@catalysis.nsk.su*

The real far future of our civilisation depends mostly on our ability to resolve the expected energy problems. In case of absence of some rigid limitations on the amount of energy at humankind's disposal, there will be no danger of shortage of food, artificial motor fuel and chemicals, etc., even for a 10 billion population on the Earth [1,2].

There are two evident ways to overcome future energy problems. First of all, one should increase the efficiency of usage of conventional energy carriers, that means simultaneously a necessity to diminish drastically the wastes or losses of energy. The second way is to enlarge utilisation of non-exhaustible sources of energy, which still do not create the basis of nowadays energetics. A principal role in these movements belongs to catalytic technologies.

A traditional way of application of catalytic technologies in energetics is their use for improvement of incineration of conventional or available fuels in various large- or small-scale thermal power plants. This allows increasing the heat-producing efficiency of these plants as well as to diminish pollution of the environment by toxic products of fuel combustion.

However, there are also some not so evident applications of catalytic technologies, which may appear to be of principal interest for the future.

This presentation concerns modern trends in application of catalytic technologies to: producing heat or high quality liquid fuels from renewable sources of carbon-containing raw materials (primarily bio-mass), utilising nuclear and non-traditional sources of energy, producing mechanical or electrical energy from the energy of chemical energy carriers, and recovering middle- or low-potential heat wastes or utilising some unexpected heat-energy sources (see also Refs. 2-4). The main attention in the presentation is devoted to the most elaborated catalytic technologies of these kind. These are ecologically pure incineration of biomass (including wet biomass and sludges too) in fluidised bed of catalysts, thermocatalytic conversion of nuclear and solar energy, and recuperation of low-potential heat or heat wastes using new kind of composite materials like selective water sorbents.

Efficient incineration of wet biomass can be achieved in fluidized bed of copper chromite or iron oxide based catalysts. In this case at a relatively low temperature (400-700°C) one can arrange an efficient mass exchange and interaction of the particles of solid organic substrates with air and the surface of the catalyst through the gas phase, while the volatilized intermediates are oxidized at the surface of the catalyst. The Boreskov Institute of Catalysis has developed and tested bench and semi-industrial pilot plants based on these principles and fed with highly wet sludges from the waste waters cleaning facilities as well as with wastes of the pulp and paper industry.

Two non-exhaustible sources of primary energy are of the most interest for far future. These are nuclear energy and solar light. The direct use of both these primary energies is impossible, since they have to be converted into a suitable form. Catalytic processes are capable of converting into energy of chemical bonds any of the above mentioned kinds of energy and to store it in the form of chemical fuels.

The simplest idea for conversion and storage of such energy is utilization of highly reversible *thermocatalytic* processes capable to shift their equilibrium at changing the temperature of the system like at the reaction of catalytic steam or carbon dioxide reforming of methane. In the nuclear fission energetics, the so-called EVA-ADAM catalytic technology is well known for indirect accumulation of released nuclear energy in the form of syngas, its storing and transportation on large distances. Recently, a new much more efficient ICAR (Immediate Catalytic Accumulation of ionized Radiation energy) process was suggested for direct nuclear-to-chemical energy conversion. The peculiarity of ICAR technology consists of placing the energy-converting catalysts immediately into the active energy-releasing zone of a nuclear reactor or even usage of special multifunctional physico-chemical structures serving simultaneously as a nuclear fuel and a catalyst for the energy-storing chemical reaction (e.g. porous uranium oxide impregnated with catalytically active metal Ni or Ru). ICAR process has exhibited a high efficiency of nuclear energy conversion combined with ability to maintain the useful specific power loading of the energy conversion up to 100-200 kW/dm³, that corresponds to flux of energy release in the modern fission nuclear power plants.

In the last two decades serious efforts were made to develop catalytic processes for solar energy conversion. Advanced are developments for *nonquantum thermocatalytic* processes of conversion of concentrated solar energy. Already in 80th the prototypes of thermocatalytic energy converting installations of a reasonable useful power (more than 2 kW) and of a very high (more than 40%) efficiency of solar-to-chemical energy conversion were tested.

PL-4

An interesting application of catalytic technologies to the thermochemical methods of nuclear or solar energy conversion could be “Zero Emission Turbines” (ZET) which utilize chemically reversible “monofuels”, e.g. mixtures of H₂ and CO, etc. which do not need a separation or additional mixing of their components during enrichment of the mixture with energy (its “charging”) or utilization of the stored energy (“discharging” the monofuel). The main idea of ZET is to use hot and recyclable reaction mixture at the outlet of the energy releasing catalytic reactor directly as the working body of a turbine. Evidently, ZET allows combination of total ecological safety of the power plants with a highly efficient conversion of the energy of the chemical fuel into mechanical energy without intermediate heat exchangers.

An ability to accumulate and store the low- and middle-potential heat is given by new solid materials with large absorption capacity. The most attractive materials are the so-called chemisorbents. When using very simple substrates as adsorbates (say, water, carbon dioxide, oxygen, etc.), the latter materials are able to accumulate up to 2000 kJ/dm³ of heat even in the ambient temperature interval. This provides a new powerful tool for recovery of heat wastes, efficient utilization of day-to-night and season temperature gradients, design of nontraditional freon-less air-conditioning systems, etc. Note, that in countries with the rigid continental climate, day-to-night and season temperature gradients seem to create a nonexpected renewable energy source with enormous potential.

References

1. V.N. Parmon, *Chemistry for Sustainable Development*, 1 (1993) 59.
2. ‘Chemistry for the Energy Future’, A ‘Chemistry for the 21st Century’ Monograph, Eds. V.N. Parmon, H. Tributsch, A. Bridgwater, D.D. Hall, Blackwell, Oxford (1999).
3. V. N. Parmon, *Catal. Today*, 35 (1997) 153.
4. E.A. Levitskij, Yu.I. Aristov, M.M. Tokarev, V.N. Parmon. *Solar Energy Mater. Solar Cells*, 44 (1996) 216.

SELECTIVE OXIDATION OF CARBOHYDRATES WITH FOCUS ON TEMPO CATALYSIS

H. van Bekkum* and **A.C. Besemer****

**Laboratory of Applied Organic Chemistry and Catalysis, Delft University of Technology
Julianalaan 136, 2628 BL Delft, The Netherlands*

***SCA Hygiene Products, PO Box 360, 3700 AJ Zeist, The Netherlands*

Converting carbohydrates into carboxylates or polycarboxylates is an obvious way of upgrading renewables. The (poly)carboxylates obtained may display unique properties or may enter the competition with fossil-based materials such as poly-acrylates.

Methods to introduce carboxylate groups include carbohydrate oxidation and carboxy-alkylation. Sometimes chemo- and bio-catalysis are in open competition (C₁-oxidation and C₁-dehydrogenation, C₂-oxidation), in other oxidations (e.g. glycolic splitting) the choice is limited, so far.

Progress in oxidation is still substantial. Some old methods are revisited (noble metal catalysis, nitrate/nitrite oxidation) and new methods come to the fore. Some excellent results have been obtained^[1] by applying bimetallic catalysts in carbohydrate oxidation. The focus of the lecture will be on the amazingly selective TEMPO-catalyzed primary alcohol oxidation of low and high molecular mass carbohydrate systems^[2,3]. Further trends are to apply cheap TEMPO derivatives^[4] and to develop immobilized TEMPO systems^[5-7], and a major challenge is to find a salt-free method^[8].

References:

- [1] M. Besson and P. Gallezot, in *Fine Chemicals through Heterogeneous Catalysis*, R.A. Sheldon and H. van Bekkum (eds.), Wiley-VCH, 2001, p. 507
- [2] A.E.J. de Nooy, A.C. Besemer and H. van Bekkum, *Synthesis* 1996, 1153 (review)
- [3] A.E.J. de Nooy, A.C. Besemer and H. van Bekkum, *Carbohydr. Res.* 269 (1995) 89
- [4] P.L. Bragd, A.C. Besemer and H. van Bekkum, *J. Mol. Catal. A* 170 (2001) 35
- [5] M.J. Verhoef, J.A. Peters and H. van Bekkum, *Stud. Surf. Sci. Catal.* 125 (1999) 465
- [6] C. Bolm and T. Fey, *Chem. Commun.* (1999) 1795
- [7] A. Dijkman, I.W.C.E. Arends and R.A. Sheldon, *Chem. Commun.* (2000) 271
- [8] Recent SCA Patent Applications

STRUCTURAL STABILITY AND CATALYTIC REACTIVITY OF ZINC ION SPECIES IN ZEOLITES

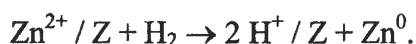
**G.M. Zhidomirov¹, A.A. Shubin¹, V.B. Kazansky², V.N. Solkan², R.A. van Santen³,
A.L. Yakovlev³, and L.A.M.M. Barbosa³**

¹ *Borshkov Institute of Catalysis, Siberian Branch of the Russian Academy of Sciences, Pr. Akad. Lavrentieva 5, Novosibirsk 630090, Russia. Phone: +7 3832 341064 Fax: +7 3832 343056; E-mail: zhi@catalysis.nsk.su, A.A.Shubin@catalysis.nsk.su*

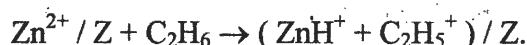
² *Zelinsky Institute of Organic Chemistry of Russian Academy of Sciences, Leninsky prospect 47, Moscow 117913, Russia. Phone: +7 095 1377400; Fax: +7 095 1355328 E-mail: vbk@ioc.ac.ru, solkanvn@ioc.ac.ru*

³ *Schuit Institute of Catalysis, Eindhoven University of Technology, P.O. Box 513, 5600 MB, Eindhoven, The Netherlands. Phone: +31 40 247 3082; Fax: +31 40 245 5054 E-mail: R.A.v.Santen@tue.nl, A.L.Yakovlev@tue.nl, Luis.Barbosa@ici.com*

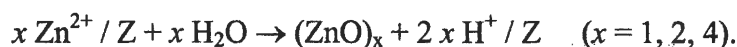
Ab initio cluster model calculations of comparative stabilisation energies of Zn²⁺ in different zeolite structures have been carried out. Zinc cation localisation in cationic positions of faujasites and MFI zeolites, as well as formation of oxygen-bridged zinc ion pairs in MFI and small neutral zinc oxide clusters have been considered. Cationic positions have been modelled by six-, five- and four-membered zeolitic rings containing two Al atoms in their structure.^{1,2} Stabilisation energy (E_{st}) of Zn²⁺ has been evaluated as the energy of the reaction



Calculations indicated that sterical restrictions associated with the size and geometrical peculiarities of the zeolitic rings in real zeolite lattice are essentially important for E_{st} . For example, E_{st} was evaluated as comparatively low for four-membered ring and α -position in ZSM-5 zeolite structure. It was also shown that Zn²⁺ in these cationic positions is mostly active in the heterolytic dissociation of ethane molecule

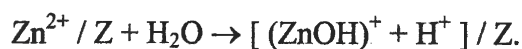


The relative stability of small intrazeolite zinc oxide clusters was calculated through the reactions



It was concluded that formation of neutral small zinc oxide clusters is strongly unfavourable for faujasites. There are more reasons for stabilisation of zinc oxide clusters in ZnZSM-5 zeolites due to the lower “average” stabilisation energies of Zn^{2+} in the cationic positions of MFI zeolites in comparison with faujasites.

The comparative stability of $(\text{ZnOH})^+$ for various cationic positions of ZnZSM-5 was evaluated by the reaction



In the case of reasonably high zeolite module (Si / Al ratio) the probability of localisation of two Al atoms in the nearest vicinity (for example, in the same zeolite ring) is essentially decreasing, and the structures with more distant Al atoms arrangement should be considered. One of the possible variants is the localisation of Al atoms in the adjacent zeolitic rings. This model was analysed³ for two neighbouring five-membered zeolitic rings in the main channel of ZSM-5 (Figs. 1, 2).

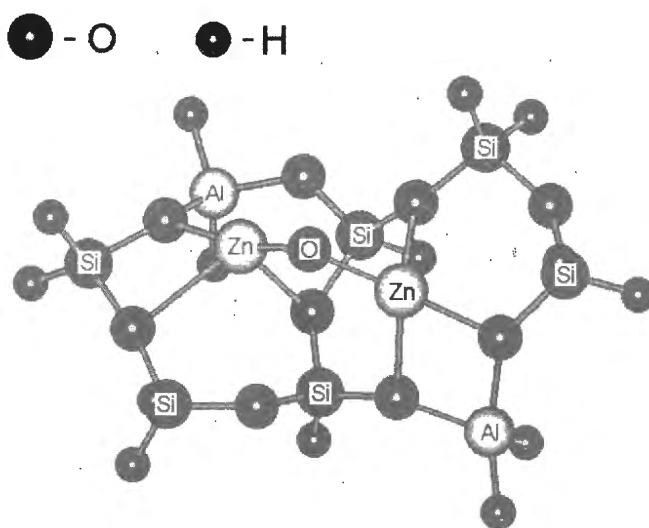


Fig. 1

Geometry of this structure is suitable for stabilisation of oxygen-bridged $[\text{Zn-O-Zn}]^{2+}$ moiety (Fig. 1). Occlusion of extra-lattice oxygen essentially affects on the chemisorption properties and catalytic activity of zinc site. It was concluded that oxygen-bridged Zn^{2+} pair is rather reactive towards ethane heterolytic dissociation, and release of dihydrogen is the key step of ethane dehydrogenation. In principle, the discussed structure can stabilise single Zn^{2+} with significantly asymmetric position of zinc cation near one of Al atoms (Fig. 2). The E_{st} energy for this cationic position is rather low and this was associated with high chemisorption and catalytic activity.

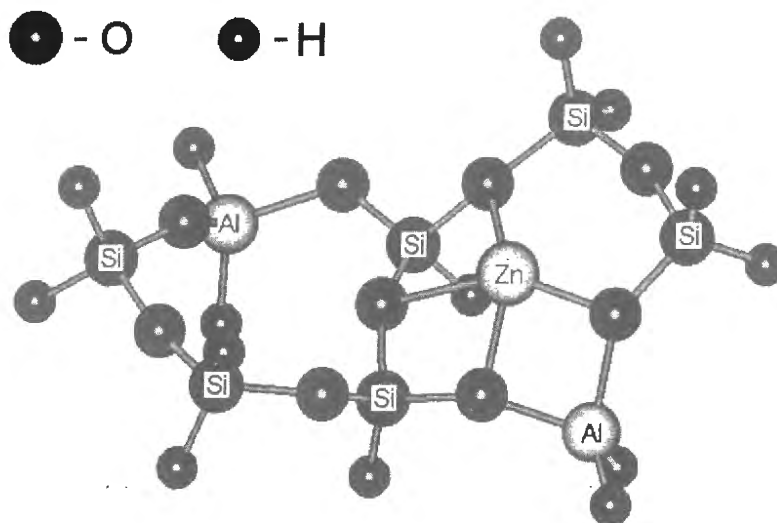
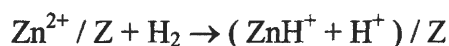


Fig. 2

Calculations of H_2 adsorption on this site (Fig. 2) have revealed a large shift of H_2 stretch vibration ($\Delta\nu \sim 270 \text{ cm}^{-1}$). The activation energy (E_a) of the first step of heterolytic H_2 dissociation



has been calculated, $E_a = 10.5 \text{ kcal/mol}$.

The adsorption and dissociation of H_2 on diverse type of active sites of Zn-containing zeolites including cation positions, $[\text{Zn-O-Zn}]^{2+}$ binuclear structures, and small oxide particles have been carried out.⁴ Frequency shifts $\Delta\nu$ evaluated for hydrogen molecule adsorbed on $\text{Zn}^{2+} / [4\text{-ring}]$, $[\text{Zn-O-Zn}]^{2+}$, $(\text{ZnO})_4$ are equal to -157 cm^{-1} , -99 cm^{-1} , and -174 cm^{-1} correspondingly. Similar study for CH_4 revealed that small oxide clusters $(\text{ZnO})_4$ and especially $(\text{ZnO})_2$ are mostly active in the perturbation of IR frequencies of adsorbed methane molecule.⁵

Acknowledgements

The authors are grateful to NWO for the financial support of this work (projects 047-005-011 and 19-0411999 NWO). GMZ and AAS also thank RFBR (project 00-15-97441) for the support of this study.

References

1. A.A. Shubin, G.M. Zhidomirov, A.L. Yakovlev, and R.A. van Santen, "Cooperative Quantum Chemical Study of Stabilization Energies of Zn^{2+} Ions in Different Zeolite Structures", *J. Phys. Chem. B* **2001**, 105, 4928-4935.
2. R.A. van Santen, G.M. Zhidomirov, A.A. Shubin, A.L. Yakovlev, and L.A.M.M. Barbosa, "Reactivity Theory of Zinc Cation Species in Zeolites", in "*Catalysis by Unique Metal Ion Structures in Solid Matrices*", 187-204, G. Centi *et al.* (eds.), **2001** Kluwer Academic Publishers, Netherlands.
3. A.L. Yakovlev, A.A. Shubin, G.M. Zhidomirov, and R.A. van Santen, "DFT Study of Oxygen-Bridged Zn^{2+} ion pairs in Zn/ZSM-5 Zeolite", *Catalysis Letters* **2000**, 70, 175-181.
4. L.A.M.M. Barbosa, G.M. Zhidomirov, and R.A. van Santen, "Theoretical Study of the Molecular Hydrogen Adsorption and Dissociation on Different Zn(II) Active Sites of Zeolites", *Catalysis Letters* **2001**, 77, 55-62.
5. L.A.M.M. Barbosa, G.M. Zhidomirov, and R.A. van Santen, "Theoretical Study of Methane Adsorption on Zn(II) Zeolites", *Phys. Chem. Chem. Phys.* **2000**, 2, 3909-3918.

**THE POTENTIAL OF STRUCTURED REACTORS IN PROCESS
INTENSIFICATION****Jacob A. Moulijn*, Andrzej Stankewicz and Freek Kapteijn***Reactor & Catalysis Engineering**DelftChemTech, Faculty of Applied Sciences, Delft University of Technology,**Julianalaan 136, 2628 BL, Delft, The Netherlands*

* Corresponding author j.a.moulijn@tnw.tudelft.nl (J.A. Moulijn)

ABSTRACT

Structured catalytic reactors have a large potential in Process Intensification. In many respects they outperform conventional reactors such as packed-bed and slurry reactors, both for gas and for gas-liquid systems. The most important structured reactors are based on gauzes, foams, and monoliths. In general, monoliths are the most satisfactory structured reactors. In gas-phase applications they are often preferred due to their favourable properties with respect to selectivity, pressure drop, and robustness. Their millisecond characteristics have potential in syngas production and selective conversions into valuable products. In gas-liquid applications they exhibit high rates, high selectivity (for serial kinetics), and they operate close to plug-flow behaviour. They are compact reactors with excellent performance in activity and selectivity. They allow co- as well as counter-current operation at common industrial conditions and can be used in multifunctional reactors, e.g. catalytic distillation. The use of a structured reactor allows the decoupling of intrinsic reaction kinetics, transport phenomena, and hydrodynamics. In this way these processes in a catalytic reactor can be optimised independently, giving rise to an excellent reactor performance. Structured catalysts and reactors will play a major role in Process Intensification.

1. INTRODUCTION

Chemical reactors form the heart of a (petro-)chemicals production plant. Given the large variety of plants it is no surprise that many different chemical reactors are used. Catalytic reactors roughly can be divided in random and structured reactors. It is useful to start with a summary of the major basic concerns (apart from high activity, selectivity, etc.) for catalytic reactors:

- catalyst quality on a microscopic length scale (quality, number of active sites);
- catalyst quality on a mesoscopic length scale (diffusion length, loading, profiles);
- ease of catalyst separation and handling;
- heat supply and removal;
- hydrodynamics (regimes, controllability, predictability);
- transport resistance (rate and selectivity);
- safety and environmental aspects (runaways, hazardous materials, selectivity);
- costs.

With regard to these aspects random and structured reactors behave quite differently. In terms of costs and catalyst loading randomly packed-bed reactors usually are most favourable. So, why would one use structured reactors? It will become clear that in many of the concerns listed structured reactors are to be preferred. Precision in catalytic processes is the basis for process improvement. It does not make sense to develop the best possible catalyst and then use it in an unsatisfactory reactor. Both the catalyst and the reactor should be close to perfect. Randomly packed beds do not fulfil this requirement. They are not homogeneous because mal-distributions always occur; at the reactor wall these are unavoidable, originating from the looser packing there. These mal-distributions lead to non-uniform flow and concentration profiles and even hot spots may arise [1]. A similar analysis holds for slurry reactors. For instance, in a mechanically stirred-tank reactor the mixing intensity is highly non-uniform and conditions exist where only a relatively small annulus around the tip of the stirrer is an effective reaction space.

Catalytic conversion and separation are conventionally carried out in separate pieces of equipment. A combination of functions in single units is an elegant form of Process Intensification. When one of the functions is a chemical reaction, such a unit is referred to as a *multifunctional reactor*. A good example is catalytic distillation [2]. Structured reactors will play a key role in the design of novel processes based on multifunctional reactors [3]. A monolith is a good example.

2. STRUCTURED REACTORS

Structured reactors and catalysts are encountered in a large variety [3,4]. Structured catalytic reactors can be divided in two categories. The first category contains a structured catalyst, whereas the second one contains 'normal' catalyst particles arranged in a non-random way. In the first category the catalyst and reactor are essential identical entities.

PL-7

Because of their low pressure-drop, structured reactors in practice dominate the field of treating tail gases. Figure 1 gives an impression of the major types of reactors. The monolithic reactor represents the class of 'real' structured catalytic reactors, whereas the parallel-passage and the lateral-flow reactor are based on a structured arrangement of packings with 'normal' catalyst particles.

Monoliths usually are made from ceramics, but metals are also used. Monoliths can be produced by extrusion of support material (often cordierite is used, but various types of clays or typical catalyst carrier materials such as alumina, titania, etc. are also used), a paste containing catalyst particles (e.g. zeolites, V-based catalysts), or a precursor for the final product (e.g. polymers for carbon monoliths). Alternatively, catalysts, supports, or their precursors can be coated onto a monolithic support structure ('washcoating'). Zeolites have been coated by growing them directly on the support during the synthesis [5]. Coating literature and patents is a large field and, in principle, a variety of preparation procedures are available. All major catalyst support materials, ceramic and polymeric, have been extruded as monolith [4,6]. Metallic support structures are used for automotive applications [7].

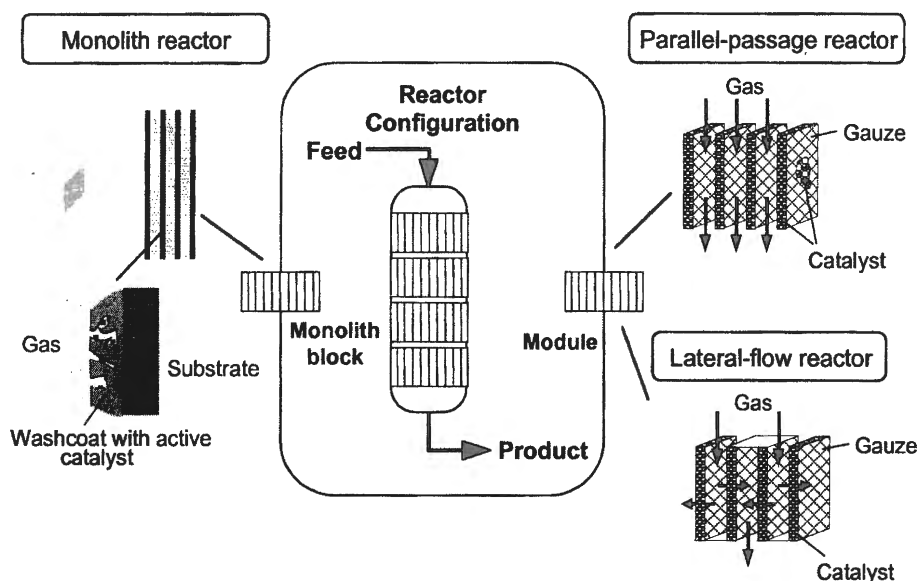


Figure 1. Low pressure-drop reactors used for tail gas treating

Monoliths are the dominant catalyst structures for three-way catalysts in cars [8-11], selective catalytic reduction catalysts in power stations [12-15], and for ozone destruction in aeroplanes. What causes this popularity? The catalyst consists of one piece, so no attrition due to moving particles in a vibrating case occurs. The large open frontal area and straight channels result in an extremely low pressure-drop essential for end-of-pipe solutions like exhaust pipes and stack gases. The straight channels prevent the accumulation of dust.

Of course, monolithic catalysts have disadvantages. They share with packed-bed catalysts the requirement of a sufficient stability or in any case a good regenerability. With respect to mass- and heat-transfer characteristics, the major limitations are the laminar flow through the channels, no interconnectivity between the channels, and a poor radial heat conductivity. The latter two properties are much better for the foam-type monoliths, but with a trade-off in a higher pressure-drop and/or lower catalyst loading (sites/m³). In principle, a laminar flow velocity profile is associated with low mass-transfer rates and a large residence time distribution. Fortunately, due to the small channel size and high diffusivity (D), for gases this radial transport in the channels is sufficiently fast. Typical time scales for diffusion ($l_D^2/2D$) are given in Table 1. In liquid phases the diffusivity is three orders of magnitude smaller and this is one of the reasons that monoliths do not enjoy a high popularity in liquid-phase operations. It will be shown that this is based on a misconception.

Table 1. Diffusion time scales in catalytic reactors ($=l_D^2/2D$) for three diffusion lengths (l_D)

	D (m ² /s)	$l_D = 1$ mm	$l_D = 0.1$ mm	$l_D = 1$ μ m
Gas	10^{-5}	50 ms	0.5 ms	50 ns
Liquid	10^{-9}	500 s	5 s	500 ns
liquid in cat pore	10^{-10}	5000 s	50 s	5 ms
liquid in zeolite pore	10^{-11}	50.000 s	500 s	50 ms

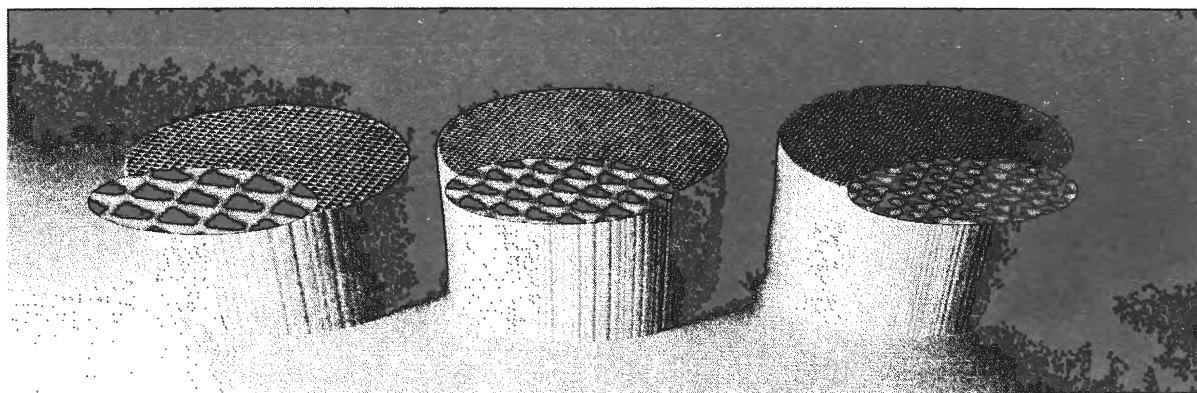


Figure 2. Square-channel cordierite monoliths with cell densities of 200, 400, and 600 cells per square inch (cpsi).

The honeycomb type monoliths are characterised by a very high geometric surface area. Dependent on the cell density this can exceed $3000 \text{ m}^2/\text{m}^3_{\text{reactor}}$! Figure 2 shows square-channel cordierite monoliths with cell densities of 200, 400, and 600 cpsi (cells per square inch). These examples are quite realistic. At present the monolith commonly used for cars is a 400 cpsi monolith. The value for the geometrical surface amounts to $3440 \text{ m}^2/\text{m}^3_{\text{reactor}}$. In packed beds this value is much lower in order to avoid unrealistic pressure-drops. It is to be

PL-7

expected that future monoliths will exhibit even larger geometric surface areas. That alone makes them highly useful for Process Intensification programs.

3. GAS-PHASE REACTIONS

It is fair to state that the most important application of structured reactors by large is in environmental catalysis. The major applications are in automotive emission reduction. For diesel exhaust gases a complication is that it is overall oxidising and it contains soot. New ideas have emerged, all of them involving structured reactors. The truck market is dominated by diesel engines. In that application space requirement is a major issue and Process Intensification is badly needed. Space velocities exceeding 100.000 h^{-1} are demanded. Other important areas are reduction of NO_x from power plants and the oxidation of Volatile Organic Compounds (VOCs). In synthesis gas production also structured reactors suggest themselves, for instance in catalytic partial oxidation (CPO) of methane.

4. MULTIPHASE REACTION SYSTEMS

Various types of reactors are being used commercially for multiphase applications, the major ones being the slurry reactor, bubble-column reactor, and the trickle-bed reactor [16]. Each reactor has its own advantages and disadvantages. Slurry catalysts are small (typically $50\ \mu\text{m}$), while trickle-bed particles are larger (millimetre scale) in view of the allowable pressure-drop over the bed. The particle size is a crucial parameter. In general it can be stated that larger particles are less efficient and, even more important, are less selective in those reactions where the desired product is subject to an undesired following reaction ($A \rightarrow B \rightarrow C$ with B the desired product). In that often-encountered case the slurry reactor is more selective than the trickle-bed reactor. In terms of Process Intensification a mechanically stirred-tank reactor often is not a good choice. In practice it is no exception that gas-liquid mass transfer is rate determining. That implies that only the part of the space close to the tip of the stirrer(s) is well used. A large part of the reactor does not contribute much to the productivity and dependent on the kinetics will lead to low selectivity. Moreover, major disadvantages of the slurry reactor are the often difficult separation of product and catalyst and catalyst attrition. The trickle-bed reactor is much more convenient but large particle sizes are unavoidable. An important limitation of trickle-bed reactors is that in practice they are nearly always operated co-currently to avoid liquid entrainment by the gas ('flooding'). Some important commercial applications, however, would benefit from counter-current operation, especially equilibrium-limited reactions and reactions with strong product inhibition [17].

4.1. Hydrodynamics and Mass Transfer in Monoliths

4.1.1. Hydrodynamics for co-current operation

For co-current gas-liquid flow, several flow regimes can occur. The preferred one usually is the so-called Taylor or slug flow [18,19]. This type consists of gas bubbles and liquid slugs flowing consecutively through the small monolith channels. The gas bubble fills up the whole space of the channel and only a thin liquid film separates the gas from the catalyst. The rate of mass transfer is large as a result of two effects. Firstly, the liquid layer between bubble and catalyst coating is thin, increasing mass transfer. Secondly, the liquid slugs show an internal recirculation during their travel through a channel. Because of this, radial mass transfer is increased. Moreover, the gas bubbles push the liquid slugs forward as a piston and a type of plug flow is created. Compare this with single-phase liquid flow through the channels. Because of the low channel diameter the flow will be laminar and, as a consequence, the radial transport will be extremely slow, leading to a very poor reactor performance: rates are slow and the reactor exhibits strong non-plug-flow behaviour. For multiphase operation at slug flow conditions the increase in the mass-transfer rate is an order of magnitude larger than for single-phase liquid flow, whereas the increase in friction, that is pressure-drop, is much less. A fortunate finding is that Taylor flow conditions are easily realised under practical conditions.

Ideally, in contrast to packed beds, scale-up of monolithic reactors is very simple. When we know the behaviour of one channel, we should be able to predict the whole reactor. Is this really true? Compared to a packed bed, a monolithic reactor differs in radial transport. When the initial distribution of liquid in the radial direction is non-ideal, going down through the reactor, this unfavourable distribution does not change. In contrast, in a packed-bed reactor some redistribution occurs. Therefore, in scale-up the reactor inlet system has to be designed well so that the distribution of the liquid in the top of the reactor is ideal. We found that if a bubble emulsion on top of the monolith is present a satisfactory distribution seems to be guaranteed, similar as found for trickle-bed reactor operation. It appeared that the flow rate has to be above a specified minimum value (linear velocities > 0.1 m/s) in order to guarantee a good distribution of liquid over the cross-section of the reactor. It might be worthwhile to investigate whether systems can be developed or conditions established that allow low flow rates. Combinations of monolithic-catalyst packages with Sulzer-type contactors are being conceptually investigated in our group. They might increase the window of operability towards lower flow rates. Moreover, they might lead to flexibility allowing more compact reactor systems. The first results are promising.

PL-7

4.1.2. Mass transfer for co-current operation

Mass transfer was studied experimentally in various ways. As an example of the performance, a monolith was compared with a trickle-bed reactor under identical reaction conditions in co-current mode for the hydrogenation of α -methylstyrene. The washcoated 400 cpsi monolith yielded a ten times higher hydrogenation rate per unit volume of reactor. This stresses the high mass-transfer rate in the monolith [16,20]. Mass transfer is usually expressed as the factor $k_t a$, the mass-transfer coefficient times the exposed surface area per unit volume. In Table 2 the three common reactor types are compared. Obviously, operation of the monolithic reactor in the Taylor flow regime leads to a high degree of Process Intensification [1].

Table 2. Comparison of mass-transfer rates for three common reactor types

Reactor Type	$k_t a$ (s^{-1})
Trickle bed	0.05 - 0.2
Slurry	0.1 - 0.3
Monolith	> 1

The corresponding production rate in the monolith at 373 K and a hydrogen pressure of 10 bar amounted to 40 mol/ ($m^3_{\text{reactor}} \cdot s$).

4.1.3. Counter-current operation

Under practical conditions counter-current operation in a packed-bed reactor is not feasible because flooding occurs [21,22]. The reason is that in the small interstitial space extended momentum transfer takes place between the liquid flowing down and the gas flowing up. At velocities used in industry this would imply that the particle size has to be increased by an order of magnitude. This leads to unacceptable internal-diffusion limitations. Clearly, momentum transfer has to be decreased while maintaining high rates. This can be done by structuring the catalyst or by clever arrangement of the catalyst particles in the reactor. From an extensive study, it appeared that also in structured reactors, counter-current operation is possible at industrially relevant conditions. The breakthrough was the design of optimal monolithic structures and dedicated inlet and outlet systems. See [23] for details.

4.2. Potential of Monolith Reactors

The catalyst to be used in a reactor operation can be coated as a thin layer on the channel walls, and, hence, the reactor can be described as a 'frozen slurry reactor'. The diffusion length is small and well controllable. The high cell density of the monoliths creates a high geometric surface area. Using a packed bed, unrealistically small particles would be needed to achieve this. Catalyst separation and handling are as convenient as in a common packed bed.

Monolith reactors are intrinsically safe. The monolith channels have no radial communication in terms of mass transport and the development of runaway by local hot spots in a trickle bed reactor cannot occur. Moreover, when the feed of liquid or gas is stopped, the channels are quickly emptied.

From the above, it should be evident that monolithic reactors (and other structured reactors) in many respects are superior to conventional reactors. Indeed, for several reactions, monolithic catalysts have been reported, although only at the bench or pilot scale except for one case. The interesting points are to demonstrate that the 'theoretically' outlined advantages are indeed present. They in fact boil down to larger reactor productivity, better selectivity control, and higher efficiency compared to conventional reactors. The first also implies better catalyst utilisation. Obvious is the fact that the catalyst is fixed in a reactor and pressure-drops are low.

The hydrogenation step in the anthraquinone process of AKZO-Nobel is an industrial realisation of a monolithic reactor and includes a lot of pioneering work by the Anderson group [24-28]. More examples of the use of monoliths can be found in [27,29].

In our own group in co-operation with a chemical company, we have studied the selective hydrogenation of pyrolysis gasoline. This study [30] demonstrated the plug-flow behaviour needed for such a selective conversion and the efficient use of the active phase, which was at least a factor three to four better than in trickle-bed operation. The hydrogenation of α -methylstyrene mentioned above, is an even more appealing example of better active-phase utilisation and confirms the good mass-transfer properties.

The co-current monolith reactor, with its plug-flow characteristics, can in principle be used in downflow, upflow and horizontal-flow mode, provided a good gas-liquid distribution is secured [31]. The latter mode might solve a major problem in practical applications of monoliths: because for hydrodynamic reasons high flow rates are needed, the reactor length tends to be very large. Research with respect to this type of reactor is in progress. An important outcome of the research might be that coupling of monolithic elements, mixing units and heat exchangers leads to flexible cascade-reactor systems enabling multistep synthesis in one pass.

The best-studied mode is co-current downflow. A monolith reactor operating in this mode is an alternative to the bubble-column reactor often used in biotechnological applications. Since bubble-column reactors have a large height and large gas flow rates are required, the energy input to introduce and compress the gas for injection at the bottom is relatively high. In the down-flow monolith reactor, this gas injection is automatically achieved. The co-current reactor type can easily be used as a stirred reactor type by a large recirculation flow

PL-7

without extremely large energy input due to the low pressure-drop. An external heat exchanger can be scaled independently of the reactor to deliver the required heat duty [1,16].

Of course, monoliths have disadvantages. Currently, they are more expensive than particle catalysts. In fixed-bed operation, they will have to exhibit a sufficiently long lifetime. In quickly (irreversibly) deactivating reactions, they cannot be used. It is of extreme importance that the inlet distribution should be secured. In co-current flow, both gas and liquid have to be contacted evenly with the catalyst at the monolith walls.

In the evaluation of the properties of catalytic reactors there are three important aspects that strongly determine the overall performance: the amount of catalyst and intrinsic kinetics, the transport phenomena (diffusion in and outside the catalyst), and the hydrodynamics in the reactor. In classical reactors these are strongly interrelated and cannot be defined and designed independently. As an example, for fast reactions small catalyst particles are desired from the point of view of catalyst effectiveness, but a packed bed with small particles will result in an unacceptable pressure drop. Therefore, an optimum has to be sought for the particle size. The elegance of structured reactors is that these three aspects can be designed and optimised fairly independently, resulting in an optimised reactor performance.

In slow reactions the intrinsic reaction kinetics control the process, so the catalyst inventory should be as high as possible. Increasing the wall thickness of a monolith can have the desired effect. In fast reactions mass transfer or intraparticle diffusion becomes controlling. Thinner catalyst coatings, Taylor flow, etc. can be applied to optimise these requirements. If mass transfer is controlling the productivity is proportional to the geometric surface area of the monolithic structure. Increasing the cell densities is recommended, of course not to the point where unacceptable pressure-drops arise.

5. CONCLUSIONS

Monolithic and other structured catalysts exhibit favourable properties with respect to practical convenience, high rates, high selectivity, and low energy consumption. From an engineering point of view, also the easy scale-up and the potential of high safety are appealing. Monoliths are not limited to single-phase processes but they are also well placed for multiphase processing.

Monoliths exhibit a large flexibility in operation. They are suited well for optimal semi-batch, batch, continuous, and transient processing. Catalytic conversion can be combined with in-situ separation, catalytic reactions can be combined, heat integration is possible, and all lead to Process Intensification. Monoliths allow the efficient use of small catalyst particles, e.g.

zeolites, and have a substantial flexibility with respect to catalyst inventory in a reactor. Multifunctional reactor operations like reactive stripping or distillation are challenging applications that are not too far away.

The essence of the use of a structured reactor is that it allows the decoupling of intrinsic reaction kinetics, transport phenomena, and hydrodynamics. In this way these phenomena, which control the overall behaviour of a catalytic reactor, can be optimised independently, giving rise to an excellent reactor performance.

REFERENCES

1. J.J. Heiszwolf, L.B. Engeltaart, M.G.v.d. Eijnden, M.T. Kreutzer, F. Kapteijn, and J.A. Moulijn, *Chem. Eng. Sci.*, 56 (2001) 805.
2. F.M. Dautzenberg, *Cattech*, 3 (1999) 54.
3. A. Cybulski and J.A. Moulijn (Eds.), *Structured Catalysts and Reactors*, Chemical Industries, Vol. 71, Marcel Dekker, New York, 1998.
4. A. Cybulski and J.A. Moulijn, *Catal. Rev.-Sci. Eng.*, 36 (1994) 179.
5. J.C. Jansen, J.H. Koegler, H. v. Bekkum, H.P. Calis, C.M. v. d. Bleek, F. Kapteijn, J.A. Moulijn, E.R. Geus, and N. V.d. Puil, *Microporous and Mesoporous Materials*, 21 (1998) 213.
6. S.T. Gulati, S.T., in A. Cybulski and J.A. Moulijn (Eds.), *Structured Catalysts and Reactors*, Chemical Industries, Vol. 71, Marcel Dekker, New York, 1998, p. 15.
7. M.V. Twigg and D.E. Webster, in A. Cybulski and J.A. Moulijn (Eds.), *Structured Catalysts and Reactors*, Chemical Industries; Vol. 71, Marcel Dekker, New York, 1998; p. 59.
8. M.V. Twigg and A.J.J. Wilkins, in A. Cybulski and J.A. Moulijn (Eds.), *Structured Catalysts and Reactors*, Chemical Industries; Vol. 71, Marcel Dekker, New York, 1998, p. 91.
9. R.M. Heck and R.J. Farrauto, *Cattech*, 1 (1997) 117.
10. G.B. Marin and J.H.B.J. Hoebink, *Cattech*, 2 (1997) 137.
11. M. Misono, *Cattech*, 2 (1998) 53.
12. A. Beretta, C. Orsenigo, E. Tronconi, P. Forzatti, and F. Berti, *Kinetics and Catalysis*, 39 (1998) 646.
13. A. Beretta, E. Tronconi, G. Groppi, and P. Forzatti, in A. Cybulski and J.A. Moulijn (Eds.) *Structured Catalysts and Reactors*; Chemical Industries; Vol. 71, Marcel Dekker, New York, 1998, p. 121.
14. E. Tronconi and P. Forzatti, *AIChE Journal*, 38 (1992) 201.
15. N.-Y. Topsøe, *Cattech*, 1 (1997) 125.
16. F. Kapteijn, F., J.J. Heiszwolf, T.A. Nijhuis, and J.A. Moulijn, *Cattech*, 3 (1999) 24.

PL-7

17. S.T. Sie and P.J.M. Lebens, in A. Cybulski and J.A. Moulijn (Eds.), *Structured Catalysts and Reactors*, Chemical Industries, Vol. 71, Marcel Dekker, New York, 1998, p. 305.
18. S. Irandoust and B. Andersson, *Computers Chem. Eng.*, 13 (1989) 519.
19. T.C. Thulasidas, M.A. Abraham, and R.L. Cerro, *Chem. Eng. Sci.*, 52 (1997) 2947.
20. T.A. Nijhuis, M.T. Kreutzer, A.C.J. Romijn, F. Kapteijn, and J.A. Moulijn, *Catalysis Today*, 66 (2001) 157.
21. P.J.M. Lebens, R.v.d. Meijden, R.K. Edvinsson, F. Kapteijn, S.T. Sie, and J.A. Moulijn, *Chem. Eng. Sci.*, 52 (1997) 3893.
22. P.J.M. Lebens, F. Kapteijn, S.T. Sie, S.T., and J.A. Moulijn, *Chem. Eng. Sci.*, 54 (1999) 1359.
23. P.J.M. Lebens, R.K. Edvinsson, S.T. Sie, and J.A. Moulijn, *Ind. Eng. Chem. Res.*, 37 (1998) 3722.
24. B. Andersson, B., S. Irandoust, and A. Cybulski, in A. Cybulski and J.A. Moulijn (Eds.), *Structured Catalysts and Reactors*, Chemical Industries, Vol. 71, Marcel Dekker, New York, 1998, p. 267.
25. V. Hatziantoniou and B. Andersson, *Ind. Eng. Chem. Fundam.*, 23 (1984) 82.
26. V. Hatziantoniou, V., B. Andersson, and N.-H. Schön, *Ind. Eng. Chem. Process Des. Dev.*, 25 (1986) 964.
27. S. Irandoust and B. Andersson, *Catal. Rev.-Sci. Eng.*, 30 (1988) 341.
28. S. Irandoust and B. Andersson, *Chem. Eng. Sci.*, 43 (1988) 1983.
29. A. Cybulski and J.A. Moulijn in A. Cybulski and J.A. Moulijn (Eds.), *Structured Catalysts and Reactors*, Chemical Industries, Vol. 71, Marcel Dekker, New York, 1998, p. 239.
30. H.A. Smits, A. Stankiewicz, W.Ch. Glasz, T.H.A. Fogl, and J.A. Moulijn, *Chem. Eng. Sci.*, 51 (1996) 3019.
31. A. Stankiewicz, A. and J.A. Moulijn, *Chemical Engineering Progress*, 96 (2000) 22.

**DEVELOPMENT OF ADVANCED CATALYSTS
FOR ENVIRONMENTAL PROTECTION**

**Z.R. Ismagilov, O.Yu. Podyacheva, L.T. Tsykoza, V.N. Kruchinin,
S.A. Yashnik, V.V. Kuznetsov, T.V. Reshetenko, H.J. Veringa***

*Boreskov Institute of Catalysis SB RAS, Pr. Acad. Lavrentiev 5, 630090 Novosibirsk, Russia
ECN, The Netherlands

The overview of main results of three joint Dutch-Russian projects supported by NWO will be presented in this paper:

1. Development of catalytic heat exchangers for high efficiency combustion application
2. Development of novel effective catalytic systems for selective reduction of NO_x by hydrocarbons
3. New ways into catalytic production of fuels out of renewable resources.

Many of industrial processes, such as methane steam reforming or methane pyrolysis are endothermic and consequently consume heat. The promising way to solve problems of heat consumption efficiency and NO_x abatement is use of the catalytic heat exchangers (HEX) [1,2]. The HEX reactor comprises a combustion catalytic layer supported on metallic carrier on one side of the reactor wall providing good heat transfer for the endothermic reaction proceeding on the other side of the wall. Catalysts supported on metal foam materials are most suitable for this purpose as they combine high combustion output, heat transfer characteristics and optimum geometric structure of the support [3]. The primary objective was the development of a catalytic HEX tubular reactor for the combination of the methane catalytic combustion and methane reforming processes.

Metal foam HEX reactors have been manufactured by placing the thermally stable high-permeable Ni-Cr (20% Cr) or SiC foam on the external surface and Ni metal foam on the internal surfaces of a stainless steel metal tube (additional information in PP 24).

Different combustion catalysts (LaCoO₃, Pt, Pd, LaMnAl₁₁O₁₉) on the external metal foam of the tube were deposited by means of impregnation or suspension technique. Metal foams were preliminary coated by dense alumina layer using plasma spraying technique to increase the adhesion of the catalytic layer on the metal surface. The prospects of plasma spraying technique for the synthesis of supported catalysts will be presented in the paper "Some applications of plasma spraying technique for the preparation of supported catalysts" (PP-24).

Ni-containing reforming catalysts were deposited on the internal Ni foam of the tube by impregnation technique. The washcoating layers with different composition (CeO₂, Al₂O₃-MgO, Al₂O₃-MgO-CeO₂, Al₂O₃-MgO-La₂O₃ and industrial steam reforming catalyst GIAP-18, 12%Ni/α-Al₂O₃) were placed on metal foams by the use of suspension technique.

PL-8

The special series of the Ni-containing catalysts were synthesized also on spherical alumina modified by Mg, Ce, La for methane reforming activity test in a regular batch reactor.

Comparative analysis of the initial activity in methane oxidation reaction of metal foamed combustion catalysts calcined at 1000°C and having different type of active component allowed to find the best compositions for methane combustion at high temperatures: $\text{Pd/CeO}_2\text{-}\gamma\text{-Al}_2\text{O}_3 > \text{LaMnAl}_{11}\text{O}_{19}/\text{La-Al}_2\text{O}_3 \sim \text{Pd-LaCoO}_3 > \text{LaCoO}_3/\text{La-}\gamma\text{-Al}_2\text{O}_3$. Thermal stability of these catalysts was studied and the first two catalysts were recommended to be used in catalytic HEX for high temperature methane combustion.

It was shown that Ni-containing catalysts supported on metal foams prepared by the use of cerium oxide washcoat showed the superior activity in methane steam reforming compared with the commercial catalyst GIAP-18. Certain mixed oxide supports ($\text{MgO-La}_2\text{O}_3\text{-Al}_2\text{O}_3$) were found to be promising materials for synthesis of Ni catalysts for dry methane reforming due to their high stability to coke formation.

Different types of catalytic HEX reactors were tested in methane combustion reaction combined with methane steam reforming or methane dry reforming. When methane was used for combustion, its conversion during operation of the HEX reactor with perovskite or Pt active component used as combustion catalyst was close to 100%. The temperature profile along the external combustion foam catalyst of the HEX reactor was not uniform with a maximum of 1000-1050°C on the side of the combustion catalyst. Methane in steam reforming conversion in these experiments was equal to 50%. Addition of a certain amount of hydrogen to the combustion feed leads to positive effect on the steam reforming catalyst performance. The temperature profile in the combustion catalyst becomes more uniform in the range of 850-900°C. Methane conversion in the reforming section increases to 64% due to better uniformity of the temperature profile in the reforming catalyst as well [4].

It was found that methane conversion in dry reforming process (CO_2) can achieve value from 71 to 82% depending on the volume space velocity of reaction mixture in catalytic HEX reactor with $\text{LaMnAl}_{11}\text{O}_{19}/\text{La-Al}_2\text{O}_3$ catalyst used for methane combustion and reforming catalyst of $\text{Ni/CeO}_2\text{-MgO-Al}_2\text{O}_3$ composition.

The second project is devoted to:

- The development of an ion exchange technique for the preparation of stable Cu-substituted zeolites (Ce or/and TiO_2 modified) to be washcoated onto monolithic honeycomb supports;
- Catalytic activity tests in the selective catalytic reduction of NO by C_3H_8 to N_2 ;
- Activity tests of copper-substituted zeolite catalysts in the presence of water and sulfur compounds [5-7].

Two zeolites of H-ZSM-5 type with different zeolite module: Si/Al=73 and Si/Al=34 have been used as the starting materials.

A powder of zeolite (particle size $\approx 30 \mu\text{m}$) was introduced into the suspension of sol-aluminum hydroxide with a pseudoboehmite structure, which serves as a binder for washcoating to the monolithic honeycomb supports made on the base of silica-alumina ceramics.

Bulk catalysts of following composition: 1-4%CuZSM-5; 1-4%Cu[80%ZSM-5+20% γ -Al₂O₃]; 1-4%Cu[80%ZSM-5+10%TiO₂+10% γ -Al₂O₃]; 1-4%Ce{1-4%Cu[80%ZSM-5+20% γ -Al₂O₃]}, and supported catalysts having the same composition of washcoating layer have been prepared. The activity tests in NO reduction with C₃H₈ were conducted in a flow reactor in the temperature range of 200-600°C, GHSV = 42 000 h⁻¹.

On the bulk catalysts the NO conversion achieves 96% at 400°C, and on supported monolithic catalysts 70% at 500°C.

Aging of these catalysts during 12 and 18 months leads to deactivation. Our study of FTIR spectra of adsorbed CO demonstrated that in aged catalyst the amount of Cu¹⁺ (2157 cm⁻¹) decreases, new clusters Cu¹⁺-O-Cu²⁺ (2149 cm⁻¹) appeared and the amount of Cu¹⁺ in CuO clusters (2137 cm⁻¹) increases.

Special experiments on the catalyst poisoning are performed introducing of H₂S ~ 300 ppm or/and of H₂O ~ 6 vol.% into the reaction mixture.

At 400°C the NO conversion over monolithic samples decreases from 60% to 35%, and at 500°C from 70% to 60%, but in both cases regeneration at 500°C leads to recovery of initial activity.

The third project consists of a combination of several subprojects and in this paper we will report results on biomass gasification, production of hydrogen and catalytic filamentous carbon (CFC) and storage of hydrogen in CFC [8-10]. Some results are presented in (PP 10, PP 26).

The series of alloy catalysts Ni-Cu-Al₂O₃, Ni-Co-Al₂O₃, Ni-Fe-Al₂O₃ have been designed and tested in the process of decomposition of methane at 550-675°C.

The samples of catalysts were investigated by TEM, XRD methods.

In one series of Ni-Cu catalysts the Cu concentration was varied: 8, 15, 25, 35, and 45 wt.%. The XRD data show that the catalysts are of the Ni-Cu alloy type in all cases. As the Cu:Ni ratio increases, the lattice parameter also increases, which results in formation of two phases of nickel-copper alloys [1]. In contrast to the Ni-Al₂O₃ system [2], the spinel phase was not observed in the diffraction pattern of Ni-Cu catalysts. The presence of the copper phase was identified for the sample with a high Cu content.

Methane decomposition with the aim of high output of CFC formation was carried out in the reactor with a fluidized bed of a catalyst. Reaction was carried out in the conditions of stationary concentration of methane and temperature.

PL-8

Ni-Al₂O₃ catalysts were stable in reaction of methane decomposition at the temperatures < 575°C, carbon capacity was about 100g/g_{cat}. Fiber CFC_{Ni} had turbostratic structure with coaxially arranged graphite planes as cones at that graphite layers were packed at an angle of 45° to the filament axis. The BET surface area is equal to 100 m²/g.

Cu adding to Ni-Al₂O₃ was defined to increase the thermal stability and carbon capacity of the catalyst. Furthermore, it varied microstructure of carbon fiber so that graphite like layers in filament was oriented perpendicularly to their axis CFC_{Ni-Cu}.

We investigated also the influence of Co and Fe addition on the properties of the Ni-Al₂O₃ catalyst and on the properties of formed CFC.

The adsorption of hydrogen and methane on CFC's was measured in the statical volumetric high pressure setup.

The highest value of hydrogen adsorption 20.0 mg/g is obtained for the catalyst 70wt%Ni+30wt%Cu.

Acknowledgements

Authors are grateful to NWO for financial support by 3 NWO grants in 1994-1996, 1997-1999 and 2001-2003.

References

1. C.Ramshaw and A.Gough, Catalytic Combustion, SanDiego, USA, April 1-16 (1999) 43.
2. Z.R.Ismagilov, O.Yu.Podyacheva, V.V.Pushkarev, V.N.Antsifirov, Yu.V.Danchenko, O.P.Solonenko and H.Veringa, Catalytic Combustion, SanDiego, USA, April 1-16 (1999) 97.
3. A.A.Fedorov, Foam Catalysts, Ekaterinburg, Russia, 1993.
4. Z.R.Ismagilov, V.V.Pushkarev, O.Yu.Podyacheva et al., Chemical Engineering, 82 (2001) 355.
5. Z.R.Ismagilov, R.A.Shkrabina, L.T.Tsykoza, N.V.Shikina, V.A.Sazonov, S.A.Yashnik, V.V.Kuznetsov and H.J.Veringa, The Sulfur and Water Resistance of Modified Washcoated Cu-Exchanged ZSM-5 Monolith Catalysts for NO Reduction by Propane, International Symposium Devoted to 70th Anniversary of Prof. J. Haber, 4-7 May, Crakow, Poland. Proceedings, (2000) p. 71.
6. Z.R.Ismagilov, R.A.Shkrabina, L.T.Tsykoza, S.A.Yashnik, V.A.Sazonov, V.V.Kuznetsov, M.V.Luzgin, A.V.Kalinkin and H.J.Veringa, Stability of Monolith Cu-ZSM-5 Catalysts for CSR-NOx by Hydrocarbons. Part I. Synthesis and Investigation of Cu-ZSM-5 Catalysts, Kinet. Katal., 42, 6 (2001) 928-934 (In Russian).
7. Z.R.Ismagilov, R.A.Shkrabina, L.T.Tsykoza, V.A.Sazonov, S.A.Yashnik, V.V.Kuznetsov, N.V.Shikina and H.J.Veringa, The Sulfur and Water Resistance of Modified Washcoated Zeolite-Exchanged Monolith Catalysts for SCR of NOx with Propane, Topics in Catalysis, 16/17 (2001) 307-310.
8. T.V.Reshetenko, L.B.Avdeeva, Z.R.Ismagilov, A.L.Chuvilin, V.A.Likholobov, Eurasian ChemTech Journal, 2 (2000) 237.
9. L.B.Avdeeva, T.V.Reshetenko, Z.R.Ismagilov, V.A.Likholobov, Appl. Catal. A, 228 (2002) 53.
10. V.B.Fenelonov, T.Ye.Podruzhdina, A.Yu.Derevyankin, L.B.Avdeeva, T.V.Reshetenko, Z.R.Ismagilov, Ch.N.Barnakov, A.P.Kozlov, S.K.Seit-Ablaeva, V.V.Chesnokov, V.N.Parmon, Adsorption Methods of Hydrogen and Methane Storage for the Fuel Cell Application (in press).

**OXIDATION REACTIONS OVER MULTICOMPONENT CATALYSTS
CONSISTING OF GOLD AND A TRANSITION/RARE EARTH METAL OXIDE**

C.J. Weststrate, A. Gluhoi, R.J.H. Grisel and B.E. Nieuwenhuys

*Leiden Institute of Chemistry, Leiden University
P.O.Box 9502, 2300 RA Leiden, The Netherlands
(tel. +31 71 5274545)/email: b.nieuwe@chem.leidenuniv.nl*

This research project is motivated by:

- a) The search for improved automotive catalysts and alternative fuels in connection with more stringent legislation concerning automotive exhaust gas catalysis.
- b) The search for catalysts selective in CO oxidation in the presence of hydrogen. These catalysts are required for the generation of electric energy by using PEFC fuel cells.

In this context the following reactions have been studied.

- 1) The oxidation of a number of selected hydrocarbons including propene and methane.
- 2) The oxidation of hydrogen at low temperatures.
- 3) The oxidation of CO at low temperatures.
- 4) The selective oxidation of CO by O₂ in the presence of hydrogen.

The catalysts used in our studies include gold on γ -Al₂O₃ and several Au-MO_x on γ -Al₂O₃ catalysts with MO_x being a metal oxide. The effect of the gold particle size and the effect of the presence of MO_x on the activity and the selectivity will be discussed. It will be shown that, both the presence of very small gold particles and the presence of MO_x are of great importance to obtain a high activity.

Large synergistic effects were found for all the reactions, i.e. the activity of the multicomponent Au-MO_x on γ -Al₂O₃ catalysts exhibit a superior behavior compared to the Au/ γ -Al₂O₃ and MO_x/ γ -Al₂O₃ catalysts.

Results concerning the performance of a number of gold based catalysts in the selective oxidation of CO in the presence of hydrogen will be shown. The effect of the gold particle size and the effect of the presence of MO_x will be discussed. The behaviour of gold based catalysts in the relevant reactions will be compared with those of other noble metal catalysts, including Pt, Pd, Rh and Ru-MO_x on Al₂O₃.

On the basis of our results we propose a formulation for a novel catalyst for the selective oxidation of CO. In addition, a mechanism is proposed for the relevant processes.

ORAL PRESENTATIONS

THE CHARACTERIZATION OF FeZSM-5 BY ^{57}Fe MÖSSBAUER SPECTROSCOPY

A.R. Overweg¹, M.W.J. Crajé¹, A.M. van der Kraan¹, I.W.C.E. Arends²

¹ *Interfacultair Reactor Instituut, Delft University of Technology,*

E-mail: A.R.Overweg@iri.tudelft.nl

² *Section Biocatalysis and Organic Chemistry, Department of Biotechnology, Delft University of Technology*

FeZSM-5 zeolites have attained considerable interest for applications in catalysis. Although these types of materials already exist for over two decades it is only since the last five years or so that they are being regarded as promising catalysts for reactions, such as the catalytic decomposition of nitrous oxide, the de-NO_x HC-SCR and benzene to phenol oxidation.

One of the key issues related to these FeZSM-5 zeolites is the identification and chemical behavior of the iron centers. Although the precise nature of these iron centers is not yet known it is widely thought that these centers play an important role in the catalysis. Panov [1] suggests that the active site, at least for the benzene to phenol oxidation, is a binuclear iron species, which is immobilized in the pores of the ZSM-5 zeolite. As such, it would resemble the iron oxidant in the enzyme methane monooxygenase, which is capable of transferring an oxygen atom from the enzymatic di-iron center to an activated C-H bond.

It is widely known that the catalytic performance of FeZSM-5 zeolites strongly depends on the preparation method chosen, as well as subsequent pretreatment steps. A highly promising route has been developed by Panov and coworkers [1]. Their method was based on the isomorphous substitution of iron by a hydrothermal method, followed by a high-temperature vacuum treatment. Following this pioneering work an FeZSM-5 material was developed in our laboratories, which showed high activities in both benzene to phenol oxidation [2], as well as nitrous oxide decomposition [3].

We have studied this FeZSM-5 catalyst by ^{57}Fe Mössbauer spectroscopy. ^{57}Fe Mössbauer spectroscopy is an excellent tool for studying the nature of the iron centers of these catalysts, not only in the as-prepared state but also under in-situ conditions. By doing so, several iron species could be discriminated. In addition, the redox behavior of these iron species has been studied by exposure of the catalyst to different treatments, such as heat treatments and exposure to different gases, e.g. hydrogen, nitrous oxide and nitrogen. The outcome of these investigations will be presented in this contribution.

[1] Dubkov, K.A., Sobolev, V.I., Talsi, E.P., Rodkin, M.A., Watkin, N.H., Shteinman, A.A. and Panov, G.I., *J. Mol. Catal. A: Chemical* 123 (1997) 155 and references cited therein.

[2] Ribera, A., Arends, I.W.C.E., de Vries, S., Pérez-Ramirez, J. and Sheldon, R.A., *J. Catal.* 195 (2000) 287.

[3] Pérez-Ramirez, J., Kapteijn, F., Mul, G. and Moulijn, J.A., *Chem. Comm.* (2001) 693.

OP-2

ON THE MECHANISM OF OSCILLATION PHENOMENA IN THE NO+H₂ REACTION ON NOBLE METAL SURFACES: SEMI-EMPIRICAL CALCULATIONS

A.R.Cholach, N.N.Bulgakov, B.E.Nieuwenhuys *

Boreskov Institute of Catalysis SB RAS, Novosibirsk, Russia

Fax: (007) 3832-34-37-66, e-mail: cholach@catalysis.nsk.su

**Leiden Institute of Chemistry, P.O.Box 9502, 2300 RA Leiden, The Netherlands*

Summary

The semi-empirical Method of Interacting Bonds was used in the present work to clarify the mechanism of the title process. Various single crystal planes of Pt, Rh, Ir, Fe, and Re were examined with respect to the stability of the adsorbed NH_n species (n = 0; 1; 2; 3); to the reactivity of NH_n (n = 0; 1; 2) species towards adsorbed hydrogen atoms; and to the possibility of proceeding the combination reactions between two NH or two NH₂ particles resulting in the formation of gaseous H₂ and N₂ molecules. All the surfaces studied were found to form readily stable NH species. The principal difference between Pt, Rh, Ir single crystal planes, on which the reaction exhibits rate oscillations, and Fe, Re surfaces, which do not show an oscillatory behavior, is that the combination reaction can easily proceed in the former case, but this reaction is not allowed on the latter surfaces. This result is consistent with an earlier suggested mechanism for the oscillatory behaviour that attributes the surface wave propagation to the intermediate formation of NH species.

Re and Fe surfaces form stable NH₂ species, whereas the noble metal surfaces can form weakly stable NH₂ particles only at the very edge of their thermodynamic existence region. The combination reaction between two NH₂ species is prohibited in all cases.

1. Introduction

The nature and properties of surface intermediates formed in the course of adsorption and sequential reactions in the adsorbed layer are obviously important for understanding the detailed mechanism of heterogeneous catalytic reactions. In the case of the NO reduction reactions, they are also of practical interest since, in particular, platinum and rhodium are currently used in catalytic ammonia oxidation, and as active component of the automotive three-way catalyst [1,2]. Recent experimental studies report on the formation and properties

of various $\text{NH}_{n,\text{ads}}$ species (where $n = 0; 1; 2; 3$) on platinum single crystal surfaces [3-6]. It was found that the intermediate NH_{ads} species are formed when a NO_{ads} layer is exposed to 0.15L (Langmuir) of hydrogen at room temperature. Upon further hydrogen exposure of up to 4 L, all nitrogen containing species are removed from the surface. On the other hand, an excess of initially adsorbed hydrogen results in formation of stable $\text{NH}_{2,\text{ads}}$ species, which occurs in the course of the $\text{NO}_{\text{gas}} + \text{H}_{\text{ads}}$ reaction on the Pt(100)-(1×1) surface at 300 K [6]. It was established that stable NH_{ads} and $\text{NH}_{2,\text{ads}}$ species are intermediates in ammonia oxidation on the Pt(111) surface [3]. These species were also identified on a Pt(111) single crystal plane after electron bombardment of molecularly adsorbed ammonia at 100 K [4]. It was reported that $\text{NH}_{2,\text{ads}}$ were the dominant species below room temperature. An increase in temperature resulted in $\text{NH}_{2,\text{ads}}$ dissociation and NH_{ads} became the main surface species in the temperature range 300-400 K.

There is also a lot of reliable experimental data, which evidently demonstrate the formation of stable NH_{ads} and $\text{NH}_{2,\text{ads}}$ species on various single crystal surfaces of Rh [7], Ir [8,9], Fe [10-12], and Re [13].

Several noble metal surfaces are known to reveal a nonlinear kinetic behavior in the reaction of $\text{NO} + \text{H}_2$. More specifically, such a behavior was reported for a number of platinum, rhodium, and iridium single crystal surfaces as well as for monocrystalline tips [14-17]. Processes such as surface explosions, surface wave propagation, and oscillations in reaction rate display these nonlinear phenomena. The proposed mechanisms usually involve a reversible surface reconstruction or an autocatalytic increase in formation of vacancies in the course of reaction. Besides that, the reversible formation of intermediate NH_n species can also make an important contribution to oscillation phenomena [15,18,19].

In our previous papers we reported on the properties of $\text{NH}_{n,\text{ads}}$ species formed on various single crystal surfaces of Rh and Pt studied by the Method of Interacting Bonds (MIB) [18,19]. It was found that stable $\text{NH}_{3,\text{ads}}$ species are not formed, and formation of NH_{ads} is more favorable in comparison with that of $\text{NH}_{2,\text{ads}}$, thus being in line with the known experimental data [15,20].

In the present work we report on a similar comparative MIB study of Pt(100)-(1×1), Rh(111), Rh(100), Ir(110)-(1×1), Ir(110)-(1×2), FCC Fe(111), and Re(0001) single crystal planes in order to find out the regularity in properties of various NH_n species. Iron and Rhenium do not reveal non-linear behavior in the $\text{NO} + \text{H}_2$ reaction, but they are known to

OP-2

form various NH_x species. The aim of including the latter metals in the present work is to elucidate the role of intermediate NH_n species in the title process.

In our calculations, n hydrogen atoms of the $\text{NH}_{n,\text{ads}}$ particle are set to bind to the nitrogen atom only, but not to surface platinum atoms. We considered that the strongly bound species, i.e. the N atom of NH_n is triply bound to surfaces with C_{3v} symmetry, and fourfold bound to surfaces with C_{4v} symmetry. Rh(111) and Rh(100) surfaces were considered as components of the Rh(533) plane, which is known to reveal oscillations in the reaction rate of the $\text{NO}+\text{H}_2$ reaction [14]. The results obtained are compared with the available experimental data.

2. Theory

The method of interacting bonds considers a certain multi-atomic system as a set of two-center bonds [20]. Each i -th bond is characterized by an empirical parameter E_i similar to the well-known bond energy by its nature. Usually E_i depends only on the type of bond forming atoms. Besides, for each i -th bond we introduce a variable bond coefficient v_i ($0 < v_i < 1$), whose value and, thus, contribution of the i -th bond to the total energy of the system is characterized by the whole system structure. The interaction (repulsion) between the i -th and k -th bonds sharing an atom is also allowed for. This interaction is characterized by an empirical parameter Δ_{ik} which depends on the type of the atoms involved into a certain system formation. Atomization energy is written as:

$$H_a = \sum_i E_i v_i (2 - v_i) - \sum_{i>k} \Delta_{ik} v_i v_k$$

Bond coefficients v_i are found from the maximum of the H_a value (energy minimum):

$$\partial H_a / \partial v_i = 0$$

The simplicity of MIB permits one to investigate any complex system of the desired structure without any additional assumptions such as surfaces, interfaces, extended defects of solids, etc. It should be noted that MIB does not deal with the electronic properties of the system considered. Therefore, determination of atomic coordination numbers, bond angles and other similar features of this system is beyond the model action. For proper use of the MIB results, one certainly has to take into account the molecular geometry, valence, steric features and some other properties of the system considered, which were determined theoretically and/or experimentally.

The bond parameters used in the present work are listed in Table 1. All E_{MM} parameters were determined from corresponding evaporation enthalpies. All Δ_M parameters were estimated from the empirical ratio $E_{MM}/\Delta_M = 4.3$ [22].

Table 1. Bond parameters used in MIB calculations, kJ/mole

	E_{MM}	Δ_M	E_{MN}	E_{NH}	Δ_N
Fe	246.34 ^(a)	57.29	405.0 ^(b)	583.25 [18]	313.8 [22]
Re [23]	456.6	106.2	555.3		
Rh [18]	333.0	77.4	405.8		
Ir	392.9	91.4	453.1 ^(c)		
Pt [19]	334.3	77.7	384.9		

^(a) E_{FeFe} is determined from the sublimation heat of γ -Fe; ^(b) E_{FeN} is determined from the atomization heat of Fe_4N ; ^(c) E_{IrN} is determined from the empirical correlation between E_{IrN} and E_{IrO} [22], that is determined from the formation enthalpies of IrO and IrO₃.

MIB assumes that the parameters used must be reliable for all the considered systems of rather different properties, though one is not always sure of this. Thus one cannot take for granted a high precision of all the calculated values. However, MIB is able to provide results with high comparative accuracy. This is very useful for examination of various systems in order to establish the conditions of their formation, and select favorable structures and determine their relative stability. We tried to use these potentialities of MIB in the present paper. The method was successfully applied to systems of various chemical origin such as oxides [21,24,25], sulfides [26,27], and metals [22] etc.

3. Results and discussion

The following key points concerning NH_{ads} and $NH_{2,ads}$ species, have been considered for a set of single crystal surfaces in order to clarify the title process:

- The stability characteristics of adsorbed species. A given $NH_{x,ads}$ species is forbidden to form if any of its bond parameters is negative, i.e. $v_{MN} < 0$ and/or $v_{NH} < 0$; the particle is stable if $v_{MN} > 0.1$ and $v_{NH} > 0.1$; the particle is weakly stable for intermediate values of bond parameters.
- The heat of formation Q_1 in the adsorbed layer according to the reactions:



OP-2

The formation of a given species is allowed if $Q_1 > 0$.

The value of Q_1 was determined as:

$$Q_1 = Q_{NH} - Q_N - Q_H \quad (\text{for } NH_{ads} \text{ formation})$$

And as:

$$Q_1 = Q_{NH_2} - Q_{NH} - Q_H \quad (\text{for } NH_{2,ads} \text{ formation}).$$

Where Q_H stands for the half of the experimental heat of adsorption of hydrogen presented in Table 2. This value is assumed to be independent of coverage for a given surface;

Q_N , Q_{NH} , Q_{NH_2} stand for heat of formation of the respective species calculated by the MIB:



- The possibility of proceeding the combination reaction according to the equations:



A given reaction is supposed to be favorable if the heat of reaction $Q_2 > 0$.

Table 2. The heat of H_2 adsorption on the metal surfaces examined, kJ/mole

	Fe(110)	Re(0001)	Rh	Ir(110)	Pt
Q_{ads} , kJ/mole	83.0	83.4	77.8	83.2	66.9
Refs.	[32]	[31]	[28,29]	[33]	[30]

Fig. 1 and Fig. 2 show the results of the calculations concerning adsorbed NH species on a set of single crystal surfaces at various coverages. In all cases NH_{ads} species are quite stable as shown in Fig. 1. The ν_{MN} bond coefficient (i.e. M-N bond strength) decreases and the ν_{NH} bond coefficient (i.e. N-H bond strength) slightly increases as the coverage rises. The latter value even exceeds $\nu_{NH} = 0.65$, the value found by MIB calculations for gaseous NH_3 molecule.

Fig. 2 (a) shows that NH_{ads} species readily form in the adsorbed layer. It means that not N_{ads} , but NH_{ads} species are favorable in the presence of adsorbed hydrogen. An excess of H_2 in the reaction mixture $NO+H_2$ corresponds to the experimental conditions required for sustained oscillations in the reaction rate [14,16,17].

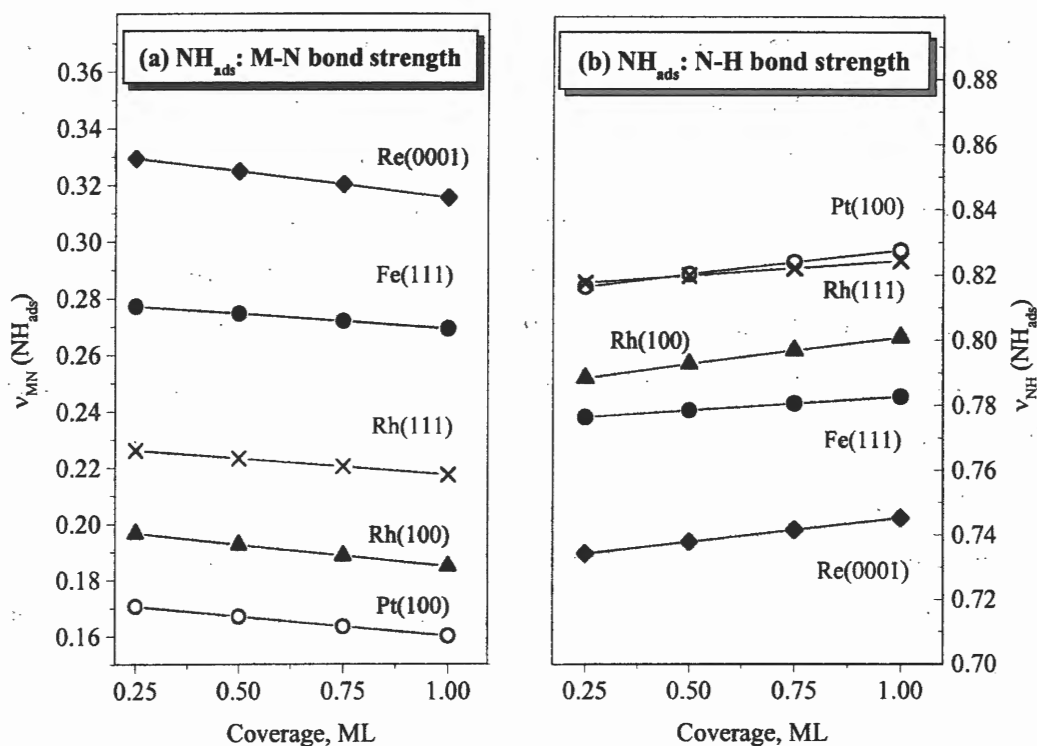


Fig. 1. The bond coefficient v_{MN} (a) and v_{NH} (b) of NH species adsorbed on different single crystal planes as a function of coverage, where M= Pt(100)-(1 \times 1) - open circles; Rh(111) - crosses; Rh(100) - up triangles; Fe(111) - solid circles; Re(0001) - diamonds.

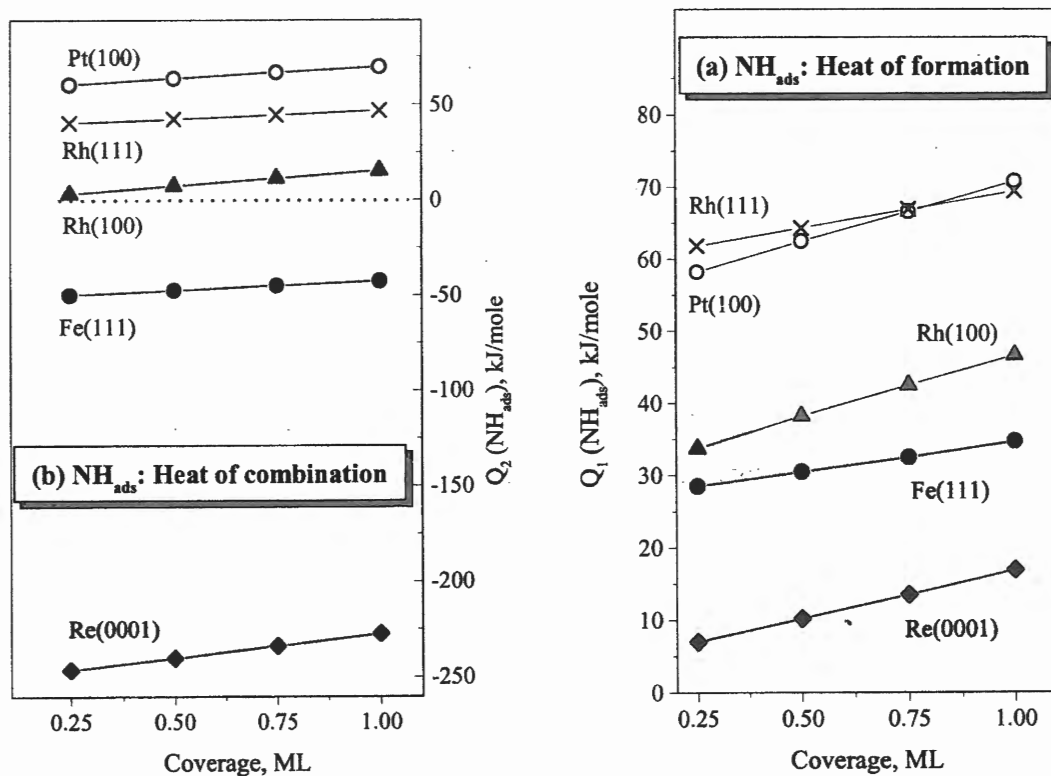


Fig. 2. Heat of formation (a) by equation (1) and heat of combination reaction (b) by equation (4) of NH species on different single crystal planes as a function of coverage.

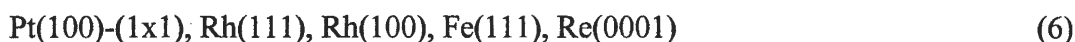
OP-2

Fig. 2 (b) illustrates an important feature of NH_{ads} particles. Namely, the combination reaction is allowed on those surfaces, which reveal oscillatory behavior, and it is forbidden for surfaces, which do not reveal oscillations. Besides that, the heat of the combination reaction increases (i.e. Gibbs energy change decreases) as the coverage rises. This result is in line with another experimental characteristic of oscillation phenomena; because a certain critical coverage is always necessary to start the regular surface wave propagation.

Fig. 3 demonstrates the stability of adsorbed NH_2 particles. The same dependence on coverage was found in the case of the NH species: M-N bond strength slightly decreases, and the N-H bond strength slightly increases as the coverage rises. $\text{Re}(0001)$ and $\text{Fe}(111)$ surfaces exhibit a rather high v_{MN} value, i.e. strong M-N bond, whereas this value obtained for the noble metal surfaces corresponds to weakly bound NH_2 particles ($v_{\text{MN}} < 0.1$, this boundary value is marked by the dashed line in Fig. 3a). In this case the N-H bond is even stronger than in NH species.

Fig. 4 shows the thermodynamic properties of NH_2 particles. In contrast to NH species, the formation of NH_2 species in the adsorbed layer by equation (2) is favorable for $\text{Pt}(100)$ and $\text{Rh}(111)$ surfaces only, and the combination reaction by equation (5) is not allowed for all surfaces.

Even a brief analysis of the data presented in the Figures 1-4 evidences that our calculations revealed a steady regularity in the row of examined surfaces:



In this order the following properties of NH and NH_2 species sequentially change:

- The heat of formation (equations 1 and 2) decreases;
- The heat of the respective combination reaction (equations 4 and 5) decreases;
- The N-H bond strength decreases;
- The M-N bond strength increases.

Table 3 is designed to find out those characteristics among the collection of experimental and theoretical data, which may be responsible for the title process.

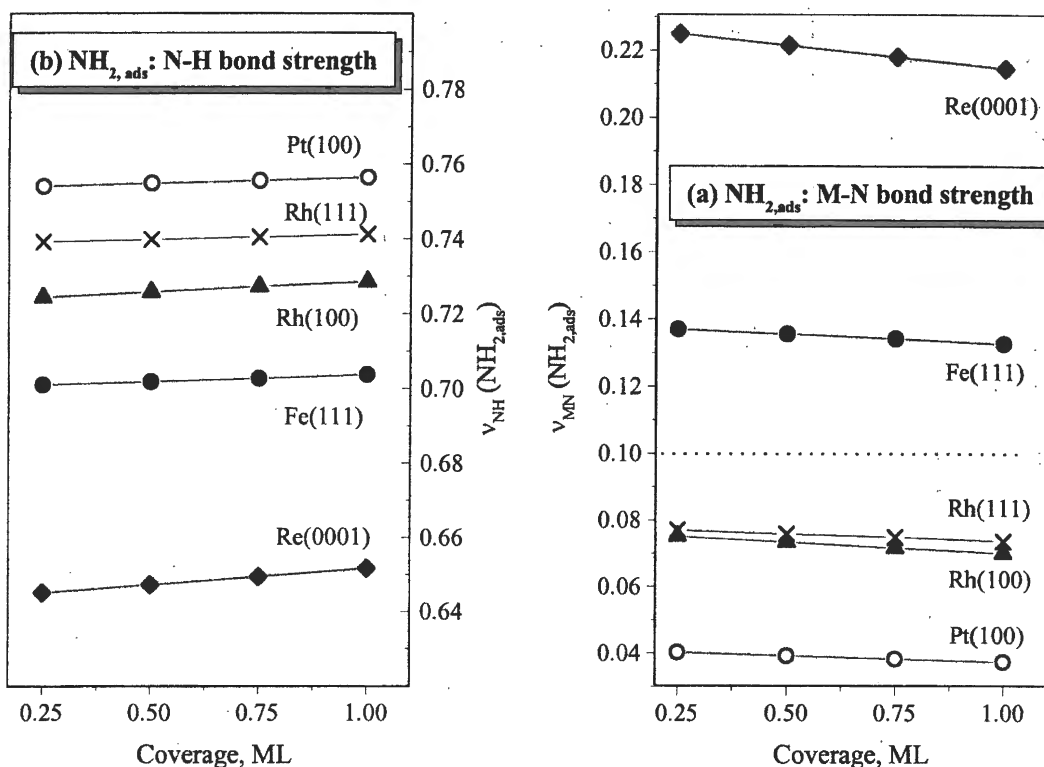


Fig. 3. The bond coefficient v_{MN} (a) and v_{NH} (b) of NH_2 species adsorbed on different single crystal planes as a function of coverage, where M= Pt(100)-(1 \times 1) - open circles; Rh(111) - crosses; Rh(100) - up triangles; Fe(111) - solid circles; Re(0001) - diamonds.

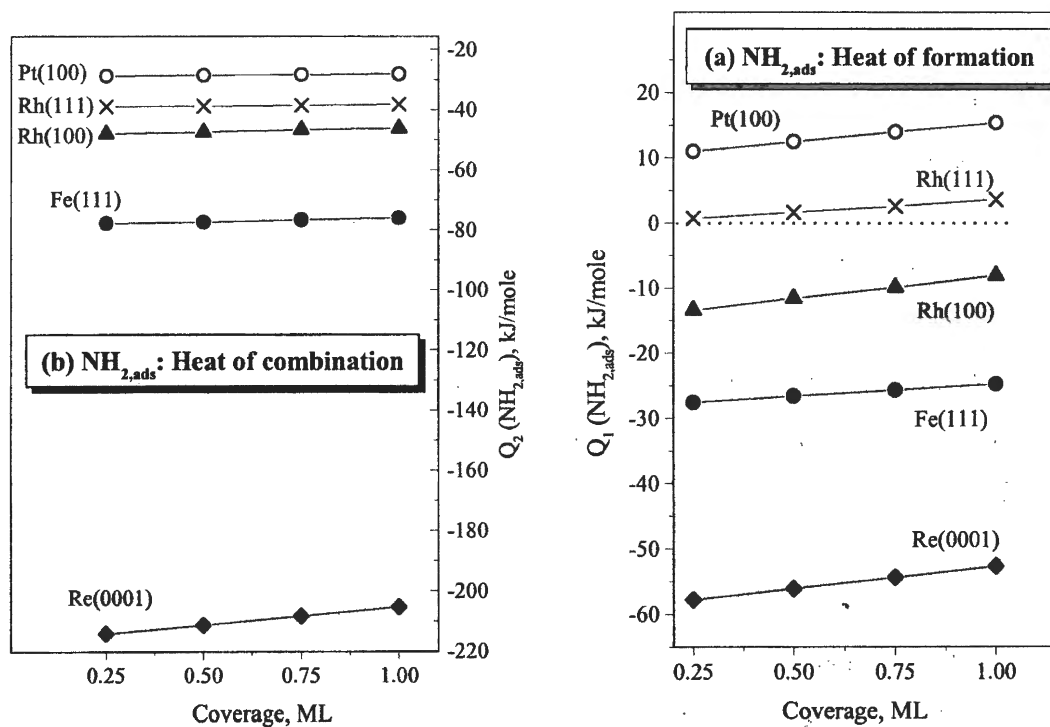


Fig. 4. Heat of formation (a) by equation (2) and heat of the combination reaction (b) by equation (5) of NH_2 species on different single crystal planes as a function of coverage.

OP-2

Table 3. Combined experimental (*) and calculated data on single crystal surfaces.

#	Characteristic	Pt(100)-(1×1)	Rh(111)/(100)	Fe(111) FCC	Re(0001)
1.	*Oscillatory behavior	+	+	-	-
2.	*NO dissociation	+	+	+	+
3.	*Surface reconstruction	+	-	-	-
4.	*Availability of NH_x species	+	+	+	+
5.	NH formation	+	+	+	+
6.	NH stability	+	+	+	+
7.	NH combination	+	+	-	-
8.	NH₂ formation	+	+	-	-
9.	NH₂ stability	-	-	+	+
10.	NH₂ combination	-	-	-	-

Table 3 evidences that line 1 (oscillatory behavior) meets coincidence at two another lines only – 7, and 8, corresponding to NH combination, and NH₂ formation, respectively. The formation of adsorbed NH₂ species cannot be responsible for oscillations, because the stability of NH₂ (line 9) reveals opposite characteristics. Moreover, the combination reaction of NH₂ particles (line 10) is not allowed thermodynamically.

In contrast to that, the reaction of NH combination may be quite responsible for oscillations. Indeed, N_{ads} species can be readily formed (line 2 in Table 3), both the further formation of NH particles in adsorbed layer, and the combination reaction are significantly exothermic as shown in Fig. 2. In addition, the intermediate NH species are quite stable as demonstrated in Fig. 1.

A preliminary consideration of the Ir(110) single crystal surface shows that the (1×1) structure should be inactive in oscillations since its properties are close to that of Fe(111). On the contrary, the properties of the Ir(110)-(1×2) surface are close to that of Rh(111). It means that the reconstructed iridium surface should be active in oscillations. It agrees with the experimental observations, which demonstrate that non-linear kinetic behavior of the Ir(110) surface in the NO+H₂ reaction proceeds under experimental conditions at which the surface is reconstructed [16,34].

Conclusions

1. The semi-empirical Method of Interacting Bonds was used to analyze the properties of adsorbed NH_n species on a set of single crystal planes of transition metals. The regularity in the following row of examined surfaces is established: Pt(100)-(1×1), Rh(111), Rh(100), Fe(111), Re(0001). In this order the properties of NH and NH₂ species sequentially change as:

the heat of formation, the heat of respective combination reaction, and N-H bond strength decreases, whereas the M-N bond strength increases.

2. The combination reaction between two adsorbed NH species may be responsible for the oscillatory behavior of the single crystal planes of noble metals considered in the NO+H₂ reaction. It means that the earlier suggested mechanism for the rate oscillations, which attributes the surface wave propagation to the intermediate formation of NH species, is quite acceptable.

Acknowledgements

The authors appreciate the financial support from INTAS99-01882.

References

1. K.C. Taylor, in: *Automotive catalytic converters* (Springer, Berlin, 1984).
2. B.E.Nieuwenhuys, *Adv.Catal.* 44 (1999) 259
3. W.D. Miehler, W. Ho, *Surf.Sci.* 322 (1995) 151.
4. Y.-M. Sun, D. Sloan, H. Ihm, J.M. White, *J.Vac.Sci.Technol. A* 14 (3) (1996) 1516.
5. D.Yu. Zemlyanov, M.Yu. Smirnov, V.V. Gorodetskii, J.H. Block, *Surf.Sci.* 329 (1995) 61.
6. D.Yu. Zemlyanov, M.Yu. Smirnov, V.V. Gorodetskii, *Surf.Sci.* 391 (1997) 37.
7. A. Vavere, R.S. Hansen, *J. Catal.* 69 (1981) 158.
8. B.J. Wood, H. Wise, *J.Catal.* 39 (1975) 471.
9. V.V. Gorodetskii, V.A. Sobyenin, *Proc. 7th ICC* (Tokyo, 1980), Tokyo: Kadansha Ltd., 1981, p. 566.
10. K. Kishi, M.W. Roberts, *Surf.Sci.* 62 (1977) 252.
11. M. Grunze, F. Bozso, G. Ertl, M. Weiss, *Appl.Surf.Sci.* 1 (1978) 241.
12. M. Drechsler, H. Hoinkes, H. Kaarmann, H.W. Wilsch, G. Ertl, M. Weiss, *Appl.Surf.Sci.* 3 (1979) 217.
13. Y. Fukuda, F. Honda, J.W. Rabalais, *Surf.Sci.* 99 (1980) 289.
14. N.M.H. Janssen, B.E. Nieuwenhuys, M. Ikai, K. Tanaka, A.R. Cholach, *Surf.Sci.* 319 (1994) L29.
15. A.R. Cholach, M.F.H. van Tol, B.E. Nieuwenhuys, *Surf.Sci.* 320 (1994) 281.
16. C.A. de Wolf, B.E. Nieuwenhuys, A. Sasahara, K. Tanaka, M.M. Slinko, M.Yu. Smirnov, *Surf.Sci.* 411 (1998) L904.
17. J. Siera, P.D. Cobden, B.E. Nieuwenhuys, *Catal.Lett.* 10 (1991) 335.
18. A.R. Cholach, N.N. Bulgakov, *Catal.Lett.*, 48 (1997)191.

OP-2

19. A.R. Cholach, N.N. Bulgakov, *Catal.Lett.*, 58, #4 (1999)183.
20. M.F.H.van Tol, A. Gielbert, B.E. Nieuwenhuys, *Catal.Lett.* 16 (1992) 297.
21. N.N. Bulgakov, Yu.A. Borisov, V.V. Popovskii, *Kinet.Katal.* 14 (1973) 395, in Russian
22. A.I. Boldyrev, V.I. Avdeev, N.N. Bulgakov, I.I. Zakharov, *Kinet.Katal.* 17 (1976) 706, in Russian
23. N.E. Henriksen, G.D. Billing, *Surf.Sci.* 227 (1990) 224.
24. N.N. Bulgakov, V.Yu. Aleksandrov, V.V. Popovskii, *React.Kinet.Catal.Lett.* 4 (1976) 473.
25. N.N. Bulgakov, V.Yu. Aleksandrov, V.V. Popovskii, *React.Kinet.Catal.Lett.* 8 (1978) 53, 59, 65.
26. Yu.I. Yermakov, A.N. Startsev, V.A. Burmistrov, O.N. Shumilo, N.N. Bulgakov, *Appl.Catal.* 18 (1985) 33.
27. N.N. Bulgakov, A.N. Startsev, *Mendeleev Commun.* 1 (1991) 98.
28. V.V.Gorodetskii, B.E.Nieuwenhuys, V.M.Sachtler, G.K.Boreskov, *Surf.Sci.* 108 (1981) 225.
29. A. Crucq, G. Lienard, L. Degols, A. Frennet, *Appl.Surf.Sci.* 17 (1983) 79.
30. B. Hellsing, B. Kasemo, V.P. Zhdanov, *J.Catal.* 132 (1991) 210.
31. R. Ducros, M. Housley, G. Piquard, M. Alnot, *Surf.Sci.* 109, 2 (1981) 235.
32. K. Yoshida, *Japan J.Appl.Phys.* 19 (1980) 1873.
33. J.M. Derochette, *Surf.Sci.* 118 (1982) 145.
34. D.E. Ibbotson, T.S. Wittrig, W.H. Weinberg, *Surf.Sci.* 111 (1981) 149.

SILICON-WAFER BASED PLANAR MODELS FOR HYDROTREATING CATALYSTS

E.J.M. Hensen, L. Coulier, A. Borgna, J.A.R. van Veen and J.W. Niemantsverdriet

*Schuit Institute of Catalysis, Eindhoven University of Technology, P.O. Box 513,
5600 MB Eindhoven, The Netherlands, E-mail: e.j.m.hensen@tue.nl*

ABSTRACT

In the present study the use of planar silicon-based models for hydrotreating catalysts is discussed. The specific flat nature makes these models amenable to high resolution surface-sensitive techniques such as XPS. The additional possibility to measure the activity of such model catalysts in thiophene hydrodesulfurization provides a powerful tool to determine structure-activity relations. Here, we study the effect of chelating agents (NTA and EDTA) on the sulfidation order of NiMo catalysts. The XPS results clearly show that the use of these chelating agents retards the sulfidation of Ni with respect to Mo. Especially, EDTA is effective by postponing Ni sulfidation after Mo is completely sulfided. The latter catalyst also displays the highest activity which is attributed to the highest amount of 'Ni-Mo-S'-type phases. In essence, the results underpin the notion that such 'Ni-Mo-S' phase can be formed effectively when Ni sulfidation proceeds after MoS₂ has been formed. When Ni sulfides at too low temperature, inactive bulky Ni₃S₂ clusters are formed.

INTRODUCTION

General

Supported mixed transition metal sulfide catalysts play a pivotal role in refineries for the production of clean motor fuels. They are employed not only to hydrotreat the final products like gasoline and diesel, but also to pretreat fluid catalytic cracking or reformer feed [1]. Furthermore, they provide the hydrogenation functionality in most hydrocracking catalysts that upgrade vacuum residue to more valuable products.

Two major drivers for the development of more active hydrotreating catalysts are (i) dwindling oil supplies forcing refiners to use heavier feedstock and (ii) ever-tightening motor fuel specifications (for instance, the EU Auto Oil programme II [2]). Noteworthy is that mostly the use of an improved catalyst is more economic than modifications to the process.

OP-3

In addition to the demand for more active catalysts, selectivity is also an issue to consider. Whereas the desulfurization of gasoline is not a difficult task in itself due to the thiophenic nature of the sulfur compounds, concomitant olefin hydrogenation leads to a dramatic loss in octane rating when aiming at very low sulfur levels. Here, there is room for the development of catalysts with an increased hydrodesulfurization/hydrogenation ratio [3,4]. For the near future, the introduction of the fuel cells in mobile applications may set zero sulfur limits when oil-derived fuels are to be used to generate hydrogen via onboard partial oxidation [5].

While research on hydrotreating catalysts has been extensive over the last 50 years [6-11], it has proven very difficult to relate catalyst structure to catalyst activity and selectivity on the molecular level. Partly, this is to be attributed to the heterogeneous nature of such catalysts in the sense that various metal sulfide phases are present.

In recent years, we have employed the model catalyst approach to heterogeneous catalysis. The essential point is to prepare planar model catalysts by spincoating which mimics the industrial pore volume impregnation method. In this way, realistic models can be obtained which are easily amenable to high-resolution spectroscopic studies. The specific catalytic activity of such well-defined models can also be evaluated. Here, we will show that the strong tandem-mix of characterization and reactivity evaluation of these realistic models enables one to obtain detailed insight into the relation between sulfidation behavior of the transition metals and their activity.

Preparation of model catalysts

Models of catalysts are used to circumvent the disadvantages of industrial catalysts (Figure 1).

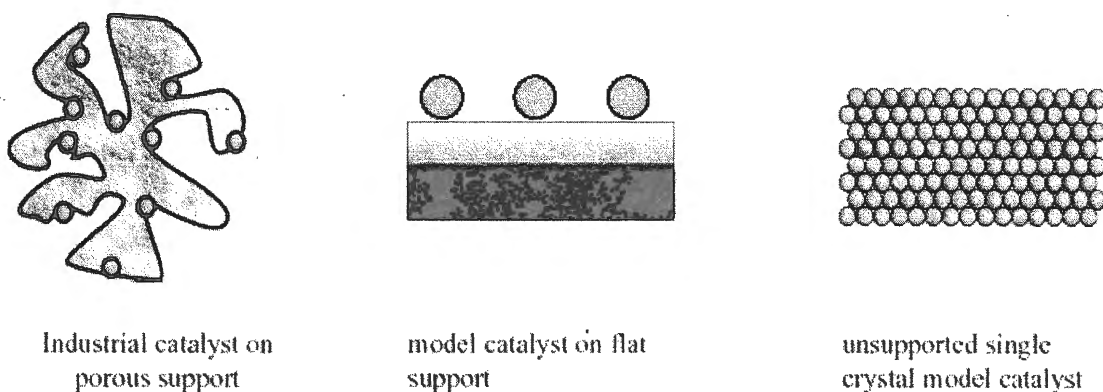


Figure 1. Schematic drawing of a porous catalyst (left), a flat supported model catalyst (middle) and a single crystal.

The ultimate and most simple model is a well-defined single crystal surface. These single crystals have been used successfully in ultra high vacuum (UHV) to study fundamental adsorption

behaviour of molecules on metal surfaces and its dependence on surface geometry and composition. A major drawback of single crystal surfaces is the so-called pressure- and material-gap with respect to industrial catalysts. Planar silicon-based model catalysts provide opportunities to bridge these gaps. These models consist of a flat model support covered by the precursor material. The model support is made up by a thin layer of SiO_2 or Al_2O_3 on a conducting substrate. The precursor material can be applied by evaporation, electron beam lithography or wet chemical preparation [12]. Especially the latter method has gained increasing importance. Spincoating introduced by Kuipers et al. [13] mimics the widely applied pore-volume impregnation used on the industrial scale and allows full control over the loading (Figure 2) [14].

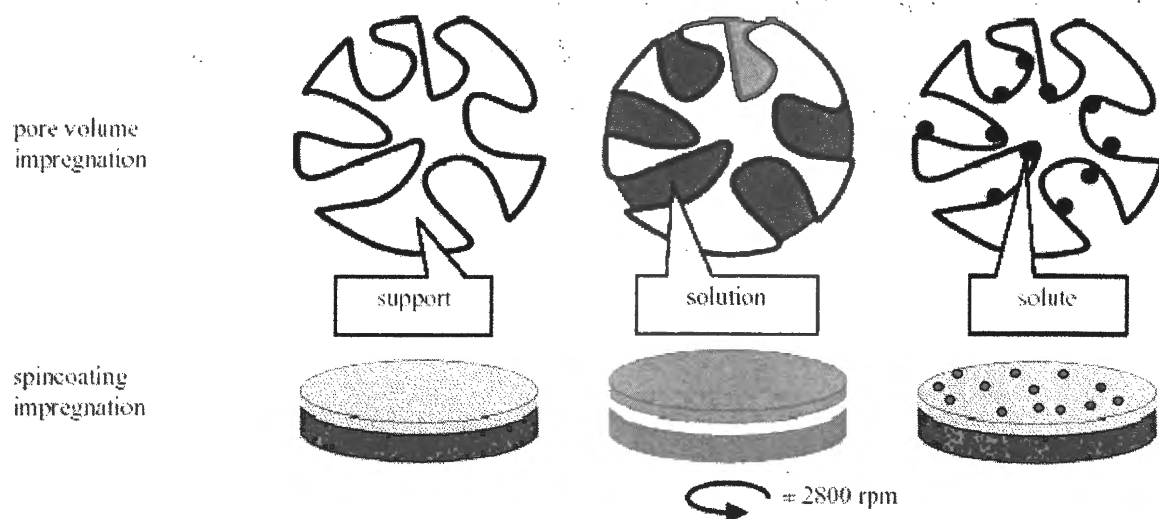


Figure 2. Analogy between the spincoating technique used for model catalysts in this thesis and impregnation of a porous catalyst.

Due to the non-porous conducting support all active particles are on top of the substrate and are thus 'visible' for various surface sensitive techniques. Furthermore, charging phenomena during electron- or ion-spectroscopies are largely eliminated due to the conducting substrate. The absence of pores allows the measurements of intrinsic kinetics without effects of diffusion limitations due to small pore sizes. The majority of studies on model catalysts concern the 'classic' metals on oxidic supports. However, recently model catalysts have also been applied in different fields of catalysis such as polymerization [15] and transition metal oxide and sulfide catalysts [16]. An excellent review on the preparation and applications of model supports and catalysts has been published by Gunter et al. [12].

OP-3

Characterization by X-ray photoelectron spectroscopy

Where in industrial practice the feed is spiked with sulfur-containing molecules to slowly convert catalyst precursors to their active sulfided form, a mixture of hydrogen sulfide and hydrogen is generally applied in laboratory practice. The group of Niemantsverdriet [17,18] has used the model catalyst approach to study the sulfidation of SiO₂-supported MoO₃ in great detail. X-ray photoelectron spectroscopy is an ideal tool [19] to study this transformation since essential information of the different types of molybdenum and sulfur species can be obtained. It was found that the sulfidation of Mo occurred via Mo⁵⁺-oxysulfides and that no MoO₂ or elemental sulfur was involved, as proposed by Arnoldy *et al.* [20]. More recently, De Jong *et al.* [16] prepared CoMo-NTA/Al₂O₃ and CoMo-NTA/SiO₂ model catalysts and concluded that these catalysts exhibit activities and product distributions for thiophene HDS similar to those of their high surface area counterparts.

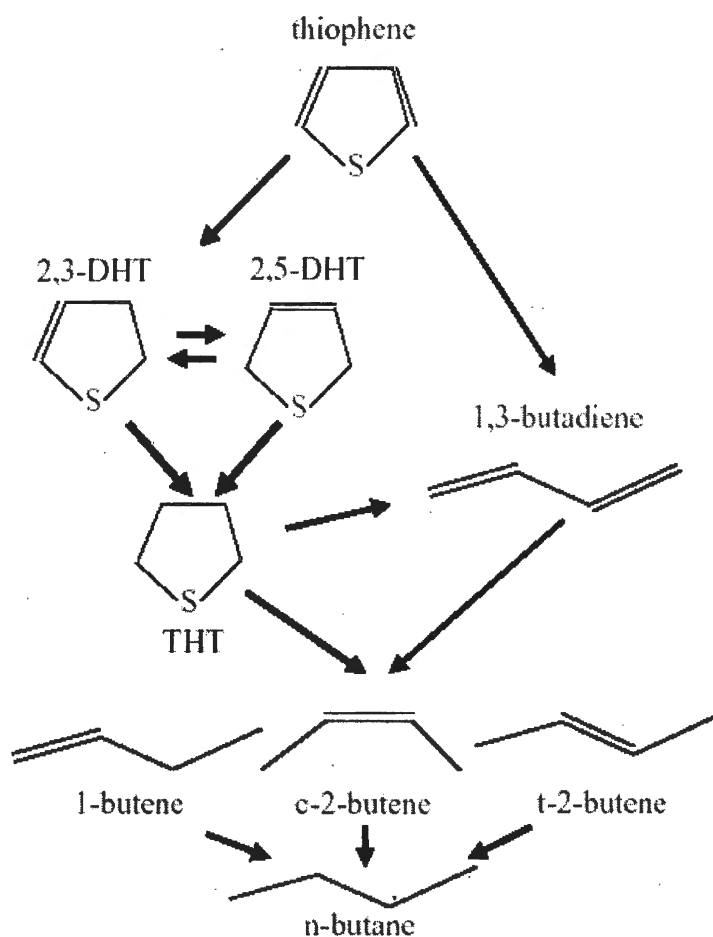


Figure 3. Possible reaction pathways for the desulfurization of thiophene.

Reactivity evaluation

Thiophene is one of the most used model compounds for studying hydrodesulfurization reactivity. Despite intensive research (see [21-23]) there is still debate on the exact reaction

mechanism. The possible reaction paths for thiophene HDS are collected in Figure 3. Direct C-S cleavage was proposed by Lipsch and Schuit [24], whereas others [25,26] have proposed partially hydrogenated intermediates, *i.e.* tetrahydrothiophene (THT) or dihydrothiophenes (DHT), which are very difficult to observe under standard reaction conditions [27]. Recently, low temperature experiments by Hensen et al. [28,29] provided evidence for DHTs and THT as intermediates in thiophene HDS.

EXPERIMENTAL

Preparation of model catalysts

A silica model support was prepared by oxidizing a Si (100) wafer with a diameter of 75 mm in air at 750°C for 24 h. Rutherford back scattering (RBS) measurements indicated that the SiO₂ layer is about 90 nm thick. The roughness of the SiO₂ surface is below 5 Å as derived from AFM experiments. After oxidation the wafer was cleaned in a solution of ammonia and hydrogen peroxide at 65°C for 10 min. The surface was rehydroxylated by boiling in water for 30 min. Cobalt and molybdenum were applied by spincoating the SiO₂/Si (100) wafers at 2800 rpm in N₂ with aqueous solutions of cobalt nitrate (Co(NO₃)₂ · 6H₂O, Merck) and ammonium heptamolybdate ((NH₄)₆Mo₇O₂₄ · 4H₂O, Merck), respectively. The concentration of Co and Mo in the aqueous solutions was adjusted to result in a loading of 2 Co atoms/nm² and 6 Mo atoms/nm² after spincoating, which was checked by RBS. The mixed phase model catalysts were prepared by spincoating with aqueous solutions containing Co and Mo with an atomic ratio of 1:3, respectively. Catalysts containing nitrilo triacetic acid (NTA) were prepared by spincoating ammoniacal solutions containing ammonium heptamolybdate (Merck), cobalt nitrate and NTA (Acros Organics) as described by van Veen *et al.* [30]. The NTA solutions contained Co:Mo:NTA ratios of 1:3:4. Calcination was carried out in a glass reactor under a 20 vol.% O₂ in Ar flow at 1.5 bar. The catalysts were heated to 500°C at a rate of 5°C/min and kept at the desired temperature for 30 min. Sulfidation of the model catalysts was carried out in a glass tube reactor with a mixture of 10 vol.% H₂S in H₂ at a flow rate of 60 ml/min. The catalysts were heated at a rate of 5°C/min (NTA-containing samples: 2 °C/min) to the desired temperature and kept there for 30 min. After sulfidation, the reactor was cooled to room temperature under a helium flow and brought to the glovebox, where the model catalyst was mounted in a transfer vessel for transport to the XPS under N₂ atmosphere.

OP-3 RESULTS

XPS characterization

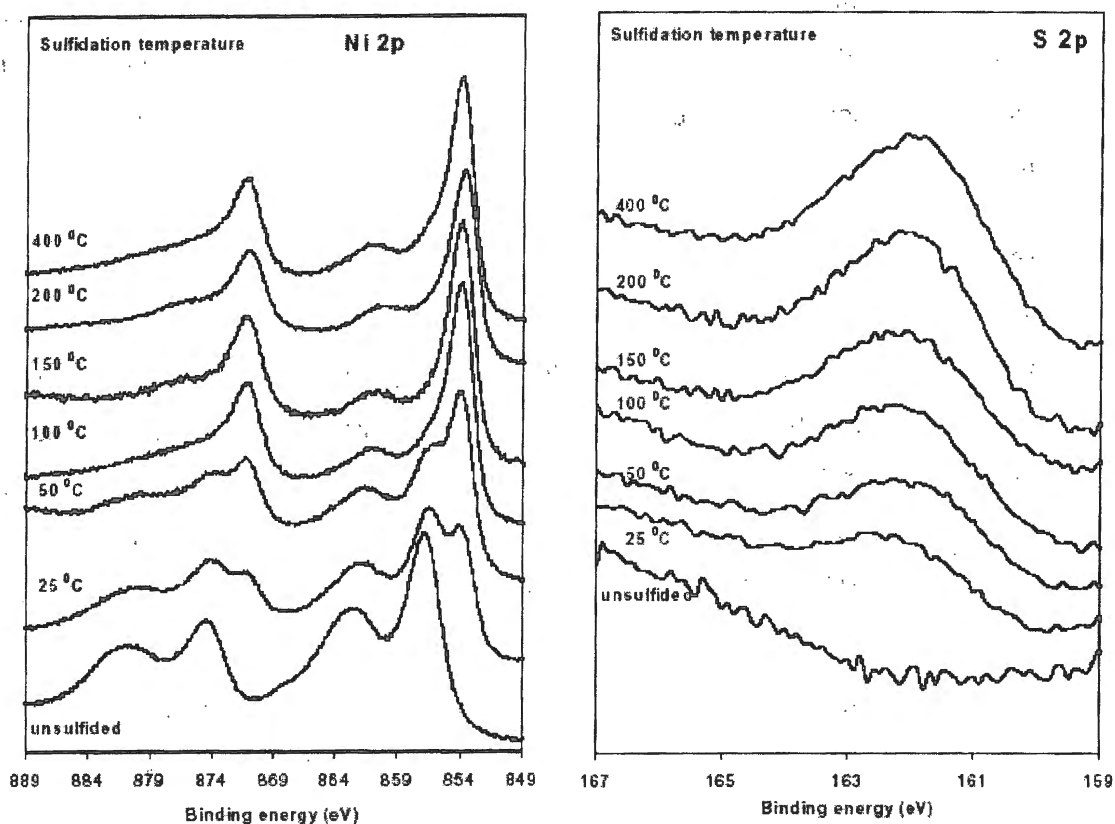


Figure 4. Ni 2p and S 2p spectra of calcined NiO_x/SiO₂/Si(100) sulfided in 10% H₂S/H₂ for 30 min at various temperatures.

The sulfidation behaviour of molybdenum was described in earlier reports [16-18,31,32]. Briefly, the sulfidation of Mo proceeds at moderate temperatures, starting around 50°C. Complete transformation to MoS₂ occurs at temperatures above 150°C. The Mo 3d spectra of the catalysts sulfided at intermediate temperatures can be all interpreted in terms of Mo⁶⁺, Mo⁵⁺ and Mo⁴⁺ doublets as described earlier [16,17]. Addition of chelating agents in the preparation stage did not affect the sulfidation behaviour of Mo significantly.

Figure 4 shows the Ni 2p and S 2p spectra during progressive sulfidation of a calcined NiO_x/SiO₂ model catalyst. The Ni 2p spectrum of the calcined catalyst shows the characteristic pattern of oxidic nickel with a Ni 2p^{3/2} peak at 856.8 eV and a shake up feature at higher binding energy [33]. The binding energy of 856.8 eV corresponds well with that of Ni₂O₃ [33]. Sulfidation at room temperature shows the appearance of a second doublet at lower binding energy. At higher temperatures this doublet increases in intensity, while the doublet with Ni 2p^{3/2} at 856.8 eV decreases and finally disappears at temperatures above 50°C. The Ni 2p^{3/2} peak at 853.8 eV obtained after sulfidation at 400°C corresponds well with

that of bulk Ni_3S_2 [33]. Sulfur is present in the S^{2-} state as derived from the binding energy of 161.8 eV. Ni 2p spectra of a Ni-EDTA/ SiO_2 /Si model (not shown) show that the sulfidation of Ni is retarded to temperatures above 200°C. The sulfidation is complete at 300°C. N 1s spectra indicate that EDTA decomposes at temperatures above 200°C.

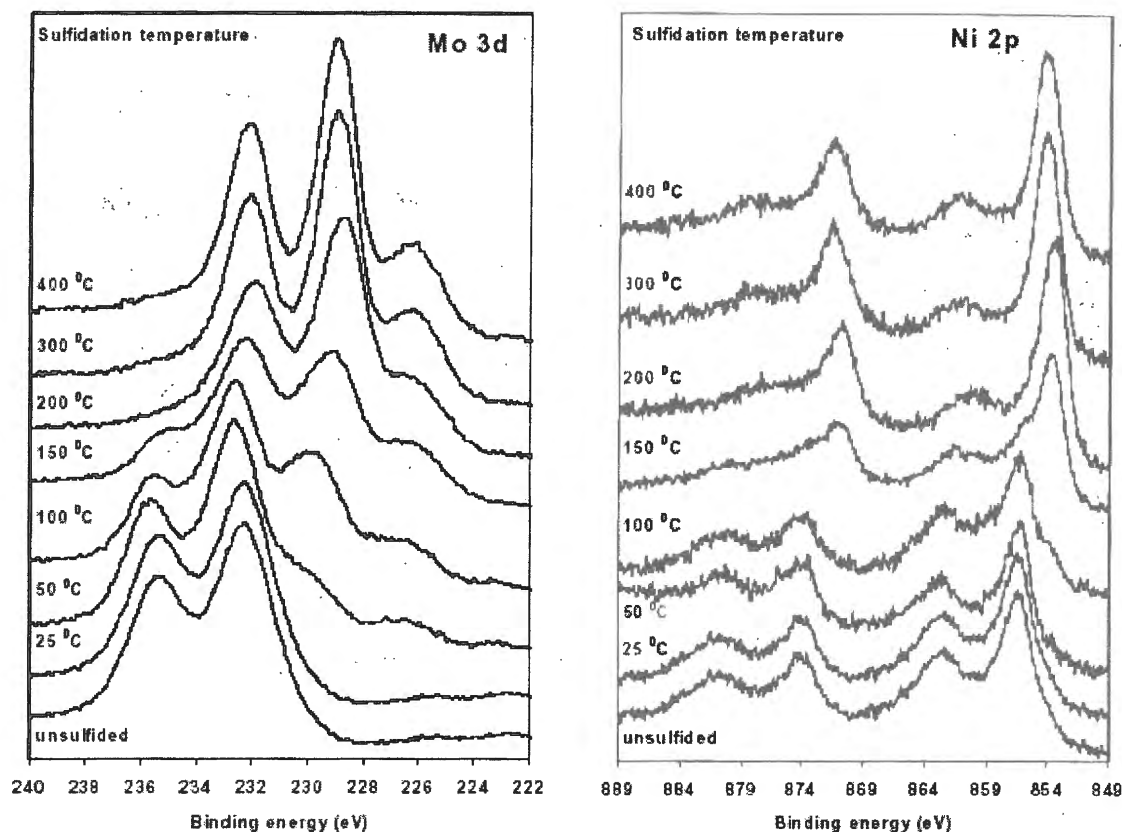


Figure 5. Ni 2p and Mo 3d spectra of calcined NiMo/ SiO_2 /Si(100) sulfidated in 10 % $\text{H}_2\text{S}/\text{H}_2$ for 30 min at various temperatures.

Figure 5 shows the Ni 2p and Mo 3d spectra of NiMo/ SiO_2 at various sulfidation stages. The Mo 3d spectra are identical to those of Mo/ SiO_2 [31]. However, the Ni 2p spectra reveal a much slower conversion of nickel oxide to the sulfided state than for Ni/ SiO_2 . Ni sulfidation only starts at temperatures around 100°C, which is some 75°C higher than for the calcined Ni/ SiO_2 . At these temperatures a second doublet with small shake up features appears at a Ni $2p^{3/2}$ binding energy of 854.2 eV. Above 150°C the sulfidation is complete. A small, but significant higher binding energy for sulfided Ni in NiMo/ SiO_2 compared to that of Ni/ SiO_2 is observed. Comparing Ni and Mo, one observes that the rates of sulfidation are similar, *i.e.* starting around 50°C and being complete between 150°C and 200°C. The XP spectra of uncalcined NiMo/ SiO_2 catalysts (not shown) are similar to those of the single-phase catalysts. Sulfidation of Ni precedes that of Mo, although the temperature regime where sulfidation occurs shows some overlap.

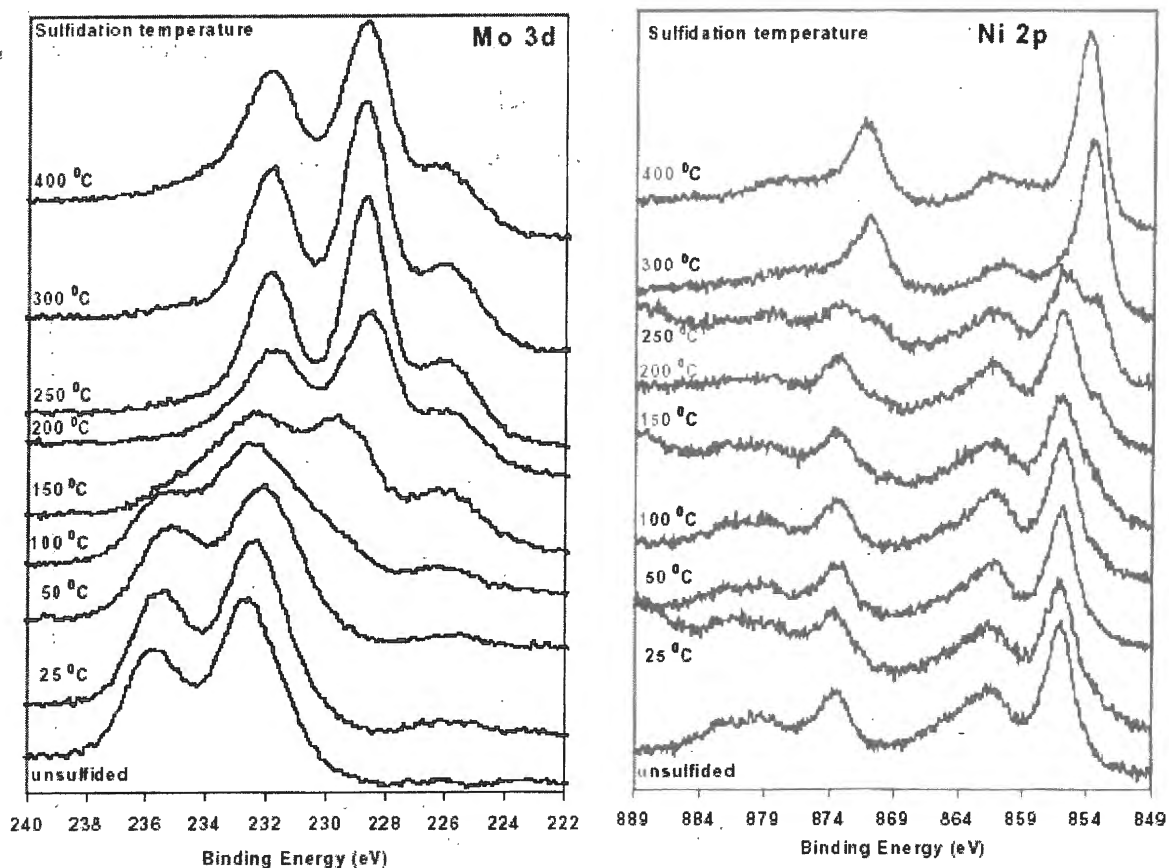


Figure 6. Ni 2p and Mo 3d spectra of calcined NiMo-EDTA/SiO₂/Si(100) sulfided in 10% H₂S/H₂ for 30 min at various temperatures.

Figure 6 shows the Ni 2p and Mo 3d spectra of a NiMo-EDTA/SiO₂ model catalyst. The Mo 3d spectrum of the fresh catalyst shows one doublet with a Mo 3d^{5/2} binding energy of 232.2 eV characteristic of molybdenum complexed to chelating agents. The sulfidation behaviour of Mo is identical to that of Mo in Mo/SiO₂ and NiMo/SiO₂. The doublet with Mo 3d^{5/2} binding energy at 229.0 eV is characteristic for MoS₂. The Ni 2p spectra show that EDTA retards the sulfidation of Ni significantly. The spectrum of the fresh catalyst shows a single doublet with Ni 2p^{3/2} at 856.1 eV, corresponding to Ni complexed to EDTA, and shake up features at higher binding energy. Sulfidation does not start until temperatures around 200 °C where a second doublet at lower binding energy appears. Ni sulfidation is complete at 300 °C. The same sulfidation behaviour was observed for Ni-EDTA/SiO₂ catalysts. Note however that the Ni 2p^{3/2} binding energy of the sulfided Ni in NiMo-EDTA/SiO₂, *i.e.*, 854.1 eV, is 0.3 eV higher than that of the fully sulfided Ni-EDTA/SiO₂ catalyst, *i.e.*, 853.8 eV.

The sulfidation behavior of a NiMo-NTA/SiO₂/Si(100) model catalyst was studied in a similar way (spectra not shown here). While Mo sulfidation proceeded qualitatively in the same way as in NiMo-EDTA/SiO₂ and NiMo/SiO₂, Ni sulfidation is faster than in the EDTA case and starts already at 125 °C. This corresponds well with the sulfidation of Co

in a CoMo-NTA/SiO₂ model catalyst [31]. In contrast to the EDTA case, there exists an overlap in temperature where Ni and Mo are converted to their sulfided state. The Ni 2p^{3/2} binding energy of the nickel in the sulfidic state (854.2 eV) equals that in NiMo-EDTA/SiO₂ and differs from that of bulk nickel sulfide.

Hydrodesulfurization activity measurements

Table 1 compares the thiophene HDS activities of the various model catalysts. The activity is expressed as yield of products per 5 cm² of catalyst after 1 h of batch reaction at 400°C and has been corrected for blank measurements (bare silica support and empty reactor).

TABLE 1 Thiophene conversion after 60 min. at 400°C in batch reactor

Catalyst	Conversion (%)
Mo/SiO ₂ /Si	0.2
NiMo-uncalcined/SiO ₂ /Si	0.7
NiMo-calcined/SiO ₂ /Si	1.1
NiMo-NTA/SiO ₂ /Si	3.5
NiMo-EDTA/SiO ₂ /Si	6.4

The activity of Ni/SiO₂ corresponds to a pseudo turnover frequency of $1.8 \cdot 10^{-3}$ mol thiophene per mol Ni per second. Similar low activities were also found for Ni/SiO₂ and Ni-EDTA/SiO₂ (not shown). The activities of Mo/SiO₂ and Mo-NTA/SiO₂ were similar. The addition of Ni to such catalysts clearly points to the known synergy between these two metals. The activity of calcined NiMo/SiO₂ is higher than that of uncalcined NiMo/SiO₂, which we attribute to an increase in Ni-Mo interaction due to calcination. The highest activities are observed in NiMo/SiO₂ catalysts prepared with chelating agents. NiMo-EDTA/SiO₂ is the most active one amongst the studied catalysts.

DISCUSSION

It is generally accepted that the high activity in CoMo sulfide catalysts derives from the presence of 'Co-Mo-S' type phases. This phase is thought to be present as MoS₂ slabs with Co species located at their edges. Although not proven beyond doubt, 'Ni-Mo-S' analogues of these phases have been proposed [34-36]. Next to these mixed transition metal sulfide phases, also segregated metal sulfides, *i.e.* MoS₂ and Ni₃S₂ may be present with a considerable lower activity. The amount of the different phases will strongly depend on the preparation procedure and the sulfidation mechanism. We will discuss the sulfidation mechanism of the model catalysts under study. While small Ni-sulfide species are mobile and able to adsorb on MoS₂

OP-3

slabs resulting in 'Ni-Mo-S'-type particles, it is expected that large bulky Ni_3S_2 particles redisperse more difficult. In that sense, it appears that sulfidation of Mo prior to Ni leads to a higher amount of 'Ni-Mo-S' phase.

Ni/SiO₂. Ni sulfidation proceeds through progressive oxygen-sulfur exchange. The transformation to the sulfided state is clearly indicated by the shift in the binding energy to lower values. Sulfidation starts already at room temperature and is completed around 100 °C. The resulting phase is most probably Ni_3S_2 and presents a low activity for thiophene HDS. The addition of EDTA hardly affects the thiophene HDS activity, although Ni sulfidation is considerably retarded to higher temperatures.

Mo/SiO₂. Mo sulfidation takes place at moderate temperatures and through different intermediates [17,31]. The sulfidation mechanism proceeds by O-S exchange transforming oxidic Mo into MoS_2 . In the intermediate temperature range Mo^{5+} and oxysulfide species are present [32,37]. These MoS_2 slabs are active in thiophene HDS. No significant differences in activity were found between uncalcined and calcined Mo catalysts. Here, we should note that an alternative explanation for the chelating ligand effect is a decreased Mo-support interactions as forwarded for alumina-supported catalysts [10,38]. On the other hand, silica displays a much lower Mo-support interaction which probably makes this effect of minor importance.

NiMo/SiO₂. The Ni 2p and Mo 3d XP spectra of uncalcined NiMo/SiO₂ are similar to those of the single phase Ni and Mo catalysts. Since no calcination took place, the metals are not in combined phases. Ni sulfidation clearly precedes Mo sulfidation apart from some small overlap. We surmise that the amount of 'Ni-Mo-S' phase is not optimal since part of the nickel will form Ni_3S_2 phases. Although this appears to be of overriding importance, one notes that small Ni-sulfide clusters may redisperse and form 'Ni-Mo-S' and 'Ni-W-S' phases. Calcination of NiMo/SiO₂ prior to sulfidation results in a more active catalyst. Interestingly, the XP spectra show that Ni sulfidation is retarded to higher temperatures and starts around 100°C and being complete around 200°C. We attribute this to a Ni-Mo interaction, which hinders low temperature Ni sulfidation. Similar results were obtained for CoMo/SiO₂ model catalysts [31]. Based on XP spectra of a reference NiMoO_4 sample, we can exclude that this compound is formed upon calcination. Nickelmolybdate has been suggested to be an ineffective precursor for 'Ni-Mo-S' type phases [39]. Although Mo sulfidation still lags behind that of Ni, there is a significantly larger temperature range where Ni and Mo sulfide simultaneously, with a greater chance to form the desired 'Ni-Mo-S' phase. This explains the higher activity of the calcined NiMo/SiO₂ catalyst.

NiMo-EDTA/SiO₂. Ethylene diamine tetraacetic acid (EDTA) - known to form very stable complexes with ions of nickel and cobalt [40] - is the most successful chelating agents with respect to stabilizing nickel against sulfidation. Whereas Mo sulfidation is similar to that of Mo/SiO₂, the sulfidation of Ni is effectively retarded to temperatures above 200°C. Hence, all Mo is present as MoS₂ when the sulfidation of Ni starts. In our simple model, this represents an ideal situation for the formation of a maximum amount of 'Ni-Mo-S' phase. This agrees with the highest thiophene HDS activity for the catalysts under study. The activity is almost two times higher than that of NiMo-NTA/SiO₂. This is in qualitative agreement with Prins et al. [41,42]. Although we surmise that the sulfidation order is most important with respect to the final activity, we cannot exclude that the chelating agents have some effect on the dispersion of MoS₂ particles as well, although one generally observes that NTA addition leads to a somewhat larger MoS₂ crystallite size. A general observation is that there is still a lack of a reliable method to determine the edge dispersion of these catalysts.

NiMo-NTA/SiO₂. Adding NTA to the impregnating solution leads to complexation of Ni and stabilizes Ni against low temperature sulfidation, whereas Mo sulfidation is not strongly affected by the NTA ligands. This leads to a large overlap of Mo and Ni sulfidation (results not shown). In fact, Ni sulfidation starts around 75°C and is completed at about 200°C. This means that both Ni and Mo sulfidation are essentially completed at the same temperature. Although this would provide more efficient 'Ni-Mo-S' formation than in the NTA-free case, it will probably form a lower amount of such species than in the EDTA case. A similar NTA effect was observed earlier for a CoMo/SiO₂ model catalysts [13,14]. The activity of NiMo-NTA/SiO₂ is indeed between those of NiMo/SiO₂ and NiMo-EDTA/SiO₂.

CONCLUSIONS

Planar model catalysts offer new possibilities to study the sulfidation mechanism of hydrotreating catalysts in detail. Combined XPS and thiophene HDS measurements applied to a series of NiMo-based model catalysts on a flat silica support allow one to correlate the sulfidation order of the respective transition metals with their activity. Conventional impregnation leads to a low activity catalyst in which Ni sulfidation proceeds at lower temperatures than Mo. Chelating agents are effective in retarding Ni sulfidation. EDTA is most effective and yields the most active catalyst. It is proposed that in order to form a high amount of the active 'Ni-Mo-S' phase, Mo has to be sulfided to MoS₂ to accommodate small Ni-sulfide particles. If Ni sulfidation takes place at too low temperature, bulky Ni₃S₂ particles are formed with low activity, which are not able to redisperse on MoS₂ edges.

OP-3

REFERENCES

1. J.W. Gosselink, *CatTech* **4** (1998) 127.
2. Auto-Oil II Programme, Commission of the European Communities, Com 626, 2000.
3. J.T. Miller, W. J. Reagan, J.A. Kaduk, C.L. Marshall and A.J. Kropf, *J. Catal.* **193** (2000) 123.
4. U.S. Patent 5851382, 1998; US Patent 5846406, 1998; US Patent 5770046, 1998.
5. B. Höhlein, P. Biedermann, T. Grube and R. Menzer, *J. Power Sources* **84** (1999) 203.
6. Weisser, O., and Landa, S., "Sulphide catalysts, their properties and applications" Pergamon Press, Oxford, 1973.
7. R.R. Chianelli, *Catal. Rev.-Sci. Eng.* **26** (1984) 361.
8. R. Prins, V.H.J. de Beer and G.A. Somorjai, *Catal. Rev.-Sci. Eng.* **31** (1989) 1.
9. B.C. Wiegand and C.M. Friend, *Chem. Rev.* **92** (1992) 491.
10. H. Topsøe, B.S. Clausen and F.E. Massoth, "Hydrotreating catalysis" Springer, Berlin, 1996.
11. S. Eijsbouts, *Appl. Catal. A* **158** (1997) 53.
12. P.L.J. Gunter, J.W. Niemantsverdriet, F.H. Ribeiro and G.A. Somorjai, *Catal. Rev.-Sci. Eng.* **39** (1997) 77.
13. E.W. Kuipers, C. Laszlo and W. Wieldraaijer, *Catal. Lett.* **17** (1993) 71.
14. R.M. van Hardeveld, P.L.J. Gunter, L.J. van IJzendoorn, W. Wieldraaijer, E.W. Kuipers and J.W. Niemantsverdriet, *Appl. Surf. Sci.* **84** (1995) 339.
15. P.C. Thüne, Ph.D. thesis, Eindhoven University of Technology, The Netherlands, 2000.
16. A.M. de Jong, V.H.J. de Beer, J.A.R. van Veen and J.W. Niemantsverdriet, *J. Phys. Chem.* **100** (1996) 17722.
17. A.M. de Jong, H.J. Borg, L.J. van IJzendoorn, V.G.M.F. Soudant, V.H.J. de Beer, J.A.R. van Veen and J.W. Niemantsverdriet, *J. Phys. Chem.* **97** (1993) 6477.
18. J.C. Muijsers, Th. Weber, R.M. van Hardeveld, H.W. Zandbergen and J.W. Niemantsverdriet, *J. Catal.* **157** (1995) 698.
19. J.W. Niemantsverdriet, "Spectroscopy in Catalysis: An Introduction", VCH, Weinheim, 1993.
20. P. Arnoldy, J.A.M. van den Heijkant, G.D. de Bok and J.A. Moulijn, *J. Catal.* **92** (1985) 35.
21. M.L. Vrinat, *Appl. Catal.* **6** (1983) 137.
22. H. Schulz, M. Schon and N. Rahman, *Stud. Surf. Sci. Catal.* **27** (1986) 201.
23. A.N. Startsev, *Catal. Rev.-Sci. Eng.* **37** (1995) 353.
24. J.M.J.G. Lipsch and G.C.A. Schuit, *J. Catal.* **15** (1969) 179.
25. J. Kraus and M. Zdrzil, *React. Kinet. Catal. Lett.* **6** (1977) 475.

26. E.J. Markel, G.L. Schrader, N.N. Sauer and R.J. Angelici, *J. Catal.* **116** (1989) 11.
27. B.T. Carvill and M.J. Thompson, *Appl. Catal.* **75** (1991) 249.
28. E.J.M. Hensen, M.J. Vissenberg, V.H.J. de Beer, J.A.R. van Veen and R.A. van Santen, *J. Catal.* **163** (1996) 429.
29. E.J.M. Hensen, H.J.A. Brans, G.M.H.J. Lardinois, V.H.J. de Beer, J.A.R. van Veen, and R.A. van Santen, *J. Catal.* **192** (2000) 98.
30. J.A.R. van Veen, E. Gerkema, A.M. van der Kraan and A. Knoester, *J. Chem. Soc. Chem. Commun.* **22** (1987) 1684.
31. L. Coulier, V.H.J. de Beer, J.A.R. van Veen, and J.W. Niemantsverdriet, *Topics in Catal.* **13** (2000) 99.
32. Th. Weber, J.C. Muijsers, J.H.M.C. van Wolput, C.P.J. Verhagen, and J.W. Niemantsverdriet, *J. Phys. Chem.* **100** (1996) 14144.
33. J.F. Moulder, W.F. Stickle, P.E. Sobol, and K.D. Bomben, "Handbook of XPS", Perkin Elmer Corporation, Eden Prairie, MN, 1992.
34. N.-Y. Topsøe and H. Topsøe, *J. Catal.* **84** (1983) 386.
35. S.P.A. Louwers and R. Prins, *J. Catal.* **133** (1992) 94.
36. J.A.R. van Veen, H.A. Colijn, P.A.J.M. Hendriks and A.J. van Welsenens, *Fuel Proc. Technol.* **35** (1993) 137.
37. Th. Weber, J.C. Muijsers, and J.W. Niemantsverdriet, *J. Phys. Chem.* **99** (1995) 9194.
38. E.J.M. Hensen, V.H.J. de Beer, J.A.R. van Veen and R.A. van Santen, submitted to *Catalysis Letters*.
39. B. Scheffer, J.C.M. de Jonge, P. Arnoldy, and J.A. Moulijn, *Bull. Soc. Chim. Belg.* **93** (1984) 751.
40. L.G. Silen, and A.E. Martell, *Stability constants of metal-complexes vol. 2*, Chemical Society, London, 1964.
41. R. Cattaneo, T. Shido, and R. Prins, *J. Catal.* **185** (1999) 199.
42. R. Cattaneo, Th. Weber, T. Shido, and R. Prins, *J. Catal.* **191** (2000) 225.

E. R. Savinova^(1,2), U. Stimming⁽²⁾

⁽¹⁾*Boriskov Institute of Catalysis SB RAS, Pr. Lavrentieva 5, 630090 Novosibirsk, Russia*

⁽²⁾*Technische Universitaet Muenchen, James-Franck-Str. 1, D-85748 Garching bei Muenchen, Germany*

Direct methanol fuel cells (DMFC) are an attractive means of energy conversion, holding a number of advantages, in particular high efficiency of the fuel conversion, low emission of pollutants, availability of methanol either through natural gas processing or from biomass and high specific energy density of methanol as a fuel. DMFCs are currently being proposed as an alternative to the combustion engine for automotive applications and for portable power sources. Despite numerous efforts, the performance of DMFCs is still far from being satisfactory for practical applications. The limitations of the DMFCs reside in the yet low efficiency of the electrode materials and in the methanol permeation (crossover) through the membrane, which reduces the voltage output of the cell and poisons the cathode. In the present paper we will concentrate on the catalytic processes occurring at the anode and cathode sides of a DMFC. Recent efforts to develop methanol-resistant RuSe cathode catalysts will be highlighted along with the insights into the mechanism of their operation and origin of their tolerance to methanol. On the anode side, we will focus on the structural effects in model and technical carbon-supported Pt and PtRu fuel cell catalysts. An impact of the structure on the methanol oxidation activity and CO tolerance will be analyzed and the prospects for the development of highly efficient catalysts for low temperature DMFCs will be outlined.

**RELATIONSHIP BETWEEN SURFACE PROPERTIES OF MODIFIED
TITANOXIDES AND THEIR CATALYTIC PROPERTIES IN THE REACTION OF
ETHOXYLATION OF ETHYLENE OXIDE**

**R.A.Kozlovskiy^a, V.F.Shvets^a, A.V.Koustov^a, L.E.Kitaev^b, V.V.Yushchenko^b,
V.V.Kriventsov^c, D.I.Kochubey^c, M.V.Tsodikov^d**

^a *D.I.Mendeleev University of Chemical-Technology of Russia, Miusskaya square 9,
125047, Moscow, Russia ; tel/fax (095)978-9554; e-mail: kra@muctr.edu.ru*

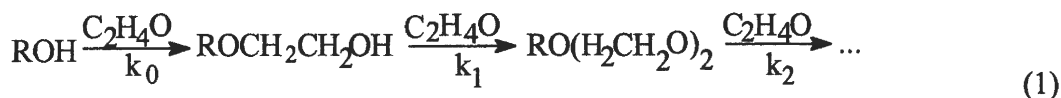
^b *M.V. Lomonosov Moscow State University, Chemical Department, Leninskii Hills,
119899, Moscow, Russia*

^c *Boreskov Institute of Catalysis SB RAS, Pr. Acad. Lavrentyeva, 5, 630090
Novosibirsk, Russia*

^d *A.V.Topchiev Institute of Petrochemical Synthesis RAS, 117912, Leninskii prospect, 29,
Moscow, Russia*

Introduction

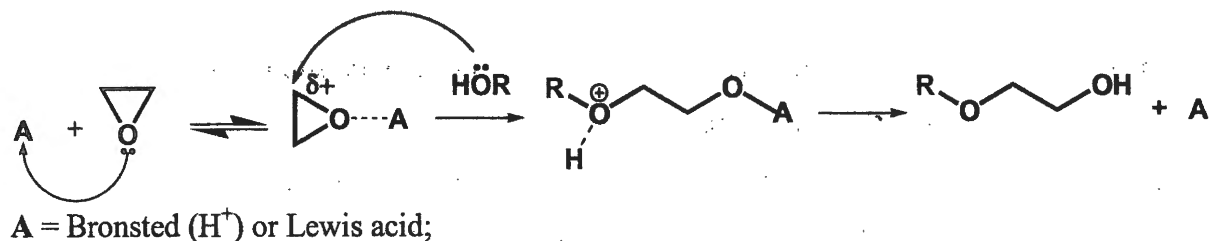
Reaction of ethoxylation of hydroxy-groups of alcohols lies in a base of many large-scale industrial processes:



in the case of ethylene glycol: R = HOCH₂CH₂-

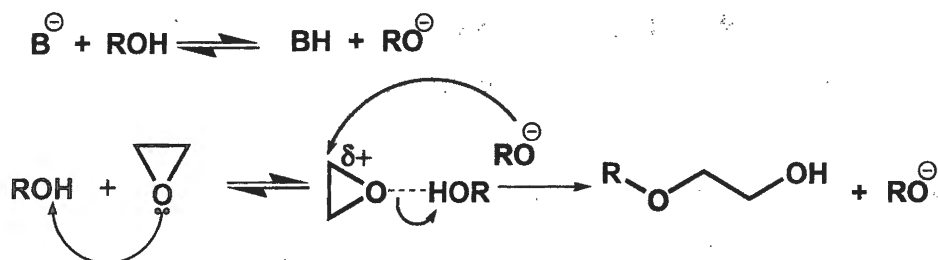
This reaction can proceed by an acid catalytic, base catalytic and noncatalytic way. All of these mechanisms are well investigated for homogeneous conditions [1-3]:

Acid catalysis:

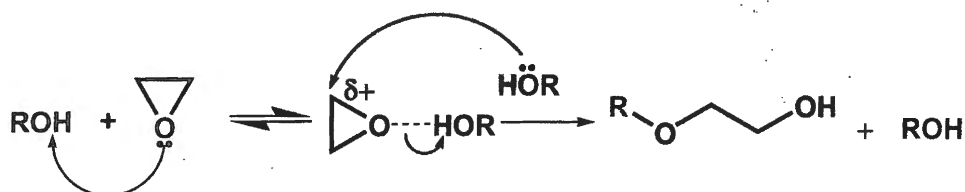


OP-5

Base catalysis:



Noncatalytic:



The effectiveness of each of these three processes is composed of two components: the rate of reaction and the selectivity. According to a value of reaction rate these processes can be arranged in the following row:

Noncatalytic < *Base catalysis* < *Acid catalysis*

The selectivity of product's formation depends on ratio of rates of consecutive stages of reaction (1) and usually is characterized by *distribution factor* (C_i) [2,4] that is equal to ratio of rate constant of corresponding stage of reaction (1) to rate constant of first stage:

$$C_i = k_i/k_0$$

So the less is the value of C_i the higher is selectivity of formation of corresponding product. For the three above mentioned mechanisms average magnitude of *distribution factor* for ethoxylation of primary alcohols is:

Acid catalysis: $C_i \approx 1$

Base catalysis: $C_i \approx 2-4$

Noncatalytic: $C_i \approx 1$

In addition there are two side reactions – ethylene oxide isomerization to acetaldehyde and dimerization to 1,4-dioxane, in the case of acidic catalysis.

Modified titanoxides synthesized by alkoxo-method using the organic derivatives of phosphoric acid as precursors, as it was shown by professor Tsodikov et al. [5,6], are a high organized nanocluster systems. So such systems are highly convenient for investigation of mechanism of reaction of ethylene glycol ethoxylation proceeding on the surface of solid.

Results and discussion

The series of kinetic experiments, with Cu-modified titanooxide systems differing in ratio of rutile and anatase showed that only system with 100% anatase structure has highest catalytic activity (Fig. 1). So only systems with 100% anatase structure were prepared for all following experiments.

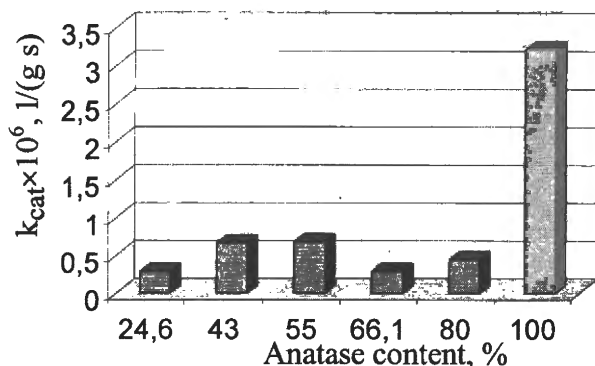


Figure 1. Changes of rate constant of catalytic reaction of etoxylation of ethylene glycol (k_{cat}) vs. content of anatase (%) in Cu-modified TiO_2 .

The precursors which were used for preparation of modified titanooxides and their phase composition and crystal lattice parameters determined by X-Ray diffraction are listed in the Table 1.

Parameters of the porous structure determined by nitrogen vapor adsorption isotherms are listed in the Table 1 as well. The specific surface area (S) was calculated using the BET method. The average pore sizes (r) were determined under the assumption of a slot-like geometry of the pores. The theoretical isotherms of polymolecular adsorption calculated by BET in coordinates *amount of adsorbate* (a) vs. *number of monomolecular layers* (n) are given in Fig. 2. Analysis of the plots shown in Fig. 2 (existence of only single break on the curves) shows that all systems are characterized by homogeneous distribution of pore sizes: around 0.8-0.9 nm for phosphorous-containing system (samples 1, 2, 10) and around 1.8-1.9 nm for metal-containing systems (samples 3, 4, 9).

The data of temperature-programmed desorption (TPD) of ammonia (Fig. 3) allowed to determine concentration of acidic sites on surface of solids (Table 2). All acidic sites were distributed to three regions depending on energy of activation of desorption (E_d): $E_d \leq 90$ kJ/mol – weak-acidic sites; 90 kJ/mol $< E_d < 130$ kJ/mol – moderate-acidic sites; $E_d \geq 130$ kJ/mol – strong-acidic sites (Table 2).

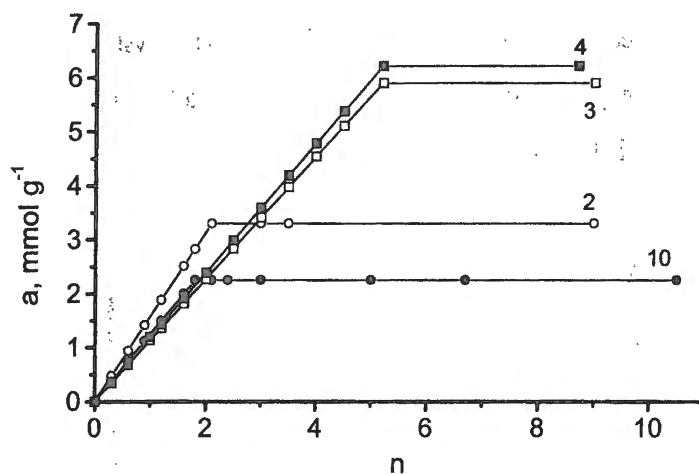


Figure 2. Changes of concentration of N_2 adsorbed (a) vs. number of monomolecular layers (n).
(Number of line corresponds to number of sample)

As it follows from data of Table 2, the doping by phosphorus leads to rising of acidity of titanooxides. This fact corresponds with XANES data showing the rising of effective positive charge of titanium atom (Fig. 4).

The experimental values of rate constant of catalytic reaction of ethyleneglycol ethoxylation at 115°C (k_{cat}), distribution factors (C) and selectivity of diethylene glycol conversion to ethylene oxide ($S_{\text{DEG}}^{\text{EO}}$) at initial molar ratio (ethylene oxide): (ethylene glycol) = 0.5 are listed in Table 2.

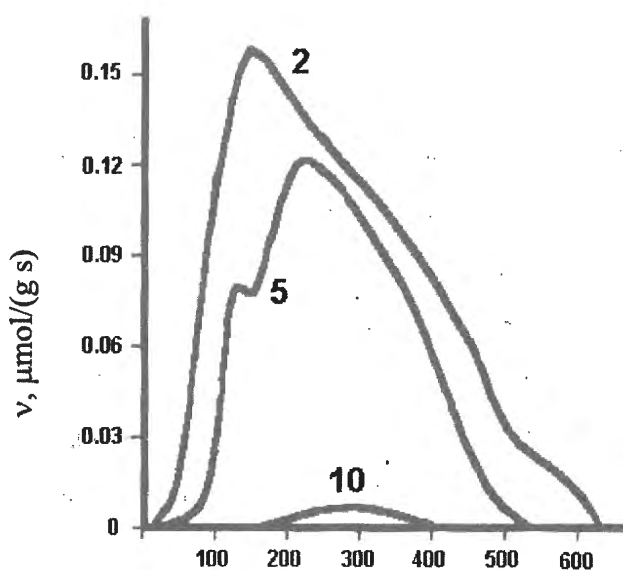


Figure 3. Temperature-programmed desorption of NH_3 . Number of curve corresponds to number of sample.

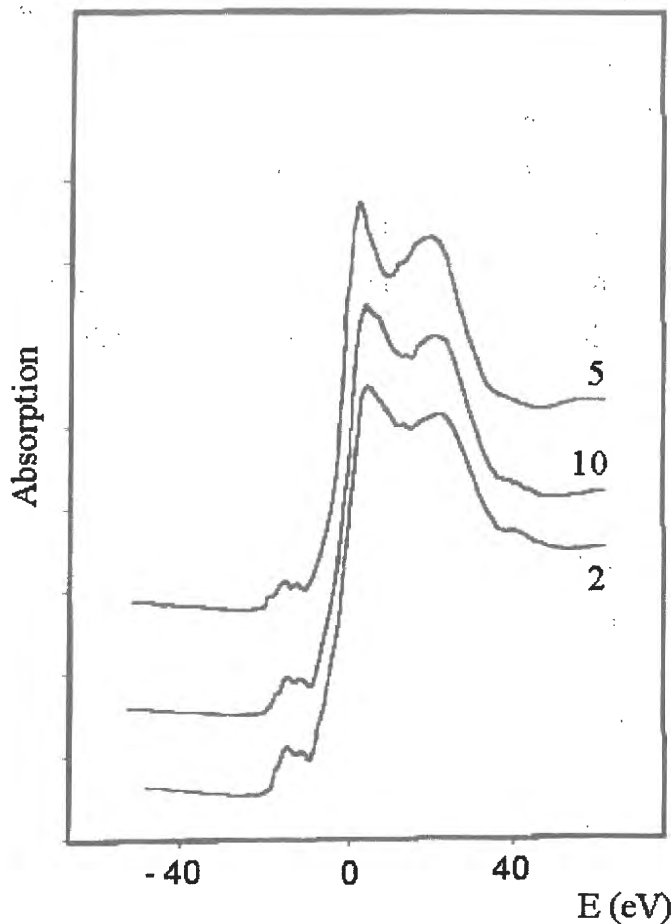


Figure 4. Titanium k-edge XANES spectra for titanate systems: samples 2, 5, 10.

Sample No	5	10	2
I (rel. un.)	0.07	0.072	0.125

Data of Table 2 show that titanooxide systems which have maximum number of acidic sites (samples 1, 2, 8) provide the highest catalytic activity. But in contrast to P-modified titanooxides the Al-modified catalyst (sample 8) yields 1,4-dioxan, that indicates that nature of acidity of the surface of these solids is different. It corresponds with the fact that during the experiment of TPD of ammonia on sample 8 some amount of NH_3 does not desorb even at temperature 600°C and higher.

As to selectivity of the reaction of ethoxylation of ethylene glycol the distribution factor for Al-modified titanooxide (sample 8) is equal 1.02, that is close to experimental one for homogeneous acid catalyzed reaction of ethoxylation of ethylene glycol (Table 2).

Above mentioned facts allow to suppose existing of strong Bronsted acidic sites on the surface of Al-modified titanooxide.

OP-5

The unique selectivity was obtained in case of P-modified titanoxides. The distribution factors for samples 1-4 are in a range of 0.37-0.52. Such level of distribution factor can not be achieved neither at acidic nor basic homogeneous catalysis (Table 2).

In this connection it is interesting to note that spectra of TPD of CO₂ for samples 1 and 2 have narrow peaks in region of 120°C, that indicates the existence of basic sites of uniform strength on their is surface (Fig. 5). Samples 1 and 2 demonstrate the combination of high activity and high selectivity (in other words the highest catalytic efficiency among all titanoxides tested).

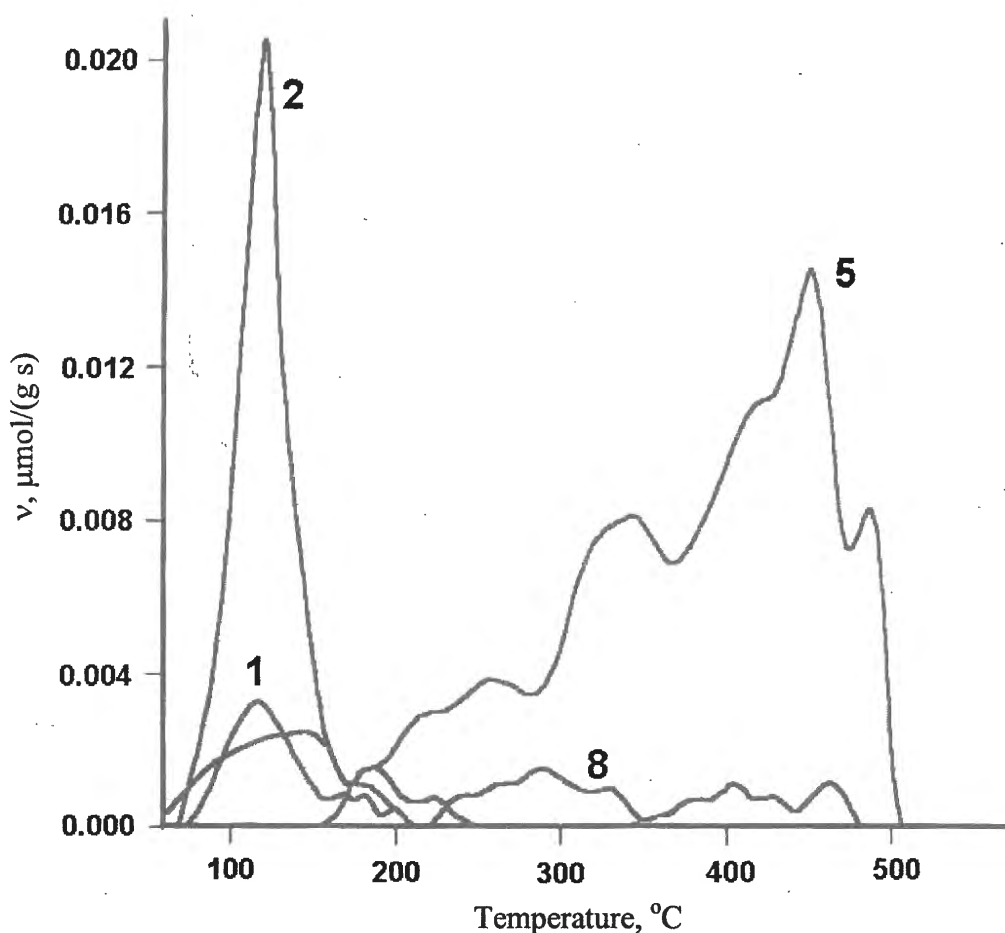
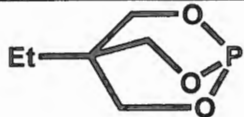
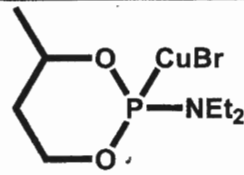


Figure 5. Temperature-programmed desorption of CO₂. Number of curve corresponds to the number of sample.

Table 1. Structural and porous properties of titanooxides

N° of Sample	Precursor	X-Ray diffraction			Parameters of porous structure		
		Oxide's composition	C, nm	Average microcrystallite size (D), nm	S, m ² /g	V, cm ³ /g	r, nm
1	2	3	4	5	6	7	8
6	Ti(OBu) ₄	TiO ₂ (rutile + anatase)					
5	Ti(OBu) ₄	TiO ₂ (anatase)	0.947	39.7	3.2	0.009	3.0
10		P _{0.07} Ti _{0.94} O _{2-δ}	0.941	8.2	83	0.082	0.9
3		Cu _{0.07} P _{0.07} Ti _{0.88} O _{2-δ}	0.944	10.5	85	0.15	1.9

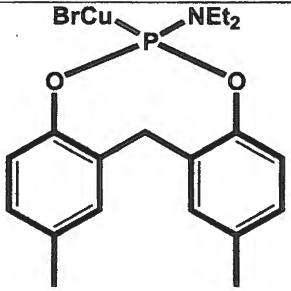
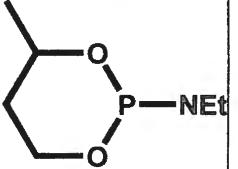
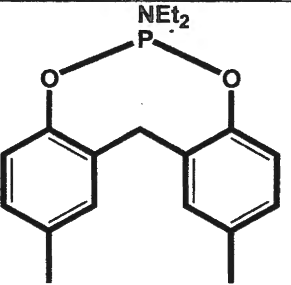
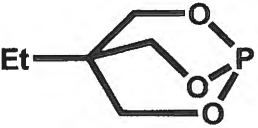
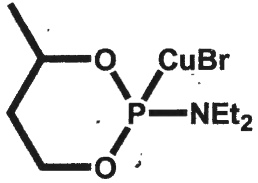
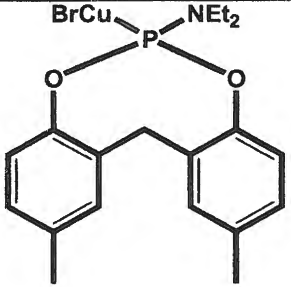
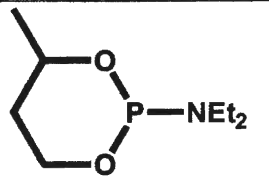
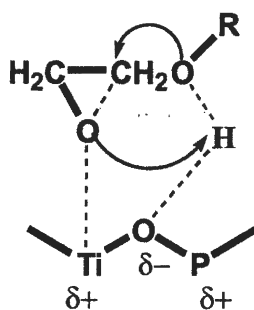
	2	3	4	5	6	7	8
4		$\text{Cu}_{0.07}\text{P}_{0.07}\text{Ti}_{0.88}\text{O}_{2-\delta}$	0.94 5	12.9	93	0.2 6	1.8
1		$\text{P}_{0.07}\text{Ti}_{0.91}\text{O}_{2-\delta}$	0.94 5	7.7	91	0.1 1	0.8
2		$\text{P}_{0.07}\text{Ti}_{0.91}\text{O}_{2-\delta}$	0.94 1	7.6	16 0	0.1 2	0.9
8	$\text{Al}_2(\text{SO}_4)_3 \times 18$ H_2O	$\text{Al}_{0.09}\text{Ti}_{0.93}\text{O}_{2-\delta}$ $(\text{SO}_x)_y$					

Table 2. Acidity and catalytic properties of titanooxides

N° of Sample	Precursor	Distribution of acidic sites over the activation energy of desorption (E_d , kJ/mol) of the ammonia, $\mu\text{mol/g}$				$k_{\text{cat}} \times 10^{-4}$, l/(g s)	Distribution factor, C	Selectivity, $S_{\text{DEG}}^{\text{EO}}$
		Overall capacity, (a_0)	$E_d \leq 90$	$90 < E_d < 130$	$E_d \geq 130$			
1	2	3	4	5	6	7	8	
6	Ti(OBu) ₄					0.0	0.9	62.9
5	Ti(OBu) ₄					0.00008	0.9	62.9
10						0.0015	0.78	65.9
3		324	71	249	4	0.3	0.52	73.7

4		300	78	222	0	0.5	0.37	79.3
1		386	67	306	13	2.1	0.38	78.9

On the base of these facts the mechanism of simultaneous acid-base catalysis of ethylene oxide's ring opening on the surface of P-modified titanoxides can be supposed:



And at last one more reason of so high selectivity that P-modified titanoxides demonstrate may be sieve effect due to the limiting of accessibility of active sites located in pores of these catalysts for reaction products.

To estimate contribution of each type of acidic sites (Table 2) to overall catalytic activity, the experimental rate constant of catalytic reaction was described by following equation using least-squares method:

$$k_{\text{cat}} = \sum_{j=1}^3 a_j k_{aj}$$

where: a_j – concentration of acidic sites of j -th region, ($\mu\text{mol/g}$); k_{aj} – specific regional constant of rate in j -th region, ($l/(\mu\text{mol s})$).

The diagram on Fig. 6 shows a satisfactory conformity of experimental and calculated rate constants of catalytic reaction.

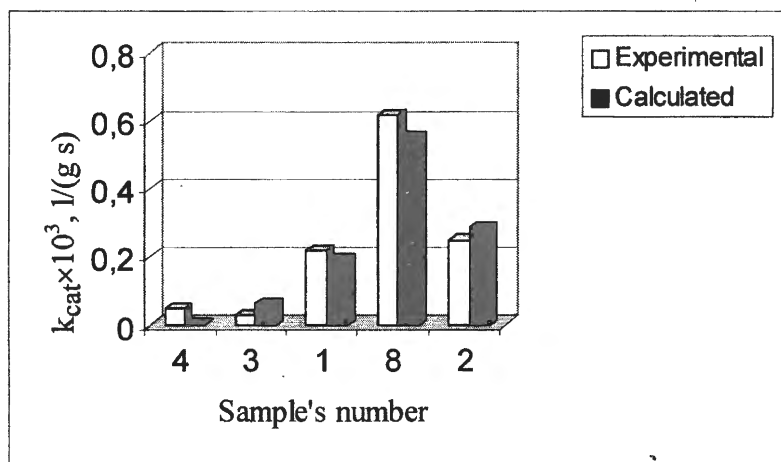


Figure 5. Experimental and calculated rate constants of catalytic reaction (k_{cat})

The calculated values of k_{aj} are: $k_{a1} = 3 \times 10^{-8}$; $k_{a2} = 2.3 \times 10^{-17}$; $k_{a3} = 1.5 \times 10^{-5}$ ($l/(\mu\text{mol s})$). As it follows from results obtained ($k_{a3} \gg k_{a1} \gg k_{a2}$) the exactly strong acidic sites

OP-5

provide a governing contribution to overall catalytic activity of modified titanooxides systems in the reaction of ethoxylation of ethylene glycol.

Acknowledgments

The authors wish thank the Russian Fundation for Basic Research (RFBR) Project 000332407A.

References

1. N.Schounfeldt, Grenzflächenaktive Athylenoxid, MBH, Stuttgart, 1976.
2. M.Nico, V.Os, Nonionic Surfactants, Surfactant science series, V.72, Marcel Dekker Inc., New York, 1998.
3. N.N.Lebedev, V.P.Savelyanov, Yu.I.Baranov, Zh. Prikl. Khim., 42 (1969) 1815.
4. B.Weibull, B.Nycander, Acta Chem.Scand, 8 (1954) 847.
5. M.V.Tsodicov, O.V.Bukhtenko, E.B.Slivinskiy, L.N.Slastikhina, A.M.Voloshuk, V.V.Kriventsov, L.E.Kitaev, Izvestiya RAN (Ser. khim), 11 (2000) 1829.
6. M.V.Tsodicov, E.B.Slivinskiy, V.V.Yushenko, L.E.Kitaev, V.V.Kriventsov, D.I.Kochubey, A.T.Teleshev, Izvestiya RAN (Ser. khim), 12 (2000) 2037.

INVESTIGATION OF HETEROGENEOUS CATALYTIC REACTIONS BY THE *IN SITU* ^1H NMR MICROIMAGING

A.A. Lysova^{1,2,3}, I.V. Koptug¹, A.V. Kulikov², V.A. Kirillov², V.N. Parmon²,
R.Z. Sagdeev¹

¹*International Tomography Center, Institutskaya St. 3A, Novosibirsk 630090, Russia*

²*Boreskov Institute of Catalysis SB RAS, Pr. Acad. Lavrentiev 5, Novosibirsk 630090, Russia*

³*Novosibirsk State University, Pirogova St. 2, Novosibirsk 630090, Russia*

Tel: 7 (3832) 333561, fax: 7 (3832) 343269, e-mail: lysova@tomo.ncs.ru

Abstract

The NMR microimaging is used for the first time as an *in situ* method to study two model three-phase heterogeneous catalytic reactions with strong exothermicity. It is shown for the α -methylstyrene hydrogenation that in the course of the reaction, two domains coexist inside the catalyst grain which differ in the liquid phase content. The 2D maps of the liquid distribution in the course of this reaction are obtained. The reaction of the hydrogen peroxide decomposition at moderate activity of the catalyst and the H_2O_2 concentrations in the range of (0.03-3) M is shown to occur only in a thin layer near the catalyst surface. The influence of the medium inhomogeneity on the behavior of the BZ chemical oscillator reaction is investigated as well.

Introduction

Heterogeneous catalytic processes occur inside the porous catalyst grains and are affected strongly by the spatial distributions of reagent, intermediate and product concentrations, temperatures, etc., which are specific for each catalyst and each reaction. The experimental investigation of the spatial organisation and progress of catalytic processes inside catalyst grains seem to be accessible only by the application of an *in situ* imaging methods.

Recently, a number of tomographic methods has been suggested for a direct visualisation of chemical processes inside catalyst grains. The ^1H NMR imaging has been shown in the last years as a powerful nondestructive method for the *in situ* studies of various physical-chemical processes in porous media, e.g. liquid sorption and desorption [1,2]. A much more challenging task is to apply the ^1H NMR imaging for studying *in situ* some chemical reactions, especially those inside porous catalyst pellets.

OP-6

In our study we have applied for the first time the NMR microimaging for the *in situ* investigation of three heterogeneous catalytic reactions in order to visualise the progress of these reactions inside the catalyst grains, including the catalytic processes at elevated temperatures. Besides, NMR flow imaging which can yield liquid and gas flow velocities [3,4] was employed to demonstrate the possibility to observe the convection of liquid outside the catalyst grain induced by a catalytic reaction.

As the first objects of the investigation we have selected several model heterogeneous catalytic processes such as hydrogen peroxide decomposition and α -methylstyrene hydrogenation. These catalytic processes proceed inside the catalyst grain in the three-phase regime. The NMR imaging allows to visualise the content of the liquid phase and its distribution within the grain and thus to get information on the catalyst state during the progress of the catalytic reaction.

The investigation of the reactions mentioned above is of both theoretical as well as practical interest. Indeed, many heterogeneous catalytic reactions in industry, especially in petrochemical synthesis, occur in the reactors with the fixed bed of catalyst and the co- or counter-current gas-liquid flow. Usually such reactors work in the stationary regime, but under certain conditions the occurrence of dangerous critical phenomena such as hot spot formation, temperature and phase composition oscillations, exothermic reaction by-passing is possible. All this can result in a rapid heating of the catalyst grain because of the possibility of porous structure drying and a subsequent reaction acceleration due to transition of reaction from a liquid phase to a gaseous phase. Such processes are known to lead to the reactor runaway [5].

Thus, it is highly desirable to investigate experimentally the critical phenomena on a porous catalyst grain under conditions of an exothermic reaction which is accompanied by evaporation in order to determine the safety conditions of the reactor operation. In particular, it is important to investigate the distribution of the liquid phase inside the porous catalyst grain, the dynamics of the grain drying for an exothermic reaction and particle runaway.

The state of the catalyst grain in the reactors with the fixed catalyst bed and the co-current gas-liquid downward flow is studied using the exothermic α -methylstyrene hydrogenation mentioned above as a representative example. As a different example, we have investigated also the three-phase exothermic reaction of hydrogen peroxide decomposition. Also, we studied some peculiarities of the occurrence of the Belousov-Zhabotinsky (BZ) reaction in an inhomogeneous medium.

Experimental part

All ^1H NMR microimaging experiments were performed at 299 MHz on a Bruker DRX spectrometer equipped with a vertical bore superconducting magnet and an imaging add-on device capable of providing pulsed magnetic field gradients of up to 100 G/cm.

Acquisition of the spatially resolved images by the ^1H NMR microimaging method is based on the use of the pulsed magnetic field gradients [6-8]. Since the resonance frequency of the NMR signal depends linearly on the strength of the magnetic field applied to the sample, the resonance frequency becomes the function of the nuclear spin coordinate along the direction of the gradient when the field gradient is turned on. This allows to determine the distribution of the spin density (the quantity of a substance) in the sample under study with the spatial resolution of some hundreds or even some tens of microns. The use of the selective radio-frequency pulses with the magnetic field gradients allows one to detect only the NMR signal of those nuclear spins which are located within a slice of a certain thickness and orientation. This gives a possibility to obtain a two-dimensional projection of the selected slice which characterises the distribution of the substance in the slice plane. Sufficiently short nuclear spin relaxation times of solid materials and low density of gas and vapour in the experiments ensure that only the NMR signal of the liquid phase is detected.

Catalytic decomposition of hydrogen peroxide

The NMR imaging experiments were carried out on an individual $\text{Ag}/\gamma\text{-Al}_2\text{O}_3$ catalyst grain. The impregnation with silver was performed from a salt solution, after that the grain was calcined at high temperature. The initial $\gamma\text{-Al}_2\text{O}_3$ had $134\text{ m}^2/\text{g}$ surface area and $0.31\text{ cm}^3/\text{g}$ pore volume. The experiments were carried out at an atmospheric pressure and an ambient temperature. The H_2O_2 solution of 3 M concentration was prepared from the 30% H_2O_2 by its dilution with distilled water.

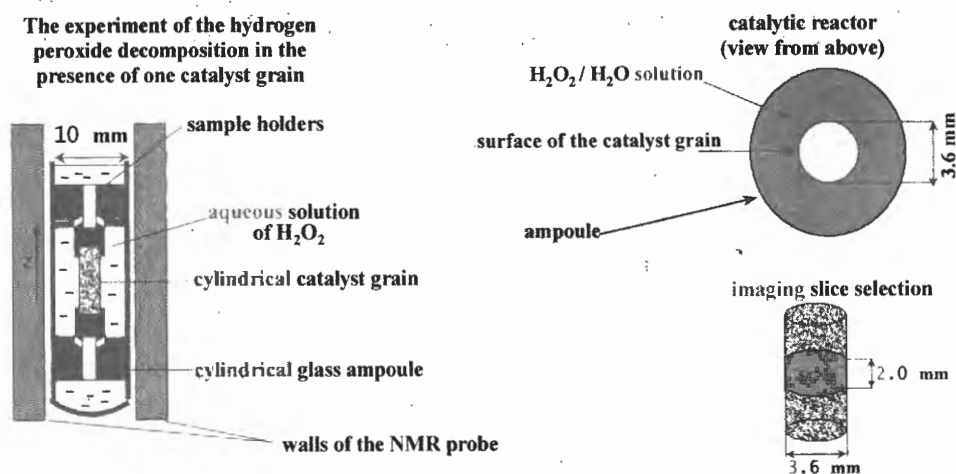


Fig. 1. A scheme of the imaging experiments on the hydrogen peroxide decomposition.

OP-6

A catalytic cell which was placed in an NMR probe is shown in Fig. 1. A cylindrical grain of the catalyst (diameter 3.6 mm) was located in the centre of a glass ampoule (inner diameter 9 mm). The grain was placed into the aqueous solution of H_2O_2 . The sample holders contained several holes so that the dioxygen gas produced in the reaction could escape from the reactive volume. We obtained two-dimensional projections of the NMR signal intensity in the plane perpendicular to the axis of the grain (Fig. 2). This figure demonstrates the dynamics of the dioxygen bubble formation on the grain surface and the evolution of the O_2 bubbles in the course of the hydrogen peroxide decomposition. The NMR signal of water outside the grain was initially partially suppressed by the fast repetition of the pulse sequence of the experiment, and thus the area outside the grain appears dark. The colour outside the grain is seen to become lighter (i.e., the signal of water protons outside the grain becomes stronger) during the first minutes of the experiments due to shortening of the T_1 time of water protons which results from the release of the paramagnetic dioxygen molecules into water.

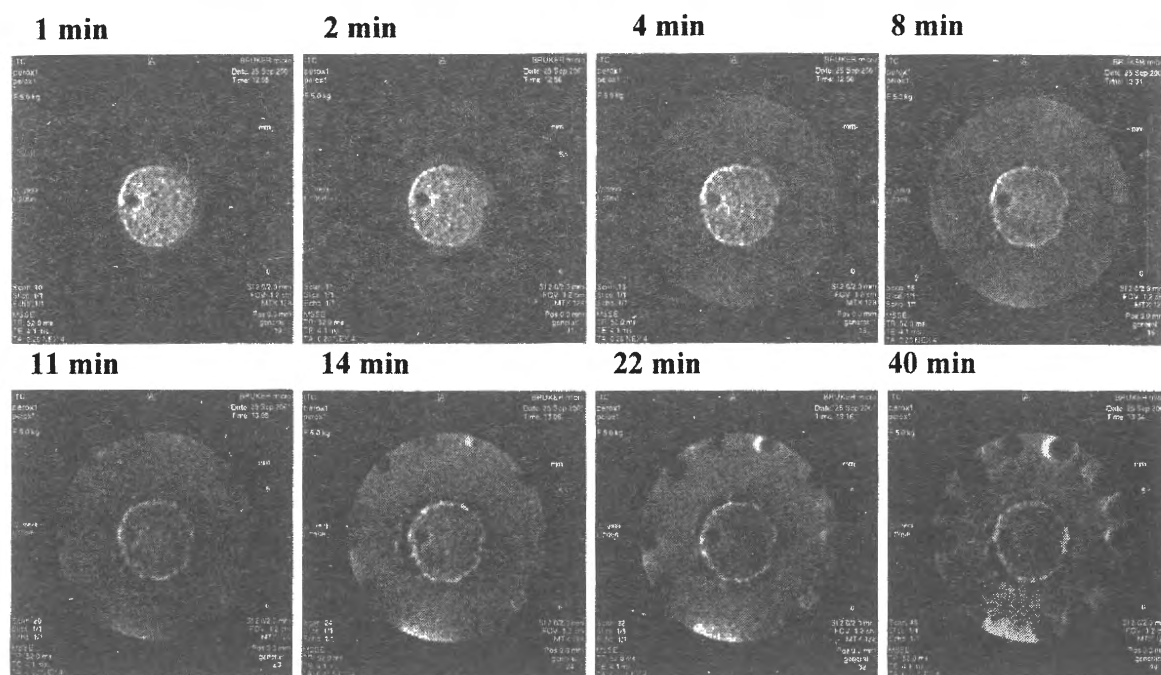


Fig. 2. Formation and evolution of the dioxygen bubbles in the course of the hydrogen peroxide decomposition over $Ag/\gamma-Al_2O_3$: two-dimensional projections.

The detection time of each projection is 27 s. The time corresponding to each two-dimensional projection is specified in the figure. 128×128 pixels correspond to $(1.2 \times 1.2) \text{ cm}^2$. The spatial resolution is $SR = (90 \times 90) \mu\text{m}^2$.

Note, that the dioxygen concentration appears to increase uniformly in the entire volume of the liquid. It means that during the time between the detection of the first and the second 2D images (1 min) the dioxygen molecules have enough time to travel from the grain surface to the ampoule wall (the distance is equal to 3.2 mm). The coefficient of the dioxygen

diffusion calculated from these data appear to be significantly greater than the corresponding reference data [9].

Thus, we think that the evolved dioxygen molecules are transferred by a convection flow rather than due to diffusion. To verify this we have carried out the experiment which confirms the existence of a convection flow of the liquid along the catalyst grain because of the vigorous bubble formation on the grain surface (Fig. 3). In this figure, the spatial map of the flow velocities of water flowing along the catalyst grain is depicted. One can see that near the grain surface where the bubble formation occurs, the liquid flow is upwards while near the ampoule walls it moves in the opposite direction. The velocity of the convective liquid transfer is ca. 0.2-0.3 mm/s. Since the height of the grain is 15 mm, during the time between the detection of the first and the second 2D projections a uniform concentration of dioxygen can be established in the entire volume of the liquid.

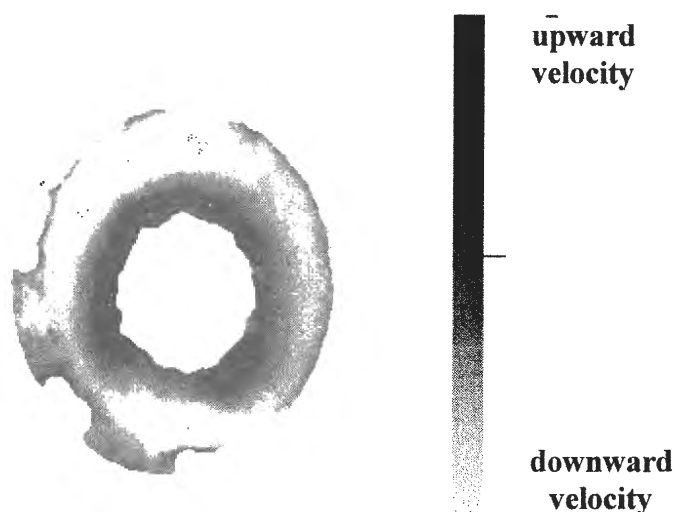


Fig. 3. A typical spatial map of the flow velocities of water flowing along the cylindrical catalyst grain in the course of the hydrogen peroxide decomposition

We have carried out experiments intended to establish the state of the grain in the course of the hydrogen peroxide decomposition. For these experiments, a composite catalyst grain consisted of an activated part and a non-activated part was prepared. Such composite grain is necessary to perform a meaningful comparison of the one-dimensional projections of the liquid content in the activated and the non-activated parts of the grain in the course of hydrogen peroxide decomposition, see Fig. 4. In the NMR imaging experiments, by changing the resonance frequency we could reposition the selected slice so that the interleaved detection of the separate projections of the slices in the activated and non-activated parts of the grain could be performed (see Fig. 4).

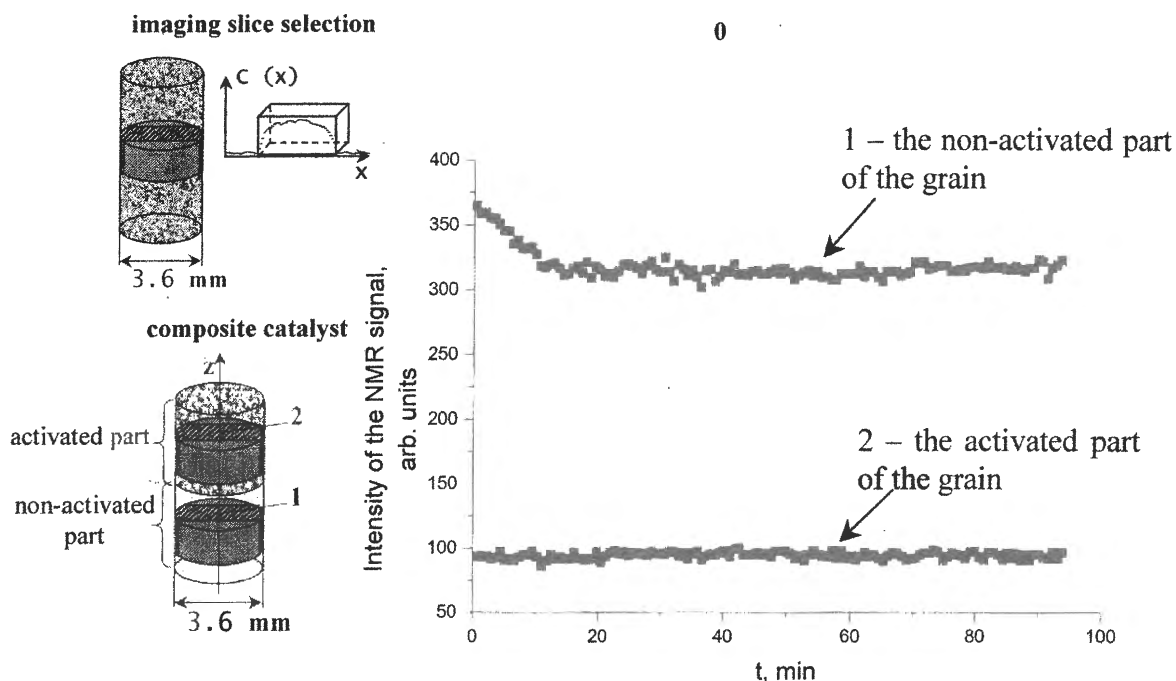


Fig. 4. The change of the NMR signal intensity in the center of the composite $\text{Ag}/\gamma\text{-Al}_2\text{O}_3$ catalyst grain in the course of the 3 M H_2O_2 decomposition.

The composite catalyst grain was initially filled with water and then placed into the 3 M H_2O_2 solution. Since the T_2 relaxation time of the H_2O_2 aqueous solution is much shorter than the T_2 relaxation time of pure water, the signal intensity in the non-activated part of the grain decreases after immersing the grain into the H_2O_2 solution due to the hydrogen peroxide diffusion into the grain (Fig. 4, curve 1). An estimation of the H_2O_2 diffusion coefficient from this curve gives $1.5 \cdot 10^{-5} \text{ cm}^2/\text{s}$ that is about two times lower than the self-diffusion coefficient of the water molecules. It is known that the diffusion coefficient in the porous medium is lower than in the bulk liquid by a factor which is equal to the ratio of the porosity and tortuosity of the medium (a factor of 2-3 for $\gamma\text{-Al}_2\text{O}_3$).

One can see that the intensity of the NMR signal inside the activated part of the grain practically does not change during the experiment in contrast to the non-activated part of the grain (Fig. 4, curve 2). It means that under the experimental conditions, hydrogen peroxide does not diffuse into the catalyst grain in the course of the reaction and that the decomposition occurs only in a thin surface layer of the grain. Thus, the ^1H NMR imaging of the hydrogen peroxide catalytic decomposition shows that for the 0.03-3 M hydrogen peroxide concentrations at moderate activity of the catalysts.

Catalytic hydrogenation of α -methylstyrene

The most interesting results concern the three-phase exothermic catalytic reaction of the α -methylstyrene (AMS) hydrogenation. For the first time we have carried out the experiments under conditions when the operating reactor was placed directly inside the NMR imaging probe. Note that the experiments were carried out for the first time at elevated temperatures (the gas flow temperature was 68 °C and the pellet temperature was 185°C).

It is known [5] that α -methylstyrene hydrogenation (boiling point 165°C) to cumene (boiling point 152°C) inside a porous catalyst grain can proceed in several stationary heat regimes: (i) when the catalyst grain is situated in the stream of dry hydrogen and the liquid reagent is supplied simultaneously, the process is characterized by a hysteresis of the grain temperature. In this case, the grain temperature on the upper branch of the hysteresis curve is higher than the temperature of the flowing gas, while on the lower branch it is lower than the temperature of the flowing gas; (ii) when the catalyst grain is positioned in the stream of hydrogen gas saturated with α -methylstyrene vapour, and simultaneously the liquid reagent supplied, the grain in the stationary regime is either practically dry and strongly overheated or flooded with the liquid phase. In the latter case, the grain temperature is equal to the temperature of the flowing gas.

The earlier studies of these regimes were carried out by monitoring the grain temperature with thermocouples [5]. For a chemical reaction accompanied by the liquid phase evaporation, such monitoring gives only the indirect possibility to observe the distribution of the liquid phase inside the porous structure. In our work, the different regimes of the catalyst grain operation mentioned above were investigated to characterise experimentally the liquid phase distribution inside the porous particle directly in the course of the catalytic reaction.

The experiments were carried out on an individual cylindrical catalyst grain of 15(wt)% Pt/ γ -Al₂O₃ (diameter 4.7 mm and height 4.7 mm). The catalyst has the specific surface area of 206 m²/g and the pore volume of 0.65 cm³/g. AMS and gaseous hydrogen was used without a preliminary purification.

A scheme of the catalytic reactor which was placed directly into the NMR probe is shown in Fig. 5. The 2D projections of a 2 mm thick axial slice of the grain saturated with the liquid phase are obtained with the in-plane spatial resolution of 230×140 μ m². The acquisition time of each image was 4 min-22 s. The time corresponding to the middle of the detection period of each image is indicated in Fig.6. A stream of hydrogen heated to 67-69°C and saturated with AMS was supplied to the pellet at the flow rate of 18.5 cm³/s. A thermocouple was implanted into the pellet through its left side and appears in the images as an area void of signal (see Fig. 6).

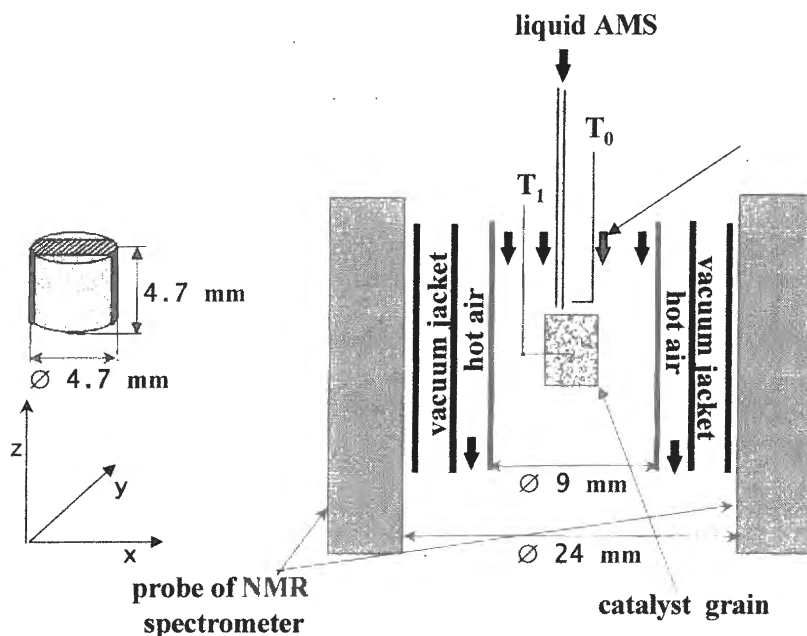


Fig. 5. A scheme of NMR imaging of the AMS hydrogenation. The location of the central slice within the grain in which the distribution of the liquid phase in the course of the experiment was detected is shown.

One can see that the pellet temperature raised 40°C above that of the gas due to the exothermic nature of the reaction. The grain temperature is also shown in Fig. 6. The first image in Fig. 6 shows the existence of the liquid phase within the pellet even though no liquid is supplied to the pellet at this stage, possibly due to the adsorption/condensation of AMS and cumene within the pores. Then, before the detection of the second image was stated, a supply of liquid AMS to the top of the pellet via a capillary was turned on (the flow of liquid AMS was 0.43×10^{-3} g/s). This led to the increase of the liquid content in the pellet (Fig. 6, image 2).

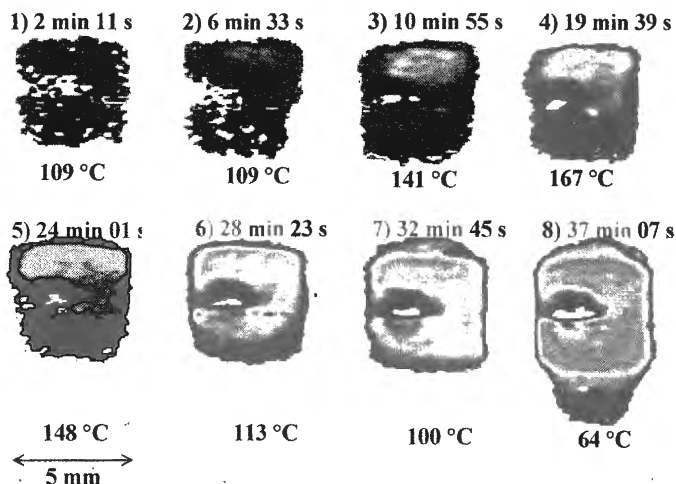


Fig. 6. The spatial distribution of the liquid phase inside the Pt/ γ -Al₂O₃ catalyst pellet in the course of the AMS hydrogenation under conditions of the simultaneous supply on the dry heated grain of the liquid AMS and hydrogen saturated with AMS vapour. See text for the details.

The brighter color of the image corresponds to the stronger NMR signal intensity and therefore to a higher liquid concentration, while the darker shade of the image corresponds to the weaker signal intensity and to the smaller liquid content. In the upper part of the grain to which liquid AMS is permanently supplied, the NMR signal intensity is much stronger than in the lower part of the grain. This corresponds to the higher liquid phase content in the upper part of the grain. The NMR signal intensity is lower in the periphery of the grain as a result of the evaporation process that occurs in this part of the grain. The evaporation front of the liquid is located inside the catalyst grain and the vapor produced reacts on the non-wetted part of the porous structure. This leads to a temperature increase (from 141°C at 11 min of the experiment to 167°C at 20 min of the experiment). The increase of the liquid AMS supply up to 0.57×10^{-3} g/s was made during the detection of the 4th. As a result, the evaporation front moves deeper into the grain and the grain temperature decreases to 113°C (image 6). In this regime the catalyst grain is almost completely filled with the liquid phase. A narrow front of evaporation and the vapor-phase reaction is located near the lower end of the grain. The front of the liquid phase propagation inside the grain is uneven. It is bound with the intensive evaporation process and hydrogenation process. The front of the liquid phase propagation deep into the grain in the experiment without the reaction (without hydrogen supply) is even.

When the liquid AMS supply was increased to 0.71×10^{-3} g/s the grain became completely filled with the liquid (image 7). The grain temperature decreased rapidly to 64°C which is lower than the gas flow temperature (image 8). It is related with the absence of the reaction in the gas-vapor phase and endothermic evaporation of the liquid phase from the catalyst grain surface. On the lower end of the pellets a drop of the liquid is formed.

The other regimes of the reaction proceeding on the individual catalyst grain were also investigated: (i) We have obtained several images illustrating the dynamics of the liquid phase distribution inside the catalyst grain when dry hydrogen flow is used with the simultaneous supply of liquid AMS; (ii) The distribution of the liquid phase inside the catalyst grain in the course of the AMS hydrogenation under conditions of the decreasing of the liquid AMS supply to the grain initially fully saturated with liquid AMS was studied.

Thus, the *in situ* NMR imaging demonstrates that impregnation of the porous catalyst with a liquid reagent under conditions of the simultaneous endothermic reagent evaporation and its exothermic hydrogenation can lead to the formation, inside the catalyst grain, of the two domains with the strongly differing liquid phase content: the upper part of the grain completely filled with the liquid phase and the lower part of the grain which is almost dry and

OP-6

filled with the gas-vapor phase where the vapor-phase hydrogenation occurs. The evaporation process occurs at the boundary between these two domains inside the grain. The location of the boundary depends on the liquid flow rate, thermal conductivity of the grain, and the ratio of the evaporation and hydrogenation rates.

The Belousov-Zhabotinsky reaction in homogeneous and heterogeneous media

There are only a few publications concerning the use of the NMR imaging to study chemical reactions, mostly the polymerisation processes and the oscillating Belousov-Zhabotinsky (BZ) reaction [10,11]. The latter reaction is the oxidation of some organic compounds by bromate-anions catalysed by transition metals ions. This reaction is characterised by the oscillations of the reactant concentrations and the generation of propagating waves due to an inherent coupling of the molecular diffusion and the chemical reaction.

All reported NMR imaging investigations of the BZ reaction were performed in homogeneous media in the presence of agar-agar in order to prevent the distortion of chemical waves by convective flow of the liquid solvent. We have studied the BZ reaction in a homogeneous medium modified with starch. The oscillations of the homogeneous catalyst (Mn^{2+}) concentration were recorded as changes in the water protons relaxation times because the oxidised and reduced states of the manganese cations have different influence on these times.

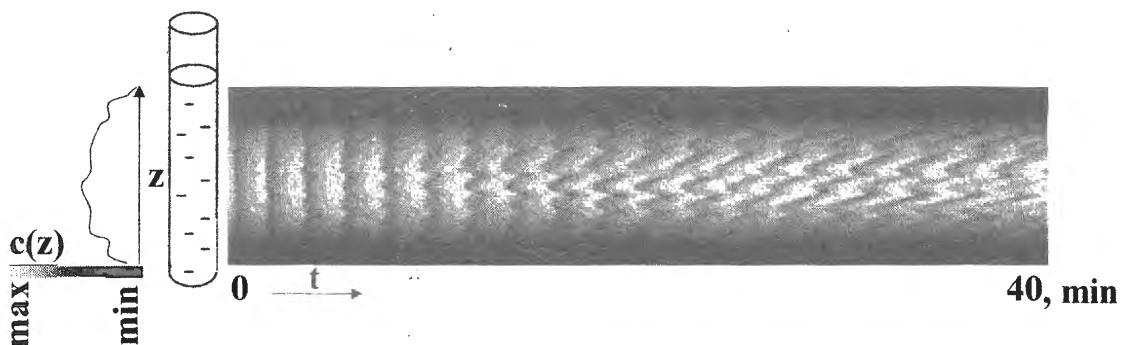


Fig. 7. Displacement-time graphs in the starch solution of the following starting composition: $[\text{KBrO}_3] = 0.05 \text{ M}$, $[\text{KBr}] = 0.06 \text{ M}$, $[\text{MA}] = 0.15 \text{ M}$, $[\text{MnSO}_4] = 0.0006 \text{ M}$, $[\text{H}_2\text{SO}_4] = 0.2 \text{ M}$, $[\text{H}_3\text{PO}_4] = 3.0 \text{ M}$, 0.7 wt % starch.

Fig. 7 shows the propagation of the concentration waves in the homogeneous reaction medium stabilised by starch. The figure shows the one-dimensional projections of the signal intensity on the vertical axis of a 4.7 mm glass ampoule filled with the reaction medium. The space resolution of the image patterns in these projections was $320 \mu\text{m}$. The acquisition time of each projection was 3.2 s. The signal intensity in each pixel of the image depends on the concentrations of Mn^{2+} and Mn^{3+} ions. It is known that the Mn^{2+} ions affect the T_1 relaxation time of water protons much stronger than the Mn^{3+} ions. Since we carried out the experiment

in such a way that the contrast of the images was governed by the T_1 time, the brighter shade in the image corresponds to a higher Mn^{2+} concentration while the darker shade corresponds to the higher Mn^{3+} concentration. It is obvious that the waves are emitted periodically by at least several pacemakers. Each pacemaker emits a spherical wave, and we see in Fig. 7 two branches of the wave, that are the projections of the upper and lower boundaries of a spherical wave. The downward moving front of the wave that was emitted by one of the pacemakers collides and annihilates with another upwards travelling wave emitted by another pacemaker. The plane in which the pacemaker is located as well as the plane in which the wave trains collide and annihilate move down with time.

We studied also the behaviour of the propagating waves inside model porous media consisted of small glass beads of 0.5 and 3 mm in diameter and filled with an aqueous solution. In such system, we also observed formation of spherical propagating waves. The velocity of the waves practically does not depend on the size of the beads and remains practically constant in comparison with the homogeneous reaction media stabilised by starch. Indeed the velocity v of the wave front in a reaction diffusion system is proportional to $(kD)^{1/2}$ [11], where k is the rate constant of the rate-determining step in an autocatalytic sequence and D is the diffusion coefficient of the autocatalytic species. It is known that in heterogeneous system D depends on the ratio of porosity and tortuosity of the grains, this ratio being only weakly dependent on the size of the beads. Also, one can assume that D in heterogeneous systems consisting of the beads is close to that in the homogeneous media stabilized by starch. Thus, the replacement of the starch stabilized homogeneous medium by the heterogeneous system consisting of small beads influence the behavior of the system only slightly.

Conclusion

The above results demonstrate the first application of the 1H NMR imaging to the *in situ* investigation of model heterogeneous catalytic reactions. The NMR imaging investigation was carried out for different systems and demonstrates its productivity.

Acknowledgment

The work was supported by grants of the Russian Foundation for Basic Research (02-03-32770, 00-15-97446, 00-15-97450) and of the Siberian Branch of the Russian Academy of Sciences (Integration project #46). A.A. Lysova gratefully acknowledges a scholarship awarded by the Zamaraev International Charitable Scientific Foundation.

OP-6

References

1. I.V. Koptyug, V.B. Fenelonov, L.Yu. Khitrina, R.Z. Sagdeev, V.N. Parmon, *In situ NMR Imaging Studies of the Drying Kinetics of Porous Catalysts Support Pellets*, Journal of Physical Chemistry B, 102, 3090, 1998.
2. I.V. Koptyug, S.I. Kabanikhin, K.T. Iskakov, V.B. Fenelonov, L.Yu. Khitrina, R.Z. Sagdeev, V.N. Parmon, *A Quantitative NMR Imaging Study of Mass Transport in Porous Solids During Drying*, Chemical Engineering Science, 55, 1559, 2000.
3. I.V. Koptyug, L.Yu. Ilyina, A.V. Matveev, R.Z. Sagdeev, V.N. Parmon, S.A. Altobelli, *Liquid and gas flow and related phenomena in monolithic catalysts studied by ^1H NMR microimaging*, Catalysis Today, 69, pp. 385-392, 2001.
4. E. Fukushima, *Nuclear magnetic resonance as a tool to study flow*, Annual Reviews, 31, pp. 95-123, 1999.
5. A.V. Kulikov, N.A. Kuzin, A.V. Shogarov, V.A. Kirillov, A.E. Kronberg, K.R. Westerterp, *Experimental study of vaporization effect on steady state and dynamic behavior of catalytic pellets*, Catalysis Today, 66, pp. 255-262, 2001.
6. P.T. Callaghan, *Principles of Nuclear Magnetic Resonance Microscopy*, Oxford: Clarendon Press, 1991. 369 p.
7. W. Kuhn, *Angew. Chem. Int.*, Ed. Engl., 29, pp. 1-19, 1990.
8. S.L. Talagala, I.J. Lowe, *Concepts Magn. Reson.*, 3, pp. 145-159, 1991.
9. A. Tzalmona, R.L. Armstrong, M. Menzinger, A. Cross, C. Lemaire, *Chemical Physics Letters*, 174, p. 199, 1990.
10. Y. Gao, A.R. Cross, R.L. Armstrong, *Journal of Physical Chemistry*, 100, p. 10159, 1996.
11. L. Kuhnert, H.J. Krug, L. Pohlmann, *Journal of Physical Chemistry*, 89, p. 2022, 1985.

THE APPLICATION OF MÖSSBAUER EMISSION SPECTROSCOPY TO INDUSTRIAL COBALT BASED FISCHER-TROPSCH CATALYSTS

M.W.J. Craje¹, A.M. van der Kraan¹, J. van de Loosdrecht² and P.J. van Berge²

¹ *Interfacultair Reactor Instituut, Delft University of Technology, Mekelweg 15, 2629 JB Delft*

² *Sasol Technology (Pty) Ltd, PO Box 1, Sasolburg 1948, South Africa*

For several environmental reasons the Fischer-Tropsch synthesis has regained world-wide attention. In the Fischer-Tropsch process transportation fuels are produced from CO and H₂, known as synthesis gas, and therefore provides a means to produce transportation fuels with very low concentrations of hetero-atoms like sulphur, nitrogen and heavy metals. The Fischer-Tropsch synthesis forms an integral part of the Gas-To-Liquids (GTL) process, which is currently receiving serious attention as a way of exploiting remote gas fields and/or associated gas at crude oil production fields, i.e. gas that is currently being flared. The Fischer-Tropsch process (i.e. coal based) has been applied commercially for several decades, using precipitated and fused Fe catalysts. However, the lifetime of the Fe catalysts is limited and the disposal of the catalysts causes environmental pollution. To overcome these problems, cobalt has received widespread attention [1-3] as preferred catalyst in the GTL process. Metallic cobalt is the active catalytic phase. During Fischer-Tropsch synthesis, supported cobalt catalysts may deactivate due to oxidation of the metallic cobalt. The oxidation of cobalt has been studied in the literature [4], but the analytical techniques used were always ex-situ. As the validity of these analytical tools can be questioned, there is still a need for a feasible in-situ technique that can determine the extent of oxidation under realistic Fischer-Tropsch conditions.

Mössbauer Emission Spectroscopy (MES) is one of the few techniques that can be considered for in-situ characterisation studies of supported cobalt based Fischer-Tropsch catalysts. In this study it is shown that MES can be used for in-situ analysis during model experiments at atmospheric pressure and low water partial pressures. For the characterisation under real industrial conditions by means of MES (catalyst contains radioactive ⁵⁷Co) a reactor has been designed that enables long-term (deactivation) studies at pressures up to 20 bar and at temperatures up to 773 K. The design of this reactor and preliminary results will be presented.

[1] B. Eisberg and R.A. Fiato, *Natural Gas Conversion V, Studies in Surface Science and Catalysis*, Vol. 199 (1998) 961-966.

[2] M.M.G. Senden, A.D. Punt, A. Hoek, *Natural Gas Conversion V, Studies in Surface Science and Catalysis*, Vol. 199 (1998) 943-948.

[3] P.J. van Berge, S. Barradas, J. van de Loosdrecht, and J.L. Visagie, *Erdöll Ergas Kohle* 117:3 (2001) 138-142.

[4] D. Schanke, A.M. Hilmen, E. Bergene, K. Kinmari, E. Rutter, E. Adanes, and A. Holmen, *Catal. Lett.* Vol. 34 (1995) 26.

A.N. Salanov and A.I. Titkov

Boriskov Institute of Catalysis SB RAS, Prospekt Akademika Lavrentieva 5, Novosibirsk 630090, Russia

Various ordered adsorption structures are developed during chemisorption of gases on single crystal surfaces at relatively low temperatures of solid surfaces ($\leq 500-700$ K), when diffusion of chemisorbed species through the surface is limited considerably. Ordered adsorption structures are formed due to the distinct surface structure and to the balance between the energies of the adsorbate/surface bonds and the energy of interaction between chemisorbed species. Structural transformations in adsorbed layers have a significant effect on chemisorption and catalytic reactions, therefore the mechanisms of formation and evolution of adsorption structures are of particular interest. At the limited surface diffusion of chemisorbed species, during chemisorption, the formation of adsorption structures usually proceeds according to the island scenario. At the beginning of the chemisorption adsorption islands are nucleated, grow gradually and merge into a continuous layer. Islands with a more dense structure are nucleated within this layer; they also grow, merge and form another continuous adsorption layer with a more dense structure. The studies of O_2 chemisorption on Pd(100), Rh(100) and Ni(100) by LEED revealed the nucleation and growth of $p(2 \times 2)$ adsorption islands with an ideal coverage of 0.25 monolayers (ML) during dissociative oxygen chemisorption on (100) surface at $\theta \leq 0.25$ and at $100 \text{ K} \leq T \leq 400 \text{ K}$. The islands gradually grow and merge into a saturated $p(2 \times 2)$ layer at O_2 exposures of about 1 L. At $\theta \geq 0.25$ $c(2 \times 2)$ adsorption islands with an ideal coverage of 0.5 ML are nucleated in the $p(2 \times 2)$ adsorption layer, then, at $\theta \geq 0.4$, they grow gradually and merge into a saturated layer. It is usually accepted that adsorption islands are formed due to lateral attraction between chemisorbed species. However, since the attraction between chemisorbed species are much weaker than the repulsion, it is assumed that the formation of adsorption islands is driven not by attraction between the chemisorbed species but by chemisorption via different adsorption pathways. Numerous adsorption data indicate that direct and indirect adsorption pathways are the basic mechanisms of chemisorption of gases on metals. The former implies that molecules chemisorb immediately after collision with the surface, surmounting a considerable activation barrier (direct adsorption pathway), while the latter means that molecules collide with the surface, are trapped into a precursor, migrate over the surface and, finally, chemisorb

practically without activation barrier (precursor-mediated adsorption pathway). The nucleation, growth and merging of (1×1) adsorption islands during chemisorption on (100) surface were described taking into account that the direct adsorption pathway results in the nucleation of adsorption islands and the indirect one includes capture of molecules into a precursor, their diffusion over chemisorbed particles and chemisorption at the edge of the adsorption island. The nucleation, growth and merging of the p(2×2) adsorption islands at $\theta < 0.25$ and of the c(2×2) islands at $0.25 < \theta < 0.5$ during dissociative chemisorption of oxygen on a metal surface with a square lattice of adsorption sites was explained in terms of this adsorption model involving repulsive lateral interactions between particles chemisorbed on the adjacent next-nearest neighbor adsorption sites (2NN). The ratio of activation energies of the direct to indirect adsorption pathways ($E_{\text{dir}}/E_{\text{indir}}$) determines the character of structural transformations in the adsorption layer which, in its turn, accounts for the dependencies of the sticking probability (S) on the surface coverage (θ).

The present study is devoted to the investigation of the influence of the direct and indirect adsorption pathways on the dynamics of formation and growth of the p(2×2) and c(2×2) adsorption structures on the (100) metal surface during O₂ chemisorption at 300 K. With this purpose, dissociative chemisorption of O₂ on the surface with a square lattice of adsorption sites was simulated by the Monte Carlo method using the model involving the direct and indirect adsorption pathways, lateral interactions in the adsorption layer and immobility of chemisorbed atoms.

OP-9

APPLICATION OF POLYFUNCTIONAL CATALYSIS IN TRANSFORMATION OF CO₂ AND BIOSILTS TO MOTOR FUELS AS A METHOD OF ENVIRONMENTALLY DANGEROUS WASTES UTILIZATION

V.M. Mysov, K.G. Ione

Scientific Engineering Centre "Zeosit" of SB RAS, Pr. Ak. Lavrentieva, 5, Novosibirsk 630090, Russia, Tel./Fax: (3832) 30-05-96, 39-62-51, E-mail: zeosit@batman.sm.nsc.ru

The development of civilization is inseparably connected with the increase of energy consumption. Nowadays the main part of energy is produced through incineration of organic fuel – natural gas, coal, and black oil. The fuel combustion products, CO₂ and H₂O, together with deleterious admixtures (dust, chemical compounds) are therefore discharged into atmosphere. It is only in the last decade of the 20th century that the ecological problems impelled the world community to intensify activity in order to decrease CO₂ emission. In May 1992 in Rio de Janeiro, 143 countries ratified an agreement on supervision upon the global warming and on decreasing CO₂ emission into atmosphere [1]. The consequent conferences held in 1994 and 1997 in Japan supported the Agreement with a special protocol which legitimated the international sanctions against increased rates of CO₂ emission into atmosphere.

There are several methods to reduce the growth of CO₂ content in atmosphere:

- 1) To retard deforestation and to plant vegetation highly effective in CO₂ absorption;
- 2) To reduce the world production of thermal energy and to increase the portion of alternative energy resources: atomic, solar, and hydro-electric energy;
- 3) To extract carbon dioxide from the exhaust gases and to dispose it in ocean depths and in geological cavities;
- 4) To convert CO₂ chemically into useful products.

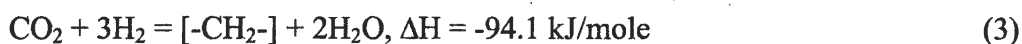
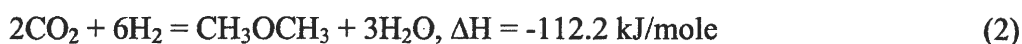
All the methods above are practicable, but the way of involving CO₂ into chemical conversion seems to be most attractive. There is a great number of known chemical reactions, both catalytic and non-catalytic, which bound CO₂ chemically into various products. Among them, the processes of carbon dioxide reduction seem to be most advantageous for CO₂ utilization [1].

An effective reducing agent for carbon dioxide is hydrogen. The following processes can be used for its industrial production :

- 1) Vapour conversion of methane $\text{CH}_4 + \text{H}_2\text{O} = \text{CO} + 3\text{H}_2$,
- 2) Water electrolysis $2\text{H}_2\text{O} = 2\text{H}_2 + \text{O}_2$,
- 3) Pyrolysis of methane $\text{CH}_4 = \text{C} + 2\text{H}_2$.

All these methods of hydrogen production require high power expenditure – from 1 (processes 1 and 3) to 3 (process 2) kw·h per 1 m³ of hydrogen produced [2-4]. The process of water electrolysis user in the case of pure products production, namely hydrogen and oxygen. Vapour conversion of methane is considered to be the cheapest way of large-scale production of industrial hydrogen. The process of methane pyrolysis has the best theoretical background for hydrogen production with minimal CO₂ emission.

The products of hydrogen reduction of CO₂ may be methanol, dimethyl ether (DME), methane, light hydrocarbons, or liquid motor fuels. The reactions of obtaining these substances from CO₂ and H₂ are as follows:



All the reactions are exothermal and besides, one to two water molecules accompany each one carbon atom in the desired product molecule (CH₃OH, CH₃OCH₃ or motor fuel fragment [-CH₂-]), so the major part of the expensive reagent, hydrogen, proves to be just spent for the production of water. On the other hand, the thermodynamic calculations show that generation of water, which is a high-stable compound, facilitates deep proceeding of CO₂-reducing reactions. The most thermodynamically advantageous reactions of CO₂+H₂ mixture conversion are the reactions of hydrocarbons synthesis.

Many publications are devoted to the process of CO₂ hydrogenation over Ni, Fe, Co, Rh, Ru-catalysts into hydrocarbons [5-10], aliphatic alcohols and hydrocarbons [11], C₂-C₂₀ olefins [12-16]. In [5], the mixture of 80% H₂ and 20% CO₂ was converted over catalysts Co/SiO₂, Ru/SiO₂, Ni/SiO₂ and Fe/SiO₂ at temperatures 180-280°C and pressures 1-11 atm. The main products of the mixture conversion were CH₄ (12.9-99.8% mol.) and CO (10.7-83.2% mol.), the conversion of CO₂ being 6-11%. Over the rhodium catalysts, a high selectivity of CH₄ (35-37% mol.) and CO formation (16-42% mol.) was also observed [11]. In this investigation, the mixture CO₂:H₂ = 1:2 was converted into alcohols, mainly into methanol (19-40% mol.), under 260°C and 50 atm. A high selectivity of light olefins formation was reported in [12], the catalyst composition 40% (Fe₅C₂/2% K)+60% amorphous carbon being used. This investigation showed that reducing

OP-9

the molar ratio H_2/CO_2 from 7.0 to 1.7 increased the content of olefins in C_2-C_4 hydrocarbons from 80 to 99%, decreased the selectivity towards CH_4 from 16.5 to 4.2%, and decreased the conversion of CO_2 from 37 to 13%.

In publications [14,17,18], the stability of Fe-containing catalysts in CO_2 hydrogenation and possibility of regeneration of their activity were studied in detail. Fe-Cu-K-Al-catalysts showed a high stability in $CO_2:H_2 = 1:3$ mixture long-run conversion under 10 atm. and $300^\circ C$ [14]. During over 1500 hours the CO_2 conversion degree remained 40-41%. The composition of the hydrocarbons produced also remained practically constant throughout the period. It was only after having been in operation for 1536 hours that the catalyst began to lose gradually its activity. After 2005 hours of operation, the CO_2 conversion degree diminished to 36.8%. The consequent redox treatment of the catalyst didn't succeed in restoring its initial activity.

After the unique acid and structural properties of high-siliceous zeolites of ZSM-5 type had been discovered, the bifunctional systems were developed composed of a component active in synthesis of hydrocarbons and/or oxygen-containing products (particularly, methanol) from synthesis-gas and of a high-siliceous zeolite catalysing the reactions of dehydration, oligomerization, isomerization, and aromatization of the intermediates [19-22]. The bifunctional catalysts of hydrocarbons synthesis were used both in the reactions of CO hydrogenation [23-39] and of CO_2 hydrogenation [40-58].

In [38,39], transformations of $CO+CO_2+H_2$ mixtures are studied in the presence of the Co-MgO-ZSM-5 catalyst under atmospheric pressure in the temperature range $150-250^\circ C$. It is shown that the gaseous hydrocarbons synthesis can involve CO, CO_2 and hydrogen while the liquid hydrocarbons can be produced only through CO and H_2 interaction. Introducing CO_2 into the mixture CO/H_2 (1/2) considerably decreases the yield of hydrocarbons. It would also change the composition of the liquid hydrocarbons produced, namely, increase the content of iso-paraffins and decrease the chain length of the hydrocarbons.

A process is developed for production of liquid hydrocarbons from the products of vegetative biomass gasification – gaseous mixtures of CO, CO_2 , H_2 and N_2 [59-65]. Even with the 50% content of nitrogen in the producer gas, under 1 atm. and $210^\circ C$ and in the presence of bifunctional catalyst 32% Co-3% MgO-ZSM-5, liquid hydrocarbons were produced with selectivity 60% [59]. As the pressure was increased to 10 atm., the content of n-paraffins in the reaction products grew from 69 to 87% [65].

Under certain condition, a strong dilution of the CO_2+H_2 mixture facilitates formation of light paraffins and olefins over bifunctional catalysts [43,54]. Thus, ethylene was produced from $\text{CO}_2/\text{H}_2/\text{Ar} = 3/6/91$ mixture over $\text{Fe}_3(\text{CO})_{12}/\text{ZSM-5}$ catalyst at temperature 260°C and pressure 1 atm. with selectivity 91.7 mol.%. The degree of CO_2 conversion was 18.5% [43].

Considerable changes in the selectivity of CO_2+H_2 conversion over bifunctional catalysts 17% Fe/HY (LiY, NaY, KY, RbY) were reported in [55]. Hydrogenation of CO_2 ($\text{H}_2/\text{CO}_2=3$) was carried out under flow conditions at 10 atm. and 300°C . The subsequent substitution of the acid carrier of the catalyst, HY, for each member of the series: LiY, NaY, KY, RbY gradually decreases methane content in the produced hydrocarbons from 72.56 to 9.54% and increases selectivity towards the C_{5+} hydrocarbons from 1.49 to 54.39%.

In many investigations, bifunctional catalysts composed of a metal-oxide catalyst of methanol synthesis and an acid component, for instance, mechanical mixtures of Cu-containing catalysts of methanol synthesis and HZSM-5 [42,47], HY [40,41], de-aluminised HY [44], SAPO-5, 44 [47], or ferrosilicate [58] were used in the process of CO_2 hydrogenation. The pressure range of the process was 14-50 atm. and the temperature range was $220-400^\circ\text{C}$. The main products of the synthesis were found to be C_1-C_3 paraffins [42,58], C_2-C_5 paraffins [44] or propane-butane fraction [47]. Aromatic hydrocarbons either were absent in the reaction products or comprised less than 1% of the hydrocarbons sum. To intensify the synthesis of hydrocarbons, small quantities of ethylene were added to the synthesis-gas [47], which increased the yield of C_3-C_4 hydrocarbons and especially of C_5 hydrocarbons. In order to obtain C_{5+} hydrocarbons, the attempts were made to use bifunctional catalysts including Cu, Zn, Cr oxides and HY zeolites at a high temperature (400°C) and pressure 50 atm. but the maximal achieved selectivity towards C_{5+} hydrocarbons wouldn't exceed 25% mol. [40]. The main results of CO_2 and CO hydrogenation over various Cu, Zn, Cr, Pd, Zr / H^+ bifunctional catalysts are shown in the Table 1.

It is due to substituting Cu, Zn,Cr oxides for a mixture of Cs-Cu-Zn chromates that the authors of [56,57] managed to considerably increase (up to 49% mol.) the selectivity towards C_{5+} hydrocarbons. It was reported that, while the maximal methanol yield over Cu-Zn-chromates was achieved at 300°C , the maximal yield of hydrocarbons over Cu-Zn-chromate/HY catalysts was, none the less, achieved at the temperature 400°C . The authors of the above works concluded that for obtaining the gasoline fraction hydrocarbons from CO_2 and H_2 , a relatively high temperature (over 300°C) was required as well as an active metal-oxide component with a lower hydrogenating activity and a highly-active coking-resistant zeolite.

Table 1. CO + H₂ and CO₂ + H₂ conversion to hydrocarbons over Cu, Zn, Cr, Pd, Zr / H⁺ bifunctional catalysts

Catalyst	Cu-Cr-Zn/ Zn/Al ₂ O ₃	Cu-Cr-Zn/ H-ZSM-5	Cu-Cr-Zn/ Zn/Al ₂ O ₃	Cu-Cr-Zn/ H-ZSM-5	Cu-Cr-Zn/ H-ZSM-5	Cu-Cr-Zn- Pd-Na/ H-ZSM-5	Zn-Cr/ Amorph. SiO ₂ -Al ₂ O ₃	Pd/SiO ₂ + H-Y	Cu-Zn-Zr/ H-Fe- silicate
H ₂ /CO	2	2	-	-	-	-	2	2	-
H ₂ /CO ₂	-	-	2.7	2.7	2.7	2.7	-	-	3
Pressure, atm.	20	20	20	20	50	50	11	20	28
Temperature, °C	290	290	320	320	320	320	390	357	400
SV, h ⁻¹	6000	6000	6000	6000	6000	6000			
W/F, g-cat· h/mol.							340	9	20
Hydrocarbons distribution, % mass									
Aliphatics									
C ₁	44.4	2.3	85.3	67.9	61.4	28.2	24.0	5.3	64.0
C ₂	24.0	15.2	11.1	25.5	35.3	31.9	20.4	23.1	30.8
C ₃	17.3	32.6	3.2	4.9	2.5	17.4	17.3	34.9	5.2
C ₄	13.4	25.4	0.3	1.3	0.4	10.3	22.8	25.8	0
C ₅₊	0.9	24.0	0	0.4	0.4	12.2	13.0	10.9	0
Aromatics	0	0.3	0	0	0	0	2.5	0	0
References	[102]	[102]	[102]	[102]	[102]	[102]	[116]	[117]	[118]

We have studied the conversion of CO, CO₂ and H₂ mixtures to motor fuels (DME, gasoline and diesel fractions) over different bifunctional catalysts [66-74]. The oxides of Zn, Cr, Fe, Co, Ru, La combined with acid components were used as bifunctional catalysts. The influences of the catalysts composition, the type of the metal oxides (Zn, Cr, Fe, Co, Ru, La etc.), the type of the acid component (ZSM-5, Beta, SAPO-5, mordenite etc.), mass ratio of the metal oxides to the acid component, pressure (from 5 to 80 atm.), temperature (210-420°C), (H₂-CO₂)/(CO+CO₂) ratio (0.5-10), duration of the test run (up to 1000 h) on the activity and selectivity of the bifunctional catalysts were studied.

Active catalysts and various technological versions were developed allowing CO+CO₂ conversion into DME, DME + CH₃OH, high-octane gasoline, diesel fraction or valuable alkyl aromatic products. By optimization of the catalysts composition and of the technological implementation of the process, we achieved high values of the yield and productivity towards the desired products. Utilization of carbon in CO and CO₂ was 70 to 95%, depending on the composition of the liquid organic products obtained. The quality of the produced gasoline fractions was high due to the low content of benzene and of 1,2,4,5-tetramethylbenzene in them. The diesel fractions contained C₁₃-C₁₈ iso-paraffins (50-60% mass) and the content of the aromatic hydrocarbons was less 1% mass. Using bifunctional catalysts with active acid components of a specially fitted structure allowed a considerable depression of formation of high-molecular compounds which are produced over the traditional Fischer-Tropsch catalysts. The C₁-C₂₀ hydrocarbons composition with respect to the carbon atom number had considerable differences against Schultz-Flory distribution typical for Fischer-Tropsch products. These differences are caused by the proceeding of some reactions on the acid component of the bifunctional catalysts – reactions of hydrogen redistribution, oligomerization, isomerization, alkylation of aromatics.

We have performed syntheses of the gasoline fraction hydrocarbons with a high aromatics content (from 20 to 80% mass) both from CO₂ and H₂ mixtures and from synthesis-gas with various percentage of CO₂ additives [72]. The syntheses were carried out in the presence of Zn-Cr/HZSM-5 catalysts at temperatures 340-420°C and pressures 40-80 atm. Using bifunctional catalysts composed of a metal-oxide component, with a low hydrogenating activity (Zn and Cr oxides) and a HZSM-5 zeolite selective towards gasoline fraction formation resulted in the production of liquid hydrocarbons consisting mainly of the aromatics and isomerised C₅-C₁₀ paraffins. The mean selectivity towards the gasoline fraction comprised about 74% mass. The degree of CO₂ conversion exceeded 87% while the methane content in the hydrocarbon products was from 2 to 7% [72].

OP-9

Table 2. Dependence of C_{5+} productivity (g/L cat/h) upon pressure and temperature for CO_2 hydrogenation ($H_2/CO_2 = 3$) over Zn-Cr/ZSM-5 catalyst

Pressure, atm	40	60	80
Temperature, °C			
320	not measured		11
340	11	14	18
360	12	24	41
380	15	38	47
400	24	56	67

Table 3. Dependence of the selectivity upon pressure and temperature for CO_2 hydrogenation ($H_2/CO_2 = 3$) over Zn-Cr/ZSM-5 catalyst

Reactant	$CO_2 + H_2$				$CO + H_2$
	340	340	400	400	400
Temperature, °C	340	340	400	400	400
Pressure, atm.	40	80	40	80	80
HC distribution, % mass:					
C_1	2.2	4.2	6.9	4.5	4.1
C_2	1.6	3.3	3.0	2.1	3.4
C_3	28.6	13.7	10.0	13.9	5.3
i- C_4	6.8	2.7	7.5	3.1	9.0
n- C_4	0.5	0.7	1.3	0.8	2.0
C_{5+}	60.4	75.4	71.3	75.6	76.2
C_{5+} distribution, % mass:					
Aromatics	62.8	65.6	41.0	44.6	28.1
n- C_{5+}	0.1	0.2	0.2	0.9	3.3
Other C_{5+}	37.1	34.2	58.8	54.5	68.6

The Tables 2 and 3 show the influence of the reaction pressure (from 40 to 80 atm.) and temperature (320-400°C) on productivity and selectivity of Zn-Cr/HZSM-5 catalyst towards C_{5+} hydrocarbons in the reaction of CO_2 hydrogenation. It can be seen that in the studied range, productivity and selectivity towards C_{5+} hydrocarbons grow as the reaction pressure and temperature increase. Comparing the processes of conversion of gaseous mixtures CO_2+H_2 , $CO+H_2$ and $CO+CO_2+H_2$ of various composition (see Tables 2-4) we can conclude that replacing CO by CO_2 in the initial gas decreases the bifunctional Zn-Cr/HZSM-5 catalyst activity in hydrocarbons synthesis but facilitates formation of the liquid gasoline-fraction hydrocarbons with a high aromatics content and low n-paraffins content (less than 1% mass). The produced gasoline fractions have a high octane number (above 93 RON) and contain practically no benzene (less than 0.5% mass).

Table 4. CO+CO₂ hydrogenation over Zn-Cr/ZSM-5 catalyst depending upon CO/CO₂ ratio, P = 80 atm., T = 400°C, H₂/CO = 2.8-2.9

CO/CO ₂ mol. ratio	98.9	3.7	1.6	0.7
V _{inlet} , h ⁻¹	1200	1000	600	300
Conversion, %:				
CO	96	90	78	28
CO ₂	90	81	80	52
Productivity, g/L cat/h	167	125	67	15
Mol. wt of the liquid HC	91	100	104	111

Thus, the results of the above investigations prove the possibility of bifunctional catalysis application in the conversion of CO₂-containing gases into valuable chemical products. We have developed bifunctional catalysts that allow more than 70% utilization of carbon in CO₂ under the optimal reaction conditions by its conversion into liquid motor fuel.

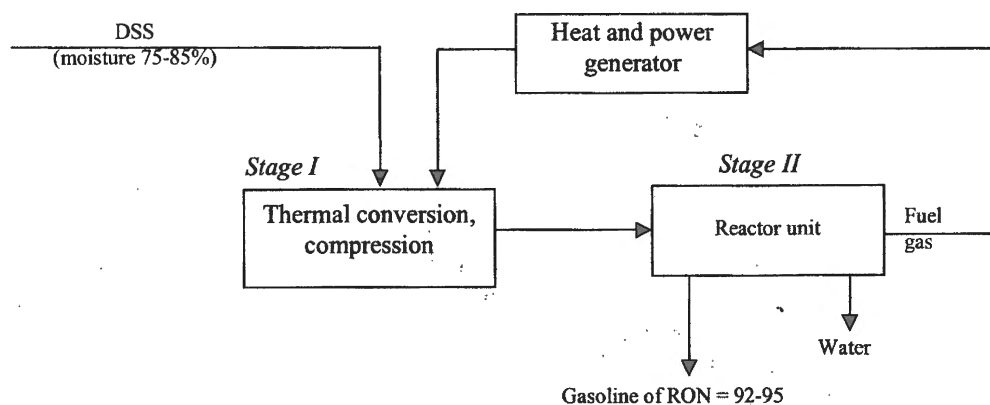
Nowadays the techniques for wastes utilization, particularly for utilization of the biological wastes of megalopolises, are of great importance for the human civilization.

At present, it is a usual situation for a large city when above 1-10 million tons of domestic silt sediments (DSS) of 75-85% moisture has been accumulated in the city sewage tanks and 40-50 thousand tons of DSS keeps being added annually.

There are known methods for utilization of these silt sediments via drying them up and then either incineration of the dry residue or using it, after disinfection, as a fertilizer. The processes are power-consuming and unprofitable.

An alternative method for DSS processing is presented in this report. The final product of the process is high-octane gasoline.

The proposed scheme of DSS conversion is the following:



The installation process 80%-moisture DSS of the incoming wastes and of the wastes having been already accumulated in the sewage tanks into motor fuels. The proposed capacity of the installation with respect to DSS feedstock would comprise about 180-200 thousand ton per year.

OP-9

The composition of the gasoline obtained (% wt.) and the catalyst characteristics are as follows:

iso-paraffins	55-65
olefins	no more than 1-2
n-paraffins	10-15
aromatics	25-35
benzene	0.2-0.8
catalyst productivity	150-250 kg of gasoline/m ³ of catalyst/hour
catalyst lifetime	not less than 20-25 thousand hours

References

1. O.V. Krylov, Mamedov A.H., *Uspehi Himii*, 64 (1995) 935.
2. V.D. Rusanov, in *Hydrogen Energy Progress XI, Proc. 11th World Hydrogen Conf., Stuttgart, 23-28 June, 1996, Vol.1*, 37.
3. V.N. Parmon, in *Hydrogen Energy Progress XI, Proc. 11th World Hydrogen Conf., Stuttgart, 23-28 June, 1996, Vol.1*, 51.
4. F.N. Pekhota, V.D. Rusanov, S.P. Malysenko, in *Hydrogen Energy Progress XI, Proc. 11th World Hydrogen Conf., Stuttgart, 23-28 June, 1996, Vol.1*, 293.
5. G.D. Weatherbee and C.H. Bartholomew, *J. Catal.*, 87 (1984) 352.
6. G.D. Weatherbee and C.H. Bartholomew, *J. Catal.*, 68 (1981) 67.
7. M.D. Lee, J.F. Lee, C.S. Chang, T.Y. Dong, *Appl. Catal.*, 72 (1991) 267.
8. G.D. Weatherbee and C.H. Bartholomew, *J. Catal.*, 77 (1982) 460.
9. N. Takezawa, H. Terunuma, M. Shimokwabe, H. Kobayashi, *Appl. Catal.*, 23 (1986) 291.
10. R.A. Migone, M.A. Ulla, E.A. Lombarbo, J.O. Petunchi, *Appl. Catal.*, 37 (1988) 115.
11. W.J. Ball and D.G. Steward, *Eur. Pat. Appl.* 0 079 207 A1 (1982).
12. R.A. Fiato, S.L. Soled, G.W. Rice, S. Miseo, U.S. Patent 5,140,049 (1992).
13. V.M. Gryaznov, Y.M. Serov, N.B. Polyansky, *Doklady Akademii Nauk*, 359 (1998) 647.
14. J.S. Hong, J.S. Hwang, K.W. Jun, J.C. Sur, K.W. Lee, *Appl. Catal. A: Gen.*, 218 (2001) 53.
15. P.H. Choi, K.W. Jun, S.J. Lee, M.J. Choi, K.W. Lee, *Catal. Lett.*, 40 (1996) 115.
16. S.R. Yan, K.W. Jun, J.S. Hong, M.J. Choi, K.W. Lee, *Appl. Catal. A: Gen.*, 194 (2000) 63.
17. J.S. Hwang, K.W. Jun, K.W. Lee, *Appl. Catal. A: Gen.*, 217 (2001) 208.
18. C.G. Frye, H.L. Pickering, H.C. Eckstrom, *J. Phys. Chem.*, 62 (1959) 1508.
19. C.D. Chang and A.J. Silvestri, *J. Catal.*, 47 (1977) 249.
20. C.D. Chang, W.H. Lang, A.J. Silvestri, U.S. Patent 4,086,262 (1978).
21. C.D. Chang, W.H. Lang, A.J. Silvestri and R.L. Smith, U.S. Patent 4,096,163 (1978).
22. C.D. Chang and W.H. Lang, U.S. Patent 4,180,516 (1979).
23. P.D. Caesar, J.A. Brennan, W.E. Garwood, J. Ciric, *J. Catal.*, 56 (1979) 274.
24. C.D. Chang, W.H. Lang and A.J. Silvestri, *J. Catal.*, 56 (1979) 268.
25. G.V. Isagulyanz, K.M. Gitis, A.A. Greish, G.L. Markaryan, *Neftehimiya*, 23 (1983) 765.
26. L.S. Egorova, G.P. Snytnikova, K.G. Ione, *Kinetika i Kataliz*, 25 (1984) 86.
27. K.M. Gitis, A.A. Greish, V.N. Kornyshev, G.V. Isagulyanz, *Neftehimiya*, 27 (1987) 638.
28. H. Nguyen-Ngoc, in P.A. Jacobs (Ed.), "Structure and Reactivity of Modified Zeolites", *Stud. Surf. Sci. Catal.*, Amsterdam, 18 (1984) 291.
29. W.H. Seitzer, U.S. Patent 4,139,550 (1979).
30. F.G. Dwyer and W.E. Garwood, U.S. Patent 4,172,843 (1979).
31. S.J. Lucki and J.A. Brennan, U.S. Patent 4,207,208 (1980).
32. S.A. Butter and H.S. Sherry, U.S. Patent 4,207,250 (1980).
33. S.A. Butter and A.W. Chester, U.S. Patent 4,255,349 (1981).
34. J.A. Brennan, P.D. Caesar, J. Ciric, W.E. Garwood, R.E. Holland, U.S. Patent 4,269,783 (1981).
35. S.A. Butter, A.W. Chester, A.B. Schwartz, U.S. Patent 4,298,695 (1981).

36. M.J. Desmond and M.A. Pepera, U.S. Patent 4,568,698 (1986).
37. Y.F. Chu, J.A. Brennan, A.W. Chester, U.S. Patent 4,595,702 (1986).
38. A.Y. Krylova, A.L. Lapidus, F.T. Davlyatov, Y.M. Paushkin, *Himiya Tverdogo Topliva*, 2 (1990) 55.
39. A.Y. Krylova, F.T. Davlyatov, N.E. Varivonchick, Y.M. Paushkin, H.M. Minachev, A.L. Lapidus, *Himiya Tverdogo Topliva*, 1 (1989) 103.
40. M. Fujiwara, R. Kieffer, H. Ando, Y. Souma, *Appl. Catal.*, 121 (1995) 113.
41. M. Fujiwara, H. Ando, M. Tanaka, Y. Souma, *Appl. Catal.*, 130 (1995) 105.
42. T. Inui, K. Kitagawa, T. Takeguchi, T. Hagiwara, Y. Makino, *Appl. Catal.*, 94 (1993) 31.
43. Y. Huang, X. Meng, Z. Dang, S. Weng, C. Zhang, *J. Chem. Soc., Chem. Commun.*, 1995, p.1025.
44. K. Fujimoto and T. Shikada, *Appl. Catal.*, 31 (1987) 13.
45. B. Denise, C. Hamon, M. Sanes, R. Sneaden, EP 0 084 469 B1 (1984).
46. M. Fujiwara and Y. Souma, *J. Chem. Soc., Chem. Commun.*, 1992, p.767.
47. J.K. Jeon, K.E. Jeong, Y.K. Park, S.K. Ihm, *Appl. Catal.*, 124 (1995) 91.
48. H. Schultz, G. Schaub, M. Claeys, T. Riedel and S. Walter, in *The proceeding of ICCDU IV, Kyoto, Japan, 1997*.
49. Y. Souma, M. Fujiwara, R. Kieffer, H. Ando, Q. Xu, in *The proceeding of ICCDU IV, Kyoto, Japan, 1997*.
50. Q. Xu, D. He, M. Fujiwara, M. Tanaka, Y. Matsumura, Y. Souma, H. Ando, H. Yamanaka, in *The proceeding of ICCDU IV, Kyoto, Japan, 1997*.
51. H. Hara, T. Takeguchi, T. Inui, in *The proceeding of ICCDU IV, Kyoto, Japan, 1997*.
52. N.K. Lunev, N.V. Pavlenko, Y.I. Shmyrko, in *The proceedings of the II Ukrainian Scientific-Technological Conference on Catalysis, Severodonetsk, Ukraine, 2000*, 36.
53. Y.I. Shmyrko, N.V. Pavlenko, in *The proceedings of the II Ukrainian Scientific-Technological Conference on Catalysis, Severodonetsk, Ukraine, 2000*, 38.
54. N.P. Samchenko, I.S. Alcheev, Z.M. Zdornaya, *Ukrainskiy Himicheskiy Zhurnal*, 58 (1992) 382.
55. S.S. Nam, H. Kim, G. Kishan, M.J. Choi, K.W. Lee, *Appl. Catal. A*, 179 (1999) 155.
56. R.A. Comelli and N.S. Figoli, *Ind. Eng. Chem. Res.*, 32 (1993) 2474.
57. K. Fujimoto, Y. Kudo, H. Tominaga, in *Pan-Pacif. Synfuels Conf., Tokyo, 1982*, 123.
58. Y.K. Park, K.C. Park, S.K. Ihm, *Catalysis Today*, 44 (1998) 165.
59. A.L. Lapidus, A.Y. Krylova, F.T. Davlyatov, Y.M. Paushkin, *Himiya Tverdogo Topliva*, 5 (1988) 134.
60. A.Y. Krylova, A.L. Lapidus, F.T. Davlyatov, Y.M. Paushkin, *Doklady AN SSSR*, 304 (1989) 162.
61. A.L. Lapidus, A.Y. Krylova, F.T. Davlyatov, Y.M. Paushkin, *Doklady AN SSSR*, 313 (1990) 129.
62. Y.M. Paushkin, G.S. Golovin, A.L. Lapidus, *Himiya Tverdogo Topliva*, 3 (1994) 62.
63. A. Lapidus, A. Krylova, Ya. Paushkin, *Science and Technology of Fuel and Energy*, 73 (1994) 583.
64. Y.M. Paushkin, A.L. Lapidus, S.V. Adelson, *Himiya i Tehnologiya Topliv i Masel*, 6 (1994) 3.
65. Y.M. Paushkin, G.S. Golovin, E.G. Gorlov, *Himiya i Tehnologiya Topliv i Masel*, 2 (1996) 10.
66. V.M. Mysov, K.G. Ione, RF patent 2089533 (1997).
67. K.G. Ione and V.M. Mysov, in B.N. Kuznetsov (Ed.), *Catalysis in coal conversions, Proc. Third Intern. Symp., Russia, Novosibirsk, 1997*.
68. V.M. Mysov, K.G. Ione, in V.V. Lunin, A.L. Lapidus et al. (Ed.), *Coal chemistry at the boundary of millennia: collection of reports of the Int. Scien. Conf. and of UNESCO Seminar School, Klyazma, March 13-15, 2000, Moscow, Moscow State University publishing house, 2000*, p. 69.
69. K.G. Ione and V.M. Mysov, in *Actual problems of petrochemistry, the proceedings of RF conf., Moscow, April 17-20, 2001*, p. 34.
70. K.G. Ione, V.M. Mysov, N.V. Savostina, G.P. Snytnikova, RF patent 1173696 (1996).
71. V.M. Mysov, K.G. Ione, V.N. Parmon, RF patent № 2143417 (1999).
72. V.M. Mysov and K.G. Ione, RF patent 2089533 (1997).
73. V.M. Mysov and K.G. Ione, RF patent 2175960 (2001).
74. V.M. Mysov and K.G. Ione, RF patent 2180651 (2002).

OP-10

**NEW BIS-(ARYLIMINO)PYRIDYL AND BIS-(ARYLIMINO)ACENAPHTHYL
COMPLEXES AS COMPONENTS OF CATALYST SYSTEMS FOR ETHYLENE
POLYMERIZATION**

**S.S.Ivanchev, G.A.Tolstikov, V.K.Badaev, I.I.Oleinik, N.I.Ivancheva,
D.G.Rogozin, I.V.Oleinik, M.V.Tikhonov**

*St-Petersburg Department of the Boreskov Institute of Catalysis
of the Siberian Branch of the Russian Academy of Sciences
14, prospect Dobrolubova, 197198, St-Petersburg, Russia*

Phone +7 812 238-08-90, Fax +7 812 233-00-02, E-mail: ivanchev@SM2270.spb.edu

In order to enhance the potential of polymerization catalysts based on bis-imines and bis-(imino)pyridines new compounds of these classes with cycloaliphatic substituents in the ortho-position of the aryl ring were synthesized. Iron halide bis-(arylimino)pyridyl and nickel bromide 1,2-bis(arylimino)acenaphthyl complexes obtained therefrom and activated with methylaluminoxane (MAO) are studied as ethylene polymerization catalysts. The kinetics of ethylene polymerization performed using all of the considered complexes is shown to feature with a non-steady behavior with the polymerization rate initially increasing and reaching the maximum in 10-30 min since the process onset and subsequently decreasing. The maximum rate value depends on the temperature as well as on the type and position of substituents in the aryl ring. A certain combination of substituents in the ortho-position of the aryl ring is found to afford carrying out the reaction with high rates at temperatures applicable for commercial processes (70-80°C) and yielding high-molecular products.

The application of bis(arylimino)pyridines results in high density (964-967 kg/m³) polyethylenes with a small methyl group content in the macromolecules (2.5-5.0 CH₃ groups / 1000 C).

In the case of using nickel bromide 1,2-bis(arylimino)acenaphthyl complexes as a catalyst component the variation of aryl ring substituents or polymerization temperature allows the control over the amount of methyl groups in the side chain of the resulting polymer in a wide range (up to 70 CH₃ groups / 1000 C).

The synthesized complexes provide catalysts with increased polymerization activity compared to the previously described counterparts.

**ACCESSIBILITY OF THE IRON SPECIES IN OVEREXCHANGED Fe/ZSM5
PREPARED BY CHEMICAL VAPOR DEPOSITION OF FeCl₃**

J.H. Bitter, A.A. Battiston, S. van Donk, K.P. de Jong and D.C. Koningsberger

Utrecht University, Department of Inorganic Chemistry, Utrecht, The Netherlands

Fe/ZSM5 possesses unique catalytic activity in HC-SCR (HydroCarbon Selective Catalytic Reduction) and phenol synthesis. It is believed that the presence of binuclear iron clusters in these materials is the reason for this behavior. These binuclear clusters have sizes comparable to the size of the zeolite channel. This might invoke difficulties for reactants to reach all the active sites with a sufficiently high rate. In order to investigate the availability of the zeolite

Table 1. Some properties of the catalysts used in this study

Sample	Si/Al	Fe/Al	Calcination	V _{micro} (ml/g)	Relative activity
HZSM5	17	-	-	0.15	-
Fe/ZSM5-mc	17	1	Mild	0.12	1.00
Fe/ZSM5-sc	17	1	Severe	0.13	0.98

channels with binuclear iron species present, we measured the uptake of the probe molecule *n*-hexane using a tapered element oscillating microbalance (TEOM).

For this study we have used three samples for which some of the properties are compiled in Table 1. A thorough characterization of the Fe containing samples with EXAFS and STEM/EELS revealed that the number of binuclear iron species is significantly lower in the Fe/ZSM5-sc sample compared to the Fe/ZSM5-mc sample. Nevertheless the activity of both samples in HC-SCR is similar (Table 1). This points to a similar number of accessible sites in both materials. In order to check the accessibility of the zeolite channels for the reactants we determined the uptake of the probe molecule *n*-hexane with a TEOM. For HZSM5 the uptake stabilizes quickly at a value of 0.03g/g_{catalyst}. The uptake of the Fe-containing samples is lower (Figure 1) but it does not stabilize during the experiment.

For the latter two regions of uptake can be distinguished. During short times on stream (TOS) the uptake is fast, visible as a steep slope of the uptake curve, while at longer TOS (>150 s) the slope decreases i.e., the rate of uptake is dramatically lowered. This indicates that for the Fe-samples part of the space in the zeolite is quickly accessible while another part is more difficult to access for *n*-hexane. Nevertheless the micropore volume, determined by N₂

OP-11

physorption, of all samples is similar (table 1). This in combination with the continuous slow uptake shows that the micropore volume is only slightly decreased by incorporating Fe in the sample but that part of the micropores are more difficult to access after iron incorporation. The latter being more pronounced for the mild calcined sample.

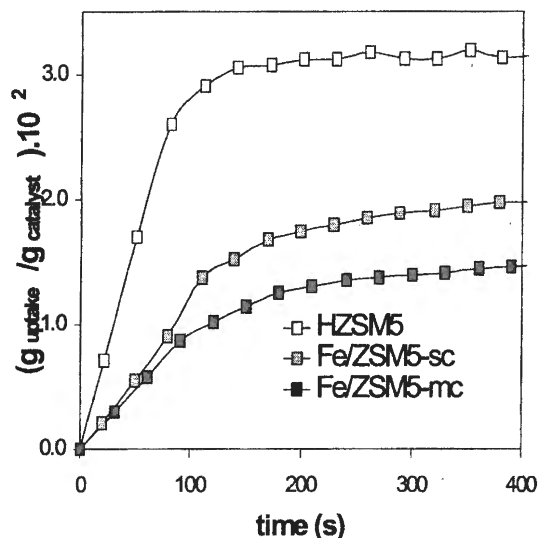


Figure 1. Uptake by different (Fe)/ZSM5 samples. T=523 K

There fore, it is concluded that for both Fe containing samples all HC-SCR catalysis takes place at the first complexes encountered by the reactants entering the micropores leaving part of the complexes unused. But for the severe calcined sample these complexes are located deeper inside the zeolite channel explaining the higher final uptake of this sample (Figure 2).

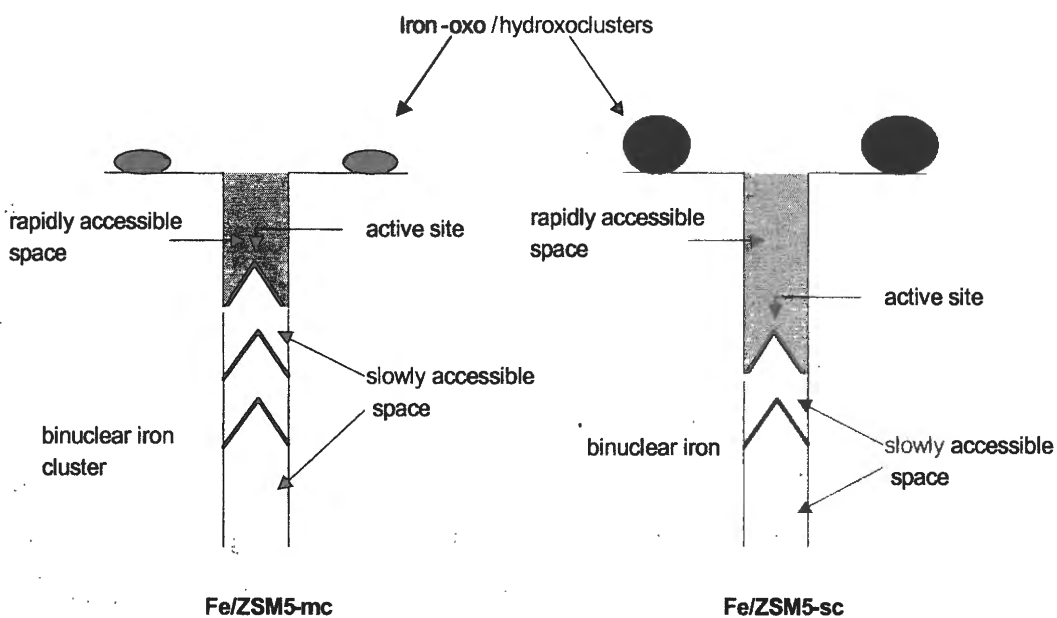


Figure 2. Micropore accessibility after mild and severe calcination

OXIDATION OF BENZENE TO PHENOL BY NITROUS OXIDE. ACTIVITY OF IRON IN ZEOLITE MATRICES OF VARIOUS COMPOSITION

L.V. Pirutko, V.S. Chernyavsky, A.K. Uriarte*, G.I. Panov

Boriskov Institute of Catalysis SB RAS, Novosibirsk, Russia

**Solutia Inc., P.O. Box 97, Gonzales, FL 32560-0097, USA*

The catalytic properties of Fe introduced in pentasil zeolite matrices of various chemical compositions (B-ZSM-5, Al-ZSM-5, Ga-ZSM-5, Ti-ZSM-5) have been studied. All the matrices were shown to be inert in the title reaction. However, upon iron introduction they may serve as a basis for the development of very active and selective catalysts. The amount of iron needed for this purpose depends dramatically on the matrix composition. For example, while Al-ZSM-5 and Ga-ZSM-5 zeolites exhibit high activity even in the presence of 0.01-0.03 wt% Fe, B-ZSM-5 and Ti-ZSM-5 zeolites need a 10-100 times more Fe.

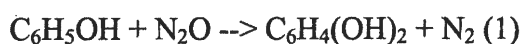
The distinctions in zeolite activity relate to the fact that the formation of Fe-containing α -sites, catalyzing the reaction, strongly depends on the Bronsted acidity and proceeds with different efficiency in various matrices, indicating charge compensating position to be a locus of active iron species. But being formed, α -sites in their catalytic performance have only slight dependence on the matrix composition. Activity of B-ZSM-5, Al-ZSM-5, and Ti-ZSM-5 zeolites is described by a common dependence on α -site concentration, which reveals their identity in these matrices. In Ga-ZSM-5 matrix, α -sites exhibit a 2-3 times higher activity.

The role of Fe admixtures in the literature disagreement on the nature of zeolite catalytic activity is discussed.

**DIRECT HYDROXYLATION OF PHENOL TO DEHYDROXYBENZENES
WITH N₂O****V.I. Sobolev, D.P. Ivanov, G.I. Panov**

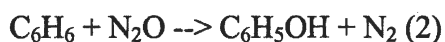
*Boreskov Institute of Catalysis SB RAS, Novosibirsk, Russia
Pr. Akad. Lavrentieva, 5, Fax +7 383 2 34 30 56*

Dihydroxybenzenes (DHB) are among the most important fine chemicals. Existing methods of their production are complex and not efficient. Therefore, oxidation of phenol by nitrous oxide seems to be a very promising new way:



Oxidation of aromatics by N₂O was suggested to perform under large excess of the substance to be oxidized [1]. Due to high heat capacity of the aromatic compound, its excess decreases heating of the reaction mixture and provides better selectivity and stability. This approach proved to be very useful for the benzene oxidation to phenol. However, in case of phenol oxidation this approach has some drawbacks. Phenol is a solid up to 42°C. It has high boiling temperature and big evaporation heat. If we add high viscosity of phenol vapor, it becomes clear that conducting reaction (1) in a large phenol excess may cause substantial complications of the process.

There is a new idea to overcome these difficulties, i.e. to add benzene to the reaction mixture as a component increasing its heat capacity. In this case, along with reaction (1) oxidation of benzene should also occur:



In the present work we study the oxidation of phenol to DHB over ZSM-5 zeolite depending on the benzene:phenol ratio in the reaction mixture. Experiments were carried out with a flow setup providing full on-line GC analysis of the reaction mixture. The basic mixture had the following composition: 50% C₆H₆, 5% N₂O, He balance. To study the effect of phenol, the latter was added to the mixture at various concentrations, from zero to 6.7 mol%. It was shown that increasing phenol concentration resulted in a remarkable increase of DHB productivity, which at 6.7 mol% phenol attained nearly 2 mmol/gh. Besides, effect of the reaction temperature and contact time on DHB productivity, N₂O selectivity, and DHB isomers distribution was studied.

[1] G.I. Panov, A.S. Kharitonov, G.A. Sheveleva, US Patent 5 756 861 (1998)

CONVERSION OF ETHANOL OR DIMETHYL ETHER TO HYDROGEN-RICH GAS

V.V. Galvita, A.V. Frumin^{*)}, V.D. Belyaev, G.L. Semin, V.A. Sobyenin

Borshkov Institute of Catalysis SB RAS, Pr. Akademika Lavrentieva 5,

Novosibirsk 630090, Russia, e-mail: galvita@catalysis.nsk.su

^{)}Novosibirsk State University, Pirogova st. 2, Novosibirsk 630090, Russia*

Analysis of current literature shows that ethanol, a widely available renewable material, and dimethyl ether (DME) that can be synthesized directly from synthesis gas, will play an important role in energy transfer. If so, hydrogen-rich gas or syngas produced from ethanol and DME seem to be very attractive for fuel cells and other applications.

This presentation reports the results on ethanol and DME steam reforming to hydrogen-rich gas. In particular, we demonstrated that:

- Two-layer fixed-bed reactor is quite promising for conversion of ethanol to syngas. In this reactor, ethanol is first decomposed to H₂, CO, CO₂ and CH₄ gas mixture over a suitable catalyst (for example, Pd/C or Pd-Cu/C) and then the mixture produced is converted to hydrogen-rich gas over another appropriate catalyst. (for example, Ni-containing catalyst for methane steam reforming);
- Both mechanical mixture of catalysts for DME hydration to methanol and methanol steam reforming to hydrogen-rich gas, as well as bifunctional catalyst containing copper and heteropoly acid possess sufficient activity for the reaction of DME steam reforming.

Acknowledgement

The authors highly appreciate partial financial support provided by INTAS (Project № 987)

I.V. Babich, L. Leveles, K. Seshan, L. Lefferts

*Catalytic Processes and Materials, Faculty of Chemical Technology, University of Twente,
Postbus 217, 7500 AE, Enschede, The Netherlands*

The present industrial capacity for lower olefins is expected to be insufficient, as the demand for these important building blocks in the modern petrochemical industry grows [1,2]. Dehydrogenation of alkanes is an option and has the advantage that it generates olefins with the same carbon number as the alkanes, but has some major disadvantages: yields are limited by thermodynamic equilibrium, and high tendency to coking and consequently short catalyst lifetime [3].

Oxidative dehydrogenation (ODH) could be a conceptually interesting route as limitations of the chemical equilibrium are removed by the coupling of dehydrogenation and hydrogen oxidation, moreover the presence of oxygen limits coking and extends therefore catalyst lifetimes. Catalysts based on transition metal oxides with pronounced redox properties such as supported vanadia catalysts have been explored, but have not been seen promising, as readsorption of olefins (leading to total oxidation) appears to limit the olefin yield [4,5]. Maximum olefin yields obtained are limited to 30 mol% [3]. Conway *et al.* [6,7] reported that magnesia based catalysts containing rare-earth oxides, promoted with alkali halide (mainly chlorides) show high activity and selectivity for forming olefins [8-12]. Over 70% ethene selectivity was reported at 75% conversion of ethane at 845 K. Somewhat later Landau *et al.* [13,14] reported on the ODH of light alkanes such as propane and butane. The mixed oxides based on rare-earth and Li oxides yielded up to 50% of total olefins at 860 K at 62% alkane conversion (>85% olefin selectivity). These catalysts present a significant improvement (>50% olefin yields) in comparison to earlier generation catalysts and thus provide intense interest currently. The composition of product stream after oxidative dehydrogenation and consisting of olefins, hydrogen, water, and carbon oxides suggests that the reactions that take place can include oxidative dehydrogenation, combustion and cracking. Key problems in the application of these catalysts include (i) catalyst stability; (ii) presence of chloride in the catalyst composition; (iii) formation of a mixture of olefins due to cracking activity of the catalysts.

Our work was directed on identification of essential catalyst components to simplify catalyst formulation without loss in catalyst efficiency, determination of the structure of the active

sites which catalyze each route of alkane conversion, and provide the data on the mechanism of the oxidative conversion of alkanes over the studied catalytic system.

It has been shown that Li appears to be the most essential component in the catalyst composition to make an active and selective catalyst (Fig. 1). Addition of Dy_2O_3 to the catalyst decreases the activity by about a factor of two. Slight decrease in selectivity is also observed. Chloride addition to Mg-Li-Dy based catalyst slightly improves activity and selectivity but stability of the catalyst decreases. After a few hours on stream the conversion and selectivity for Cl-containing catalyst declines so the Cl-free catalyst possesses higher activity and selectivity. Chlorine free catalysts also give olefin yields, which is 15% more than that obtained over conventional catalysts. High olefin selectivity is maintained even at high conversions – very little secondary conversion of the olefins formed to CO_x occurs. It is appropriate to mention at this point that development of a chlorine free efficient oxidation catalyst is a significant factor from the point of commercial application.

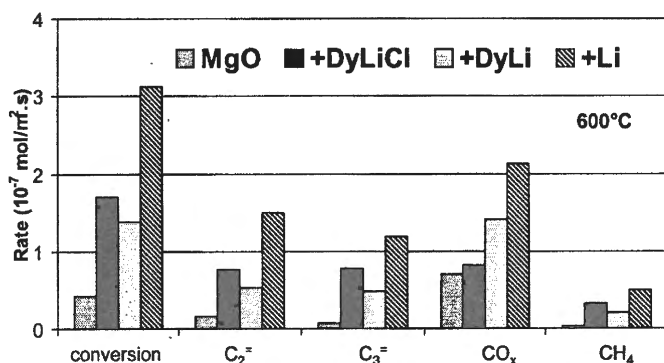


Fig. 1. Catalytic activity of the MgO-based catalysts of different composition.

It is generally accepted that the presence of Li on the magnesia surface generates the oxygen vacancies, which form highly nucleophilic centers *via* dissociative adsorption of O_2 . The resulting sites are commonly noted as $[\text{Li}^+\text{O}^-]$ and are considered to be active in methane coupling [15,16]. We suggest that the similar active sites are responsible for the extraordinary properties of Li/MgO in formation of olefins compared to MgO. The $[\text{Li}^+\text{O}^-]$ active site is able to initiate dehydrogenation reaction *via* splitting the most active hydrogen from an alkane. The crucial role of Li in the creation of the ODH active sites is confirmed by the increase in the activity and selectivity of Li-based catalysts with increase of Li content. In addition, a strong correlation between catalytic activity and CO_2 concentration has been observed. Adding up to 8 vol% CO_2 to the reaction mixture led to a marked decrease in the reactivity, while the selectivity did not change. Kinetic measurements indicate that the reaction order is -1 , which is attributed to the formation of Li^+CO_3^- species that results in the deactivation of the active sites.

OP-15

The observed linear dependence between conversions and yields for the products (Fig. 2) over the catalysts studied clearly indicates, that only the rates of olefin and CO_x formation are of significance, while readsorption of olefins (for e.g. propene as shown in Fig. 2) and subsequent oxidation did not occur. Thus, carbon oxides and olefins are concluded to be primary products. Even more strikingly, for a reaction temperature of 600°C such an inter conversion was not observed up to conversions of more than 60%. The fact that high olefin selectivity is maintained at high alkane conversions implies that secondary combustion of formed olefin is not important. This provides a significant advantage for commercial application because it makes the use of fluidized bed reactor with back mixing (ideal for heat removal) possible.

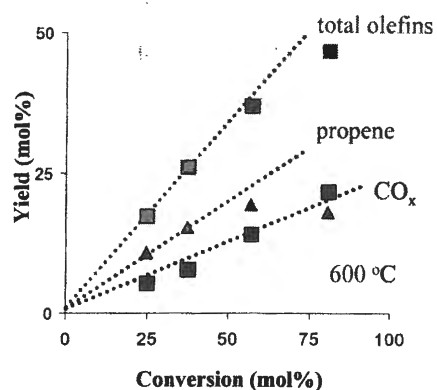


Fig. 2. ODH of propane over chlorine free Li-Dy-MgO based catalysts

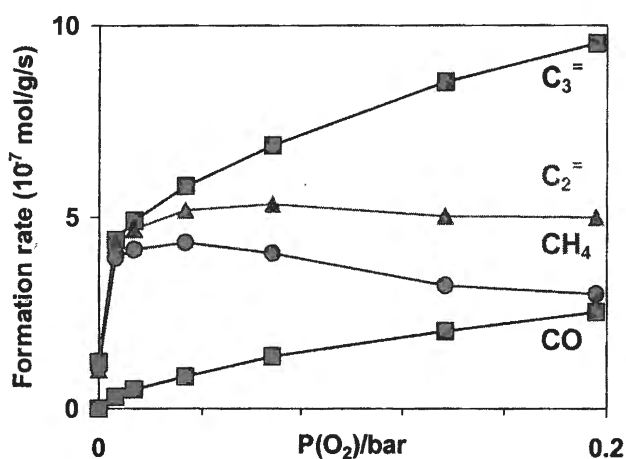


Fig. 3. Rates of ODH products formation at different oxygen partial pressure.

The influence of oxygen upon activity and selectivity in the reaction is complex (Fig. 3). At very low partial pressures of oxygen (0-5 mbar) the activity steeply increased while selectivity to dehydrogenation and cracking (to ethene and methane) remained unaffected. At higher oxygen partial pressures the rates of propene and CO_x formation

increase, while those of cracking slightly decrease. It is interesting to note that the sum of production rates of CH_4 and CO equals the formation rate of ethane independent of the partial pressure of oxygen. This fact seems to indicate that a common C_1 intermediate leads to formation of CH_4 and CO .

Mechanism of propane ODH over Li-Mg-based catalysts has been elucidated from the data of kinetic measurements varying the propane partial pressure. It has been determined that activation of the alkane is rate determining step. At low propane partial pressure (typically below 0.3 bar) propane activation takes place predominantly on the catalyst surface (active sites are $[\text{Li}^+\text{O}^-]$) via hydrogen abstraction. This results in the transformation of the active sites

to the $[\text{Li}^+\text{OH}^-]$ and formation of n- or iso-propyl radicals depending on whether the hydrogen was bonded to a primary or secondary carbon atom. The propyl radicals are released into the gas phase where they undergo decomposition reaction. Iso-propyl radicals give propene and H_2 whereas n-propyl radicals are transformed to ethane and CH_4 . The radicals that result from the decomposition activate new propane molecules and continue the reaction chain. In the presence of oxygen the reaction goes much faster due to fast reaction of oxygen with the propyl radicals to form propene and HO_2 . Oxygen also regenerates $[\text{Li}^+\text{OH}^-]$ sites closing the catalytic cycle. At high partial pressure of propane (typically above 0.3 bar) the gas-phase activation of propane molecules becomes important and predominates over the activation at the catalyst surface. It is interesting to mention that contribution of gas-phase activation of alkane is much smaller in the presence of catalyst than in the empty reactor. This can be explained by the quenching role of the catalyst, which limits the formation of a pool of radicals to accelerate the reaction.

The presented results clearly indicate that Li-Mg-based catalysts are very promising in oxidative dehydrogenation of light alkanes and are an improvement over the redox-based catalysts providing higher yield of desired products, olefins.

References

1. S. Zehnder, in: *Hydrocarbon processing*, Feb. 1998.
2. P. K. Niccum, M. F. Gilbert, M. J. Tallman, and Ch. R. Santner, *NPRA 2001 Annual Meeting* March 18-20, 2001, Marriott Hotel, New Orleans, LA, AM-01-61.3. F. Cavani, and F. Trifiro, *Catal. Today* 24 (1995) 307.
4. T.C. Watling, G. Deo, K. Seshan, I.E. Wachs, and J.A. Lercher, *Catal. Today* 28 (1996) 139.
5. R. H. H. Smits, K. Seshan, J. R. H. Ross, and A. P. M. Kentgens, *J. Phys. Chem.* 99, 9169 (1995)
6. S. J. Conway, D. J. Wang, and J. H. Lunsford, *Appl. Cat. A* 79 (1991) L1-L5.
7. S. J. Conway, and J. H. Lunsford, *J.Catal.* 131 (1991) 513.
8. C. Mazzocchia, C. Aboumradi, C. Diagne, E. Tempesti, J. M. Herrmann and G. Thomas, *Catal. Lett.* 10 (1993) 1253.
9. P. M. Michalakos, M. Kung, I. Jahan and H. H. Kung, *J. Catal.* 140 (1993) 226.
10. M. A. Char, D. Partel, M. C. Kung and H. H. Kung, *J. Catal.* 105(2) (1987) 483.
11. H. H. Kung and M. A. Char, *U.S. Patent 4777319* (1987). 12. M. A. Char, D. Partel and H. H. Kung, *J. Catal.* 109(2) (1988) 463.
13. M. V. Landau, M. L. Kaliya, M. Herskowitz, P. F. van den Oosterkamp and P. S. G. Boque, *Chemtech* 26(2) (1996) 24.
14. M. Herskowitz, M. Landau, M. L. Kaliya, *US Patent 6130183* (2000).
15. D. J. Driscoll, W. Martir, J. X. Wang, J. H. Lunsford, *Adv. Catal.* 35 (1987)139.
16. C. Shi, M. Hatano, J. H. Lunsford, *Catal. Today*, 13(2-3) (1992) 191.

FISCHER-TROPSCH SYNTHESIS WITH THE USE OF A POROUS CATALYST PACKING. FEASIBILITY STUDY OF PERFORMING MULTIPHASE CATALYTIC PROCESS USING PENETRABLE COMPOSITE MONOLITHS

**A.G. Sipatroy, A.A. Khassin, T.M. Yurieva, V.A. Kirillov, G.K. Chermashentseva,
and V.N. Parmon**

*Boriskov Institute of Catalysis SB RAS, Pr. Lavrentieva, 5, Novosibirsk, 630090, Russia
e-mail: los@catalysis.nsk.su tel: +7-3832-344109 fax: +7-3832-343056*

Introduction

The conversion of renewable energy sources (in particular, that of biomass) to conventional motor fuels may be performed by junction of biomass gasification and Fischer-Tropsch synthesis. At present, both stages of the process are in the focus of numerous studies [1,2]. Use of the biomass as a raw material lays some specific constrains on the Fischer-Tropsch technology which are mainly related with a comparatively small scale of production. The traditionally proposed slurry bed or monolith trickle-bed reactors are characterized by a high extent of the catalyst dilution (by slurry filling or by monolith block). Thus, the productivity of the volume unit of a reactor is low, leading to high capital costs of the process. The operation of the "small" scale plants using these types of reactors seems to be not self-supporting. Therefore the challenge is to design a new type of the Fischer-Tropsch three-phase reactor, which should combine the advantages of the slurry bed and trickle-bed reactors (isothermal catalyst bed, high rates of mass transfer) with high concentration of the catalytically active substance in the reactor volume [3].

It is noteworthy, that high concentration of the active component loading must not be accompanied by the decrease of:

- catalyst bed heat conductivity (isothermal catalyst bed is important for retaining high selectivity of the process, see e.g. [4]);
- gas-liquid interface specific area;
- internal diffusion rates inside the porous structure of the catalyst grain (this is important not only for providing a high effectiveness factor of the catalyst usage but also for ensuring a high selectivity of the process [5]);
- hydraulic penetrability of the catalyst bed.

Only in the case that all above criteria are maintained at the highest level, the increase of the catalyst concentration in the reactor volume can lead to better process performance.

Here we present an experimental study on the possibility of providing the Fischer-Tropsch synthesis in a new type of three-phase reactor, which combines the dense catalyst bed and high rates of mass and heat transfer.

Proposed concept of the porous catalyst packing: Penetrable Composite Monolith (PCM)

The origin of the PCM concept is high loading of the active component in the catalyst grain combined with the low void volume in the reactor volume. In this case, an intense mass-transfer can be achieved by directing the gas flow through the catalyst grain via a set of transport pores, provided that concentration of the transport pores is high enough.

Then, the effective diffusion length will be about the mean distance between the neighboring transport pores. In [5], it was concluded that for typical Fischer-Tropsch catalyst, internal diffusion constrains do not worsen the process selectivity at catalyst grain size less than 50 μm . Assuming the close packing of pores, this corresponds to the concentration of the transport pores $n_{tp} > 7 \cdot 10^8 \text{ m}^{-2}$.

A high area of the gas-liquid interface could be created by an organization of the gas flow through the transport pores partially filled by liquid in the “annular” regime, provided the concentration of such pores is high enough and their effective diameter is quite small. Assuming the mass-transfer coefficient on the gas-liquid boundary, k_L , to be about 10^{-4} m/s (estimated by the Moo-Young equation [6]), the reaction rate to be not higher than 6 moles(CO)/($\text{m}^3 \text{ s}$) (i.e. 300 kg/($\text{m}^3 \text{ hr}$) of hydrocarbons produced), and solubility of CO in hydrocarbons to be about 52 moles(CO)/($\text{m}^3 \text{ MPa}$) (measured for octacosane, $T = 250 \text{ }^\circ\text{C}$ [7]), one can estimate that the specific area of the gas-liquid interface should be above $20 \text{ cm}^2/\text{cm}^3$ to relax the mass-transfer restrictions at the interface for the typical Fischer-Tropsch conditions (2 MPa, 33% of CO).

At the same time, the effective radius of the transport pores should be high enough to provide a low pressure drop. Let us estimate the minimal penetrability (the Darcy’s law coefficient) of a PCM grain, assuming that the gas feed rate in the industrial Fischer-Tropsch synthesis can hardly exceed $1 \text{ m}^3/(\text{m}^3 \cdot \text{s})$, and the minimal reasonable catalyst bed length is about 0.1 m. Then, the reasonable pressure drop, $\Delta P < 0.5 \text{ MPa}$, can be achieved, if the penetrability of the catalyst bed is above $1.2 \cdot 10^{-14} \text{ m}^2$ (12 mDarcy).

The challenge is to prepare the catalyst grain, which satisfies all the above criteria. We have made an attempt to prepare the catalyst grain using the combination of the state-of-the-art techniques known for the preparation of composite materials. Below we demonstrate that this

OP-16

attempt was successful. This new type of catalyst grains we will further denote as “penetrable composite monolith” (PCM) catalyst.

Experimental

PCM catalyst grains were prepared basing on the Co-containing catalyst. The cobalt loading in the catalyst powder was 24% wt. Concentration of the catalyst in the PCM samples varied from 0.7 to 1.1 g/cm³. The PCM particles under the study have cylinder geometry with the base diameter 15 mm and height 5-7 mm.

Porosity of the PCM samples was calculated by relating the true volume of the catalyst grain to its geometrical volume. The true volume was measured using a Helium picnometer Micromeritics 1320 (USA). Independently, the porosity was estimated by flooding the PCM grain with liquid n-tetradecane, n-C₁₄H₃₀, and by comparing the weight of the flooded grain to its initial weight.

Penetrability of the PCM samples was estimated by the Darcy equation from the dependence of the pressure drop vs. the gas flow through the PCM grain at room temperature.

Thermal conductivity was estimated from the experimental data on the electric conductivity by the well-known Wiedemann-Franz correlation [8].

Mechanical strength was estimated from experiments when the glass vessel with the catalyst PCM grain was vibrating with frequency 100 Hz and amplitude 5 mm. The PCM sample was free and stroke against the vessel wall at each oscillation. The weight fraction retained by PCM sample after 20 min treatment was used as a measure of its mechanical strength. These studies were performed after all the other tests are over.

The catalytic tests were performed at T = 483 K, P = 0.1 MPa, H₂:CO = 2 (mol). 10 vol.% of N₂ was introduced into the gas flow as an internal standard for gas chromatography. The gas mixture was saturated by vapor of n-tetradecane (at 483 K) for uniformity of all the catalytic test series. Thus, the partial pressure of CO in the gas feed was ca. 20 kPa, that of H₂ was ca. 40 kPa.

The PCM samples used in the catalytic tests were sealed into a solid ring for insulation of the cylinder element. The volume of the PCM sample was ca. 1.05 cm³. The amount of the active catalyst loading varied slightly from 0.9 to 1.03 g per the PCM sample. Before starting a test, the PCM samples were pre-activated (reduced) in hydrogen flow and placed into liquid n-tetradecane under the protection of flowing Ar in order to avoid contact with air oxygen. Then the sample was moved into a plug-flow reactor with the ascending gas flow.

Two series of tests were made: in a “gas” mode (i.e. with no additional liquid hydrocarbon introduced into the reactor volume) and in a “gas-liquid” mode (i.e. with having the layer of

liquid n-tetradecane of 1-2 cm in height maintained over the top of the PCM cylinder). Note, that the PCM sample was initially dried by argon flowing through for the “gas” test series.

Reference data for the evaluation of the PCM performance were obtained by testing the Co-containing catalyst used for the PCM preparation in a slurry bed reactor (n-tetradecane as the slurry filling). The sample size was 1.1 g, the catalyst powder particle size was less than 0.1 mm. The catalyst was activated in the fluidized-bed reactor and placed into liquid n-tetradecane under the protection of flowing Ar in order to avoid contact with air oxygen.

Results and discussion

Estimation of integral values for the PCM samples:

Figure 1 illustrates, that the experimental dependencies of the gas flow through the dry PCM grain on the pressure drop follows the Darcy’s law for ideal gas:

$$Q_{vol} = K \cdot \frac{S}{l \cdot \eta} \cdot \Delta P \quad (1)$$

Here Q_{vol} is volume gas flow (m^3/s), K is penetrability (m^2), η – dynamic viscosity (Pa’s), l – grain height (m), ΔP – pressure drop (Pa), S – PCM grain cross-section area (m^2).

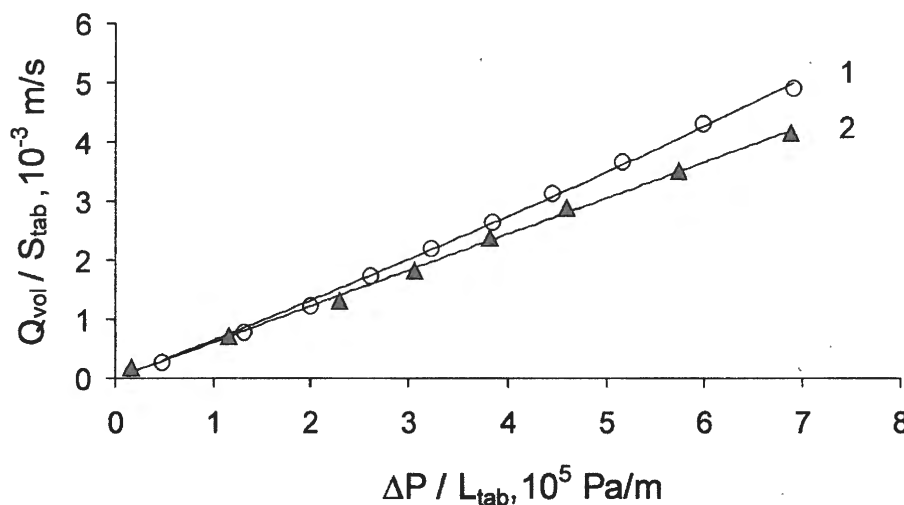


Figure 1. The experimental data on the dependence of the volume gas flow *versus* the pressure drop for the PCM operated in the “gas” regime: 1 – sample PCM-5; 2 – sample PCM-6. $T = 22 \text{ }^\circ\text{C}$, $P = 1 \text{ bar}$; gas composition: 30% vol. CO , 60% vol. H_2 , and 10% vol. N_2 .

By varying the composition and conditions of the PCM preparation, we found that it is possible to obtain PCM samples which differ a lot by their penetrability. However, the samples with the higher penetrability are less mechanically strong. At Figure 2 the correlation between these two parameters is shown. It is quite clear from the plot, that the PCM grains with the penetrability,

OP-16

K_{gas} , ranging from 10^{-14} - $5 \cdot 10^{-13} \text{ m}^2$ (10-500 mDarcy) are optimal. Thus, the scope of the study was contracted by a few selected PCM samples with similar preparation conditions and composition. Table 1 summarizes the experimental data on the catalyst loading, mechanical strength, penetrability and thermal conductivity of the selected PCM samples.

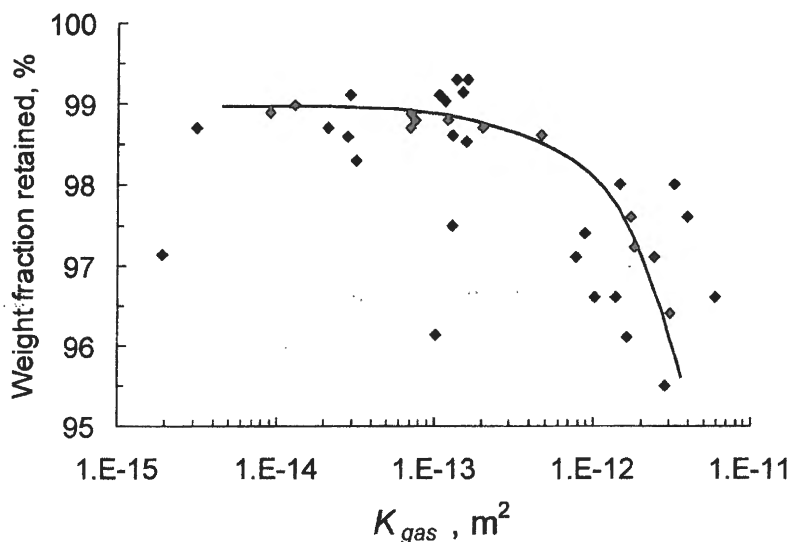


Figure 2. The correlation of the penetrability, K_{gas} , and the mechanical strength for PCM samples in a wide range of the PCM sample composition and preparation conditions. The mechanical strength is expressed in weight fraction of sample retained after intense vibration treatment (see the text).

Table 1. The experimental data on the PCM samples under the study.

Sample	Catalyst loading, g/cm^3	Mechanical strength ^(a)	Porosity ^(b)	Porosity ^(c)	Penetrability, K_{gas} , mDarcy	Heat conductivity, $\text{W}/(\text{m}\cdot\text{s})$
PCM-1	0.92	98.5%	0.77	0.64	120	4
PCM-2	0.99	98.8 %	0.72	0.71	106	4
PCM-3	0.90	98.7 %	0.74	0.66	71	3.5
PCM-4	1.04	99.2 %	0.66	0.60	130	4.5
PCM-5	1.0	98.8 %	0.56	0.46	75	> 5
PCM-6	0.97	98.6%	0.77	0.64	158	4

^(a) measured as the weight fraction retained by sample after 20 min of intense vibrations;

^(b) estimated from the true PCM density measured by Helium picnometer

^(c) measured by n-tetradecane porometry

Estimation of the transport pores distribution by size.

Figure 3 represents the effect of the pressure drop on the volume gas flow in the case, when the layer of liquid n-tetradecane is maintained on the top of the PCM grain (i.e. at the

“gas-liquid” mode of operation). The data on the PCM-1 sample at 22°C, $P = 1$ bar were selected for the illustration. It is quite clear from the presented plot, that the observed pressure drop originates from a superposition of the capillary pressure and the resistance of the pores to the viscous gas flow:

$$\Delta P = \frac{l \cdot \eta}{K S} \cdot Q_{vol} + P_{cap}, \quad (2)$$

and therefore is not linear to the gas flow.

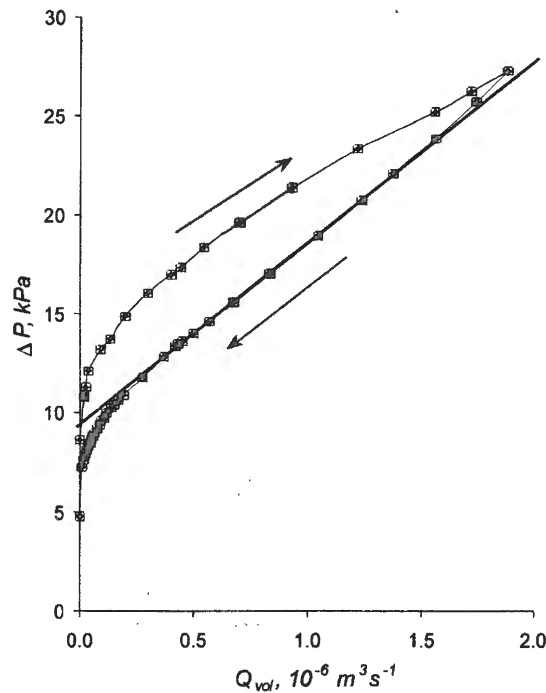


Figure 3. The experimental dependence of the pressure drop on the volume gas flow for PCM-1 at the “gas-liquid” operation mode.

At low values of the gas flow, only the widest transport pores are open for the gas flow, i.e. those satisfying the necessary condition $P_{cap} < \Delta P$. The observed hysteresis loop indicates the complicated geometry of the pores: the critical value of the pressure drop needed to open a transport pore corresponds to the most narrow spot in the pore, while, at decreasing the gas flow, the same pore can be closed only at a somewhat lower pressure drop value equal to the capillary pressure at the pore exit. The experimental dependence $Q_{vol}(\Delta P)$ allows to estimate the density of the transport pores distribution by diameter $n(D)$ by equation (3):

OP-16

$$n(D) = \frac{128}{\pi} \left(\frac{4\sigma}{\Delta P} \cos(\Theta) \right)^{-5} \eta l \Delta P \left\{ \frac{P_{atm}}{\Delta P + P_{atm}} \cdot \frac{d^2 Q_{vol}}{d\Delta P^2} - \frac{P_{atm}}{(\Delta P + P_{atm})^2} \cdot \frac{dQ_{vol}}{d\Delta P} \right\}, \quad (3)$$

$$D = \frac{4\sigma}{\Delta P} \cos(\Theta)$$

which follows from Eq. (2) and Hagen-Poiseuille equation [9] for the cylindrical shape of pores. In Eq. (3), σ is surface tension of the liquid phase; Θ is the wetting angle; D – diameter of the transport pore. A laminar flow of gas through the transport pore was assumed. Derivatives $\frac{d^2 Q_{vol}}{d\Delta P^2}$ and $\frac{dQ_{vol}}{d\Delta P}$ were calculated from the 6th degree polynomial approximation of the experimental data on $Q_{vol}(\Delta P)$. An example of the estimated pore distribution density, $n(D)$, is presented by Figure 4 (curve 1).

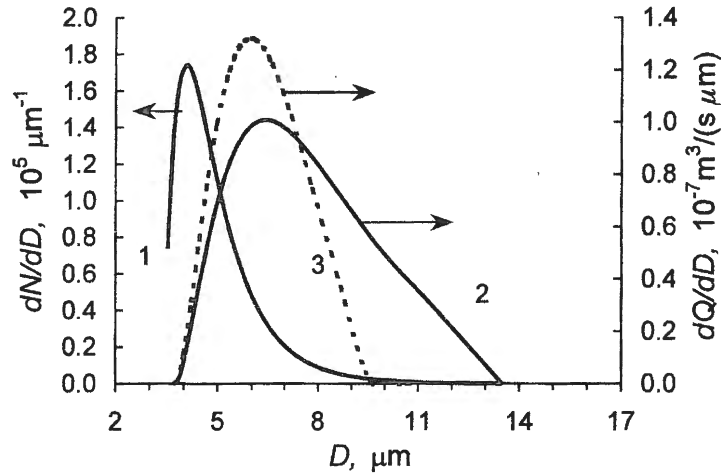


Figure 4. The estimated density functions: 1 – of the transport pore distribution by size for PCM-5; 2 – of the gas flow distribution by the pore size for PCM-5; 3 – of the gas flow distribution by the pore size for PCM-6.

Curves 2 and 3 at Figure 4 correspond to the calculated densities of the gas flow distribution by the transport pore size $\frac{dQ(D)}{dD}$ at the value of $\Delta P = 14$ kPa:

$$\frac{dQ(D)}{dD} = n(D) \frac{\pi}{128} \frac{D^4}{\ln \eta} \left(\Delta P - \frac{4\sigma \cos(\Theta)}{D} \right) \left(1 + \frac{1}{2P_{atm}} \left(\Delta P - \frac{4\sigma \cos(\Theta)}{D} \right) \right) \quad (4)$$

The measured values of the PCM penetrability K_{g-t} , estimated transport pores size, $R_{tp\ cap}$, concentration, n_{tp} , volume fraction, ε_{tr} , their specific surface area, a_{tp} , as well as the transport pore size measured by optical microscopy, $R_{tp\ opt}$, are summarized in Table 2.

Table 2. The estimated transport pore structure parameters

Sample	Penetrability, K_{g-l} , mDarcy	$R_{tp\ cap}$, μm	$R_{tp\ opt}$, μm	TP concentration, n_{tp} , $10^9\ \text{m}^{-2}$	Volume of TP, ε_{tp}	TP surface area, a_{tp} , cm^2/cm^3	Distance TP – TP, L_{tp} , μm
PCM-1	66	3.6	-	1.0	3.6 %	210	38
PCM-2	30	2.5	2.5	2.7	4.5 %	370	23
PCM-3	60	3.6	-	1.2	3.6 %	230	35
PCM-5	53	3.9	5.0	2.0	4.2 %	320	27
PCM-6	42	3.2	-	2.1	4.3 %	330	26

The penetrability, K_{g-l} , corresponds to the slope of the $Q_{vol}(\Delta P)$ plot at $\Delta P > 15$ kPa (see Fig. 3).

The effective size of transport pores, $R_{tp\ cap}$ was estimated by the expression (5):

$$R_{tp\ cap} = \frac{\frac{1}{2} \frac{D_{min}}{D_{max}} \int_{D_{min}}^{D_{max}} Q'(D) D dD}{\int_{D_{min}}^{D_{max}} Q'(D) dD} \quad (5)$$

where $Q'(D)$ is the density of the pore size distribution calculated by Eq. (4). The concentration of the pores was calculated as the total amount of the pores related to the area of the PCM grain cross-section, S . Similarly, the volume of the transport pores and their specific surface area were calculated:

$$n_{tp} = \frac{\int_{D_{min}}^{D_{max}} n(D) dD}{S}, \quad \varepsilon_{tp} = \frac{\int_{D_{min}}^{D_{max}} n(D) \pi D^2 dD}{S}, \quad \text{and} \quad a_{tp} = \frac{\int_{D_{min}}^{D_{max}} n(D) 2\pi D dD}{S} \quad (8)$$

The data of Tables 1 and 2 evidence that the PCM catalysts satisfy all the requirements postulated in the first section of this article. Thus, it is quite natural to expect their performance to be high. Below, the performance of the PCM catalyst in the Fischer-Tropsch synthesis at $P = 0.1$ MPa is discussed.

Catalytic performance of the PCM samples in CO hydrogenation at 0.1 MPa

The experimental data on the performance of the PCM samples in the Fischer-Tropsch synthesis at 0.1 MPa are summarized in Table 3. Each experimental point refers to 12 hours on run at constant reaction conditions for the PCM tests and for 18 hours on run for the slurry bed tests.

In the “gas” mode of the operation, the activity of the PCM samples is close to that observed in a slurry reactor over the catalyst powder, i.e. at the conditions, when nor internal

OP-16

neither external mass-transfer restrictions can be considered as significant. Thus, almost all the active component particles are accessible to the gas (the “closed” pores aren’t present in the packing). A high value of propylene-to-propane ratio indicates, that the mass-transfer limitations are not strong enough to provide the high probability of propylene re-adsorption. From the other hand, the low value of ASF parameter α for the olefin fraction of the products indicates that for higher olefins a re-adsorption process is still probable. Some decrease of the C_3 =/– ratio at the high contact time appears to be a quite expected result: at longer residence time, the probability of propylene re-adsorption should apparently be higher.

Table 3. The Fischer-Tropsch synthesis performance of the PCM samples in comparison to that of the original catalyst powder in the slurry bed reactor, $P = 0.1$ MPa, $H_2:CO:N_2 = 6:3:1$, the $n-C_{14}H_{30}$ saturated vapors.

Sample	T, K	$V_g^{(a)}$, NI/hr	Operation mode	CO conversion	Activity, $\mu\text{mol}/(\text{hr } g_{\text{cat}})$		Selectivity parameter $\alpha^{(b)}$		C_3 =/–
					CO converted	CH_4 formed	paraffins	olefins	
SBR	484	0.32	slurry bed	24 %	1180	170	0.83	0.80	1.9
	484	0.42		21 %	1340	180	0.84	0.81	2.0
PCM-2	484	0.94	gas	11.5%	1560	100	0.81	0.59	4.8
	483	0.68		14.6%	1570	130	0.80	0.61	4.9
	484	0.46		19.3%	1410	130	0.75	0.58	4.6
	484	0.32		25.2%	1280	130	0.73	0.56	3.7
	484	0.93	g-l	6.4%	940	110	0.79	0.57	3.8
	483	0.67		11.2%	1180	140	0.80	0.50	3.3
	484	0.33		21.2%	1090	140	0.70	0.41	2.3
	484	0.50		11.6%	910	130	0.77	0.54	2.8
PCM-3	483	0.75	gas	7.6 %	1050	60	0.84	0.54	5.4
	484	0.31		18.8 %	1080	120	0.81	0.53	4.9
	484	0.47		13.2 %	1140	110	0.83	0.56	4.6
	484	0.85	g-l	5.3 %	820	90	0.78	0.65	4.2
	483	0.34		15.6 %	950	80	0.81	0.63	2.7
	484	0.50		10.0 %	880	80	0.80	0.66	3.3
PCM-5	484	0.50	g-l	11.6%	910	130	0.77	0.54	2.8
	473	0.50		8.8 %	630	27	0.82	0.75	1.6
	483	0.50		10.6 %	750	60	0.72	0.74	1.9
	493	0.50		13.2 %	900	130	0.65	0.63	2.5
	493	0.30		20.1 %	800	150	0.65	0.63	2.4
	494	0.67		10.1 %	1030	150	0.67	0.63	3.0
	494	0.91		8.2 %	1130	150	0.68	0.64	3.4

^(a) the volume flow of the syn-gas before saturation by the n-tetradecane vapors

^(b) the values of the Anderson-Schulz-Flory parameter α are calculated from the composition of $C_4 - C_9$ fraction of corresponding products

The “gas-liquid” mode of the operation is, probably, more close to the steady-state of the catalyst in realistic conditions, when the reaction represents a three-phase process. For this mode of the operation, the most narrow transport pores are plausibly flooded, i.e. “closed” for

the gas flow through due to a high capillary pressure according to the data of Fig. 3. This provides a less effective usage of the catalyst (60-70% in respect to the original catalyst powder in the slurry bed reactor).

The propylene-to-propane ratio for the “gas-liquid” operation mode is lower, than that for the “gas” mode. This indicates that the effective residence time of non-saturated products in the PCM pore structure is higher than the gas residence time due to the existence of additional mass-transfer constrains at the gas-liquid interface. The propylene selectivity in the “gas-liquid” regime seems to be close to the marginal case of a well mixed liquid, when it increases monotonously with the gas velocity. A simple estimation leads to the following equation for the model of gas flowing through the well mixed liquid phase:

$$\left\{C_3\right\}_{observed} = \frac{\left\{C_3\right\}}{1 + \frac{k RT}{V_g P^0}}, \quad (9)$$

which accords to the experimental data on the PCM samples provided $\left\{C_3\right\} = 6.1$ (see Fig. 5).

Here $\left\{C_3\right\}$ is the rate of the propylene production related to the rate of the propane production (in the supposition of the absence of the re-adsorption); V_g is the volume flow of gas through the PCM grain related to 1 g of the catalyst loading; P^0 is the saturated vapor pressure of propylene; k is the first order kinetic rate constant for the propylene re-adsorption.

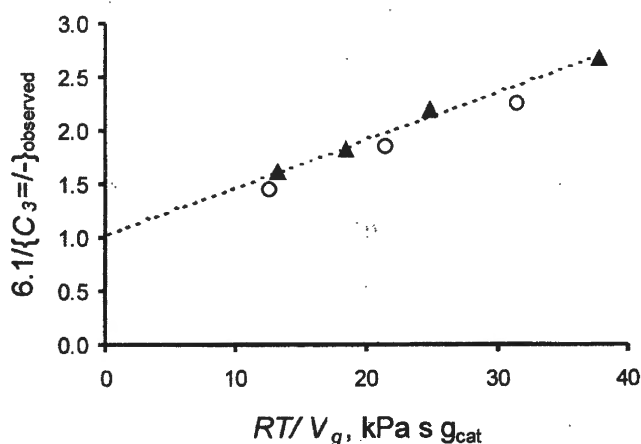


Figure 5. A linear anamorphosis of the impact of the volume gas flow, V_g , through the PCM-2 (▲) and PCM-3 (O) samples on the propylene selectivity

The above data evidence that mass-transfer constrains are not very severe for the PCM catalysts. Despite that, the selectivity towards heavy hydrocarbons (the ASF α parameter) is quite low at high degree of the CO conversion for the PCM-2 sample, while this tendency is

OP-16

not so pronounced for the other two samples. From Table 2 it is clear that the PCM-2 sample is characterized by the smallest mean size of transport pores. Thus, it is quite natural to suppose, that the most of transport pores are flooded and the mass-transfer limitation affects the performance of this sample to a much greater extent.

Conclusions

1. In this paper we demonstrate that it possible to prepare penetrable composite monoliths (PCM) which are characterized by:
 - a high concentration of a catalytically active compound (0.9-1.1 g/cm³);
 - a high heat-conductivity (above 3 W/(m s));
 - a high mechanical strength;
 - the penetrability, which is reasonable for the Fischer-Tropsch synthesis ($4 \cdot 10^{-14}$ - 10^{-13} m²);
 - a well developed transport pore structure with mean size *ca.* 2-5 μm and concentration *ca.* $1-3 \cdot 10^9$ m⁻².
2. The effectiveness factor of the PCM catalyst usage in the three-phase operation mode is enough (60 – 70%) to provide the high productivity of the PCM volume (2 – 3 times higher, than for the conventional slurry bed reactor). No catalyst is located in the closed pores.
3. Despite the PCM pore structure favors the intense mass-transfer and the mass-transfer restrictions are rather mild, the selectivity of the process is still sensitive to the mean size of transport pores and, probably, to the dispersion of their size distribution. Therefore, studies on the way of the preparation of PCM samples with more homogeneous pore size distribution is necessary.
4. The results of the study encourage to consider PCM as prospective catalysts for the Fischer-Tropsch synthesis [10], the catalytic tests in more realistic reaction conditions (P = 2 MPa) could give the basis for better-grounded conclusions [11].

Acknowledgements

We highly appreciate assistance of Dr. I.Sh.Itenberg. This research is financially supported by grant Copernicus ICAS2-2000-10004 and Grant of the Programm “Leading Science Schools of Russia” # 00-15-97446.

References

1. M. Kaltschmitt and A.V.Bridgewater (Eds.), Biomass Gasification and Pyrolysis, CPL press, Newbury, UK, 1997.
2. H. Schulz, M. Clayes (Eds.), Recent advances in Fischer-Tropsch synthesis, Appl. Catal. A: Gen., 186, 1999.
3. A.A. Khassin, V.A. Kirillov, Kataliz v Promyshlennosti (Catalysis in Industry), 2 (2002) (*in Russian*)
4. A.A.Khassin, V.N.Parmon, Doklady Phys. Chem., 368(4-6), 283 (1999) (Official English translation from Doklady RAN, 368(4), 503 (1999))
5. E. Iglesia, Appl. Catal. A.: Gen., 161, 59 (1997).
6. P.A.Ramachandran and R.V.Chaudhari, Three-phase catalytic reactors, Gordon and Breach Science Publishers, NewYork, 1983.
7. C.N. Satterfield, H.G. Stenger, Ind. Eng. Chem. Process Des. Dev., 24, 407 (1985)
8. N.W. Ashcroft, N.D. Mermin, Solid State Physics, Holt, Rinehart & Winston, NewYork, 1976.
9. R. B. Bird, W.E. Stewart, E.N. Lightfoot, Transport phenomena, Wiley, New York, 2002.
10. I.Sh. Itenberg, V.A. Kirillov, N.A. Kuzin, V.N. Parmon, A.G. Sipatrov, A.A. Khassin, G.K.Chermashentseva, T.M. Yurieva. Patent Application RU 2001135572, priority date 21.12.2001.
- 11 A.A. Khassin, T.M. Yurieva, A.G. Sipatrov, V.A. Kirillov, G.K. Chermashentseva and V.N. Parmon. *Submitted to Catal. Today, 2002*

**MICROSPHERES OF FLY ASH AS A SOURCE FOR CATALYTIC SUPPORTS,
ADSORBENTS AND CATALYSTS**

**S.N. Vereshchagin, N.N. Anshits, A.N. Salanov*, O.M. Sharonova, T.A. Vereshchagina,
A.G. Anshits**

*Institute of Chemistry and Chemical Technology SB RAS, K.Marx St., 42, Krasnoyarsk,
660049, Russia. tel./fax 8-3912-43943, e-mail snv@krsk.infotel.ru*

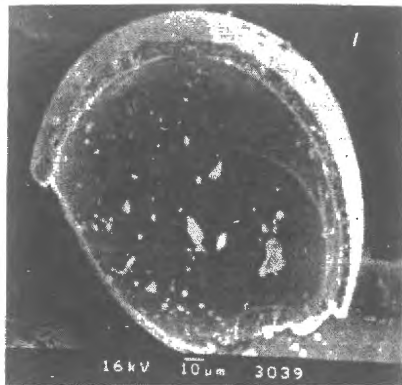
** Borekov Institute of Catalysis SB RAS, Lavrent'eva Pr. Acad., 5, Novosibirsk, 630090, Russia*

1. Introduction

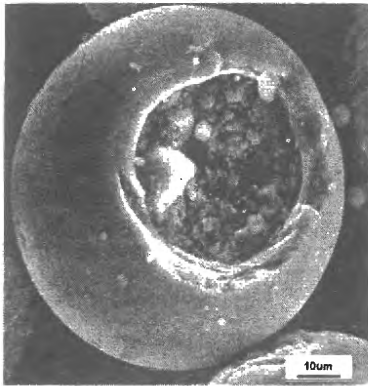
Vast amount of fly ash produced by power stations causes development of efficient ash utilization processes. The spherical particles called microspheres constitute the substantial part of fly ashes, which are used at the moment mostly in construction and material industries. But it is known that microspheres reveal outstanding thermal, magnetic and some other properties combined with the unique spherical design and chemical inertness. These features make them very promising material for development on their basis new special products of high technological importance. The present paper reviews the processes of separation of microspheres from fly ash and their possible applications for the creation of catalytic supports, adsorbents and catalysts.

2. Classification and recovery of glass crystalline microspheres from fly ash

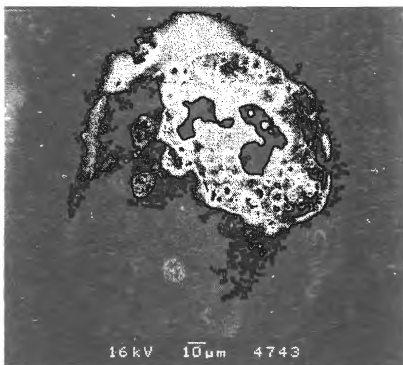
The accepted classification of microspheres includes three main groups of different morphology (Fig. 1): microspheres (magnetite or aluminosilicate glass crystalline spherical particles, monolith or porous), cenospheres (hollow microspheres based on aluminosilicate glass in which the ratio of the particle diameter to the wall thickness can reach more than 50) and plerospheres (hollow glass crystalline microspheres filled with tiny spherical particles) [1-3]. In real fly ashes the proportion between these types of microspheres as well as their chemical and mineral-phase composition vary in a very wide range and depend on the nature and composition of initial coal and on the coal combustion modes. From the point of the practical application of microspheres as catalysts and supports, magnetite microspheres with high content of the ferrosphenel phase (magnetic microspheres) and cenospheres are the most interesting objects.



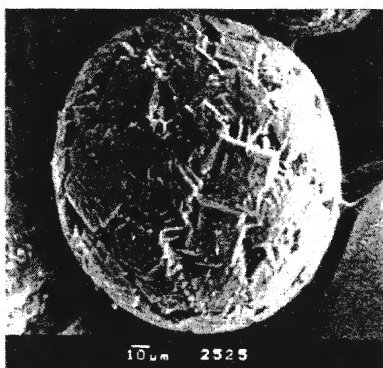
cenosphere



plerosphere



porous microsphere



crystalline microsphere

Figure 1. Typical appearance of microspheres found out in fly ashes

The primary separation of fly ash to recover the mentioned microspheres includes hydrostatic isolation of cenospheres (concentrate) having the lowest density compared to other ash components (bulk density 0.3-0.6 g/cm³) and magnetic separation of the rest part resulting in the recovery of the magnetic product (magnetic concentrate). Concentrates of microspherical products (cenospheres and magnetic microspheres) are mixed materials that are heterogeneous by their grain size, chemical and mineral phase composition.

To obtain materials with predictable properties from the microspheres, an additional stabilization of composition of the primary products is required. The further separation of concentrates is based on the difference of physical characteristics of microspheres (density, content of the magnetic constituent, particle size). The process flowsheets of concentrate separation based on the combination of hydro- or aerodynamic and granulometric classification followed by magnetic separation in magnetic field of different intensity have been realized to isolate magnetic microspheres and cenospheres of stabilized composition [4-7].

The scheme to illustrate the principle of hydro- and aerodynamic separation of magnetic microspheres and cenospheres using up flow or down flow gas or liquid is presented in Figure 2. The scheme has been applied to separate the concentrates of magnetic microspheres and cenospheres. As a result a wide range of microspherical products with stabilized physicochemical properties and chemical compositions has been produced. The detailed study of their properties and morphology by methods of scanning electron microscopy, Mossbauer

OP-17

spectroscopy, X-ray diffraction and electron spin resonance has been carried out. Based on the results obtained the promising fields of application of stabilized products including the production of catalysts, supports and adsorbents have been defined and some examples are given below.

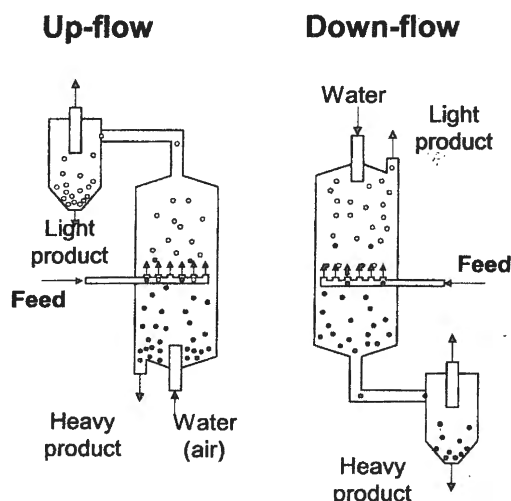


Figure 2. Scheme of hydro- and aerodynamic separation of concentrates

3. Modification of microspheres

3.1. Preparation of porous microspherical glasses

The porous structure of glasses is known to be formed by removing soluble components from two-phase sodium-boron-silicate glasses as a consequence of chemical etching with mineral acids [8]. Cenospheres can be also precursors of porous glasses due to the entering of acid soluble phases into the composition of aluminosilicate glass.

The chemical etching of cenospheres was performed by treatment of non-perforated cenospheres of Novosibirsk Power Plant with hydrochloric acid at given temperature, processing time and volume ratio of sample to etching solution resulting in the formation of three products, such as two perforated products (P1 and P2) and one non-perforated product (NP) with 4, 20 and 74% volume yields, accordingly (losses-2%). All the products have been isolated and characterized by SEM. Texture parameters of products obtained (specific surface area, pore volume and pore size distribution) were calculated from low temperature isotherms of nitrogen sorption (ASAP 2400 Micromeretics) and from the volume of adsorbed argon at 77 K (method of thermal desorption of argon - TDA).

According to TDA the specific surface area of the porous cenospheres obtained are equal to the values of 51 m²/g (P1), 15 m²/g (P2) and 3.4 m²/g (NP). The total single point pore volume of pores less than 2400Å at P/P₀ = 0.99 for P1 is as much as 0.016 cm³/g. The

differential curve of pore size distribution has a well-defined maximum at 35 angstrom (Å), it spans the range of 50-80 Å pore size and sufficiently large pores of 100-500 Å. The presence of macropores is confirmed also by SEM. Two types of regular macropores having size less than 0.05 microns and 0.05-0.5 microns are distinctly observed on the surface of porous cenospheres formed as a result of acid etching.

Thus, the data obtained have shown the possibility to form the mesoporous microspherical glasses with specific surface area of 3-50 m²/g based on cenospheres of stabilized composition. Perforation of the cenosphere wall can be reached under these conditions resulting in the formation of 0.05-0.5 micron open pores.

3.2. Fe₂O₃ supported cenospheres

Table 1. Specific surface area of neat Fe₂O₃ and Fe₂O₃ supported on cenospheres

Fe ₂ O ₃ content, wt.%	Calcination temperature, °C	S ^{TDA} , m ² /g Fe ₂ O ₃
2.1	600	200
10.1	600	50
2.1	900	90
10.1	900	10
Fe ₂ O ₃	600	7.7
Fe ₂ O ₃	900	3.5

Thin films of iron oxide deposited on cenospheres were prepared by thermal decomposition of iron (3+) nitrate on the support surface including impregnation of cenospheres with Fe(NO₃)₃ solution of given concentration, drying at 110-120°C and thermal treatment of the samples at 500°C for 2 hours followed by calcination at 600-900°C

for 6 hours. Samples with the supported iron oxide content in the range of 0.95-10.1wt.% have been obtained. After every step of the thermal treatment the specific surface area of the samples was determined by TDA method using the standard procedure. The morphology of iron oxide films was studied by SEM. The specific surface area of iron oxide is equal to 10-200 m²/g Fe₂O₃ depending on the Fe₂O₃ content and pretreatment temperature. The increase of Fe₂O₃ content and treatment temperature results in the decrease of specific surface. It is important to note that the value of specific surface area for supported Fe₂O₃ is higher than that for the individual Fe₂O₃ treated under the same condition. Thus, using method of thermal decomposition of iron nitrate on the surface of cenospheres, the supported iron oxide systems with specific surface area of 50-200 m²/g Fe₂O₃ at 600°C and 10-90 m²/g Fe₂O₃ at 900°C have been obtained.

3.3. Synthesis and application of zeolite-coated cenospheres

The molar SiO₂/Al₂O₃ ratio for the most fraction of cenospheres resides in the range of 2-6 that is very close to the low silica zeolites. It is known that low silica zeolites with FAU,

OP-17

LTA and GIS types of framework are widely used as ion-exchangers, adsorbents and catalysts. Earlier it has been shown by numerous studies that fly ash can be effectively converted to the up to 13 different zeolitic products by hydrothermal synthesis or alkaline fusion. Process of fly ash to zeolite conversion was evaluated at pilot plant scale [9] and their application for water treatment technology was suggested [10-12]. The main disadvantage of the zeolite produced in such a way was powder-like character of the resulting materials, which required additional formation with binder to form granules. Moreover, the substantial heterogeneity of chemical and mineral composition of coal fly ash usually leads to unreproducible results, the products being contaminated with iron.

One of the possible way to achieve a better reproducibility and eliminate the need for additional granules formation is to utilize glassy microspheres with stabilized composition obtained by separation procedures described above.

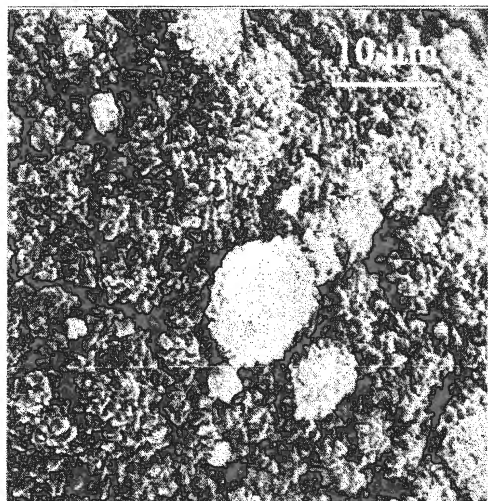


Figure 3. Zeolite NaP1 coating on the surface of cenosphere

The zeolitization process was performed in a Teflon vessel at 80-150°C and autogenous pressure with 1-4 M sodium hydroxide solution. XRD, optical and scanning electron microscopy were used to follow the progress of reaction. As a starting material for zeolitization a fraction of cenospheres with stabilized composition was used, which was additionally purified from magnetic impurities prior to conversion. Depending on the reaction condition three type of zeolite framework are formed, namely NaA (LTA), NaX (FAU) and

NaP1 (GIS) either as a mixture or as a single phase. Formation of zeolite crystals is found to occur both on the surface of cenospheres and in the liquid phase. Longer reaction time results in total conversion of cenosphere material to zeolites to form large crystals (3-20 micron) as well as dendrites which are irregularly attached to the surface, this process entailing almost complete destruction of cenospheres. When a special attention has been paid to preserve the intactness of cenosphere walls by adjusting process parameters, tiny crystals of zeolites (<1 micron) were formed which cover the surface of the cenosphere forming a kind of a coating (Fig. 3). Under this experimental condition it is possible to fulfil the conversion of the most part of glass phase to zeolites keeping intact initial spherical shape.

These spherical zeolite containing sorbents were tested as ion-exchangers for cesium and strontium removal from dilute and technological solutions and demonstrated up to 2 meq/g total cation exchange capacity and a good selectivity for the heavy metal ion removal.

4. Application of microspheres in catalysis

4.1. Catalytic properties of Fe₂O₃/cenosphere catalysts in deep oxidation of methane

Catalytic properties of Fe₂O₃/cenosphere catalysts were studied in a microcatalytic set-up with a quartz fixed bed reactor with 0.1-0.3 g of the catalyst. Specific catalytic activity of Fe₂O₃/cenospheres catalysts in the reaction of deep oxidation of methane is presented in Figure 4.

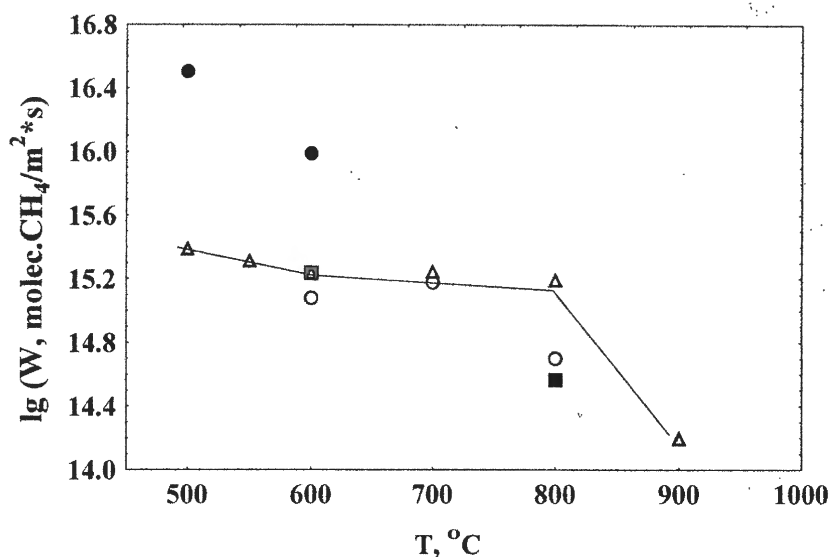


Figure 4. Variation of specific catalytic activity of Fe₂O₃/cenospheres in the reaction of deep oxidation of methane as a function of pretreatment temperature. CH₄:O₂=2:98; reaction temperature 400°C. Fe₂O₃ loading, wt.%: ○ - 1; ■ - 2.1; △ - 10; ● - 100.

Catalytic runs have shown that at 400°C the specific catalytic activity in the reaction of deep oxidation of methane does not depend with an experimental error on the content Fe₂O₃ and the pretreatment temperature of 2.1wt.% Fe₂O₃/cenosphere catalysts in the range of 500-700°C and 10wt.% Fe₂O₃/cenosphere catalysts in the 500-800°C range. The specific catalytic activity of Fe₂O₃/cenospheres is lower compared to the individual Fe₂O₃. The decrease of activity is likely to be caused by the interaction between iron oxide and the support of catalysts. The activity of Fe₂O₃ decreases very strong as a result of the rise of treatment temperature from 500 up to 600°C.

4.2. Catalytic properties of magnetic microspheres

It is known that catalysts of deep oxidation based on ferrosinels is less active than other oxide systems, in particular, cobaltites and chromites [13-16]. Nevertheless, iron oxide

OP-17

catalysts including ferrospinels are more resistant to catalytic poisons. They are also cheaper and nonpolluting. It was shown that magnetic microspheres of stabilized composition isolated from ashes contain substantial part of iron in the form of a solid solution based on Fe_3O_4 or ferrospinels, therefore they can possess activity in reactions of catalytic oxidation.

Catalytic activity of magnetic microspheres were tested both in the reaction of oxidative coupling and deep oxidation of methane. At a high temperature the selectivity of formation of C_2H_6 , C_2H_4 and CO from $\text{CH}_4\text{-O}_2$ feeds ranges up to 76-81% corresponding to characteristics of the best known catalysts of oxidative coupling of methane [5,17]. Activity of deep oxidation of methane was found to be lower than that for neat $\alpha\text{-Fe}_2\text{O}_3$ ($(4\text{-}8)\cdot 10^{16}$ and $31.5\cdot 10^{16}$ molec. $\text{CH}_4/\text{s}\cdot\text{m}^2$ correspondingly; 500°C , $\text{CH}_4:\text{O}_2 = 2:98$) but the same order of magnitude as for magnesium ferrite MgFe_2O_4 ($3.2\cdot 10^{16}$ molec. $\text{CH}_4/\text{s}\cdot\text{m}^2$) [13,14].

At present time the quantitative composition of (Ca,Mg,Al,Mn)-ferrites being part of the active component of microspheres is not established. Nevertheless, taking into account that formation of ferrospinels takes place from ferrosilicate melts, it could be presumed that the Ca,Mg-ferrite content in the composition of solid solution is determined by the total content of calcium and magnesium. It was found that microspheres with (CaO + MgO) being equal to

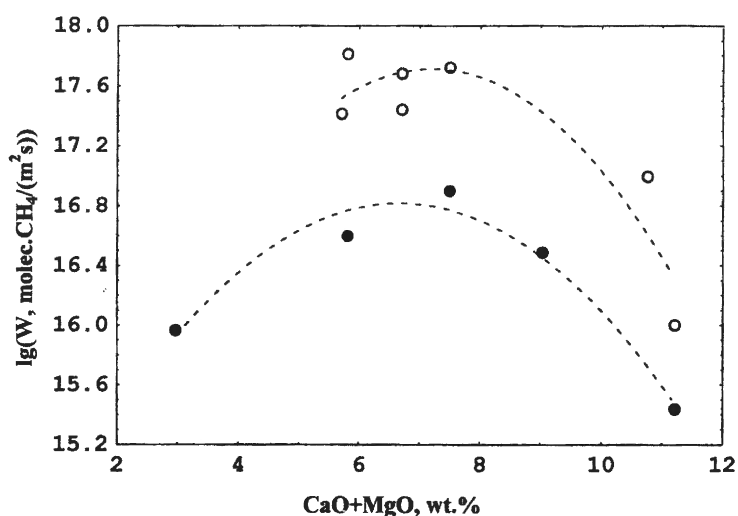


Figure 5. Catalytic activity of magnetic microspheres in reaction of methane deep oxidation.

○ - 520°C , $\text{CH}_4:\text{O}_2 = 85:15$ (vol.%); ● - 500°C , $\text{CH}_4:\text{O}_2 = 2:98$ (vol.%)

5-8 wt.% display the highest catalytic activity (Fig. 5). This fact is likely to be caused by the peculiarities of the active component formation.

Thus, magnetic microspheres are active in the reactions of oxidative conversion of methane, ferrospinel of (Ca,Mg,Al,Mn)-ferrite composition being the active component of magnetic microspheres. The range of compositions of magnetic microspheres displaying the highest catalytic activity in deep oxidation of methane has been established.

References

1. Kizilshstein L.Ya., et al. "Components of power plant ashes and slags", Moscow: Energoatomizdat, 1995.-176 p. In Russian.
2. Vassiliev S.V., *Fuel* 71(1992) 625.
3. Fisher G.L., Chang D.P.J., Brummer M., *Science*, 192 (1976) 553.
4. RU Patent No 21299470, 1999.
5. Anshits A.G., Kondratenko E.V., Fomenko E.V., et al, *Chemistry for sustainable development* 7(1999) 105 – In Russian.
6. RU Application No 2001112067.
7. Vereshagina T.A., Anshits N.N., Zykova I.D., et al., *Chemistry for sustainable development* 9 (2001) 379 – In Russian.
8. Zhdanov S.P., *Porous Glasses and Their Structure*, Wiss.Z. Friedrich Schiller-Univ. Jena: Naturwiss. Reihe 36(5)(1987) 817.
9. Querol X., Umana J.C., Plana F., et al., *Fuel* 80 (2001) 857.
10. Steenbruggen G., Hollman G.G., *Journal of geochemical exploration* 62 (1997) 305.
11. Wei-Heng Shih, Hsiao-Lan Chang., *Material Letters* 28 (1996) 263.
12. Mimura H., Yokota K., Akiba K., Onodera Y., *Journal of Nuclear Science and Technology* 38 (2001) 766.
13. Popovskii V.V., *Kinetika i kataliz* 13 (5) (1972) 1190 – In Russian.
14. Popovskii V.V., Boreskov G.K., Dzeventsi Z., et al, *Kinetika i kataliz* 12(4) (1971) 979. In Russian.
15. "Mechanisms of heterogeneous catalytic reactions of oxidation", Ed. Muzikantov V.S., Novosibirsk, Boreskov Institute of Catalysis SB RAS, 1993.- P.49. - In Russian.
16. Vodyankin A.Yu., Kurina L.N., Popov V.N., *Kinetika i kataliz* 40(4) (1999) 636.- In Russian.
17. Fomenko E.V., Kondratenko E.V., Salanov A.N., et al, *Catalysis Today* 42 (1998) 267.

MODELING OF HEAT AND MASS TRANSPORT IN WALL-COOLED TUBULAR REACTORS

G.W. Koning*, A.E. Kronberg, W.P.M. van Swaaij

University of Twente, Faculty of Chemical Technology

P.O. Box 217 7500 AE Enschede the Netherlands

Ph. xx-31-53-4315057 Fax. xx-31-53-4894738

email: gwkoning@hetnet.nl

Abstract

Heat transfer experiments with and without chemical reaction were performed in a wall-cooled tubular reactor. The oxidation of carbon monoxide over a CuO/ γ -alumina catalyst was used as a model reaction. A two-dimensional heterogeneous reactor model was used for calculation of the temperature and concentration profiles inside the packing. The experiments were performed at Re between 200 and 1400, reactor pressures of 3, 5.9 and 8 bara, wall temperatures of 156, 180 and 200°C and CO inlet concentrations ranging from 0.1 to 1.5vol%. The obtained data show that a radial distribution of the axial fluid velocity should be taken into account to reconcile the effective heat transport parameters obtained from experiments with and without reaction.

Introduction

For a proper design of a wall-cooled tubular reactor an accurate knowledge of the heat transfer properties of the catalyst bed is required because of the high parametric sensitivity of the reactor behavior towards these parameter, especially at conditions near runaway. Nowadays most cooled tubular reactors are not designed on the basis of kinetic data and model calculations, but experiments are carried out using single tubes in pilot scale reactors at conditions similar to those if the industrial process. Previous studies of heat transport phenomena in wall-cooled tubular reactors have shown a discrepancy between the effective radial conductivities of the catalyst bed measured with and without reaction [1-4]. Schwedock [3] found that the effective radial thermal conductivity was about 50% higher in the presence of reaction than when no reaction occurs. Borman et al. [4] used partial oxidation of ethylene to ethylene oxide over a silver/ γ -alumina catalyst in their work. The main disadvantages of this reaction system is its complicated kinetics, caused by the occurrence of complete combustion of ethylene as a parallel reaction, the large number of reactants that influence the reaction rate and

a slow deactivation of the catalyst. This investigation is a continuation of their work using a more simple reaction system. The oxidation of carbon monoxide to carbon dioxide over a copper oxide catalyst supported on γ -alumina has been chosen as model reaction. An advantage of this reaction is its large enthalpy of reaction of 283 kJ mole^{-1} , which causes a large temperature increase at a small change in the composition of the gas mixture. The kinetics of this reaction was studied separately using an integral and an internal-recycle reactor.

Reactor model

The reactor model used is commonly referred to in literature as a 'two-dimensional heterogeneous model without axial dispersion', in which the heat and mass balance equations and their boundary conditions are the following:

Heat balance

$$\epsilon \rho_f c_{p,f} \frac{\partial T_f}{\partial t} = \frac{1}{r} \frac{\partial}{\partial r} \left(\lambda_{e,r} r \frac{\partial T_f}{\partial r} \right) - u \rho_f c_{p,f} \frac{\partial T_f}{\partial z} + \alpha_p a (T_s - T_f) \quad (1)$$

$$(1-\epsilon) \rho_s c_{p,s} \frac{\partial T_s}{\partial t} = -\alpha_p a (T_s - T_f) + \sum_{i=1}^n -\Delta H_i R_i (c_s, T_s) \quad (2)$$

Mass balance component j

$$\epsilon \frac{\partial c_f^j}{\partial t} = \frac{1}{r} \frac{\partial}{\partial r} \left(D_{e,r}^j r \frac{\partial c_f^j}{\partial r} \right) - u \frac{\partial c_f^j}{\partial z} + k_g^j a (c_s^j - c_f^j) \quad (3)$$

$$(1-\epsilon) \frac{\partial c_s^j}{\partial t} = \sum_{i=1}^n -v_i^j R_i (c_s^j, T_s) - k_g^j a (c_s^j - c_f^j) \quad (4)$$

$$z=0 \quad T=T_0 \quad c=c_0 \quad (5)$$

$$r=0 \quad \frac{\partial T}{\partial r} = 0 \quad \frac{\partial c}{\partial r} = 0 \quad (6)$$

$$r=R_t \quad -\lambda_{e,r} \frac{\partial T}{\partial r} = \alpha_w (T - T_w) \quad \frac{\partial c}{\partial r} = 0 \quad (7)$$

$\lambda_{e,r}$ and α_w are the effective radial thermal conductivity and wall heat transfer coefficient. All the transport parameters in the model depend on the physical properties of the fluid and the

OP-18

solid and of the flow conditions inside the reactor. $D_{e,r}^j$ is the effective radial dispersion coefficient of component j . The general form of correlations for the dependence of $\lambda_{e,r}$ on the system parameters is:

$$\lambda_{e,r} = \lambda_r^0 + \lambda_r^f \quad (8)$$

The static contribution λ_r^0 depends on bed properties as particle shape and porosity, and on the thermal conductivity of the solid and the fluid. Well-known are the predictive correlations of Yagi and Kunii [5] and Bauer and Schlünder [6]. The contribution of fluid flow, which is the result of mixing of fluid elements moving with different velocities, is usually expressed as function of the fluid Peclet number:

$$\frac{\lambda_r^f}{\lambda_f} = \frac{Pe_h^0}{Pe_{h,r}^\infty}; \quad Pe_h^0 = \frac{u_0(\rho c_p)_f d_p^e}{\lambda_f} = RePr \quad (9)$$

$Pe_{h,r}^\infty$ is the Peclet number at fully developed turbulent flow and is a function of the tube-to-particle diameter ratio [7-9]. Distinguishing of heat conduction through the solid and the fluid phase, as is often made in literature, is not applied here. Direct heat transfer through the solid-solid contacts is usually of little importance and cannot be estimated accurately except for beds of particles of simple shape, consisting of certain materials, for which the contact area can be calculated [6]. Particle-to-particle heat transfer occurs mainly through the fluid phase in the interstices between the particles [10] and can therefore not be separated from the fluid-phase contribution.

The wall heat transfer coefficient is usually expressed in the form of a wall Nusselt number as:

$$Nu_w = C_1 + C_2 Re^{n_1} Pr^{n_2} \quad (10)$$

with n_2 close to 1/3 and n_1 between 0.5 and 1. The flow-independent contribution C_1 is often omitted. The wall heat transfer coefficient is also expressed as in the form of a Biot number, for which Dixon and Creswell [11] propose the following correlation:

$$Bi = \frac{\alpha_w R_t}{\lambda_{e,r}} = 1.5 N Re^{-0.25} \quad (11)$$

Literature agrees on the fact that correlations for Nu_w obtained by simultaneous optimization of $\lambda_{e,r}$ and α_w to fit the model prediction to the experimental data differ greatly. One possible explanation, based on heat transfer investigations not discussed in this paper, is

the neglecting of the influence of the wall roughness, which is recognized as an important parameter in heat exchanger design. It was found that the resistance of a quasi-stagnant fluid film at the reactor wall accounts for 70% for the total resistance to heat transfer for $Re > 500$. In case the distribution of the axial fluid velocity over the radius is non-uniform due to variation of the local porosity over the radius, $\lambda_{e,r}$ and $D_{e,r}$, as well as the fluid-to particle heat and mass transfer coefficient α_p and k_g^j will be a function of the radial position.

Experimental

Fluid and catalyst temperatures were measured by 32 thermocouples inside a 1 m reactor with an internal diameter of 53 mm. A scheme of the reactor is shown in Figure 1. The 0.5 mm type K thermocouples were fixed to a 'thermocouple ladder' placed inside the reactor tube prior to filling it with catalyst. The ladder consists of two 1 mm metal wires resting on the trough-shaped feed distributor, in between which crosses of glass-fiber reinforced poly-ether-ether-keton crosses are clamped. The thermocouples protrude 5 mm from the holes that are drilled in these crosses. Fluid temperatures were measured at 0, 8, 15, 21 and 25 mm from the centerline of the reactor at 6 axial positions. Close to the centerline, the temperature of a catalyst particle was measured by a thermocouple inserted into a 0.5 mm hole drilled in it. At 8 axial positions, a sample was withdrawn (100 ml min^{-1}) for analysis of the fluid composition. The concentrations of CO and CO₂ in the samples was measured by two infrared analyzers (Mayhak) put in series. The reactor feed consists mainly of air, which was supplied by a centrifugal compressor at a maximum flow rate of 600 NI min^{-1} at a pressure of 10 bara. The water content of the air was fixed at a concentration of 1400 ppm by passing it through a heat exchanger. After cooling, excess water is removed in two coalescing filters. Initially, air was dried using a dessicant dryer to achieve a water content smaller than 20 ppm. It was found, however, that the catalyst activity could not be kept constant due to fast, reversible adsorption of these traces of water. After a decrease in reactor temperature, the activity would slowly decrease. When exposing the bed to the maximum temperature of approximately 250°C , the original activity could be brought back only partially over a period of several days. Since it is impossible to achieve the exact same conditions during catalyst pretreatment and during reactor operation in the kinetic

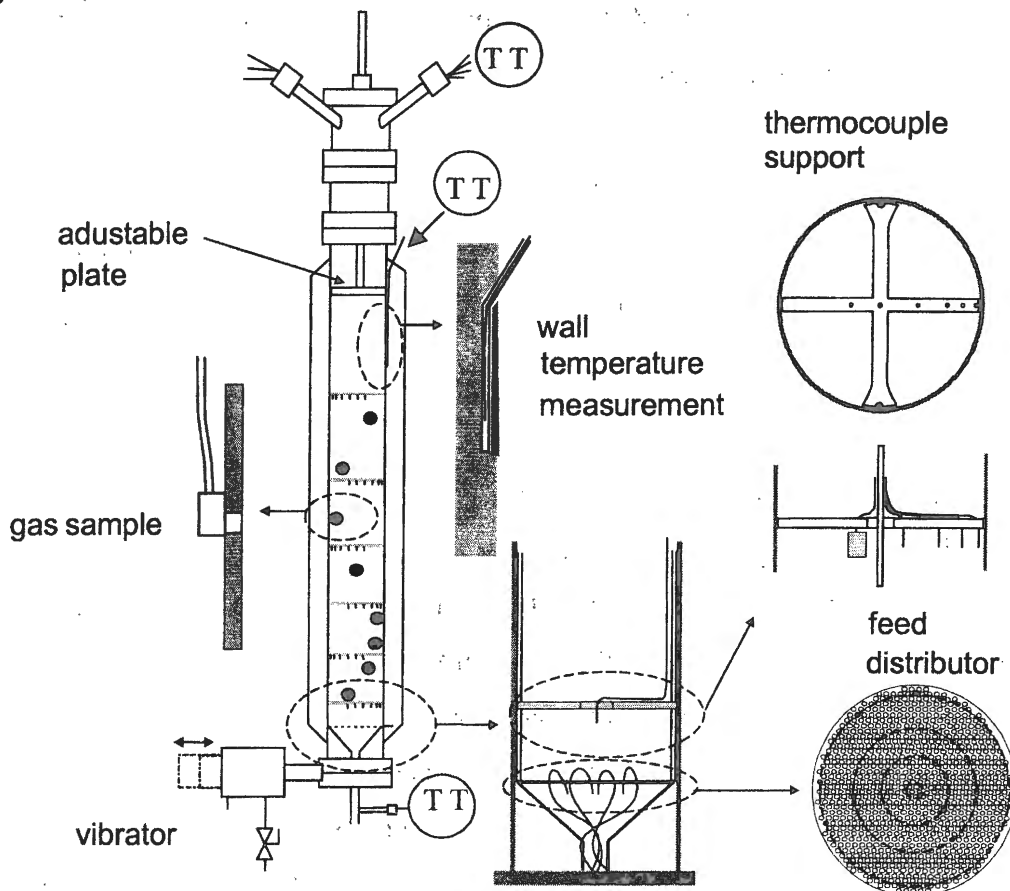


Fig. 1. Pilot scale wall-cooled tubular reactor

reactors and the pilot-scale tubular reactor, it was chosen to operate at constant air humidity, at which the activity was found to be constant and reproducible. Deactivation by water is extremely fast. When deliberately adding a few drops of water to the dry reactor feed, the CO conversion and the maximum reactor temperature initially increased. This observation can only be explained if the water is absorbed almost instantaneously by the catalyst near the inlet. This would cause so-called 'wrong-way behavior': A decrease in the reaction rate near the entrance causes an increase of the concentration further downstream, where the temperature of the catalyst is still high. Here the reaction rate will temporarily increase, causing the overall conversion to be higher than those of the steady states before and after the perturbation.

After removal of the excess water, the air is passed through three columns filled with active carbon to remove organic contaminants. The flow of air and that of CO and CO₂ (99% purity) was controlled by electronic mass flow controllers. Before the mass flow controller, CO was passed through a bed of SiC particles heated at 250°C to decompose any iron carbonyls present. When operating without this filter, deposition of rust-like material was found on the catalyst particles close to the reactor inlet. After mixing, the total flow rate is measured using an impeller flow meter.

Instead of relying on the mass flow controllers, the inlet concentration of CO was measured by analyzing the CO₂ concentration in a sample of the reactor effluent after passing it through a small catalyst bed in which all CO is converted. The reactor feed was preheated in a tubular oven and entered the reactor through a metal funnel. Just below the sieve plate covering this funnel, the fluid temperature was measured at 4 radial positions. The reactor wall was cooled by boiling water which pumped through the cooling jacket at 4 m³ h⁻¹ using a centrifugal pump. By varying the pressure in the cooling system, the coolant temperature could be varied between 100 and 250°C with an accuracy of 0.3°C. At 4 axial positions, the wall temperature was measured by thermocouples inserted into capillaries welded into slits in the reactor wall. After pretreatment of the catalyst, which consisted of heating it at 500°C for 30 hours in dry air, the reactor was filled with 1.5 kg of it. The bed was then repacked by fluidization. The flow rate was slowly increased and decreased whilst vibrating the reactor using a pneumatically driven vibrator. During this process, catalyst particles are thoroughly mixed over the length of the reactor, as was observed in a glass reactor. A reproducible porosity of 0.42 ± 0.01 could be achieved when vibrating the reactor for one minute after abruptly stopping the air supply. The reactor setup was fully automated using a Hewlett Packard data acquisition unit coupled to a PC. This allowed series of experiments at different flow rates, wall- and inlet temperatures, concentrations and reactor pressures to be performed automatically, whilst simultaneously safeguarding the setup using the control software. After changing a setpoint, steady state was assumed to be achieved when – after a minimum period- the slope of some relevant temperatures and concentrations versus time had become small enough. In case of no chemical reaction, the fluid temperature at the reactor inlet was approximately 50°C above the wall temperature. Despite the fact that the feed distributor was insulated from the reactor wall, a non-uniform radial temperature distribution was observed at the inlet low flow rates. When calculating the effective heat transport parameters, this temperature distribution was used as boundary condition at $z = 0$. Similarly, the measured wall temperature, which showed a slight increase, was used in the boundary conditions at the reactor wall. In experiments with chemical reaction, the inlet temperature was uniform and equal to the wall temperature. After changing the reactor temperature or pressure, the reactor was flushed with air for a night to allow the water content of the catalyst to come at equilibrium with that of the fluid. When applying this procedure, experiments performed at different concentrations were very well reproducible, as is shown in Figure 2. The CO conversion near the end of the reactor and the maximum temperature do not change when twice varying the CO inlet concentration in the same manner over a period of 40 hours. Temperature and concentration profiles were found to be reproducible after repacking of the catalyst bed by fluidization, during which the

OP-18

catalyst is redistributed over the reactor. This means that no change of the catalytic activity over the reactor length occurred, which could be caused by fouling or exposure to different temperatures.

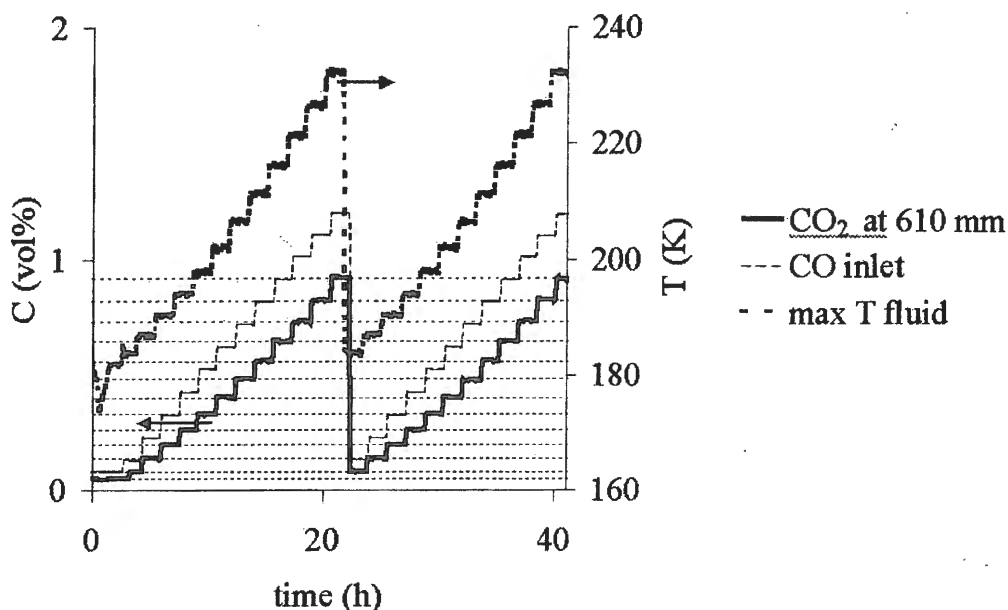


Fig. 2. Reproducibility of experiments performed at $T_{\text{inlet}}=T_{\text{wall}}=178^{\circ}\text{C}$, $P=3.8$ bara, and a gas load of $3.55 \text{ kg m}^{-2} \text{ s}^{-1}$. Shown are the maximum reactor temperature and CO_2 concentration near the bed exit as function of the CO inlet concentration. Dashed lines are drawn through CO_2 concentrations measured at the same CO inlet concentrations, which shown no inclination with respect to the horizon axis.

Catalyst properties and kinetics

The used catalyst is a γ -alumina extrudate containing 29 wt% copper (II) oxide. The particles have an average length of 11.5 mm and a constant diameter of 5.5 mm. An integral reactor with a length of 10 cm and an internal diameter of 8 mm, filled with a mixture of 2-5 wt% crushed catalyst (0.2 mm) and silicium carbide particles of the same size was used to study the intrinsic reaction kinetics. Experiments were performed at temperatures between 130 and 240°C , pressures between 2 and 9 bara and fluid flow rates between 0.15 and $0.75 \text{ kgm}^{-2}\text{s}^{-1}$. The inlet concentrations of CO and CO_2 were varied between 0.1 and 1.2 and between 0.1 and 1 vol% respectively. The overall reaction rate for the entire catalyst particles was measured in an internal recycle reactor, which is described in [12]. The reactor was modified in order to increase the maximum rotational speed of the impeller. In the original configuration, the catalyst pellets were placed inside the blades of the axial impeller used for mixing of the fluid in the reactor. During the experiments performed in this investigation, catalyst pellets with small (0.5 mm) holes were mounted on metal pins or thermocouples on ring just below the impeller. At this position, the mass and heat transfer rate between the fluid and the catalyst are smaller than in

the first case. The more important advantage is, however, that the catalyst and fluid temperatures are known accurately, making it possible to correct the measured reaction rate for particle-to-fluid heat and mass transfer limitations. In this reactor, experiments were performed at temperatures between 115 and 225°C, pressures between 2 and 8 bara and CO and CO₂ concentrations between 0.2 and 1.4 vol%. Due to the large sensitivity of the catalyst activity to water, the same air was used as in the pilot-scale wall-cooled tubular reactor. The intrinsic kinetics of CO oxidation is described by the following Langmuir-Hinshelwood type of reaction rate expression:

$$R = \frac{k_3 [\text{CO}]}{1 + \frac{k_3}{k_{-6}} [\text{CO}] + K_7 [\text{CO}_2] + K_8 [\text{H}_2\text{O}]} \quad (12)$$

$$k_j = k_{0j} \exp\left(\frac{-E_a}{RT}\right); \quad K_j = K_{0j} \exp\left(\frac{-\Delta H_{\text{ads}}}{RT}\right)$$

Eq. (12) implies that CO reacts from the gas phase according to an Eley-Rideal mechanism. A distinction is made between CO₂ which adsorbs from the gas phase on an active site ($K_7 [\text{CO}_2]$) and CO₂ that is present as a result of reaction of CO with adsorbed oxygen ($k_3/k_{-6} [\text{CO}]$). This equation has been taken from [12], with an additional term to account for the influence of the water concentration. The reaction rate measured in the integral reactor was found to decrease with increasing reactor pressure. When using intra-particle diffusion limitation to account for this decrease, the average pore size should be unrealistically small. Water adsorption does seem the only plausible explanation for the influence of pressure on the reaction rate. The overall reaction rate over the entire catalyst particles is affected by intra-particle diffusion limitation:

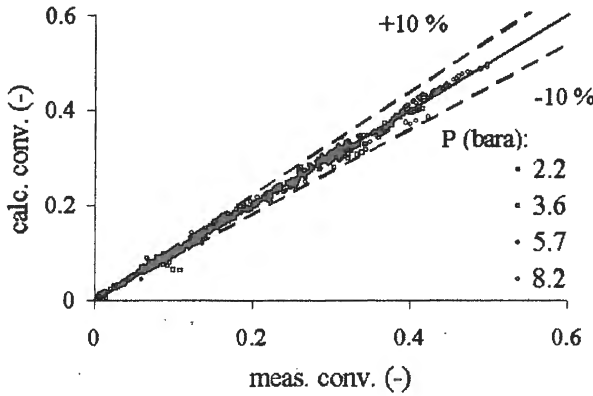
$$\frac{1}{V} \int_V R(C, T) dV = \eta R(C_s, T_s) \quad (13)$$

C_s and T_s are the concentration and temperature at the surface of the catalyst and η is the effectiveness factor, which is a function of the size and geometry of the catalyst particles, the internal pore structure and of temperature and pressure. The effectiveness factor is approximated analytically using a method similar to that of [13], in which the particle shape is taken into account.

The effective diffusivities of CO and CO₂ were calculated from the pore size distribution measured by mercury porosimetry, combined with the results of permeation experiments

OP-18

using helium. The effective diffusivity is the result of weighed contributions of the different pore sizes, assuming that the pores are in parallel. Figure 3 shows a parity plot of the calculated versus the measured conversion for all experiments in the internal recycle reactor, together with the values of the intrinsic kinetic constants. The obtained kinetics expression accurately describes the effect of different CO₂ inlet concentrations on the temperature and concentration profiles measured in the pilot-scale wall-cooled tubular reactor.



Values of parameters in eq. 12:

$k_{0,3}$	43	$\text{kg}^{-1}\text{s}^{-1}$
E_{a3}	33	kJ mole^{-1}
$k_{0,3}/k_{0,.6}$	$6.3 \cdot 10^{-6}$	$\text{kg}^{-1}\text{s}^{-1}$
$E_{a,.6} - E_{a3}$	-49	kJ mole^{-1}
$K_{0,7}$	$2.0 \cdot 10^{-9}$	$\text{kg}^{-1}\text{s}^{-1}$
ΔH_7	-79	kJ mole^{-1}
$K_{0,8}$	$1.2 \cdot 10^{-6}$	$\text{kg}^{-1}\text{s}^{-1}$
ΔH_8	-60	kJ mole^{-1}
E_a apparent	50	kJ mole^{-1}
Average error	4 %	

Fig. 3. Parity plots of the reaction rate of CO oxidation over entire catalyst particles after optimization of the constants in the expression of the intrinsic reaction kinetics. $K_{0,8}$ and ΔH_8 as in integral reactor.

Results

Experiments without reaction have been performed using 6 catalyst beds which were obtained by catalyst repacking by fluidization. A total of 113 experiments were performed at reactor pressures between 2 and 8 bara, flow rates of 0.1 to 5.5 $\text{kg m}^{-2} \text{s}^{-1}$, wall temperatures between 100 and 200°C and temperature differences of 6 to 70°C. The effective radial thermal conductivity and wall heat transfer coefficient were optimized to minimize the difference between the measured and the calculated temperatures as:

$$f(\lambda_{e,r}, \alpha_w) = \sum_{i=1}^n \frac{(T_i^{\text{calc}} - T_i^{\text{exp}})^2}{T_{r=0}^{\text{calc}} - T_{r=1}^{\text{calc}}} \quad (14)$$

Figure 4 shows $\lambda_{e,r}/\lambda_f$ and Nu_w as function the fluid Peclet number. The dashed lines in this figure are calculated by averaging the heat transfer parameters obtained for individual experiments, whereas the solid lines were obtained by using the entire set of experimental data. In the latter case, $\lambda_{e,r}$ and α_w were assumed to comply with eqs. (8) and (11).

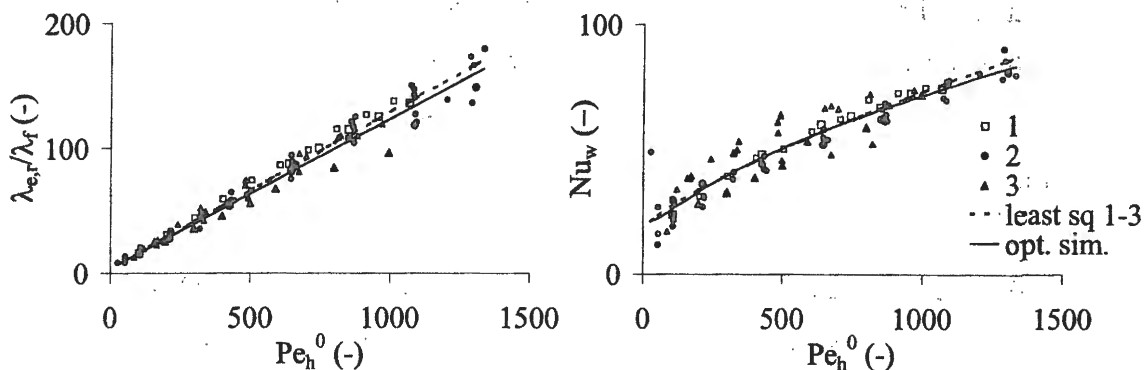


Fig. 4. Effective radial thermal conductivity and wall Nusselt number as function of the fluid Peclet number. Experiments after re-assembly of the thermocouple ladder are shown as different series.

Both approaches agree very well, considering the non-linear differences between both averaging methods. Axial dispersion of heat, omitted in the balance equations, was found to be of negligible influence on the obtained heat transport parameters and on the target function of the minimization procedure. A possible influence of a radial velocity distribution cannot be detected when evaluating temperature fields measured without chemical, as was observed earlier by Borman et al. [13], who made a theoretical investigation using a two-region model. When applying a radial velocity distribution in eq. (1), assuming the fluid contribution to the effective radial thermal conductivity to be independent of the radial position, the wall heat transfer coefficient remains unchanged, whilst λ_r^f changes proportionally to the ratio of the velocity at the centerline of the reactor and the average axial fluid velocity. The shape of the radial temperature profile does not depend on the shape and extent of the velocity maldistribution.

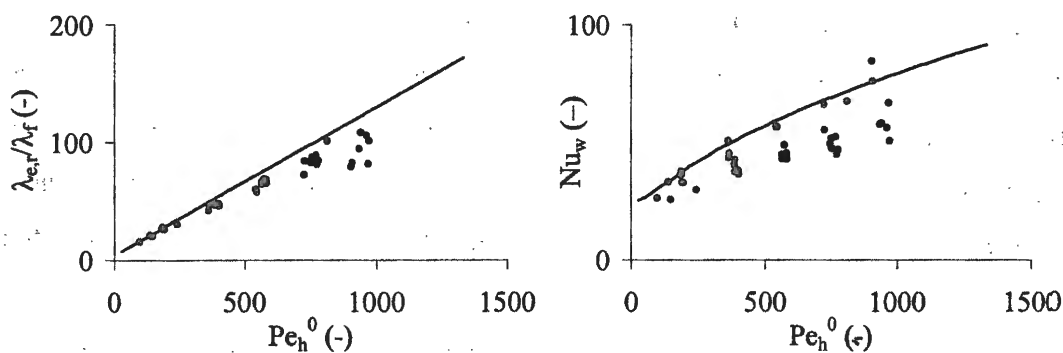


Fig. 5. Effective radial thermal conductivity and wall Nusselt number from experiments with chemical reaction at $CO_{in}=1$ vol %. Lines show the heat transfer parameters obtained by optimization of eqs. (8) and (11) to all experiments without chemical reaction. $Pe_m=Pe_h$.

OP-18

Temperature and concentration profiles with chemical reaction have been measured at Re between 200 and 1400, reactor pressures of 3, 5.9 and 8 bara and CO inlet concentrations between 0.1 and 1.5 vol %. The wall- and inlet temperatures were the same and varied between 156 and 200 °C. The maximum bed temperature was 265 °C. A fair description of the measured temperature and concentration profiles was obtained when using the independently measured reaction kinetics and the heat transfer parameters measured without reaction. In the model, radial mass transport was assumed to be analogous to radial heat transfer, so that $Pe_{m,r} = Pe_{h,r}$.

The measured temperature difference between the fluid and solid phase did agree with the predictions for the fluid-to-particle heat and mass transfer coefficient taken from [15] and [16]. However, it was found that the effective heat transfer parameters are very sensitive to the reaction kinetics. Therefore, the reaction rate was optimized to match the measured conversion. This was done by multiplying constant $k_{0,3}$ in eq. (12) by a constant. The used conversion is the maximum measured value smaller than 80%. The maximum change of the reaction rate with respect to the reaction rate measured in the kinetic reactors is rather small and corresponds to an error in the apparent activation energy of $\pm 2.5\%$. Figure 5 shows the effective heat transfer parameters calculated for experiments at different pressures, wall and inlet temperatures and flow rates with a CO inlet concentration of 1 vol%. At low Pe_0^f , the values of $\lambda_{e,r}$ agree with the values measured without chemical reaction. At higher fluid velocities, however, the effective radial thermal conductivity tends to become significantly smaller. After optimization of the transport parameters, the temperature profiles close to the inlet are underestimated, whilst the calculated temperatures after the hot spot are higher than measured. The discrepancy between the heat transfer parameters with and without reaction cannot be attributed to the neglecting of heat and mass dispersion in axial direction, since their influence on the calculated profiles is negligible at the applied fluid velocities. The use of a non-uniform radial velocity distribution is the most plausible reason for the discrepancy. The effect of such velocity distribution on the predictions of the model has been investigated by [14,17-29]. Hennecke and Schlünder [17] and Hein [27] observed a significant improvement of their model's agreement with experimental data at low Re when including a velocity distribution. The most important effect of a decreased fluid velocity at the core of the bed is the increase in the ratio of the rate heat production by reaction and the rate of heat removal through convection. The reaction rate is affected only moderately affected by radial differences in the fluid velocity. Radial concentration differences are usually much smaller

than radial temperature differences and the reaction rate is much less sensitive to the concentration than it is to temperature. To improve our model, the porosity- and velocity distributions will be calculated according to Gies et al. [25], who experimentally investigated porosity and velocity profiles for packings of spheres. For cylindrical particles with a height equal to the diameter, the following correlation for the porosity is proposed:

$$\epsilon(r) = \epsilon_{\infty} \left[1 + \left(\frac{\epsilon_w}{\epsilon_{\infty}} - 1 \right) \exp \left(-C \frac{(R_t - r)}{d_p^e} \right) \right], \quad (15)$$

in which ϵ_w is the porosity at the wall and ϵ_{∞} the porosity at infinite distance from the wall, to be calculated from the known average bed porosity. For cylinders, $\epsilon_w = 0.65$ and $C = 6$. The velocity distribution over the radius is obtained assuming radial pressure gradients to be negligible. The radial velocity distribution for different values of ϵ_w . $u_{r=0}/u_0$ was found not to depend on u_0 for $140 < Re < 1400$.

When applying the non-uniform radial porosity and velocity distributions, the dependence of $\lambda_{e,r}^f$ on r should be defined. The radial porosity distribution has two opposite effects. The increased porosity near the wall results in an increased fluid velocity and in a decreased tortuosity of the fluid path in between the catalyst pellets. These two effects oppositely influence $\lambda_{e,r}^f$ at high fluid flow rates. In accordance with [3] and [17], the effects are assumed to cancel each other, so that $\lambda_{e,r}$ is constant over the radius. The reaction rate and the fluid-to-particle heat and mass transfer coefficients are corrected for the radial porosity- and velocity distribution. It was found that, for constant ratio of the velocity at the core of the bed and the average fluid velocity, the model predictions are not sensitive to the exact shape of the velocity profile. Changing of the value of C in eq. (15) or even the assumption of full slip conditions at the wall does hardly affect the calculated concentration and temperature fields.

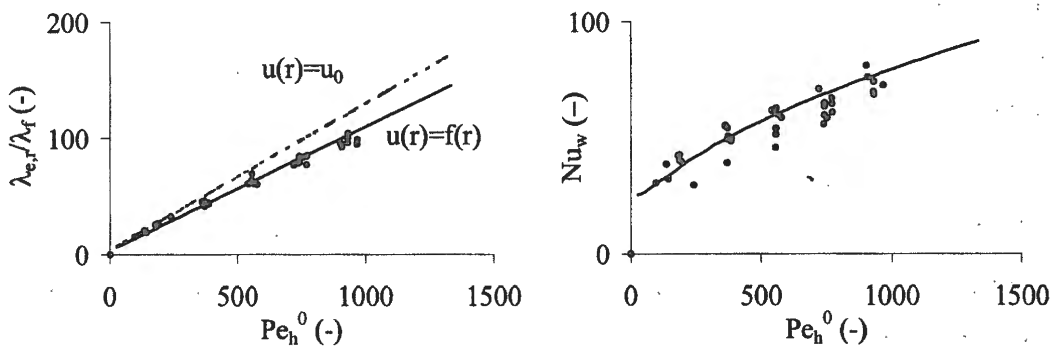


Fig. 6. As Fig. 5, with radial distribution of the axial fluid velocity. $C = 6$, $\epsilon_w = 0.75$. $u_{r=0} = 0.85 u_0$. Effective radial thermal conductivity in case of uniform velocity distribution is shown as dashed line.

OP-18

Figure 6 shows the effective heat transfer parameters with and without chemical reaction for the case $u_{r=0} = 0.85 u_0$, corresponding to $\epsilon_w = 0.75$. This distribution was found to give optimum agreement between the effective heat transfer parameters obtained with and without chemical reaction. $\epsilon_w = 0.75$ is between the value suggested for the cylinders with a height-over-diameter ratio of 1 and the value recommended for spheres, which is 0.87. The improvement becomes more clear when lumping $\lambda_{e,r}$ and α_w into an overall heat transfer coefficient U , which is the proportionality coefficient between the heat flux to the wall and the difference between the average bed temperature and the wall temperature.

With assumption of a radial velocity distribution, the results of the model are closer to the experimental data, as is shown in Figure 7. The initial axial temperature gradient at the reactor inlet is not sensitive to radial heat transport, but is determined mainly by the ratio of the heat production rate and the rate of heat removal through convection. When overestimating the velocity at the core of the reactor, the initial temperature is underestimated. As a result, $\lambda_{e,r}$ is decreased during parameter estimation, causing overestimating of the temperature after the hot spot in the reactor.

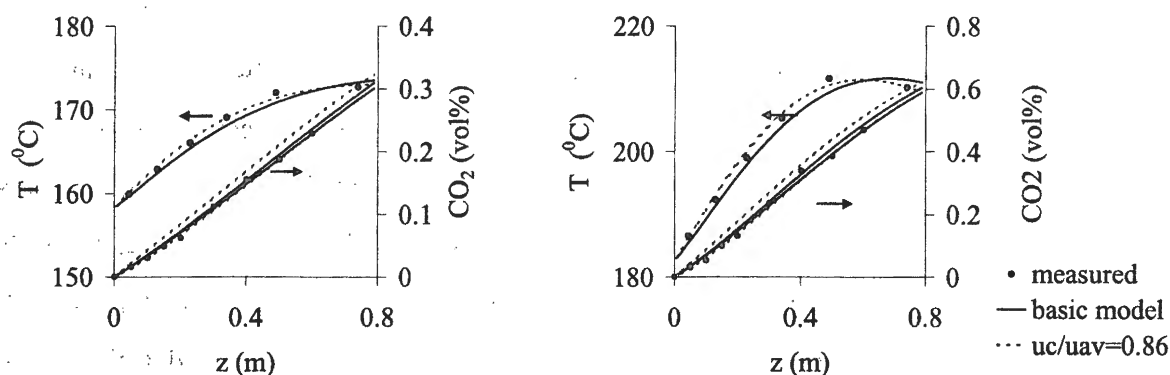


Fig. 7. Temperature at $r=0$ and CO_2 concentration at $r=0$ and $r=R_i$ for experiments at different wall- and inlet temperatures. $Re=1100$, $P=8$ bara, $\text{CO}_{in}=1$ vol%.

Conclusions

Experiments performed in a pilot-scale wall-cooled tubular reactor using a wide range of operating conditions were evaluated using a two-dimensional heterogeneous reactor model. It was found that the assumption of a non-uniform radial distribution of the axial fluid velocity improves the agreement between the effective heat transport parameters obtained from experiments with and without reaction and results in a better description of the measured temperature and concentration profiles.

Notation

a	specific area per m ³ of bed	m ² m ⁻³
a _p	surface of a particle	m ²
C	constant or dimensionless concentration	-
c	concentration component j	mole m ⁻³
c _p	heat capacity	J kg ⁻¹ K ⁻¹
d _p	particle diameter	m
d _p ^e , d _p	(volume-equivalent) particle diameter	m
D	diffusion coefficient	m ² s ⁻¹
E _a	activation energy	J mole ⁻¹
ΔH _{ads}	adsorption enthalpy	J mole ⁻¹
ΔH _r	reaction enthalpy	J mole ⁻¹
h _p	length of a cylindrical particle	m
K _#	adsorption constant	kg ⁻¹ s ⁻¹
k	reaction rate constant, order n:	mole ⁽¹⁻ⁿ⁾ m ³ⁿ kg ⁻¹ s ⁻¹
k _g	particle-to-fluid mass transfer coefficient	m s ⁻¹
n	constant or reaction order	-
Pe _{h,r}	fluid Peclet number at fully developed turb. flow	-
R	gas constant	8.3143 J mole ⁻¹ K ⁻¹
R _i	reaction rate i	mole kg ⁻¹ s ⁻¹
R _t	bed radius	m
r	radial coordinate	m
r _p	radius of a cylindrical particle	m
T	temperature	K
t	time	s
U	overall heat transfer coefficient	W m ⁻² K ⁻¹
u	superficial fluid velocity	m s ⁻¹
v _p	volume of a particle	m ³
z	axial coordinate	m
<i>Greek</i>		
α _p	particle-to-fluid heat transfer coefficient	W m ⁻² K ⁻¹
α _w	wall heat transfer coefficient	W m ⁻² K ⁻¹
ε	bed porosity	-
ε _w , ε	porosity at the wall and at infinite distance from the wall	-
η	dynamic viscosity	Pa s
	or: effectiveness factor	-
λ _{e,r}	effective radial thermal conductivity	W m ⁻¹ K ⁻¹
λ	thermal conductivity	W m ⁻¹ K ⁻¹
λ _r ⁰	static contribution to λ _{e,r}	W m ⁻¹ K ⁻¹
λ _r ^f	dynamic contribution to λ _{e,r}	W m ⁻¹ K ⁻¹
v	stoichiometry constant	-
ρ	density	kg m ⁻³
<i>dimensionless groups</i>		
Bi	Biot number for heat transfer at the wall	$\frac{\alpha_w R_t}{\lambda_{e,r}}$
Nu _w	wall Nusselt number	$\frac{\alpha_w d_p^e}{\lambda_f}$
Pe _h ⁰	fluid Peclet number	$\frac{u_0 (\rho c_p)_f d_p^e}{\lambda_f}$
Pe _{h,r}	fluid Peclet number for radial heat transport	$\frac{u_0 (\rho c_p)_f d_p^e}{\lambda_{e,r}}$

OP-18

$Pe_{m,r}$	fluid Peclet number for mass heat transport	$\frac{u_0 d_p^e}{D_{e,r}}$
Pr	fluid Prandtl number	$\frac{\eta c_{p,f}}{\lambda_f}$
Re	Reynolds number	$\frac{u_0 \rho_f d_p^e}{\eta}$

sub- / superscripts

0	average value at inlet conditions
calc	calculated
e	effective
exp	experimental
f	fluid
h	heat
i	reaction number
j	component number
m	mass
r	radial
s	solid

Literature cited

- 1 Hall, R.E. and Smith, J.M., Chem. Eng. Prog., 45 (1949) 459.
- 2 Hoffman, H., Chem. Ing. Techn., 51 (1979) 257
- 3 Schwedock, M.J., Windes, L.C., Ray, W.H., Chem. Eng. Comm., 78 (1989) 45
- 4 Schouten, E.P.S., Borman, P.C., Westerterp, K.R., Chem. Eng. Sc., 49 (1994) 4725.
- 5 Yagi, S., Kunii, D., AIChE J., 3 (1957) 373.
- 6 Bauer, R., Schlünder, E.U., Int. Chem. Eng., 18 (1978) 189.
- 7 Schlünder, E.U., Chem. Ing. Techn., 38 (1966) 967
- 8 Fahien, R.W., Smith, J.M., AIChE J., 1 (1955), 28
- 9 Specchia, V., Baldi, G., Sicardi, S., Chem. Eng. Comm., 4 (1980) 361
- 10 Eigenberger, G., Chem. Eng. Sc., 27 (1972) 2909
- 11 Dixon, A.G., Creswell, D.L., AIChE J., 25 (1979) 663
- 12 Borman, P.C., Bos, A.N.R., Westerterp, K.R., AIChE J., 40 (1994) 862
- 13 Wijngaarden, R., J., 'The scaling-up of cooled tubular reactors', thesis, University of Twente (1988)
- 14 Borkink, J.G.H., Westerterp, K.R., Chem. Eng. Sc., 49 (1994), 863
- 15 Beek, W.J., Drinkenburg, Proc. Int. Symp. Fluidization, Neth. Univ. Press, Amsterdam (1967) 507
- 16 Gnielinski, V., Verfahrenstechnik, 16 (1982) 36
- 17 Hennecke, F.W., Schlünder, E.U., Chem. Engng. Technol. 45 (1973) 277
- 18 Kalthoff, O., Vortmeyer, D., Chem. Eng. Sc., 35 (1980) 1637
- 19 Vortmeyer, D., Schuster, J., Chem. Eng. Sc., 38 (1983) 1691
- 20 Tsotsas, E., Schlünder, E.U., Chem. Eng. Sc., 43 (1988) 1200
- 21 Ziólkowski, D., Szustek, S., Chem. Eng. Sc., 44 (1989) 1195
- 22 Foumeny, E.A., Pahlevandahzeh, H., Chem. Eng. Technol., 14 (1990) 161
- 23 Vortmeyer, D., Haidegger, E., Chem. Eng. Sc. 46 (1991) 2651
- 24 Ziólkowska, I., Ziólkowski, D., Chem. Eng. Sc., 48 (1993) 3283
- 25 Bey, O., Eigenberger, G., Chem. Ing. Techn., 68 (1996) 1294
- 26 Latifi, M.A., Lesage, F., Midoux, N., Computers Chem. Engng 22(1998) 5905
- 27 Hein, S., 'Modellierung wandgekühlter katalytischer Festbettreaktoren mit Ein- und Zweiphasenmodellen', Fortschrittberichte VDI, Reihe 3, Nr. 593, VDI Verlag, Düsseldorf (1999)
- 28 Winterberg, M., Tsotsas, E., Krischke, A., Vortmeyer, D., Chem. Eng. Sc. 55 (2000) 967
- 29 Winterberg, M., Tsotsas, E., Chem. Eng. Sc., 55 (2000), 5937
- 30 Giese, M., Rottschäfer, K., Vortmeyer, D., AIChE J., 44 (1998) 484

INVESTIGATION OF PARAMAGNETIC PROPERTIES OF CATALYSTS ON THE BASIS of $\text{Ca}_{1-x}\text{Sr}_x\text{FeO}_{2.5+y}$ BY EPR METHOD

Z.A. Mansurov, Y.A. Ryabikin, M.I. Tulepov, O.V. Zashkvara, O.Yu.Podyacheva^a,
A.P.Nemudry^b

Al-Farabi Kazakh National University, Almaty

^a *Borekov Institute of Catalysis SB RAS, Pr. Akad. Lavrentieva 5, 630090 Novosibirsk, Russia*

^b *Institute of Solid State Chemistry and Mechanochemistry, Kutateladze st. 18, 630128 Novosibirsk, Russia*

Introduction

The problem of environment protection both from emissions of mobile and stationary sources is the real challenge for world scientific community. The catalytic methods seem to be the best solution for this set of problems [1-2]. To date, however, there are no efficient catalysts, which operate at low temperatures for purification of gases from nitrogen oxides. To fill this gap we suggest to use innovative approach based upon development of principally new perovskite catalysts, and which requires interdisciplinary research unifying specialists in catalysis and solid state chemistry.

Following the data [3-7], catalysts on the basis of perovskites are considered to be perspective. In connection with this, synthesis of perovskite catalysts with the general formula $\text{Ca}_{1-x}\text{Sr}_x\text{FeO}_{2.5+y}$ and different x and y and investigation of their paramagnetic structure are of interest for determining the correlation of their parameters with catalytic activity in NO_x decomposition.

Experimental

$\text{Ca}_{1-x}\text{Sr}_x\text{FeO}_{2.5}$ samples were prepared by standard solid state technique. Stoichiometric amounts of CaCO_3 , SrCO_3 and Fe_2O_3 (analytical grade) were ground and calcined in air at 900°C for 12h. The samples were pelletized and heated in air at temperatures 1200°C (24h), 1000°C (12h) and quenched thereafter in liquid N_2 . To remove the rest of the oxygen excess, the pellets of $\text{Ca}_{1-x}\text{Sr}_x\text{FeO}_{2.5+y}$ were placed into a quartz ampoule heated at 1000°C under dynamic vacuum (10^{-2} Torr) for 6h and quenched under vacuum in liquid N_2 . [8]

EPR spectra were recorded on modernized IRES-1001 Spectrometer operating in 3-cm. wave band (in X-band), magnetic field modulation amplitudes were chosen to be 3E, the value of SHF microwave power was taken so that to avoid possible effects of saturation, the samples were ground in a porcelain mortar to 0.1-0.5 mm.

OP-19

The sample amounts were 80-100 mg. For $\text{Ca}_{0.5}\text{Sr}_{0.5}\text{FeO}_{3.0}$ sample, its amount was reduced to 15 mg due to its strongly pronounced ferromagnetic properties. The sample was placed into an ampoule of optical quartz, which was set into EPR spectrometer resonator to be measured.

To record TPR spectra, a gas chromatograph equipped with heat conductivity detector was used. The catalyst sample was placed into a quartz reactor, which, in its turn, was inserted into an oven with the controlled rate of heating. After the reactor there was a trap with askarite for absorption of reaction products from the reaction mixture (H_2O).

8% H_2 -Ar (TPR) was used as a mixture, the heating rate was 8°C per minute. The rate of linear heating varied within $5\text{-}25^\circ\text{C}/\text{min}$. After carrying out the experiment by TPR, the sample was quenched to room temperature in H_2 -Ar mixture.

Results and discussion

Five samples of the following compositions: I- $\text{Ca}_{0.3}\text{Sr}_{0.7}\text{FeO}_{2.5}$, II- $\text{Ca}_{0.5}\text{Sr}_{0.5}\text{FeO}_{2.5}$, III- $\text{Ca}_{0.7}\text{Sr}_{0.3}\text{FeO}_{2.5}$, IV- $\text{Ca}_{0.7}\text{Sr}_{0.3}\text{FeO}_{3.0}$, V- $\text{Ca}_{0.5}\text{Sr}_{0.5}\text{FeO}_{3.0}$ were studied. This paper presents some preliminary results on the investigation of paramagnetic properties of these systems and search for correlations between their catalytic activity and EPR spectra parameters. It should be noted right away that for all these samples EPR spectra differ significantly. It is surprising. The thing is that the radii of Ca and Sr atoms are practically equal, and these two elements very readily substitute one another in different compounds, e.g. in bone tissue and some minerals. Therefore, it seems, one might have expected much identical in EPR spectra for a group consisting of the first three samples, and in the spectra of samples IV and V.

EPR spectrum of $\text{Ca}_{0.3}\text{Sr}_{0.7}\text{FeO}_{2.5}$ sample has a complex rarely observed form. A wide line with the width $\Delta H=900$ Oe and $g=2.028$ may be marked out. Spin concentration for this line is $N=1.7 \cdot 10^{18}$ sp/g. Beside this line with a gradually increasing intensity up to the weakest fields there is a line, which may be regarded as bending around several lines having g -factors from 4.3 to higher values. These lines may be caused by isolated Fe^{3+} ions, which are in the field of a quasi-rhombic symmetry (rhombic-like). EPR line with $g=2.028$ appears due to interaction of Fe^{3+} ions, which are in the field of a slightly distorted octahedron. Beside these lines between components 3 and 4 of the spectrum of a bench sample of bivalent manganese there was detected a weak signal of a free radical nature with $\Delta H=7.2$ Oe and $N=3.8 \cdot 10^{14}$ sp/g.

The spectrum of $\text{Ca}_{0.5}\text{Sr}_{0.5}\text{FeO}_{2.5}$ sample has a wide line too with $\Delta H=1000$ Oe and $g=2.021$ due to the interaction of Fe^{3+} ions, which are in the field of a slightly distorted octahedron. Beside these lines in the spectrum there is a faint line with $g=4.2$ and $H=220$ Oe due to isolated Fe^{3+} ions, which are in the field of low symmetry caused by ortho-rhombic distortions of the crystalline grid. For

this sample also one can observe a bending line but of much less intensity, several lines with small g-factors. There is also a "free radical" line with $\Delta H=7.2$ Oe, but its intensity is five times less than it is for $\text{Ca}_{0.3}\text{Sr}_{0.7}\text{FeO}_{2.5}$ sample.

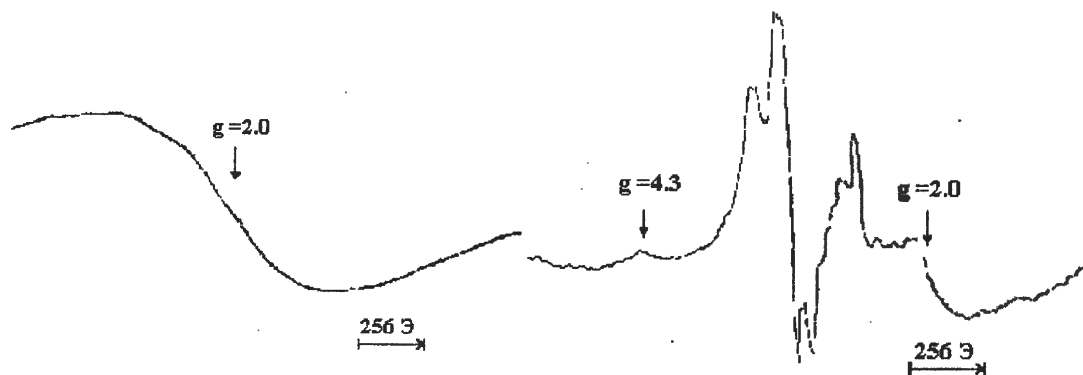


Fig. 1. EPR spectrum of $\text{Ca}_{0.7}\text{Sr}_{0.3}\text{FeO}_{3.0}$ sample

Fig. 2. EPR spectrum of $\text{Ca}_{0.7}\text{Sr}_{0.3}\text{FeO}_{2.5}$ sample

$\text{Ca}_{0.7}\text{Sr}_{0.3}\text{FeO}_{2.5}$ sample (Fig.2) is clearly non-uniform. EPR spectra of these samples for different parts of the plate have different intensity and form. The most interesting feature of this sample is a superfine structure in the spectrum, interpretation of which is difficult at the present time.

We consider it necessary to carry out a repeated synthesis of this sample. The total spin concentration for this sample is $N=1.5 \cdot 10^{18}$ sp/g.

Spectrum of $\text{Ca}_{0.7}\text{Sr}_{0.3}\text{FeO}_{3.0}$ sample (Fig.1) consists of one wide, quite intensive line with $\Delta H=1500$ Oe and $g=1.92$. It may be caused by small clusters of Fe^{3+} ions, bounded by exchange interaction. Equivalent concentration of spins for this sample is $N=4.1 \cdot 10^{18}$ sp/g.

Spectrum of $\text{Ca}_{0.5}\text{Sr}_{0.5}\text{FeO}_{3.0}$ sample also consists of one intensive line with $\Delta H=1100$ Oe and $g=1.90$. This line is narrowed on account of stronger ferromagnetic exchange interactions. This allows to suppose that in this sample state with larger clusters of Fe^{3+} ions is realized.

It is of interest to predict the catalytic activity of these samples on the basis of analysis of EPR spectra. Isolated ions of iron are considered to have a tendency to develop physical adsorption and interaction between each other ions ($g=2$) exhibit chemisorption properties. It is also considered that iron ions with high values of g-factors have higher catalytic activity. On the basis of these analyses of EPR spectra of the five samples investigated one can come to the conclusion that $\text{Ca}_{0.3}\text{Sr}_{0.7}\text{FeO}_{2.5}$, $\text{Ca}_{0.5}\text{Sr}_{0.5}\text{FeO}_{2.5}$ must have maximum catalytic activity. Minimum catalytic activity may be expected for $\text{Ca}_{0.5}\text{Sr}_{0.5}\text{FeO}_{3.0}$ sample.

If we suppose that catalytic activity of these samples is directly related with EPR signal intensity, the investigated samples may be aligned by catalytic activity as follows:



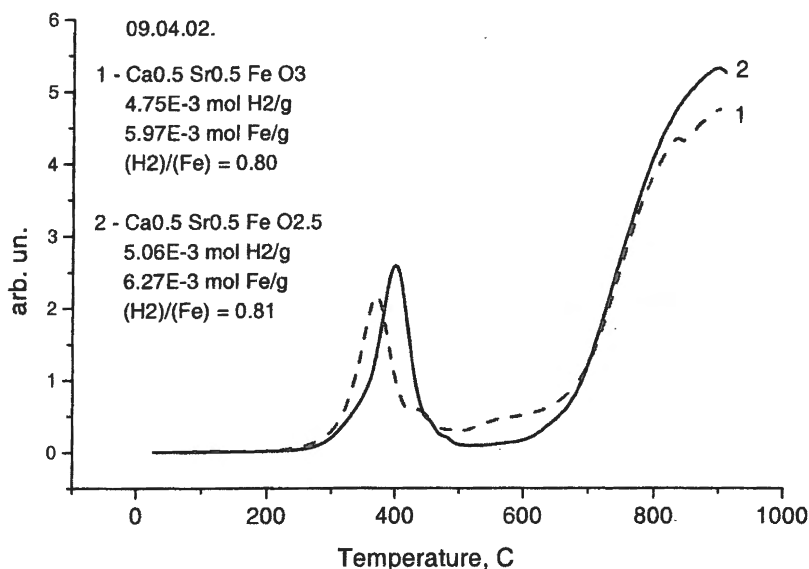


Fig 3. TPR spectra of two catalyst samples

There is a possibility, however, that some peculiarities of the structure of these compounds may introduce corrections into this alignment. The samples of $\text{Ca}_{0.5}\text{Sr}_{0.5}\text{FeO}_{3.0}$, $\text{Ca}_{0.5}\text{Sr}_{0.5}\text{FeO}_{2.5}$ catalysts were tested in the process of thermoprogrammed reduction (Fig. 3).

Reduction of iron oxides by TPR method proceeds, as a rule, in two steps, first Fe^{3+} to Fe^{2+} , then Fe^{2+} to Fe^0 . These data are confirmed by X-ray phase analysis. Therefore, the first peak of TPR in the range 300-500°C is related with reduction of Fe^{3+} to Fe^{2+} evidencing the presence of these ions in the catalyst. Since the peak within 600-1000°C is significantly larger by area than the first one, iron in the catalyst is mainly in the form of Fe^{2+} with a certain amount of Fe^{3+} . These data are confirmed, for example, by EPR and X-ray phase analysis methods.

Acknowledgements

This work was supported by INTAS grant 2000-00180.

References

1. Z.R. Ismagilov: Monolithic catalyst design, engineering and prospects of application for environmental protection in Russia, *React. Kinet. Catal. Lett.*, v. 60, N 2, 1997, P. 215-218
2. Z.R. Ismagilov, R.A. Shkrabina, M.A. Kerzhentsev, G.B. Barannik "New catalysts and catalytical processes for environmental protection". *React. Kin. Cat. Lett.*, 1995, v. 55, N 2, p. 489
3. A. Wattiaux, L. Fournes, A. Demourgues, N. Bernaben, J.-C. Grenier and M. Pouchard, *Solid St. Commun.* 77 (1991) 489.
4. A. Nemudry, P. Rudolf and R. Schoellhorn, *Chem. Mat.* 8 (1996) 2232.
5. L. Qiu, T.H. Lee, L.-M. Liu, Y.L. Yang and A.J. Jacobson, *Solid State Ionics*, 76 (1995) 321.
6. J.S. Anderson, *The thermodynamics and theory of nonstoichiometric compounds*, in *Nonstoichiometric compounds*. Pergamon Press, 1973, p. 1-76
7. E. Goldberg, A. Nemudry, V. Boldyrev and R. Schoellhorn, *Solid State Ionics*, 110 (1998) 223.
8. A. Nemudry, A. Rogatchev, I. Gainutdinov, R. Schöllhorn / Reactivity of the perovskite system $\text{Ca}_{1-x}\text{Sr}_x\text{FeO}_{2.5}$ in topotactic electrochemical oxidation at ambient temperature. / *Solid State Electrochem* (2001) 5 P.450-458.

MANGANESE OXIDE MONOLITH CATALYSTS MODIFIED BY Fe AND Cu FOR HIGH-TEMPERATURE AMMONIA DECOMPOSITION AND H₂S REMOVAL

Z.R. Ismagilov, S.A. Yashnik, N.V. Shikina, I.P. Andrievskaya, S.R. Khairulin,
V.A. Ushakov, J.A. Moulijn*, I.V. Babich*

Boriskov Institute of Catalysis SB RAS, Prosp. Akad. Lavrentieva, 5, Novosibirsk 630090, Russia

Phone: +7 3832 341219, Fax: +7 3832 397352, E-mail: zri@catalysis.nsk.su

** Delft University of Technology, 136 Julianalaan 2628 BL Delft, The Netherlands*

Phone: 31 15 2785008, Fax: 31 15 2785006, E-mail: J.A.Moulijn@tnw.tudelft.nl

Abstract

Monolith sorbents/catalysts that have potential in simultaneous removal of H₂S and NH₃ from hot fuel gas were developed. Preparation methodology and composition of supported honeycomb sorbents/catalysts, based on manganese oxides modified by Fe and Cu oxides, have been optimized. Impregnated and washcoated monolith catalysts were tested in ammonia high temperature decomposition and H₂S sorption. Approaches for improving the thermal stability and catalytic activity under reaction conditions are described.

Introduction

An effective direct usage (e.g. high temperature turbines) of the gases, obtained in the Integrated Gasification Combined Cycle, is substantially limited, since those gases contain undesirable impurities, first of all, ammonia (up to 0.3 vol.%, [1]) and hydrogen sulfide (0.1-1.5 vol.%, [2]). Development of an effective monolith sorbents/catalysts that allow the high temperature abatement of ammonia via its decomposition toward N₂ and H₂ and simultaneous H₂S sorption is the most promising way to solve this problem.

It is known, that the most important processes for high temperature regenerative H₂S removal use sorbents on the base of single or mixed-metal oxides, such as: ZnO [3], zinc ferrite [4], zinc titanate [3,5], CuO [6], MnO/ γ -Al₂O₃ [2,7] and FeO [8] or FeO/ γ -Al₂O₃ [2]. The sorbents usually provide H₂S removal from the fuel gas to levels less than 20 ppm due to the sulfidation reaction. Manganese and iron oxides sorbents are preferable, since they can be regenerated by steam [2,7,8].

On the other hand, transition metal oxides – Fe₂O₃, CuO, Cr₂O₃, MnO_x [9-12] are known to be the most active catalysts for ammonia decomposition. However, these bulk catalysts have low thermal stability and their selectivity in the reaction drops with temperature elevation. Deposition of these oxides on the supports allows to raise substantially their thermal stability under the reaction conditions [9].

OP-20

Published data allow to conclude that the oxides of transition metals Mn, Fe and Cu are the most perspective candidates for active components of the sorbents/catalysts for simultaneous cleaning of the hot coal gas from hydrogen sulfide and ammonia. Development of the sorbents/catalysts in the form of monolith increases their technical merit due to the easy operation, regeneration, low pressure drop, small dust and attrition sensitivity. Titania is widely used as a support to improve thermal, mechanical and chemical properties of the catalysts and sorbents [13], but its application in the form of honeycomb support is rather limited [12].

Individual Mn, Fe and Cu salts were used as the precursors to prepare monolith sorbents/catalysts based on titania honeycomb support and alumina-silica monolith washcoated with titania [12]. The monolith sorbents/catalysts combine high catalytic activity in the ammonia decomposition with acceptable mechanical strength of the monolith supports. It was shown [12], that the iron- and copper-containing catalysts, prepared by the impregnation, exhibit higher activity and stable performance at high temperatures in comparison with the manganese oxides-containing samples, so that 95% and 80% of NH_3 conversion is achieved at 780-800°C, respectively, on monolith sorbents/catalysts, containing individual Fe, Cu and Mn oxides. Supported manganese oxide catalysts above 700°C show a high initial activity, but lose their activity in the temperature range 800-900°C due to a strong interaction with the monolith support material [14]. There are two ways to stabilize the monolith catalysts: modification of the monolith support, and introduction of modifying elements into the supported active component.

This work is devoted to the study of physico-chemical properties of the manganese oxides-supported monolith sorbents/catalysts modified by Fe and Cu, and to their testing in ammonia decomposition and H_2S sorption.

Experimental

Catalysts preparation

The monolith supports were prepared by extrusion of the masses based on titanium dioxide (anatase) or silica-alumina precursors followed by drying at 110°C and calcination at 700°C in accordance with [12]. Ca-forms of montmorillonite (denoted as Ca-f) were used as a binder for preparation of the extrusion masses. The mullite-silica fibers (2 wt.%) were added to the extrusion mass for improvement of the mechanical strength of titania-based monolith. Monolith supports have diameter 18 mm, square channels 1.5x1.5mm, wall thickness 1 mm. The physico-chemical properties of the samples are given in Table 1.

Preparation of the impregnated monolith catalysts

The impregnated catalysts were prepared by wet impregnation of the TiO₂-monolith supports (MS-1) with the aqueous solution of manganese nitrate (110 mg Mn/ml) with subsequent drying at 110°C and calcination at 500, 700 and 900°C. To obtain manganese loading equal to 15 wt.% (hereafter calculated for MnO₂), the impregnation-drying-calcination procedure was repeated three times.

The manganese-containing catalysts modified by Fe₂O₃ were prepared by impregnation of the Mn-catalyst by aqueous solution of the iron nitrate (112 mg Fe/ml) or iron (III) ammonium oxalate (56 mg Fe/ml), with subsequent drying at 110°C and calcination at 500, 700, 900°C. Iron loading was 4-8 wt.% (hereafter calculated for Fe₂O₃).

The manganese-containing catalysts modified by CuO were prepared by impregnation of the Mn-catalyst by aqueous solution of the copper nitrate (192 mg Cu/ml), with subsequent drying at 110°C and calcination at 500, 700, 900°C. Copper loading was 4-8 wt.% (hereafter calculated for CuO).

Table 1. Properties of the monolith supports.

	Composition of the monoliths	T, °C	S _{sp} , m ² /g	Phase composition	Mechanical strength, kg/cm ²
MS-1	63%TiO ₂ +35%Ca-f ^{a)} + + 2%MSF ^{c)}	700	86	TiO ₂ (anatase) Ca-montmorillonite ^{b)}	8
MS-2	75% alumina-silica (clay) ^{d)} + 25%Ca-f ^{a)}	700	33	Al ₂ O ₃ ·SiO ₂ +α-SiO ₂	19.5

a) Ca-f means the Ca-form of montmorillonite with general formula Ca_{0.2}(Al,Mg)₂Si₄O₁₀(OH)₂· 4H₂O.

b) Product of Ca-montmorillonite dehydration.

c) MSF – mullite-silica fibers with diameter 0.25mm and length 10 mm, made in Russia, State Standard (GOST) 23 619-79.

d) Obskaya clay – clay from Ob'river region (Russia), after calcination at 500°C represents silica-alumina.

Preparation of the washcoated monolith catalysts

Washcoated catalysts were prepared using the aluminosilicate monolith supports (MS-2). Bulk MnO₂ or Mn₂O₃, obtained by the decomposition of Mn(NO₃)₂, were mixed with TiO₂ and γ-Al₂O₃ (as a binder), and a suspension based on this mixture was prepared. After the suspension had been deposited on the monolith support, the catalysts were dried and calcined at 500, 700 and 900°C. Active component – Fe and Cu oxides were introduced into the washcoating by impregnation with Fe or Cu nitrate solutions.

Preparation of the model catalysts

The model Mn-containing catalysts on granulated TiO₂ (anatase) and Ca-montmorillonite were prepared by procedure written above. Mn loading in these catalysts was 15 wt.%.

OP-20

The bulk MnO_2 , Mn_2O_3 , MnO were prepared by the decomposition of manganese nitrate at temperatures 300, 700 and 900°C respectively.

The bulk MnTiO_3 and FeTiO_3 were prepared by the mechanical mixing of equimolar quantities of $\text{Mn}(\text{NO}_3)_2 \cdot 4\text{H}_2\text{O}$ or $\text{Fe}(\text{NO}_3)_3 \cdot 9\text{H}_2\text{O}$ and TiO_2 (anatase), with subsequent calcination at 800°C/8h in air and 900°C/2h in gas mixture 1 vol.% NH_3 + helium.

Activity test

Reaction of ammonia decomposition was studied in a flow reactor within temperature range of 400-1000°C and space velocity of 1000 h^{-1} . Ammonia concentration in the initial gas mixture was 1 vol.% in helium. Catalytic activity was defined as ammonia conversion (X, %) at the given temperature.

The study of hydrogen sulfide sorption was carried out in a flow reactor at the temperature 700°C and space velocity 3600 h^{-1} ; hydrogen sulfide concentration in initial gas mixture was 2.8 vol.% in argon. The sorption capacity was determined as the amount of sorbed H_2S in mmol of H_2S per 1 gram of the catalyst, or in wt.%.

XRD (X-ray diffraction) characterization of catalyst samples was conducted with HZG-4 diffractometer (Germany) using the $\text{Cu K}\alpha$ radiation. The patterns were recorded over a range of 2θ angles from 10° to 60° with the sweep rate 1°/min.

Formation of sulfur compounds on the catalyst surface after hydrogen sulfide sorption was studied using a MAP-3 microanalyzer. The probe diameter was 1-2 mm, the working voltage was 25 kW. The $\text{Al K}\alpha$, $\text{Ti K}\alpha$, $\text{Cu K}\alpha$, and $\text{S K}\alpha$ were analytical lines.

Results and discussion

Testing of the catalyst activity in ammonia decomposition

The dependencies of properties of the catalysts and their activity on the nature of active component (Mn, Fe, Cu), loading of the active component (5-20 wt.%), type of the support and calcination temperature have been studied earlier [12].

It was found [12,14], that manganese oxides deposited on the TiO_2 -monolith support (MS-1) and calcined at 700°C have rather high activity in NH_3 decomposition (Sample 2, Table 2). At 740°C the NH_3 conversion is more than 80%. Considerable decrease of the activity for the samples is observed upon their exposure to the reaction mixture at temperatures above 750-800°C. Then, NH_3 conversion over these catalysts, preliminary calcined at 500 and 700°C, decreases from 70-80% to 55% when the reaction temperature is above 850°C. The catalysts with 15 wt.% Mn, prepared on TiO_2 -monolith and preliminary calcined at 900°C (Sample 3, Table 2), demonstrate high conversion (up to 90%) only at the reaction temperature above 950°C.

Deactivation of the manganese oxide-containing catalysts calcined at 500 and 700°C may be explained by the chemical interaction of the Mn oxides and the support materials resulting in the formation of inactive phases of Mn cations with the Ca-montmorillonite (binder) or the titanium dioxide. Comparison of the initial phase composition of these catalysts (Table 2) and those after ammonia decomposition, done using XRD shows, that at the reaction conditions MnO_2 and Mn_2O_3 (initial active phase in samples 1, 2) were partially reduced with the formation of interaction phase of manganese oxides with TiO_2 . This interaction phase is a solid solution on the basis of hexagonal structure of MnTiO_3 with partial substitution of Ti^{+4} by Mn^{+3} or Al^{+3} (from binder).

The phases similar to MnTiO_3 are formed after the calcination at 900°C of the catalysts based on TiO_2 -monolith with Ca-montmorillonite, and these catalysts are active only at the high temperatures (Sample 3, Table 2). Taking into account all the presented above, it is believed that $\beta\text{-Mn}_2\text{O}_3$ phase is more active than MnTiO_3 phase in ammonia decomposition.

To elucidate the nature of catalyst deactivation due to the interaction of the catalytically active Mn species with the material of monolith support, the samples of bulk MnO_2 , Mn_2O_3 , MnO , MnTiO_3 and special series of the samples, supported on granulated Ca-montmorillonite and TiO_2 (anatase), were prepared.

The manganese oxides supported on granulated Ca-montmorillonite (Sample 4, Table 2) after the operation at 900°C lose their activity to 55%. According to the XRD data, the active manganese oxide, $\beta\text{-Mn}_2\text{O}_3$, interacts with the support forming a solid solution similar to $\text{MnMn}_6\text{SiO}_{12}$. Because of the complicated composition of the products, which are formed upon the thermal decomposition of manganese oxides supported on Ca-montmorillonite, it is impossible to state exactly, that nature of montmorillonite affects on the deactivation of monolith catalysts at the reaction condition.

For the impregnated 15% $\text{Mn}_2\text{O}_3/\text{TiO}_2$ catalysts (Sample 6, Table 2), the NH_3 decomposition attains 100% conversion at 855°C. Operation of this catalyst under reaction mixture at 850°C within 1-2 hours leads to the transformation of active manganese oxide Mn_2O_3 into MnTiO_3 .

It should be underlined, that the ammonia conversion curves for bulk MnO_2 and Mn_2O_3 are similar in the temperature range of 500-700°C (Fig.1). The conversion on these oxides reaches maximum value at 700°C (100%), but for MnO_2 decreases to 20% within 2 hours of operation at this temperature. At the reaction temperatures above 700°C, the ammonia conversion curve for bulk MnO_2 is similar to that of MnO . 100% NH_3 conversion is achieved at 830°C. For bulk Mn_2O_3 , ammonia conversion remains high (~100%) up to 900°C. In accordance with the XRD data for both precursors, the manganese oxides are reduced to MnO

OP-20

and Mn_3O_4 . In comparison with MnO , the ammonia conversion curve for bulk MnTiO_3 is shifting by 50°C into the high-temperature region. Therefore, the reduced forms of manganese oxide, such as MnO and MnTiO_3 (or solid solution on the basis of MnTiO_3), which are thermodynamically stable at high temperatures, can be considered as the active components in NH_3 decomposition at temperatures above 700°C .

Table 2. The properties of Mn-containing (15 wt.%) catalysts in ammonia decomposition

N	Catalyst calcination T, $^\circ\text{C}$	Properties of fresh catalyst		NH ₃ conv., %, at temperature, $^\circ\text{C}$		Properties after reaction	
		S_{sp} , m^2/g	XRD composition	800	900	S_{sp} , m^2/g	XRD composition
1.	$\text{MnO}_2/(\text{TiO}_2+\text{Ca-f}^*)/500$	93	Anatase MnO_2	75	55	11	Anatase + rutile = 3:1 $\text{Mn}(\text{Ti,Al,Mn})\text{O}_3$ **
2.	"-"-" /700	42	Anatase $\beta\text{-Mn}_2\text{O}_3$	60	60	6,8	Anatase + rutile = 2:3 $\text{Mn}(\text{Ti,Al,Mn})\text{O}_3$ **
3.	"-"-" /900	0.8	Rutile $\text{MnMn}_6\text{SiO}_{12}$ ***	15	35	0.7	Rutile + $\text{MnMn}_6\text{SiO}_{12}$ $\text{Mn}(\text{Ti,Al,Mn})\text{O}_3$ **
4.	$\text{MnO}_2/\text{Ca-f}/700$	3.6	$\alpha\text{-SiO}_2$ Ca-montmorillonite**** $\beta\text{-Mn}_2\text{O}_3$	45	55	0.6	$\alpha\text{-SiO}_2$ $\text{Ca}(\text{Al,Si})_2\text{Si}_2\text{O}_8$ $\text{MnMn}_6\text{SiO}_{12}$
5.	"-"-" /900	0.7	$\text{Ca}(\text{Al,Si})_2\text{Si}_2\text{O}_8$ + $\text{MnMn}_6\text{SiO}_{12}$ ***	40	60	0.2	$\alpha\text{-SiO}_2$ + $\text{Ca}(\text{Al,Si})_2\text{Si}_2\text{O}_8$ $\text{MnMn}_6\text{SiO}_{12}$ ***
6.	$\text{MnO}_2/\text{TiO}_2/700$	11	Anatase (~85%) Rutile (~15%) $\beta\text{-Mn}_2\text{O}_3$	85	100	4.1	Rutile MnTiO_3
7.	"-"-" /900	0.8	Rutile MnTiO_3	50	95	0.5	Rutile MnTiO_3

*) Ca-f means Ca-form of montmorillonite

**) hexagonal structure, like MnTiO_3

***) structure, like $\text{MnMn}_6\text{SiO}_{12}$, with substitution of the part of Mn-cations by Si^{4+} .

****) product of Ca-montmorillonite dehydration

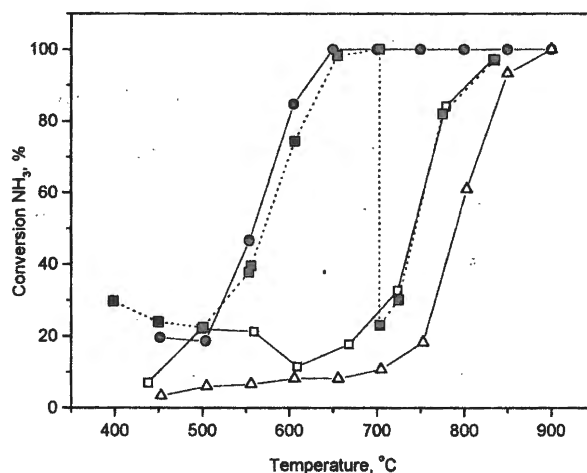


Fig. 1. Ammonia conversion vs temperature over bulk MnO_2 (■), Mn_2O_3 (●), MnO (□), MnTiO_3 (Δ).

There are two ways to stabilize the monolith catalysts: (1) modification of the monolith support, (2) introduction of modifying elements in the supported active component. In this work the second way is considered. To stabilize the impregnated manganese-containing catalysts, 4-8 wt.% of iron oxide were introduced into the supported active component. The modified catalyst with 7-8 wt.% of Fe_2O_3 demonstrates high activity and stability at elevated temperatures. It is seen from Fig.2, that ammonia conversion over the manganese-containing catalyst, modified by 8 wt.% Fe_2O_3 , is reduced from 94% to 73% at 860°C. For comparison, ammonia conversion for the unmodified catalyst is decreased to 46% at this temperature. According to XRD data (Table 3) interaction of Fe_2O_3 and Mn_2O_3 with the support material, namely TiO_2 , resulting in the formation of solid solution with the hexagonal structure similar to $(\text{Fe}, \text{Mn})\text{TiO}_3$ is observed for all the studied modified catalysts after testing in NH_3 decomposition.

The symbasis of Ti K_α , Mn K_α and Fe K_α profiles, which were obtained for the modified catalyst using X-Ray microanalysis, indicates the interaction of Mn and Fe oxides with TiO_2 (Fig. 3). It should be emphasized, that the interaction of these components occurs in the initial catalyst (Fig. 3A), and is strengthened in catalyst after ammonia decomposition test (Fig. 3B).

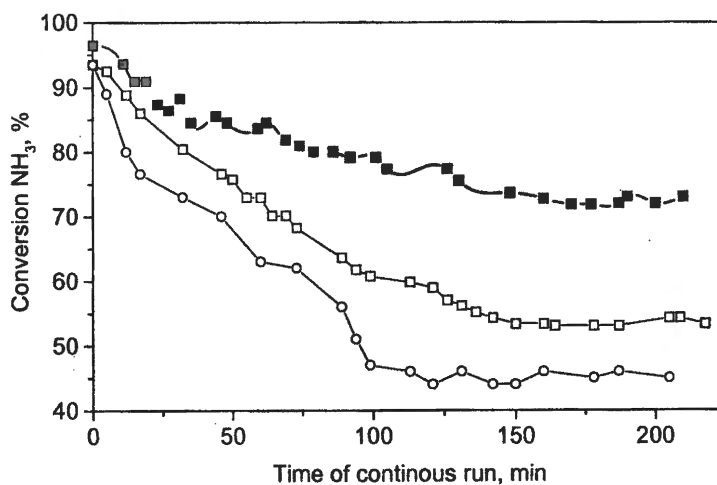


Fig. 2. Stability of 15%MnO₂ (○), (5%Fe₂O₃+15%MnO₂) (□), (8%Fe₂O₃+15%MnO₂) (■) catalysts prepared on MS-1 upon ammonia decomposition at 860 °C.

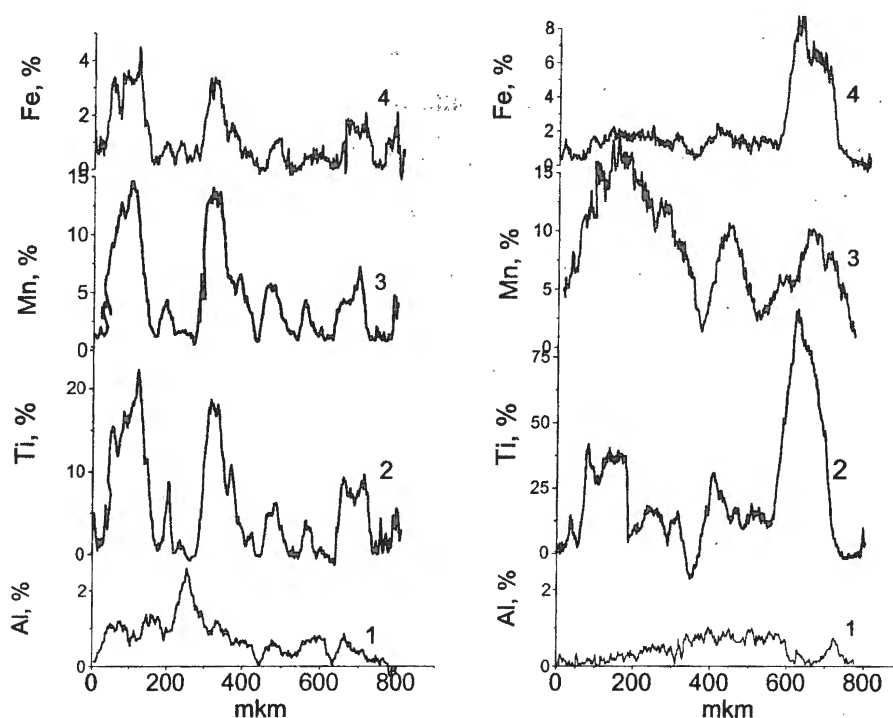


Fig. 3. Intensity of Al K α (1), Ti K α (2), Mn K α (3) and Fe K α (4) radiation for 8%Fe₂O₃+15%MnO₂ catalyst prepared on MS-1: initial (A) and after NH₃ decomposition testing (B).

As it is illustrated in Fig.4, the specially prepared bulk FeTiO₃ demonstrates higher catalytic activity and stability in ammonia decomposition at temperatures above 600°C than bulk MnTiO₃. For instance, temperatures at which 50% ammonia conversion is achieved are 540°C and 790°C, respectively, for FeTiO₃ and MnTiO₃. It should be pointed out that, as it is shown in Fig. 4, catalytic activities of bulk FeTiO₃ and pure α -Fe₂O₃ are the same at temperatures above 600°C. Accordingly, it is believed that high activity and stability of the modified catalysts at elevated temperatures are provided by the formation of phase FeTiO₃ under the reaction conditions.

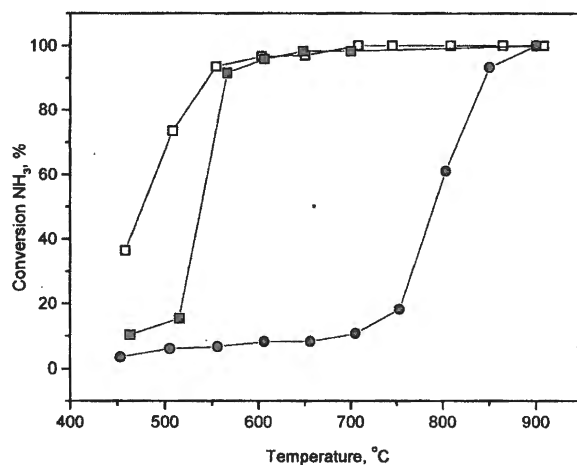


Fig. 4. Ammonia conversion vs temperature over bulk Fe₂O₃ (□), FeTiO₃ (■), MnTiO₃ (●).

The main goal of this work is the development of optimal catalysts for the simultaneous ammonia and H₂S removal from hot coal gases. In order to combine high efficiency of the systems on the basis of iron and copper oxides in ammonia decomposition, and high activity of the manganese-containing catalysts in regenerative hydrogen sulfide removal, the samples with two active components were synthesized by the impregnation of monolith support. The properties of catalysts based on Fe-Mn- or Cu-Mn-oxides are presented in Tables 3 and 4. Temperature at which 90% NH₃ conversion is achieved on the Cu-Mn-oxides impregnated catalysts was about 790-810°C. System on the basis of manganese oxide doped with iron oxide (8 wt.%) is the most active catalyst.

It should be noted, that XRD data of all the spent catalysts show that NH₃ decomposition on the oxide systems is accompanied by the partial or complete reduction of the active component, and its interaction with the support, resulting in the formation of hexagonal structures like MnTiO₃ or FeTiO₃ (Tables 3 and 4). In the case of Cu oxide-containing catalysts, reduction of the CuO and spinel structure like CuMn₂O₄ into metallic state (Cu⁰) at the reaction conditions was observed.

Table 3. Properties of Mn-Fe-containing monolith catalysts

N	Catalyst calcination T, °C	Initial properties		Activity in NH ₃ decomposition		Properties after reaction	
		S _{sp} , m ² /g	Phase composition	T _{50%} , °C	T _{max conv.} , °C (% conv.)	S _{sp} , m ² /g	Phase composition
Impregnated catalysts*							
1	8%Fe ₂ O ₃ (N) + 15%MnO ₂ /500	58	Anatase β-Mn ₂ O ₃ , D<5nm α-Fe ₂ O ₃ , D<5nm	690	790°C (90%)	6.0	Rutile, Anatase (tr) (Fe, Mn)TiO ₃ ***
2	8%Fe ₂ O ₃ (O) + 15%MnO ₂ /500	49	Anatase β-Mn ₂ O ₃ , D<5nm α-Fe ₂ O ₃ , D<5nm	720	760°C (85%)	7.2	Rutile, Anatase (tr) (Fe, Mn)TiO ₃ ***
3	“-“- /700	33	Anatase β-Mn ₂ O ₃ , D<20nm Fe(Fe,Mn,Ti)O ₃ **	725	845°C (80%)	3.2	Rutile, Anatase (tr) (Fe, Mn)TiO ₃ ***
4	“-“- /900	0.2	Rutile (Fe,Mn)TiO ₃ *** MnMn ₆ SiO ₁₂	810	985°C (95%)	<1	Rutile (Fe, Mn)TiO ₃ ***
Washcoating composition							
5	60%TiO ₂ + 17%Al ₂ O ₃ + 15%MnO ₂ + 8%Fe ₂ O ₃ /500	155	Anatase MnO ₂ α-Fe ₂ O ₃ Fe(Fe,Al)O ₃ **	550	800°C (100%)	24	Rutile(70%) Anatase (30%) FeTiO ₃ (Mn,Fe)(Al,Ti)O ₃ ***
6	“-“- /700	73	Anatase Mn ₂ O ₃ α-Fe ₂ O ₃ Fe(Fe,Mn,Al)O ₃ **	575	750°C (100%)	19	Rutile(70%) Anatase (30%) FeTiO ₃ (Mn,Fe)(Al,Ti)O ₃ ***

*) For the preparation of impregnated catalysts was used monolith support MS-1. Samples 1 and 2-4 were prepared by impregnation of Mn-catalyst by Fe-nitric solution and by Fe-ammonia-oxalate solution, respectively. **) hexagonal structure, like α-Fe₂O₃; ***) hexagonal structure, like MnTiO₃

OP-20

Table 4. Properties of Mn-Cu-containing monolith catalysts

N	Catalyst calcination T, °C	Initial properties		Activity in NH ₃ decomposition		Properties after reaction	
		S _{sp} , m ² /g	Phase composition	T _{50%} , °C	T _{max conv.} , °C (% conv.)	S _{sp} , m ² /g	Phase composition
Impregnated catalysts*							
1	8%CuO (N) + 15%MnO ₂ /500	56	Anatase MnO ₂ , D<30 nm CuO, D<20 nm	690	790°C (90%)	5.6	Anatase MnTiO ₃ Cu ⁰ , D > 40 nm
2	8%CuO (N) + 15%MnO ₂ /700	23	Anatase β-Mn ₂ O ₃ CuMn ₂ O ₄ , CuO	700	820°C (90%)	5.5	Anatase MnTiO ₃ Cu ⁰ , D > 40nm
3	8%CuO (N) + 15%MnO ₂ /900	3	Rutile MnTiO ₃ CuMn ₂ O ₄	800	900°C (75%)	2.4	Rutile MnTiO ₃ Cu ⁰ , D > 50 nm
Washcoating composition**							
4	60%TiO ₂ + 17%Al ₂ O ₃ + 15%MnO ₂ + 8%CuO /700	54	Anatase, γ-Al ₂ O ₃ β-Mn ₂ O ₃ (Cu,Mn)[Al] ₂ O ₄ ^b	725	775°C (100%)	27	Anatase MnTiO ₃ CuO
5	60%TiO ₂ + 17%Al ₂ O ₃ + 15%MnO ₂ + 8%CuO /900	15	Rutile, α-Al ₂ O ₃ (Cu,Mn)[Al] ₂ O ₄ ^b	560	700°C (100%)	1.8	Rutile + α-Al ₂ O ₃ Mn(Mn,Ti)O ₃ ^a (Cu,Mn)[Al] ₂ O ₄ ^b Cu ⁰

*) For the preparation of impregnated catalysts was used monolith support MS-1. Samples 1-3 were prepared by impregnation of Mn-catalyst by Cu-nitric solution. **) For Samples 4, 5, CuO was introduced via impregnation of 60%TiO₂+ 17%Al₂O₃ + 15%MnO₂ by Cu-nitric solution;

a) hexagonal structure, like MnTiO₃; b) structure, like CuMn₂O₄

Washcoated monolith catalysts

To optimize compositions of the washcoated monolith catalysts, bulk samples of the washcoating precursors have been prepared and tested. As it is indicated in [12], the activity of manganese oxide-containing washcoating materials and of washcoated catalysts is rather high. For example, 100% of NH₃ conversion is achieved at 850-900°C for all the bulk samples of washcoating precursors. The most active among the bulk manganese-containing washcoating compositions was the sample, in which MnO₂ was introduced as a bulk oxide. For the manganese-containing washcoating material, higher conversion of ammonia is observed at lower temperatures than that for the impregnated catalysts.

Our intentions were to improve these compositions by modifying them with iron or copper oxides. The modification of manganese-containing washcoating composition 65%TiO₂+15%MnO₂+20%Al₂O₃ by Fe₂O₃ leads to the substantial increasing of its activity. For example, the temperature of attaining of 100% NH₃ conversion (T_{100%}) was 870°C and 720°C for unmodified and modified catalysts, respectively (Fig. 5). The effect of CuO additives on the activity of washcoating composition 65%TiO₂+15%MnO₂+20%Al₂O₃ was weaker (T_{100%} = 780°C, Fig. 5).

The effect of Fe_2O_3 and CuO additives on the activities of washcoated catalysts prepared on aluminosilicate (MS-2) or cordierite (Corning, 400 cell/inch) monolith was less pronounced (Fig. 6). For example, temperature of 95% NH_3 conversion was 870°C, 760°C and 820°C for unmodified, modified by Fe_2O_3 and CuO catalysts, respectively, in case of MS-2 monolith. The modification effect of CuO additives was smoother when using the cordierite (Fig. 6B)

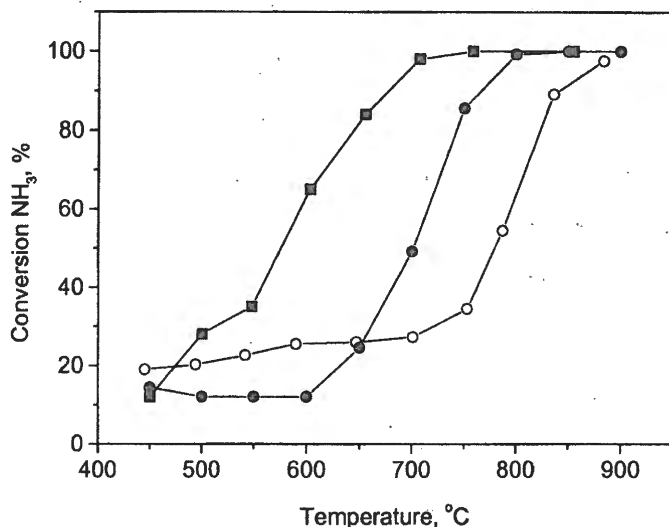


Fig. 5. Ammonia conversion vs temperature over bulk washcoating materials calcined at 700°C.

○ - 15% Mn_2O_3 +20% Al_2O_3 +65% TiO_2 ; ■ - 8% Fe_2O_3 +15% Mn_2O_3 +17% Al_2O_3 + 60% TiO_2 ;
● - 8% CuO +15% Mn_2O_3 +17% Al_2O_3 + 60% TiO_2

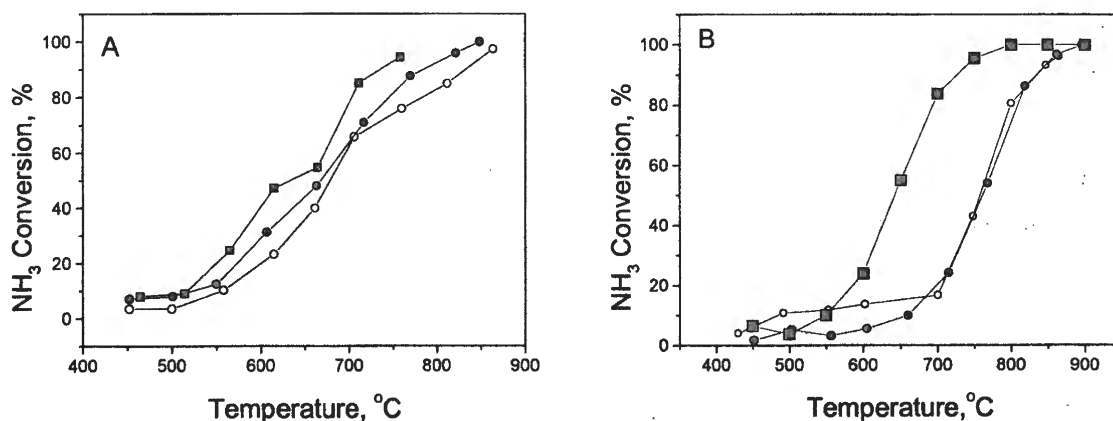


Fig. 6. Ammonia conversion vs temperature over washcoated monolith catalysts based on aluminosilicate (A) and cordierite (B) after calcination at 700°C:

○ - 15% Mn_2O_3 +20% Al_2O_3 +65% TiO_2 ;
■ - 8% Fe_2O_3 +15% Mn_2O_3 +17% Al_2O_3 + 60% TiO_2
● - 8% CuO +15% Mn_2O_3 +17% Al_2O_3 + 60% TiO_2

Testing of the catalyst in hydrogen sulfide sorption

The samples chosen in accordance with the results of catalytic activity tests in the ammonia decomposition have been tested in the hydrogen sulfide sorption. All experimental data are

OP-20

presented in Table 5. The sorption capacities of pure monolith support MS-1 and impregnated catalyst containing only 15%MnO₂ are presented in Table 6 for comparison. The sorption capacity of original monolith support MS-1 achieved 1.3 wt.%, which can be explained by the presence of 2 wt.% CaO and 1.8wt.% Fe₂O₃ as admixtures in Ca-montmorillonite, used as the binder. It has been found, that the sorption capacity of impregnated Mn-containing catalysts on TiO₂-monolith support depends on the Mn content. The increasing of Mn content from 5 wt.% to 20 wt.% leads to the proportional rise of sorption capacity from 1.6% to 6.3 wt.%.

The sorption capacities of the impregnated catalyst and bulk washcoating material, containing simultaneously 15%MnO₂ and 8%Fe₂O₃, were 6.8 and 6.0 wt.%, respectively. These data are in a good correlation with those previously reported by Bakker [3]. By means of the XRD analysis formation of the MnS and Fe_{1-x}S_x phases was detected.

Sorption capacity of the Mn-containing catalyst modified by 8 wt.% CuO was similar to unmodified catalyst. The sorption capacities of the impregnated catalyst and bulk washcoating material, containing simultaneously 15%MnO₂ and 8%CuO, were 6.1 and 4.4 wt.%, respectively. By means of the XRD analysis, formation of the MnS, Cu₂S and CuS phases was detected for the impregnated catalyst.

The sulfidation degree of supported oxides, calculated from the stoichiometric reaction for all the studied catalysts, was estimated to be around 70%. Thus, it is believed that part of the active component may remain in the forms of Mn, Fe and Cu oxides, although this fact was not confirmed by the XRD analysis.

The increase of calcination temperature of Mn-containing catalyst modified by Fe₂O₃ up to 900°C leads to the substantial reduction of H₂S sorption capacity. Similar decrease of the sorption capacity (to 1.4 wt.%) was observed for this catalyst after testing in NH₃ decomposition. It should be noted, that sorption capacity of the catalyst modified by CuO after testing in NH₃ decomposition was close to zero.

Testing of the catalyst in ammonia decomposition after hydrogen sulfide sorption

The catalysts after hydrogen sulfide sorption were tested consequently in ammonia decomposition reaction. As it can be seen from the data of Table 5 samples exhibited the activity equal to the activity of fresh catalysts, or even higher. These results can be explained in terms of formation of partially reduced iron and manganese cations, which are known to be more active in ammonia decomposition [1].

Table 5. Properties of monolith catalysts in the H₂S sorption

Catalyst/ calcination T, °C	Testing H ₂ S sorption at 700°C			Testing in NH ₃ decomposition after H ₂ S sorption		
	sorption capacity mmol/g, (wt.%)	S _{sp} , m ² /g	XRD phase	T _{50%} before, °C	T _{50%} after, °C	XRD phase
MS-1/ 700	0.4 (1.3 %)	62	Anatase α-SiO ₂ (tr) Ca-montm ^a (tr)	725°C	640°C	Anatase α-SiO ₂ (tr)
15%MnO ₂ /*700	1.7 (5.8%)	18	Anatase+rutile MnS	780°C	710°C	Anatase+rutile MnS
8%Fe ₂ O ₃ + 15%MnO ₂ /*700	2.1 (6.8 %)	15	Anatase+rutile MnS Fe _{1-x} S	725°C	670°C	Anatase+rutile MnS Fe _{1-x} S
8%Fe ₂ O ₃ + 15%MnO ₂ /*700 after NH ₃ test	0.4 (1.4%)	1.5	Rutile MnS	-	-	-
8%CuO+ 15%MnO ₂ /* 700	2.7 (6.1 %)	5.4	Anatase+rutile MnS CuS, Cu ₂ S	740°C	750°C	Anatase+rutile MnS CuS
8%CuO+ 15%MnO ₂ /* 700 after NH ₃ test	(0.2%)	5.5	Rutile MnS	-	-	-
60%TiO ₂ + 17%Al ₂ O ₃ + 15%MnO ₂ + 8%Fe ₂ O ₃ /** 500	1.9 (6.0 %)	34	Anatase MnS Fe _{1-x} S	575°C	625°C	Anatase MnS Fe _{1-x} S
60%TiO ₂ + 17%Al ₂ O ₃ + 15%MnO ₂ + 8%CuO/** 700	1.4 (4.4%)	54	Anatase MnS γ*-Al ₂ O ₃	725°C	710°C	50%Anatase 50%Rutile MnS γ*-Al ₂ O ₃

*) Impregnated catalysts on the basis of monoliths support MS-1

***) Bulk washcoating material

a) Ca-montmorillonite

The Mn-containing catalyst modified by Fe₂O₃ after testing in H₂S sorption was studied by X-Ray spectral microanalysis. The investigation of modified catalyst demonstrated that the catalyst after H₂S sorption test contains about 20 wt.% S. In this case sulphur is chemically bonded with Mn and Fe cations, that is proved by the symbasis of S K_α, Mn K_α, Fe K_α profiles (Fig. 7A). The catalyst after subsequent testing in H₂S sorption and NH₃ decomposition contains negligible amount of sulphur chemically bonded with Mn and Fe cations (not presented in Fig. 7). The catalyst after subsequent testing in NH₃ decomposition and H₂S sorption contains negligible amounts of both the sulphur chemically bonded with Mn

OP-20

and Fe cations and of the elemental sulphur (Fig. 7B). Thus, two parallel reactions: H₂S sorption and decomposition take place on this case.

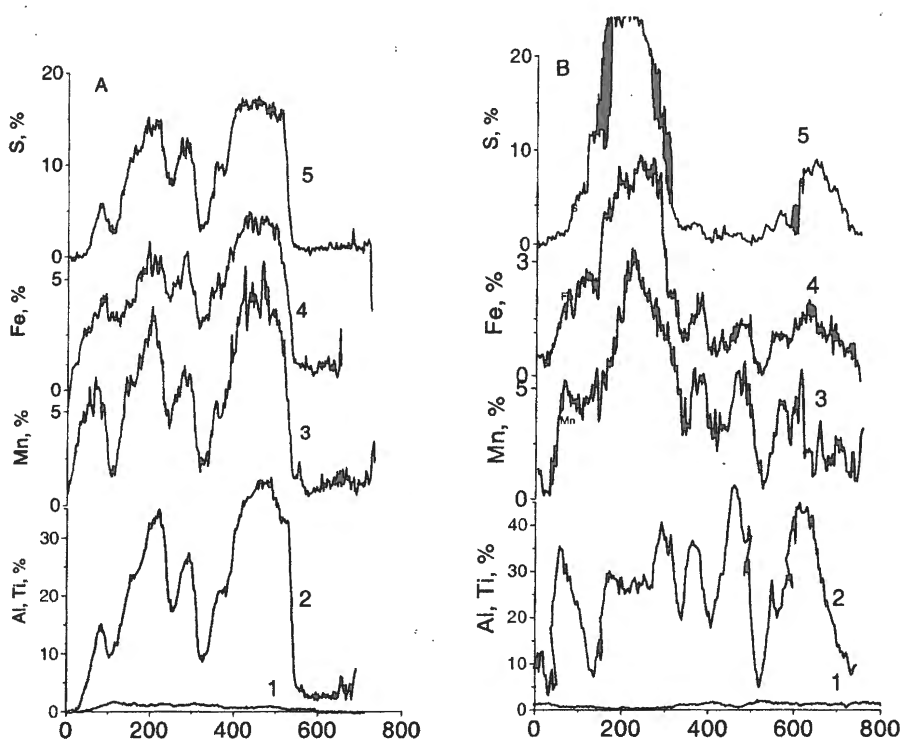


Fig. 7. Intensity of Al K α (1), Ti K α (2), Mn K α (3), Fe K α (4) and SK α (5) radiation for 8%Fe₂O₃+15%MnO₂ catalyst prepared on MS-1: A) after H₂S sorption test; B) after subsequent testing in NH₃ decomposition and H₂S sorption.

Conclusions

The introduction of 4-8 wt.% Fe or Cu oxides into Mn-containing catalyst allows to improve thermal stability at high reaction temperatures and catalytic performance.

Under the reaction conditions the manganese oxides (MnO₂ and β -Mn₂O₃) interact with support (TiO₂), which results in the formation of pure or partially substituted hexagonal structures, like MnTiO₃. The similar phenomenon was observed for the Fe oxide-containing catalysts, where α -Fe₂O₃ transformed to FeTiO₃. In the case of Cu oxide-containing catalysts, reduction of CuO into metallic state (Cu⁰) under the reaction conditions was observed. The investigation of bulk MnTiO₃, FeTiO₃ and the special series of samples supported on granulated Ca-montmorillonite and TiO₂ allows to understand the reason of high temperature deactivation of the impregnated manganese oxide catalyst. It has been found, that bulk FeTiO₃ has higher catalytic activity and stability in the ammonia decomposition at temperatures above 600°C, than bulk MnTiO₃. The obtained data indicate, that high activity and stability of the modified catalysts at elevated temperatures is provided by the formation of active phase (Fe,Mn)TiO₃.

The monolith catalysts based on $\text{Fe}_2\text{O}_3+\text{MnO}_2$ active component seem to be the most preferable among studied systems, since they possess the highest catalytic activity at lower temperatures and are the best sorbents for H_2S removal.

Acknowledgement

This work was financed by the INCO – COPERNICUS Contract No. ER BIC 15CT 980505.

References

1. E.N.Gobina, J.S.Oklany, R.Hughes, *Ind. Eng. Chem. Res.*, 34 (1995) 3777.
2. J.P.Wakker, A.W.Gerritsen, J.A.Moulijn, *Ind. Eng. Chem. Res.*, 32 (1993) 139.
3. S.Lew, K.Jothimurugesan, M. Flytzani-Stephanopoulos, *Ind. Eng. Chem. Res.*, 28 (1989), 535.
4. R.E.Ayala, D.W. Marsh, *Ind. Eng. Chem. Res.*, 30 (1991) 55.
5. S.K.Gangwal, J.M. Stogner, S.M.Harkins, S.J.Bossart, *Environ. Prog.* 8 (1989) 26.
6. M.Desai, F.Brown, B.Chamberland, V. Jalan, *Prepr. Pap.-Am. Chem. Soc., Div. Fuel Chem.* 35 (1990) 87.
7. W.J.W.Bakker, M.Vresendorp, F.Kapteijn, J.A.Moulijn. *Can.J.Chem.Eng.* 74 (1996), 713.
8. Hitachi Co. US Patent 4273749 (1981) by S.Kimura, T.Takahashi, Z.Tamura; Refining process of hot gas containing hydrogen sulfide and ammonia.
9. M. Grunze. *Synthesis and decomposition of ammonia*. Eds. D.A. King, D.P. Woodruff, Elsevier Sci. Publisher Comp. Inc., 1983.
10. Mitsubishi Co, US Patent 5679313 (1997) by S.Nojuma, R. Tokuyama, K.Lida; Ammonia decomposition catalysts.
11. Japan Pionics Co. LTD, US Patent 5632964, (1997) by Ishii Yasu, Akita Noboru; Cleaning method for exhaust gas containing ammonia and silane.
12. Z.R.Ismagilov, R.A.Shkrabina, S.A.Yashnik et. al., *Catal. Today* 69 (2001) 351.
13. G.Centi, S.Perathoner, B. Kartheuser et.al., *Appl. Catal. B: Environ.*, 1 (1992) 129.
14. Z.R.Ismagilov, S.R.Khairulin, R.A.Shkrabina et. al., *Catal. Today* 69 (2001) 253.

OP-21

**CATALYTIC OXIDATION OF UNSYMMETRICAL DIMETHYLHYDRAZINE AS
THE METHOD FOR NEUTRALIZATION OF HAZARDOUS LIQUID ROCKET
FUELS: TECHNOLOGY DEVELOPMENT BASED ON THE LABORATORY AND
PILOT PLANT STUDIES**

**I.Z.Ismagilov¹, M.A.Kerzhentsev¹, Z.R.Ismagilov¹, V.N.Parmon¹, V.N.Eryomin²,
L.N.Rolin², V.A.Shandakov³, G.V.Sakovich³, F.Garin⁴, H.J.Veringa⁵**

¹ *Boreskov Institute of Catalysis SB RAS, Pr. Akademika Lavrentieva 5, Novosibirsk, 630090, Russia*

² *State Rocket Center "Academician V.P.Makeyev Design Bureau", Turgoyakskoe Sh. 1,
Miass, Chelyabinsk region, 456300, Russia*

³ *Federal Research and Production Center "Altai", Ul. Socialisticheskaya 1, Biysk, Altai
region, 659322, Russia*

⁴ *Louis Pasteur University, 4, rue Blaise Pascal, Strasbourg, 67070, France*

⁵ *Netherlands Energy Research Foundation, P.O.Box 1, Petten, 1755ZG, The Netherlands*

Reduction and conversion of defense industries in Russia have made extremely important the issues of development and implementation of environmentally safe and efficient technologies for liquid rocket fuel utilization. One of the most topical problems is development of the process for neutralization of 1,1-dimethylhydrazine (CH₃)₂N-NH₂ (or unsymmetrical dimethylhydrazine – UDMH, technical name – "heptil"), by itself representing a highly toxic and explosive substance.

The Boreskov Institute of Catalysis (BIC) in collaboration with the State Rocket Center "Academician V.P.Makeyev Design Bureau" and other institutions has developed a new environmentally safe method for UDMH destruction by means of the complete catalytic oxidation to harmless products (CO₂, H₂O, N₂). In order to destroy UDMH, it is suggested to use a combination of methods of oxidation in the reactor with fluidized catalyst bed and liquid-phase catalytic oxidation of UDMH traces in the scrubber fluids of gas purification units [1,2].

A study of UDMH vapor oxidation by air has been conducted at BIC in the laboratory kinetic setup on different solid catalysts, including oxide catalysts IC-12-73 (Cu_xMg_{1-x}Cr₂O₄/γ-Al₂O₃), IC-12-74 (Fe₂O₃/γ-Al₂O₃), IC-44 (Fe₂O₃+Cr₂O₃+ZnO), noble metal catalysts AP-64 (0,64%Pt/γ-Al₂O₃), 0,5%Pd/γ-Al₂O₃, 32,9%Ir/γ-Al₂O₃, and catalysts of other types: modified zeolite Cu/(ZSM5+TiO₂+Al₂O₃)/Al₂O₃-SiO₂ and β-Si₃N₄. The temperature dependencies of various product concentrations have been examined. The reaction intermediates were identified, and a possible mechanism of UDMH catalytic

oxidation has been suggested. The catalysts and process conditions, allowing to achieve the complete oxidation of UDMH to CO_2 , H_2O and N_2 with minimal concentrations of nitrogen oxides formed, were selected. Also the study of catalysts for UDMH oxidation in the aqueous solutions has been conducted, and selection of the most efficient catalysts was done [3].

In this communication we present some results of the experiments with catalysts IC-12-73 ($\text{Cu}_x\text{Mg}_{1-x}\text{Cr}_2\text{O}_4/\gamma\text{-Al}_2\text{O}_3$), IC-12-74 ($\text{Fe}_2\text{O}_3/\gamma\text{-Al}_2\text{O}_3$), AP-64 (0,64%Pt/ $\gamma\text{-Al}_2\text{O}_3$) and modified zeolite $\text{Cu}/(\text{ZSM5}+\text{TiO}_2+\text{Al}_2\text{O}_3)/\text{Al}_2\text{O}_3\text{-SiO}_2$. These experiments were conducted under the following conditions: catalyst temperature 200-400°C, C(UDMH) in the initial reaction mixture $0,55 \pm 0,05$ mmol/L ($1,2 \pm 0,1$ vol.%), catalyst loading 1 cm³, catalyst fraction 0,25-2 mm, reaction mixture gas hourly space velocity (GHSV) 7200 h⁻¹.

It was found that the most active catalysts for UDMH deep oxidation to CO_2 are IC-12-73 and AP-64, while catalysts IC-12-74 and $\text{Cu}/(\text{ZSM5}+\text{TiO}_2+\text{Al}_2\text{O}_3)/\text{Al}_2\text{O}_3\text{-SiO}_2$ can be used for UDMH deep oxidation only at the temperatures above 400°C. In the case of IC-12-73, noticeable increase of conversion to CO_2 begins at 200°C, and at the temperatures above 300°C practically complete UDMH transformation into the deep oxidation products CO_2 , H_2O and N_2 is observed. For all the studied catalysts, at 200-300°C, along with the products of deep oxidation, a number of intermediate products forming from UDMH were revealed on the chromatograms, among them – methane CH_4 , dimethylamine $(\text{CH}_3)_2\text{NH}$, methylenedimethylhydrazine $(\text{CH}_3)_2\text{N-N=CH}_2$, dimethyl ether $(\text{CH}_3)_2\text{O}$, 1,2-dimethyldiazene $\text{CH}_3\text{-N=N-CH}_3$, acetonitrile $\text{CH}_3\text{-C}\equiv\text{N}$, dimethylformamide $(\text{CH}_3)_2\text{N-COH}$, dimethylnitrosoamine $(\text{CH}_3)_2\text{N-N=O}$. It was determined, that the most toxic product dimethylnitrosoamine is usually formed only at the low temperatures near 210°C, and is absent at the temperatures above 400°C.

The highest NO concentrations are formed on AP-64 catalyst, while the lowest – on IC-12-74 and IC-12-73 catalysts. $\text{Cu}/(\text{ZSM5}+\text{TiO}_2+\text{Al}_2\text{O}_3)/\text{Al}_2\text{O}_3\text{-SiO}_2$ catalyst demonstrates rather high C(NO), however it becomes lower at the temperatures above 360°C. In summary, IC-12-73 catalyst exhibited the best results of UDMH oxidation to CO_2 , and low selectivity of nitrogen oxides formation [2]. Consequently, this catalyst was selected for the usage in fluidized bed reactor of the pilot plant for catalytic destruction of UDMH.

Based on the studies conducted, a pilot plant for UDMH catalytic destruction with a capacity of 10 tons/year was developed and fabricated. In this plant, the adjustment and optimization of the process of UDMH catalytic destruction was carried out.

OP-21

References

1. Z.R.Ismagilov, V.N.Parmon, M.A.Kerzhentsev et al, Proc. Scientific and Technical Seminar "Problematic Questions in the Methodology of Utilization of Composite Solid Rocket Propellants, Wastes and Residues of Liquid Rocket Propellants in the Elements of Rocket and Space Technology", Federal Research and Production Center "Altai", Biysk, Russia, November 16-17, 1999, p.13 (in Russian)
2. V.N.Parmon, O.P.Pestounova, G.L.Yelizarova et al, Proc. Memorial Prof. V.V.Popovskii Conference "Regularities of the Deep Oxidation of Substances on the Solid Catalysts", Boreskov Institute of Catalysis, Novosibirsk, Russia, May 22, 2000, p.235 (in Russian)
3. O.P.Pestounova, G.L.Elizarova, Z.R.Ismagilov et al, Abstr. 3rd European Workshop on Environmental Catalysis "Environmental Catalysis - a Step Forward", Maiori (Amalfi Coast), Italy, May 2-5, 2001, p. 137

Acknowledgements

The authors would like to thank the International Science and Technology Center (ISTC, Moscow, Russia) for the financial support of this work (Project No 959), and Dr. V.A.Rogov (BIC) for the assistance with GC/MS analysis of some of the UDMH partial oxidation products.

MATHEMATICAL MODELLING OF OSCILLATORY BEHAVIOUR DURING $\text{N}_2\text{O}+\text{H}_2$ REACTION OVER IR (110)

N.V. Peskov, M.M. Slinko*, Sónia A. C. Carabineiro**, Bernard E. Nieuwenhuys**

*Moscow State University, Department of Computational Mathematics & Cybernetics,
Moscow, Russia*

**Institute of Chemical Physics, Moscow, Russia*

***Leiden University, Leiden Institute of Chemistry, Surface Science and Catalysis,
Einsteinweg 55, 2333 CC, Leiden, The Netherlands*

1. Introduction

Oscillatory behaviour during the $\text{NO}+\text{H}_2$ reaction has been widely studied over Pt, Rh and Ir single crystal surfaces and a review of these studies can be found in ref [1]. The reaction of $\text{NO}+\text{H}_2$ was the first oscillatory system, where the problem of the understanding of oscillations in selectivity was arisen. Two of three possible products, namely N_2 and NH_3 were oscillating with different phase shifts for various single crystal surfaces. While for Pt(100), Ir(100) and Ir(510) N_2 and NH_3 were oscillating in phase, there was the phase shift between the N_2 and NH_3 production rates over Rh(111), Rh(110), Ir(110) and Ir(210) single crystal surfaces. Mathematical modelling was used to understand the mechanism of the non-linear behaviour of the $\text{NO}+\text{H}_2$ reaction over Pt(100) [2,3,4] and Rh(533), Rh(111) [5] single crystal surfaces. It was demonstrated, that the anti-phase oscillations in the N_2 and NH_3 production rates could be explained on the basis of the character of the lateral interactions between adsorbed species [5].

Less studies were devoted to the $\text{N}_2\text{O}+\text{H}_2$ reaction over noble metal surfaces and only recently self-sustained reaction rate oscillations in this system were discovered over the Ir(110) surface [6]. The oscillatory behaviour was found in the narrow temperature range between 460 K to 464 K at a N_2O pressure of 10^{-6} mbar with $\text{H}_2/\text{N}_2\text{O}$ ratios close to 1. The period of oscillations was about 60 s. The reaction products were N_2 and H_2O . N_2O oscillates in anti-phase with N_2 and the maxima in H_2O formation were “delayed” compared to the maxima in N_2 formation during the oscillations. The goal of the present study is the development of a mathematical model, which can describe the experimentally observed oscillatory behaviour and to explain the origin of the phase shift between oscillations in N_2 and H_2O production rates.

2. Experimental

Reactions were performed in a UHV system (Leybold Heraeus) equipped with facilities for LEED, AES and a differentially pumped (60 l/s) quadrupole mass spectrometer (UTI 100 C). The system was pumped by a turbo molecular pump (170 l/s) and an ion pump (150 l/s). The base

OP-22

pressure was always better than 2×10^{-10} mbar. The crystal was cleaned by repetitive cycles of heating in an oxygen or hydrogen atmosphere, Ar^+ ion sputtering ($p(\text{Ar}) = 1 \times 10^{-5}$ mbar, incident energy = 1.5 kV) and flashing in UHV to 1400 K. The Ar^+ ion sputtering and flashing treatments were repeated at the beginning of each series of experiments and the surface cleanliness was checked by AES and LEED. Further details about the experimental procedure are described elsewhere [6].

The oscillations were obtained by slowly heating the crystal in N_2O (1×10^{-6} mbar) with a very low amount of H_2 , the smallest possible to be read on the ion gauge (resulting in a $\text{H}_2/\text{N}_2\text{O}$ ratio of approximately 0.4) from room temperature to 800 K and then cool it down to a temperature between 450 K and 470 K. Then the pressure of H_2 was increased stepwise until sustained oscillations in rate started. Figure 1 shows oscillations in the partial pressures of N_2O , H_2O and N_2 , which were detected at 460 K for a N_2O pressure of 1×10^{-6} mbar and $\text{H}_2/\text{N}_2\text{O}$ ratio of 1.2.

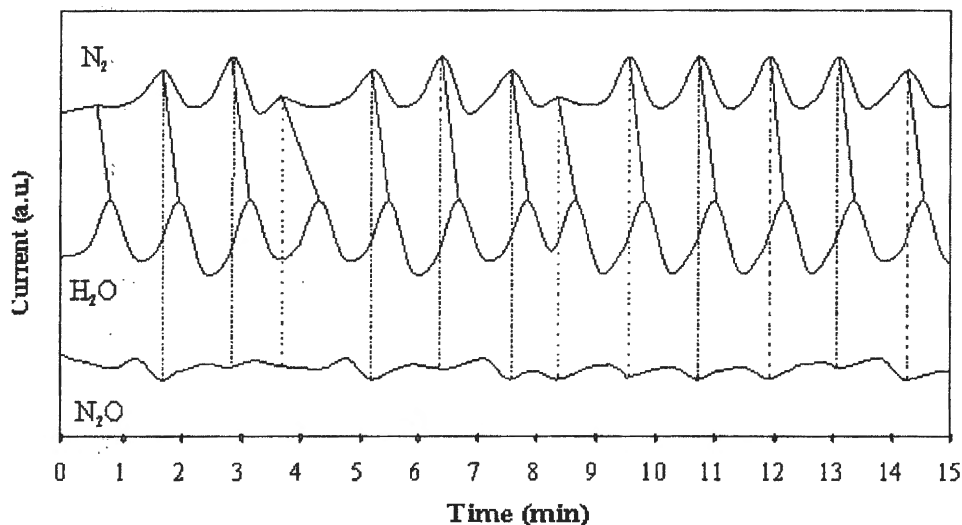


Figure 1. Oscillations in the partial pressures of N_2O , H_2O and N_2 , on the Ir(110) surface, at a N_2O pressure of 1×10^{-6} mbar. The temperature was 460 K and the $\text{H}_2/\text{N}_2\text{O}$ ratio was 1.2. From reference [6].

As can be seen from this figure, the product N_2 pressure oscillates in anti-phase with the reactant N_2O pressure, as can be expected. However it can also be noted that the oscillations in H_2O formation are “delayed” compared to the oscillations in rate of N_2 formation. The oscillations are very sensitive to changes in the $\text{H}_2/\text{N}_2\text{O}$ ratio or temperature, fading away easily.

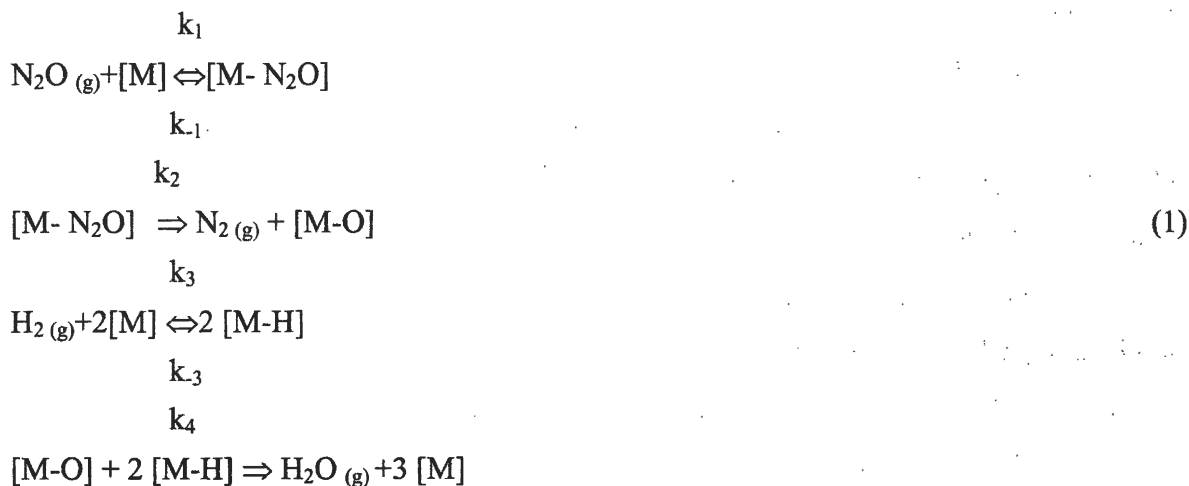
AES measurements were also carried out during the oscillations. For that purpose the rate oscillations were started and the crystal was taken away from the front of the MS hole to the front of the CMA hole. Since the period of oscillations is of the order of 1 minute and a full AES spectrum takes about 2.5 minutes, the evolution of the oxygen peak ($\text{O}_{510\text{eV}}$) could

not be followed during one oscillation cycle. However it was observed that the O-concentration varies from zero to a maximum value during the rate oscillations [6].

3. Mathematical Modelling and Discussion

The TDS studies revealed some interesting features of this system [6]. Usually adsorption of N₂O over metals such as Pt and Rh results in the formation of N₂ and O_{ads} on the surface, whereas on the more active metal surfaces also N_{ads} can be detected. However TDS studies showed that on Ir(110) only N₂ and N₂O were released from the surface in the temperature range from 350 K to 500 K and no NO desorption was detected. In addition it was demonstrated, that oxygen could modify the rates of N₂O desorption and decomposition in a very complicated manner. At small oxygen precoverages, N₂O decomposition is accelerated by oxygen, while at higher oxygen coverages a large increase in the N₂O desorption peak with increasing O precoverage was identified (see Figure 2a from ref.[6]). It was concluded that the presence of oxygen on the surface could modify the N₂O desorption rate.

To model the experimental observations the following set of elementary steps was formulated:



The reaction mechanism includes the adsorption/desorption of N₂O, H₂ and N₂O dissociation. According to the data of TPD studies [6] the reaction products N₂ and H₂O produced at T>400 K desorb immediately after their formation on the catalyst surface.

Mathematical modelling has been done on a macroscopic level and is based on the standard mean field approximation. The nonideality of the adsorbed layer was accounted for through the parameters of lateral interactions ϵ_α where α denotes the number of the step. For the developing of the mathematical model the following assumptions are made:

- 1) H₂ and N₂O adsorption proceed on separate sub-lattices of surface adsorption centres.
- 2) Each adsorbate can occupy only one site on the sub-lattice and the species compete for free sites only on the same sublattice

OP-22

3) On a microscopic scale a randomly well-mixed adlayer is formed in spite of lateral interactions.

4) The variations of the gas phase partial pressures P_{N_2O} and P_{H_2} are very small during the reaction.

Following the proposed reaction mechanism, one arrives at a set of three coupled ordinary differential equations (ODE), describing the temporal variation of surface coverages during the reaction:

$$\begin{aligned} \dot{x} &= p_1 k_1 (1 - x - y) - k_{-1} x - k_2 x, \\ \dot{y} &= k_2 x - k_4 y z^2, \\ \dot{z} &= p_3 k_3 (1 - z)^2 - k_{-3} z^2 - k_4 y z^2. \end{aligned} \quad (2)$$

where p_1 and p_3 are the partial pressures of N_2O and H_2 and x , y , z denote the coverages of N_2O , O, and H.

Mathematical analysis demonstrates, that there is no any limit cycle solutions in the system (2) at any values of the constants k_i , where $i = \pm 1, 2, \pm 3, 4$. The origin of oscillations in this system is supposed to be due to the lateral interactions existing in this system. The analysis of the TPD spectra presented in ref.[6] demonstrates that oxygen greatly modifies the rates of N_2O desorption and dissociation. It was supposed, that due to lateral interactions adsorbed oxygen accelerates the rate of N_2O desorption and the rate of N_2O dissociation. A linear dependence of the activation energies of the following steps on the oxygen coverages were introduced in the model (2) as $E_{-1} + \mu_{-1}y$ and $E_2 + \mu_2y$ where $\mu_{-1}, \mu_2 < 0$. The nonlinearity, which is necessary for the production of rate oscillations in the system (2) is presented via the dependence of the rate constants k_{-1} and k_2 upon the oxygen coverage:

$$k_{-1} = \tilde{k}_{-1} \exp(\varepsilon_{-1}y), \quad k_2 = \tilde{k}_2 \exp(\varepsilon_2y).$$

The values of model parameters were chosen in such a way that they are in agreement with the known literature data and produce the best qualitative similarity of model solutions and experimental data. The obtained values of parameters are shown in the Table:

k	k_1	\tilde{k}_{-1}	\tilde{k}_2	k_3	k_3	k_4
k_0^*	6.2×10^4	10^{12}	5.0×10^{22}	8.3×10^5	2.58×10^8	3.04×10^6
E cal/mol	0	35000	51700	0	23000	15000
k^{**}	0.062	0.001	0.014	1	0.003	0.225

* - dimension of k_1 and k_3 is $(s \times \text{mbar})^{-1}$, dimension of k_i for $i = -1, 2, -3$ and 4 is s^{-1} .

** - the value of the constant at $p_1 = 10^{-6}$ mbar, $p_3 = 1.2 \times 10^{-6}$ mbar, and $T = 460$ K.

The parameters of lateral interaction energies in the rates k_{-1} and k_2 were chosen as $\mu_{-1} = -3640$ cal/mol, $\mu_2 = -9100$ cal/mol, so that at $T = 460$ K, $\varepsilon_{-1} = 4$, $\varepsilon_2 = 10$.

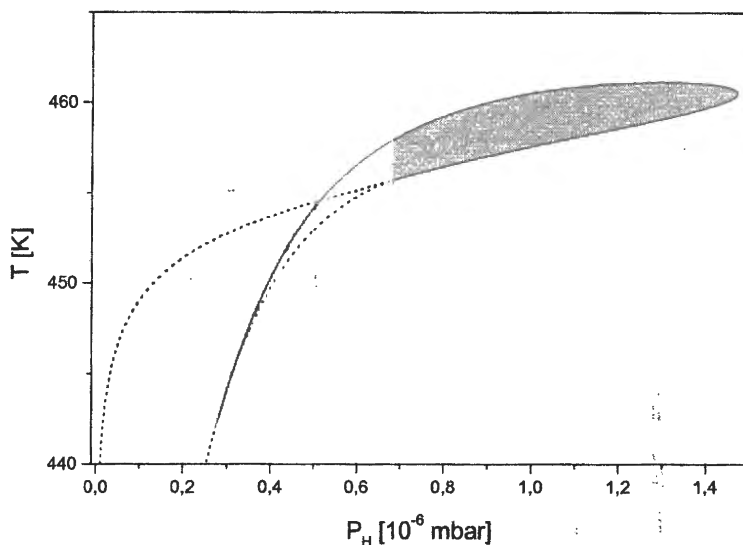


Figure 2. The phase diagram of the model (2) at $p_1 = 10^{-6}$ mbar

The results of the bifurcation analysis at the chosen values of parameters are presented in Figure 2 that shows the phase diagram of the system (2) in the plane (p_3, T) . The solid line denotes the line of the Andronov-Hopf bifurcation and the dashed line represents the line of a saddle-node bifurcation. The region of oscillations is shown by the grey area. As can be seen from this Figure, the temperature region where oscillatory solutions originate is rather narrow. This fact is in excellent agreement with the experimental observations.

Figure 3 displays oscillatory behaviour of the coverages of the adsorbed species, obtained as a result of mathematical modelling. The period of oscillations and the conditions of their appearance closely coincide with the experimental data.

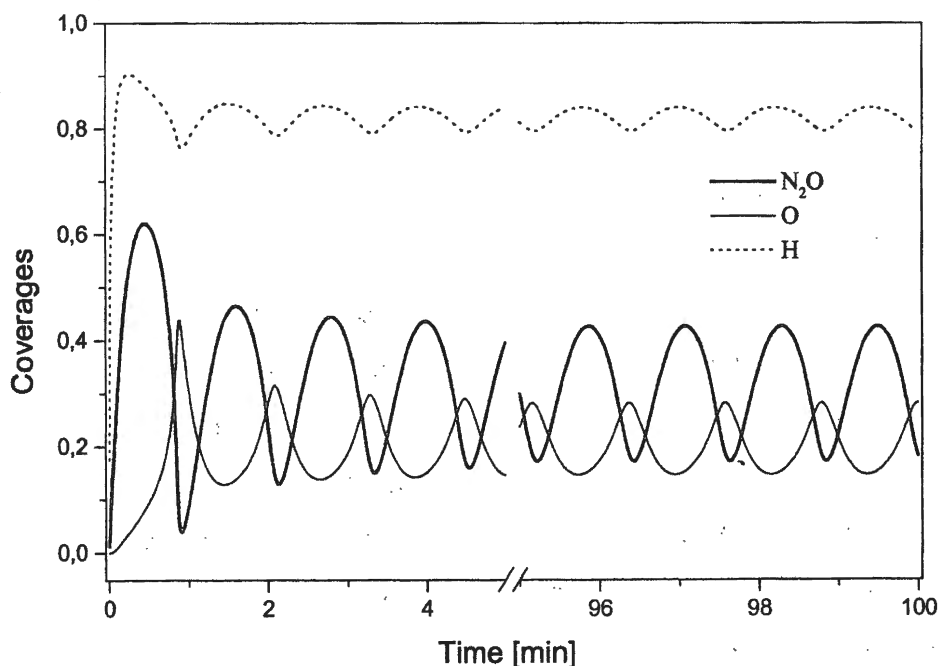


Figure 3. Oscillatory behaviour of surface coverages at $p_1 = 10^{-6}$ mbar, $p_3 = 1.2 \times 10^{-6}$ mbar, and $T = 460$ K.

OP-22

Figure 4 shows oscillations in the production rate of H_2O and in the rate of N_2O decomposition. The last value coincides with the rate of N_2 formation, because following experimental data N_2 molecules desorb immediately after their formation on the catalyst surface.

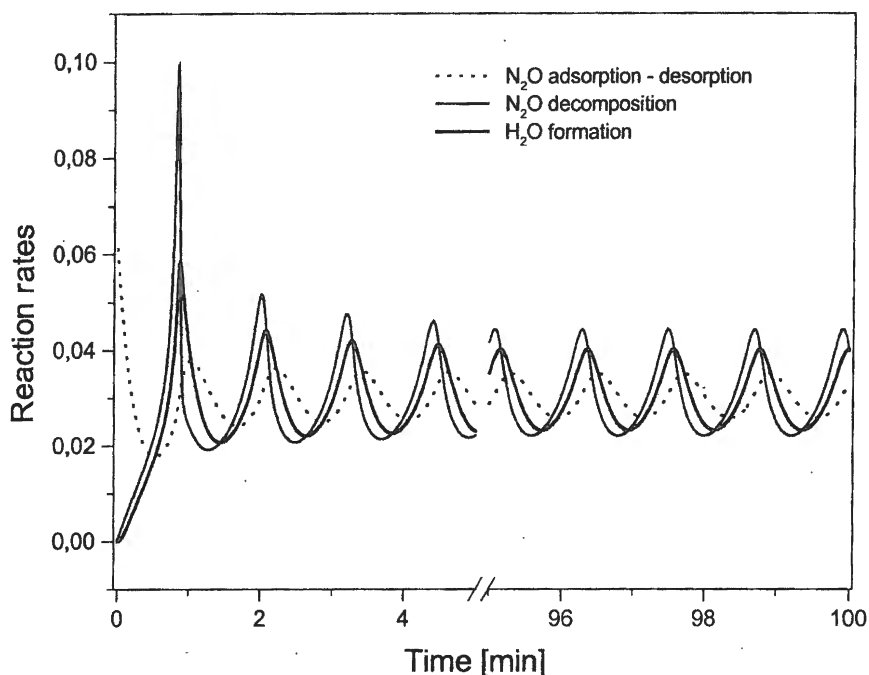


Figure 4. Rates of N_2O decomposition and H_2O formation at the same conditions as in Figure 3.

Figure 4 demonstrates that the results of mathematical modeling reproduce the experimental observations, including the observation that the oscillations in the H_2O formation rate are “delayed” compared to the oscillations in the rate of N_2 formation. The origin of this time delay is connected with the phase shift between the surface concentrations of N_2O and O as shown in Figure 3. The mechanism of oscillations (see Figures 3 and 4) may be presented as follows: starting with the clean surface, hydrogen immediately occupies all sites on its sub-lattice and hydrogen has a minor role in the appearance of oscillations. The concentration of N_2O on the surface increases. Due to the dissociation of N_2O the concentration of adsorbed oxygen increases. Oxygen accelerates N_2O dissociation and the N_2O surface concentration drastically decreases (solid line in Figure 3), while the O coverage increases in an autocatalytic way. However, due to the reaction with hydrogen the concentration of surface oxygen starts to decrease. The decrease of the oxygen concentration causes an increase of the N_2O surface concentration. As the result of this process the rate of N_2O dissociation again increases, leading to an increase of the surface concentration of oxygen. Oxygen again accelerates the N_2O dissociation rate and the cycle of oscillations starts again.

4. Conclusions

A mathematical model is presented, which simulates the oscillatory behaviour reported for the $\text{N}_2\text{O}+\text{H}_2$ reaction over the Ir (110) surface. It is shown that lateral interactions in the adlayer can be the origin of the observed oscillatory behaviour. The character of lateral interactions was obtained from the analysis of the TPD spectra.

The results of the simulation demonstrate that nearly all peculiarities of the experimentally observed kinetic oscillations mentioned in Sec. 2, can be modelled rather well with the model presented in this paper. The model simulates successfully the very narrow temperature range for the appearance of oscillations and the properties of oscillations, including their period and the waveform.

The model presented simulates the phase shift, between the maxima of H_2O and N_2 production rates. It is demonstrated, that this unusual phase shift between production rates of two reaction products is closely connected with the character of lateral interactions in the adlayer. According to the proposed mechanism hydrogen plays a minor role in the appearance of oscillations by removing the oxygen from the surface, resulting in H_2O production. This result of the simulation is supported by the recent observation of isothermal sustained oscillations in the rate of $\text{N}_2\text{O}-\text{CO}$ reaction. This observation demonstrates that the oscillations can be produced with different reducing agents [7].

Acknowledgements

The authors acknowledge financial support from INTAS (99-01882).

References

1. C.A. de Wolf, B.E. Nieuwenhuys "Oscillatory behaviour in the NO-hydrogen reactions over Pt-group metal surfaces", *Catal. Today* 70, 2001, 287-301
2. S.J. Lombardo, T. Fink, R. Imbihl "Simulations of the $\text{NO}+\text{NH}_3$ and $\text{NO} + \text{H}_2$ reactions on Pt(100)", *J. Chem. Phys.*, 98, 1993, 5526-5539
3. M. Gruyters, A.T. Pasteur, D.A. King "Simulation of oscillatory behaviour in the reduction of NO by hydrogen on Pt(100): The role of nonlinear restructuring" *J. Chem. Soc., Faraday Trans. 92*, 1996, 2941-2949
4. A.G. Makeev, B.E. Nieuwenhuys "Simulation of oscillatory behaviour in the $\text{NO}+\text{H}_2/\text{Pt}(100)$ reaction: «surface explosion», kinetic oscillations and chaos", *J. Chem. Phys.*, 108, 1998, 3740-3749
5. A.G. Makeev, M.M. Slinko, N.M.H. Janssen, P.D. Cobden, B.E. Nieuwenhuys, "Kinetic oscillations and hysteresis phenomena in the $\text{NO}+\text{H}_2$ reaction on Rh(111) and Rh(533): Experiments and Mathematical modelling", *J. Chem. Phys.*, 105, N16, 1996, 7210-7222
6. S.A. Carabineiro, B.E. Nieuwenhuys, "Reduction of N_2O by H_2 on the Ir(110) surface. Oscillations in rate", *Surf. Sci.* 2001, 495, 1-7.
7. S.A.C. Carabineiro, W.D. van Noort, B. E. Nieuwenhuys, "A comparative study of the $\text{N}_2\text{O}-\text{CO}$ and $\text{N}_2\text{O}-\text{H}_2$ reactions on the Ir(110) surface with emphasis on the oscillatory behaviour", *Surf. Sci.*, in review.

**¹³C NMR STUDY OF Ti(IV) SPECIES FORMED VIA ACTIVATION OF Cp*TiCl₃
WITH METHYLALUMINOXANE (MAO)**

K.P. Bryliakov^{a,b}, N.V. Semikolenova^a, V.A. Zakharov^a, E.P. Talsi^{a,b}

^a *Boreshkov Institute of Catalysis, SB RAS Pr. Akademika Lavrentieva 5, Novosibirsk 630090, Russia Fax: +7 (383 2) 343 766; e-mail: talsi@catalysis.nsk.su*

^b *Novosibirsk State University, ul. Pirogova 2, Novosibirsk 630090, Russia Fax: +7 (383 2) 343 766; e-mail: bryliako@catalysis.nsk.su*

The discovery of syndiotactic polystyrene (sPS) was an important milestone in stereospecific polymerization.¹ Catalytic system Cp*TiCl₃/MAO (Cp* = C₅Me₅) is one of the most practicable for sPS production.² The mechanism of (C₅Me₅)TiCl₃ activation by MAO to form effective catalysts for α-olefins polymerizations is an extremely important and still unsolved problem. In this work, the titanium(IV) species formed in the catalytic systems Cp*TiMe₃/MAO and Cp*TiCl₃/MAO (Cp* = C₅(CH₃)₅) in toluene and chlorobenzene were studied within the temperature range 253-293 K and at Al/Ti ratios 30-80, by means of ¹³C NMR spectroscopy.

It was shown that two types of titanium(IV) complexes are formed upon activation of Cp*TiMe₃ with MAO. The major complex was identified as a 'cation-like' intermediate Cp*Me₂Ti⁺ ← Me⁻ - Al ≡ (MAO). The minor complex was tentatively assigned to a heterodinuclear cationic complex [Cp*TiMe(μ - Me)₂AlMe₂]⁺[Me - MAO]⁻.

Four types of titanium(IV) complexes were observed in the Cp*TiCl₃/MAO catalytic system. They are: two methylated complexes, Cp*TiMeCl₂ and Cp*TiMe₂Cl; the 'cation-like' intermediate Cp*MeCITi⁺ ← Me⁻ - Al ≡ (MAO) and the heterodinuclear cationic complex [Cp*TiCl(μ - Me)₂AlMe₂]⁺[Me - MAO]⁻. According to the EPR measurements, the relative concentration of Ti(III) species in the Cp*TiCl₃/MAO system is smaller than 1% of total Ti concentration at Al/Ti ratio 35 and 10% at Al/Ti ratio 700.

Acknowledgements. This research was supported by grant INTAS 00-00841. The authors are grateful Dr. D. E. Babushkin for the help in synthesis of Al(¹³CH₃)₃ and the fruitful methodology of using ¹³C enriched MAO.

1. N. Ishihara, T. Seimiya, M. Kuramoto, M. Uoi, *Macromolecules*, 19 (1986) 2464.
2. N. Tomotsu, N. Ishihara, T. H. Newman, M. T. Malanga, *J. Mol. Catal.*, 128 (1998) 167.

ENVIRONMENTAL CATALYSIS: SELECTIVE REDUCTION OF NO BY ALKANES OVER MECHANICALLY MIXED OXIDE CATALYSTS

Valentin F. Tretyakov, Tatyana N. Burdeynaya, Valerii A. Matyshak¹

A.V. Topchiev Institute of Petrochemical Synthesis, Russian Academy of Sciences, Moscow, Russia

¹*N.N. Semenov Institute of Chemical Physics, Russian Academy of Science, Moscow, Russia*

Selective catalytic reduction (SCR) of NO to N₂ by hydrocarbons attracts attention nowadays as an important process for NO_x removal from exhaust emissions in both mobile and stationary sources. Basic achievements in this field of ecological catalysis are connected with development of such catalysts as metal ion-exchanged zeolites and metal oxides-supported alumina. Recent studies have shown that the mechanical mixing of different metal oxides or metal oxides with zeolites considerably enhanced the rate of the reduction of NO by hydrocarbons.

In our research we investigated commercial oxide catalysts that do not relate to SCR process and do not contain neither zeolites nor noble metals.

Peculiarities of redox reactions in the process of NO reduction by alkanes (CH₄ or C₃H₈) in the presence of O₂ were investigated over mechanically mixed commercial oxide Cu-Zn-Ni-Al(I) + Fe-Cr(II)-containing and Cu-Zn-Ni-Al(I) + Fe-Cr(III)-containing catalysts. The catalytic reactions were conducted in flow reactor with catalyst in the fixed bed, N₂ being the carrier gas. Activity tests were carried out in the temperature range 200-600°C at GHSV range 10,000-17,000 h⁻¹. Analysis was carried out with gas chromatograph (Chrom - 5) and gas analyzer (TestoTerm). The synergistic effect in the reaction of NO_x reduction by methane and propane was originally discovered over these catalytic systems in the temperature range 300-550°C under the atmospheric pressure.

It was shown by temperature-programmed desorption of NO that oxygen does not block the adsorption of NO on the surface of these catalysts.

The synergistic effect in the reaction of NO reduction by propane over mechanically mixed oxide catalysts (I) + (II) was investigated using IR-spectroscopy *in situ*. It was concluded that observed synergistic effect could be explained by partial propane oxidation over Cr-containing component (II) and NO reduction by this product over Cu-containing component (I) of the binary catalytic system.

OP-24

The effect of mechanochemical activation on the activity of these compositions in the reaction of selective reduction of nitrogen oxides by propane in the presence of O₂ and severe oxidation of hydrocarbons (using toluene as an example) were examined. The interaction of the components of a reaction medium with the catalyst surface was studied by the technique of temperature programmed desorption (TPD) as the most informative method for such systems. The effect of reduction/reoxidation processes on the surface of oxide catalytic systems on the absorption capability was investigated. A correlation between the surface properties of the catalysts and their catalytic activity in the reaction of selective NO reduction by propane was established.

The obtained data show the possibility of using the technology of mechanochemical synthesis of catalysts with various compositions and better properties than analogous industrial catalysts prepared by conventional procedures. In the view of high environmental safety of the technology of catalyst preparation by the mechanochemical method, opportunities for the synthesis of catalysts with properties superior to those of analogous industrial catalysts, for rapid launching of production of catalysts of any prescribed composition, this method was shown to be much be promise.

The worked-out catalytical systems showed high effectivity in the process of simultaneous removing of several toxic components: NO_x, CO, hydrocarbons from model gas mixtures as well as from real exhausts of automobile transport.

IRON CLUSTERS OCCLUDED IN ZEOLITE ZSM5 MICROPORES

**Emiel J.M. Hensen, Qingjun Zhu, Pieter C.M.M. Magusin
and Rutger A. van Santen**

*Schuit Institute of Catalysis, Laboratory of Inorganic Chemistry and Catalysis,
Eindhoven University of Technology, P.O. Box 513, 5600 MB, Eindhoven,
The Netherlands*

Abstract

The effect of high temperature calcination and steaming on iron-containing zeolite was studied. Iron was introduced by sublimation of FeCl_3 . FTIR measurements clearly show the disappearance of Brønsted acid sites upon such treatments. This is attributed to a reaction between small occluded Fe oxide clusters obtained after initial low temperature calcination and the zeolite protons to give cationic Fe species compensating the negative zeolite charge. High temperature calcination and especially steaming considerably increase the catalyst activity in nitrous oxide decomposition. The two treated catalysts exhibit a higher apparent activation energy than the original sample. This high apparent activation energy is compensated by a high pre-exponential factor. In Fe/ZSM-5 the activity mainly derives from small Fe oxide clusters, while upon treatment more active cationic species are generated. The kinetic parameters point to a stronger Fe-O bond for the latter case.

Introduction

Transition metals in zeolite host matrices provide unique catalytic properties [1]. A prime example is the ability of small occluded Fe-oxide particles in pentasil zeolite to selectively hydroxylate benzene to phenol with nitrous oxide as oxidant [2-8]. Fe/ZSM5 also provides possibilities for selective reduction of NO_x [9-15] and the decomposition of N_2O [15-19].

Various preparation methods are available to introduce Fe in the zeolite micropores. Generally, ion exchange leads to bulky iron oxide agglomerates on the zeolite external surface. While the preferred preparation route for catalysts active in benzene hydroxylation appears to be steaming of isomorphously Fe-substituted zeolites [2-8,20,21], sublimation of FeCl_3 provides a controlled way to deposit a higher amount of Fe in the zeolite micropore space [11-17,22,23]. The amount of Fe can be tuned by the choice of the Si/Al ratio of the parent

OP-25

zeolite. These catalysts have shown a high activity in SCR of NO_x [19] and nitrous oxide decomposition [19,22].

In the present contribution, we further study the effect of various high temperature pretreatments on catalysts prepared by the sublimation method. The catalysts are extensively characterized by FTIR and ²⁷Al NMR and tested in the decomposition of N₂O. Furthermore, their ability to produce phenol from benzene and nitrous oxide was evaluated.

Experimental

Catalyst preparation

NH₄ZSM5 (Akzo Nobel, Si/Al = 19.4) was calcined in pure oxygen at 823 K for 2 h to yield HZSM5. Anhydrous FeCl₃ (Aldrich, reagent grade 99.9%) was sublimed onto HZSM5 (Akzo Nobel, Si/Al = 19.4) [11,12]. The temperature of the iron precursor and zeolite were 573 K and 593 K, respectively. Subsequently, the sample was washed in 2500 ml deionized water twice by stirring for 1 h each time. After drying in an oven at 383 K overnight, 1 g of the resulting material (Fe/ZSM5) was calcined in 20vol.% O₂ in He at a flow rate of 200 Nml/min for 2 h. Further treatment of the original catalyst was carried out: (a) 200 mg Fe/ZSM5 was calcined in 20vol.% O₂ in He at a flow of 200 ml/min at 973 K for 3 h (Fe/ZSM5-HTC), (b) 200 mg Fe/ZSM5 was steamed in mixture of 20 vol.% O₂ and 10 vol.% water vapor at a flow rate of 200 ml/min at 973 K for 3 h (Fe/ZSM5-HTS).

Characterization

The samples contained approximately 3.6 wt.% Fe (ICP-OCES), which corresponds to a Fe/Al ratio of 0.97. The Fe content of the three samples were found to be identical.

Infrared spectra of self-supporting 10 mg catalyst wafers were recorded at room temperature on a Bruker IFS113 Fourier Transform IR spectrometer with DTGS detector at a resolution of 4 cm⁻¹. Prior to IR measurement, the catalyst was pretreated *in situ* at 773 K for 1 h *in vacuo* (pressure <10⁻⁶ mbar). Normalization of the overtones of the zeolite lattice vibrations (1870 cm⁻¹-1950 cm⁻¹) was applied to quantitatively determine the number of Brønsted acid sites.

Solid-state ²⁷Al magic-angle spinning NMR spectra were obtained on a 11.7-T Bruker DMX500 spectrometer equipped with a 2.5-mm MAS probe head, and operating at a ²⁷Al NMR frequency of 130 MHz. The sample-rotation rate was 30-kHz. Rotor-synchronized echoes were recorded with a two-pulse sequence p₁-τ-p₂-τ-acquisition with p₂ = 2p₁ = 2.4 μs, and τ = 31.5 μs. The interscan delay, 1 sec, was long enough to avoid ²⁷Al-saturation effects. Chemical shifts were referenced to a saturated Al(NO₃)₃ solution.

Reactivity studies

Activity measurements were carried out in an atmospheric gas-phase single-pass fixed-bed reactor system (quartz reactor, i.d. 4 mm). Gas-phase reactants were fed by thermal mass flow controllers (Brooks). The reactant composition for nitrous oxide decomposition was 3500 ppm N_2O in He, which was fed to the reactor at a GHSV of 24000 h^{-1} . Effluent products (N_2O , N_2 and O_2) were detected by an online quadrupole mass spectrometer. An amount of 40 mg catalyst (sieve fraction $125\text{-}425\mu\text{m}$) was diluted with carborundum to fulfill plug flow conditions. Prior to reaction, catalysts were pretreated in a 100 Nml/min He flow at 723 K for 1 h after heating at a rate of 2 K/min .

The catalysts were qualitatively tested for the production of phenol at 648 K . To this end, benzene was vaporized by a syringe in the nitrous oxide stream before the catalyst bed. The effluent products were condensed after the reactor and analyzed by GC-MS.

Results

Characterization

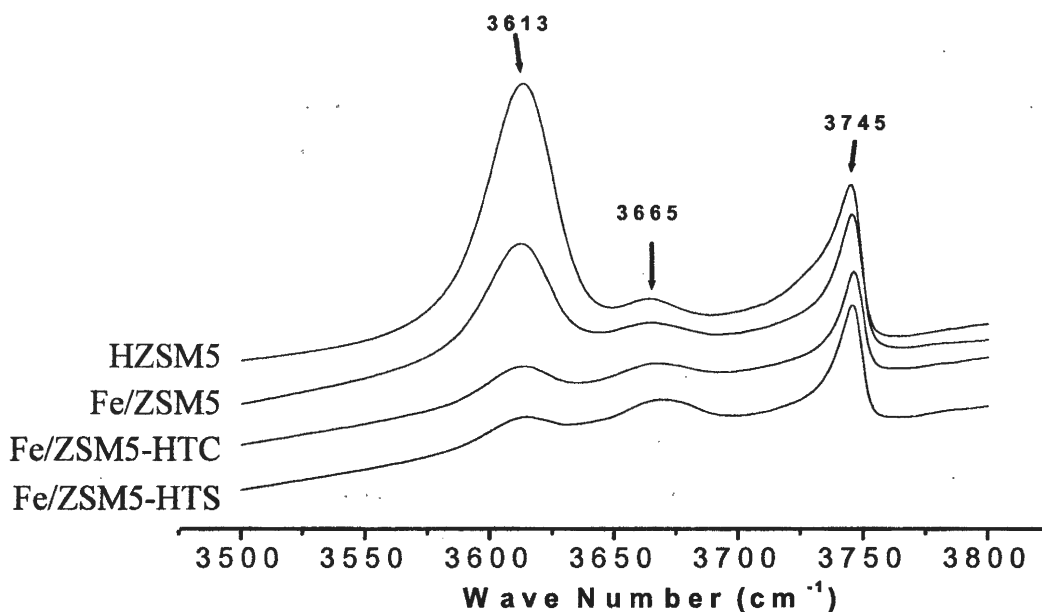


Figure 1. Infrared spectra of the parent zeolite, Fe/ZSM5, Fe/ZSM5-HTC and Fe/ZSM5-HTS at room temperature after drying.

Figure 1 displays infrared spectra for the various catalysts including the parent HZSM5. The band at 3613 cm^{-1} is the stretching vibration of the Brønsted hydroxyl groups, while the band at 3745 cm^{-1} relates to the vibration of terminal Si-OH groups (26, 27). Generally, the weak band at 3665 cm^{-1} is assigned to the hydroxyl groups connected to extra-lattice aluminium [24]. By calibration with the overtone of lattice vibrations, a quantitative

OP-25

comparison of the number of Brønsted hydroxyl groups was possible. While Chen and Sachtler [11] described the disappearance of bridging hydroxyl groups after FeCl_3 sublimation, our IR data indicate that approximately 45% of these groups are regenerated after washing and calcination at 723 K. The remaining charge-compensation derives from the coordination of cationic Fe-species to the zeolite framework. After calcination at 973 K, the band at 3613 cm^{-1} has further decreased in intensity and we calculate that approximately 8% of the original Brønsted acid sites persist. A similar effect is found for Fe/ZSM5-HTS. In this case, a small increase in the band at 3665 cm^{-1} points to partial dealumination of the zeolite structure. XRD spectra of the various samples showed that the MFI structure remains intact, while the steaming treatment results in a small increase of amorphous phases in Fe/ZSM5-HTS.

The magic-angle spinning (MAS) ^{27}Al NMR spectra of the various samples are collected in Figure 2. The signal at 57 ppm is assigned to tetrahedrally coordinated aluminium in the zeolite lattice. The signal at 0 ppm in the spectra of Fe/ZSM5-HTC and Fe/ZSM5-HTS belongs to a fraction of octahedrally coordinated extra-lattice Al, which is particularly significant for the steamed zeolite. This is consistent with the findings of a signal of hydroxyl groups associated with extra-lattice aluminium at 3665 cm^{-1} . For Fe/ZSM5-HTS spectral intensity is also detected between the 57-ppm and the 6-ppm signal. Typically, a broad peak in this shift-range is attributed to non-lattice tetrahedrally or pentacoordinated aluminum [25]. Such Al species may exist in the zeolite micropores as small Al_2O_3 particles without associated hydroxyl groups. This explains why we cannot detect the increase of the 3665 cm^{-1} band in Fe/ZSM5-HTS. A quantitative comparison with the parent ZSM5 indicates that only ~10% of the Al species is detectable in the echo spectra. This is probably a result of the line broadening caused by paramagnetic Fe and indicates that Fe is located close to the Brønsted sites in the zeolites, although a decrease of the symmetry around Al nuclei can also play a role.

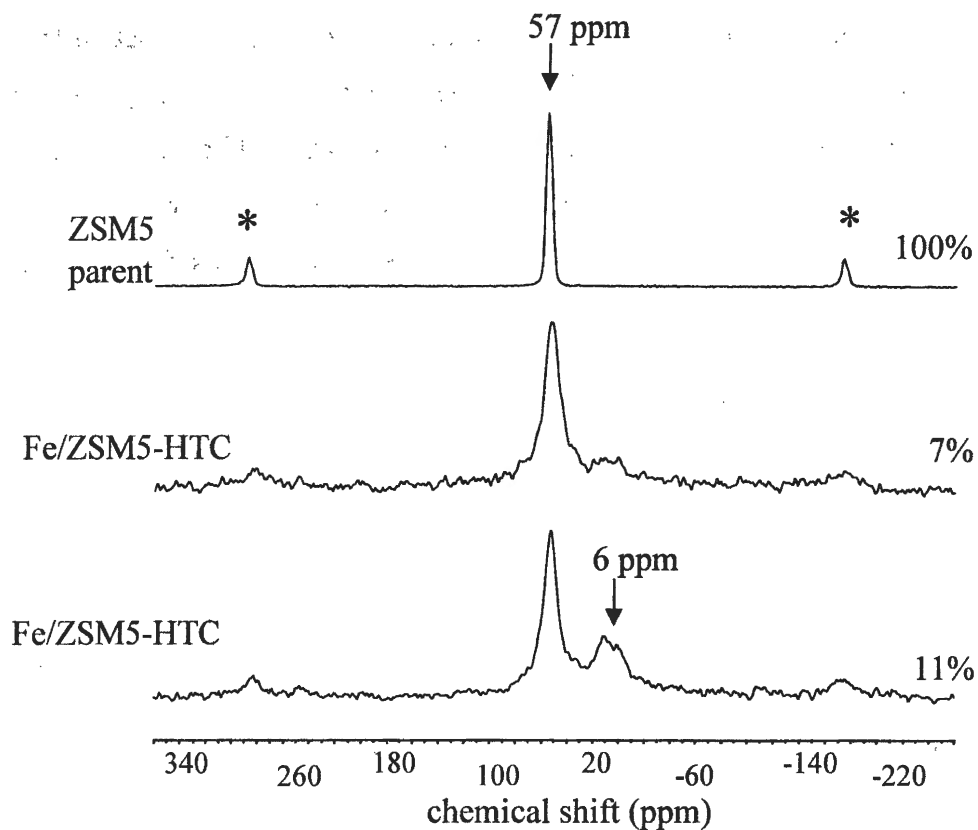


Figure 2. ^{27}Al NMR MAS spectra of parent H/ZSM5(15), Fe/ZSM5-HTC and Fe/ZSM5-HTS. MAS sidebands are indicated with an asterisk.

Reactivity

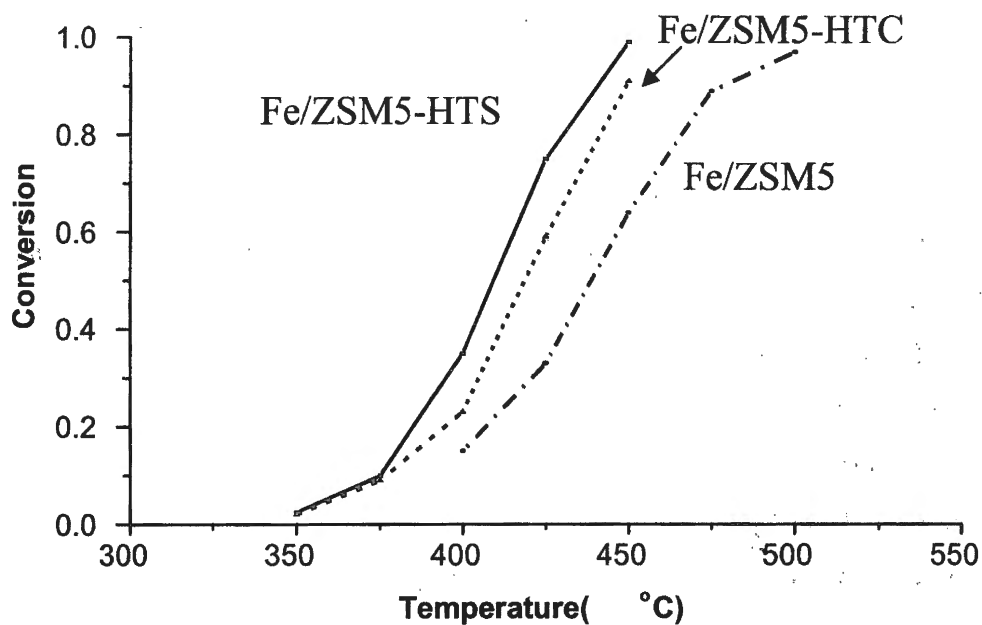


Figure 3. Nitrous oxide conversion as a function of temperature for Fe/ZSM5, Fe/ZSM5-HTC and Fe/ZSM5-HTS (GHSV = 24000 h⁻¹).

OP-25

Figure 3 shows the nitrous oxide conversion as a function of the reaction temperature for the catalysts under study. The activity of Fe/ZSM5 can be efficiently increased by high temperature treatments (Fe/ZSM5-HTC and Fe/ZSM5-HTS). While Fe/ZSM5-HTC decreases the temperature needed for 50% conversion by 30 K, steaming allows a further reduction of 10 K. The apparent activation energies and pre-exponential factors for the various catalysts are condensed in Table 1.

Table 1. Kinetic parameters for Fe/ZSM5 catalyst in nitrous oxide decomposition (activation energies: ± 8 kJ/mol; pre-exponential factors: $\pm 10\%$)

Catalyst	Apparent activation energy(kJ/mol)	Pre-exponential factor(1/s)
Fe/ZSM5	136	4.10^{10}
Fe/ZSM5-HTC	186	5.10^{14}
Fe/ZSM5-HTS	195	4.10^{15}

The benzene hydroxylation tests showed that phenol was not formed on the Fe/ZSM5 catalysts. Both Fe/ZSM5-HTC and Fe/ZSM5-HTS showed phenol production with the latter one producing considerably more phenol.

Discussion

The sublimation procedure effectively replaces all Brønsted acid sites with iron chlorine complexes [11]. The IR results show that approximately 45% of these Brønsted acid sites are regenerated after washing, drying and calcination at 773 K. This results in various Fe species including bulky iron oxide agglomerates on the external zeolite surface, and positively charged Fe^{3+} species and neutral nanoclusters in the zeolite micropores. For such intracrystalline species, diiron species have been advanced by several authors [5,11] in analogy with the active center in methane monooxygenase enzyme [26]. High temperature calcination (Fe/ZSM5-HTC) or steaming (Fe/ZSM5-HTS) results in the disappearance of nearly 90% of the bridging hydroxyl groups. This dramatic decrease is explained by the reaction of neutral iron oxide nanoclusters with the Brønsted acid sites at elevated temperatures [22]. Dehydroxylation can only play a minor role since high temperature calcination of the parent zeolite only resulted in a small decrease of Brønsted acidity. Furthermore, Brønsted acid sites in Fe/ZSM5-HTC can be regenerated by exposure to water vapor at 773 K [23]. This shows that cationic Fe species generated in Fe/ZSM5-HTC can be rehydrolysed. Neutral species include Fe oxide particles at the external zeolite surface and Fe oxide nanoclusters occluded in the zeolite micropores. We propose that such nanoclusters

which is in close proximity to the Brønsted acid sites reacts with the zeolitic protons. Bulky Fe oxide clusters, prepared by impregnation of $\text{Fe}(\text{NO}_3)_3$ on a silica support, are not active in N_2O decomposition below 773 K, while Fe oxide agglomerates formed on the external zeolite surface after steaming iron-substituted ZSM-5 cannot activate nitrous oxide as oxidant for aromatics [21]. This indicates that the active species in Fe/ZSM-5 are Fe oxide nanoclusters and cationic Fe species. High temperature calcination results in an increase of the number of cationic Fe species. The almost complete disappearance of Brønsted acidity may indicate that such further treatment leads to a catalyst with almost exclusively cationic Fe species present in the micropore space. It appears that these cationic species display a much higher nitrous oxide decomposition activity than small Fe oxide species. Alternatively, the high temperature treatment may lead to migration of Fe species from the zeolite pores to the external surface, thus opening up the micropores. However, preliminary TEM measurements show that the amount of external Fe-oxide clusters does not increase to a large extent upon high temperature treatments. Moreover, the reaction of Fe oxide species and zeolite protons appears to be reversible upon exposure to water vapor at 773 K [23]. Large crystals on the external surface will not redistribute again under such conditions.

The large change in apparent activation energy between original Fe/ZSM-5 and further treated Fe/ZSM-5 as determined over a wide temperature range indicates that indeed the catalytic nature of Fe oxide and cationic Fe species are very different. This is taken as further evidence that the neutral nanoclusters are also able to catalyze N_2O decomposition although at a much lower rate. The much higher apparent activation energy for the more active species is compensated by a high pre-exponential factor. The difference is 4-5 orders of magnitude. Thus, we draw the main conclusion that in Fe/ZSM-5 various iron species are responsible for nitrous oxide decomposition.

While the reaction between Fe oxide nanoclusters upon high temperature calcination is partly reversible, steaming essentially leads to partial dealumination as derived from the presence of pentacoordinated Al species. However, the fact that part of the aluminium is not detected by NMR due to the presence of the paramagnetic iron nuclei makes this interpretation inconclusive.

The rate limiting step for nitrous oxide decomposition over Fe/ZSM5 is proposed to be the removal of adsorbed oxygen, generated by the reaction of N_2O with an iron center, by N_2O [27]. The large change in kinetic parameters can thus be explained by the nature of the adsorbed oxygen atom (O^*). From its higher apparent activation energy, we conclude that the Fe- O^* bond energy is higher for the more active catalyst. Such a strong Fe- O^* bond leads to a large

OP-25

gain in entropy in the rate limiting step, thus providing a tentative explanation for the increase of the pre-exponential factor. The difference in the nature of the Fe species can partly be proven by their oxidation ability towards hydrocarbons. We have done some preliminary tests of the conversion of benzene to phenol using N_2O as the oxidant on various Fe/ZSM-5 samples. In our initial qualitative analysis, the original Fe/ZSM-5 has a very low activity whereas the high temperature calcined and especially steamed Fe/ZSM-5 show good catalytic performance.

Conclusions

High temperature treatments of Fe/ZSM-5 prepared by the sublimation of $FeCl_3$ on H-ZSM5 is found to strongly increase the rate of nitrous oxide decomposition. The activity strongly depends on the nature of Fe species inside the zeolite micropores. In Fe/ZSM-5 the catalytic activity mainly derives from Fe oxide nanoclusters. Calcination or steam treatments at 973 K induces a reaction between these nanoclusters and zeolite protons, resulting in cationic Fe species. Such species have an appreciably higher activity, while kinetic parameters point to a stronger Fe-O bond for this case.

Acknowledgement

The Dutch National Research School Combination Catalysis is gratefully acknowledged for the financial support.

References

1. P.M.M. Blauwhoff, J.W. Gosselink, E.P. Kieffer, S.T. Sie and W.H.J. Stork, in *Catalysis and Zeolites Fundamentals and Applications*, (J. Weitkamp and L. Puppe, eds.), chapter 7, Springer Press, 1999.
2. G.I. Panov, V.I. Sobolev and A.S. Kharitonov, *J. Mol. Catal.* **61** (1990) 85.
3. V.I. Sobolev, G.I. Panov, A.S. Kharitonov, V.N. Romannikov, A.M. Volodin and K.G. Ione, *J. Catal.* **139** (1993) 435.
4. V.I. Sobolev, K.A. Dubkov, E.A. Paukshtis, L.V. Pirutko, M.A. Rodkin, A.S. Kharitonov and G.I. Panov, *Appl. Catal. A* **141** (1996) 185.
5. G.I. Panov, V.I. Sobolev, K.A. Dubkov and A.S. Kharitonov, *Stud. Surf. Sci. Catal.* **101** (1996) 493.
6. G.I. Panov, V.I. Sobolev, K.A. Dubkov, V.N. Parmon, N.S. Ovanesyan, A.E. Shilov and A.A. Shteinman, *React. Kinet. Catal. Lett.* **61** (1997) 251.

7. K.A. Dubkov, V.I. Sobolev, E.P. Talsi, M.A. Rodkin, N.H. Watkins, A.A. Shteinman and G.I. Panov, *J. Mol. Catal.* **123** (1997) 155.
8. G.I. Panov, *CatTech* **7** (2000) 18.
9. X. Feng and W.K. Hall, *Catal. Lett.* **41** (1996) 45.
10. X. Feng and W.K. Hall, *J.Catal.* **166** (1997) 368.
11. H.Y. Chen and W.M.H. Sachtler, *Catal. Today.* **42** (1998) 73.
12. H.Y. Chen and W.M.H. Sachtler, *Catal. Lett.* **50** (1998) 125.
13. H.Y. Chen, T.V. Voskoboinikov and W.M.H. Sachtler, *J.Catal.* **180** (1998) 171.
14. T.V. Voskoboinikov, H.Y. Chen and W.M.H. Sachtler, *Appl. Catal. B* **19** (1998) 279.
15. Q. Sun, Z.X. Gao, H.Y. Chen and W.M.H. Sachtler, *J. Catal.* **201** (1998) 89.
16. El-M. El-Malki, R.A. van Santen and W.M.H. Sachtler, *Microporous Mesoporous Mater.* **35-36** (2000) 235.
17. El-M. El-Malki, R.A. van Santen and W.M.H. Sachtler, *J. Catal.* **196** (2000) 212.
18. G. Centi and F. Vazzana, *Catal. Today* **53** (1998) 683.
19. F. Kapteijn, J. Rodríguez-Mirasol and J.A. Moulijn, *J.Catal.* **167** (1997) 256.
20. E. Selli, A. Isernia and L. Forni, *PCCP* **2** (2000) 3301.
21. A. Ribera, I.W.C.E. Arends, S. de Vries, J. Pérez-Ramírez and R.A. Sheldon, *J.Catal.* **195** (2000) 287.
22. Q. Zhu, B.L. Mojet, R.A.J. Janssen, E.J.M. Hensen, J. van Grondelle, P.C.M.M. Magusin and R.A. van Santen, accepted for publication in *Catalysis Letters*.
23. Q. Zhu, E.J.M. Hensen, B.L. Mojet, J.H.C. van Wolput and R.A. van Santen, submitted.
24. P.O. Fritz and J.H. Lunsford, *J.Catal.* **118** (1989) 85.
25. D. Goldfarb, M. Bernardo, K.G. Strohmaier, D.E.W. Vaughan and H. Thomann, *J. Am. Chem. Soc.* **116** (1994) 6344.
26. N. Elango, R. Radhakrishnan, W. A. Froland, B. J. Wallar, C. A. Earhart, J. D. Lipscomb and D. H. Ohlendorf, *Protein Sci.* **6** (1997) 556.
27. F. Kapteijn, J. Rodriguez-Mirasol and J.A. Moulijn, *Appl. Catal. B* **9** (1996) 25.

Hessel L. Castricum¹, Vladislav V. Malakhov², Tamara M. Yurieva², Hans Bakker³
and Eduard K. Poels¹

¹ *Department of Chemical Engineering, Universiteit van Amsterdam, The Netherlands*

² *Borekov Institute of Catalysis SB RAS, Novosibirsk, Russia*

³ *Van der Waals-Zeeman Institute, Universiteit van Amsterdam, The Netherlands*

Cu/ZnO catalysts are traditionally prepared by coprecipitation or homogeneous deposition precipitation. Mechanochemical preparation by mechanical milling may also result in the formation of active catalysts [1,2]. After reduction in hydrogen, all types of catalyst are active for the synthesis of methanol. However, the stoichiometry of the metal part can be controlled much better for mechanochemical preparation than for classical chemical preparation techniques.

We have obtained a range of well-defined and intimately mixed Cu/ZnO compounds from various precursors and by mechanical milling in different atmospheres. Differential Dissolution has proved to be an effective technique for monitoring the intimacy of these mixtures. Intimate mixtures are formed during mechanochemical reactions of oxides with the milling atmospheres, as well as by milling of Cu and Zn hydroxides and hydroxy-carbonates. The poor mutual solubility of Cu and Zn oxides improves for anion-modification, i.e. in the presence of hydroxide or carbonate anions. Both Cu⁰ specific surface areas and total surface areas are substantially increased for all milled Cu/ZnO mixtures, but a strong dependency on the type of anion-modification is found. Despite their high intimacy, Cu/Zn hydroxide mixtures exhibit low Cu⁰ areas. This can be explained by the high reduction temperatures of these mixtures that lead to excessive sintering. On the other hand, the presence of carbonates is advantageous for obtaining a structure with a high Cu⁰ area and correspondingly a high activity. As the catalytic activity of these mechanochemically prepared catalysts is of the same order as that of their coprecipitated counterparts, mechanical milling provides an interesting alternative for study and preparation of promoted heterogeneous catalysts.

[1] L. Huang, G.J. Kramer, W. Wieldraaijer, D.S. Brands, E.K. Poels, H.L. Castricum and H. Bakker, *Catal. Lett.* 48 (1997) 55

[2] H.L. Castricum, H. Bakker, B. van der Linden and E.K. Poels, *J. Phys. Chem. B* 105 (2001) 7928

INTAS SESSION

CATALYTIC MATERIALS

**Z.R. Ismagilov¹, S.A. Yashnik¹, O.Yu. Podyacheva¹, N.V. Shikina¹, L.M. Kustov²,
V.N. Antsifirov³, P.G. Tsyrunnikov⁴, A. Kalugin⁵, P. Siffert⁶, R. Keiski⁷, J. Herguido⁸**

¹*Boriskov Institute of Catalysis SB RAS, Novosibirsk, Russia*

²*Zelinsky Institute of Organic Chemistry RAS, Moscow, Russia*

³*Republican Engineering Center "Powder Metallurgy", Perm, Russia*

⁴*Omsk Department of Boriskov Institute of Catalysis SB RAS, Omsk, Russia*

⁵*Steel-Rolling Plant, St. Petersburg, Russia*

⁶*European Materials Research Society (E-MRS), Strasbourg, France*

⁷*University of Oulu, Oulu, Finland*

⁸*University of Zaragoza, Zaragoza, Spain*

Efficiency of catalytic reactions for environmental protection and hence their economic performance primarily depends on the properties of catalytic materials: BET and external surface area, morphology, diffusion, capability for heat transfer, thermal stability, and mechanical strength.

The main idea of this INTAS Network project #1044 is to develop new catalytic materials in the different geometric forms such as foil, metal and ceramic fibers, metal or ceramic foams, and honeycomb monoliths.

At the Steel-Rolling Plant (St. Petersburg) special alloys with an optimal chemical composition were developed for application as a high temperature catalyst carrier. They are called Aluchroms of various modifications, containing Al and Cr. The particular feature of these alloys is the presence of Y_2O_3 used as a modifying additive. These alloys can be used for production of foil with thickness of 0.05 mm, resistant to oxidation in the air at 1050°C for 500 hours.

Non-metal incorporations in the foil have an adverse effect on thermal resistance. These incorporations are represented mainly by carbides and nitrides of titanium with a particle size of 2-8 μ , which content should be kept below 0.027 vol.%. Methods for the optimization of alloy smelting in order to reduce concentration of non-metal incorporations were developed.

It is shown, that further increase of the heat resistance of the Aluchrom alloys can be achieved by the introduction of hafnium and the increase of aluminum content up to 7% wt. The alloy of such composition can be used for the production of refractory foil with thickness of 0.025 mm.

At the Republican Engineering Center "Powder Metallurgy" (Perm) new materials for the preparation of highly porous reticulated ceramic foam monoliths were developed [1]. They are cordierite-containing compositions, having additional phases of quartz (α - SiO_2),

IN-1

corundum ($\alpha\text{-Al}_2\text{O}_3$) or mullite ($3\text{Al}_2\text{O}_3 \times 2\text{SiO}_2$). The coefficient of linear thermal expansion of the mullite and quartz containing composition is close to that of pure cordierite. However, quartz is subjected to the high temperature induced phase transformations, and the mullite-quartz compositions tend to deteriorate after multiple thermal cycles. The mullite and corundum containing compositions were shown to have sufficiently high thermal durability.

The regularities of formation and sintering of large-size foam monolithic supports were studied. Pilot batch of mullite and corundum-containing cordierite monoliths was manufactured and tested in catalytic combustion of methane.

At the Zelinsky Institute of Organic Chemistry (Moscow) the work was focused on the preparation and investigation of new catalysts supported on metallic carriers for the process of catalytic combustion [2]. In this part of the work two types of metallic carriers were used:

1) stainless steel gauze and 2) thermally stable Fe-Cr-Al foil. For the deposition of a washcoating layer and an active component on the surface of the metallic carriers the method of electrophoretic deposition was applied. The catalytic activity of Pt- and Pd-containing catalysts, supported on the stainless steel gauze washcoated with alumina, was studied in the reaction of deep oxidation of methane and butane. A series of monolithic catalysts based on the mixed metal oxide and modified zeolite, supported on the Fe-Cr-Al foil, were prepared and the catalytic properties and thermal stability of these catalysts in methane combustion were investigated.

At the Boreskov Institute of Catalysis (BIC, Novosibirsk) the ceramic monolithic supports with a washcoat containing ZrO_2 and Y_2O_3 were used for the preparation of impregnated catalysts. The aqueous solutions of the following reagents were used for impregnation: copper nitrate, cobalt nitrate, palladium chloride, and platinum hydrochloric acid. The catalysts were dried at room temperature for 10 h and at $70\text{-}110^\circ\text{C}$ for 2 h and then calcined at 600°C for 4 h. The catalysts were tested in the reaction of methane catalytic combustion, and also were shown to be promising for the treatment of the industrial exhaust gases containing VOCs.

The methane combustion catalysts of perovskite structure were synthesized on the Ni-Cr foams preliminary manufactured on the wall of metal heat exchanging tube of the catalytic heat exchanging reactors and washcoated by means of plasma spraying of alumina. It was shown that plasma-sprayed alumina does not change the genesis of the formation of the perovskite active component but allows to improve substantially the adhesive properties of the active layer at high temperature [3].

At the Omsk branch of BIC (Omsk) the new catalytic materials for fuel combustion were developed. Different types of supported oxide and noble metal catalysts were tested in the reaction of methane and butane combustion. The kinetic parameters of methane oxidation over catalysts Co_3O_4 , NiO , Fe_2O_3 , CuO , ZnO , V_2O_5 , Pt and Pd at the temperatures 360-500°C were determined. The comparison of specific catalytic activity (per m^2) extrapolated to 300°C allows to place the catalysts in the following activity series:



The most appropriate catalyst for the low temperature methane oxidation should be based on Pd , deposited on a thermally stable support with high specific surface area.

The study in a flow setup, carried out under the following conditions: composition of the gas mixture - 0.03 vol.% methane in air, GHSV = 20000 h^{-1} , $V = 0.1$ m/s, volume of catalyst - 4 cm^3 , residence time - 0.18 s, showed that the catalyst 1% $\text{Pd}/\gamma\text{-Al}_2\text{O}_3$ provides the best efficiency in CH_4 oxidation, close to 100% at the temperatures about 300°C.

Similar study of the activity of catalysts in the reaction of low temperature butane oxidation showed that the most active catalysts (at 200°C) are those based on Pt supported on $\gamma\text{-Al}_2\text{O}_3$.

The catalysts were characterized by BET surface area measurements, TPR, SEM, ESDR, diffuse reflectance IR spectra of adsorbed molecules: NO and CH_4 .

At BIC these catalysts were tested in the catalytic combustion of CH_4 [4], steam reforming of CH_4 [3], DENOX [5], oxidation of 1,1-dimethylhydrazine, and H_2S oxidation and decomposition.

The catalytic heat exchangers were constructed by means of the variation of composition of the metal foam, nature of the active component, and geometry (thickness) of the combustion catalyst supported foam layer.

At the University of Zaragoza the bulk iron oxide, prepared by the precipitation and by citrates method, has been studied as an alternative catalyst for methane combustion. While hematite was the dominant phase in all the samples prepared, significant differences were observed regarding the activity and stability of the catalysts, depending on the preparation method. The catalysts prepared by precipitation presented higher surface areas and lower light-off temperatures. Catalyst deactivation is due to the sintering under reaction conditions, and becomes more severe if the operating temperature exceeds the calcination temperature used in catalyst preparation. The best performance in terms of stability and steady-state conversion was obtained with the catalyst prepared by precipitation and calcined at 600°C.

IN-1

The deactivation of bulk iron oxide during methane combustion also has been studied. The observed deactivation behavior has been explained as the result of two simultaneous deactivation mechanisms. In the initial phase of reaction both mechanisms are in action, and the activity drops rapidly as a consequence of both catalyst sintering and of the depletion of lattice oxygen in the outer layers, due to a partial reduction of the catalytic surface. At the later stages, catalyst deactivation is almost exclusively due to the sintering under reaction conditions. A kinetic model of deactivation is presented, together with the physicochemical characterization of fresh and partially deactivated catalysts.

The samples of catalysts developed at BIC and in other Russian laboratories will be tested in methane combustion at the University of Zaragoza, in DENOX with propane and specific VOC's oxidation at the University of Oulu (Oulu, Finland).

Acknowledgements

This work was supported by INTAS grant 99-1044.

REFERENCES

1. Yu.V. Danchenko. Highly porous permeable foam materials. Structure, properties and applications. Vestnik PGU (Bulletin of Perm State Technical University), No 2 (Dynamics and Strength of Machines), p. 54-60, 2001, (in Russian) 2001.
2. M.P. Vorob'eva, A.A. Greish, A.Yu. Stakheev, N.S. Telegina, A.A. Tyrlov, E.S. Obolonkova, L.M. Kustov, Stud. Surf. Sci. Catal.,130 (2000) 1127.
3. Z.R. Ismagilov, V.V. Pushkarev, O.Yu. Podyacheva, N.A. Koryabkina, H. Veringa., Chem. Eng.J, 82 (2001) 355.
4. S.A. Yashnik, L.T. Tsykoza, Z.R. Ismagilov, V.V. Kuznetsov, V.A. Ushakov, EnviCat 2001 Workshop "Environmental Catalysis – A Step Forward", Maiori (Amalfi Coast), Italy, May 2-4, 2001, pp. 255-256.
5. Z.R. Ismagilov, R.A. Shkrabina, L.T. Tsykoza, V.A. Sazonov, S.A. Yashnik, N.V. Shikina, H. Veringa, Topics in Catalysis, 16/17 (2001) 307.

PARTICLE SIZE EFFECT OF REACTION RATE OSCILLATIONS DURING CO OXIDATION OVER ZEOLITE SUPPORTED Pd CATALYSTS

N.V. Peskov, M.M. Slinko^a, N.I. Jaeger^b

Department of Computational Mathematics & Cybernetics, Moscow, Russia

^aInstitute of Chemical Physics, Moscow, Russia

^bInstitut für Angewandte und Physikalische Chemie, FB 2, Universität Bremen, Bremen, Germany

The oscillating oxidation of CO on zeolite supported nm-sized palladium particles is a good model reaction for the study of a particle size effect in the nonlinear behaviour of heterogeneous catalytic systems. The microporous structure of a zeolite host allows the preparation of various metal dispersions with narrow particle size distributions within the matrix.

The effect of the size of the palladium crystallites on the activity and the dynamic behavior of the catalysts has been studied under shallow bed conditions in a CSTR. The activity and the dynamic behavior of the system have been analyzed under similar experimental conditions for pre-oxidized catalysts with the same Pd loading, equal to 0.05%, the same surface area but different size of the Pd particles. It was demonstrated, that

(1) in the case of catalyst with 4 nm Pd particles the activity is higher, the region of oscillations more extended and the amplitudes larger compared to a catalyst loaded with 10 nm Pd particles;

(2) the size of the Pd particles has a significant influence upon the length of the transient periods during which a stationary oscillatory state is attained. The reaction rate slowly increases during the slow reduction of the catalyst and the transient period is shorter in the case of 4 nm particles as compared to 10 nm particles;

(3) while for a small region of CO inlet concentration (0.3 – 0.32%) regular periodic oscillations could be established in the case of a catalyst with 10 nm Pd particles, this was not possible for a catalyst containing 4 nm particles for any region of CO concentrations.

The particle size effect upon the oscillatory behaviour during the CO oxidation over zeolite supported Pd catalysts is simulated with the help of a deterministic point model and a stochastic mesoscopic model. The point model is developed on the basis of a model proposed by Sales, Turner and Maple, which is modified to consider the slow processes of bulk Pd oxidation and its reduction as well as the effects of the bulk oxidation upon the catalyst activity. It is demonstrated that the developed point model can simulate many experimental trends, e.g., the dependence of the catalytic activity and the waveform of the oscillations upon the particle size and the pre-treatment of the catalyst as well as the anticlockwise hysteresis in the dependence of the reaction rate during the cyclic variation of the CO inlet concentration. The stochastic model simulates the reaction by a Markovian chain of elementary steps of the reaction. The model variables are the numbers of reagent atoms. Transition probabilities of the stochastic model are chosen in accordance with the rates of the developed point model. It is shown that intrinsic fluctuations and correlations of stochastic variables can significantly change the reaction dynamics on nm-sized particles.

N.V. Peskov, M.M. Slinko^a, I.A. Gainova^b, S.I. Fadeev^b

Department of Computational Mathematics & Cybernetics, Moscow, Russia

^a*Institute of Chemical Physics, Moscow, Russia*

^b*Sobolev Institute of Mathematics, SB RAS, 630090 Novosibirsk, Russia*

The experimental studies of oscillatory behavior during CO oxidation over Pd catalysts reveal the high sensitivity of the properties of oscillations to the preliminary treatment of catalysts, including oxidation or reduction processes. This effect was found to be the most prominent for zeolite supported Pd catalysts, where the microporous structure of a zeolite host allows the preparation of nm size particles with narrow size distributions within the matrix [1].

To simulate the effect of the degree of the oxidation of Pd particles upon the properties of self sustained oscillations during the CO oxidation the new mathematical model was developed [2]. The model is based on the well-known Sales, Turner and Maple model [3], which is modified to consider the slow processes of the bulk Pd oxidation and its reduction as well as the effects of the bulk oxidation upon the catalyst activity.

The goal of this study is the bifurcation analysis of the developed model, including the identification of regions of oscillatory behaviour and multiplicity of steady states. The main attention will be paid to the character of the Andronov-Hopf bifurcations (subcritical or supercritical) at the boarder of oscillatory region. These data represent the important information for the analysis of the sensitivity of the system to fluctuations present in the system and for the simulation of stochastic oscillations over nm sized particles.

References

- [1]: M.M. Slin'ko, A.A. Ukharskii, N.V. Peskov, N.I. Jaeger, *Catal.Today*, 2001, 70, 341
- [2]. M.M. Slin'ko, N.V. Peskov, N.I. Jaeger "Mathematical modelling of a particle size effect upon the oscillatory behaviour during CO oxidation over zeolite supported Pd catalysts" PCCP, 2002 to be published
- [3]. B.C. Sales, J.E. Turner and M.B. Maple, *Surf. Sci.*, 1982, 114, 381.

THE CONJUGATE ELECTRON EXCITATION IN A SUBSTRATE-ADSORBATE SYSTEM

A.R.Cholach and V.M.Tapilin

*Boreshkov Institute of Catalysis SB RAS
Prosp. Akademika Lavrentieva 5, Novosibirsk 630090, Russia
Fax: (007)3832-34-37-66, e-mail: cholach@catalysis.nsk.su*

Abstract

The electronic peculiarity of the Pt(100)-(1×1) surface affected by various adsorbates and interaction in adsorbed layer was studied by Disappearance Potential Spectroscopy (DAPS). Two below types of features were developed in DAPS spectra. The first type corresponds to an ordinary threshold excitation of platinum core electron to available vacant state. These features are attributed to the substrate properties, and their locations are in good agreement with corresponding LDOS calculations. The second type of features evidences for a new way of the primary electron energy consumption – the conjugate electron excitation, which includes the above threshold transition of the substrate core electron accompanied by excitation of the valence electron of adsorbed species to vacuum level. Locations of the respective spectral satellites are close to corresponding ionization potentials of a given species in adsorbed layer. Our experimental data show altogether more than 10 satellites providing the reliability of the conjugate electron excitation process to proceed. The present results as a whole testify experimentally to the substantial unity of the substrate and adsorbate electronic structure.

1. Introduction

Disappearance Potential Spectroscopy (DAPS) is known to provide information on density of vacant state structure (DVS) of a given sample [1-3]. The DAP spectrum represents a current of quasi-elastically scattered electrons versus energy of primary electrons. Whenever the primary electron energy slightly exceeds the threshold energy, an incident electron can transmit its energy to the core electron so that both electrons move to states just above the Fermi level E_F . The DAP spectral features are mainly determined by self-convolution of density of states above E_F [1-3]. Using DAPS, one can find additional information on the chemical bond origin and on the density of unoccupied states in the surface region. However, DAPS is not widely used by now, and there is insufficient number of papers dealing with this technique. DAPS loses in comparison with Auger-electron Spectroscopy (AES), X-ray

IN-4

Photoelectron Spectroscopy (XPS), Ultraviolet Photoelectron Spectroscopy (UPS), etc. as an analytical method. However, the sensitivity of DAP spectra features to the origin of surrounding surface species and to the presence of impurities or adsorbed residual gases make this technique very promising for studying adsorption and catalysis.

We have previously shown [4-6] that DAPS can be successfully used for examination of platinum electronic properties. The DAP spectra are in agreement with the local density of states (LDOS) calculations and the known model of hydrogen adsorption on the unreconstructed Pt(100) single crystal surface. The present paper is aimed at studying the effect of chemisorption on the electronic peculiarities of platinum surface.

2. Theory

We present here the calculations of bulk platinum DOS that have been performed with the ADF-BAND (Amsterdam Density Functional) code [16]. This code uses the density functional formalism, numerical atomic and Slater functions as a basis set, and numerical integration over the real space for calculations of the Hamiltonian matrix elements that permitted to avoid muffin-tin approximation for the crystal potential. We use local density approximation with Vosko – Wilk – Nusair formulas for exchange-correlation potential [17] and the spin restricted nonrelativistic option of the program. Numerical atomic functions from 1s up to 6s, calculated with Herman – Skillman program [18], and 5d, 6s and 6p Slater functions are used as the basis functions. The integration over the Brillouin zone was performed with the quadratic interpolations of the band structure.

Fig. 1A presents the results of DOS calculations for the bulk platinum in the vicinity and above the Fermi level. For assignment of the DAPS peaks the important features are as: a relatively small part of d-electron states above the Fermi level and the DOS peak around 10 and 15 eV. The corresponding energy regions are shaded and denoted by *a*, *b* and *d*. The region *c* between *a* and *b* states corresponds to the broad peak of DOS. According to the self-convolution model of Lander [19], working quite well for a number of solids, the line-shape in DAPS is determined by the following equation:

$$\frac{dW}{dE} = \frac{d}{dE} \int_0^E \rho(\varepsilon) \rho(E - \varepsilon) d\varepsilon = \rho(0) \rho(E) + \int_0^E \rho(\varepsilon) \frac{d\rho(E - \varepsilon)}{dE} d\varepsilon \quad (2)$$

where ρ and W stand for Pt bulk DOS and DOS self-convolution, respectively.

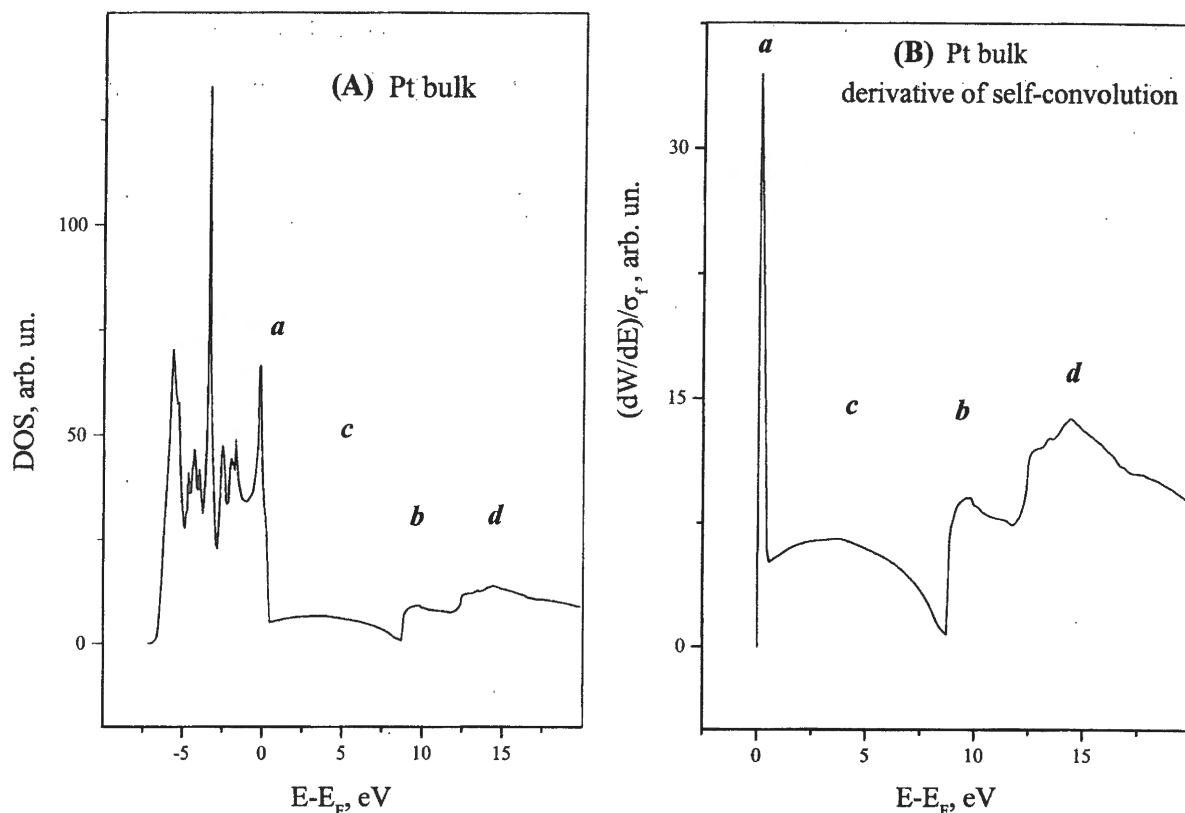


Figure 1. (A) Pt bulk DOS (the number of states per energy unit per atom); *a*, *b*, *c*, and *d* are the DOS features revealed in DAP spectra (see Fig. 4); (B) Derivative of the Pt bulk DOS self-convolution W normalized at state density at the Fermi level σ_f . The features *a*, *b*, *c* and *d* correspond to those in DOS.

The result of this expression calculation with DOS, shown in Fig. 1A, is presented in Fig. 1B. One can expect the features in the DAP spectra just above the Fermi level (peak *a*), at 10 and 15 eV (peaks *b* and *d*) above the Fermi level and a broad feature *c* between *a* and *b* peaks. All the mentioned features, excepting *d*, are in agreement with our earlier calculations based on the LMTO-TB approximation [5].

3. Experimental

Experiments were performed in an UHV chamber with a residual gas pressure of $<1 \cdot 10^{-10}$ mbar, which was equipped with the low-energy electron diffraction (LEED), Auger-electron spectroscopy, a dipole mass-spectrometer and an Ar^+ ion gun. The DAPS technique was arranged by use of 3-grid LEED optics. The central LEED electron gun with a tungsten cathode was used as a source of primary electrons of variable energy. The surface cleanliness was checked by AES. The finally observed LEED pattern was typical for the Pt(100)-hex surface [8,9]. The clean unreconstructed Pt(100)-(1x1) surface was obtained using "NO-receipt" of [10,11]. The detailed description of experimental technique and sample treatment can be found elsewhere [4]. The

IN-4

apparent Pt4d_{5/2} core level energy of 314.8±0.5 eV (i.e. E_F location) was determined as an intersection of background and leading edge of the spectrum peak [2,4], and it is close to the reference value of 314.6 eV [7].

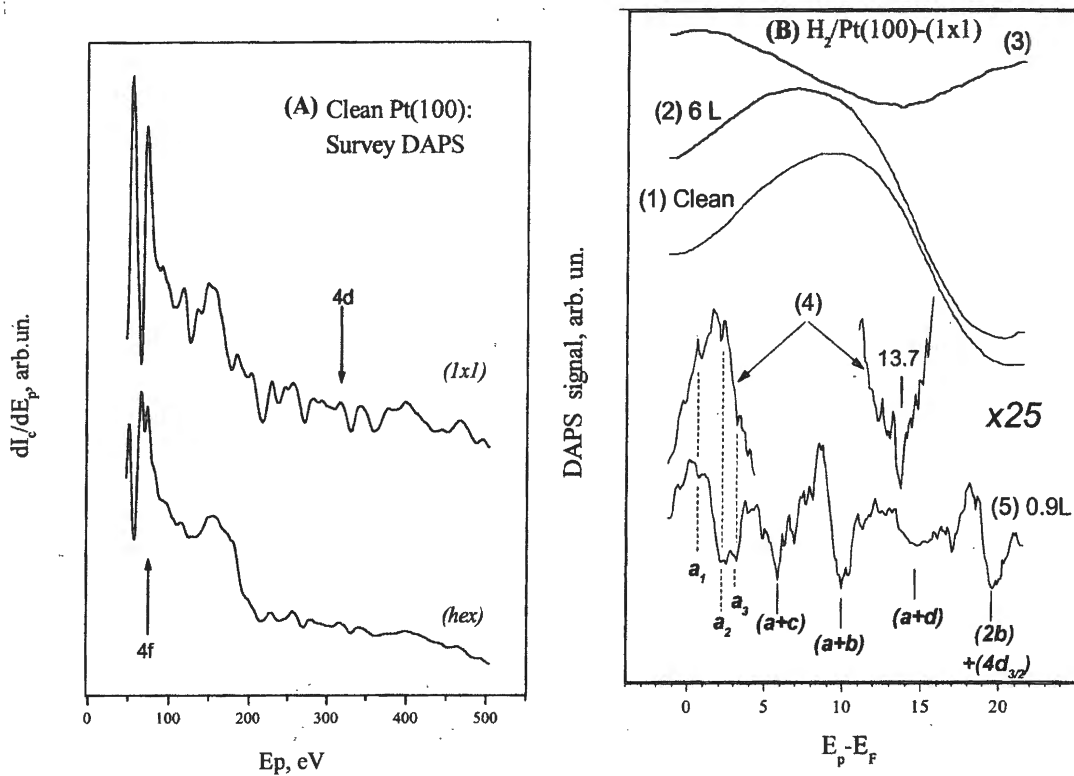


Figure 2. (A) Survey DAP spectra of the clean Pt(100) single crystal surface with (1×1) and (hex) structures of the top layer; (B) Hydrogen adsorption on the Pt(100)-(1×1) surface: curves (1) and (2) - original DAP spectra corresponding to the clean surface and after H₂ exposure of 6 L (Langmuir), respectively; curves (3) and (4) – difference DAP spectra, (4) is identical to (3) but magnified by 25 times; (5) – difference DAP spectrum corresponding to a 0.9 L exposure of H₂, curves (4) and (5) are displayed at the same ordinate scale.

Since DAPS deals with an elastic electron collection, it certainly accumulates the attendant diffraction features, which are to 10³ times as large as that of true DAPS peaks, that is why the latest are completely hidden. It is particularly pronounced for the well-ordered substrate, such as a single crystal surface. In Fig. 2A, the survey DAP spectra exhibit a continuous sequence of such peaks with mean width at the base of about 15-20 eV, which is a typical characteristic of the diffraction features [12].

In order to get rid of the strong diffraction background we followed the difference between DAP spectra of clean and adsorbate covered surfaces. Thus the diffraction features suppress each other in difference spectrum under subtraction. The difference DAPS spectrum S_{dif} was computed from recorded spectra of clean S_{cl} and adsorbate covered surface S_{ads} according to equation:

$$S_{dif} = \alpha(\theta) \cdot S_{ads} - S_{cl} \quad (1)$$

where $\alpha(\theta)$ accounts for the screening effect of the adsorbed layer at coverage θ corresponding to the given exposure; this procedure we described earlier in more detail [4].

The sequent construction of difference spectrum is demonstrated in Fig. 2B. In the present work we studied the Pt(100)-(1×1) surface in order to maintain the stable substrate structure, because the Pt(100)-hex surface is known to reconstruct readily under influence of various adsorbates [13,14]. The threshold excitation of platinum 4f core electrons is expected to be more effective in comparison with that of 4d electrons [15]. Nevertheless, we have investigated an energy range of 300-350 eV around the Pt4d core level. Fig. 2A shows that this energy interval is more convenient due to a smaller diffraction peak intensity compared to energy interval of 70-80 eV around the Pt4f binding energy.

4. Results and Discussion

Figures 2, 3 present a set of difference DAP spectra corresponding to various adsorbed layers on the clean Pt(100)-(1×1) surface. The vacant states in DAP spectra shown in below figures and in the text are labeled in accordance with LDOS features in Fig. 1.

Fig. 2B shows spectra obtained after two different H₂ exposures. A considerable difference between these spectra results from the ordering in the H_{ads} layer at higher hydrogen exposure. Indeed, low and high-energy parts in spectrum (4) correspond to the top and bottom of the total spectrum (3), respectively, whereas spectrum (5) does not show the attending diffraction feature. Spectra (4) and (5) reveal a triply splitted *a*-state corresponding to the DOS structure of Pt5d band [4-6]. The other spectral features are labeled in accordance with location of two interactive electrons (incident and excited) at different DOS states shown in Fig. 1 [4].

The peak at 19-20 eV above Pt 4d_{5/2} threshold is most probably contributed by the sum of double occupation of the *b*-state and the threshold excitation of the 4d_{3/2} core level [4]. Beside the splitted *a*-state, the high-energy region in curve (4) reveals a pronounced peak at 13.7 eV whose origin will be discussed below.

Fig. 3A shows DAP spectra obtained after various CO exposures. The strong diffraction background resulted from the ordered adsorbed layer formation, significantly hampers the expected fine spectra structure just above the Fermi edge. However, two unresolved peaks at ~ 12.6 eV and 13.8 eV are quite pronounced. As CO exposure rises, the intensity of both peaks increases and the intensity ratio changes in favor of the latter peak. In addition, the feature at ~ 18.3 eV is also seen. To assign peaks, its location is compared to the reference data on the respective ionization potentials of CO_{ads} (Table 1). It should be noted that different platinum surfaces reveal similar features in the UPS spectra obtained after O₂, NO, and CO

IN-4

adsorption [20,21,25,30,34-36]. Unfortunately, the values of corresponding work functions required for determination of ionization potentials are not available. In Fig. 3A, the spectrum feature at ~ 20.9 eV likely belongs to platinum DOS [4].

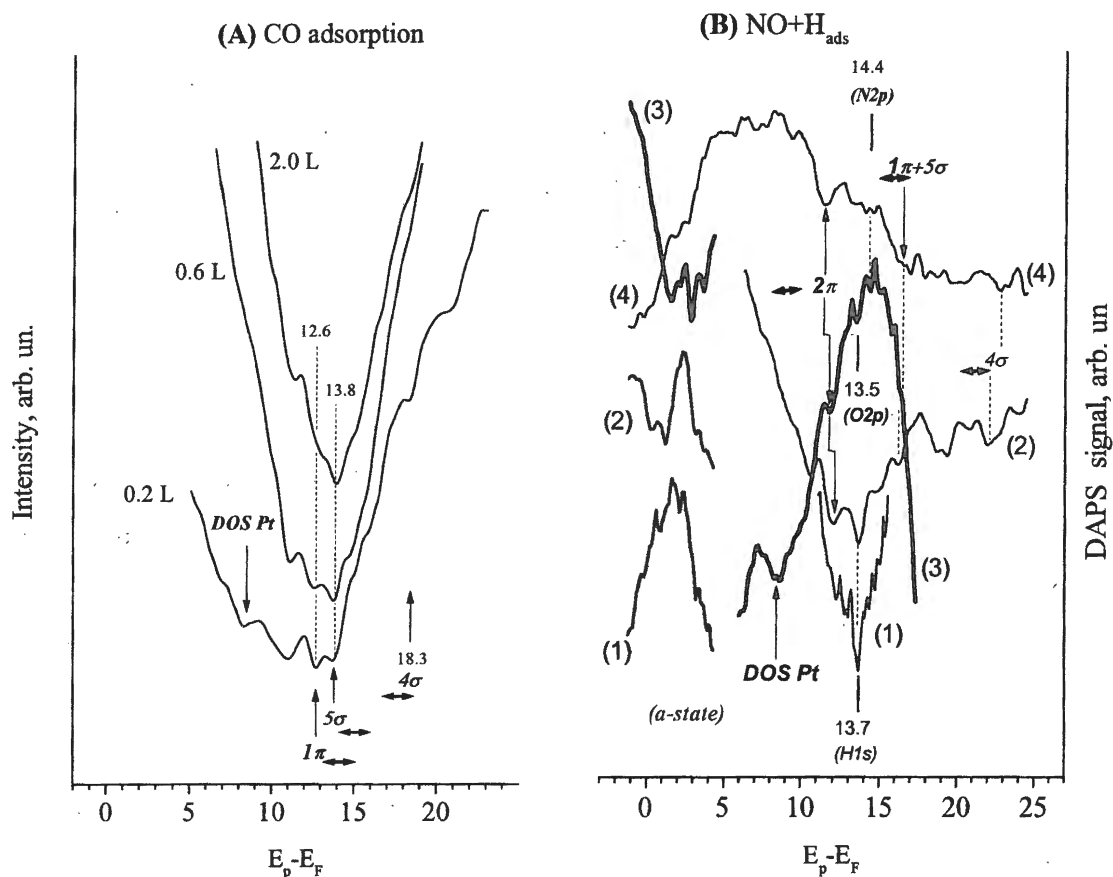


Figure 3. (A) Difference DAP spectra related to CO adsorption on clean Pt(100)-(1×1) surface at 300 K and shown exposures (in Langmuirs); (B) Comparative set of difference DAP spectra related to interaction of NO with hydrogen covered Pt(100)-(1×1) surface: (1) – after 6 L H₂ adsorption on clean surface; (2) – after exposure of surface (1) to 0.7 L of NO; (3) – after further exposure of surface (2) to NO up to total NO exposure of 1.0 L, this curve is displayed in bold type in order to distinguish it from other spectra at intersection points; (4) – after exposure of clean Pt(100)-hex surface to 20 L of NO at 300 K. The double side arrows correspond to the width and locations of the respective valence states quitted from the reference UPS data.

Fig. 3B shows DAP spectra obtained after separate adsorption of H₂ and NO, and in the course of interaction NO_{gas}+ H_{ads}. There is also a set of additional features, which cannot be treated as a combination of platinum LDOS peculiarities. Even a brief revision of data presented in Table 2 shows the correspondence between location of DAPS peaks and respective values of the valence band ionization potential.

Table 1. Comparison of high-energy DAPS features locations (the peak minimum above E_F , eV) revealed after CO adsorption on Pt(100)-(1×1) surface as shown in Fig. 3A with ionization potentials (eV) estimated for the similar systems. Ionization potentials are determined as a sum of UPS peak location with respect to E_F and the corresponding work function.

	CO			References
	1π	5σ	4σ	
Gaseous	14.01	16.53	19.68	[23,24]
CO/Pt(100)-hex	14.6 ($1\pi+5\sigma$)		17.2	[24]
CO/Pt(111)	14.2	15.05	17.45	[24,29, 32]
CO/Pt-foil	14.6 ($1\pi+5\sigma$)		17.1	[33]
CO/Pt(100)-(1×1)	12.7	13.7	18.3	This work
0.2 L	12.6	13.8	~18.3 (hidden)	
0.6 L				
2.0 L	12.6	13.9	~18.3 (hidden)	

Table 2. Comparison of high-energy DAPS features locations (the peak minimum above E_F , eV) revealed after H_2 and NO adsorption and $NO+H_{ads}$ interaction on Pt(100)-(1×1) surface as shown in Fig. 3B with ionization potentials (eV) estimated for the similar adsorbed species^(a).

Inquiry object	H	O	N	NO				Ref.
				2π	1π	5σ	4σ	
gaseous	13.60	13.62	14.54	9.3	16.9	17.4	21.0	[23,29]
O/Pt(100)		12.7						[24]
O/Pt(111)		14.2 (O2p)						[28]
O/Pt(111)		12.1						[31,32]
H/Pt(111)	12.8 (H1s)							[31]
NO/Pt(100)-hex		12.1 (O2p/N2p)		8.9	15.7 ($1\pi+5\sigma$)		20.7	[21,24]
NO/Pt(100)-hex				8.4	15.5 ($1\pi+5\sigma$)		20.2	[13]
NO/Pt(111)				7.9	14.9	18.0	20.7	[29]
H_2 /Pt(100)-(1×1) 6 L	13.7 (H1s)							This work
$NO_{gas} + H_{ads}$ 0.7 L	13.7 (H1s/O2p)			12.0	16.3 ($1\pi+5\sigma$)		22.2	
$NO_{gas} + H_{ads}$ 1.0 L		13.5 (O2p)	14.4	11.8	15.9 ($1\pi+5\sigma$)		22.5 ^(b)	
NO/Pt(100)-hex 20 L		13.8 (O2p/N2p)		1 1.4	15.9		23	

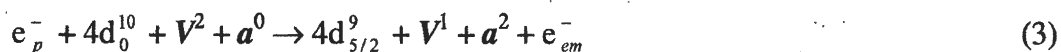
^(a) Ionization potentials are determined as a sum of UPS peak location with respect to E_F and the corresponding work function;

^(b) peak is not shown in Fig. 3B; location is estimated after subtraction of the linear background.

IN-4

Indeed, if the hydrogen covered surface (curve (1) Fig. 3B) is exposed to NO for 0.7 L, peak H_{1s} at 13.7 eV depletes and a new strong peak appears at 12.0 eV and weak features appear at 16.3 and 22.2 eV. A decrease of the former peak intensity is in line with a remove of H_{ads} from the surface due to the NO_{ads} dissociation [21,22] followed by reaction $2\text{H}_{\text{ads}} + \text{O}_{\text{ads}} \rightarrow \text{H}_2\text{O}_{\text{gas}}$. It should be noted that spectrum (2) in Fig. 3B was obtained under the same experimental conditions as in ref. [22], where authors have shown the formation of stable NH_{2,ads} species. We suppose that in the present case formation of the same species attribute the pronounced feature at 12.0 eV, which location is close to ionization potential of the gaseous NH₂ particle 11.14 eV [23]. The peak at 12.0 eV slightly shifts and diminishes at further NO exposure (curve (3) Fig. 3B), which is in line with removal of NH_{2,ads} species under these experimental conditions [22]. The location of the new pronounced peak at 14.4 eV and the weak features at 15.9 and 22.5 eV in spectrum (3) are also close to the respective ionization potentials of N_{ads} and NO_{ads} particles (Table 2). The presence of molecularly adsorbed NO_{ads} on platinum surface is quite possible in our experimental conditions [13], and atomic N_{ads} species may form due to the NO_{ads} dissociation and/or the primary electron damage of NO_{ads} [20]. Because of the last reason the peak at 13.5 eV in spectrum (3) should be related not to H_{ads}, but to O_{ads} particles as noted in Table 2. The additional strong feature at 8.5 eV in spectrum (3) is probably associated with excitation of Pt5d electrons since it is localized within the characteristic energy region of the strong UPS peaks attributing the different platinum surfaces [13,23,24]. Peak locations revealed after a 20 L exposure of the clean Pt(100)-hex surface to NO (spectrum (4) in Fig. 3B) are close to the corresponding ionization potentials, which were determined under similar experimental conditions (Table 2).

According to data listed in Tables 1-2, DAP spectra generally reveal high-energy satellites, which can not be described according to our earlier approach as a combination of platinum vacant states occupied by operating electrons [4-6]. Moreover, location of these satellites with respect to the substrate Fermi level is close to ionization potentials of the given species in adsorbed layer. This evidences for a new way of the primary electron energy relaxation, which includes the excitation of the substrate core level accompanied by the threshold ionization of atoms and/or molecules forming the adsorbed layer. The simultaneous energy transfer followed by localization of the primary and core electrons at the vacant *a*-state just above E_F may be realized as follows:



where e_p^- is a primary electron, e_{em}^- is electron emitted from the given valence state *V*.

Then the energy conservation should be written according to the below equation:

$$E_p = E_B + I + 2 \varepsilon_a \quad (4)$$

where E_p , E_B and I stand for absolute values of the primary electron energy, core level binding energy, and ionization potential of valence state V , respectively; ε_a stands for the energy of the vacant a -state above E_F .

On the one hand, the location of the DAPS satellite should exceed the respective ionization potential by $2 \varepsilon_a$ according to equation (4). On the other hand, the satellite location should be lower than the ionization potential determined from UPS data. This is due to the derivative mode of experimental DAP spectra, because location of the DAPS peak minimum should correspond to the leading edge of the broad UPS feature. However, the agreement between DAPS and UPS data (Tables 1, 2) seems to be significant, though one cannot expect a precise conformity. It is very unlikely that the above DAPS satellites are originated from a spectra subtraction technique and/or imperfection of the surface structure because of the significant difference between width of satellite and diffraction peaks [12]. Our experimental data show altogether more than 10 satellites providing the evidence of reliability of the conjugate electron excitation process [4].

Core and valence electrons separately are an ordinary objects for admission of external energy. The DAPS technique is actually a probe, which reveals energy thresholds of the primary electron current consumption. Our data indicate that a threshold conjugate excitation of both, core and valence, electrons becomes possible if E_p in equation (4) overcomes the sum of E_B and I . This process is not considered as an excitation of the core electron of a Pt atom directly to the atomic orbital of the adsorbed atom. We suggest that ionization of the adsorbed species results from excitation of the metal core electron to the metal valence orbital, which is strongly bounded through a chemical bond with an orbital of the adsorbed species. Moreover, the intensity of such features in DAP spectra may be considered as a measure of the chemical bond strength. The presence of similar features at 8-9 eV above E_F in DAP spectra, related to clean and adsorbate covered surface (see Fig. 3B and ref. [4]), indicates that valence state V in equation (3) may belong to substrate and to adsorbed species as well. Moreover, on the basis of the detailed analysis of DAP spectra, we assume that the platinum plasmons characterized by a neighbor distance of 6.0 ± 0.8 eV are distinguishable [4].

The DAPS spectral satellites corresponding to joint excitation are in qualitative accordance with electronic peculiarities of solids revealed by other techniques. Indeed, these features are similar to those of shake-off satellites in AES and XPS spectra [32,33]. The latest correspond

IN-4

to relaxation of the core hole accompanied by emission of the valence electron of the *same atom* in continuum. On the other hand, the UPS technique evidences that the substrate and adsorbate electronic properties are quite specific. Besides, emission of *both the substrate and adsorbate* valence electrons is readily exhibited in UPS spectra. The DAPS principle differs significantly from that of AES, XPS and UPS. It concerns the incident particles, the excitation mechanism, the conformational interaction, and the final state structure, etc. However, all these techniques deal with the similar electronic peculiarities, which should be of the same origin. To summarize, our data show that excitation of the *substrate* core electron accompanied by excitation of the valence electron of the *neighboring adsorbed species* does not seem to be improbable. Moreover, it emphasizes a strong correlation between the substrate and adsorbate electronic structure.

Conclusions

1. The electronic peculiarity of the Pt(100)-(1×1) surface affected by different adsorbates was studied by Disappearance Potential Spectroscopy. Two below types of features were revealed in DAP spectra:

(i) The first type of features corresponds to the ordinary threshold excitation of the platinum core electron to available vacant state. These features are mainly attributed to substrate properties and faintly depend on the adsorbate origin. Peak locations are in good agreement with LDOS calculations related to platinum unoccupied states;

(ii) The second type of features evidences for the conjugate electron transition, which includes the above excitation of the substrate core electron and excitation of the valence electron of adsorbed species to vacuum level. The location of the respective satellites in DAP spectra strongly depend on the adsorbate origin.

2. The present results testify to the substantial unity of the substrate and adsorbate electronic structure and display potentials of the DAPS technique to reveal peculiarities of the surface unoccupied states and valence states corresponding to both the substrate and adsorbate.

Acknowledgements

The authors appreciate the financial support from INTAS99-01882.

References

- [1] J. Kirschner, in: Electron Spectroscopy for Surface Analysis, Ed. H. Ibach, Springer-Verlag, 1977, chap. 3.
- [2] R.L. Park, Surf. Sci. 48, 1 (1975) 80;

- [3] L. Ecertová, *Surf. Sci.* 200 (1988) 490.
- [4] A.R. Cholach, V.M. Tapilin, *Appl. Surf. Sci.*, 180 (2001) 173; *J. Molec. Catal.*, 158 (2000) 181; A.R. Cholach, V.M. Tapilin, in: *Heterogeneous Catalysis*, Eds. L. Petrov, Ch. Bonev, G. Kadinov (Proc. 9th Intern. Symp. on Heterog. Catalysis, Varna, Bulgaria, 23-27 Sept. 2000), Sofia, 2000, p. 73.
- [5] A.R. Cholach, V.M. Tapilin, *Abstr. Intern. Memorial K.I.Zamaraev Conf. "Physical Methods for Catalytic Research at the Molecular Level"*, Novosibirsk, Russia, 1999, p.56.
- [6] A.R. Cholach, V.M. Tapilin, *React. Kinet. Catal. Lett.*, 71, 1 (2000) 65.
- [7] *Handbook of Chemistry and Physics*, 73rd edn., Ed. D.R. Lide, CRC Press, Inc., 1992-1993, p.10-281.
- [8] Ch. Romainczyk, J.R. Manson, K. Kern, K. Kuhnke, R. David, P. Zeppenfeld, G. Comsa, *Surf. Sci.* 336 (1995) 362.
- [9] A.T. Pasteur, St.J. Dixon-Warren, D.A. King, *J. Chem. Phys.* 103 (6) (1995) 2251.
- [10] G. Brodén, G. Briden, H.P. Bonzel, *Surf. Sci.* 72 (1978) 45.
- [11] D.Yu. Zemlyanov, M.Yu. Smirnov, V.V. Gorodetskii, *Catal. Lett.* 43 (1997) 181.
- [12] D.P. Woodruff, in: *The Chemical Physics of Solid Surfaces and Heterogeneous Catalysis*, v.1 *Clean Solid Surfaces*, Eds. D.A. King and D.P. Woodruff, Elsevier Sci. Publ. Comp., 1981, chapter 2, p.81-181.
- [13] H.P. Bonzel, G. Brodén, G. Pirug, *J. Catal.* 53 (1978) 96.
- [14] H. Miki, T. Nagase, K. Sato, H. Watanabe, S. Sugai, T. Kioka, *Surf. Sci.* 287/288 (1993) 448.
- [15] *Practical Surface Analysis by Auger and X-Ray Photoelectron Spectroscopy*, Eds. D. Briggs and M.P. Seach, John Wiley & Sons Ltd, Chichester, New York, Brisbane, Toronto, Singapore, 1983.
- [16] G. de Velde and E.J. Baerends, *Phys. Rev.* B44 (1991) 7888.
- [17] S.H. Vosko, L. Wilk and M. Nusair, *Can. J. Phys.* 58 (1980) 1200.
- [18] F. Herman and S. Skillman, in: *Atomic structure calculations*, Englewood Cliffs, Prentice-Hall, 1963.
- [19] J.J. Lander, *Phys. Rev.* 91 (1953) 1382.
- [20] D.M. Collins, W.E. Spicer, *Surf. Sci.* 69 (1977) 114.
- [21] S. Sugai, K. Takeuchi, T. Ban, H. Miki, K. Kawasaki, T. Kioka, *Surf. Sci.* 282 (1993) 67.
- [22] D.Yu. Zemlyanov, M.Yu. Smirnov, V.V. Gorodetskii, *Surf. Sci.* 391 (1997) 37.
- [23] *Handbook of Chem. and Phys.*, 73rd ed., Ed. D.R.Lide, CRC Press, 1992-1993.
- [24] H.P. Bonzel, T.E. Fischer, *Surf. Sci.* 51 (1975) 213.
- [25] S.R. Bare, K. Griffiths, P. Hofmann, D.A. King, G. L. Nyberg, N.V. Richardson, *Surf. Sci.* 120 (1982) 367.
- [26] T.A. Carlson, *Photoelectron and Auger Spectroscopy*, Plenum Press, NY, 1975, Chaps. 4 and 5.
- [27] D.P. Woodruff, T.A. Delchar, *Modern Techniques of Surface Science*, Cambridge Univ. Press, 1986, Chap. 3.
- [28] C. Puglia, A. Nilsson, B. Hernnäs, O. Karis, P. Bennich, N. Mårtensson, *Surf. Sci.* 342 (1995) 119.
- [29] M.E. Bartram, B.E. Koel, E.A. Carter, *Surf. Sci.* 219 (1989) 467.
- [30] J.L. Gland, B.E. Sexton, G.B. Fisher, *Surf. Sci.* 95 (1980) 587.
- [31] J.E. Demuth, *Surf. Sci.* 65 (1977) 369.
- [32] A. Ramstad, F. Strisland, S. Raaen, A. Borg, C. Berg, *Surf. Sci.* 440 (1999) 290.
- [33] A.I. Boronin, P.A. Zhdan, *Izv. Akad. Nauk SSSR, ser. Phis.*, 46, 7 (1982) 1247, and private communication.
- [34] S. Sugai, K. Shimizu, H. Watanabe, H. Miki, K. Kawasaki, T. Kioka, *Surf. Sci.* 287/288 (1993) 455.
- [35] H. Miki, T. Kioka, S. Sugai, K. Kawasaki, *Vacuum* 41 (1990) 105.
- [36] J. Küppers, G. Ertl, *Surf. Sci.* 77 (1978) L647.

ANISOTROPIC EFFECT OF ADSORBED CO DIFFUSION ON THE OSCILLATORY BEHAVIOR DURING CO OXIDATION OVER Pd(110) - MONTE-CARLO MODEL

A.V. Matveev, E.I. Latkin, V.I. Elokhin, V.V. Gorodetskii

Boreskov Institute of Catalysis SB RAS Novosibirsk, 630090, Russia

Fax: 007-3832-343056, e-mail: elokhin@catalysis.nsk.su

The modelling of self-oscillations and surface autowaves in CO oxidation reaction over Pd(110) has been carried out by means of the Monte-Carlo technique. The synchronous oscillations of the reaction rate and surface coverages are exhibited within the range of the suggested model parameters (under the conditions very close to the experimental observations). It has been established that the surface phase transition $(1 \times 1) \rightarrow (1 \times 2)$, modelled as the adsorbed CO diffusion anisotropy, does not influence the oscillation kinetics but leads to the appearance of the reaction fronts elliptically stretched along the $[1\bar{1}0]$ direction in close agreement with the known experimental data.

1. Introduction

Experimental study of CO oxidation over Pd(111), Pd(110), Pd(210) single crystals has evidently shown that the modification of the catalytic properties of the palladium surface occurs under the particular reaction conditions caused by the penetration of the adsorbed oxygen atoms into the subsurface layer. These modifications could manifest in the reaction kinetics as the critical effects - hysteresis, self-oscillations and chemical waves on the surface. The oscillation mechanism is usually assumed to be connected with the change of the oxygen sticking coefficient caused by the reversible subsurface oxygen formation: $O_{ads} \leftrightarrow O_{ss}$.

Based on the «oxide model» proposed for the explanation of the critical phenomena in CO oxidation reaction over platinum metals [1] different catalytic systems has been modelled using the so-called «traditional approach (the analysis and solving of differential equation systems build on the detailed reaction mechanism), e.g., the rate and concentration oscillations in CO oxidation reaction over Pd(110) [2] and Pt(110) [3]. However, due to the use of modern physical methods for studying catalytic surfaces, the adsorbate distribution even on the single-crystal surfaces has been found to be substantially non-uniform, and a wide spectrum of spatiotemporal structures

(solitons, spiral and travelling waves, chaotic alternating of islands of different adsorbates resembling the turbulent motions, etc.) is observed on the surface in the course of numerous catalytic reactions. To describe such phenomena, it is insufficient to use the systems of ordinary differential equations, which, in some cases, describe quite satisfactorily the complicated dynamic behavior of such integral characteristics as the reaction rate and the dimensionless coverage of the surface with adsorbates. A very promising approach, being actively used in the recent decade for the description of interrelated and competing physicochemical processes on catalytic surfaces, is the imitation simulation of these processes by means of the statistical lattice models (Monte Carlo technique). This approach makes it possible to describe most adequately the spatiotemporal dynamics of the behavior of adsorbates on the catalytic surface.

Recently the statistical lattice model has been studied for the $(\text{CO} + \text{O}_2) / \text{Pd}(110)$ [4], which takes into account the change of surface properties due to the penetration of the adsorbed oxygen into subsurface layer. This model demonstrates oscillations in the rate of CO_2 formation and in the concentrations of the adsorbed species, as well as the autowave processes on the model palladium surface. But the model surface in our previous study [4] was assumed to be homogeneous, i.e., the surface structure of the palladium single crystal was not taken into account. However it is well known, that CO or oxygen adsorption over the Pd(110) surface leads to the surface structure transformation [5] into the so called «missing row» structure: $(1 \times 1) \rightarrow (1 \times 2)$, Fig. 1. The presence of steps introduces diffusion anisotropy and the diffusion rate of CO_{ads} along and across the rows can differ noticeably, e.g., three times as many for the Pt(110) [6] (unfortunately, there is no experimental data for the Pd(110), for a review see [7]).

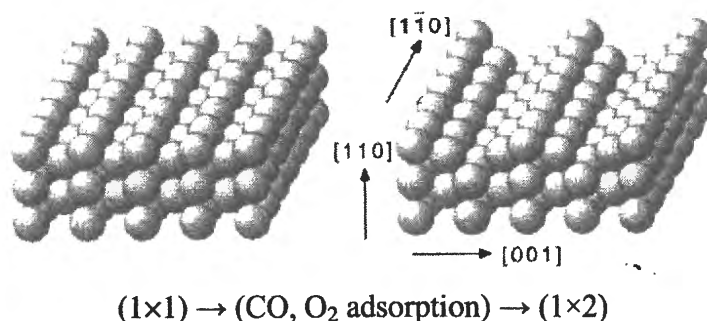


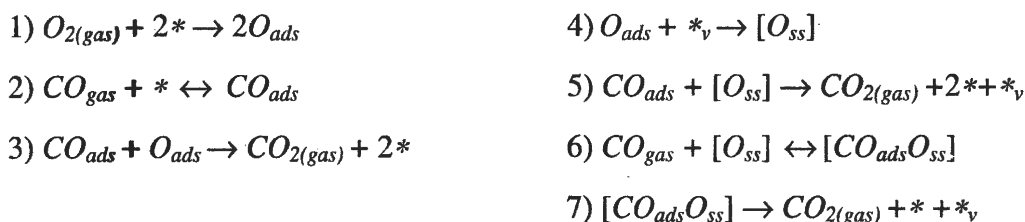
Fig. 1. Reconstruction of the Pd(110)-(1×1) surface into the (1×2) "missing-row" structure

IN-5

The anisotropy of surface diffusion should reflect in the shape of the chemical wave propagation observed in the oscillatory reaction regimes. In fact, elliptically shaped target patterns and spiral waves have been observed experimentally in numerous catalytic systems on stepped surfaces: CO oxidation on Pt(110) [8-10], H₂ oxidation on Rh(110) [11], NO + H₂ and H₂ + O₂ reactions on Rh(553) [12], etc. In our work we have studied the anisotropic effect of CO_{ads} diffusion on the reagent distribution over the surface and on the adsorbed species dynamics in the oscillatory regime of CO oxidation over Pd(110) using the statistical lattice model developed in [4] as a basis.

2. The model

The following reaction mechanism based on our FEM data was used in simulation [4]:



Here * and *_ν are the active centres of the surface and subsurface Pd layer, respectively. Formation of the subsurface oxygen proceeds according to step 4, reduction of the initial surface – due to reactions 5 and 7 («cork-screw» reaction). The adsorbed CO_{ads} species can diffuse over the surface according to the following rules: i) CO_{ads} + * ↔ * + CO_{ads}, ii) CO_{ads} + [*O_{ss}] ↔ * + [CO_{ads}O_{ss}], iii) [CO_{ads}O_{ss}] + [*O_{ss}] ↔ [*O_{ss}] + [CO_{ads}O_{ss}].

The simulation was performed on the lattice with a size of $N \times N$ square cells with periodic boundary conditions (for the most part of our simulations $N = 768$). Each lattice cell can exist in one of five states: *, CO_{ads}, O_{ads}, [*O_{ss}], [CO_{ads}O_{ss}]. The states of the cells are determined according to the rules specified by the detailed reaction mechanism. For steps 1), 2), -2), 4), 5), 6), -6), 7), the values of k_i were specified as a set of numbers, which can be considered as the rate constants of these elementary steps taking into account the partial pressures of O₂ (step 1) and CO (steps 2 and 6). That is, the values for O₂ and CO adsorption (k_1 , k_2 , and k_6) can be treated as a product of the impingement rate ($k_i \times P_i$) and of the sticking coefficient (S_i). The following set of the rate coefficients was used in simulation:

k_1	k_2	k_{-2}	k_4	k_5	k_6	k_{-6}	k_7
1	1	0,2	0,03	0,01	1	0,5	0,02

We suppose that reaction 3 proceeds immediately as soon as adsorbed CO_{ads} and O_{ads} appear in nearest neighbourhood. After each successful attempt of CO or O_2 adsorption as well as of CO_{ads} diffusion, the neighbouring cells were checked to find the partners in reaction 3. If the partners were found then the cells were given the state *, and one more CO_2 molecule was added to the reaction rate counter.

The method for processing the steps i)-iii) of CO_{ads} diffusion over the surface will be discussed below. The prescribed constants were recalculated as a probabilities of the realization of elementary processes w_i by the formula: $w_i = k_i / \sum k_i$. Using a generator of random numbers uniformly distributed over the (0, 1) interval, we chose one of these processes according to the specified ratio of their occurrence (the «comb» of probabilities). Then, also using pairs of random numbers, the coordinates of one cell (or two adjacent cells, depending on the chosen process) were determined from $N \times N$ cells of lattice. This algorithm (first, choice of the process and second, choice of the cell) makes it possible to take into account the dependence of the step rates on the adsorbate coverage. The detailed description of the algorithm can be found in [4].

The so-called MC-step (MCS) consisting of $N \times N$ attempts of choice and realisation of «main» elementary processes {1-2,4-7} is used as a time unit in the Monte Carlo models. During the MCS, each cell is tested on the average once. The reaction rate and surface coverages were calculated after each MCS as a number of CO_2 molecules formed (or the number of cells in the corresponding state) divided by the total value of the lattice cells N^2 . In the course of each MCS after every choice of one of the above-named processes and an attempt to perform this process the inner cycle of CO_{ads} diffusion was processed, which included $(M_x + M_y)$ attempts of random choice of a pair of adjacent cells of the lattice. For the sake of simplicity we did not model in direct way the process of $(1 \times 1) \rightarrow (1 \times 2)$ surface reconstruction, we only proposed that the intensity of CO_{ads} diffusion was different in x (M_x attempts) and in y (M_y attempts) directions on our square lattice representing the catalytic surface (diffusion anisotropy, x is the $[1\bar{1}0]$ direction). If the $\{\text{CO}_{\text{ads}}, *\}$, $\{\text{CO}_{\text{ads}}, [*O_{\text{ss}}]\}$, $\{*, [\text{CO}_{\text{ads}}O_{\text{ss}}]\}$, $\{[\text{CO}_{\text{ads}}O_{\text{ss}}], [*O_{\text{ss}}]\}$ pairs turned out to be these pairs, the states in these cells were interchanged according to the rules i)-iii), i.e. diffusion took place. Otherwise, the attempt of diffusion was rejected.

IN-5

3. Results and discussion

The simulation was performed on the lattices with N varied from 50 to 1500 cells at the ratio of the diffusion cycle parameters M_x/M_y being equal to 75/25, 80/20 and 85/15. The values of the rate coefficients are referred above. Surprisingly, but the integral oscillations of the reaction rate and of the surface coverages (Fig. 2) do not vary with the change of the ratio M_x/M_y and do not differ from the case with isotropic diffusion $M_x = M_y = 50$, [4]. The amplitude, the period and the shape of oscillations remain invariable.

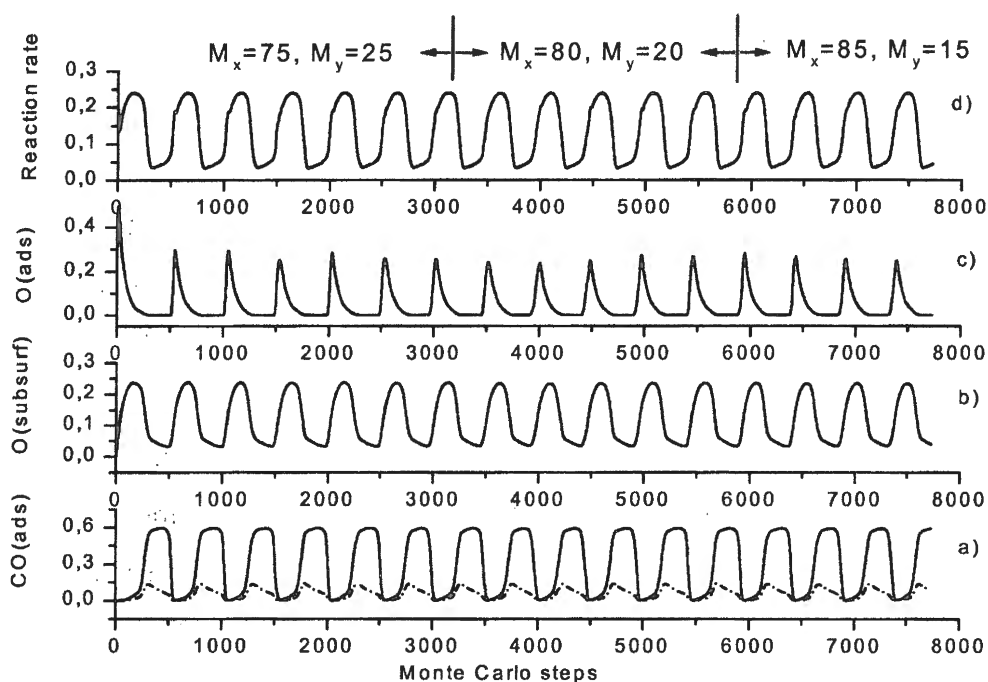


Fig. 2. Dynamics of changes in surface coverages $CO(ads) = CO_{ads}$ (solid line) and $[CO_{ads}O_{ss}]$ (dash-dotted line), $O(subsurf) = *O_{ss}$, $O(ads) = O_{ads}$ and the specific reaction rate at different ratios M_x/M_y (the instants of switching of diffusion parameters are shown by arrows). $N = 768$, the rate coefficients are listed in the table.

But the chemical wave pattern observed on the model surface in the oscillation regime becomes anisotropic and the shape of the propagation of the reaction fronts reflects the increasing value of the M_x/M_y ratio. This signifies that the kinetic measurements of the reaction rate and concentrations only could not reveal the anisotropic effect of the adsorbed species diffusion, this effect could be observed only by using the physical methods for the direct surface imaging. Let us compare the simulated snapshots showing the adsorbate distribution over the surface during surface oxygen wave propagation at the instants of the reaction rate ignition. For the correct comparison the snapshots are chosen having the approximate equal oxygen coverages ($O_{ads} \sim 0.05$) and different M_x/M_y , Fig. 3.

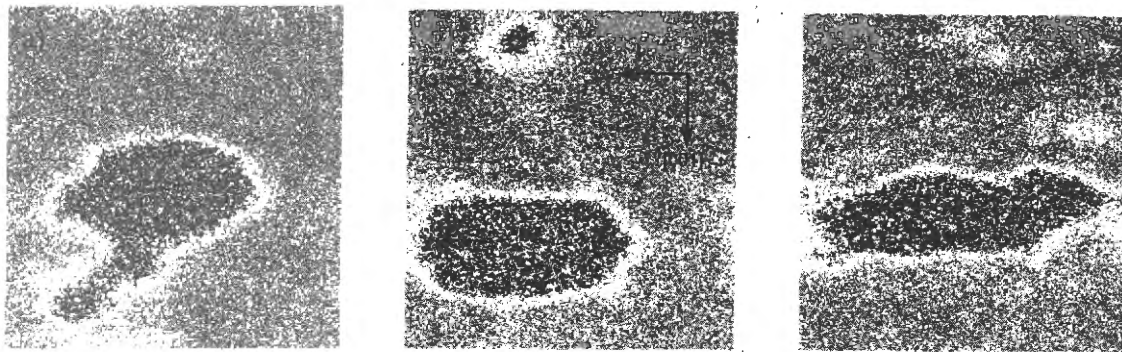


Fig. 3. Snapshots reflecting the adsorbate distribution over the surface during oxygen wave propagation: O_{ads} is black, O_{ss} is 75% grey, CO_{ads} is 50% grey, $[CO_{ads}O_{ss}]$ is 25% grey and the adsorbate-free surface is white. a) 2979 MCS, $M_x/M_y = 75/25$; b) 3951 MCS, $M_x/M_y = 80/20$; c) 7344 MCS, $M_x/M_y = 85/15$.

The snapshots show the elliptically deformed along the $[1\bar{1}0]$ direction (in our case x direction) oxygen islands surrounded by the narrow regions with elevated concentration of the free active centers, reaction zone [4]. Due to the rapid O_2 adsorption and subsequent fast reaction with neighboring CO_{ads} the formation of CO_2 molecules proceeds most intensively just in that reaction zone.

Acknowledgement: *The financial support of the INTAS Grant # 99-01882 and RFBR Grant # 02-03-32568 is highly appreciated.*

References

- [1] B.C. Sales, J.E. Turner, M.B. Maple. *Surface Sci.*, **114** (1982) 381.
- [2] M.R. Basset, R. Imbihl. *J. Chem. Phys.*, **93** (1990) 811.
- [3] A.L. Vishnevskii, V.I. Elokhin, M.L. Kutsovskaya. *React. Kinet. Catal. Lett.*, **51** (1993) 211.
- [4] E.I. Latkin, V.I. Elokhin, A.V. Matveev, V.V. Gorodetskii. *J. Mol. Catal. A: Chem.*, **158** (2000) 161.
- [5] H. Tanaka, J. Yoshinobu and M. Kawai. *Surface Sci.*, **327** (1995) L505.
- [6] H. H. Rotermund, S. Nettesheim, A. von Oertzen, G. Ertl. *Surface Sci.*, **275** (1992) L645.
- [7] M. U. Kislyuk. *Kinet. Katal.*, **39** (1998) 246 [*Kinet. Catal.*, **39** (1998) 229, Engl. Transl.].
- [8] A. von Oertzen, H.H. Rotermund, S. Nettesheim. *Surface Sci.*, **311** (1994) 332.
- [9] S. Jakubith, H.H. Rotermund, W. Engel, A. von Oertzen, G. Ertl. *Phys. Rev. Lett.*, **65** (1990) 3013.
- [10] A.J. Patchett, F. Meißer, W. Engel, A.M. Bradshaw, R. Imbihl. *Surface Sci.*, **454-456**(2000)341.
- [11] F. Mertens, R. Imbihl. *Chem. Phys. Lett.*, **242** (1995) 221.
- [12] A. Schaak, B. Nieuwenhuys, R. Imbihl. *Surface Sci.*, **441** (1999) 33.

OXYGEN-INDUCED RECONSTRUCTION AND SURFACE EXPLOSION PHENOMENA IN THE NO+CO/Pd(110) SYSTEM: THEORETICAL AND EXPERIMENTAL STUDIES

A.V. Matveev, A.A. Sametova, N.N. Bulgakov, V.V. Gorodetskii

Boriskov Institute of Catalysis SB RAS, Pr. Ak. Lavrentieva 5, Novosibirsk 630090, Russia

Fax: +7-3832-343056; E-mail: matveev@catalysis.nsk.su

1. Introduction

The NO+CO reaction on Pt and Pd surfaces is of practical importance due to the key role of NO_x emission in air pollution and interest due to the dynamic behavior, especially in connection with new experimental data, allowing to throw light upon the nature of sustained kinetic oscillations [1]. In contrast to the CO+O₂ reaction on a Pt(100) surface, the adsorbate-induced Pt(100) 1×1 ⇌ hex phase transition is not considered to be essential for the NO+CO oscillation mechanism [2]. Under heating of Pt(100) surface at the coadsorbed NO_{ads} and CO_{ads} layer up to T ~ 400 K, the reaction product forms in an “explosive” way giving rise to extremely narrow desorption peaks (FWHM ~ 5 K) CO₂ and N₂. This surface “explosion” is due to an autocatalytic increase of vacant sites for NO dissociation being as a main driving force for kinetic oscillations under steady-state conditions. Some studies of CO+NO reaction over palladium surfaces have shown that the decomposition of nitric oxide to N₂ molecules is the rate limiting step followed by rapid CO_{ads} + O_{ads} reaction to yield CO₂. Bimolecular reaction step (NO_{ads} + CO_{ads} → N_{ads} + CO₂) to be a limiting stage in CO+NO reaction at higher pressures also has been shown [3].

The purpose of the present work was (i) to investigate the coadsorption of NO and CO on Pd(110) surface; (ii) to examine the effect of coadsorbed oxygen (O_{ads} and O_{ss}) on both the NO_{ads} + CO_{ads} reaction and adsorption of NO; (iii) to calculate the adsorption heats of oxygen in a dissociative form on the Pd(110) and Pd nanocrystals by the method of interacting bonds.

We have studied the reaction between ¹⁵NO_{ads} and CO_{ads} molecules on the Pd (110) single crystal surface by temperature-programmed reaction spectroscopy (TPR). The effect of the metal particle size on catalytic properties has been studied using the semi-empirical method of interacting bonds (MIB) by calculating the heats of adsorption of O₂ and NO in a dissociative form on the Pd(110) and Pd nanocrystals.

2. Experiment

The TDS and TPR experimental device used on the single crystal Pd(110) surface is described in detail in ref. [4]. The UHV chamber is equipped with VG QXK 400 quadrupole mass spectrometer, sputtering ion gun and a molecular beam doser. The TD spectra were obtained with a heating rate of 6 K s^{-1} . Steady-state rates for the catalytic NO+CO reaction on Pd(110) surfaces have been measured with the gas flow controlled by mass spectrometer.

3. Theoretical and experimental results

MIB Effect of the metal particle size on catalytic properties has been studied by the semi-empirical method of interacting bonds (MIB) [5] by calculating the heats of oxygen adsorption in a dissociative form on the Pd(110) and Pd nanocrystals. This technique permits (i) to study the influence of the subsurface oxygen (O_{ss}) on the stability of palladium nanoparticles and Pd(110) single crystal surface reconstruction and (ii) to reveal the mechanism of O_{ss} layer action on the adsorption heat of CO_{ads} molecules and on the bond strength of the atomic O_{ads} state. The simulation has shown that the most energy favourable states for palladium are the multiple bonded states of atomic O_{ads} in the structures $\text{Pd}_3\text{-O}_{\text{ads}}$ and $\text{Pd}_4\text{-O}_{\text{ads}}$ as shown in Fig. 1. The adsorption heat of oxygen in multiple bonded states $\text{Pd}_4\text{-O}_{\text{ads}}$ (hollow) is much higher in comparison with $\text{Pd}_2\text{-O}_{\text{ads}}$ (bridged) state: this species is likely to exist in the initial steps of adsorption as an intermediate state which converts into the more multiple bonded forms.

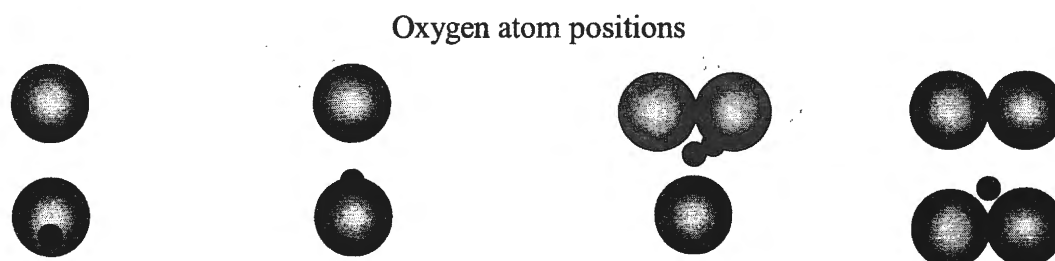


Fig. 1. On-top, bridge and hollow sites location of O_{ads} on the (111), (110) and (100) surfaces.

Calculated heats of oxygen adsorption ΔH (kcal/mol)

on-top	bridge	hollow	hollow	cluster
-2.5	18	29	35	octahedron
-4.5	15	26		icosahedron

Using MIB, for the first time the morphological convertibility of palladium nanoclusters under the influence of the O_{ads} adlayer has been provided. In accordance with simulations the most stable cluster configuration for the 13-atomic cluster is the regular icosahedron. But adsorption of 9 oxygen atoms in the Pd_3-O_{ads} and Pd_4-O_{ads} states is accompanied by the structure transition and by transformation of the icosahedron into the cuboctahedron as shown in Fig. 2. That is of special interest in oxidative catalysis because of the morphological stability of nanoclusters in oxygen presence. The six-oriented metal cluster has been shown to be the most stable for the 20-atomic cluster in toroidal structure. The adsorption of 17 oxygen atoms leads to the reconstruction of the six-oriented 20-atomic cluster into the four-oriented one. Taking into account the interactions of the palladium atoms situated in the second and third cluster layers with the upper layer of the metal atoms, the drastic decrease of the oxygen atoms concentration has been observed (up to 6 O_{ads} atoms) resulting in the reconstruction of the 20-atomic cluster into the four-oriented one.

Model clusters

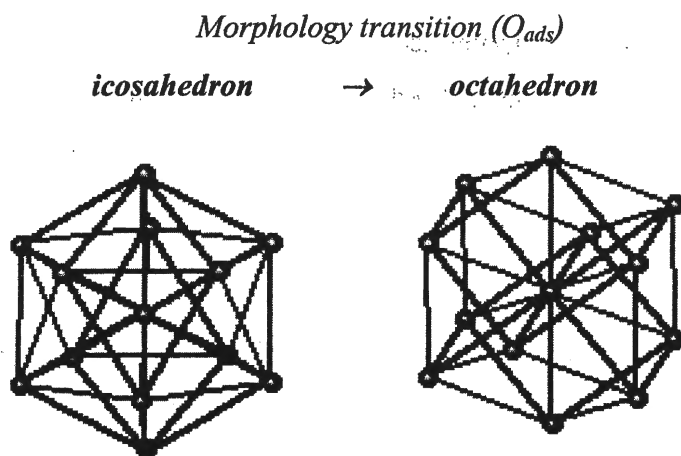


Fig. 2. The equilibrium configurations of the icosahedron and cuboctahedron clusters.

NO dissociation TD spectra of ^{15}NO adsorbed on Pd(110) surface at 100 K have one desorption peak at 490 K, when the surface coverage is low at ^{15}NO exposure (0.2÷1.0 L), Fig. 3. If the NO coverage increases up to 2 L (1 L=10⁻⁶ torr s), additional desorption peaks at 347, 262 and around ~ 200 K will appear. During these experiments single desorption peaks N_2 (496 K), N_2O (496 K) and O_2 (822 K) were observed as a result of NO decomposition according to [6].

The adsorption of NO on palladium surfaces has been studied for the (100), (111),

(110), (112) and (320) surfaces [7-9]. It is reported that molecular NO states desorb at low temperature ($T < 300$ K) and then NO_{ads} molecules dissociate partially at room temperature [10]. It is concluded that the produced N and O atoms diffuse into the metal at 300 K and diffuse back to the surface at increasing temperature. The diffusion of O_{ads} atoms into Pd is well known to be a result of presence of a small energy barrier for $\text{O}_{\text{ads}} \rightarrow \text{O}_{\text{sub}}$ process [2]. The order of activity for the N-O bond breaking is as follows [10]: $\text{Pd}(100) > \text{Pd}_{\text{poly}} > \text{Pd}(111) \geq \text{Pd}(110)$.

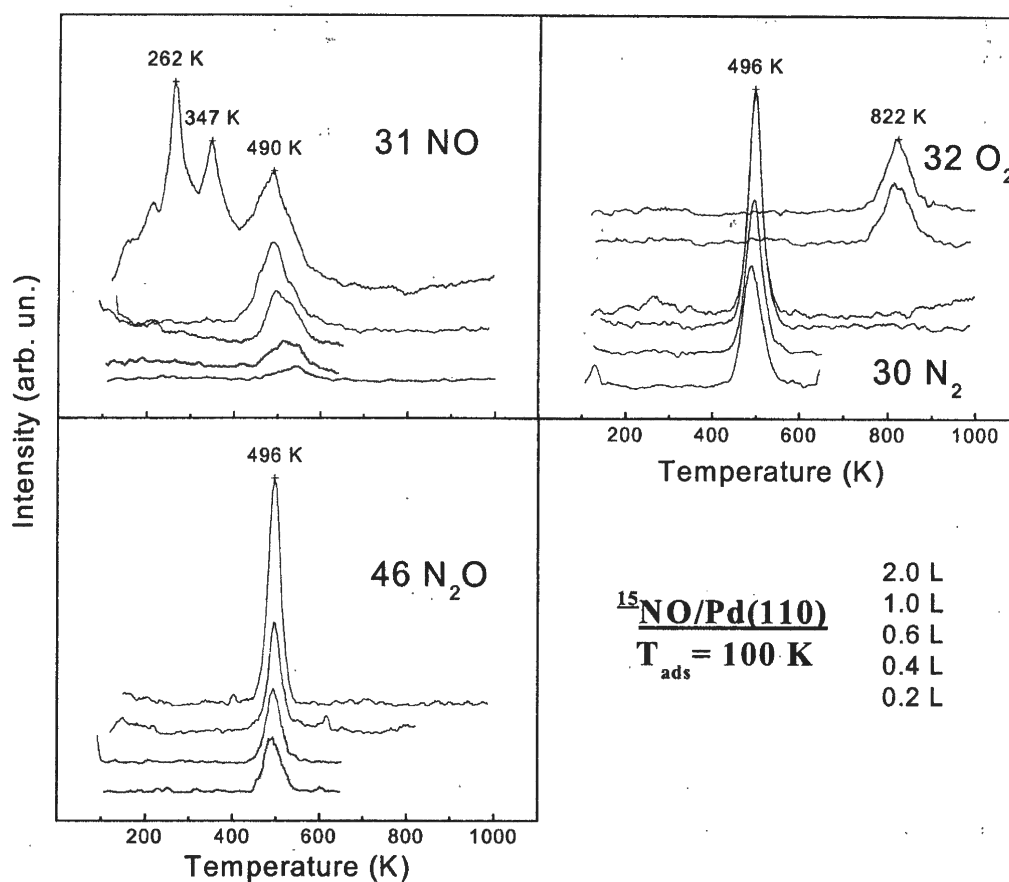


Fig. 3. TD spectra of NO (31), N_2 (30), N_2O (46) and O_2 (32) after exposure the Pd(110) surface to various doses of NO at 100 K.

The effect of oxygen preadsorption has been studied at an initial coverage of oxygen and NO applying both adsorption sequences. Desorption/decomposition processes occurring upon heating of NO layer on clean Pd(110) and O/Pd(110) surfaces can be deduced from Fig. 4a-b. As an example in Fig. 4b TD spectra are shown the increase of amount of molecular NO_{ads} states after exposing of O/Pd(110) surface to nitric oxide. Two NO desorption peaks are observed at 450 and 290 K and a shoulder occurs at around 200 K. Intensity of N_2 and N_2O peaks in the temperature range where dissociation occurs is strongly decreased. It has been suggested that the probability of NO dissociation decreases on oxygen-covered Pd surfaces in

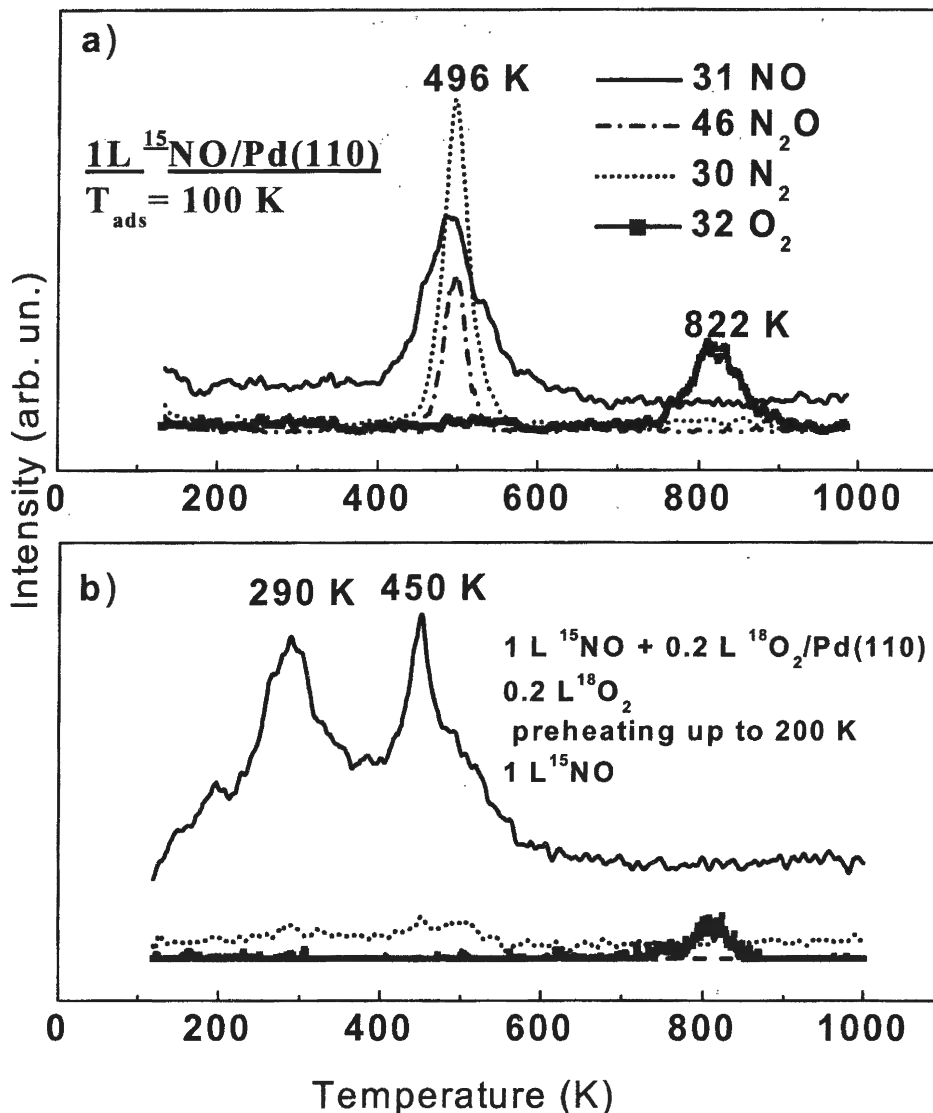


Fig. 4. TD spectra after exposure clean Pd(110) surface to NO at 100 K (a) and of mixed O/NO layers at fixed oxygen 0.2 L preexposure surface (b).

comparison to the clean palladium surfaces. Similar results have been observed on the Pd(331) single crystal: small amounts of oxygen block the step sites and inhibit NO dissociation [11].

NO+CO reaction in Fig. 5 shows series of spectra produced when the Pd(110) surface is exposed to 0.1 L of CO followed by 0.05÷0.3 L of ¹⁵NO. Comparison of these spectra with those in Fig. 3 shows that the N₂ and N₂O peaks (482 K) look different from the peaks (496 K) seen at the surface exposure to pure NO. Oxygen desorbs as a peak centered at 820 K. The products, N₂ and CO₂, desorb in simultaneous peaks within the temperature interval 460÷480 K. Thus, it is indicative of a so-called "surface explosion" [12]. Recent studies of the CO+NO reaction have reported an explosive CO₂ production over Pd(100) surface which does not reconstruct [13,14]. The behaviour of the N₂ and CO₂ desorption peaks for (NO+CO)/Pd(100) does not differ

from that for (NO+CO)/Pd(110). The peak temperatures of N₂ (483 K) and CO₂ (471 K) for Pd(100) are close to those for Pd(110).

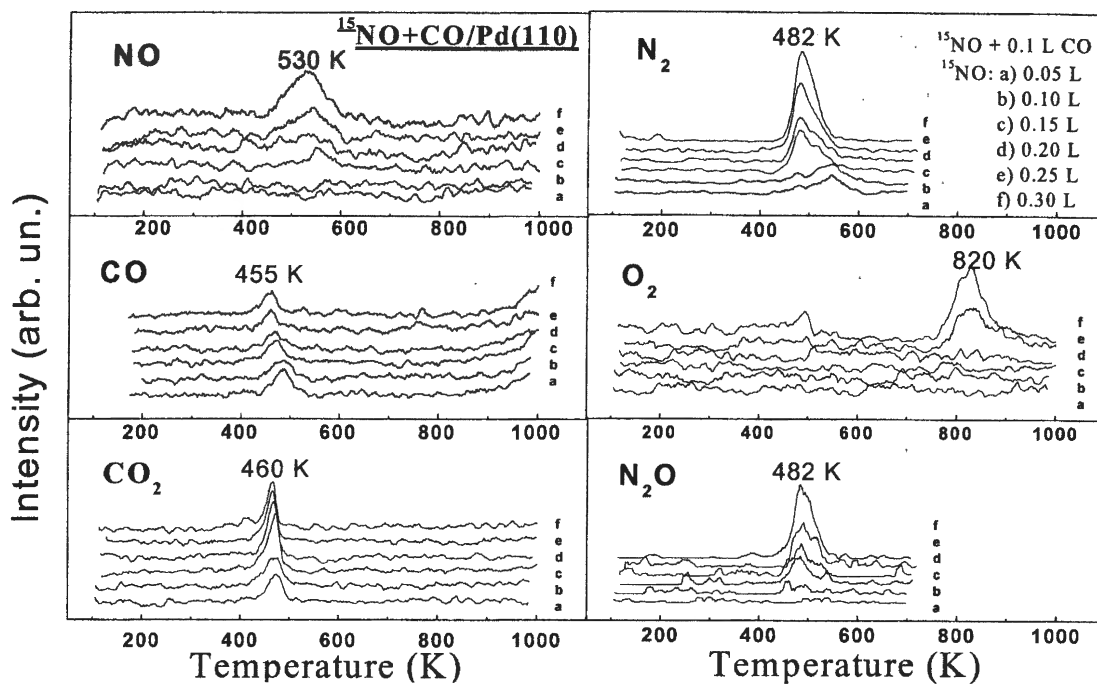


Fig. 5. TPR spectra for Pd(110) precovered with CO and exposed to ¹⁵NO at 100 K. The heating rate is 6 K s⁻¹.

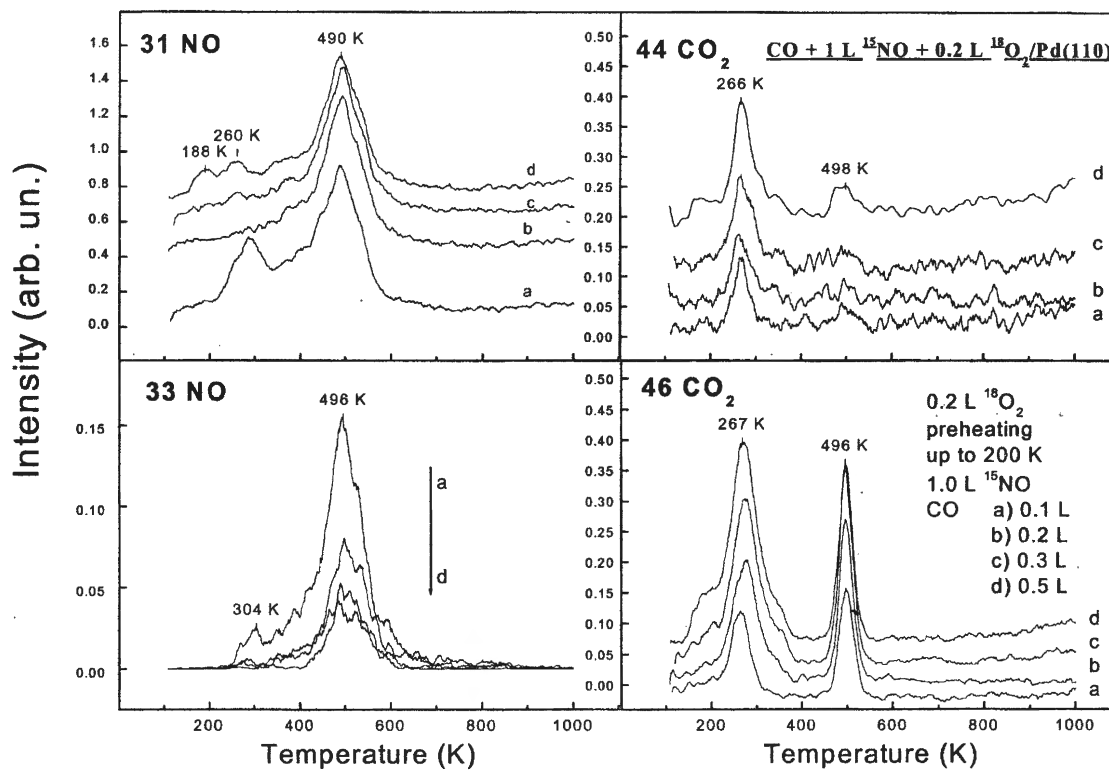


Fig. 6. TPR spectra after exposure of mixed O/NO layers at fixed oxygen 0.2 L and nitric oxide 1 L preexposure Pd(110) surface to CO at 100 K.

IN-6

Preadsorption of oxygen and nitric oxide on Pd(110) surface has a dramatic effect on the $\text{CO}_{\text{ads}} + \text{O}_{\text{ads}}$ reaction at low coverages. Fig. 6 shows TPR spectra obtained after $^{18}\text{O}_2$ (0.2 L) + ^{15}NO (1 L) exposure on the clean surface, followed by exposure to CO (0.1÷0.5 L). Comparing the spectra in Fig. 5 and Fig. 6, we see that two new CO_2 peaks at 267 K and at 496 K are observed. The low temperature production of carbon dioxide molecules is due to the reactions:

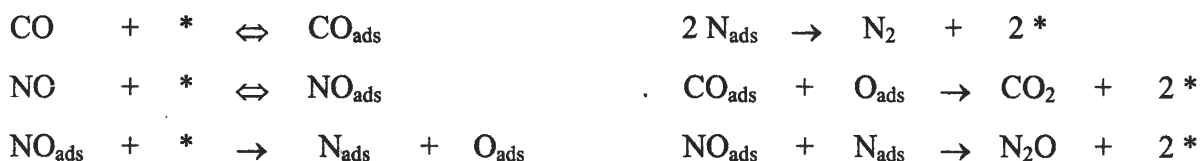
1. $\text{CO}_{\text{ads}} + ^{15}\text{NO}_{\text{ads}} \rightarrow \text{CO}^{16}\text{O}^{16}_{\text{gas}} (44 \text{ m.e}) + ^{15}\text{N}_{\text{ads}} + *$ (empty site)
2. $\text{CO}_{\text{ads}} + ^{15}\text{NO}_{\text{ads}} + ^{18}\text{O}_{\text{ads}} \rightarrow \text{CO}^{16}\text{O}^{18}_{\text{gas}} (46 \text{ m.e}) + ^{15}\text{NO}_{\text{ads}} + 2*$ (empty site)

In summary the low temperature $\text{CO}_{\text{ads}} + ^{15}\text{NO}_{\text{ads}}$ interaction on a precovered layer of atomic oxygen on the Pd(110) surface shows a possibility of realization of bimolecular reaction mechanism.

3. Discussion

Reaction mechanism Several mechanisms have been proposed in the literature for the “surface explosion” over platinum metals [13-15]. The $1 \times 1 \leftrightarrow \text{hex}$ structural phase transition is proposed on $(\text{NO} + \text{CO})/\text{Pt}(100)$ [15]. Since no structural phase transition was observed over Pd single crystal surfaces, a “vacancy model” mechanism has been proposed [14,15].

It has been shown that the NO_{ads} dissociation on the Pd(100) and Pd(110) surfaces requires the adjacent vacant adsorption sites. A clean-off reaction between CO_{ads} and O_{ads} results in the $\text{CO}_{2\text{gas}}$ formation; then a recombination of two N_{ads} atoms leading to the N_2 formation occurs accompanied by the release of the vacant adsorption sites, necessary for the dissociation of further NO_{ads} molecules and for the CO adsorption. The reaction mechanism is described as follows:



The unreconstructed Pt(100)- 1×1 surface shows a high activity in the $\text{NO}_{\text{ads}} + \text{CO}_{\text{ads}}$ reaction accompanied by N_2 and CO_2 peaks formation (350 K). The reconstructed Pt(100)-hex surface appears to be less active under the same conditions (395 K). The Pd(110) surface shows a low

activity (460 ÷ 482 K). The $1 \times 1 \leftrightarrow \text{hex}$ phase transition is related with the “surface explosion” on $(\text{NO}_{\text{ads}} + \text{CO}_{\text{ads}})/\text{Pt}(100)$. Since no structural phase transition was observed on the $\text{Pd}(110)$ surface, the low activity of palladium is considered to reflect the different bonding energy of oxygen and nitrogen adatoms for Pt and Pd surfaces.

Acknowledgement

This work is supported in part by RFBR Grant # 02-03-32568 and INTAS Grant # 99-01882

References

- [1] B.E. Nieuwenhuys, *Adv. Catal.* 44 (2000) 259.
- [2] R. Imbihl, *Progr. Surface Sci.*, 44 (1993) 185.
- [3] R.L. Klein, S. Schwartz, L.D. Schmidt, *J. Phys. Chem.* 89 (1985) 4908.
- [4] V.V. Gorodetskii, A.V. Matveev, P.D. Cobden, B.E. Nieuwenhuys, *J. Molec. Catal. A: Chemical* 158 (2000) 155.
- [5] N.N. Bulgakov, Yu.A. Borisov, V.V. Popovskii, *Kinet. Katal.* 14 (1973) 468.
- [6] R.G. Scharpe, M. Bowker, *Surf. Sci.* 360 (1996) 21.
- [7] H. Conrad, G. Ertl, J. Küppers, E.E. Latta, *Surf. Sci.* 65 (1977) 235.
- [8] R.D. Ramsier, Q. Gao, H. Neergaard Waltenburg, J.T. Yates, Jr, *J. Chem. Phys.* 100 (9) (1994) 6837.
- [9] M. Hirsimäki, S. Suhonen, J. Pere, M. Valden, M. Pessa, *Surf. Sci.* 402 (1998) 187.
- [10] S. Sugai, H. Watanabe, T. Kioka, H. Miki, K. Kawasaki, *Surf. Sci.* 259 (1991) 109.
- [11] S.W. Jorgensen, N.D.S. Canning, R.J. Madix, *Surf. Sci.* 179 (1987) 322.
- [12] M.W. Lesley, L.D. Schmidt, *Surf. Sci.* 155 (1985) 215.
- [13] M. Daté, H. Okuyama, N. Takagi, M. Nishijima, T. Aruga, *Surf. Sci.* 341 (1995) L1096.
- [14] M. Daté, H. Okuyama, N. Takagi, M. Nishijima, T. Aruga, *Surf. Sci.* 350 (1996) 79.
- [15] Th. Fink, J.-P. Dath, R. Imbihl, G. Ertl, *Surf. Sci.* 245 (1991) 96.

CO, O₂ COADSORPTION AND CO + O₂ OSCILLATORY REACTION ON Pd TIP AND Pd(110) SURFACES: FEM, TPR, XPS STUDIES

V.V. Gorodetskii, A.V. Matveev, A.V. Kalinkin and B.E. Nieuwenhuys¹

Boreskov Institute of Catalysis SB RAS, Pr. Ak. Lavrentieva 5, Novosibirsk 630090, Russia

Fax: +7-3832-343056; E-mail: gorodetsk@catalysis.nsk.su

¹*Leiden Institute of Chemistry, P.O.Box 9502, 2300 RA Leiden, The Netherlands*

1. Introduction

Unslackened interest in self-oscillatory phenomena in catalytic reactions over metal surfaces [1] is for a large part caused by the possibility to perform catalytic processes more effectively using unsteady-state operation. The extensive study of model reactions (CO+O₂, CO+NO, NO_x reduction, etc.) has been stimulated by the relevance of these reactions to air pollution control [2]. The automotive catalyst is based on the precious metals, usually Pt, Rh or Pd. CO oxidation and NO_x reduction on noble metal surfaces are highly non-linear systems. Usually these reactions are operated under conditions far from thermodynamic equilibrium, where temporal and spatial organizations become possible. In the oscillating regime of the reactions, the reaction mixture periodically affects the metals properties. These processes can be accompanied by (i) surface phase transition; (ii) facetting of the surface; (iii) formation of oxide layers. Two different mesoscopic and microscopic analytical tools have been introduced and successfully applied to learn details about the reaction dynamics at catalyst surfaces [3]. During catalytic reactions the formation of the target pattern and the propagation of reaction-diffusion fronts were observed [3-8]. Inspired by these experimental results Field Electron Microscopy (FEM) with higher lateral resolution of ~ 20 Å and Field Ion Microscopy with atomic resolution of ~ 3-6 Å have been applied to investigate dynamic surface phenomena over tip surfaces. Sharp tips of Pt, Ir and Rh in size up to several hundreds of Angstroms have been used to perform in situ investigations of real dynamic surface processes in which different crystallographic nanoplanes of the emitter-tip are simultaneously exposed to the reacting gas [4-7]. These tips were used as an excellent model for metal particles on supported catalysts to study oscillations in the CO+O₂, NO+H₂, and H₂+O₂ reactions in situ. The principal result of these studies was that non-linear reaction kinetics is not restricted to macroscopic planes since: (i) planes ~ 200 Å in diameter show the same non-linear kinetics as large planes; (ii) regular waves appear under certain condition; (iii) the propagation of reaction-diffusion waves includes the participation of the different crystal nanoplanes and

indicates an effective coupling of adjacent planes.

Langmuir-Hinshelwood mechanism can be used to describe the CO oxidation on platinum group metals. In order to explain the occurrence of kinetic oscillations an additional feedback reaction is required. Mechanisms of these oscillations on platinum surfaces are connected with a reversible surface reconstruction $\{\text{Pt}(100)\text{-(hex)} \leftrightarrow (1 \times 1)\}$ [8]. Palladium surfaces do not reconstruct and isothermal rate oscillations are associated with subsurface oxygen formation ($\text{Pd}(110): \text{O}_{\text{ads}} \leftrightarrow \text{O}_{\text{sub}}$) [9].

Reaction kinetics on a Pd tip (model catalyst, grain diameter $\sim 10^3 \text{ \AA}$) might be quite different as compared to large single crystal surfaces as a result of an interplay between the various nanoplanes present on emitter surfaces [4]. On supported metal catalyst with a crystallite size of $\sim 500 \text{ \AA}$, these surfaces are formed by the most dense (111), (100), (110) nanoplanes which differ dramatically in adsorption and oscillation behaviour.

In the present work the mechanism of surface wave generation in the oscillating $\text{CO} + \text{O}_2$ reaction has been studied on a Pd tip ($\sim 2000 \text{ \AA}$ in radius) by FEM. This technique is able to image *in situ* real dynamic surface processes in which the various nanoplanes of the emitter-tip are simultaneously exposed to the reacting gas. O_2 adsorption and the reaction of adsorbed atomic O_{ads} and of subsurface atomic O_{sub} with CO on an extended Pd(110) single crystal surface have been studied as well by TDS, TPR and XPS techniques. Hysteresis phenomena of the $\text{CO} + \text{O}_2$ reaction have been studied by means of molecular beam (MB) techniques. The effect of oxygen adsorption on the subsequent $\text{CO} + \text{O}_{\text{ads}}$ reaction on an oxygen preadsorbed Pd(110) surface has been studied with TDS, TPR and XPS techniques. The results obtained have been compared with those in which CO oxidation was studied using $^{18}\text{O}_{\text{sub}}$.

2. Experimental

Experiments were performed in a UHV chamber (base pressure $< 10^{-10}$ mbar) which was used simultaneously as the catalytic reactor and field electron microscope. The catalyst was a Pd-emitter tip, prepared from spectroscopically pure Pd-wire (0.1 mm \varnothing), spot-welded to a metal heating loop of 0.25 mm diameter. The method for producing clean stable Pd tips, along with the experimental set-up has also been described elsewhere [10]. The temperature at the tip could be controlled to within 1 K and it was measured by means of a chromel/alumel thermocouple spot-welded to the metal loop near the tip. The reaction gases CO and O_2 of highest purity were introduced with a flow rate of 2.5 L s^{-1} and controlled by a quadrupole mass spectrometer. The total field electron current and FEM image were continuously

IN-7

monitored during the catalytic surface reaction at an oxygen partial pressure of $\approx 10^{-3}$ mbar and carbon monoxide partial pressure of $\approx 10^{-4}$ mbar. A double-channel plate was used as an image amplifier of a small electron emission current (< 1 nA), and CCD camera recorded *in situ* the behaviour of the tip in CO oxidation. It was demonstrated that at a pressure of up to $\approx 10^{-3}$ mbar, stable emission currents could be obtained in the absence of sputtering processes. The surface analysis of the Pd emitter is based on the fact that due to adsorption of CO and oxygen, local work function changes ($\Delta\Phi$) can be correlated with the total field electron current, as described before [10]. Electrostatic field effects at a field of ~ 0.4 V/Å during these investigations have not been observed in according with [11].

The TDS and TPR experimental device on the single crystal Pd(110) surface is described in detail in ref. [12]. The UHV chamber is equipped with a VG QXK 400 quadrupole mass spectrometer, a sputtering ion gun and molecular beam doser. A detailed description of doser setup is given in ref. [13]. The TD spectra were obtained with a heating rate of 6 K s^{-1} . Steady-state rates for the catalytic CO+O₂ reaction on Pd(110) surfaces have been measured by using a molecular beam setup with mass spectrometry detection. The crystal is exposed to a CO+O₂ molecular beam through a capillary array doser with the gas flow controlled by the mass spectrometer. XPS analysis was performed by using an X-ray photoelectron spectrometer VG ESCA-3.

3. Result and discussion

Carbon monoxide and oxygen adsorption

WF At 300 K, the work function ($\Delta\Phi$) over Pd tip increases upon increasing exposure to

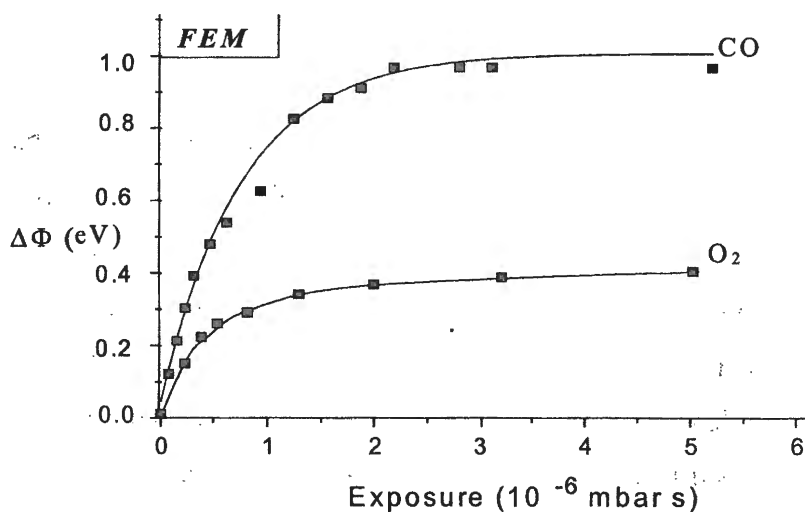


Fig. 1: Change in work function versus exposure of O₂ and CO on Pd at 300 K, using the simplified Fowler-Nordheim equation. $P(\text{CO}) = 5 \times 10^{-9}$ mbar, $P(\text{O}_2) = 5 \times 10^{-9}$ mbar.

oxygen up to a value of 0.37 eV above that of the clean surface. This value can be compared to $\Delta\Phi = 0.4$ eV reported for CO on the Pd(110) single crystal surface at $T_{\text{ads}} = 304$ K [14]. This value is already reached at an O_2 exposure of $\sim 2.3 \times 10^{-6}$ mbar s (Fig. 1), suggesting a sticking probability near unity. The change in work function ($\Delta\Phi = 0.98$ eV) with CO exposure on Pd tip at 300 K is shown in Fig. 1. Similar measurements at 300 K on Rh tips led to changes in work function, $\Delta\Phi = 1.20$ eV [15]. Measurements on different Pd single crystal surfaces give a maximum increase in work function in the range $0.75 \div 1.27$ eV for the various planes, with Pd(111) showing a maximum increase of 0.98 eV [16]. The work function variation with coverage was used for determination of the isosteric heat of CO adsorption on the clean Pd tip surface. This value was found to be ~ 154 kJ mol $^{-1}$ in the limit of zero coverage, decreasing to ~ 133 kJ mol $^{-1}$ at a coverage of 0.5 [10].

TDS Fig. 2 illustrates a series of CO TD spectra as a function of exposure. During CO

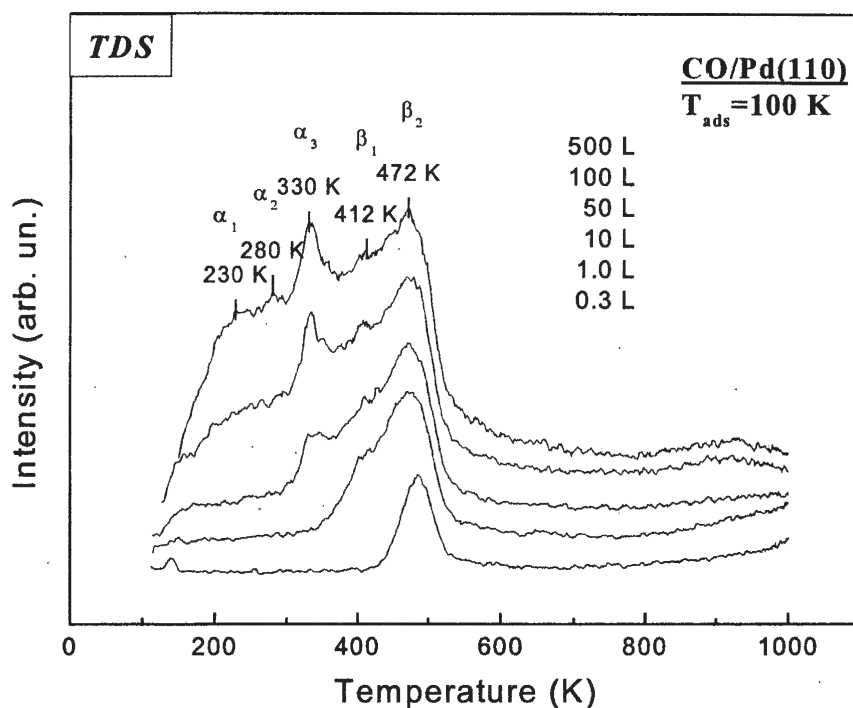


Fig. 2. Thermal desorption spectra of carbon monoxide from Pd(110) exposed at 100 K.

adsorption at 100 K on the Pd(110) surface several molecular CO_{ads} states with desorption peak temperatures at 230 (α_1), 280 (α_2), 330 (α_3) and 412 (β_1), 472 K (β_2) appear (Fig. 2) in agreement with [17].

Fig. 3 shows TD spectra of O_2 from Pd(110) surface after different oxygen exposures at 100 K. Above an exposure of 0.3 L (1L = 1.33×10^{-6} mbar s), three peaks are observed in the TD

IN-7

spectrum located around 124 (α_1 -O₂ molecular state) and 740 (β_1 -O_{sub} subsurface atomic state) and 815 K (β_2 -O_{ads} surface atomic state). The β_1 -oxygen state was attributed to subsurface oxygen formation that results in the appearance of an efficient desorption channel for recombination of oxygen adatoms. In the O/Pd(110) system, indirect evidence for the formation of subsurface oxygen layer during adsorption comes from work function measurements [18].

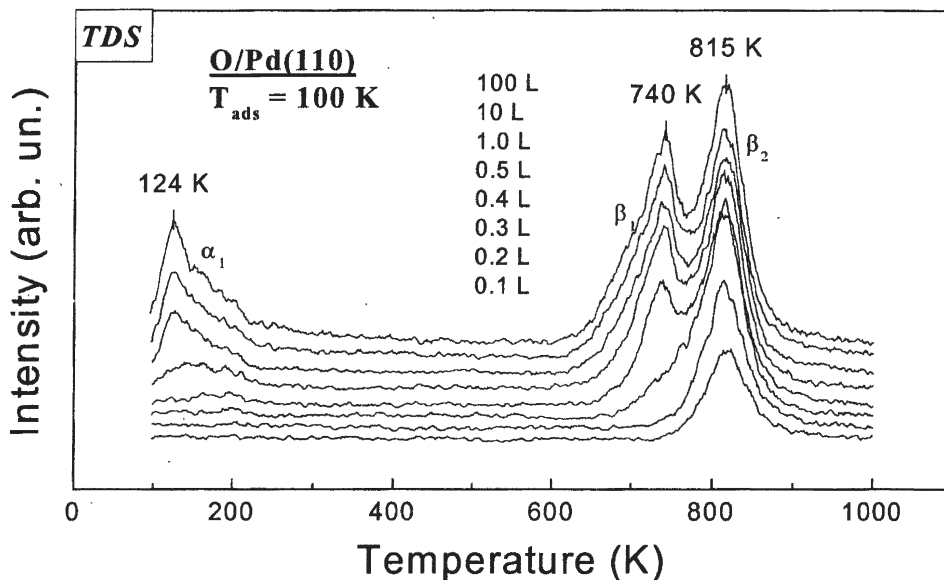


Fig. 3. Thermal desorption spectra of oxygen from Pd(110) exposed at 100 K.

TPR The effect of subsurface oxygen layer formation on the $\text{CO} + \text{O}_{\text{ads}} \rightarrow \text{CO}_2$ reaction rate has been studied by temperature programmed reaction experiments. Figure 4a shows the TPR spectra of coadsorbed oxygen and carbon monoxide. Oxygen was first adsorbed to a small coverage ($\theta \sim 0.2 \text{ ML}$) in the atomic β_2 -O_{ads} state, followed by exposure to CO at 100 K. CO₂ is evolved mainly in a peak at 415 K and in a small peak at 300 K as a result of increasing CO exposure.

Fig. 4b depicts the TPR spectra of coadsorbed oxygen (atomic β_2 -O_{ads} and β_1 -O_{sub} states) and CO. In contrast to Fig. 4a, low temperature CO₂ formation begins immediately above an oxygen exposure of 0.5 L. Five distinct CO₂ desorption peaks are observed at 160, 225, 320, 370, and 420 K from the (110) surface. This complexity of CO₂ formation may be the result of different reaction rates of adsorbed CO with the two types of adsorbed atomic oxygen: (i) $\text{CO}_{\text{ads}} + \text{O}_{\text{ads}} \rightarrow \text{CO}_{2(\text{gas})} + 2^*$; (ii) $\text{CO}_{\text{ads}} + [*_{\text{O}_{\text{sub}}}] \rightarrow \text{CO}_{2(\text{gas})} + 2^* + *_{\text{v}}$. In addition the reaction

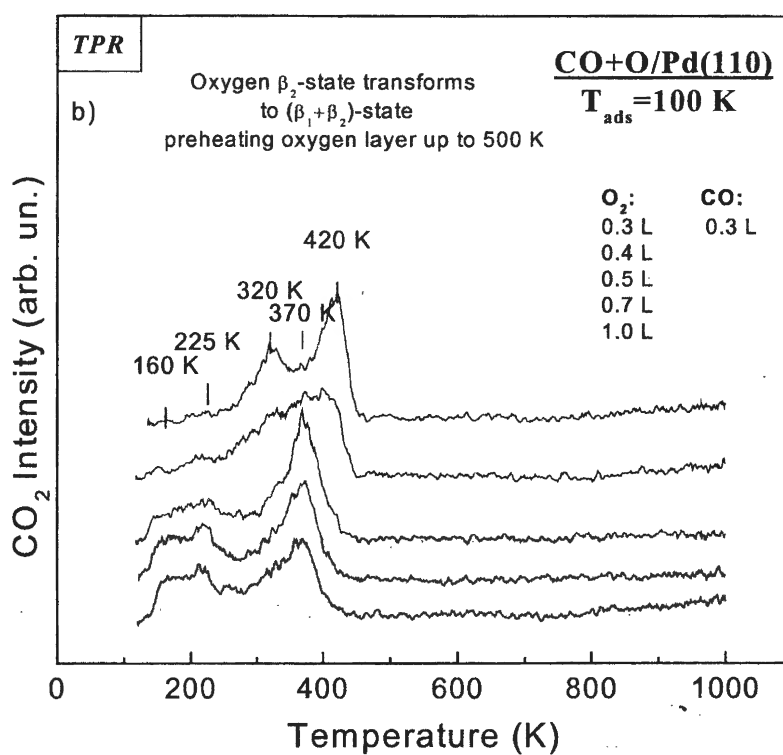
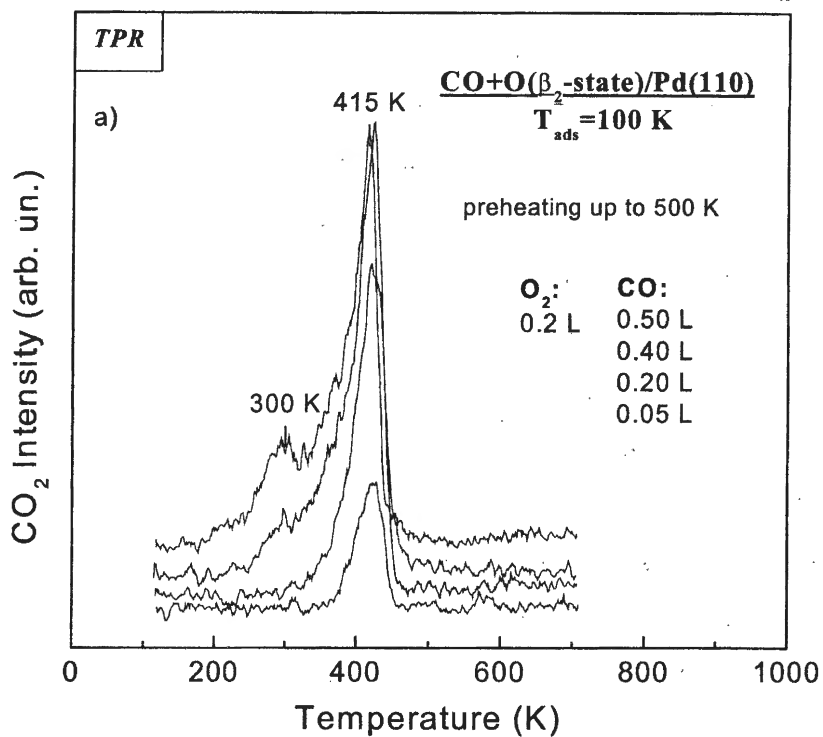


Fig. 4. Temperature programmed reaction of CO_2 formation from $\beta_2\text{-O}_{\text{ads}}$ (a) and $\beta_1\text{-O}_{\text{sub}} + \beta_2\text{-O}_{\text{ads}}$ (b) atomic oxygen layers.

IN-7

complexity might be expected since the coadsorption of CO and oxygen may result in the formation of either a segregated layer, where the CO_{ads} molecules and O_{ads} atoms form separate layer on the surface, or a mixed layer where the two adsorbates mix completely [19]. In a mixed layer new sites for the coadsorption layer are usually occupied. Adsorption of CO at low temperature on an oxygen atomic $\beta_2\text{-O}_{\text{ads}}$ and $\beta_1\text{-O}_{\text{sub}}$ layers might produce a segregated layer and form islands of each species. Annealing this adlayer to ~ 160 K in TPR experiments leads to dispersing the islands and mixing the adsorbate layer at temperatures where reaction with CO is significant. The Pd-O bond is weakened in well-mixed $\text{O}_{\text{ads}}+[*\text{O}_{\text{sub}}]+\text{CO}$ adlayer, indicating that the $\text{O}_{\text{ads}}-[*\text{O}_{\text{sub}}]$ repulsive interaction proceeds throughout the metal surface rather than directly between the adsorbed atoms. On the other hand the effect of adsorbed oxygen ($\text{O}_{\text{ads}}+[*\text{O}_{\text{sub}}]$) on the CO adsorption rate is an important part of the low temperature CO oxidation reaction. Ladas et al. [20] have shown that the formation of subsurface oxygen leads to a decrease in the CO residence time due to a decrease of the CO adsorption energy and reduction of the CO sticking probability.

Hysteresis and Oscillations

MB Fig. 5 illustrates the temperature dependence of the steady-state rate of CO oxidation over

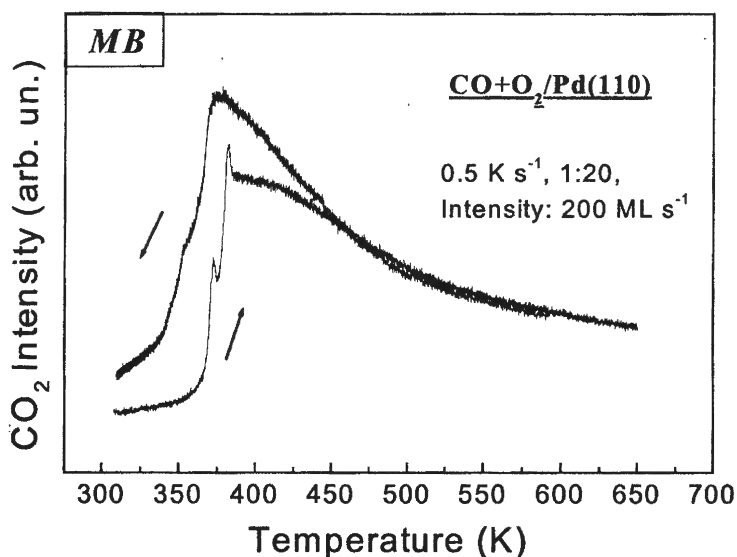


Fig. 5. The hysteresis of steady-state rates of CO_2 formation during of a heating-cooling cycle at an $\text{CO}+\text{O}_2$ molecular beam pressure.

the Pd(110) surface. At 300 K the reaction is inhibited by a high coverage of CO_{ads} . In the temperature interval $370 \div 650$ K the initial rate diminishes rapidly, presumably as a result of a low CO_{ads} coverage during the reaction. Fig. 5 shows the bistability regions and represents the anticlockwise hysteresis behavior for CO_2 formation in the temperature interval between

300 and 450 K. With increasing temperature the transfer from the θ_{CO} layer into the O_{ads} layer is delayed, with decreasing temperature it is the reverse reaction. The presence of oscillatory behavior appeared of the CO_2 rate at 372 and 382 K.

FEM The brightness of local regions of the $\text{Pd}(100)_{\text{step}}$ surface in the emission pattern was accompanied by fluctuations of the electron current. The difference in work function ($\Delta\Phi$) between CO_{ads} and O_{ads} over Pd surfaces is connected with a change in the emission current, as described by the Fowler-Nordheim equation:

$$I = AV^2 \exp\left(\frac{-B\Phi^{3/2}}{V}\right)$$

where I is the current measured at the fluorescent screen, V is the applied voltage at the tip, A and B are constants and Φ is the work function. From this equation a sensitive dependence of I on $\Delta\Phi$ is expected. This large change in $\Delta\Phi$ gives an excellent tool for observing the transition in the adsorption layers: the CO adsorption layer with low emission current, a current increase for oxygen adsorption. Using a conventional video technique to monitor the FEM brightness variation, local time oscillations of the emission current were extracted from digitized video images [21].

Fig. 6 represents a series of oscillations (FEM) when the Pd-tip with [110]-orientation is exposed at 425 K to a $\text{CO}+\text{O}_2$ reaction mixture. The oscillation amplitude from the CO_{ads} layer (low current) to the O_{ads} layer (high current) has a periodicity of 5 s. The difference in work functions between CO_{ads} and O_{ads} of ~ 0.6 eV is connected with the change in the electron current. The study of the Pd-tip surface has shown that the CO oxidation reaction is characterized by a sharp boundary between two spatially separated adlayers (CO_{ads} and O_{ads}) over the $\text{Pd}\{100\}_{\text{step}}$ surfaces forming under oscillating conditions: $370 < T < 450$ K, $P_{\text{CO}} + P_{\text{O}_2} (1:20) = 2.6 \times 10^{-3}$ mbar. The CO_{ads} -covered areas are formed only on the {100} nanoplanes, whereas O_{ads} -covered areas are formed only on the {110}, {310} and {210} nanoplanes. Chemical waves appear on the emitter surface and propagate in phase with self-sustained isothermal oscillations.

The initiating role of a *subsurface* oxygen layer formation has been established for the generation of regular waves along certain crystallographic directions on the Pd-tip surface: (i) O_{ads} wave follows the path in the direction $(110) \rightarrow (210) \rightarrow (100)$; (ii) CO_{ads} wave moves in the opposite direction.

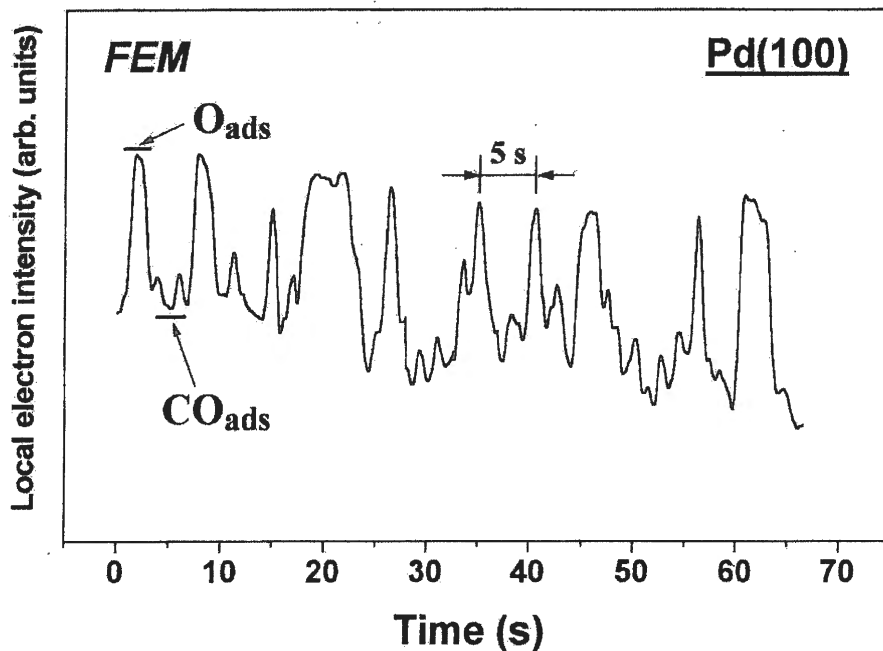


Fig. 6. The variation of the local emission current from the Pd (100)_{step} plane as a function of time during the oscillatory behaviour of the CO + O₂ reaction on a Pd field emitter tip at constant control parameters under reaction conditions: T = 425 K, P(O₂) = 2.6 × 10⁻³ mbar, P(CO) = 1.3 × 10⁻⁴ mbar. Low current levels reflect CO_{ads}-covered Pd(100) plane. F ≈ 0.4 V/Å.

XPS Fig. 7 shows a set of Pd 3P_{3/2} XPS spectra for the surface of a Pd foil before and after oxygen exposure at 525 K. The difference spectra clearly show the presence of an atomic oxygen state with an O 1s binding energy of 529.5 eV (P(O₂) = 10⁻⁷ ÷ 10⁻² Torr), which shifts to 530.5 eV after oxygen exposures for 2, 4 and 10 min at 5 Torr, showing the growth of an oxide. According to the XPS data, bulk oxide formation does not occur under the conditions (370 < T < 450 K, P_{CO} + P_{O₂} (1:20) = 2.3 × 10⁻³ Torr) of rate oscillations is not sufficient for bulk oxide formation.

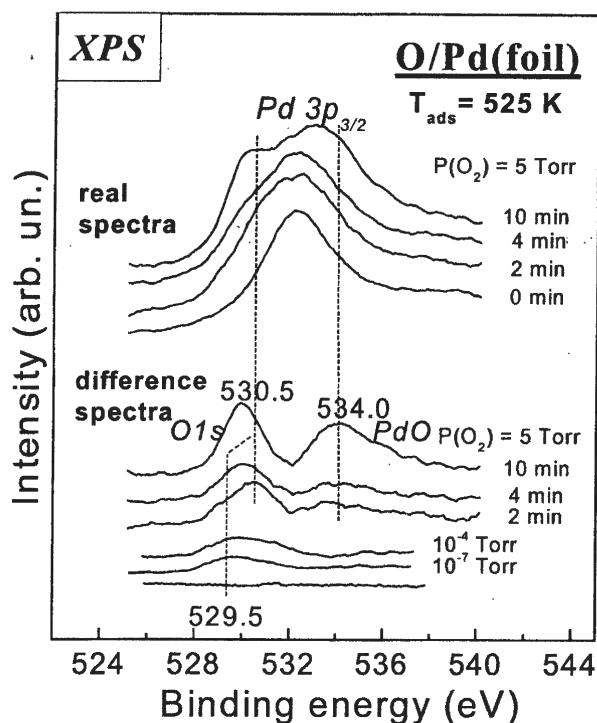


Fig. 7. XPS spectra for the clean, oxygen-covered and oxide growth Pd ($3p_{3/2}$) at 45° take-off angle.

Reaction mechanism Knowledge of the various steps is necessary to gain a better insight into the mechanism of the oscillating phenomena. The oscillating catalytic CO oxidation proceeds via a Langmuir-Hinshelwood mechanism:

1. $\text{CO}_{\text{gas}} + * \leftrightarrow \text{CO}_{\text{ads}}$
2. $\text{O}_{2\text{ gas}} + 2 * \rightarrow 2 \text{O}_{\text{ads}}$
3. $\text{CO}_{\text{ads}} + \text{O}_{\text{ads}} \rightarrow \text{CO}_{2\text{ gas}} + 2 *$

where two adjacent empty sites (*) are required for the dissociative adsorption of $\text{O}_{2(\text{gas})}$. It is well known that under reaction conditions adsorption islands CO_{ads} are formed as well as O_{ads} , whereas CO_2 immediately desorbs at reaction temperatures.

The catalytic oxidation of CO over palladium surfaces exhibits temporal oscillations in a certain range of reaction parameters: T , P_i . The feedback mechanism of these oscillations is associated with the changes in the oxygen adsorption (S_0) induced by depletion of subsurface oxygen ($\text{Pd}(110): \text{O}_{\text{ads}} \leftrightarrow \text{O}_{\text{sub}}$). The oxide model assumes that the O_{sub} layer blocks the oxygen adsorption simultaneously with the growth of a CO_{ads} layer and the surface reaction is poisoned (low rate of CO_2 formation). The slow reaction of CO_{ads} with O_{sub} removes the subsurface oxygen and O_2 adsorption is again possible (high rate of CO_2 formation). Then, the subsurface oxygen layer is formed and the cycle is restored. Probably, the subsurface oxygen

IN-7

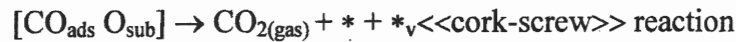
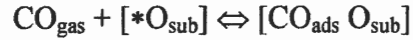
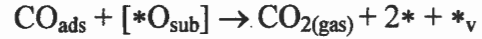
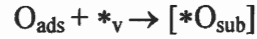
could produce a significant change in CO adsorption energies, decreasing the heat of adsorption according to [20]. Based on our TDS, TPR, XPS, MB, FEM results regarding CO oxidation over Pd surfaces, some elementary steps have been added to the LH scheme:

CO oxidation over Pd surface (model with subsurface oxygen)

Atomic oxygen route (LH)



Subsurface oxygen route (added)



CO heat of adsorption:



CO diffusion: $\text{CO}_{\text{ads}} + * \rightarrow * + \text{CO}_{\text{ads}} < [\text{CO}_{\text{ads}} \text{O}_{\text{sub}}] + [*_{\text{O}_{\text{sub}}}] \rightarrow [*_{\text{O}_{\text{sub}}}] + [\text{CO}_{\text{ads}} \text{O}_{\text{sub}}]$

By this reaction scheme the rate oscillations were simulated with a standard Monte Carlo algorithm, that had been explored in our previous modelling of oscillatory behaviour of catalytic reactions due to the influence of the «subsurface» oxygen [22].

4. Conclusions

A palladium surface is catalytically active in the CO+O₂ reaction due to its ability to dissociate O₂ molecules. At present, an O_{ads} diffusion process may be proposed for the formation of a *subsurface* oxygen layer O_{sub}, which is an important intermediate species in the CO+O₂ reaction over Pd surfaces. O_{ads} is highly active as compared to O_{sub} species due to the rapid attachment of the carbon monoxide molecules, CO_{ads}, producing CO₂. As a result of this oxidized surface local oscillations on the Pd(100)_{step} nanoplanes are obtained with fast repetition periods.

A specific structure sensitivity of the kinetics of the CO+O₂ reaction has been observed over a Pd tip: (i) the maximum initial rate has been observed on Pd(110); (ii) two spatially separated adlayers are formed on the tip surface. The oxygen layer forms only on the {110}, {320} and {210} planes, whereas a CO_{ads} layer or empty sites form on the {100} and {100}_{step} planes. Chemical waves are related to O_{ads} and CO_{ads} layers in a sequence of reaction steps with the transition of O_{ads} ↔ O_{sub} plane (*_v empty sites induced by O_{ads} adsorption), which involves the feedback reaction O_{sub} → O_{ads} during oscillations.

In summary the character of the oscillations of the CO+O₂ reaction on Pd differs remarkably from that of Pt: (i) *subsurface oxygen mechanism* (Pd) and *phase transition mechanism hex* ↔ 1×1 on Pt; (ii) oxygen front travelling in the reverse direction: on Pd starts from (110) to

(100); on Pt starts from (100) to (110). The principal result of this work lies in the following: *the appearance of regular waves* under reaction rate oscillations is an amazing example of *self-organization of a catalytic reaction* taking place when the size of the active catalyst averages *some hundreds Å*.

Acknowledgements

This work is supported in part by RFBR Grant # 02-03-32568 and INTAS Grant # 99-01882

References

- [1] M.M. Slin'ko, N.I. Jaeger. Oscillating Heterogeneous Catalytic Systems. Surface Science and Catalysis, v.86, Elsevier, Amsterdam, 1994.
- [2] B.E. Nieuwenhuys, Adv. Catal. 44 (2000) 259.
- [3] R. Imbihl, Progr. Surface Sci., 44 (1993) 185
- [4] V. Gorodetskii, J. Lauterbach, W. Drachsel, H.H. Rotermund, J.H. Block, G. Ertl. Nature 370 (1994) 276.
- [5] M.F.H. van Tol, A. Gielbert, B.E. Nieuwenhuys. Catal. Lett. 16 (1992) 297
- [6] V.V. Gorodetskii, W. Drachsel. Applied Catalysis A: General 4727 (1999) 1
- [7] V. Gorodetskii, W. Drachsel, M. Ehsasi, J.H. Block, J. Chem. Phys. 100 (1994) 6915.
- [8] G. Ertl, Adv. Catal. 37 (1990) 213
- [9] G. Veser, R. Imbihl. J. Chem. Phys. 96 (1992) 7155
- [10] P.D. Cobden, B.E. Nieuwenhuys, V.V. Gorodetskii, Appl. Catal. A: General 188 (1999) 69
- [11] Yu. Suchorski, R. Imbihl, V.K. Medvedev, Surf. Sci. 401 (1998) 392
- [12] V.V. Gorodetskii, A.V. Matveev, P.D. Cobden, B.E. Nieuwenhuys, J. Molec. Catal. A: Chemical 158 (2000) 155
- [13] C.S. Gopinath, F. Zaera, J. Catal. 186 (1999) 387
- [14] V.A. Bondzie, P. Kleban, D.J. Dwyer. Surf. Sci. 347 (1996) 319
- [15] V.V. Gorodetskii, B.E. Nieuwenhuys, W.M.H. Sachtler, G.K. Boreskov, Surf. Sci. 108 (1981) 225.
- [16] W.A. Brown, R. Kose and D.A. King, Chem. Rev. 98 (1998) 797
- [17] M. Ehsasi, C. Seidel, H. Ruppender, W. Drachsel, J.H. Block, K. Christmann, Surf. Sci. 210 (1989) L198
- [18] J.-W. He, P.R. Norton, Surf. Sci. 204 (1988) 26
- [19] T. Engel, G. Ertl, Adv. Catal. 28 (1979) 1
- [20] S. Ladas, R. Imbihl, G. Ertl, Surf. Sci. 280 (1993) 14
- [21] M.C. Reckzügel, V. Gorodetskii, J.H. Block, Appl. Surf. Sci. 49/95 (1996) 194
- [22] E.I. Latkin, V.I. Elokhin, A.V. Matveev, V.V. Gorodetskii, J. Molec. Catal. A: Chemical 158 (2000) 161

**THEORETICAL INVESTIGATION OF THE MECHANISM OF METHANOL
CARBONYLATION CATALYZED BY DICARBONYLDIIODORHODIUM
COMPLEX**

E.A. Ivanova, V.A. Nasluzov, A.I. Rubaylo, N. Rösch*

Institute of Chemistry and Chemical Technology SB RAS, Krasnoyarsk, Russia

**Institute für Physikalische und Theoretische Chemie, Technische Universität München,
Garching, Germany*

The systematic and complete theoretical study of the catalytic cycle of methanol carbonylation catalyzed by $[\text{Rh}(\text{CO})_2\text{I}_2]^-$ complex was carried out using a gradient-corrected density functional method. The main goals of our study were an exploration of the free energy profile for the entire catalytic cycle of methanol carbonylation and clarification of the detailed mechanism for each elementary step with accurate account for environment effects.

The various possible isomers for the intermediates involved in the catalytic cycle were considered and their relative stability was estimated. The complex $[\text{Rh}(\text{CO})_2\text{I}_2]^-$ was determined to have preferential *cis* conformation. The six-coordinated $[\text{RhCH}_3(\text{CO})_2\text{I}_3]^-$ and $[\text{RhCH}_3\text{CO}(\text{CO})_2\text{I}_3]^-$ species were calculated to exist in a form of *trans* isomers. These results are in agreement with the experimental data with the exception of complex $[\text{RhCH}_3(\text{CO})_2\text{I}_3]^-$ which was characterized as a *cis* isomer by IR and NMR spectroscopy. As all isomers of species $[\text{RhCH}_3(\text{CO})_2\text{I}_3]^-$ have the similar energies within 8 kJ/mol it is likely that they are easily converted to each other.

The geometrical and energetic parameters of the transition states for the activated reaction steps such as CH_3I oxidative addition, CO migratory insertion and CH_3COI reductive elimination were elucidated. The first elementary step of the catalytic cycle, CH_3I oxidative addition, was calculated to have the highest activation barrier. Its energy is 189 kJ/mol in gas phase and 135 kJ/mol in solution. According to the calculations CH_3I oxidative addition proceed via a back-side $\text{S}_{\text{N}}2$ mechanism. A front-side approach was calculated to have the higher activation barrier of 194 kJ/mol. The CO migratory insertion and CH_3COI reductive elimination in solution were calculated to proceed with smaller activation barriers of 75 and 73 kJ/mol, respectively. The activation barriers of CO migratory insertion and of CH_3COI reductive elimination are higher for the *trans* isomers than those of the corresponding *cis* isomers. Therefore, the lowest-energy path is determined by the corresponding *cis* dicarbonyl species which have to be accessed by a ligand rearrangement.

The magnitude of the solvent effect was found to decrease on going from six-fold to five-fold to four-fold coordinated complexes. While the solvent effects on the transition states are in general similar to those of the six-coordinated complexes, they affect oxidative addition and the reductive elimination steps in a crucial way.

ENVIRONMENTALLY FRIENDLY PRODUCING OF CELLULOSE BY ABIES- WOOD ORGANOSOLVENT PULPING IN THE PRESENCE OF CATALYSTS

S.A. Kuznetsova, V.G. Danilov, O.V. Yatsenkova, N.B. Alexandrova, V.K. Shambasov,
B.N. Kuznetsov

*Institute of Chemistry and Chemical Technology SB RAS, Krasnoyarsk, Russia
Krasnoyarsk State University*

Introduction

The industrial processes of cellulose production make negative influence on an environment since they use the sulfur-containing reagents for removing lignin from a wood biomass. Variety of catalysts and catalytic additives promoting the wood delignification process are known but only few of them have found at present the industrial application.

The paper describes the new environmentally benign method of cellulose production based on the use of catalysts and sulfur-free reagents – acetic acid and hydrogen peroxide for wood delignification. Organosolvent pulping is considered as an environmentally friendly way of cellulose production [1].

Methods

The pulping process was carried out in a static metallic reactor with volume 200 cm³ at the temperatures 120-150°C and liquor ratios 5:1 – 20:1 during 1-5 hours in the presence of TiO₂, Na₂MoO₄, H₂SO₄ (0.5-2.0 %) as described in [2]. In the two-step pulping, impregnation step was carried out without catalyst at liquor ratio 15:1 and temperature 60°C during 2 hours followed by replacement of the impregnation liquor with pulping one. The second step was carried out in the presence of catalyst at 130°C and liquor ratio 10:1 during 2-3 hours. The main components of cellulosic material obtained were analyzed using chemical methods according to [3].

Results and discussion

The process of wood delignification was optimized to catalyst type and its concentration, temperature and the process time, the pulping liquor composition (H₂O₂ / CH₃COOH ratio).

The data on influence of different catalysts on the pulp yield and on the composition of cellulosic product from Abies wood are given in the Table 1.

IN-9

Table 1. The influence of catalyst nature in the process of Abies wood delignification at 130°C, H₂O₂ / CH₃COOH molar ratio 0.3, liquor ratio 10:1, catalyst 2 wt. on a.d.w. and process time 3 hours

Parameters	Catalyst							
	Blank	H ₂ SO ₄	TiO ₂	Na ₂ MoO ₄	ZnO	Cr ₂ O ₃	KMnO ₄	TiCl ₃
Cellulosic product yield, (% on a.d.w.)	48,2	55,2	48,5	48,8	50,3	64,8	60,0	60,5
Cellulose content (%)*	70,5	71,9	74,3	76,7	58,4	60,7	66,4	60,4
Lignin content (%)*	24,0	15,8	16,1	8,6	39,2	30,4	24,4	31,6
Pentosanes content (%)*	3,7	3,4	3,5	3,5	0,4	0,7	0,8	2,1

*relative to cellulosic product mass

Obtained results show that the additives of H₂SO₄, TiO₂ and Na₂MoO₄ demonstrate the best catalytic properties for the delignification process. The use of these catalysts makes it possible to increase the yield of cellulose content in the obtained product to 76.7% and to reduce the content of lignin down to 8.6%.

The optimum parameters of Abies-wood delignification, which correspond to the highest yield of cellulosic product (89.5% wt. on dry wood) were selected: temperature 130°C and H₂O₂/CH₃COOH molar ratio 0.5. The highest cellulose content in cellulosic product was observed for TiO₂, Na₂MoO₄ catalysts at concentration 0.5% wt. and pulping time 3h, in the case of H₂SO₄ catalyst its optimum concentration was 2.0% wt.

The most pronounced catalytic effect was observed at the high liquor ratios 15:1 when the diffusion limitations do not play a significant role.

The novel method of microcrystalline cellulose (MCC) producing which combines the stages of Abies-wood catalytic organosolvent pulping and cellulosic product solvolysis treatment was suggested. The structural characteristics of obtained MCC were studied by γ -ray diffraction and FTIR techniques.

The promoting influence of UV-irradiation on the catalytic activity of TiO₂ in wood delignification process was established. The possible explanations of observed catalytic phenomena were discussed.

References

1. J.C. Pario, J.V. Alonso, V. Santos, *Ind. Eng. Chem. Res.* 12 (1995) 4333.
2. S.A. Kuznetsova, V.G. Danilov, B.N. Kuznetsov, *Book of Proceedings of the Sixth European Workshop on Lignocellulosics and Pulp*, Bordeaux, France, 2000, p. 421.
3. A.V. Obolenskaya, Z.P. El'nitskaya, A.A. Leonovich, *Laboratory Work on Chemistry of Wood and Cellulose, Ecology*, Moscow, 1991 (in Russian).

**NANOSTRUCTURED CATALYSTS OF NO_x SELECTIVE REDUCTION BY
HYDROCARBONS BASED UPON ZIRCONIA-PILLARED CLAYS: SYNTHESIS
AND PROPERTIES**

**V.A. Sadykov, V.P. Doronin, T.P. Sorokina, T.G. Kuznetsova, G.M. Alikina,
R.V. Bunina, D.I. Kochubei, B.N. Novgorodov, E.A. Paukshtis, V.B. Fenelonov,
A.Yu. Derevyankin, V.I. Zaikovskii, V.N. Kolomiichuk, V.F. Anufrienko,
A.Ya. Rozovskii*, V.F. Tretyakov*, T.N. Burdeynaya*, V.A. Matyshak**,
G.A. Konin**, J. R. H. Ross*****

Boreskov Institute of Catalysis SB RAS, Novosibirsk, Russia

**Topchiev Institute of Petrochemical Synthesis RAS, Moscow, Russia*

***Semenov Institute of Chemical Physics RAS, Moscow, Russia*

****University of Limerick, Limerick, Ireland*

Procedures for synthesis of thermally stable up to 750°C and well-ordered zirconia-pillared clays with specific surface area up to 300-400 m²/g prepared via intercalation of a montmorillonite clay with zirconium polyoxocations were elaborated. It was achieved through varying the nature of starting zirconium salts (oxochloride and acetate) and pH, adding modifying cations of Ce, Fe, Al, Ca, Sr, Ba along with controlled aging of pillaring solutions while monitoring the properties of zirconium macrocations in solution by EXAFAS and SAXS. The pillared clays structure (the inner arrangement of pillars and pores within crystallites) and texture (a type of crystallites packing into aggregates), was characterized by specially developed approach based upon analysis of combined XRD and high resolution absorption data in the frames of a geometrical model (1). Optimization of the preparation procedure allowed to obtain samples with the gallery height up to 8 Å, inter-pillar distance being comparable. Copper and cobalt cations were fixed at pillars using the cation exchange or wet impregnation. Pt clusters were juxtaposed on pillars using photoassisted deposition. The structural and surface properties of pillars and supported cations were elucidated using TEM, EXAFS, SAXS, ESR, UV-VIS, TPD/TPR and FTIRS of adsorbed CO/NO molecules. Specificity of copper and cobalt cations coordination in those systems is explained by their strong interaction with nanosized zirconia pillars. Strong interaction between the metal and oxide components is reflected in variation of the number of coordinatively unsaturated cations and their clustering degree as probed by FTIRS of adsorbed CO. Substantial variation of the bonding strength and coverages of ad-NO_x species due to precious metals addition was also observed.

IN-10

Catalytic properties of these systems were characterized in the reactions of NO_x selective reduction in the excess of oxygen by propane, propylene and decane. Catalytic performance of best samples in the NO_x selective reduction by hydrocarbons in the low-temperature (200-300°C) region is comparable with or higher than that of systems based upon ZSM-5 while being stable in the presence of water and sulfur dioxide. The details of the reaction mechanism were elucidated using pulse titration experiments and in situ FTIRS studies of intermediates transformation. The most efficient low-temperature route appears to include rapid HC activation on Pt clusters followed by interaction of activated CH_x species with nitrite complexes located on transition metal cations yielding organic nitrocomplexes.

Acknowledgments This work is in part supported by INTAS 97-11720 project

References

1. V.B. Fenelonov, A.Yu. Derevyankin, V.A. Sadykov, *Micropor. Mesopor. Mater.*, 47 (2001) 359.

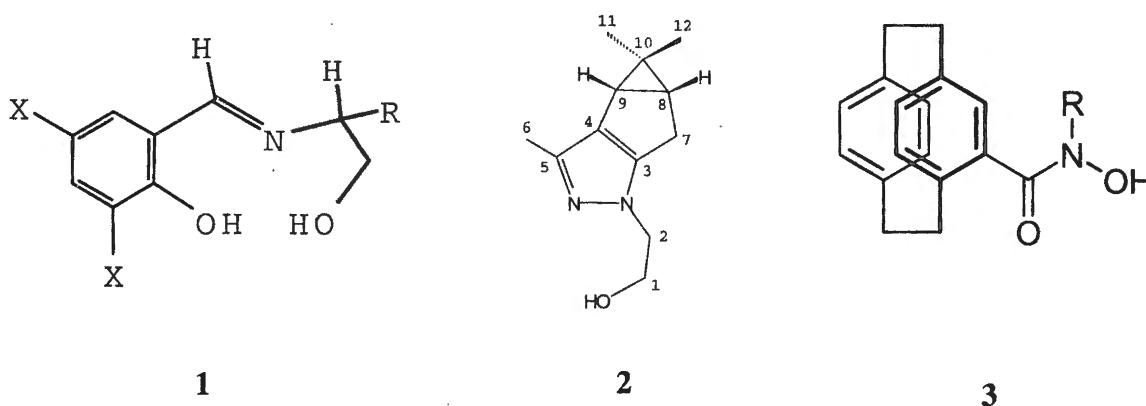
**THE REACTIVE INTERMEDIATES IN ASYMMETRIC OXIDATIONS
CATALYZED BY VANADIUM(V) COMPLEXES**

K.P. Bryliakov, E.P. Talsi

Borekov Institute of Catalysis, SB RAS Pr. Akademika Lavrentieva 5, Novosibirsk 630090, Russia

Fax: +7 3832 343766; E-mail: bryliako@catalysis.nsk.su

The detailed coordination chemistry was examined by multinuclear (^{13}C , ^{51}V , ^{17}O) NMR spectroscopy in three practical catalytic systems: 1) $[\text{VO}(\text{OAlkyl})_3]$ / chiral Schiff base ligand of the type **1** / H_2O_2 for enantioselective oxidation of sulfides [1], 2) $[\text{VO}(\text{OAlkyl})_3]$ / chiral terpenoid ligand of the type **2** / TBHP for stereoselective epoxidation of allylic alcohols [2] and 3) $\text{VO}(\text{OAlkyl})_3$ / planar-chiral hydroxamic acid of the type **3** / TBHP for stereoselective epoxidation of allylic alcohols [3]. Structure, stability and reactivity of the key intermediates were investigated.



Acknowledgements. This work was supported by Russian Foundation for Basic Research (grant 00-03-32438). K.P. Bryliakov gratefully acknowledges INTAS for financial support (grant YSF-006).

[1] C. Bolm, F. Bienewald, *Angew. Chem. Int. Ed. Engl.* 34 (1995) 2640.

[2] K.P. Bryliakov, E.P. Talsi, S.N. Stas'ko, O.A. Kholdeeva, S.A. Popov, A.V. Tkachev.

Manuscript submitted.

[3] C. Bolm, T. Kühn, *Synlett*, 6 (2000) 899.

**DIFFERENT WAYS TO WEAKLY STABLE DYNAMICS
IN A THREE-DIMENSIONAL KINETIC MODEL OF CATALYTIC HYDROGEN
OXIDATION**

Gennadii A. Chumakov and Natalia A. Chumakova*

Sobolev Institute of Mathematics SB RAS, 630090 Novosibirsk, Russia

E-mail: chumakov@math.nsc.ru Tel: +7 (3832) 334 129

**Boreskov Institute of Catalysis SB RAS, 630090 Novosibirsk, Russia*

E-mail: chum@catalysis.nsk.su Tel: +7 (3832) 341 278

A detailed study of a mathematical model of a heterogeneous catalytic system in the form of three-variable nonlinear ordinary differential equations is presented with special attention to weakly stable dynamics, a type of complex irregular behavior frequently encountered in oscillating chemical reactions. One of the most important properties of the weakly stable dynamics is “a sensitive dependence on the initial conditions” [1-4].

In the model considered we find numerically periodic orbits of rather complex structure. Bifurcation theory and precise numerical analysis of the global error in long-term numerical integration show that a high sensitive dependence on the initial conditions and weakly stable dynamics appear in the three-variable systems with fast, intermediate and slow variables due to existence of the canard cycles which occur close to Hopf bifurcation in the one-parameter family of two-variable subsystems [5].

In this paper we study another way to weakly stable dynamics and show the role of successive period doubling bifurcations in the creation of weakly stable dynamics.

Mathematical model. In this paper we present some new results concerning complex dynamics in a three-dimensional kinetic model of heterogeneous hydrogen oxidation on metallic catalysts [11]:

$$\begin{aligned} \dot{x} &= k_1(1-x-y)^2 - k_{-1}x^2 - 2k_3(y) \cdot x^2y, \\ \dot{y} &= k_2(1-x-y)^2 - k_{-2}y^2 - k_4(y,z) \cdot y - k_3(y) \cdot x^2y, \\ \dot{z} &= \varepsilon [y(1-z) - \alpha z(1-x-y)], \end{aligned} \quad (1)$$

where x and y are the catalyst surface coverages by hydrogen and oxygen adsorbed, respectively, so that $x \geq 0$, $y \geq 0$ and $x + y \leq 1$; z is the concentration of oxygen dissolved into the subsurface layer, $0 \leq z \leq 1$; $k_{\pm 1}$, $k_{\pm 2}$, k_3 , k_4 , and $k_{\pm 5}$ are the rate constants of the reaction mechanism steps, $\alpha = k_{-5}/k_5$, $\varepsilon = k_5$, and

$$k_3(y) = k_{30} \exp(-\mu_3 y), \quad k_4(y, z) = k_{40} \exp(-\mu_4 y - \mu_5 z)$$

due to the assumption that the activation energies of the reaction rates depend upon the oxygen concentrations y and z . Note that ε is a small parameter because the dissolution into the subsurface layer is a relatively slow process as compared to the chemical reaction or adsorption onto the catalyst surface.

An original iterative method for solving periodical boundary-value problem for autonomous ordinary differential equations is applied to calculations of periodic orbits and their stability in the three-dimensional kinetic model of catalytic hydrogen oxidation [6-8]. This method develops the concept of the well known multishooting method [14,15].

The model (1) has served as an important motivation for the simplest possible geometrical interpretation of weakly stable dynamics in nonlinear heterogeneous catalytic reactions [9-13,5,8].

Periodic orbits. We let parameters k_1 and k_{40} vary while fix the other parameters $k_{-1} = 0.008$, $k_2 = 20$, $k_{-2} = 0$, $k_{30} = 100$, $\mu_3 = 30$, $\mu_4 = 12$, $\mu_5 = -10$, $\alpha = 7.88$, and $\varepsilon = 0.0024$. Physically it means that the hydrogen partial pressure in the gas mixture over the catalyst surface is varied. Note that k_1 and k_{40} depend linearly upon it.

Now we give an example to illustrate that an unstable limit cycle exists (see Fig. 1). We take three local cross-sections π_1 , π_2 and π_3 passing through the points $a_1 = (0.28899502, 0.64086281, 0.51238075)$, $a_2 = (0.33714826, 0.57187779, 0.49312216)$ and $a_3 = (0.38548260, 0.52092294, 0.44677296)$. It allows us to decompose the periodic orbit into three pieces with intervals of integration T_i from π_i to π_{i+1} where $T_1 = 395.66180572$, $T_2 = 283.61493869$ and $T_3 = 598.30280382$. Thus, the period equals 1277.57954823. We remark that in this example the multipliers of the unstable closed orbit are $(1.8133, 0, 1)$ and hence a two-dimensional stable invariant manifold exists. The local dynamical behavior "transverse" to this manifold is relatively simple, since it is controlled by the exponentially contracting flow in the local stable manifold (see Fig. 2). Trajectories in the stable manifold are expanding.

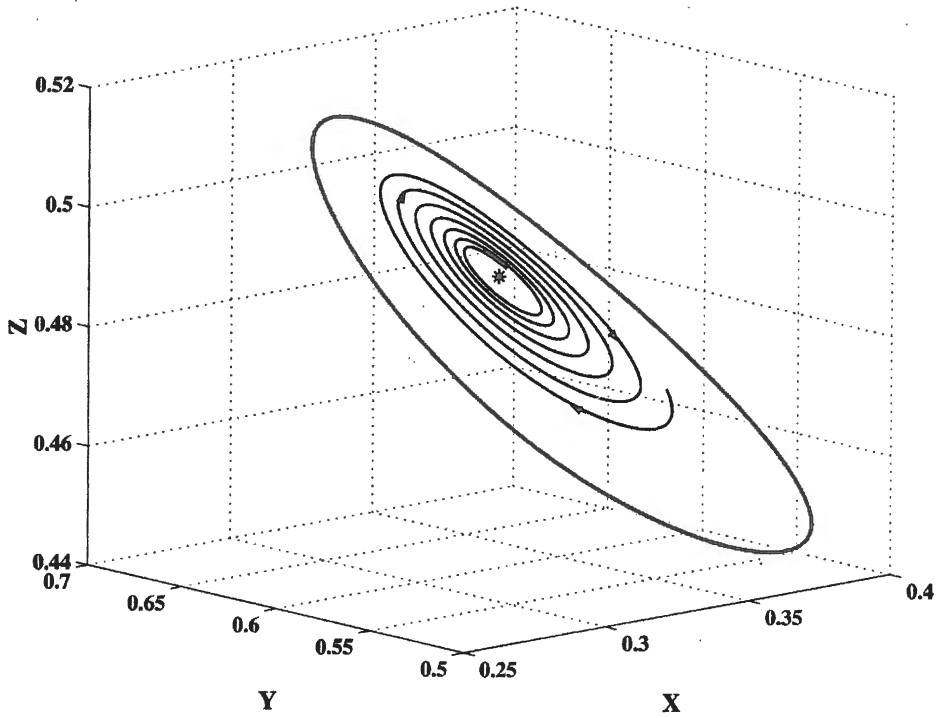


Fig. 1. Unstable limit cycle with a trajectory inside it of the system (1) for $k_1=0.135824260$ and $k_{40}=2$. The stable steady state is $(0.3252466, 0.5958083, 0.4892114)$ with the eigenvalues -1.9004268 and $-1.9769 \cdot 10^{-4} \pm i \cdot 5.05856 \cdot 10^{-3}$.

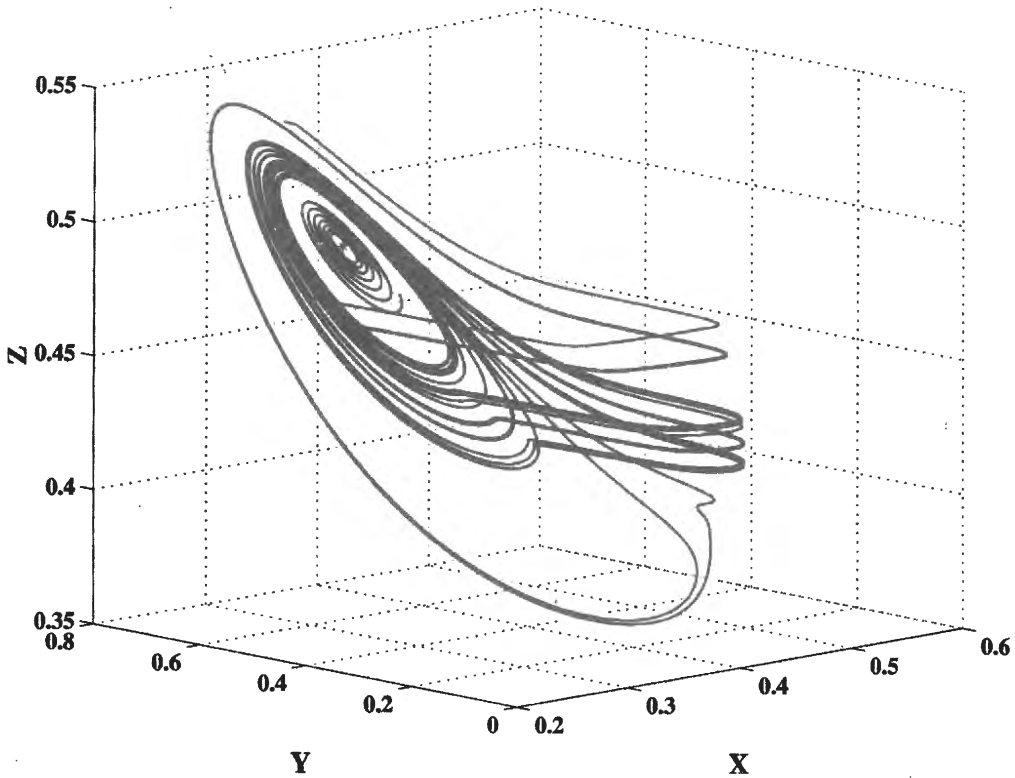


Fig. 2. Unstable limit cycle with two trajectories around it of the system (1). Parameters are the same as in Fig. 1.

Weakly stable dynamics. Numerical integration of the system (1) appears to yield trajectories that are not asymptotically periodic. In fact, in some cases we observe weakly stable dynamics followed by asymptotically periodic motions (see Fig. 3).

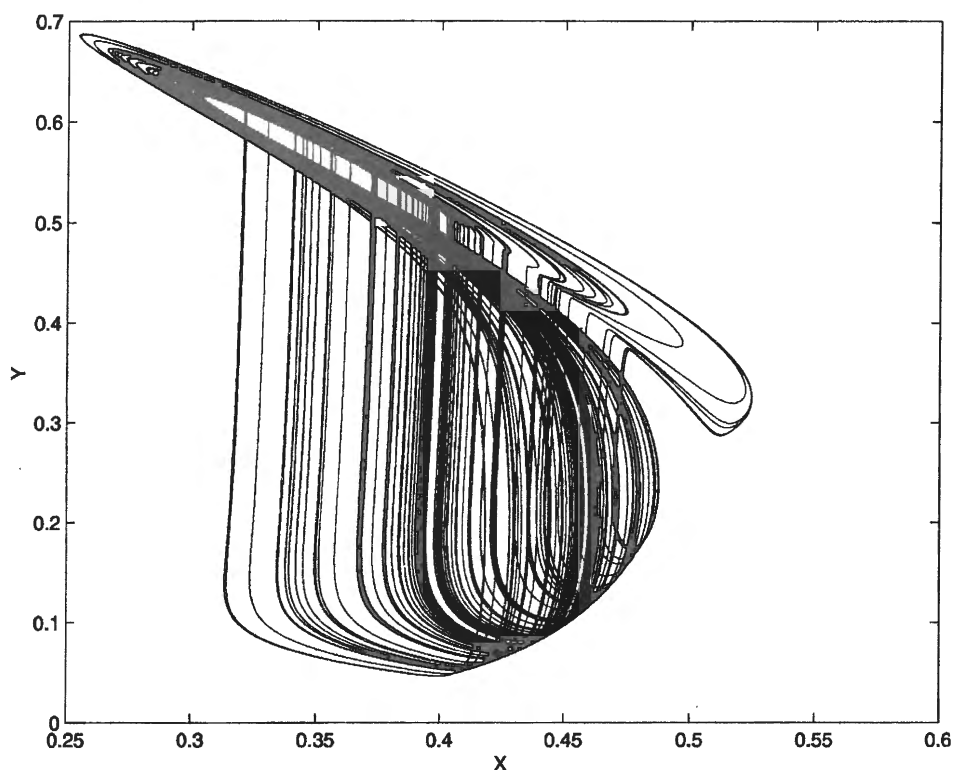


Fig. 3. Weakly stable dynamics: (x,y) -projection of the numerical solution of the system (1) for $k_1=0.144$ and $k_{40}=1.92$ with the initial conditions chosen arbitrary close to the attractor.

Following [1,2] we refer to the local expansion and consequent "independent" behavior of orbits starting arbitrary close together as sensitive dependence on the initial conditions or weakly stable dynamics. Since such "simple" differential equations of dimension three play an important role in the kinetic modelling of heterogeneous catalytic reactions [13] and can possess solutions of stunning complexity, an understanding of typical structures of their solutions is essential.

Period Doubling Sequence. We consider the role of successive period doubling bifurcations in the creation of weakly stable dynamics in Fig. 3. Following [3], we make first one remark about relationship of the Poincaré return map with eigenvalue -1 at a fixed point, to the continuous flow around the corresponding periodic orbit. The trajectories of the Poincaré map alternate from one side of the fixed point to the other along the direction of the eigenvector to -1 . It means that the two-dimensional center manifold for the periodic orbit of the three-variable system is twisted around the periodic orbit like a Möbius band around its center line.

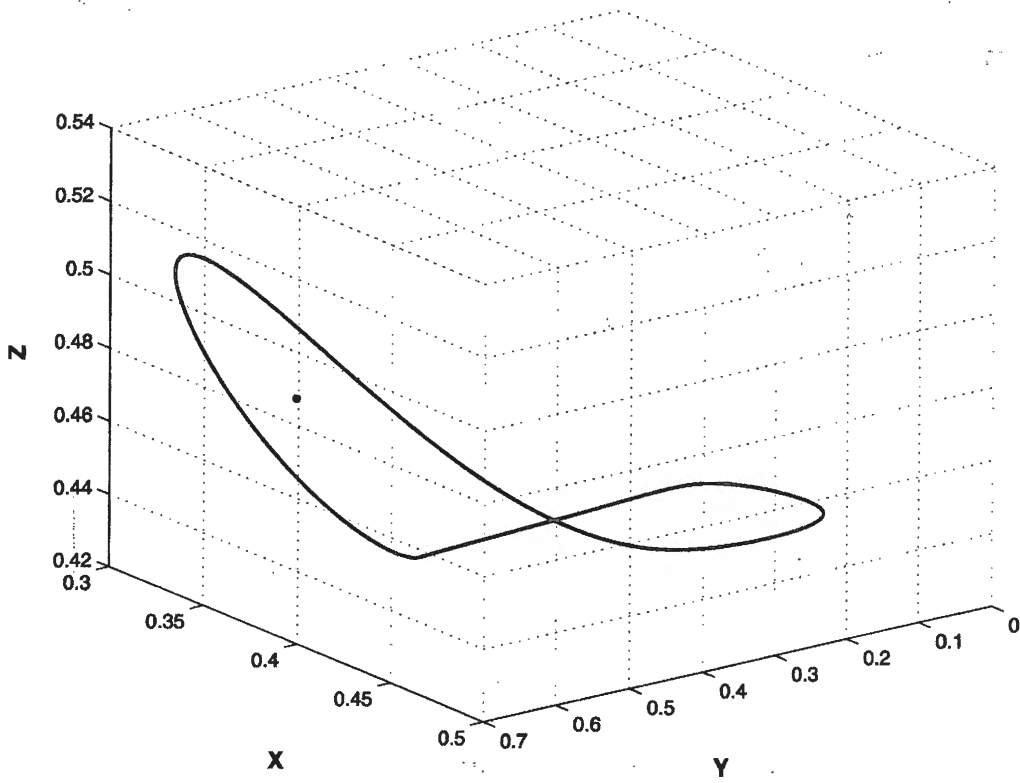


Fig. 4. T -periodic solution of the system (1) for $k_1=0.147045$ and $k_{40}=1.9606$. The unstable steady state is $(0.3487194, 0.5699204, 0.4706045)$ with the eigenvalues -1.931873 and $7.17146 \cdot 10^{-4} \pm i 5.14812 \cdot 10^{-3}$. Period equals 970.4344 .

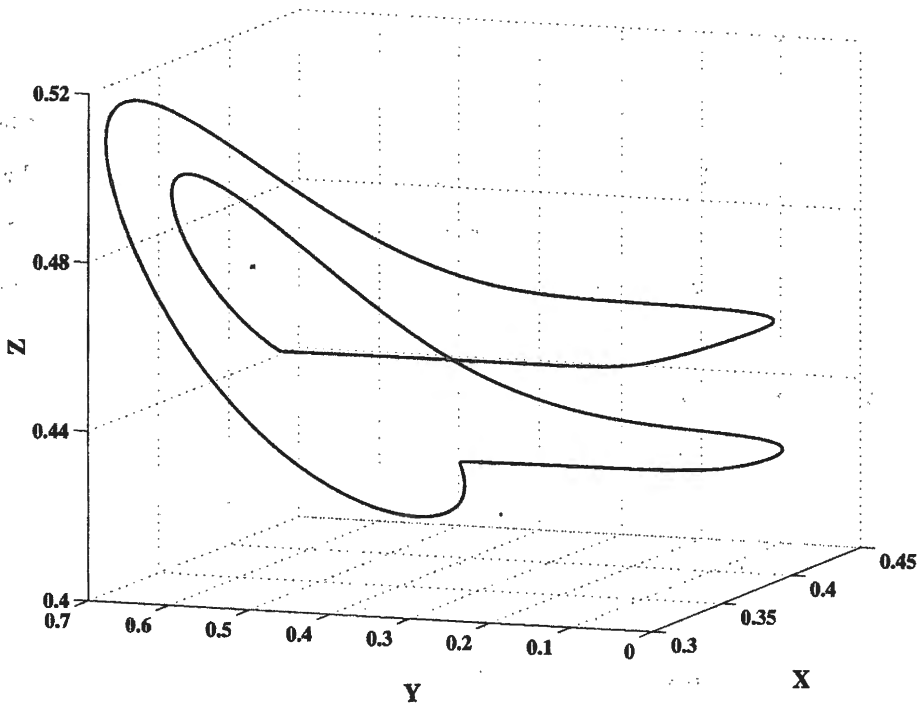


Fig. 5. $2T$ -periodic solution of the system (1) for $k_1=0.1460$ and $k_{40}=1.94666$. Period equals 1931.1277 .

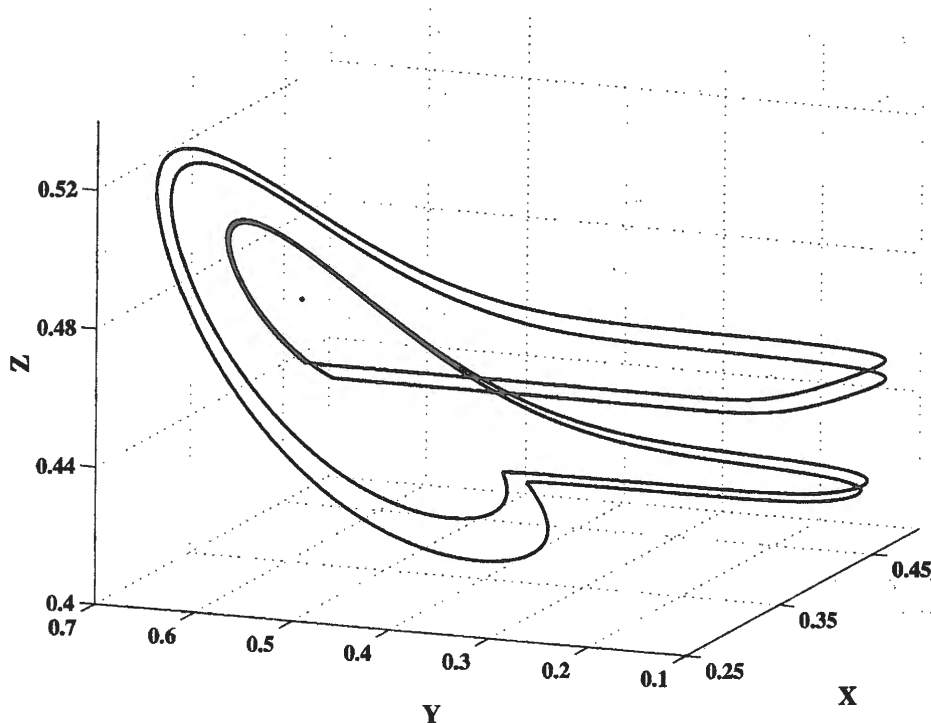


Fig. 6. $4T$ -periodic solution of the system (1) for $k_1=0.1450$ and $k_{40}=1.9334$. Period equals 3949.9572.

We have found numerically a sequence of flip bifurcations in the system (1). In Fig. 4-6 we show periodic orbits for several values of k_1 and k_{40} . Using the techniques of previous paragraphs we show that for a value k_1' where $0.146 < k_1' < 0.147045$ the periodic orbit of period T has bifurcated to an orbit of period $2T$ and then for k_1'' where $0.145 < k_1'' < 0.146$ the periodic orbit of period $2T$ has bifurcated to an orbit of period $4T$. In such a way, an infinite number of families of periodic orbits can be created in flip bifurcations as k_1 decrease. Thus, a stable orbit with period longer than any preassigned period can be found if we let k_1 vary in the interval $0.144 \leq k_1 < 0.145$. Such orbits are indistinguishable in the numerical integration from bounded non-periodic motions.

We suggest that for $k_1=0.144$ such orbits may constitute the attractor observed in a long-term numerical integration (see Fig. 3).

Conclusions. In the paper an original iterative algorithm proved to be efficient and accurate for long-term calculations of rather complex periodic orbits and their stability in a three-dimensional kinetic model of catalytic hydrogen oxidation.

Our analysis of this model demonstrates that for some parameters there exists an attractor with sensitive dependence on initial conditions. To get a clearer idea of the structure of the attracting set we find successive period doubling bifurcations in which the flow

IN-12

becomes progressively more complex until the attractor appears.

We believe that the results obtained are of importance for understanding the reasons of weakly stable dynamics in different heterogeneous catalytic systems.

Acknowledgement. This research was supported by the International Association for the promotion of co-operation with scientists from the New Independent States of the former Soviet Union (INTAS), grant No. 99-01882. We are grateful to our students Kiseleva Anna (Novosibirsk State University, Russia) and Chumakova Lyubov (University of Wisconsin-Madison, USA) for active participation in the numerical experiments.

References:

1. D.Ruelle: Sensitive dependence on initial condition and turbulent behavior of dynamical systems. In *Bifurcation Theory and Applications in Scientific Disciplines*, O.Gurel and O.E.Rössler (eds.), pp. 408-446. New York Academy of Sciences: New York, 1979.
2. P.Berge, Y.Pomeu and Ch.Vidal: *L'ordre dans le chaos*, Hermann, Paris, 1988.
3. J.Guckenheimer and Ph.Holmes: *Nonlinear Oscillations, Dynamical Systems and Bifurcations of Vector Fields*. Applied Mathematical Sciences; Vol. 42, 5th Edition. Springer-Verlag, New York, 1997.
4. M.Kubicek and M.Marek: *Computational Methods in Bifurcation Theory and Dissipative Structures*. Springer Series in Computational Physics. Springer-Verlag, New York - Berlin - Heidelberg - Tokyo, 1983.
5. G.A.Chumakov and N.A.Chumakova: Relaxation oscillations in a kinetic model of catalytic hydrogen oxidation involving a chase on canards, *Chemical Engineering Journal* (2002) (to be published).
6. G.A.Chumakov: Technology of periodic solution computation for autonomous system of ordinary differential equations, Preprint No 16, Sobolev Institute of Mathematics, Novosibirsk, 1990. (In Russian).
7. G.A.Chumakov and N.A.Chumakova: Method of computation of structurally stable periodic solutions of autonomous systems of ODE. In: *Modelling of Chemical Reaction Systems. Proceedings of an International Workshop, Heidelberg, Germany, July 24-26, 1996*. Eds.: J. Warnatz and F. Behrendt. 1996. ISBN: 3-932217-00-4.
8. N.A.Chumakova, L.G.Chumakova, A.V.Kiseleva and G.A.Chumakov, Computation of Periodic Orbits in a Three-Dimensional Kinetic Model of Catalytic Hydrogen Oxidation, *Selcuk Journal of Applied Mathematics* (2002) (to be published).
9. G.A.Chumakov, M.G.Slinko and V.D.Belyaev: Complex Behaviour of the Reaction Rate in a Heterogeneous Catalytic Reaction, *Dokl. Acad. Nauk SSSR* **253** (1980) No. 3, 654-658.
10. G.A.Chumakov and M.G.Slinko: Kinetic turbulence (chaos) of reactions rate for hydrogen oxidation on metallic catalysts, *Dokl. Acad. Nauk SSSR* **266** (1982) No 5, 1194-1198. (in Russian)
11. G.A.Chumakov: Analysis of Mathematical Models of Rate Autooscillations in Heterogeneous Catalytic Reactions. Ph.D. thesis, Novosibirsk State University, Novosibirsk, 1985. (in Russian)
12. G.A.Chumakov: Mathematical modeling of complexe behaviour of heterogeneous catalytic reaction rate, Preprint No. 233, Computing Center, Novosibirsk, 1980.
13. M.M.Slinko and N.I.Jeager: *Oscillating heterogeneous catalytic systems*. Studies in surface science and catalysis, Vol. 86. Elsevier, Amsterdam, 1994.
14. U.M.Ascher, R.M.M.Mattheij and R.D.Russel: *Numerical Solution of Boundary Value Problem for Ordinary Differential Equations*, Prentice Hall, 1988.
15. P.Deuflhard: Numerik von Anfangswertmethoden für gewöhnliche Differential-gleichungen, Technical Report TR 89-2, Konrad-Zuse-Zentrum für Informations-technik, Berlin, 1989.

SYNTHESIS AND CATALYTIC ACTIVITY OF TERTIARY
ORTHO-PHOSPHINOPHENOLS AND THEIR DERIVATIVES

D.G.Yakhvarov^a, J.Heinicke^b, Yu.H.Budnikova^a, O.G.Sinyashin^a

^a*A.E.Arbuzov Institute of Organic and Physical Chemistry of Kazan Scientific Center of
Russian Academy of Sciences, 8, Arbuzova str., 420088 Kazan, Russia*

Fax: (8432) 752253, e-mail: yakhvar@iopc.knc.ru

^b*Institute für Chemie und Biochemie, Universität Greifswald,*

Soldmannstrasse 16, D-17487 Greifswald, Germany

Fax: (internat.) +49(0)3834/864337, E-mail: heinicke@mail.uni-greifswald.de

One of the tasks of modern organoelemental chemistry is development of new more effective processes and creation of novel catalytic systems.

The polymerization of unsaturated hydrocarbons by transition metal catalysts is known since more than 50 years. Karl Ziegler discovered the polymerization of ethene by $\text{TiCl}_4\text{-AlCl}_3$ catalysts [1] and Giulio Natta realized the stereoselective polymerization of propene [2]. Since this time many processes were developed to obtain new useful materials using the homo- and co-polymerization of ethene, propene, and other α -olefins. Recent research was devoted mainly to the improved, highly active and stereoselective metallocene catalysts, bis- η^5 - or η^5 - η^1 -chelate-complexes of group 4 elements, usually Ti or Zr, and containing suitable bridged *bis*-cyclopentadienyl or suitable ω -heterofunctionalized alkyl-cyclopentadienyl derivatives as ligands [3]. For the oligomerization of ethene to give linear α -olefins the Shell Higher Olefins Process [4-6] using P-O-chelate nickel complexes as catalysts is the most important process. In order to tune the catalyst properties, various P-O-nickel complexes of varying ring sizes and bearing different functional groups have been investigated [7-10].

The aim of the present work is the synthesis of tertiary *ortho*-phosphinophenols and their ethers and testing of catalytic activity of the nickel-complexes with these ligands in the ethene polymerization and oligomerization processes.

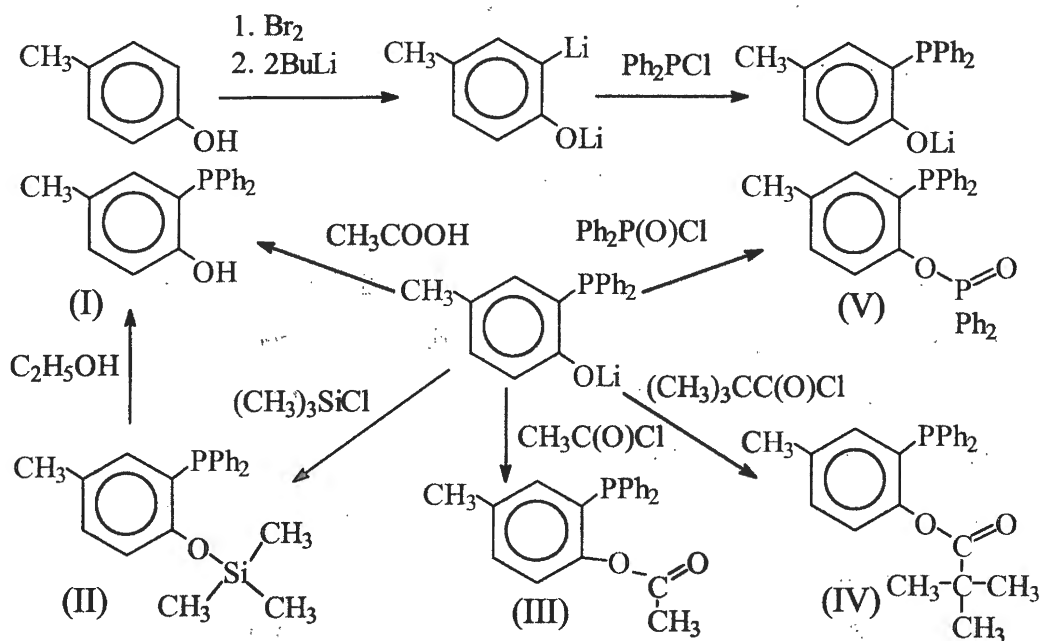
The synthesis of tertiary *ortho*-phosphinophenols and their ethers and testing of catalytic activity of the nickel complexes of these ligands in the ethene oligomerization and polymerization processes were carried out in the present investigation.

IN-13

Using dilithium reagent prepared from BuLi and *p*-cresol as a starting reagent the following tertiary *o*-phosphinophenols and their derivatives were synthesized:

1. 2-Diphenylphosphino-4-methylphenol
2. 2-Diphenylphosphino-4-methylphenyl trimethylsilyl ether
3. Acetic acid 2-diphenylphosphino-4-methyl-phenyl ester
4. Pivalic acid 2-diphenylphosphino-4-methyl-phenyl ester
5. Diphenylphosphinic acid 2-diphenylphosphino-4-methylphenyl ester

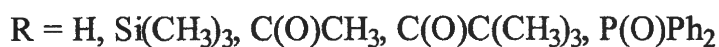
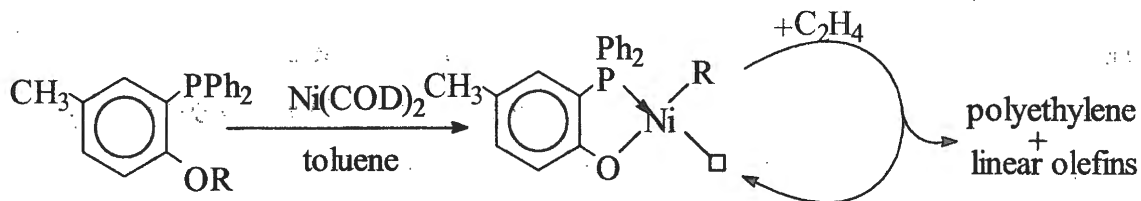
The ligand synthesis was carried out under the following procedure:



The novelty of synthesis 2-diphenylphosphino-4-methylphenole consists in the use of acetic acid at the acidolysis stage of lithium derivative, which reduces direct deriving of tertiary phosphines. The ethers of ortho-diphenylphosphino-4-methylphenole were obtained from appropriate chloroanhydrides.

All obtained compounds were tested in the ethene polymerization and oligomerization processes using $\text{Ni}(\text{COD})_2$ as starting metalcomplex under the following scheme:

Scheme of catalytical test:



The nickel complexes with tertiary *ortho*-diphenylphosphinophenols have shown high catalytic activity in the ethene polymerization processes (the yield of extracted polymer was 70-80%). Unexpectedly high results were obtained at the testing of catalytic activity of tertiary *ortho*-diphenylphosphinophenyl ethers. In this case it was possible to achieve practically full conversion of ethene to the high molecular products (98-99%). However, the lack of the free hydrogen group in the molecules of tertiary *ortho*-diphenylphosphinophenyl ethers testifies to a possibility of a course of ethene polymerization process not only through formation of nickel-hydride complexes, that is in some discordance with the postulated mechanism for ethene oligomerization via a P-C-C-O-stabilized nickel hydride species.

This work was financially supported by DFG (He 1997/8-2), RFBR (grant nos. 01-03-33210 and 01-15-99353) and INTAS 00-0018.

References

1. K.Ziegler, E.Holzkamp, H.Breil, H.Martin; *Angew. Chem.* 1955, 76, 545
2. G.Natta; *Angew. Chem.* 1956, 68, 393
3. B.Cornils, W.A.Herrmann (eds.); *Applied Homogeneous Catalysis with Organometallic Compounds, VCH-Wiley, Vol 1 and 2, Weinheim/Germany*, 1996
4. W.Keim, *J. Mol. Catal.* 1989, 52, 19.
5. W.Keim, *Angew. Chem. Int. Ed. Engl.* 1990, 29, 253.
6. W.Keim, *New J.Chem.* 1994. 18, 93.
7. W.Keim, F.H.Kowaldt, R.Goddart, C.Kruger, *Angew. Chem.* 1978, 90, 493.
8. J.Heinicke, R.Kadyrov, M.K.Kinderman, M.Koesling, P.G.Jones, *Chem. Ber.* 1996, 129, 1547-1560
9. I.Brassat, U.Englert, W.Keim, D.P.Keitel, S.Killat, G.P.Suranna, R.Wang, *Inorg. Chim. Acta* 1998, 280, 150
10. J.Heinicke, M.He, A.Dal, H-F.Klein, O.Hetche, W.Keim, U.Florke, H.J.Haupt, *Eur. J. Inorg. Chem.* 2000, 299-305.

1. The first part of the document discusses the importance of maintaining accurate records of all transactions. This is essential for ensuring the integrity of the financial statements and for providing a clear audit trail.

2. The second part of the document outlines the various methods used to collect and analyze data. These methods include direct observation, interviews, and the use of statistical techniques. Each method has its own strengths and limitations, and it is important to choose the most appropriate one for the specific situation.

3. The third part of the document describes the process of data analysis. This involves identifying patterns, trends, and anomalies in the data. It also involves testing hypotheses and drawing conclusions based on the results.

4. The fourth part of the document discusses the importance of reporting the results of the analysis. This involves presenting the findings in a clear and concise manner, and providing a summary of the key conclusions.

5. The fifth part of the document discusses the importance of maintaining the confidentiality of the data. This is especially important in cases where the data may be sensitive or proprietary.

6. The sixth part of the document discusses the importance of maintaining the accuracy of the data. This involves ensuring that the data is collected and analyzed correctly, and that any errors are identified and corrected.

7. The seventh part of the document discusses the importance of maintaining the integrity of the data. This involves ensuring that the data is not tampered with or altered in any way.

8. The eighth part of the document discusses the importance of maintaining the security of the data. This involves ensuring that the data is protected from unauthorized access and theft.

9. The ninth part of the document discusses the importance of maintaining the availability of the data. This involves ensuring that the data is accessible to those who need it.

10. The tenth part of the document discusses the importance of maintaining the reliability of the data. This involves ensuring that the data is consistent and trustworthy.

11. The eleventh part of the document discusses the importance of maintaining the validity of the data. This involves ensuring that the data is based on sound principles and methods.

12. The twelfth part of the document discusses the importance of maintaining the objectivity of the data. This involves ensuring that the data is not biased or influenced by external factors.

13. The thirteenth part of the document discusses the importance of maintaining the transparency of the data. This involves ensuring that the data is open and accessible to all relevant parties.

14. The fourteenth part of the document discusses the importance of maintaining the accountability of the data. This involves ensuring that the data is used responsibly and that any misuse is reported.

15. The fifteenth part of the document discusses the importance of maintaining the integrity of the data. This involves ensuring that the data is not tampered with or altered in any way.

16. The sixteenth part of the document discusses the importance of maintaining the security of the data. This involves ensuring that the data is protected from unauthorized access and theft.

17. The seventeenth part of the document discusses the importance of maintaining the availability of the data. This involves ensuring that the data is accessible to those who need it.

18. The eighteenth part of the document discusses the importance of maintaining the reliability of the data. This involves ensuring that the data is consistent and trustworthy.

19. The nineteenth part of the document discusses the importance of maintaining the validity of the data. This involves ensuring that the data is based on sound principles and methods.

20. The twentieth part of the document discusses the importance of maintaining the objectivity of the data. This involves ensuring that the data is not biased or influenced by external factors.

21. The twenty-first part of the document discusses the importance of maintaining the transparency of the data. This involves ensuring that the data is open and accessible to all relevant parties.

22. The twenty-second part of the document discusses the importance of maintaining the accountability of the data. This involves ensuring that the data is used responsibly and that any misuse is reported.

23. The twenty-third part of the document discusses the importance of maintaining the integrity of the data. This involves ensuring that the data is not tampered with or altered in any way.

24. The twenty-fourth part of the document discusses the importance of maintaining the security of the data. This involves ensuring that the data is protected from unauthorized access and theft.

25. The twenty-fifth part of the document discusses the importance of maintaining the availability of the data. This involves ensuring that the data is accessible to those who need it.

26. The twenty-sixth part of the document discusses the importance of maintaining the reliability of the data. This involves ensuring that the data is consistent and trustworthy.

27. The twenty-seventh part of the document discusses the importance of maintaining the validity of the data. This involves ensuring that the data is based on sound principles and methods.

28. The twenty-eighth part of the document discusses the importance of maintaining the objectivity of the data. This involves ensuring that the data is not biased or influenced by external factors.

29. The twenty-ninth part of the document discusses the importance of maintaining the transparency of the data. This involves ensuring that the data is open and accessible to all relevant parties.

30. The thirtieth part of the document discusses the importance of maintaining the accountability of the data. This involves ensuring that the data is used responsibly and that any misuse is reported.

POSTER PRESENTATIONS

PLATINUM AND RHENIUM EXTRACTION FROM DEACTIVATED CATALYST OF THE PETROLEUM-CHEMICAL INDUSTRY

V.I. Bogdanov, L.D. Gorbatova, A.A. Lavrov, S.J. Chelnokov

JSC "Ekaterinburg Non-Ferrous Metal Processing Plant", Ekaterinburg, Russia

It is a well-known fact that the catalysts containing Platinum Group Metals have been successfully used for a long time in many different chemical processes, including petroleum-chemical industry. The exhausted catalyst treatment aiming on the value components extraction and their return into turnover is a very important and completely unsolved task. Nowadays, due to the lack of rhenium-containing raw material in Russia, the ability to extract rhenium from exhausted catalysts became the decision criteria for making choice of right partner as refining company.

There are many methods of extraction of the value components from exhausted catalysts. All the hydro-metallurgical methods can be divided in two variants upon concentrate obtaining: base removal or selective value components' leaching.

The JSC "Ekaterinburg Non-Ferrous Metal Processing Plant" created the hydro-metallurgical technology of platinum and platinum-rhenium concentrates refining. This technology includes consequent selective acid leaching of the value components (rhenium first, then platinum) and subsequent extraction of rhenium from the leaching solutions as potassium perrhenate and platinum as ammonium chloroplatinate. The chosen conditions of concentrate opening allow 80% of rhenium to be converted into rhenium solution, and 98% of platinum – into platinum solution.

Different methods of concentrate opening: selective distillation, sintering with alkali, nitric acid and "aqua-regia" leaching, hydrous leaching, opening with hydrogen peroxide and mixed nitric acid with hydrogen peroxide were considered upon the development of the technology.

The high degree of rhenium extraction (appr. 85-95%) is characteristic for the "aqua-regia" concentrate opening, however, only 98% of platinum could be converted into solution. Hydrous leaching, opening with hydrogen peroxide and mixed nitric acid with hydrogen peroxide, and also selecting distillation allow to achieve 10-50% of rhenium extraction.

Maximum rhenium extraction (and minimum platinum) is provided by nitric acid leaching.

Upon using of the multiple-factor planning method an effect of nitric acid solution concentration, process temperature, grain size of concentrate on rhenium and platinum extraction degree has been examined. Also our Company developed the other methods of selective rhenium extraction from nitric acid solution, containing base metals. Rhenium can be obtained from the solution after platinum separation with the separation efficiency more than 90%.

The chemical content and crystal structure of potassium perrhenate have been studied by ICP-MS and electron-sone microanalyses. The results obtained agree with the theoretical conceptions on stoichiometric elements ratio and salt crystal structure.

**OXIDATION OF BENZENE TO PHENOL BY NITROUS OXIDE: THE
MECHANISM OF DEACTIVATION AND REGENERATION OF FeZSM-5
ZEOLITE CATALYSTS**

D.P. Ivanov, V.I. Sobolev, G.I. Panov

Boriskov Institute of Catalysis SB RAS, Novosibirsk, Russia

The reaction of direct benzene to phenol oxidation by nitrous oxide is of great applied interest. On this basis, Boriskov Institute of Catalysis and Solutia Inc. developed a new efficient process for phenol production, called the AlphOx process, which has been successfully pilot tested. This one-step process provides nearly 100% phenol selectivity and is considered as potential alternative to the three-step cumene process.

Studies on the reaction mechanism revealed that catalytic properties of zeolites are related to the presence of the so-called α -sites, which are dinuclear iron complexes stabilized in the micropore volume of zeolite matrix. In spite of its high selectivity, the benzene oxidation is accompanied by side reactions leading to coke deposition and gradual decrease in zeolite catalytic activity. This work considers the mechanism of zeolite catalyst deactivation by coke, formed in the reaction of benzene to phenol oxidation, and restoration of its catalytic activity at the regeneration in oxygen and nitrous oxide.

Deactivation by coke was shown to relate to the α -sites poisoning and impossibility of their further participation in catalytic reaction. Therewith, as deactivation increases, the activity of an individual site remains constant, despite a manifold drop in the overall catalytic activity. This indicates the absence of the zeolite porous space blocking and the absence of diffusion complications due to coke formation.

The regeneration study showed that coke burning out from the surface of FeZSM-5 zeolite proceeds selectively and primarily releases the α -sites. This is most pronounced at the regeneration in N_2O . Removal of 30-35% coke results in practically a complete restoration of catalytic activity.

DEVELOPMENT OF Fe₂O₃- BASED CATALYSTS OF DIFFERENT GEOMETRIES FOR ENVIRONMENTAL CATALYSIS

L.A. Isupova, V.A. Sadykov

Boriskov Institute of Catalysis SB RAS, Novosibirsk, Russia

Iron oxide α -Fe₂O₃ due to its large-scale production and a low cost, stability in reaction medium is very promising for development of deep oxidation catalysts for abatement of industrial emissions of CH_x, CO, NO_x. Due to stability of Fe-O bond, iron oxide is more suitable for high temperature (800-900°C) oxidation catalytic processes. Hence, for low-temperature application, it is necessary to modify it with noble metals (Pt, Pd, Au, Ag) or such active oxides as CuO, Co₃O₄, MnO_x, LaMnO₃. Due to restriction on waste-waters in the catalysts production put by ecological demands, dry methods including so called kneading technology are now of a special interest.

This study presents results on development of iron oxide-based deep oxidation catalysts of different geometric forms including monolithic ones prepared by using a kneading technology.

To solve the problem we used approaches earlier elaborated for preparation of CuO and Co₃O₄ monolith oxide catalysts. To obtain iron oxide-based plastic pastes with a good rheology, α -Fe₂O₃ was subjected to mechanical activation. Besides, Al₂O₃-based binders and different electrolytes were added. Active components (CuO, Co₃O₄, LaMnO₃) were either introduced by a wet impregnation of iron-oxide based support, or by adding oxides into the paste.

Catalysts were characterized by TA, X-Ray, IR, BET, TEM, SIMS, high-pressure mercury pores measurements and mechanical (crushing strength) methods. Catalytic activity in the processes of CO and CH₄ deep oxidation was investigated in flow-circulatory reactors loaded with the catalyst particles and granules.

Mechanochemical treatment. It was revealed that after mechanochemical treatment, α -Fe₂O₃ powder forms a plastic paste even with pure water (without acid adding) whereas untreated powder does not form such a plastic paste. The mechanochemical treatment leads to decrease of the aggregates and the crystalline sizes and to change of the surface microstructure and chemistry (hydration of surface). Consequently surface wetting improves, paste humidity decreases, pores size and their volume decrease in calcined iron oxide granules, while crushing strength increases.

Adding of alumina-based binders. Plastic pastes and granules may be prepared by adding of alumina-based binders (5-20%) even without acid adding and without mechanochemical treatment. Increasing Al_2O_3 content and acid adding lead to increase of the granules strength due to increased number of contacts and their strength. Optimization of plastic pastes properties by applying mechanochemical activation of iron oxide, varying amount of a binder and electrolytes nature and concentration allowed to produce monolithic carriers/catalysts and control their strength and pore structure.

The method of active component incorporation into $\alpha\text{-Fe}_2\text{O}_3$ supports was found to affect the catalytic activity. A low level of catalytic activity of “impregnation” catalysts can be explained by modification of active component with Fe and Al due to support dissolving during impregnation by saturated acidic nitrate solutions. In the kneading procedure acidity was much low, and added active oxides retained their high dispersion.

The data on comparative testing of $\alpha\text{-Fe}_2\text{O}_3$ – based catalysts modified with CuO or Co_3O_4 and early developed deep oxidation catalysts (IK-12-1, ICT-12-6, MPB-PC) in CO and CH_4 oxidation processes have demonstrated that new catalysts have a higher level of activity and thermal stability as compared with traditional ones, though containing smaller amounts of active components. Hence, low cost, active and stable catalysts with different geometric forms for deep oxidation processes were developed.

A.I. Jumabayeva, A.N. Sartaeva, K.A. Zhubanov

Scientific-Research Institute of Chemical Technologies and Materials,

Al-Farabi Kazakh National University,

Karasai batira, 95a, Almaty, 480012, Republic of Kazakhstan

Abstract

Utilization of sulfur dioxide is of great ecological importance since SO₂ emissions cause one of the global ecological problems – acid rains. Oxidation seems to be the most efficient way of SO₂ conversion. Though there exist many catalysts for this process, a search for active catalyst with a simple production technology is still going on. In particular, different chromium-containing catalysts are investigated.

In the present work, two different methods of chromium-aluminum oxide catalyst preparation were used: impregnation and co-precipitation. The former catalysts were prepared by alumina impregnation with chromium nitrate. The latter were co-co-precipitated from nitrate solutions.

A catalytic test of sulfur dioxide oxidation was conducted in a fixed bed reactor. The amount of SO₂ was 1 volume percent in balance air.

It was found that the conversion of SO₂ on co-co-precipitated catalysts was higher than on impregnated catalysts. For co-co-precipitated catalysts, the maximum conversion of SO₂ is 70% at 873 K. Impregnated catalysts show maximum activity of 59% at 973 K.

1. Introduction

Utilization of sulfur dioxide is of great ecological importance since SO₂ emissions cause one of the global ecological problems – acid rains. Oxidation seems to be the most efficient way of SO₂ conversion. There are many oxide catalysts for sulfur dioxide oxidation [1-3]. The preparation method of iron-chromium catalyst on aluminum oxide support was described in [1]. The suggested technique used 12-15 consecutive impregnations. This method was complicated and did not produce effective catalyst (32.8% of SO₂ conversion).

Catalysts were obtained by impregnation of support with 20-30% aqueous solutions of chromium acid [2]. The activity of catalysts was not high (51.7% of SO₂ conversion).

The co-precipitation and impregnation methods of catalyst preparation were described in [3]. Aluminum hydroxide was used to obtain alumina. Then granules of Al_2O_3 were impregnated with chromium nitrate (III). The SO_2 conversion was 95.8%.

In [4], the co-precipitation of salts of chromium and one of the metals (cobalt, copper, iron, nickel and zinc) with ammonia was used. The high activity of catalysts obtained by this technique was achieved.

In the present work, two different methods of catalysts preparation were used: impregnation and co-precipitation. Both types of catalysts were used for sulfur dioxide oxidation. It was found that the conversion of SO_2 on co-precipitated catalysts was higher than on impregnated catalysts.

2. Experimental

In order to prepare impregnated catalysts, the cylinders of aluminum oxide (gamma-type, 5x5 mm; industrial type A-1) were used as a support material. The support was washed with hot distilled water and dried in air stream at 373-383 K. Catalysts were prepared by impregnation of Al_2O_3 -cylinders with aqueous solution of chromium nitrate (III) of different concentrations. Excess water and nitrogen oxides were evaporated while stirring. The obtained solid catalysts were dried and calcined in air stream at gradually increased temperature up to 873 K.

The co-precipitated catalysts were prepared using different concentrations of aqueous solutions of $\text{Al}(\text{NO}_3)_3$ and $\text{Cr}(\text{NO}_3)_3$. After co-precipitation, the mixture of Al_2O_3 and Cr_2O_3 was washed with distilled water to remove excess ions of NO_3^- . After that, water was evaporated, and the cylinders (5x5 mm) of catalysts were formed from the obtained solid. The prepared catalysts were dried in air stream at 373-383 K and then calcined at gradually increased temperature up to 873 K.

The catalysts obtained by those two techniques were investigated in sulfur dioxide oxidation. The catalytic test of sulfur dioxide oxidation was conducted in a fixed bed reactor. A quartz tube was used as a reactor with 15 mm in diameter and 450 mm long. The volume of catalyst packing was 10 ml. Crushed quartz pieces (3-5 mm) were placed inside the reactor on both sides of catalyst.

After the catalyst was placed inside the reactor, it was preheated in air environment at 673 K for 2 hours. After that, the gas mixture of SO_2 and air was introduced into the reactor. The amount of SO_2 was 1 vol% and balance air. The flow rate of gaseous mixture was 4000 l/hr.

PP-4

3. Results and discussion

Table below illustrates the relationship between SO₂ conversion (%) and reaction temperature for sulfur dioxide oxidation over aluminum-chromium catalysts, prepared using different techniques. With the increase of reaction temperature, the conversion of SO₂ increases until it reaches maximum point. For co-precipitated catalysts, the maximum conversion of SO₂ is 70% at the reaction temperature 873 K. The impregnated catalysts show maximum activity of 59% at 973 K.

It was assumed that the activity of obtained catalysts was related to their pore structure [5]. By varying the preparation techniques, it is possible to obtain catalysts of different activity.

Table. Activity of co-precipitated and impregnated catalysts in sulfur dioxide oxidation.

Temperature, K	Co-precipitated catalysts	Impregnated catalysts
673	45	33
773	53	40
873	70	42
973	68	59
1073	65	57

References:

1. Patent USSR 493243 (1973) (in Russian).
2. Patent USSR 703132 (1979) (in Russian).
3. Patent USSR 691185 (1979) (in Russian).
4. Patent USSR 925381 (1982) (in Russian).
5. I.P. Mukhlenov, E.I. Dobkina, V.I. Deryuzhkina, V.E. Soroka, Technology of catalysts, Khimiya, Leningrad, 1979 (in Russian)

DIFFUSION OF 3-METHYLPENTANE IN SILICALITE: CONCENTRATION DEPENDENCE

Alina O. Koriabkina^{a*}, Arthur M. de Jong^b, Danny Schuring^a,
Rutger A. van Santen^a

^a*Laboratory of Inorganic Chemistry and Catalysis, Schuit Institute of Catalysis, Eindhoven University of Technology, P.O.Box 513, 5600 MB Eindhoven, The Netherlands*

^b*Accelerator Laboratory, Schuit Institute of Catalysis, Eindhoven University of Technology, P.O.Box 513, 5600 MB Eindhoven, The Netherlands*

*Author to whom correspondence should be addressed.
Fax: +31-40-245-5054, E-mail a.koriabkina@TUE.NL

1 Introduction

Many studies of the diffusive and adsorptive properties of alkane/MFI-zeolites systems have been carried out for several decades already due to great number of application of these materials in the petroleum industry as catalysts for hydrocarbon conversion processes. 3-Methylpentane is one of the main products of hydroisomerization reaction, which is one of the steps of the oil refinery process. Diffusion of the reactant/product mixture might play a significant role in the catalyst performance. Therefore, the concentration dependence of the diffusion coefficient, especially for bulky alkane (iso-hexane) is an important issue. Silicalite, which does not have any acid sites was used in order to exclude any possible influence of them on the diffusion process [2].

In the present experimental study of the concentration impact on self-diffusion of 3-methylpentane in silicalite we have tried to establish the dependence and check it with the existing models. Factors influencing the activation energy of diffusion have been also studied.

2 Experimental

The PEP technique is a radiochemical method using β^+ -emitting isotopes. In our experiments ¹¹C-labelled hydrocarbons are used.

During the experiments, a constant flow of non-labelled hydrocarbon (3-methylpentane) in a carrier gas (hydrogen) was fed in a plug flow reactor containing zeolite. In order to measure the diffusivity of the alkane, a delta-pulse containing approximately 10^{-15} moles of ¹¹C-labelled one is injected from the loop in the flow passing through the reactor. The development of the pulse (change of the radio-labelled concentration profile in time) is monitored using a

PP-5

detection system based on the principal described below.

The radioactive nuclei of ^{11}C decay with a half-life 20.4 min, emitting a positron. The annihilation of positrons with electrons from the surrounding matter results in pairs of γ -photons emitted in opposite directions. The position where the annihilation takes place (which is the position of the radiolabelled molecule) is determined by coincident detection of the photon pair. In this way the PEP technique is capable of monitoring of the concentration of labelled alkane along the cylindrical axis of the reactor with a time resolution of Is and a spatial resolution of 3 mm. An appropriate mathematical model describing transport phenomena in the catalyst bed is used in order to interpret experimental data and obtain diffusion coefficients [1].

3 Results and discussion

Using a PEP technique concentration dependence of 3-methylpentane in silicalite has been studied. Found behavior of self-diffusion coefficient can be described as monotonous decrease as the pore occupancy increases, which corresponds to the type-I of the concentration dependence according to Karger and Pfeifer [3]. Since the activation energy of diffusion of the alkane turned out to be independent on the pore occupancy (44 ± 3 kJ/mol at zero loading and 46 ± 6 at approximately 50% pore filling), the pre-exponential factor D_0 was assumed to be concentration dependent. For the molecular diffusion in silicalite, theoretical studies predict linear decrease of diffusion coefficient $D(\theta) = D_0(1 - \theta)$ (mean-field theory) and negative deviation from linear behavior, which can be approximated by stretched exponential $D(\theta) = D_0 \exp(-b \theta)$ where b is a coefficient for a particular system (approximation of Monte-Carlo simulations).

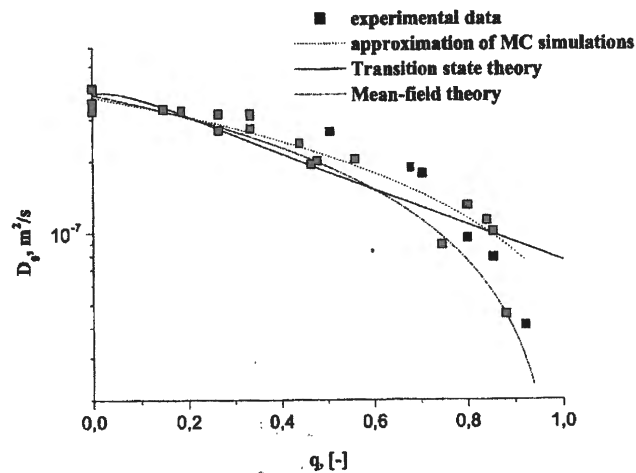


Figure 1. Pre- exponential factor D_0 for 3-methylpentane diffusion in silicalite fitted by theoretically predicted dependencies.

Analysis of the experimental data showed that stretched exponential can be a slightly better fit for the experimental data than the linear one, but the experimental accuracy does not allow to conclude it undoubtedly (Fig. 1). Moreover, theoretically predicted deviation from the linear dependence is also very small for this system. Since 3-methylpentane molecules most probably jump to the channel intersections only, the connectivity of the system is 4, which leads to a smaller deviation from the linear dependence, which is within the experimental accuracy. Therefore, we may only conclude that the observed concentration dependence of the diffusivity is close to linear one.

As a consequence of the concentration dependence of pre-exponential factor D_0 , the apparent activation energy increases with partial pressure: as the pressure increases from 0 kPa to 4.5 kPa, a significant rise in the activation energy from 44 kJ/mol to 80 kJ/mol occurred (Table 1).

Table 1. Apparent activation energies of 3-methylpentane diffusion in silicalite at different partial pressures.

Pressure, kPa	E_a , kJ/mol
0	44 ± 3
1.33	65 ± 4
2	61 ± 3
3.7	70 ± 5
4.5	80 ± 6

Usually, in the macroscopic experiments the measurement of the activation energy is performed under fixed partial pressure conditions. Due to the concentration dependence of self-diffusivity, using of different pressure conditions can be the reason for the discrepancies between different studies. Therefore, the values of true activation energy of diffusion should be compared and it should be only measured at zero pore filling or under fixed loading conditions.

References

- [1] Shuring, D.; Koriabkina, A.O.; de Jong, A.M.; Smit, B.; van Santen, R.A. *J. Phys. Chem. B*, **105**(32) (2001) 7690-7698.
- [2] Coppens, M. O.; Bell, A.T.; Chakraborty, A.K. *Chem. Eng. Sci.* **54** (1999) 3455-3463.
- [3] Karger, J. and Pfeifer, H. *Zeolites* **7** (1987) 90 – 107.

**BIOEPOXIDATION OF PROPENE BY NON-GROWING CELLS OF
RHODOCOCCUS SP.**

G.A. Kovalenko, I.B. Ivshina, E.V. Kuznetsova, I.S. Andreeva, A.V. Simakov

Boriskov Institute of Catalysis SB RAS, 630090 Novosibirsk, Russia

Biocatalysis and the biotechnological processes attract the attention as *alternatives* to traditional chemical technologies due to unique properties of biocatalysts, absence of toxic by-products, environmental safety and low energy consumption of the processes. The direct selective oxidative biotransformations of alkanes and alkenes to corresponding alcohols and epoxides are of great importance for large-scale chemical industry.

The investigations of the direct selective oxidation of propene to *1,2-epoxypropane* by non-growing cells of *Rhodococcus* sp. were carried out in homogeneous conditions. The initial rate of *1,2-epoxypropane* generation exceeded to 10 nmole/min per 1 mg of dry cells. The product epoxide accumulated extracellularly, with its concentration running up 2 mM in the reaction medium. It has been shown that *1,2-epoxypropane* had irreversible inhibition effect on the oxidative activity of cells suspensions, with the 50% lost of activity occurring at epoxide concentration above 0.4 mM.

The *immobilization* of the cells of *Rhodococcus* sp. on the solid supports to perform bioepoxidation in heterogeneous regime may solve the problem of reducing the toxic effect of the epoxide via removing the epoxide from the reaction media. The comparative study of inorganic supports to adsorb the microorganisms demonstrated that *carbon*-containing supports had the largest adsorption capacity with respect to *Rhodococcus* sp. bacteria. Besides the value of accessible surface area of support, roughness of the surface was found to be an additional key factor affecting the efficiency of the adsorption of bacterial cells. The optimal adsorbent of cells has been shown to be such that has advanced macrostructure and rough surface. Foam-like ceramics, coated with catalytic filamentary carbon, satisfied these requirements and was found to be the most effective support for adsorptive immobilization of *Rhodococcus* sp. bacteria.

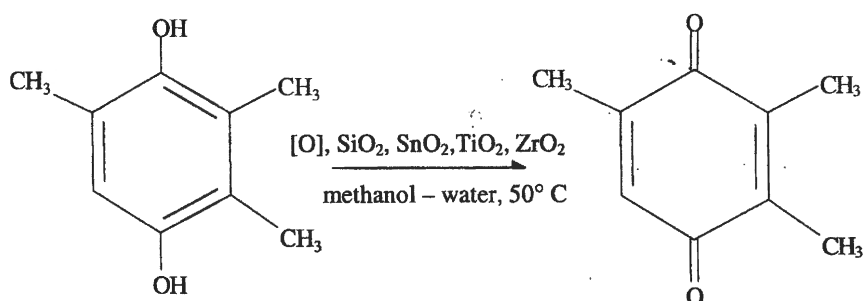
**ROLE OF DIOXIDE HYDROGELS AND THEIR SURFACE COPPER
STRUCTURES IN HYDROXYARENES CATALYTIC OXIDATIVE
TRANSFORMATION**

**E.G. Kovalyova, A.B. Shishmakov, V.G. Kharchuk, L.A. Petrov, O.V. Kuznetsova,
O.V. Koryakova, M.Yu. Yanchenko, L.A. Petrov & L.S. Molochnikov ***

*Institute of Organic Synthesis, Ural Branch of the Russian Academy of Sciences,
S. Kovalevskoy 20, 620219 Ekaterinburg GSP -147, Russia, fax: 7-(3432) 741189,
e-mail: gek@mail.ur.ru and kox@uran.ios.ru; * Department of Chemistry, Ural State Forest
Engineering Academy, Siberian highway 37, 620100 Ekaterinburg, Russia*

The ability to self-organization is a principal property of fine systems, including dioxide hydrogels. This property is conditioned by thermodynamic non-equilibrium and excess energy of the developed boundary surface between nano-sized particles and disperse phase, that determines the tendency to minimization of free energy. The resulting mobile structured hydrate lattice and high-organized surface layer of the studied hydrogels produce unique conditions for concentrating of precisely-orienting reagents and catalysts, that leads to the correction of the direction and parameters of chemical reactions with hydrogels participation. The unique properties of the finely dispersed dioxides such as high chemical stability, availability of the surface active centers over all reaction volume, capacity for intensive heat and mass transfer in the absence of brittle destruction, ease in separation from the products of reaction and possibility of repeated usage allow to develop high-effective technological processes with their participation, satisfying ecological requirements of advanced technologies.

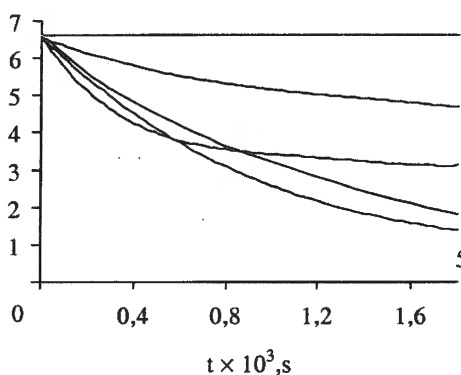
Keeping in mind the above-stated, process of liquid-phase oxidation of trimethylhydroquinone (TMHQ) as a model of hydroxyarenes in the presence of SnO_2 (I), SiO_2 (II), TiO_2 (III) and ZrO_2 (IV) hydrogels and their $\text{Cu}(2+)$ -containing structures has been studied in this work. The above-mentioned reaction proceeds yielding trimethylbenzoquinone (TMBQ) by the following scheme:



PP-7

The reaction is inhibited by binding the substrate and the resulting TMBQ into chinhydron (ChHd). Incorporation of hydrogels I-IV in reaction medium results in decreased of the inhibition of the oxidative process (Fig. 1). This effect depends on values of specific surface (S_{sp}) of the studied hydrogels, to the point of its excluding. This dependence for the hydrogel II is shown in Fig. 2. In parallel with this process there also took place inhibition of the oxidation reaction: the initial rates in the presence of the hydrogels ($W_{0\text{ I-IV}}$) were much less than that without gels. On contacting the reaction mixture with gel I the oxidation reaction is stopped. The dependences of $W_{0\text{ II-IV}}$ on the amounts of gels II-IV have complex shape (Fig. 3).

Concentration of TMHQ
($C_{\text{TMHQ}} \times 10^{-2}$, mol/l)



Concentration of TMHQ
($C_{\text{TMHQ}} \times 10^{-2}$, mol/l)

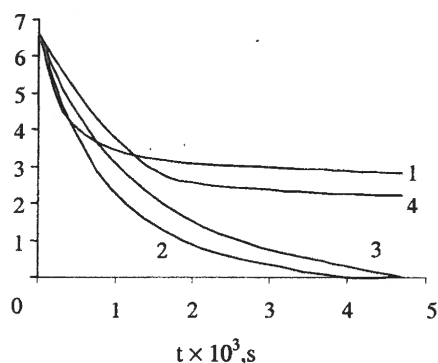


Fig. 1. Kinetic curves for the consumption of the substrate TMHQ during oxidation with oxygen: without gels (1); in the presence of gel I (2); gel II (3); gel III (4); gel IV (5). The mole ratio TMHQ : gel is 1 : 2. The specific surfaces of gels I-IV (S_{sp}) are 320, 300, 290 and 317 m^2/g , respectively.

Fig. 2. Kinetic curves for the consumption of the substrate TMHQ during oxidation with oxygen without gels (1); in the presence gel II at $S_{sp} = 226 \text{ m}^2/\text{g}$ (2); at $S_{sp} = 240 \text{ m}^2/\text{g}$ (3); at $S_{sp} = 320 \text{ m}^2/\text{g}$ (4). The mole ratio TMHQ: gel II is 1 : 2 .

$W_0 \times 10^4$, mol/(l × s)

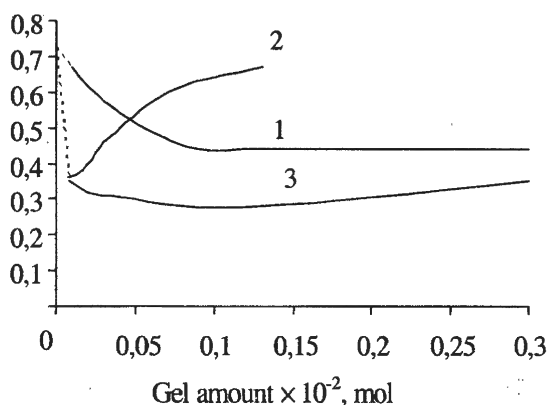


Fig. 3. The initial rates of TMHQ oxidation at different amounts of gels II-IV in the reaction zone: 1-gel II, $S_{sp} = 300 \text{ m}^2/\text{g}$; 2 - gel IV, $S_{sp} = 317 \text{ m}^2/\text{g}$; 3 - gel III, $S_{sp} = 290 \text{ m}^2/\text{g}$. The content of TMHQ in the reaction volume is $6,6 \times 10^{-4}$ mol.

The obtained results, obviously, indicate the significant role of different particle-particle interactions between substrate and gel at different ratios of these components. The associative compounds of TMHQ with gels I, II, III, obtained by sorption from water-methanol phase are found by IR spectroscopy. It was found the significant change in the parameters of sorbate - sorbent bonds vibrations as discussed earlier [1,2]. The study of the associates hydroxyarene - hydrogels II-IV of various composition with varied mole ratio of components was carried out using unsubstituted 1,4-hydroquinone (HQ). This compound was used as a model owing to convenience and reliability in interpretation of its vibration characteristics.

It is found as gel III content increases, IR spectra of the associates HQ -gel III vary. At low amounts of gel III it is bounded with aromatic ring of HQ, in so doing the gel involves in bonding a lot of OH-groups of HQ. In this case intra-molecular hydrogen bonds are disrupted. At the significant excess of gel III intra- and intermolecular hydrogen bonds dominate, in this case the bond substrate HQ -gel becomes less strength.

Similar relationships reveal themselves in spectra of the associates of HQ with gels of other element oxides. Therefore the change in character of particle-particle interactions in the system gel-substrate leads to variations in inhibition degree of TMHQ with oxygen at varying content of the finely dispersed elements dioxides II-IV in the reaction zone (Fig. 3).

Introduction of the Cu(2+)-containing hydrogels II-IV into reaction medium leads to acceleration of liquid-phase oxidation of TMHQ. Here there are two oxidants: Cu(II) ions and oxygen. The exception is gel I. In this case TMHQ participates in two parallel oxidation reactions: the first is inhibited by this hydrogel, the proceeding of the second one is conditioned by catalytic action of Cu(2+) ions. Fig.4 demonstrates this effect and non-linear dependence of W_0 on Cu(2+) content in a gels phase.

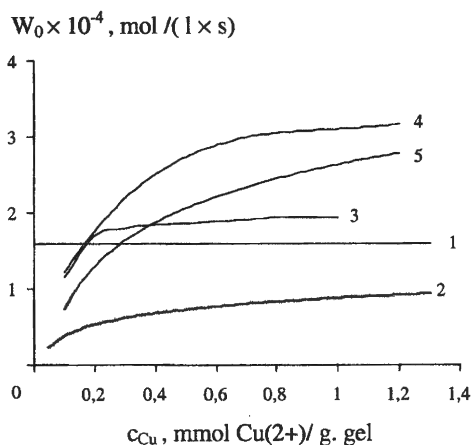


Fig. 4. The initial rates of TMHQ oxidation (W_0) without gel (1) and in the presence of the Cu(2+)-containing gels I-IV (2,3,4,5, respectively) at different content of Cu(2+) in a gel phase (c_{Cu}). The mole ratio substrate TMHQ- $CuCl_2$ is 1: 0.1.

The shape of the curves, obviously, is conditioned by the process of intercalating gels I-IV with Cu(2+) ions. It is found by ESR spectroscopy that there are three types of Cu(2+)-

PP-7

compounds in a gels phase, namely, mononuclear $\text{Cu}(2+)$ -complexes (V) ($g_{\parallel} = 2.357 \pm 0.005$; $A_{\parallel} = 13.2 \pm 0.3$ mT) (two non-protonated oxygen atoms and two hydroxyls are located within an equatorial plane of $\text{Cu}(2+)$, and two H_2O molecules, apparently, are done within an complex former axial plane), their associates with an increased local concentration of $\text{Cu}(2+)$ -ions as compared with mononuclear complexes (VI), and $\text{Cu}(2+)$ -compounds giving no ESR spectra at the used frequency and temperature (VII) [3]. They may be either a separate phase of $\text{Cu}(\text{OH})_2$ or polynuclear $\text{Cu}(\text{II})$ -compounds with bridge hydroxyls. The participation of the surface hydroxyl groups and "ethereal" oxygen of the bonds Ti-O-Ti at forming complexes V is also shown by IR spectroscopy for gel III. Varying $\text{Cu}(2+)$ ions content (c_{Cu}) various relationships between amounts of structures V-VII have been achieved.

The amounts of the above-mentioned $\text{Cu}(2+)$ -structures in a gels phase were determined by computer separation of their ESR signals. The fractions of each of these structures as a function of $\text{Cu}(2+)$ content in the phase of gels I-III are presented in Fig.5-7. The specific initial rates of TMHQ oxidation with different $\text{Cu}(2+)$ structures ($W_{0V}, W_{0VI}, W_{0VII}$) characterizing their individual reactivity were found using the obtained data. They are shown in Table. It is found that $\text{Cu}(2+)$ structures VI and VII show higher catalytic activity in the studied reaction of TMHQ oxidation than structures V. Apparently, it is caused by the greater mobility of electrons in the systems of $\text{Cu}(2+)$ ions bound to each other and by transfer of electronic density in them. Earlier, [4], by measuring microwave conductivity the correlation between mobility of electrons and catalytic activity of $\text{Cu}(2+)$ ions has been found.

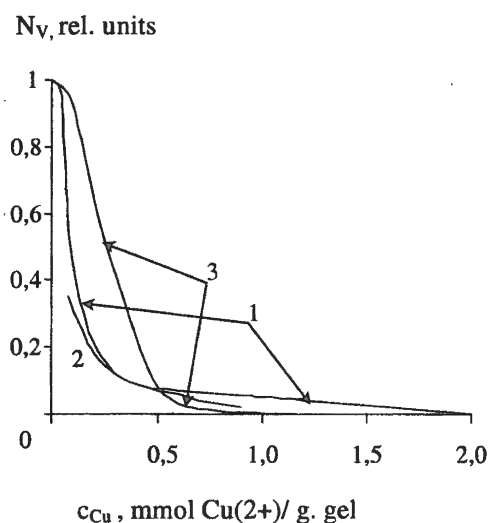


Fig. 5. The fractions of Cu^{2+} -containing structures V (mononuclear complexes) (N_V) in a phase of gel I (1), gel II (2) and gel III (3) at different content of $\text{Cu}(2+)$ in a gel phase (c_{Cu}).

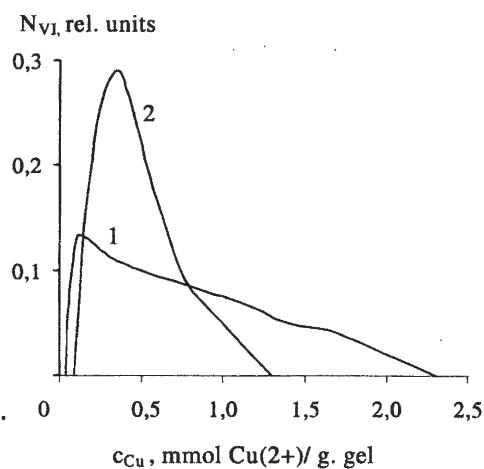


Fig. 6. The fractions of Cu^{2+} -containing structures VI (magnetic associates) (N_{VI}) in a phase of gel I (1), gel III (2) at different content of $\text{Cu}(2+)$ in a gel phase (c_{Cu}).

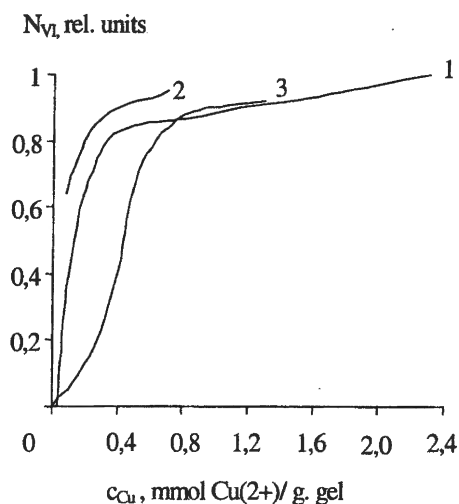


Fig. 7. The fractions of Cu^{2+} -containing structures VII (polynuclear compounds or a separate phase of $\text{Cu}(\text{OH})_2$) (N_{VII}) in a phase of gel I (1), gel II (2) and gel III at different content of $\text{Cu}(2+)$ in a gel phase (c_{Cu}).

Of interest are the results on the influence of the studied gels on physico-chemical properties of $\text{Cu}(2+)$ ions obtained using voltammetry [5]. In particular, it is shown that adsorption of $\text{Cu}(2+)$ ions on gels I-IV leads to the shift in the reduction potentials during the process $\text{Cu}(2+) \rightarrow \text{Cu}(+) \rightarrow \text{Cu}(0)$ relative to the curve of reduction of copper from a solution on carbon-pasted electrode (UPE) to the field of less negative values, so the oxidative activity of $\text{Cu}(2+)$ ions increases. The maximal shift in potentials was observed at adsorption of $\text{Cu}(2+)$ ions on gel III, and the least one was found for gel IV. For gel IV it is pointed the appearance of additive peak of $\text{Cu}(2+)$ reduction at the potential shifted to the field of more negative values (peak at $-1,05$ V). It indicates formation of another copper complex with a decreased oxidative activity (The peak at ~ -1 V for gel III appears as result of titanium reduction) (Fig. 8).

Table. Specific initial rates of oxidation reaction of substrate TMHQ with different $\text{Cu}(2+)$ structures (V, VI, VII) on gels I, II, III

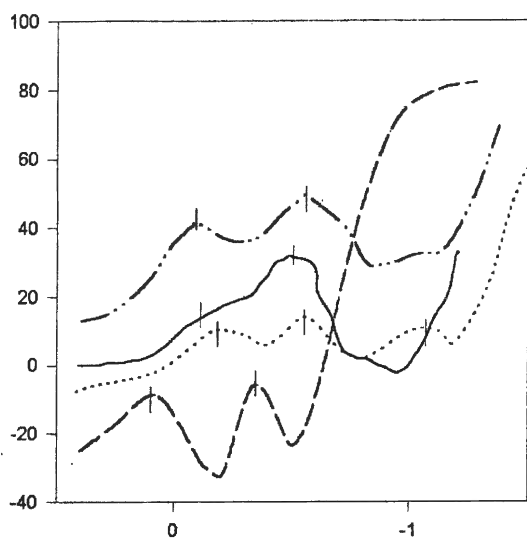
gel	$W_0, \text{mol}/(\text{l} \times \text{c}) \times 10^4$			
	$W_{0\text{V}}$	$W_{0\text{VI}}$	$W_{0\text{VII}}$	W_0 oxidation with $\text{Cu}(2+)$ ions in solution
without gel	-	-	-	1.60 ± 0.16
I (SnO_2)	0.28 ± 0.04	0.42 ± 0.06	0.67 ± 0.10	-
II (SiO_2)	1.60 ± 0.16	-	1.81 ± 0.27	-
III (TiO_2)	0.97 ± 0.14	2.78 ± 0.42	3.33 ± 0.50	-

The potentials of copper oxidation during the processes $\text{Cu}(0) \rightarrow \text{Cu}(+) \rightarrow \text{Cu}(2+)$ on the gels surface are shifted to the field of negative potentials relative to the curve of oxidation of copper from a solution. It indicates that oxidation of the reduced copper to the initial state

PP-7

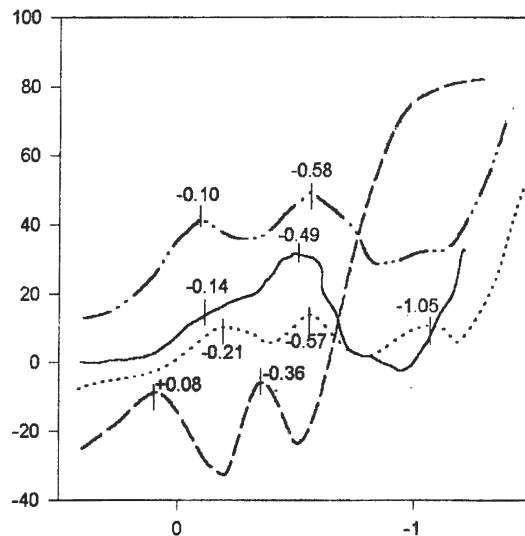
proceeds much easier (Fig.9). The redox process for copper in gel phase as a whole becomes less reversible and leads to increased standard constant of electronic transfer rate.

di / dt, rel. units



E, V

di / dt, rel. units



E, V

Fig. 8. Reduction of Cu(2+) on carbon-pasted electrodes (UPE).

— Cu — UPE
- - - adsorbed Cu — gel III
..... adsorbed Cu — gel IV
- . . . adsorbed Cu — gel II

Fig. 9. The curves of anode oxidation of copper on carbon-pasted electrodes (UPE).

— Cu — UPE
- - - adsorbed Cu — gel III
..... adsorbed Cu — gel IV
- . . . adsorbed Cu — gel II

Thus, the application of SnO₂, SiO₂, TiO₂ and ZrO₂ hydrogels and their Cu(2+)-containing structures as catalytic active ingredients during hydroxyarenes oxidation is promising. It was found that this process proceeds in the sphere of the competing particle-particle interactions with participating gel catalysts. The properties of reagents and catalysts are significantly changed due to these interactions. This work was done under support of the Russian Foundation for Basic Research. (Grant № 01-03-P 96523).

REFERENCES

1. L.Petrov, V. Charchuk, A.Shishmakov & E.Tokarev, J. Organic Chem. (Russian), 34(2) (1998) 376.
2. V.Charchuk, A.Shishmakov, O. Koryakova & E.Tokarev, J. Organic Chem. (Russian), 35(7) (1999) 1118.

3. E. Kovalyova, V. Charchuk, A. Shishmakov, L. Petrov and L. Molochnikov, Abstr. the Intern. Mem. K.I. Zamaraev Conf. "Physical methods for catalytic research at the molecular level", Novosibirsk, 1999, p.101.
4. Min' Tyau Van, Tuen Nguen Van, A. Rudenko, Bull. Moscow Univ.(Russian), Chemistry, 36(3) (1995) 278.
5. V. Charchuk, A. Shishmakov, O. Koryakova, M. Yanchenko et al, J. General Chem. (Russian), 70(6) (2000) 993.

**FORECASTING OF THE EFFICIENCY OF MODIFIED CATALYSTS IN
METHANOL SYNTHESIS****A.V. Kravtsov, A.A. Novikov, A.A. Saifulin, V.V. Samoilenko**

*Chemical technological department, Tomsk Polytechnic University,
Lenin ave. 30, Tomsk 634034, Russia, tel: +7 (3822) 415-443, fax: +7 (3822) 415-235,
E-mail: a_crow@mail.ru*

The methods to produce low-temperature catalysts for methanol synthesis are in continuous development. The characteristics of the used catalysts in many respects determined methanol synthesis efficiency. Thereby quantitative estimation of the properties of new catalysts and forecasting of their efficiency are important problems.

In this work the forecast of the efficiency of modified catalysts for methanol synthesis produced by plasmochemical method was carried out. The kinetic parameters before and after catalyst overheating were determined.

The correction of parameters of kinetic model was carried out based on the experimental data for modified catalysts. The comparative analysis of outcomes for modified catalyst and industrial (ICI 51-2) allows to mark two main features in the properties of modified catalyst - high thermostability and displacement of maximum activity to the region of 260-270°C.

The obtained results indicate to coincidence of computational and experimental data and allow forecasting of the efficiency of new catalysts.

REDUCTION OF COKE FORMATION ON Pt-Re CATALYSTS OF GASOLINES REFORMING

A.V. Kravtsov, E.D. Ivanchina, L.V. Krupenya, S.A. Galushin

Chemical Technological Department, Tomsk Polytechnic University

Lenin ave. 30, Tomsk 634034, Russia; tel: +7 (3822) 415-443, fax: +7 (3822) 415-235,

E-mail: a_crow@mail.ru

The estimation of an optimum catalytic activity is the one of the main problems upon analysis of catalysts at plants. It is determined by a ratio of reforming target reaction rates and equilibrium between reactions of formation and hydrogenation of coke structures. Quantitatively equilibrium coke formation is determined by three major factors: hydrogenating ability of Pt-catalyst; raw material component structure; technological modes. Apparently, the hydrogenating activity of Pt-catalyst is functionally determined by the nature and quantity of electronic and structural promoters, therefore, the value of optimum activity is characteristic for each type of industrial catalysts, known for us. The catalytic activity fluctuations distort the balance of the reactions of hydrogenation of carbon depositions and causes increase of coke formation. We offer an operation method of Pt-Re catalysts, which allows to keep track of activity enhancement, that increase run duration on 20-30%. For confirmation of these conclusions the assessment of unbalanced by Re catalyst R-56 at Omsk petroleum refinery plant and charging of a mixed type KP-108Y and PB-22Y at Angarsk petroleum refinery plant was fulfilled. It has been shown that the fluctuation nature of activity results in a selectivity decrease.

The mathematical model has been used for numerical evaluation of a fixed catalytic activity level a_{opt} , which is determined by total amount and structure of coke deposition on a catalyst surface. Level of a catalytic activity is an integral index of this equilibrium. It depends on its chemical composition (ratio Pt/Re), its activity and stability. This parameter changes during service cycle and its value can be used for forecasting a term of working contact regeneration.

Thus, the results reveal that the regulation of activity in dependence of the consumption and hydrocarbon raw material composition, and also circulating factor of hydrogenous gas allows to lower process of coke formation and to increase duration of service cycle. The results have the great practical importance and have been applied at Omsk, Achinsk, Angarsk petroleum refinery plants.

**THE INVESTIGATION OF PROCESSES OF BIOMASS PYROLYSIS AND
GASIFICATION IN FLUIDIZED BED REACTORS.**

V. N. Kruchinin, M. A. Kerzhentsev, Z. R. Ismagilov, V. N. Korotkikh

*Boreskov Institute of Catalysis SB RAS, Pr. Ak. Lavrentieva 5,
630090, Novosibirsk, Russia*

G. M. Zabortsev, Yu. M. Ostrovskii

*Novosibirsk State Design-Exploratory Institute VNIPIET, ul. B. Khmel'nitskogo 5, 630075,
Novosibirsk, Russia*

H. J. Veringa

*University of Twente, Faculty of Mechanical Engineering, P.O. Box 217, 7500 AE Enschede,
The Netherlands*

Biomass (yearly world growth up to $200 \cdot 10^9$ t) is considered as the main renewable resource for energy production. Amongst well-known methods of biomass processing (pyrolysis, liquefaction, gasification, combustion) catalytic gasification is of primary interest [1].

Pyrolysis and gasification processes are based on endothermic reactions demanding supply of heat to the reaction zone. Therefore, the introduction of catalytic heat generator (CHG) into the technological cycle of these processes can be a prospective approach [2-4]. Total combustion of fuels in a catalytic fluidized bed of CHG is achieved at relatively low temperatures 600-750°C. The application of CHGs allows to prevent formation of soot and carcinogenic hydrocarbons and to abate emissions of CO and NO_x.

The goal of this work was to study the processes of biomass pyrolysis and gasification in experimental facilities containing CHG reactors. Three setups used in this work were different by the way of conducting the pyrolysis and gasification processes (see Fig 1-3).

In the *setup 1* the reactor contains fluidized bed catalyst in lower part for catalytic combustion of kerosene. The height of the fluidized bed being 50 cm and biomass was fed directly to the hot fluidized bed at the height of 40 cm (see Fig. 1).

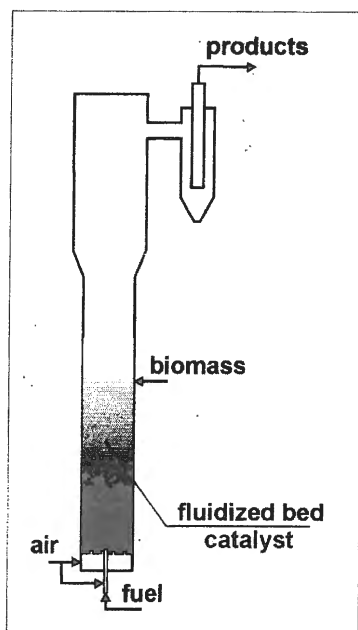


Fig. 1. Scheme of setup 1.

The *setup 2* contains two fluidized bed reactors. Lower reactor is for kerosene catalytic combustion and upper reactor loaded by inert bed material ($\gamma\text{-Al}_2\text{O}_3$). The biomass was fed into the fluidized bed of the upper reactor (see fig.2)

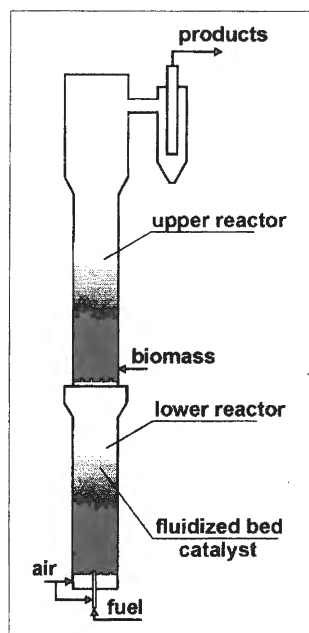


Fig. 2. Scheme of setup 2.

The *setup 3* contains two cylindrical fluidized bed reactors of different diameter. The reactor of smaller diameter is placed into the bigger one so combustion of fuel proceeds in the annulus providing heat through the wall into the fluidized bed of inert in internal reactor for biomass gasification.

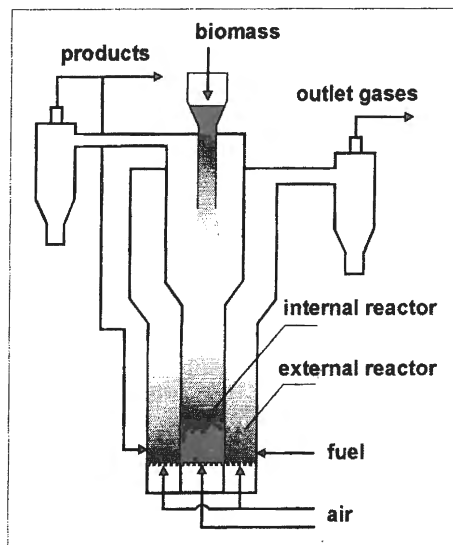


Fig. 3. Scheme of setup 3.

For the studies semolina was taken as a model object, with the following chemical composition (wt. %): hydrogen 6.92; carbon 39.18; nitrogen 1.81; ash 1.17.

The combustion catalyst $\text{Cu}_x\text{Mg}_{1-x}\text{Cr}_2\text{O}_4/\gamma\text{-Al}_2\text{O}_3$ (IC-12-73) was used in the experiments. The inert bed material used in the setups 2 and 3 was $\gamma\text{-Al}_2\text{O}_3$.

All setups were equipped with the system for on-line continuous gas sampling for GC analysis.

Experimental results

The GC analysis of the exhaust gas from the reactors showed that the gas formed at biomass pyrolysis and gasification contains substantial amounts of hydrogen, methane, carbon monoxide and carbon dioxide. The relative amounts of these gases depended on the feed rates of the biomass, air and fuel and the temperature of the process and was in the range (vol.%): hydrogen – 2-7; carbon monoxide – 3-18; methane – 1-15; carbon dioxide – 7-14 (see Table 1). These values are in good agreement with those obtained by other researchers in the studies of biomass pyrolysis and gasification [5,6].

The biomass pyrolysis and gasification in the setups 1 and 2 was performed in the flow of catalytic fuel combustion hot gases. In order to exclude additional oxygen intake, the biomass was fed by flow of an inert gas (nitrogen). As shown by the experiments, the efficiency of the process was only slightly dependent on the temperature (in the range of 650-750°C), but very sensitive to the content of oxygen in the reactor. Increase of oxygen concentration leads to the biomass deep oxidation (see Fig. 4), and at the outlet of the reactor substantial amounts of

carbon dioxide was detected. The process of gasification was occurred deeper with adding of water vapour to reaction zone (see Fig. 5 and Table 2).

Table 1. Amounts of the products of biomass pyrolysis and gasification

Feed rates of gases, fuel and biomass					T, °C	The gaseous products			
Air, m ³ /h	biomas, kg/h	N ₂ , m ³ /h	Fuel, kg/h	H ₂ O, g/h		H ₂ , % vol.	CO, % vol.	CH ₄ , % vol.	CO ₂ , % vol.
Experimental setup 1									
1.5-2	0.2-0.3	1.0	0.1-0.2	-	650-750	2.3-4.2	3.6-4.3	0.5-2.7	7.0-8.5
Experimental setup 2									
6.0	0.6-2.1	2.5	0.3	-	650-750	1.5-5.1	3.2-4.3	0.2-0.8	10-12
5.0	0.5-0.6	1.0	0.2-0.3	20-80	650-700	3.8-6.8	6.3-12	0.7-1.6	14-15
Experimental setup 3									
0.8	10	-		-	700	6-7	12-18	5-9	7-8
0.8(Ar)	10	-		-	700	6-7	1.5-2.5	12-15	2-3

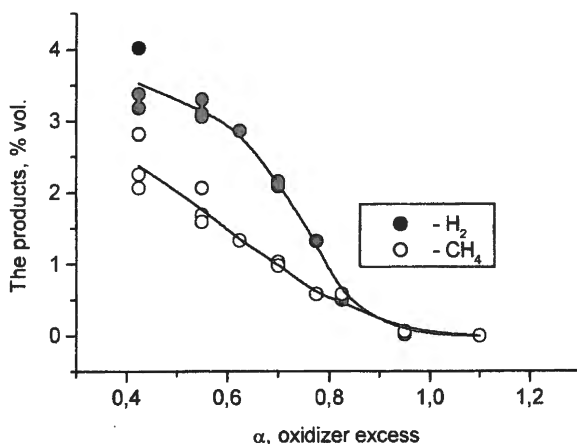


Fig. 4. Concentrations of CO and H₂ vs. coefficient of the oxidizer excess (α) (α = added oxidizer / stoichiometric needed oxidizer).

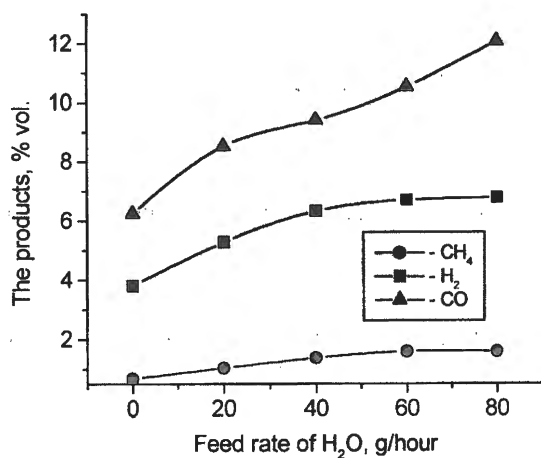


Fig. 5. Concentrations of CO, H₂ and CH₄ vs. feed rate of H₂O

PP-10

Table 2. Specific output of products of pyrolysis and gasification in setup 2

Product	Specific output of products of pyrolysis and gasification (g/kg of biomass)		
	Experiment, 700°C	thermodynamic calculations at 700°C	Torn S.Q. et. al., data at 800°C [7]
H ₂	33.9	29.4	10.8
CO	784.5	411.8	180.9
CH ₄	48.6	0.003	31.0

Conclusions

The biomass pyrolysis and gasification in the setups comprising catalytic fluidized bed reactors (CHGs) were studied. The composition of the gaseous products of these processes was shown to depend substantially on the experimental conditions and the biomass feed rate. Using steam-air mixture for biomass gasification allowed to increase of CO and H₂ concentrations in the reaction products.

Acknowledgement. This work was supported by NWO grant 2000.

REFERENCES

1. Z.R.Ismagilov, A.S.Noskov. Proceedings of 16th Mendeleev Congress on General and Applied Chemistry, 1998, part 2, p. 420.
2. G.K.Boreskov, E.A.Levitskii, Z.R.Ismagilov. Zh. Vses. Kh. Ob-va, 1984, vol. 29, p. 379.
3. V. N. Parmon, Z. R. Ismagilov, M. A. Kerzhentsev, Perspectives in Catalysis, a "Chemistry for 21st Century monograph", J. M. Thomas, K. I. Zamaraev eds., Blackwell: Oxford, 1992, p. 337.
4. Z. R. Ismagilov, M. A. Kerzhentsev, Catalysis Today, 1999, vol. 47, p. 339.
5. W. Wang, N. Padban, Z. Ye, G. Olofsson, A. Andersson, I. Bjerle, Ind. Eng. Chem. Res., 2000, vol. 39, p. 4075.
6. M. Gabra, E. Pettersson, R. Backman, B. Kjellstrom, Biomass and Bioenergy, 2001, vol. 21, p.351.
7. S. Q. Torn, C. M. Kinoshita, D. M. Ishimura, Fuel, 1998, vol. 77, No. 3, p.135.

THE INFLUENCE OF INERT IMPURITIES ON THE CATALYST LIFETIME AND PROPERTIES OF NANOFIBROUS CARBON PRODUCED BY UTILIZATION OF DILUTED HYDROCARBON GASES

D.G. Kuvshinov, G.G. Kuvshinov, A.M. Glushenkov

Boriskov Institute of Catalysis SB RAS, Prosp. Ak. Lavrentieva 5, Novosibirsk 630090, Russia

Abstract

Experimental studies were focused on feasibility of utilization of hydrocarbons diluted with inert gases (for example, associated oil gases) in the course of synthesis of nanofibrous carbon. The carbon yield and catalyst lifetime were studied depending on parameters of the initial reaction mixture. It was discovered that varying the composition of the initial gas mixture allowed textural characteristics of the carbon product to be controlled.

Introduction

Synthesis of nanofibrous carbon by decomposition of hydrocarbon gases over metal-containing catalysts has become of ever-increased interest in the recent years. Prospective application areas of this material are catalyst supports [1], electrode materials [2], supports for immobilization of biologically active substances [3] and additives to polymers [4]. Besides, nanofibrous carbon behaves as a good adsorbent that makes it useful for cleaning wastes from harmful impurities [5].

The material is a collection of carbon fibers with diameter distribution between 3 and 500 nm. Nanofibers are structured in the graphite-like manner. Depending on the catalyst type and reaction conditions, the basic graphite planes may be arranged either as a kind of coaxial cylindrical system (multi-layer nanotubes) or at some angle to the fiber axis to form a system of cones put one into another or a package. The use of high-loaded metal-containing catalysts allows the nanofibrous material to be produced not only as individual fibers or unstable conglomerates to be easily dusted but also as porous granules [6] built-up by densely packed interlaced nanofibers.

Iron, nickel, cobalt and alloys thereof are most practicable catalysts for synthesis of carbon nanofibers, hydrocarbons and carbon monoxide being used as the hydrocarbon gaseous feedstock. The process is achieved at the temperature range of 700-1200 K. Mechanisms of formation of individual nanofiber and porous granules are discussed elsewhere ([4,7] and [6], respectively).

The simplicity of the process makes it possible to use associated oil gases as the hydrocarbon feedstock. At present these gases are not utilized but torch burnt at remote little-inhabited regions of oil extraction where their utilization in ordinary way is unprofitable. The wastes cause

PP-11

environmental problems at these regions. The application of the proposed process will allow the wasteless utilization of associated oil gases to produce valuable products, hydrogen and nanofibrous carbon that also can be used to abate environmental pollution.

Associated oil gases often contain, apart from hydrocarbons, inert impurities that may have a considerable impact on the efficiency of process of hydrocarbon decomposition and on properties of the produced carbon materials. At the same time, we failed to find any papers dealing with the influence of the inert impurities in the reaction medium on the synthesis of the nanofibrous material.

The aim of the present paper was to elucidate what would be the effect of dilution of the initial mixture (the presence of inert impurities in the reaction medium) on parameters of the process of synthesis of nanofibrous carbon.

Experimental

Experiments on synthesis of nanofibrous carbon material were carried out using an installation providing ideal gas mixing in a fluidized bed reactor. The mixture was prepared and fed to a quartz microreactor with a loaded catalyst. The microreactor was thermostated at a preset temperature. During the reaction, the microreactor was forced vibrating along vertical.

Major experiments were aimed at establishment of dependencies of the total yield of the carbon product and the catalyst deactivation rate on parameters of the reaction medium. The experiments were conducted until the complete catalyst deactivation. The outlet gas mixture was analyzed chromatographically during the process that allowed the kinetics of catalyst deactivation to be studied. As soon as the process was completed, the produced carbon was unloaded from the reactor and weighed to determine the product mass.

The percentage of inert impurities was varied from 0 to 90% during experiments. Nitrogen, argon and helium were used as inert impurities. Experiments were carried out at atmospheric pressure. The mixture was fed into the reactor in the amount to provide constant consumption of the methane constituent at the level corresponding to that in experiments with pure methane ($120 \text{ l} / (\text{h} \cdot \text{g}_{\text{cat}})$). Temperature was varied in the range of 475-575°C. The carbon material was synthesized using a Ni-containing catalyst prepared by co-precipitation. The components were precipitated from aqueous solutions of $\text{Ni}(\text{NO}_3)_2 \cdot 6\text{H}_2\text{O}$ and $\text{Al}(\text{NO}_3)_3 \cdot 9\text{H}_2\text{O}$ taken in proper proportion with NaOH used as the precipitating agent [8].

Additional experiments allowed the catalyst activity and characteristic diameter of produced nanofibers to be estimated depending on the synthetic conditions. In these experiments,

nanofibrous carbon was synthesized during 2.5 hours. After that time, the reactor was detached from a thermostated furnace and immersed in cold water to provide fast cooling. Transmission electron microscopy with a microscope JEM-100CX (limit resolution 2 Å, accelerating voltage 100 kV, spherical aberration of the object lens 2.8 nm; magnification 10000 to 100000) was used for characterization of samples obtained.

Results and discussion

Fig.1 illustrates experimental results obtained with methane/argon mixtures. When the inert gas is added, the total carbon yield (the yield observed after complete catalyst deactivation) decreases. The influence of inert impurities is not noticeable at the range of low concentration but becomes more and more apparent as the argon concentration increases.

Besides, a regular decrease in the carbon yield at temperature elevation is observed at any concentration of the inert impurity. Probably, the decrease results from more rapid catalyst deactivation at relatively high temperatures.

The catalyst lifetime depends considerably on the inert impurity concentration in the gas mixture. Fig. 2 shows methane conversion *versus* process time at different argon concentration in the reaction mixture. All the curves are plotted for the same temperature (535°C) of synthesis of nanofibrous carbon. The time of complete catalyst deactivation shortens with an increase in the inert impurity concentration. In particular, the deactivation is observed just after the gas mixture starts feeding into the reactor at high concentrations of inert impurities.

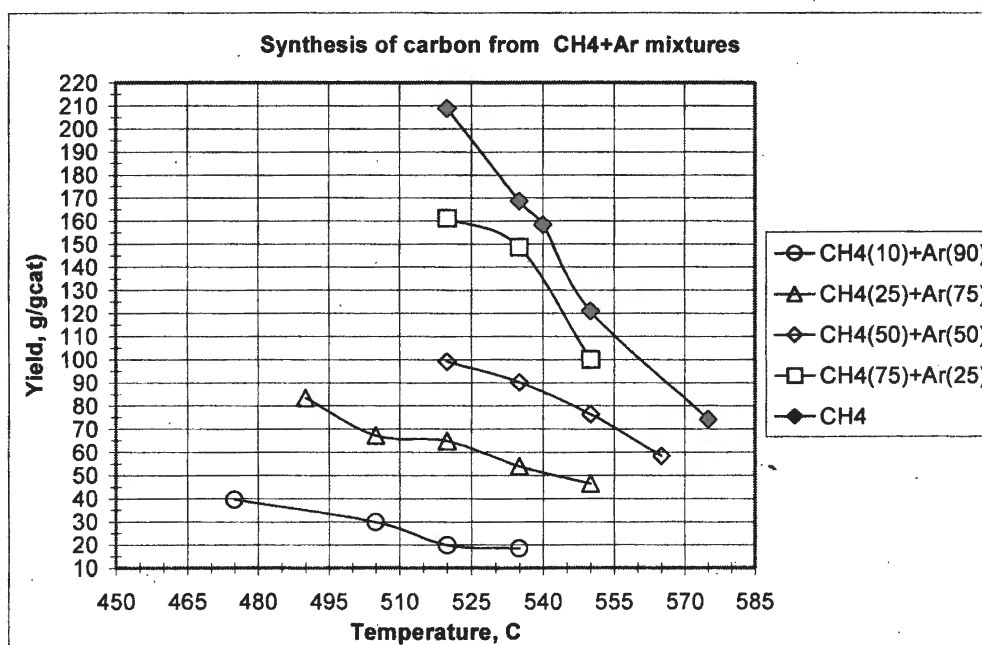
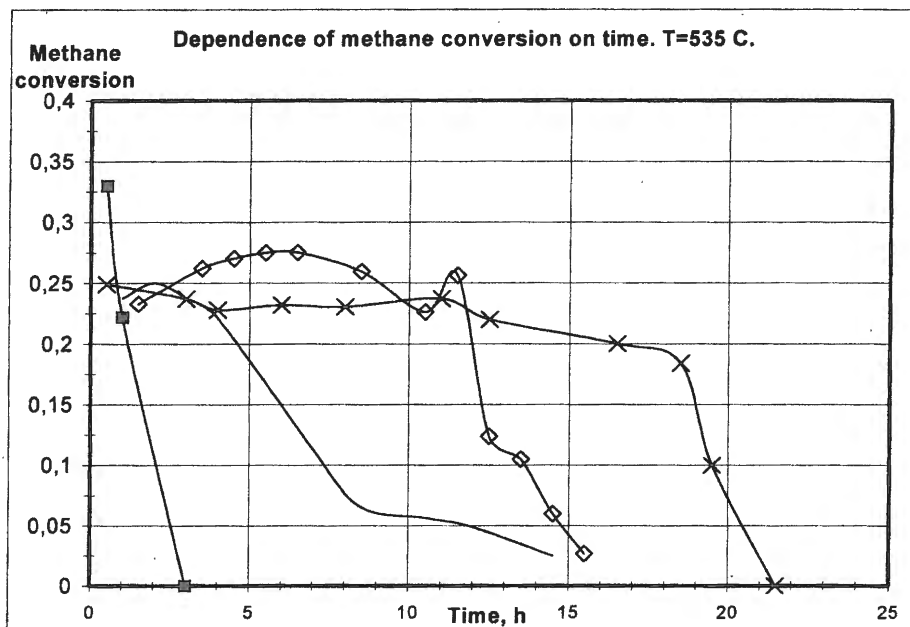


Fig. 1. Influence of argon concentration in methane on carbon yield



× - Initial mixture CH₄(100%); ◊ - Initial mixture CH₄(90%)+Ar(10%); — Initial mixture CH₄(80%)+Ar(20%); ■ - Initial mixture CH₄(10%)+Ar(90%).

Fig. 2. Dependence of methane conversion on the time of catalyst operation at different proportion of argon in the inlet mixture

Comparison of the experimental data allows the conclusion that a decrease in the carbon yield at high concentrations of the inert gas results from a faster catalyst deactivation under these conditions. The conclusion is supported by electron microscopic data. Deactivated particles of the active phase of the catalyst encapsulated with the carbon layer are observed in a considerable amount in 2.5 hour after beginning of the process in the samples synthesized at high concentrations of the inert gas.

It should be noticed that the above phenomena were independent of the nature of the inert gas. Similar behavior of methane mixtures was observed with nitrogen, helium and argon. When the mixture was diluted with these inert gases, the carbon yield and deactivation rate varied in the same manner in all the cases with close quantitative ratios.

As the concentration of inert impurities in the gas phase increases, the size distribution of catalyst nanoparticles and, as a consequence, that of fibers grown thereon changes. With 100% methane used as the feedstock, the average diameter of nanofibers ranges between 30 and 40 nm that is in agreement with the results of previous work [9] achieved with the same catalyst. At a high concentration of the inert impurities the average diameter of nanofibers decreases considerably to fall into the size range below 20 nm. This effect of changes in the characteristic size of nanofibers was unknown before. The result obtained makes it possible to predict probability of variations in the textural characteristics of the carbon material (granule

porosity and diameter of the nanofiber constituents) due to changing of the inert impurity concentration in the reaction mixture.

Analysis of experimental data on the influence of inert impurities on the carbon yield and catalyst deactivation rate led to assumption that the inert gas does not have in itself any direct effect on the process of nanofiber carbon growth. Nevertheless, the presence of the inert impurity in the system gives rise to the dilution to decrease absolute concentrations of methane and hydrogen. The presence of hydrogen in the reactor prevents deactivation of catalyst nanoparticles due to impediment to formation of the encapsulating carbon layer.

This assumption is in agreement with literature data [10]. The authors of this paper studied the catalyst deactivation during decomposition of propylene. The principal deactivation mechanism was, as in the present work, encapsulation of active catalyst particles. The authors discovered that catalyst was considerably less deactivated in the presence of hydrogen in large amount.

Additional experiment at a higher pressure and $T=550^{\circ}\text{C}$ was conducted in order to elucidate if there is indeed the influence of hydrogen. No inert impurity was used but the inlet gas was methane alone at excess pressure of 1.2 atm. As expected, the carbon yield was 205.3 g/g_{cat} that was 60% higher than that observed at standard pressure.

Conclusion

The results obtained demonstrate that inert gases can be used for synthesis of nanofibrous carbon materials. The texture of carbon material can be controlled by varying the concentration of the inert impurities in the reaction medium.

Thus, the process of synthesis of nanofibrous carbon can be used for wasteless utilization of various diluted hydrocarbon gases (including associated oil gases). Due to its good adsorption properties, the reaction product – nanofibrous carbon – also can be used for environmental protection.

Acknowledgement

The present work is supported by the U. S. Civilian Research & Development Foundation for the Independent States of the Former Soviet Union (CRDF), Award No. REC-008

References

1. Rodriguez N.M., Kim M.S. and Baker R.T.K., *J. Phys. Chem.* 98 (1994), p. 13108.
2. Frysz C.A., Shui X. and Chung D.D.L., *J. Power Sources.* 58 (1996), p. 41.
3. G. A. Kovalenko et. al., *Carbon* 39 (2001) 1033-1043.
4. K. P. De Jong, J. W. Geus, *Catal. Rev. – Sci. Eng.*, 42(4), 481-510 (2000).
5. V.I. Zheivot, E.M. Moroz, V.I. Zaikovskii et al., *Doklady Akademii Nauk*, 1995, v.343, No.6, p.781.
6. G. G. Kuvshinov et. al., *Carbon* 37 (1999) 1239-1246.
7. N. M. Rodriguez, *J. Mater. Res.*, 8 (1993), p. 3233.
8. Sh. K. Shaikhutdinov et. al., *Appl. Catal. A: General*, 1995, 126 (1), p. 125-139.
9. G. G. Kuvshinov et. al., *Carbon* 36 (1998), 87-97.
10. J. Rostrup-Nielsen, D. L. Trimm, *J. of Catalysis* 48, 155-165 (1977).

THE INFLUENCE OF STRUCTURE AND CHARACTER OF DISTRIBUTION OF
PALLADIUM ON THE SURFACE OF CATALYST ON ITS ACTIVITY IN
REACTION OF HYDROGENATION OF DIENES

A.A.Lamberov, R.G.Romanova, E.Yu.Sitnikova, Kh.Kh.Gil'manov*, S.R.Egorova

Kazan State Technological University, 420015, Kazan, K.Marx str., 68, Russia
e-mail: rrg@kstu.ru

**JSC "Nizhnekamskneftekhim", Nizhnekamskneftekhim, Russia*

In present time sufficiently strict demands are laying on the quality and purity of oil products, for example, on the content of admixtures of diene hydrocarbons. The most effective catalysts for selective hydrogenation of diene hydrocarbons are supported palladium catalysts. The main disadvantages of these catalysts are their low selectivity, leading to the loss of purpose products, and also proceeding of the-processes of coke formation. In connection with mentioned reasons, the development of scientific fundamentals of obtaining of efficient catalysts for hydrogenation of diene compounds became at present time an actual problem. The aim of this investigation is to study the influence of the support structure and also of palladium distribution on the surface of catalyst on its catalytic activity in the reaction of hydrogenation of dienes to hydrocarbon fraction C₅-C₉.

Investigation of composition, surface and structural characteristics for a number of industrial and experimental standards of catalysts for selective hydrogenation of diene hydrocarbons to fraction C₅-C₉ was carried out with the use of complex of physico-chemical methods, such as thermodesorption of nitrogen, diffractometry, X-ray-fluorescence analysis, flaming and atomic-absorbitive photometry. A number of catalysts, taken for investigation, have the wide variations of distribution and quantity of palladium, of phase composition and porous structure of aluminum oxide as supporter. Catalytic activity of investigated standards in reaction of hydrogenation of pyrobenzine in small-scale reactor of flowing type with the volume of loading 6 cm³ was determined. The carried out tests of catalytic activity of industrial and experimental standards of catalysts and analysis of structural characteristics showed, that the catalysts, having the surface distribution of active component on the support - γ -Al₂O₃ with tetragonal symmetry are the best for the process of hydrogenation of diene hydrocarbons.

XPS STUDY OF METAL-SUPPORT INTERACTION IN Ru/MgO CATALYST FOR LOW-TEMPERATURE AMMONIA SYNTHESIS

Yu.V. Larichev^{a,b}, B.L. Moroz^b, I.P. Prosvirin^b, V.A. Likholobov^{a,b}, V.I. Bukhtiyarov^b

^aNovosibirsk State University, Novosibirsk 630090 (Russia); e-mail: prsv@catalysis.nsk.su

^bBoreskov Institute of Catalysis SB RAS, Novosibirsk 630090 (Russia); fax. (+7-3832)342453;
e-mail: moroz@catalysis.nsk.su

Introduction

Metallic ruthenium catalysts has proved to permit milder operating conditions in ammonia synthesis compared with the magnetite-based systems, such as low synthesis temperatures and pressure (70-105 bars vs. 150-300 bars), while maintaining higher conversion than a conventional Fe-K₂O-Al₂O₃ catalyst [1]. The activity of Ru/support catalysts in ammonia synthesis strongly depends on the support nature and increases in the following order: support = carbon < TiO₂ < Nb₂O₅ << Al₂O₃ << MgO [2]. It has been suggested [3] that dissociative chemisorption of N₂ on Ru metal, which is the rate-determining step of ammonia synthesis, is promoted by electron donation from basic MgO surface to Ru particles. However, the experimental data, which have been published yet [4], look insufficient for making the strong conclusions on the type of electronic effect of MgO to supported Ru particles. Here we report the data of further characterization of Ru/MgO system by XPS and high-resolution transmission electron microscopy (HRTEM) techniques.

Experimental

Magnesium oxide (prepared in BIC; surface area, 135 m²/g; fraction 0.25-0.50 mm) calcined in a dry airflow at 450°C and stored under Ar was used as a support. The weighted amount of MgO was incipient wetness impregnated with an acetone solution of Ru(OH)Cl₃ at room temperature (RT) for 10-15 min. The sample was dried by blowing air at RT, than by outgassing at RT for 2h and at 60°C and 0.02 Torr for 6 h. To attain the desirable content of Ru in the sample the impregnation run was repeated 3 times due-to low solubility of Ru complex in acetone. The reduction of Ru(OH)Cl₃/MgO precursor was carried out in a tube fixed-bed glass reactor in flowing H₂ (80 ml/min) by heating the sample up to 450°C during 2 h and keeping at this temperature in a H₂ flow for another 6 h. The reduced Ru/MgO sample was cooled to RT, unloaded in an argon flow and stored in sealed glass ampoules under Ar or *in vacuo*.

PP-13

The resulting sample contains 4.2 wt.% of Ru, as determined by X-Ray fluorescence spectroscopy.

For XPS studies the samples were pressed into a Ni grid immediately after unsealing the storage ampoules and transferred to a test chamber (the duration of sample stay in air during these manipulations was ≤ 5 min). The vacuum in the test chamber was maintained at 10^{-6} mbar. H_2 was then admitted at a pressure of 1 bar, and the samples were re-reduced under static conditions at $350^\circ C$ for 1.5 h, followed by outgassing ($1-5 \cdot 10^{-8}$ mbars) the samples at RT. The XPS spectra were recorded on a VG ESCALAB HP spectrometer using the non-monochromatic radiation of AlK_{α} ($E_{hv} = 1486,6$ eV, 200 W power). The binding energy (BE) scale was calibrated relative to the peaks of $Au4f_{7/2}$ (84.0 eV) and $Cu2p_{3/2}$ (932.6 eV). Charging was corrected using the $Mg2s$ peak (88.1 eV) as internal standard. The charging factor was determined as the difference between the measured and tabulated values of BE.

The HRTEM measurements were performed on a JEM2010 electron microscope operated at 200 kV. Prior the examination, the sample powder was ground and suspended in ethanol. A drop of suspension was then mounted on a copper grid covered by carbon film, and the solvent was allowed to evaporate. Maximal resolution was 0.14 nm at 180000 magnification. From each sample about 250 particles were measured to determine a statistically justified averaged particle size and particle size distribution.

Results and discussion

Fig.1a compares XPS spectra, in the Ru 3d region, performed on the $Ru(OH)Cl_3/MgO$ and Ru/MgO samples. In this region Ru species show two peaks due to the $Ru\ 3d_{5/2}$ and $Ru\ 3d_{3/2}$ transitions. In the following the values of BE will be referred to the $Ru\ 3d_{5/2}$ peak. The BE of the peak at 282.1 eV for the $Ru(OH)Cl_3/MgO$ sample before reduction (Fig. 1a-1) coincides with the BE of $Ru\ 3d_{5/2}$ measured for the native bulk $Ru(OH)Cl_3$. Another peak around 285 eV assigned to be $Ru\ 3d_{3/2}$ is considered to contain the C 1s component; the appearance of C 1s peak is presumably caused by carbon impurity in the apparatus. After the reduction of Ru/MgO sample (Fig. 1a-2), the Ru 3d peak shifts to lower BE value (279.5 eV) indicating the presence of ruthenium in the metallic state. It should be noted that the BE value of 279.5 eV is by 0.6-0.8 eV lower than that is observed for bulk Ru metal ($E_b = 280.2$ eV). This shift of the Ru 3d peak is often interpreted as a result of electron transfer from a support to supported Ru metal particles [3].

To obtain information on the Ru particle size and size distribution, the reduced Ru/MgO sample was subjected to a HRTEM study. The electron micrographs demonstrate the contrast images of Ru particles of spherical shape, which are uniformly distributed over the support

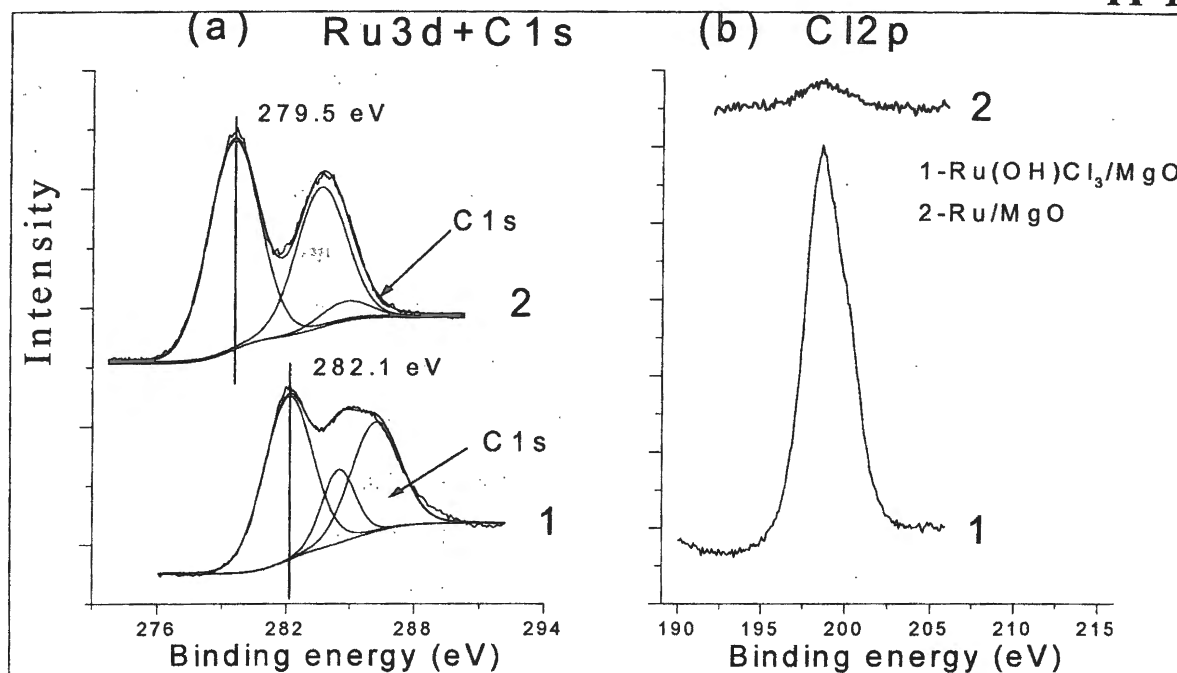


Fig. 1. Ru3d (a) and Cl2p (b) spectra of Ru/MgO sample before (1) and after reduction (2).

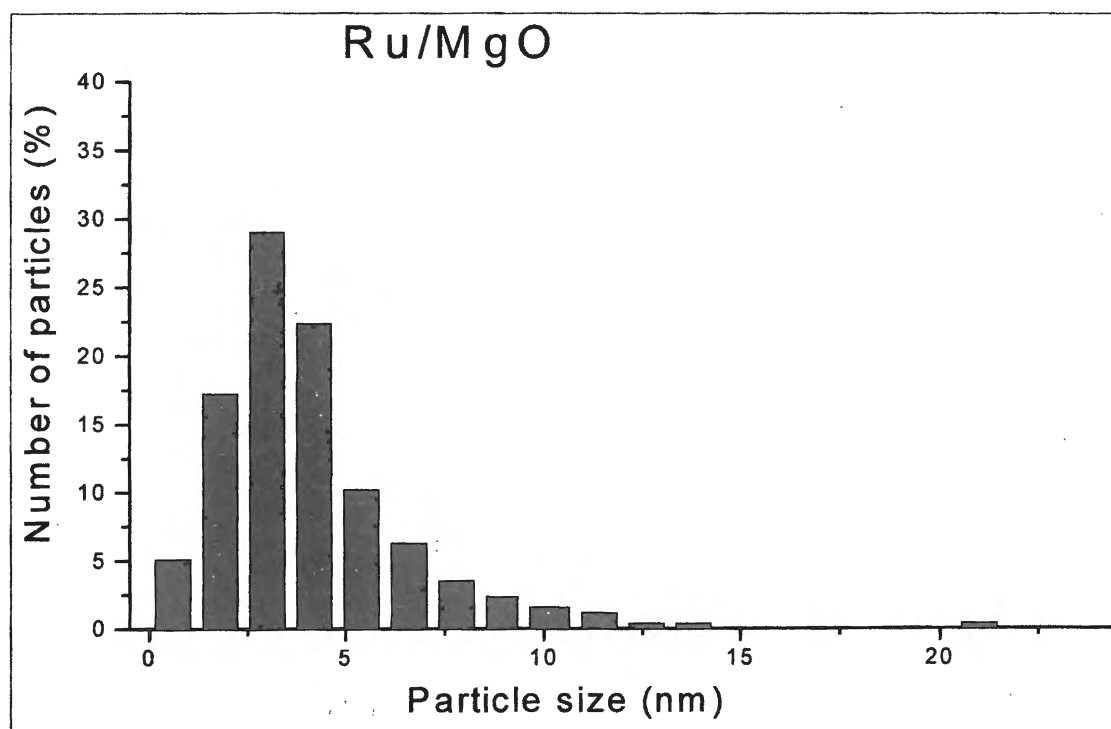


Fig. 2. Size distribution of Ru particles, supported on MgO.

The Ru crystallites having diameters d_i less than 10 nm constitute the majority of the metal particles. Besides, few larger Ru crystallites ($d_i \sim 10-18$ nm) were also present. The average diameter of Ru particles, $\langle d \rangle$ defined as $\langle d \rangle = \Sigma(n_i d_i) / \Sigma n_i$, is 4.08 ± 0.26 nm, as determined from the histogram.

PP-13

Fig. 1b exhibits XPS spectra, in the Cl 2p region, recorded for the Ru(OH)Cl₃/MgO and Ru/MgO samples. The surface Ru/Cl atomic ratio of Ru(OH)Cl₃/MgO sample, as determined from the integral intensities of Ru 3d and Cl 2p peaks (Figs. 1a-1 and 1b-1) was 0.65, *i.e.* *ca.* 2 times higher than the Ru/Cl ratio of 0.36 found for native Ru(OH)Cl₃ in agreement with the stoichiometric ratio. This increase in the Ru/Cl ratio may be caused by hydrolysis of Ru(OH)Cl₃ under H₂O traces containing in acetone and/or by partial substitution of Cl ligands of native compound for OH groups on MgO surface during the impregnation. Upon reducing the Ru(OH)Cl₃/MgO sample, the Cl 2p spectrum (Fig. 1b-2) shows a further sharp decrease in the peak intensity. The surface Ru/Cl ratio was increased by a factor of about 10 (Ru/Cl = 6.2) obviously due to conversion of hydroxychloride complexes of Ru into metallic Ru. An insignificant amount of chlorine still remains after reduction on the sample surface presumably as MgCl₂ formed due to the reactions of Ru(OH)Cl₃ and/or HCl with MgO [5].

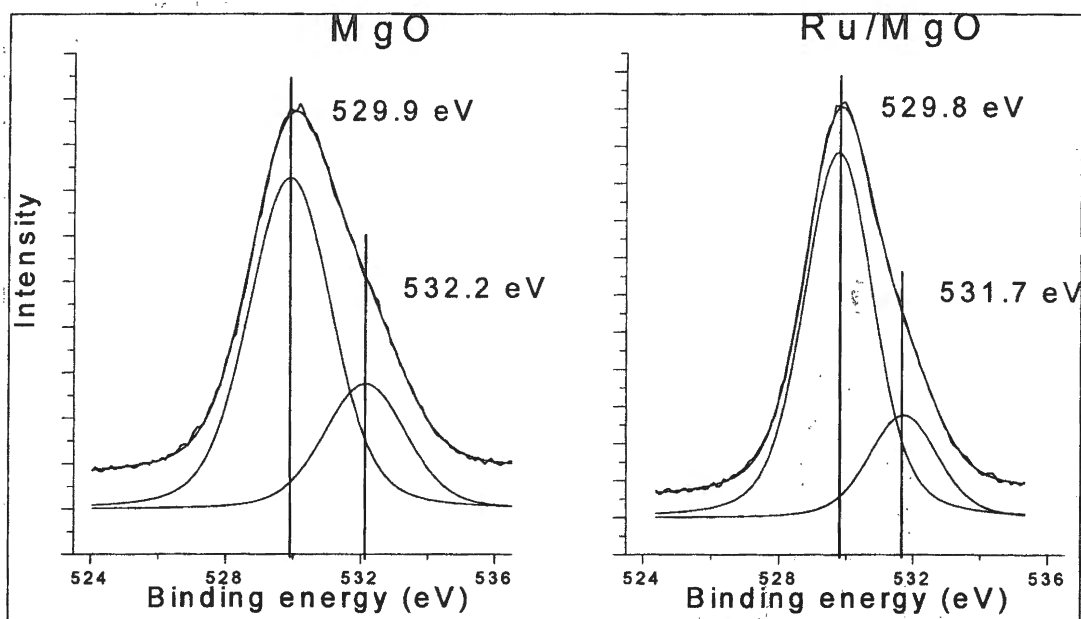


Fig. 3. O1s spectra of MgO and Ru/MgO.

Fig. 3 presents XPS spectra of MgO and Ru/MgO samples in the O 1s region. The both spectra contain a peak of asymmetric shape suggesting the presence of different surface states of oxygen. Deconvolution of this peak fits very well by using a pair of components, respectively, at 529.9 and 532.2 eV in the case of MgO bulk or at 529.8 and 531.7 eV in the case of Ru/MgO. The component at higher BE (about 530 eV for the both samples) is related to O²⁻ ions of MgO lattice, whereas the second component can be assigned to OH groups on MgO surface [6]. The shift of the second component by 0.5 eV to lower BE observed in the

spectrum of Ru/MgO as compared with the spectrum of pure MgO may derive from interaction of surface OH groups with supported Ru particles leading to the appearance of a negative charge on oxygen atoms. However, this assumption is in contradiction with the fact that the Ru 3d peak observed in the spectrum of Ru/MgO sample is shifted to lower BE values; this shift may show that Ru metal particles, when supported on MgO, also are negatively charged.

Meanwhile, the appearance of a negative charge on metal atoms may not be the only reason for the shift of corresponding XPS features towards lower BE values. Another possible reason is the differential charging effect observed, as it has been shown previously [7], for the non-conducting samples which consist of several phases significantly differing by their conductivity (for example, Ru metal and MgO support). This effect can not be corrected by using an internal standard. Indeed, the uniform shift of all peaks observed may result in underestimation of BE value for the phase possessing the higher conductivity, since its surface positive charge generated due to electron loss under photoemission would be less than that for the phase having the lower conductivity. Evidently, if the differential charging phenomenon be taken into account for the case of Ru/MgO system, the aforementioned contradiction may prove to be apparent.

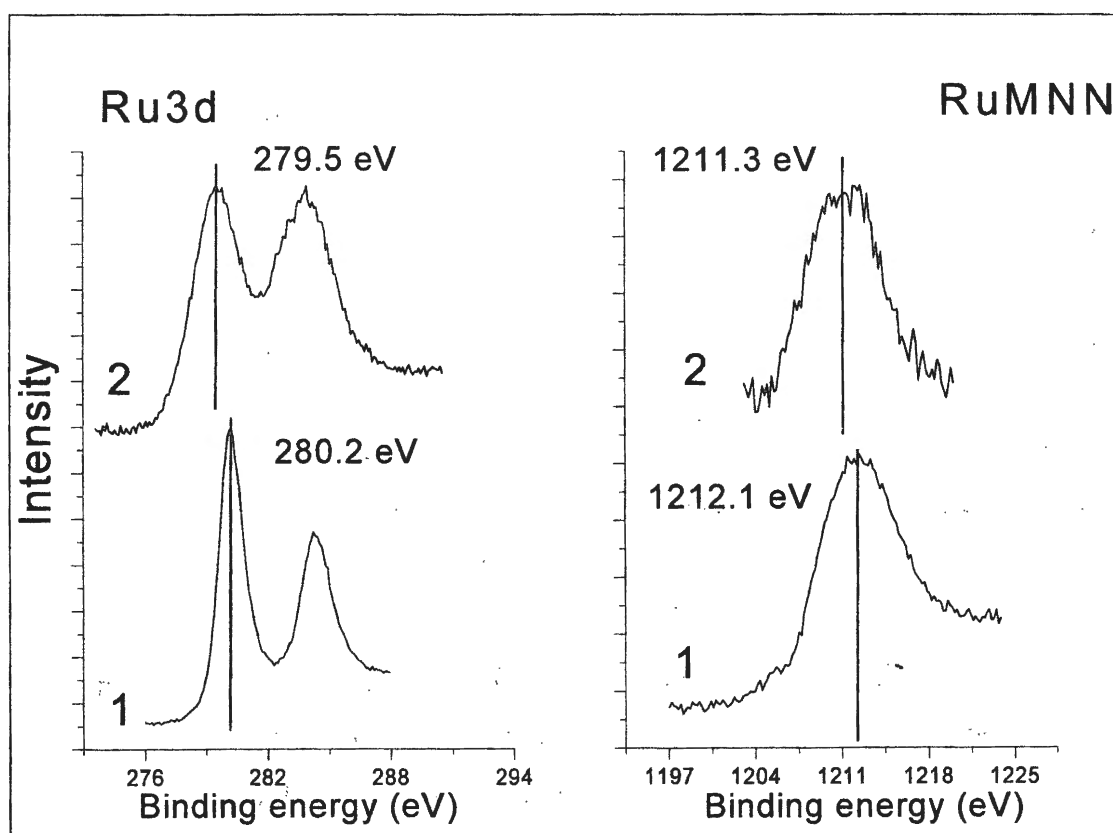


Fig. 4. Ru3d and Auger RuMNN spectra for of bulk Ru (1) and Ru/MgO (2).

PP-13

To check the presence of differential charging phenomenon, we recorded the Ru 3d and Auger Ru MNN spectra (Fig. 4) for the samples of bulk Ru metal and Ru/MgO and calculated the corresponding values of Auger parameter, α by the formula

$$\alpha = KE (\text{RuMNN}) + BE (\text{Ru3d}),$$

where KE is the kinetic energy of Auger electrons and BE is the binding energy of Ru 3d core level spectra. As a first approximation, the α value is supposed to be independent of the charging. Fig. 4 demonstrates that the values of Auger factor found for Ru bulk (554.7 eV) and Ru/MgO (554.8 eV) sample coincide confirming that the Ru/MgO sample contains metallic ruthenium. Therefore, the shift of Ru 3d peak in the spectrum of Ru/MgO to lower BE is caused by the differential charging effect and not related to the presence of a negative charge on Ru particles.

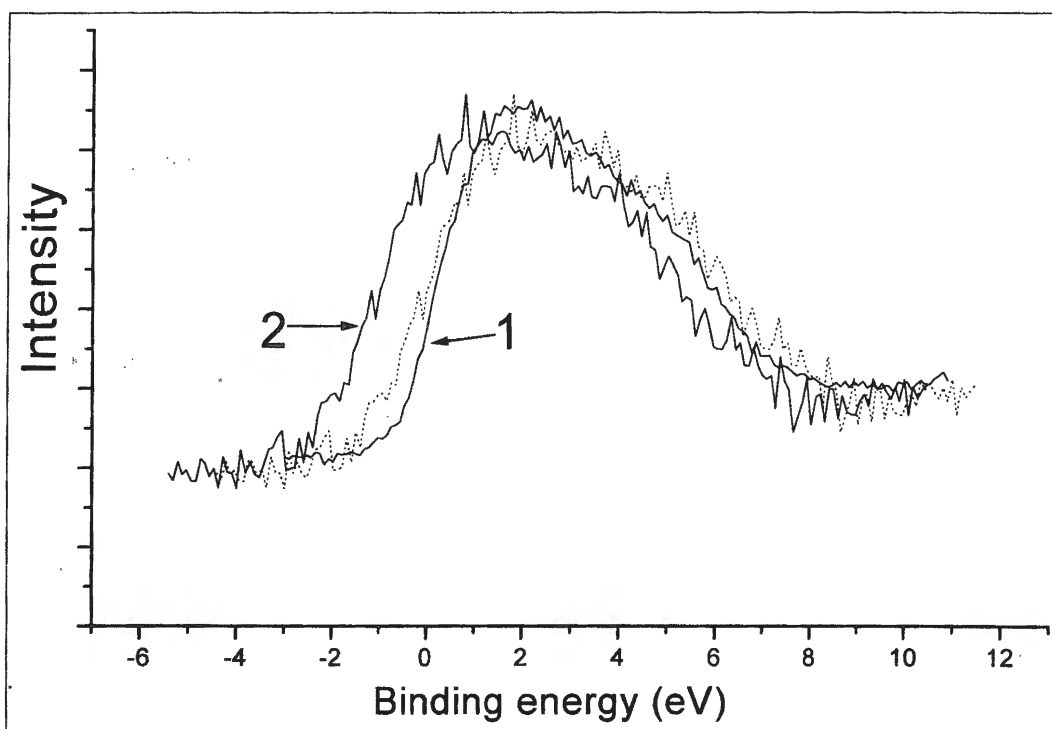


Fig. 5. Valence band spectra for bulk Ru (1) and Ru/MgO (2). The dotted curve was obtained after the shift curve 2 by 1.0 eV towards higher binding energy values.

The value of the differential charging effect can be estimated by a comparison of the valence band spectrum of supported metal particles with that of bulk metal [8]. It should be noted that this comparison gives a reliable result only if any changes of the valence band spectrum caused by the small sizes of supported metal particles may not be observed, *i.e.* if the mean diameter of these particles is higher than 2 nm [9]. Fig. 5 comprises the difference valence band spectrum of supported Ru particles (obtained by subtraction the spectrum of

MgO support from the spectrum of Ru/MgO sample) with the valence band spectrum of bulk Ru. The both spectra exhibit the lines of similar widths, but the line in the spectrum of supported Ru metal is shifted by 1.0 eV to lower BE values relatively to the line for bulk Ru. Since, according to HRTEM data, the mean diameter of supported Ru crystallites containing in the Ru/MgO sample is as large as 4.0 nm, it is reasonable to attribute this shift to the differential charging effect. Correspondingly, the value of differential charging can be estimated as equal to +1.0 eV. After the correction of the Ru3d spectrum of Ru/MgO (Fig. 1a-2) by this value, the BE of Ru 3d_{5/2} is changed to 280.5 eV and becomes by 0.3 eV higher than the BE of Ru 3d_{5/2} for bulk Ru. Based on this result, we assume the supported Ru particles are positively charged in fact. The last conclusion along with the observation of a negative shift of O 1s peak at 532.2 eV allows to suppose that Ru metal particles interact with the acidic OH groups of MgO surface, and this interaction is accompanied by transfer of electronic density from metal particles to oxygen atoms.

Thus, unlike that was suggested early [3,4,10], we found that the resulting electronic effect of MgO surface to supported Ru particles is the electron-accepting one. We did not observe any evidences for the electron-donating effect of lattice O²⁻ ions of MgO lattice to supported Ru metal, which may be manifested in a positive shift of O 1s peak at 530 eV, possibly due to the weakness of this effect or the considerably higher surface content of O²⁻ ions as compared with the atomic content of Ru. The increased electron-accepting properties of MgO support observed here may be caused by the presence of Cl⁻ impurity, which usually increases the acidity of a support [11]. In order to confirm or reject this assumption we are planning to study the Ru/MgO sample prepared by use of Cl-free Ru precursor.

In conclusion, it should be emphasized that the positive charging of Ru particles on MgO surface may be a reason for insufficiently high activity of unpromoted Ru/MgO catalyst in ammonia synthesis. The addition of alkali promoters (CsNO₃, Cs₂CO₃, potassium metal etc.) is necessary for increasing the activity of Ru/MgO catalyst up to practically acceptable level [4].

Acknowledgements

This work was supported by the Russian Foundation for Basic Research (the Project codes 00-15-99335 and 02-03-32681). Yu.V.L. and V.I.B. also acknowledge the financial support from Presidium of the Russian Academy of Sciences (integral project # 10.4). The authors wish to thank Prof. A.S. Ivanova and Mrs. N.V. Karasyuk for the preparation of MgO and Dr. V.I. Zaikovskii for the HRTEM study of Ru/MgO sample.

PP-13

References:

1. M. Muhler, F. Rosowski, O. Hinrichsen, A. Hornung, and G. Ertl, in *Stud. Surf. Sci. Catal.*, vol. 101, J.W. Hightower, W.N. Delgass, E. Iglesia, and A.T. Bell (Eds.), Elsevier, Berlin 1996, p. 101.
2. M. S. Khaja, R. K. S Rama, R. P. Kanta., *Indian J. Chem. A*, 32(1993) 383.
3. K. Aika, A. Ohya, A. Ozaki, Y. Inoue, and Y. Yasumori, *J. Catal.*, 92 (1985) 305
4. K. Aika and K. Tamary, in *Ammonia: Catalysis and Manufacture*, A. Nielsen (Ed.), Berlin: Springer, 1995. - p. 104 and references therein.
5. S. Murata and K. Aika, *Appl. Catal.*, 82 (1992) 1.
6. V.I. Nefedov, D. Gati, B.F. Dzhurinskii, N.P. Serguhin, and Ya.V. Salyn, *Zh. Neorg. Khim.*, 20 (1975) 2307 (in Russian).
7. V.I. Bukhtiyarov, I.P. Prosvirin, and R.I. Kvon, *J. Electron Spectrosc. Relat. Phenom.*, 77 (1996) 7.
8. G.K. Wertheim, *Z. Phys. B-Condensed Matter.*, 66 (1987) 53.
9. R.C. Bartzold, *Surface Sci.*, 106 (1981) 243.
10. K. Aika, T. Takano, and S. Murata, *J. Catal.*, 136 (1992) 126.
11. K. Tanabe, in *Catalysis: Science and Technology*, J.R. Anderson and M. Boudart (Eds.), Berlin:Springer, 1981 – Vol.2. - p. 231.

STUDIES OF SULFATED ZIRCONIA CATALYSTS DEACTIVATED IN ALKYLATION OF ISOBUTANE WITH BUTENES

A.V. Lavrenov*, E.A. Paukshtis, V.K. Duplyakin*, B.S. Bal'zhinimaev

Boreshkov Institute of Catalysis SB RAS, Novosibirsk, Russia

**Omsk Department of Boreshkov Institute of Catalysis SB RAS, Omsk, Russia*

Alkylation of isobutane with butenes is an essential process for production of the high quality gasoline. Sulfated zirconium oxide (SZ) have attracted considerable attention in the last few years due to its potential to form an active catalytic system to be used for hydrocarbon low-temperature conversion, including alkylation of isobutane. However, the fast deactivation of this kind of catalysts is a major drawback for commercial application.

The nature and the origin of organic residues, present in spent SZ catalysts after alkylation, have been studied by combined UV-VIS and FT-IR techniques. The bulk SZ was investigated, as well as silica supported SZ. The alkylation reaction was carried out in liquid phase at temperature 40°C in stirred tank reactor. The space velocity was $WHSV=0.05 \text{ h}^{-1}$ referred to the butenes. Deactivated SZ samples were recovered at different time-on-stream.

For all samples the three kinds of organic compounds are present: light hydrocarbons, such as alkylates and small oligomers, entrapped in the catalysts, high unsaturated byproducts as polyenes and stable alkyl substituted cyclopentadienes. The polyenes and cyclopentadienes are nonextractible and nondesorbed products. These compounds blockade active sites, which are accountable for alkylation reaction.

Deactivation of SZ by alkylation isobutane with butenes is likely the results of a series of reactions starting with the oligomerization of the butenes: butenes oligomers polyenes cyclopentadienes.

3D SIMULATION OF DIESEL ENGINE EXHAUST GASES CATALYTIC CONVERTER

A.A. Makarov, A.M. Khanov, A. Tzschatzsch*

Perm State Technical University, Perm, Russia

**ReMetall GmbH, Drochow, Germany*

Catalytic converters are a widely used approach to solve a problem of transport exhaust gases cleaning. In this paper we report on the system based on open cell nickel foam with special oxidation catalyst upstream of a particulate trap on railway diesel locomotive.

Catalytic converter should be integrated in exhaust system of diesel engine. In this case the main and the most strongest limitation for this catalytic system is that the pressure drop should not be more than 3 kPa. This limitation is due to keeping the working conditions of diesel engine without retrofitting or power loss. Also there are restrictions for converter size and shape (it should be mounted instead of locomotive muffler). Volume flow and speed of engine exhaust gases is up to $29,5 \cdot 10^3 \text{ m}^3/\text{hour}$ and 98,5 m/s. It is clear that in these hard conditions the construction of catalytic converter should be developed sophisticatedly.

The main aim of the present development is to achieve a minimum pressure drop with a maximum conversion of soot and NO_x . We used a finite elements method to simulate processes of gas distribution in converter. Three dimensional finite elements model was used, because the construction of converter did not have any symmetry axis and have only one symmetry plane. In our model there is two types of materials: free space and nickel foam, used as the catalytic supporter in our construction. Gases motion in foam structures is modeled using Darcy law. The simulated process is accepted to be stationary. Thermal conductivity and radiation processes are not modeled.

The results show that total pressure drop of catalytic converter is up to $3,25 \cdot 10^3 \text{ Pa}$ on the maximum load level of diesel engine. The results are confirmed by the tests performed in January 2002 on the real diesel locomotive in Germany. The measured pressure drop on the maximum load level is $3,22 \cdot 10^3 \text{ Pa}$. Also the analysis of simulation results shows that gas distribution in converter is significantly non-uniform along catalytic blocks. So the construction of converter should be improved to achieve low pressure drop.

REDOX NO_x ON SOOT PARTICULE TRAP**A.M. Makarov, A.A. Makarov*, A. Tzschatzsch*****Institute of Solid State Chemistry, Ural Department of RAS, Perm, Russia***Perm State Technical University, Perm, Russia****ReMetall GmbH, Drochow, Germany*

Engine and combustion improvements have substantially reduced NO_x and particulate from modern diesel engines. In this paper we report on the system based on nickel foam with special oxidation catalyst upstream of a particulate trap on railway diesel locomotive. Over the catalyst some of the engine-out NO emission is oxidized to NO₂, which is active for continuous oxidation of soot collected in the trap above 300°C. As a result of this regeneration process the trap is always lightly loaded with soot and the backpressure level is therefore very low. The oxidation catalyst naturally also leads to very low emissions of CO, hydrocarbons of fuel and soluble organic fraction of soot particles, containing carcinogenic poly-aromatic hydrocarbons. Dry carbon particulate is aggregated on three-dimensional structure of nickel-foam material of trap. The process of soot tapping is continuous when a filter is included in an exhaust assembly, but here soot destruction and reduction NO_x is also continuous at temperatures > 300°C.

The system consists of an oxidation catalyst and a particulate trap downstream the catalyst. Catalyst and trap consists of a three filter made of many porous nickel blocks and an electrical heater, which is planar shaped for wide-area and uniform heating. An electrical heater is set in the space between the blocks, so the accumulated soot in filter is heated and burnt out directly. The size and the coating of the catalyst is optimized to produce sufficient NO₂ for soot oxidation and therefore depends on the engine out NO_x and particulate emission and on the exhaust temperature. The total soot oxidized in the trap depends on the NO₂ content, temperature of exhaust gas and catalytic blocks and on the soot mass collected. Electronic control of heating devices and temperature at catalyst-trap system may be mounted with electronic engine system.

The system has been shown to reduce NO_x by 20% to 80% over a variety of cycles intended to reproduce driving conditions in railway.

OXIDATION CATALYST FOR GAS OXYGEN SENSORS

Malchikov G.D., Timofeev N.I.*, Bogdanov V. I.*, Tupikova E. N., Goryainova N.E.

The Korolev's Samara State Aerospace University, Samara, Russia

**JSC "Ekaterinburg Non-Ferrous Metal Processing Plant", Ekaterinburg, Russia*

The object of researches is the catalytic material representing metal (stainless steel, nickel and chrome steel, nickel) block prepared according to the technology of damping hardware products ("metalrubber") and covered with highly dispersed coating of Platinum Group Metals (Pt, Pd, Pt+Rh and Pd+Rh). The coatings are deposited by method of autoclave thermolysis of corresponding metal complexes. Platinum metals content does not exceed 0.1%.

The catalytic properties were investigated in model reactions of a complete oxidation of hydrocarbons (n-hexane). The high efficiency and stability of the block catalytic material in the processes of hydrocarbons combustion is shown. The conditions of the reaction transition from kinetic in outward diffusive area are defined. It is stated, that irrespective of the nature of catalytically active metal the reaction has the first order to hydrocarbon at multiple excess of oxygen. It is determined, that at contents of sulfur components (thiophene) $\leq 0.3\%$ in oxidable hydrocarbon the catalyst maintains high activity.

The developed catalyst has shown good results at laboratory's tests in the processes of the off-gases (operations, power engineering, transport) neutralisation and organic synthesis. We used the block catalyst as a nozzle for preparation of gas probe in oxygen sensors or as a nozzle at the exhaust of gases from the sensor at the server of hydrogen production.

The function of a nozzle consists in transformation of gas probe to equilibrium state at different initial non-equilibrium gas mixtures. As a result, the sensor signal does not depend on consumption and gas streams velocity.

The sensors work stable on a number of plants as a part of Automatic Control System of regulating fuel/oxidation ratio on generators of endogas, furnaces of grouting, control of shielding mediums and instillations of hydrogen production.

The work is supported by "Haldor Topse A/S" company.

STUDY OF Mo PRECURSOR SPECIES IN IMPREGNATION
SOLUTION OF AMMONIUM HEPTAMOLYBDATE

E.V. Matus, L.T. Tsykoza, Z.R. Ismagilov

*Boreskov Institute of Catalysis SB RAS, Prosp. Akad. Lavrentieva, 5
630090 Novosibirsk, Russia*

Mo/ZSM-5 catalysts are the most promising for dehydro-aromatization of methane to benzene. At the moment it is important to define the conditions of synthesis and to study the nature of active component of these catalysts [1-3].

A change in a ratio between monomeric and polymeric species of molybdenum regarding the concentration and pH of the impregnation solution will probably make a significant effect on the nature and number of active sites of Mo/ZSM-5 catalysts. We used the electron absorption spectra to study the dependence of structure of molybdenum species in the initial impregnation solutions of ammonium heptamolybdate on the concentration and pH of these solutions.

As the molybdenum concentration increases, the degree of absorption increases and an absorption edge shifts to the long-wave part of spectrum, that may indicate an increase in the degree of molybdenum polymerization [4]. The fact that the Buger-Lambert-Beer law is obeyed in two concentration ranges as $2 \cdot 10^{-6}$ – $5 \cdot 10^{-5}$ M and $2 \cdot 10^{-3}$ – 10^{-1} M suggests that the ratio of the light-absorbing molybdenum species is similar for the above solutions. When the molybdenum concentration is $5 \cdot 10^{-5}$ – $2 \cdot 10^{-3}$ M, this law does not work, suggesting that the molybdenum species are heterogeneous and their amount is different.

When the solution of ammonium heptamolybdate is alkalized, the absorption degree increases. For higher concentrations of molybdenum, the initial absorption edge shifts to the short-wave spectrum part (Fig.1). A change in the spectra shows that the polymeric molybdenum species transform into a monomeric molybdate-ion state [4,5]. In each case, as pH achieves some limiting value, there are no changes in the electron spectra. This indicates a complete transition of molybdenum into the monomeric species.

By contrast, when the ammonium heptamolybdate solution is acidated (the concentration of molybdenum is in the range of $2 \cdot 10^{-4}$ – 10^{-1} M), the initial absorption edge shifts to a more long-wave spectrum part (Fig.1). In this case, changes in the spectrum indicate an increase in the polymerization degree [4].

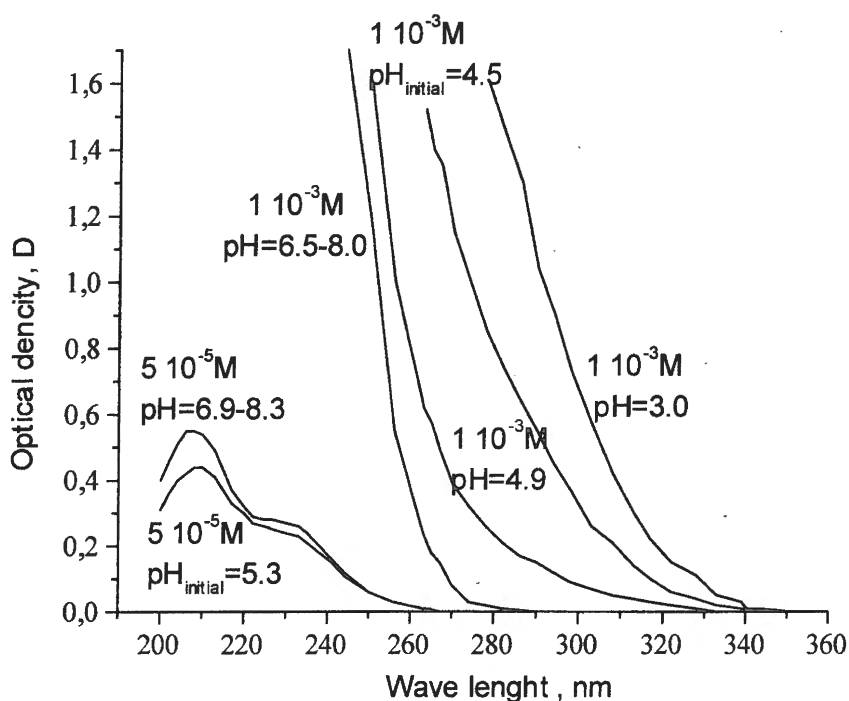


Fig. 1. Effect of pH on the shape of electron spectra of ammonium heptamolybdate solutions

The molar extinction coefficient of ammonium heptamolybdate solutions with different concentrations calculated for the fixed value of pH and specified wave length does not practically change over a wide range of molybdenum concentration, $2 \cdot 10^{-5}$ – 10^{-1} M, when $\text{pH} \geq 7$ (Fig. 2a). This indicates that the solutions contain molybdenum in the similar species. The fact that molybdenum exists only as a molybdate-ion state in the solutions with a concentration of $2 \cdot 10^{-5}$ M indicates that this monomeric species MoO_4^{2-} , typical for strongly diluted solutions of ammonium heptamolybdate, maintains at $\text{pH} \geq 7$ and high concentrations of molybdenum.

As follows from Fig. 2a, the dependence between the molar extinction coefficient and molybdenum concentration in the above solutions ($6 \cdot 10^{-4}$ – 10^{-1} M) changes also insignificantly when pH is fixed ($\text{pH} = 2$ – 4). For this concentration range, the degree of molybdenum polymerization increases and the polymeric species dominate if the solution is acidified. The fact that the molar extinction coefficient is constant in the molybdenum solutions indicates that either the ratio between different molybdenum polymeric species is equal or the species are of the same type.

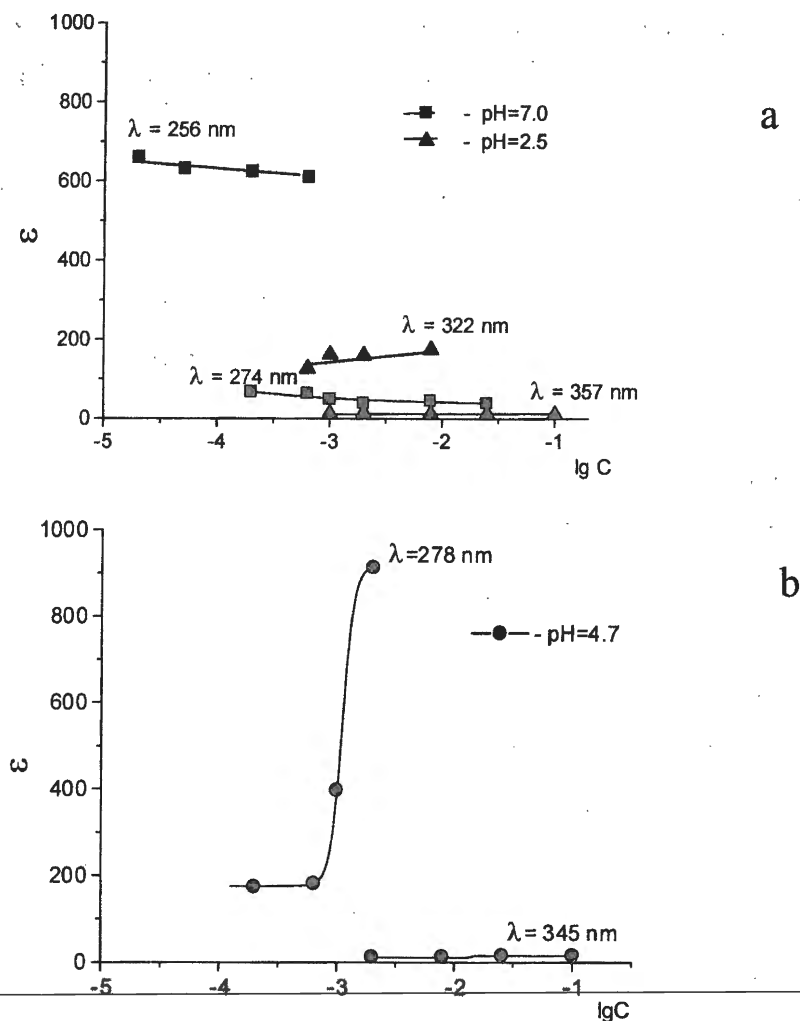


Fig. 2. Molar extinction coefficient (ϵ) vs. molybdenum concentration (C). The values of pH and wave length (λ) are fixed.

According to Fig. 2b, the molar extinction coefficient is not constant when the molybdenum concentration is varied and the fixed pH is 4-6.

Therefore, the experimental data suggest that the reaction of polymerization does not occur upon the low molybdenum concentration or increasing of the pH of solutions. In addition, there is a region where polymeric and monomeric molybdenum species exist at a time. When the concentration of molybdenum is higher or pH of the solution decreases, the monomeric species almost completely convert into the polymeric species.

ACKNOWLEDGEMENT

The authors would like to thank V.V.Kuznetsov for the discussion of results and INTAS 99-1044.

1. Wang L., Huang J., Tao L. et al // Catal. Lett. 1993. V. 21. P. 35.
2. Weskhuysen B.M., Wang D., Rosynek M.P. and Lunford J.H. // J. Catal. 1998. V.175. P. 338.
3. Chen L., Lin J., Zeng H.S., Tan K.L. // Catal. Com. 2001. V. 2. P.201.
4. Babko A.K., Pilipenko A.T. Photometric Analysis, Moskva, Khimiya 1968 (in Russian).
5. Baes C.F., Mesmer Jr.R.E. The hydrolysis of cations. John Wiley & Sons. New York. 1976. P. 253-257.

SOME ASPECTS OF THE REACTION MECHANISM OF OXIDATIVE DEHYDROGENATION OF ETHYLBENZENE TO STYRENE**N.I. Maximova, V.V. Kuznetsov*, Yu.V. Butenko*, G. Mestl, R. Schloegl***Fritz-Haber Institute, Berlin, Germany***Boreskov Institute of Catalysis SB RAS, Novosibirsk, Russia*

Because the styrene synthesis is one of the ten largest industrial processes in the world, there is a strong incentive to overcome the drawbacks of such a process. Among the several alternative processes proposed, such as dehydrogenation followed by oxidation of hydrogen, dry dehydrogenation in the presence of CO₂ and membrane technologies, the exothermic oxidative dehydrogenation (ODH) of EB to ST is one of the most elegant and promising reactions due to the absence of equilibrium limitations and lower operation temperatures.

The performances of various mainly inorganic oxidic catalysts for the ODH of EB to ST were characterized by a similar induction period, during which the increase of the catalytic activity could be correlated to coke formation. Subsequently, dehydrogenation activity was obtained over amorphous carbon catalysts, but low performances or low stability in an oxidative atmosphere hindered the potential interest of such materials. High and stable performances, as compared to technical catalysts, were recently reported for sp²-bonded carbon structures, such as graphite and carbon nanofilaments (CNF).

Non-planar sp²-bonded nanostructures are especially very active and promising for the realization of a technical application in the nearest future. It has been shown that the microstructure of the carbon materials was determining in order to obtain high and stable efficiencies. The structure-activity relationship and the nature of the active sites of such carbon catalysts still remain open questions.

The aim of the present work is to report influence of the carbon nature on the ODH performances via investigation of both non-planar sp³- and sp²-bonded nanocarbons.

Transmission electron microscopy (TEM), X-ray photoelectron spectroscopy (XPS), IR-spectroscopy, and BET surface area measurements were carried out in order to get more insight about the structure-function relationship of such nanocarbons as catalysts in the oxidative dehydrogenation reaction.

STM AND XPS STUDY OF THE MODEL SUPPORTED SILVER CATALYSTS.

Anna V. Nartova, Ren I. Kvon

Boriskov Institute of Catalysis SB RAS, Pr. Akademika Lavrentieva, 5, 630090 Novosibirsk Russia

E – mail: anna_nartova@ngs.ru

Introduction

The fundamental study of the supported metal catalysts is quite important for understanding and improving their catalytic behavior. The wide set of parameters, namely, the metal particles shape and size, the distribution at the support surface, their electron properties, etc. are known to dramatically affect the catalytic activity [1,2]. The support itself – the nature, surface structure and composition – in many respects determines these characteristics of the catalysts particles. The tandem of scanning tunneling microscopy and X-ray photoelectron spectroscopy is looking very promising when studying the supported systems as it would give the complementary information both about the particle / support morphology (STM) and about their electronic structure (XPS). Still, very often it is very difficult to apply these techniques to the direct study of “real”, i.e. industrial catalysts – either due to methodical restrictions or because the obtained data result in the overcomplicated or ambiguous interpretation. The common way to avoid these problems is the preparation of the special model catalytic systems. Me/HOPG (i.e. metal particles deposited at Highly Oriented Pyrolytic Graphite) systems are the simplest and most widely used ones. Still, the results and conclusions obtained for HOPG systems can hardly be adapted to the oxide supports (to say, alumina or silica), because the nature and the strength of the metal to substrate adhesion forces are absolutely different in these cases. On the other hand, the usual oxide support samples are non-conductive (except for titania and MgO single crystals [3]) and therefore they could not be studied directly by STM technique.

Some authors have reported on the successful application of Atomic Force Microscopy for the investigation of the alumina supported catalysts [4], and another team has achieved the interesting STM results by the preparation of very thin – and therefore remaining conductive – alumina layer over the surface of NiAl single crystal [5,6]. We have prepared another model support by the formation of the conductive alumina film over the metal substrate – Fe-Cr-Al alloy. Here we present the first results of the comparative of XPS and ex-situ STM study of two model supported catalysts – Ag/HOPG and Ag/Al₂O₃ film.

PP-20

Experimental

The microscopy study has been carried out in air by means of STM/AFM multi-microscope SMM2000T. The magnification has been varied from 2×10^4 for the maximal scan range of $6 \times 6 \mu\text{m}$ to 10^7 for the precise scans. We have used Pt tips cut by scissors. For HOPG samples STM pictures were acquired with 0.2 V bias and 3 nA tunneling current, while for alumina ones the scanning parameters were varied up to 2.2 V and 10 nA, correspondingly. The practical vertical (1 nm) and lateral (3 nm) resolution was evaluated by using fresh cleaved HOPG sample. To prove the received STM pictures are representative the sets of several (from ten to twenty) points at every chosen magnification were explored for the each sample. The histograms were plotted after analyzing of more than hundred observed particles.

All the sample preparation stages as well as XPS measurements were performed in the preparation chamber of VG ESCALAB HP electron spectrometer. XPS spectra were recorded using $\text{AlK}\alpha$ irradiation and calibrated against $\text{Au}4f_{7/2}$ ($\text{BE} = 84.0 \text{ eV}$) and $\text{Cu}2p_{3/2}$ ($\text{BE} = 932.7 \text{ eV}$) lines [7]. We have used the conventional UHV silver source with the massive Ag (99.99 purity) slab for the vapour deposition of metal particles. The temperature of the support sample and Ag source were measured by K-type thermocouples attached to back side of the sample holder and very near to the piece of silver, correspondingly. The pieces of 0.6 mm thick foil of ALFA-IV alloy (Allegheny Ludlum Corp.) have been used to prepare alumina samples. The major composition of the alloy includes Fe(74%), Cr(20%) and Al(5%).

Results and discussion

The study of Ag/HOPG system

The STM investigation of the Ag/HOPG samples has proved that the particles morphology strictly depends on the properties of the support. We have found the “decoration” effect when silver particles were preferentially located at the polyatomic steps or the damaged / distorted patches of graphite surface. Such particles had usually the hemispherical shape in contrast to their spheroid mates at flat surface. Thus we assume that silver particles have the high mobility over the graphite surface during the vapour deposition and, therefore, the temperature of the Ag source would be determinative for the particle size distribution. Indeed, just slight raising the Ag source temperature above 770 K has noticeably changed the size distribution (Fig. 1 a, b). It became more even – due to decreasing of the smallest

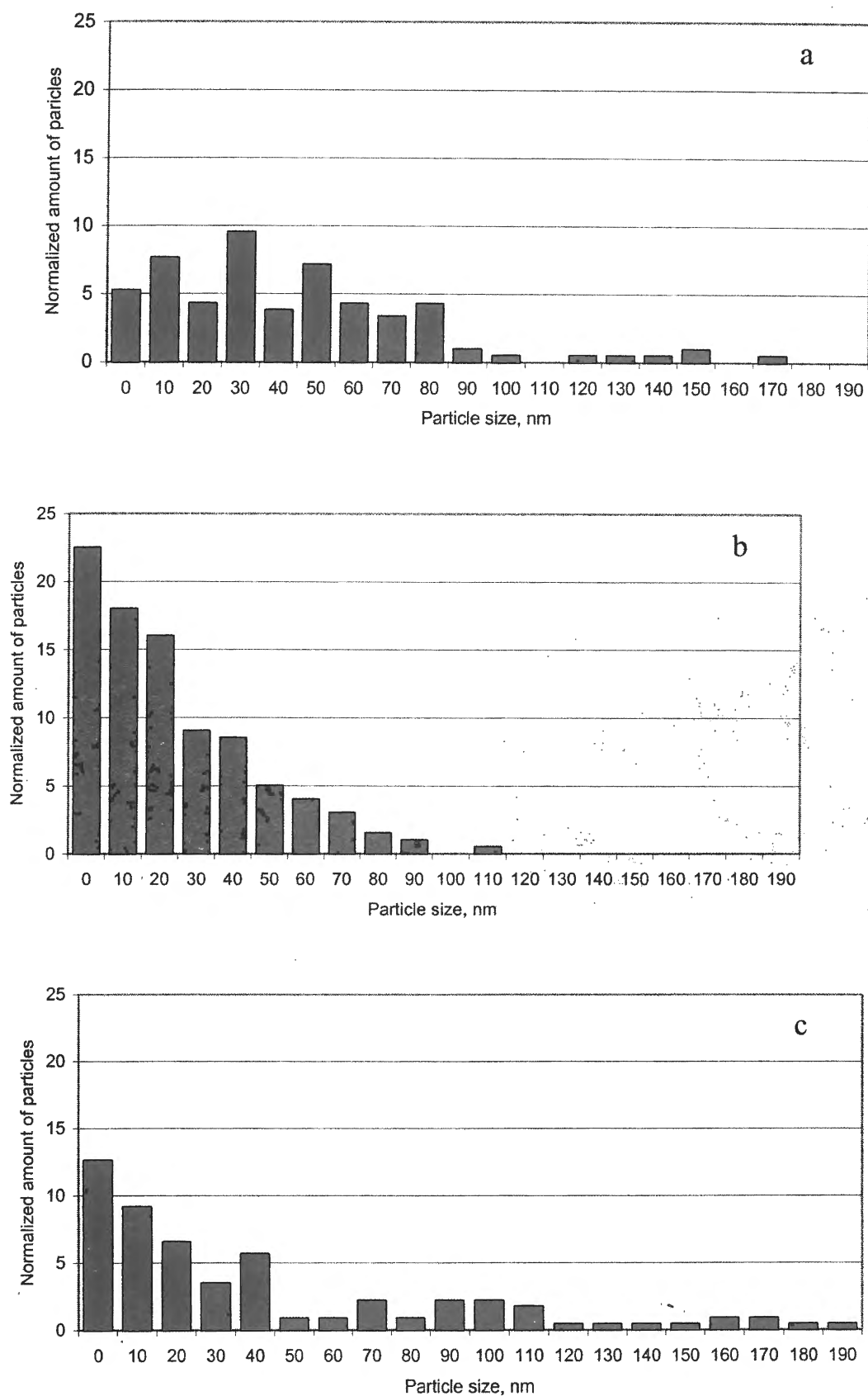


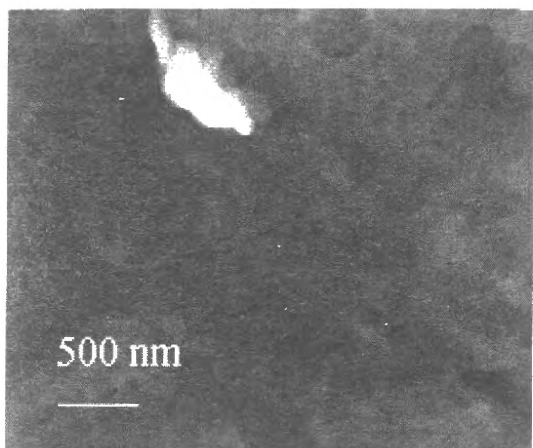
Figure 1. Particles size distribution histograms: a) for higher Ag source temperature; b) for normal Ag source temperature; c) after the normal procedure followed by the sample heating at 570 K

PP-20

(< 10 nm) particles amount and more broadened – as the very large (> 120 nm) particles appeared. The probable reasons are:

- at higher temperature the smallest particles can diffuse over the surface for the longer time and distance until they meet another one(s) or any graphite surface defect;
- the larger Ag clusters can initially leave the source;
- the incident Ag flux upon the sample surface is more dense.

The role of the surface diffusion is illustrated by the results of the 10 minutes heating of Ag/HOPG sample at 570 K (Fig. 1 b, c). One can see that again the fraction of smaller particles drops and very large Ag “pieces” are formed, but the size distribution remains asymmetric. Thus all factors listed above are likely to contribute to the resulted look of the size histogram for higher deposition temperature, but the further cross-linked experiments (with both HOPG sample and Ag source temperatures to be varied) are in need for better understanding.



As concerning with sample annealing effects (i.e. “thermal stability” of deposited silver particles), two main interdependent effects were observed: the growth of very large objects at the flat areas of the surface and the migration of smaller particles out of there. At higher magnifications we have succeeded to reveal that the appeared formations consist of the several smaller particles. Figure 2 shows a large silver particle ($3.3 \mu\text{m} \times 2.7 \mu\text{m} \times 73 \text{ nm}$) of 400 nm and the height of 40 nm (the latter is characteristics for the separate particles). We suppose that the stronger bonded to the surface particles (either fixed at point imperfections or just of larger size) are the centers of such agglomeration. One should note that we have failed to resolve the “fine structure” of medium (30-60 nm) objects. It obviously means the smallest particles are merged each other to form the united larger ones. The shape of the larger particles is mainly hemispherical while the isolated ones remain quasi-spherical, so that one probably can use the height profiles of the observed particles to rule out whether they are agglomerated or not.

The preparation of the model alumina support

Before the alumina film preparation all alloy samples were cleaned by argon etching to remove the organic contamination and oxidized layer of the surface. Then the samples were

annealed in vacuum at 870-930 K for 10-15 minutes. XPS spectra show that this procedure causes the dramatic increase of Al2s and O1s intensity (Fig. 3 a, b) indicating the surface segregation of aluminum and bulk dissolved oxygen. Al2s binding energy value of the main peak component (~ 120.1 eV) corresponds to oxide state of aluminum [7]. Still, some Al remains in metallic state, but the variation of the electron take-off angle results in the noticeable drop of its intensity, so that one could resume this component to originate from unaltered alloy lattice beneath the prepared alumina film. Indeed, the analysis of Fe2p and Cr2p peak positions demonstrates that no oxidation of these elements occurs, and the peak intensities are attenuated due to screening effect of alumina overlayer. We have used the latter effect to estimate that the thickness of the produced Al_2O_3 films does not exceed 4.5 nm [8].

STM investigation of the films shows that their surface consists of the irregular but rather plain formations of very large sizes (Fig. 4) – for $6 \times 6 \mu\text{m}$ scans the heights difference is hundreds nanometers. At higher magnifications the sample surface looks very flat (the height drop of 10 – 15 nm for 150×150 nm scans). No “particle-like” objects to misidentify them as silver particles are found.

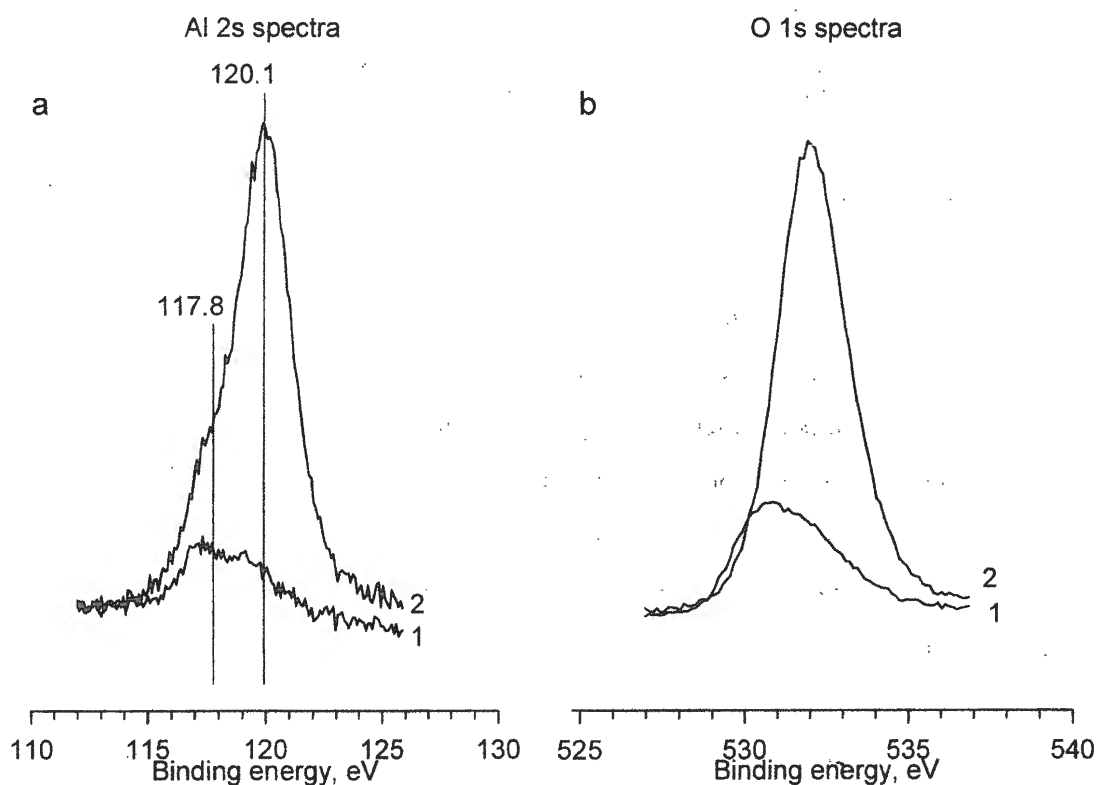


Figure 3. Al2s spectra (a) and O1s spectra (b) before (curves 1) and after (curves 2) the alloy sample annealing.

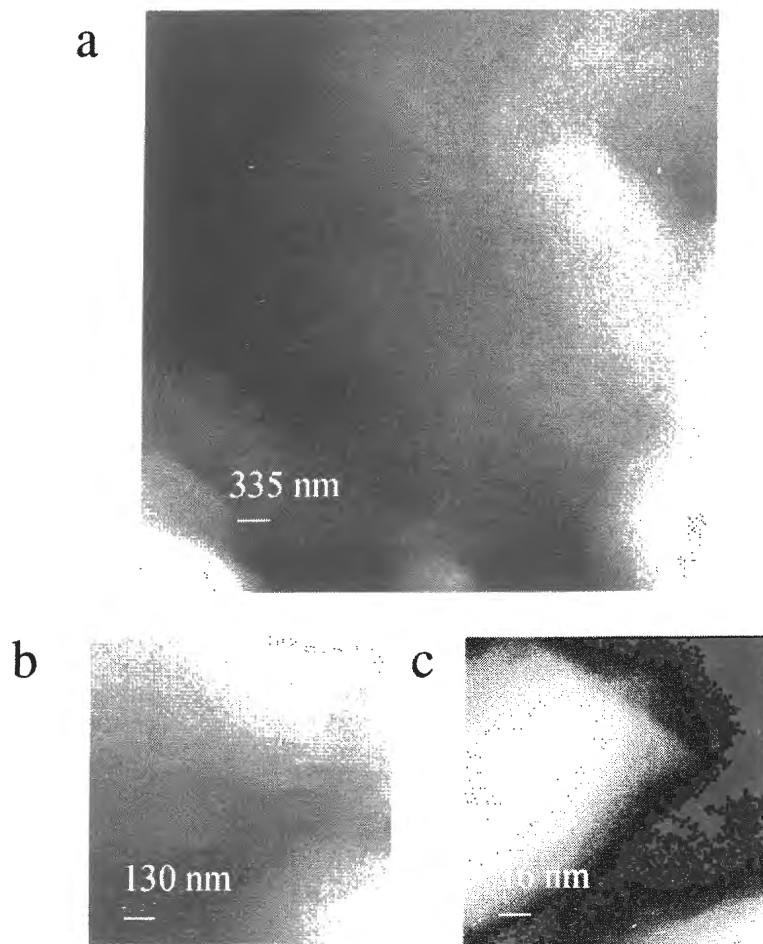


Figure 4. STM pictures of clean surface of alumina film ($U = 200$ mV, $I = 3$ nA) at various magnifications: survey scan ($5.9 \mu\text{m} \times 5.9 \mu\text{m} \times 600$ nm); b) ($1.2 \mu\text{m} \times 1.2 \mu\text{m} \times 250$ nm); c) (150 nm \times 150 nm \times 16 nm).

The study of model Ag/Al₂O₃ system

After the detailed STM and XPS characterization of the produced alumina films the vapour deposition of silver has been performed. The Ag source temperature was varied from 650 K to 850 K and the duration of evaporation ranged from 5 to 70 minutes. However, XPS estimation of silver coverage revealed that below 750 K the procedure time became too long (several hours for one monolayer of silver). Here we present the results for the samples prepared at $T \geq 750$ K. The survey STM scans of the Ag/alumina samples show that silver particles are evenly distributed over the surface. The size distribution is very narrow and the maximal size of the particles does not exceed 12 nm (Fig. 5). The shape of all observed particles is quasi-spherical and their typical height profile is shown at Fig. 6.

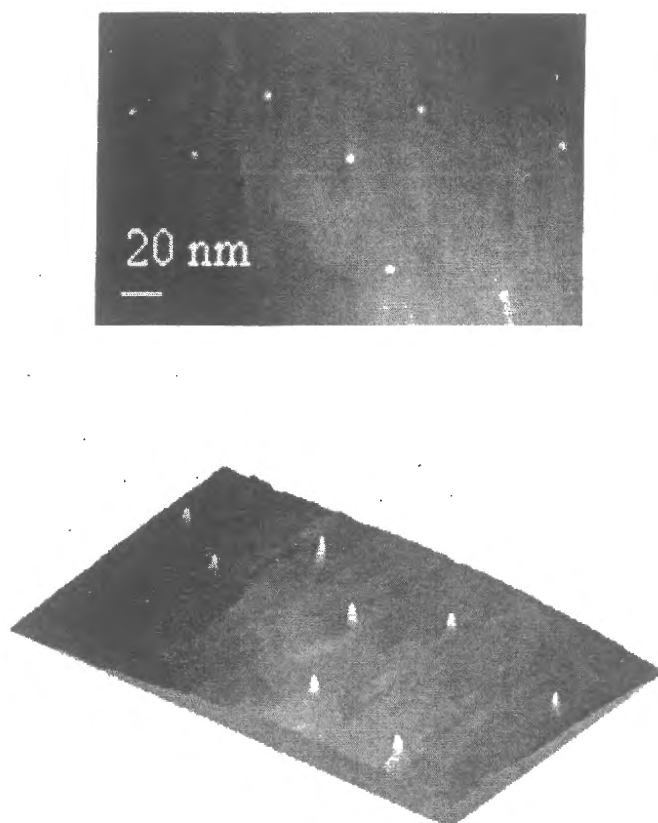


Figure 5. STM scan (upper panel) and corresponding 3D-picture (lower panel) of isolated Ag particles at alumina surface (220 nm × 136 nm × 40 nm); $U = -2000\text{mV}$, $I = 5\text{nA}$

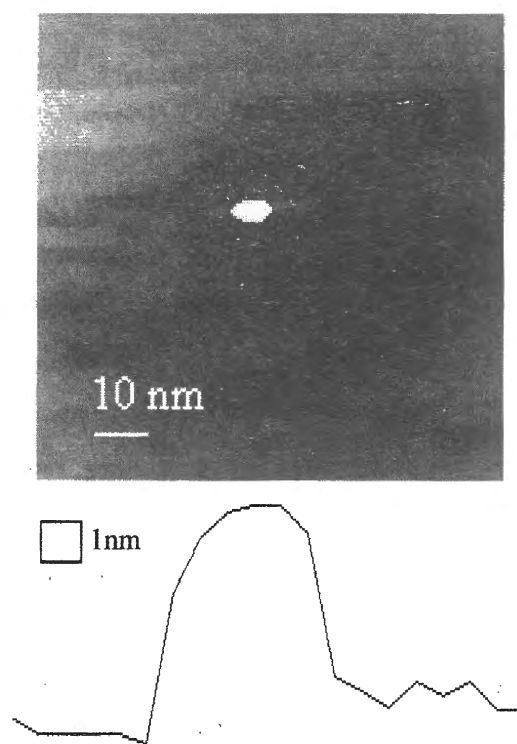


Figure 6. Upper panel: STM image of single silver particle at the Al_2O_3 - film sample (92 nm × 91 nm × 20 nm), $U = 200\text{mV}$, $I = 7\text{nA}$. Lower panel: Height profile of this particle (in vertical direction)

PP-20

Conclusion

Two model supported catalysts – Ag/HOPG and Ag/alumina – were prepared and studied by STM and XPS methods. The vacuum annealing of the HOPG supported samples at 570 K revealed silver particles to migrate over graphite surface and agglomerate to the larger formations. These observations indicated the very high mobility of silver particles at the inert support that results in the rather broad size distribution for the vapour deposited metal particles. On the contrary, we have found the very narrow size distribution for alumina supported catalysts indicating the total immobilization of deposited Ag particles, obviously due to much stronger metal – support bonding. Thus it proved again the nature of the support to be very important for the thermal stability of supported metal catalysts both during their preparation and (especially) under the reaction conditions. Our preliminary research of the specially constructed model alumina supported catalysts have shown such systems to be very useful for the further investigations on the morphology and the stability of the oxide supported metal catalysts.

Acknowledgements

The authors highly appreciated the generous and various help / assistance of our colleagues: A.V. Kalinkin, I.P. Prosvirin and M.Yu. Smirnov. R.I.K. would like to acknowledge CRDF for the financial support under BRHE Grant # REC-008.

References

1. G.K. Boreskov, *Heterogeneous catalysis*, Science, Moscow, 1988, (in Russian).
2. R.M. Lambert and G. Pacchioni, Eds., *Chemisorption and Reactivity on Supported and Thin Films*, Kluwer Academic Publishers, 1997.
3. Henry C.R., *Surf Sci. Rep.*, 31 (1998) 235.
4. E. Umbach, H.-J. Freund, Eds., *Adsorption on Ordered Surfaces of Ionic Solids and Thin Films*, Vol. 33 of Springer Series in Surface Sciences (Springer, Berlin, 1993).
5. R.M. Jaeger, H. Kuhlenbeck, H.-J. Freund, *Surf. Sci.*, 259 (1991) 235.
6. J. Libuda, F. Winkelmann, M. Baumer, H.-J. Freund, Th. Bertrams, H. Neddermeyer, K. Muller, *Surf. Sci.*, 318 (1994) 61.
7. J.F. Moulder, W.F. Stickle, P.E. Sobol, K.D. Bomben, *Handbook of X-Ray Photoelectron Spectroscopy*, Perkin- Elmer, Eden Prairie, MN, 1992.
8. D. Briggs, M.P. Seach, Eds., *Practical Surface Analysis by Auger and X- ray Photoelectron Spectroscopy*, John Wiley&Sons, 1983.

SYNTHESIS AND STUDY OF MICRODOMAIN TEXTURED PEROVSKITE CATALYSTS

A.P.Nemudry^a, O.Yu.Podyacheva^b, Z.R.Ismagilov^b, V.A.Ushakov^b and S.R.Khairulin^b

^a*Institute of Solid State Chemistry and Mechanochemistry, Kutateladze st. 18, 630128,
Novosibirsk, Russia*

^b*Boreskov Institute of Catalysis SB RAS, Pr. Akad. Lavrentieva 5, 630090 Novosibirsk, Russia*

Mixed oxides ABO_{3-d} with perovskite structure have received considerable attention as efficient heterogeneous catalysts, e.g. in oxidation of CO and reduction of NO_x for application in auto-exhaust treatment [1], membrane catalysis [2,3] and electrocatalytic processes [4]. Since these oxides are Lewis bases they are promising in terms of oxidative coupling of methane and complete or selective oxidation of hydrocarbons [5-8].

On the other hand, perovskites because of their controllable physical and chemical properties can be used as model system for basic research in catalysis: i.e. to define the influence of partial substitution of the A and B site cations, oxygen stoichiometry, oxidation state of the transition metal B, crystal structure and structural disorder, etc. on the catalytic activity. Oxygen stoichiometry and mobility which have substantial influence on functional properties of perovskites are of considerable interest in this respect. It is generally believed that in the oxidative catalysis the activity of catalysts is defined by the state and concentration of the active oxygen on the catalyst surface and controlled by its mobility. Reversible uptake of oxygen by the catalyst can provide oxygen storage capability in reactions of complete or selective oxidation of hydrocarbons and oxidative coupling of methane.

Under these aspects, it is remarkable that in a recent series of publications it has been reported that perovskite-related compounds (La_2CuO_4 [9], Ln_2NiO_4 with $Ln = La, Nd$, [10-11] and $SrMO_{2.5}$ with $M=Fe, Co$ [12-14]) are able to undergo reversible electrochemical oxygen intercalation at ambient temperature which is correlated with an unusual high oxygen ionic transport property. It is considered that low temperature oxygen transport in these compounds is related to the presence of specific microdomain texture [13-16].

Microdomain texture assumes the existence of two forms of active oxygen (lattice and interdomain oxygen ions) on the surface of perovskite type catalysts. The state and concentration of these active oxygen forms can be controlled, e.g. by the variation of the overall oxidation state of the transition metal B and oxygen stoichiometry or by the size of

PP-21

microdomains. Reversibility of the redox processes and high velocity of the oxygen ion transport provide the fast exchange between the bulk and surface of the catalyst.

Above mentioned peculiarities of microdomain textured (MDT) perovskites make them attractive in terms of complete or selective oxidation of hydrocarbons. Determination of the essential factors which define MDT perovskites catalytic activity in respect to these catalytic reactions represents the subject of this research.

In order to achieve the aim the CaFeO_{3-d} perovskites in which Ca ions were partially substituted by strontium have been synthesized. It was expected that partial substitution of A cations in CaFeO_{3-d} structure provokes microdomain formation in these phases and increases their catalytic activity in respect to methane oxidation.

$\text{Ca}_{1-x}\text{Sr}_x\text{FeO}_{2.5}$ samples were prepared by standard solid state techniques. Stoichiometric amounts of CaCO_3 , SrCO_3 and Fe_2O_3 (analytical grade) were ground and calcined in air at 900°C for 12 hours. The samples were reground, pelletized, then heated in air at temperatures of 1200°C (24 h), 1000°C (12 h) and quenched thereafter in liquid N_2 .

Oxygen stoichiometry was determined by iodometry [17]. Powder X-ray diffraction data were measured with a Siemens D 5000 diffractometer using $\text{Cu K}\alpha$ radiation. Electrochemical experiments were performed at room temperature in galvanostatic mode (three electrode cell, 1M KOH electrolyte) with working electrodes of polycrystalline material pressed into Pt grids along with 1% wt of Teflon and 15-20% wt of acetylene black. The Mössbauer spectroscopy measurements were carried out by conventional constant acceleration technique at room temperature. Electron diffraction and microscopy studies have been performed on a JEM-100CX (accelerating voltage 100 kV, point resolution 4.5 Å). Bright (BF) and dark (DF) field image regimes were used, as well as selected area electron diffraction (SAED).

In the frame of this work samples with following compositions $\text{Ca}_{1-x}\text{Sr}_x\text{FeO}_{2.5}$ ($x=0.1, 0.15, 0.2, 0.25, 0.3, 0.5, 0.7, 0.8, 0.9$) have been synthesized. Parent compounds (ABO_{3-d} , $d=0.5$) and products of their oxidation ($d=0$) are characterized by X-ray diffraction, Mössbauer spectroscopy, thermal and chemical analysis. The real microstructure of synthesized samples was studied by electron microscopy. The reactivity of the samples towards electrochemical oxidation in aqueous electrolyte at room temperature was studied by chronopotentiometry. In situ X-ray diffraction studies of structural transformations in the course of electrochemical oxygen intercalation were carried out. Activity of parent and oxidized samples was tested in methane oxidation reaction in a flow set-up; the reaction mixture was 1% CH_4 in air with a volume velocity 1000 h^{-1} .

It has been shown that doping of $\text{CaFeO}_{2.5}$ by Sr leads to both the formation of solid solutions ($x < 0.2$) and their unmixing ($0.2 < x < 0.7$) with the formation of $\text{CaFeO}_{2.5}/\text{SrFeO}_{2.5}$ microdomains in the range of tens to hundreds angstroms. Microdomain formation drastically increases the reactivity of the samples: electrochemical oxidation of $\text{SrFeO}_{2.5}$ as well as $\text{CaFeO}_{2.5}$ domains has been achieved at room temperature. According to Mössbauer spectroscopy, X-ray diffraction and chemical analysis data in the course of electrochemical oxidation at room temperature the formation of CaFeO_3 domains with unit cell parameters close to the ones of thermally prepared at 1000°C and $P_{\text{O}_2}=2\text{GPa}$ takes place.

Detailed studies of real structure, mechanism and kinetics of low temperature reactivity of MDT ferrites have been conducted on $\text{Ca}_{0.5}\text{Sr}_{0.5}\text{FeO}_{2.5}$ sample. It has been shown that the crystallites of this perovskite are composed of two types of grains having different calcium to strontium cation ratio. In turn, the grains are separated into microdomains sized from 30 to 70 Å.

By means of *in situ* X-ray studies the mechanism of electrochemical oxidation of MDT $\text{Ca}_{0.5}\text{Sr}_{0.5}\text{FeO}_{2.5}$ sample has been investigated. Using the kinetic model developed earlier [15] to describe the diffusion of oxygen in microdomain textured matrix the potentiostatic relaxation curves of the oxidation of $\text{Ca}_{0.5}\text{Sr}_{0.5}\text{FeO}_{2.5}$ have been analyzed. It is demonstrated that the limiting stage is supply of oxygen along the domain walls with the coefficient of oxygen diffusion about $D_0 \sim 5 \cdot 10^{-13} \text{ cm}^2/\text{s}$. Electrochemical oxidation resulted in the formation of $\text{Ca}_{1-x}\text{Sr}_x\text{FeO}_{3.0}$ MDT perovskites having considerably faster oxygen transport properties: oxygen diffusion coefficient along microdomain walls rises up to two order of magnitude.

Microdomain textured $\text{Ca}_{1-x}\text{Sr}_x\text{FeO}_{2.5}$ catalysts show low catalytic activity in methane oxidation reaction. Temperatures of 50% conversion vary within interval of $620\text{-}640^\circ\text{C}$, Fig.1. Electrochemical oxidation of parent catalysts leads to considerable increase of catalysts activity. Temperatures of 50% conversion are shifted to low temperature region and amount to $443\text{-}485^\circ\text{C}$. It is obvious that supplemental oxygen introduced into the structure of parent catalysts $\text{Ca}_{1-x}\text{Sr}_x\text{FeO}_{2.5}$ with the formation of $\text{Ca}_{1-x}\text{Sr}_x\text{FeO}_{3.0}$ perovskites is active in methane oxidation reaction and is stable up to the temperatures of $500\text{-}600^\circ\text{C}$.

Thus, the change of microdomain composition in the course of electrochemical oxidation and the increase of oxygen mobility considerably improve the catalytic activity of the samples.

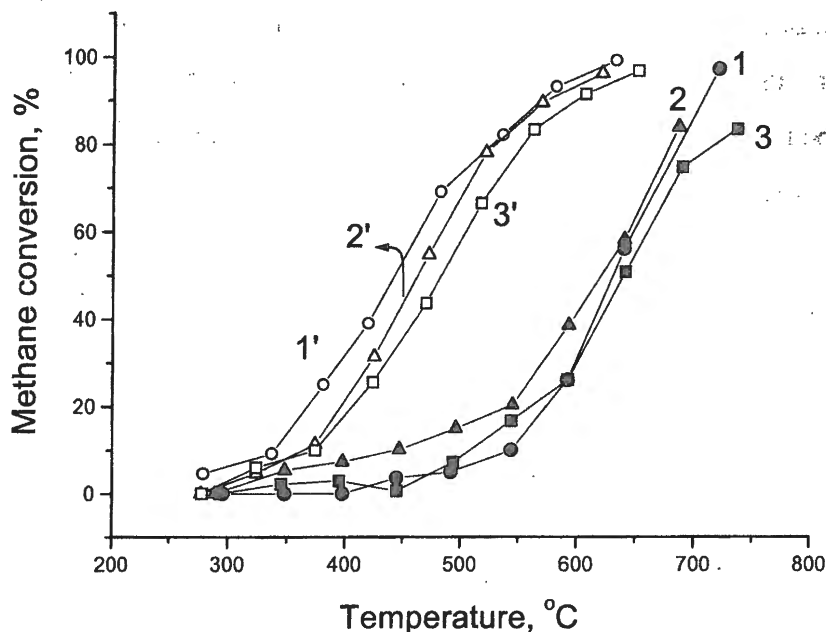


Fig. 1. Temperature dependencies of methane conversion on $\text{Ca}_{1-x}\text{Sr}_x\text{FeO}_{3-d}$ perovskites:

1, 1' - $x=0.7$; 2, 2' - $x=0.5$; 3, 3' - $x=0.3$.

Solid symbols - parent catalysts, opened symbols - oxidized catalysts.

Acknowledgements

This work was supported by INTAS grant 2000-00180.

The authors thank Mr. V.V. Kuznetsov for performance of activity tests in methane oxidation reaction.

References

1. L.G. Tejuca, J.L.G. Fierro and J.M.D. Tascón, *Adv. Catal.*, **36** (1989) 237.
2. S.Pei, M.S. Kleefisch, T.P. Kobylinski, J. Faber, C.A. Udovich, V. Zhang-McCoy, B. Dabrowski, U. Balachandran, R.L. Mieville and R.B. Poeppel, *Catal. Lett.* **30** (1995) 201.
3. C. Schinzer, R.A. Saymeh and H.M. Asfour, *Z. Naturforsch.* **52b** (1997) 927
4. S. Trasatti, Transition metal oxides: versatile materials for electrocatalysis. In *The Electrochemistry of Novel Materials*, Eds. J. Lipkowski and P.N. Ross, 1992, VCH, N.Y., 207.
5. M.M. Bettahar, G. Costenin, L. Savary and L.C. Lavalley, *Appl. Catal.*, **145** (1996) 1.
6. D. Klissurski and V. Rives, *Appl. Catal.*, **109** (1994) 1.
7. P.N. Trikalitis, T.V. Bakas, A.C. Moukarika, A.T. Sdoukos, T. Ngelidis and P.J. Pomonis, *Appl. Catal.*, **167** (1998) 295.
8. M. Caldararu, A. Ovenston, and J.R. Walls, *Appl. Catal.*, **167** (1998) 225.
9. A. Wattiaux, J.C. Park, J.C. Grenier and M. Pouchard, *C. R. Acad. Sci. Ser.2*, **310** (1990) 1047.
10. J.-C. Grenier, A. Wattiaux, J.-P. Doumerc, P. Dordor, L. Fournes, J.-P. Chaminade and M. Pouchard, *J. Solid State Chem.* **96** (1992) 20.
11. I. Yazdi, S. Bhavaraju, J.F. DiCarlo, D.P. Scarfe and A.J. Jacobson, *Chem. Mater.* **6** (1994) 2078.
12. A. Wattiaux, L. Fournes, A. Demourgues, N. Bernaben, J.-C. Grenier and M. Pouchard, *Solid St. Commun.* **77** (1991) 489.
13. A. Nemudry, P. Rudolf and R. Schöllhorn, *Chem. Mat.* **8** (1996) 2232.
14. A. Nemudry, I. Gainutdinov, V. Boldyrev, M. Weiss, and R. Schöllhorn, *Chem. Mat.* **10** (1998) 2403.
15. E. Goldberg, A. Nemudry, V. Boldyrev and R. Schöllhorn, *Solid State Ionics*, **122** (1999) 17.
16. A. Nemudry, A. Rogatchev, I. Gainutdinov, R. Schöllhorn, *J. Solid State Electrochem.* **5** (2001) 450
17. E.H. Appelman, L.R. Moriss, A.M. Kini, *Inorg. Chem.*, **26** (1987) 3237.

**DOUBLE STEREOSELECTION IN HYDROGENATION OF PROCHIRAL
DEHYDROCARBOXYLIC ACIDS ON $\text{Rh}(\text{S,S-DIODMA})_2^+ \text{TfO}^-$ COMPLEX IN THE
PRESENCE OF (+)-NEOMENTHYLDIPHENYLPHOSPHINE**

L.O.Nindakova, O.V.Gamzikova, B.A.Shainyan, F.K.Schmidt

Irkutsk Institute of Chemistry, Siberian Division of Russian Academy of Sciences,

1 Favorsky St., 664033, Irkutsk, Russia. E-mail: bagrat@irioch.irk.ru

Abstract

Enantioselective hydrogenation of α -acetamidocinnamic (AACA) and itaconic (IA) acids has been studied on rhodium complexes $\{[\text{Rh}(\text{COD})_2]^+ \text{TfO}^- + n\text{MDPP}\}$ COD = 1,5-cyclooctadiene, $n\text{MDPP} = (1S,2S,5R)\text{-}(+)\text{-neomenthyldiphenyl phosphine}$] and $\{[\text{Rh}(\text{S,S-DIODMA})_2]^+ \text{TfO}^- + n\text{MDPP}\}$ [(S,S)-DIODMA = 4S,5S-(+)-N⁴,N⁴,N⁵,N⁵,2,2-hexamethyl-1,3-dioxolane-4,5-dimethaneamine]. Addition of nMDPP decreases the activity of the catalyst increases the optical yield with retention of the direction of stereoselection. Optical yields for hydrogenation on $\{[\text{Rh}(\text{S,S-DIODMA})_2]^+ \text{TfO}^- + n\text{MDPP}\}$ exceed those obtained on the diamine complex in the presence of Ph₃P as well as those obtained on $\{[\text{Rh}(\text{COD})_2]^+ \text{TfO}^- + n\text{MDPP}\}$. The result of combined action of two ligands may be considered as manifestation of 'matched' effect. Transformations of complexes have been studied by the use of ¹H and ³¹P NMR spectroscopy. At least three complexes exist in the catalytic system, namely, diamine complex $[\text{Rh}(\text{S,S-DIODMA})_2]^+ \text{TfO}^-$, solvate complex $[(n\text{MDPP})_2\text{Rh}(\text{solV})_2]^+ \text{TfO}^-$ and diamine-phosphine complex $[(n\text{MDPP})_2\text{Rh}(\text{S,S-DIODMA})]^+ \text{TfO}^-$.

Introduction

Term 'double stereoselection' denotes symbate or antibate action of two chiral species in enantioselective reactions. The two chiral species may be a chiral ligand and a substrate possessing chiral center, or two different chiral ligands. Combination of chiral species resulting in a higher or lower enantioselectivity is designated as 'matched' or 'mismatched', respectively. Recently we have studied enantioselective hydrogenation of α -acetamidocinnamic (AACA) and itaconic (IA) acids on rhodium complex $[\text{Rh}(\text{S,S-DIODMA})_2]^+ \text{TfO}^-$ 1, where (S,S)-DIODMA is 4S,5S-(+)-N⁴,N⁴,N⁵,N⁵,2,2-hexamethyl-1,3-dioxolane-4,5-dimethaneamine [1]. Complex 1 is formed by replacement of both cyclooctadiene (COD) ligands from complex $[\text{Rh}(\text{COD})_2]^+ \text{TfO}^-$ by two molecules of DIODMA. The reached optical yields are moderate (<30%), which is not

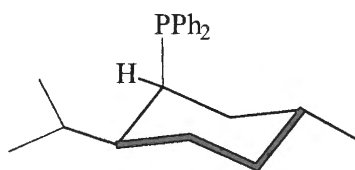
PP-22

only due to the nature of the ligand but, probably, also because of reduction of rhodium(+1) to rhodium metal. To prevent this reduction, we introduced an equivalent amount of triphenylphosphine ($\text{PPh}_3/\text{Rh} = 1$) into the catalytic system, that led to a decrease of chemical yields but increased optical yields. Effect of an achiral P-ligand may consist in stabilization of the diamine rhodium complex during the process of hydrogenation due to formation of a new complex possessing both ligands in the coordination sphere of the metal. Besides, we cannot rule out steric hindrances in the coordination sphere of rhodium arising from its coordination with Ph_3P . This must give rise to more rigid selection of the *re* or *si* side of the $\text{C} = \text{C}$ double bond during formation of the substrate rhodium complex, that is, to an increase of free energy difference of the two diastereomeric rhodium olefin complexes.

Formation of the phosphine-diamine rhodium complex $[(\text{Ph}_3\text{P})_2\text{Rh}(\text{DIODMA})]^+ \text{TfO}^-$ **2** by the reaction of complex $[\text{Rh}(\text{COD})_2]^+ \text{TfO}^-$ with molecular hydrogen in the presence of two moles of triphenylphosphine was corroborated by ^1H and ^{31}P NMR studies [1].

Hydrogenation of prochiral substrates on rhodium complexes

Here we report on the results of enantioselective hydrogenation of AACA and IA on rhodium complex $[\text{Rh}(\text{COD})_2]^+ \text{TfO}^-$ in the presence of chiral phosphine **3**, (1*S*,2*S*,5*R*)-(+)-neomenthyldiphenyl phosphine (nMDPP) and on rhodium diamine complex **1** also in the presence of nMDPP.



3 (nMDPP)

Phosphine **3** was used by Morrison et al. in hydrogenation of prochiral acids, like atropic, *E*- α -methyl cinnamic and *E*- β -methylcinnamic acids on the *in situ* formed rhodium complex $\text{Rh}[(+)\text{nMDPP}]_3\text{Cl}$ [2,3]. The optical yields reached 28% for (*S*)-2-phenylpropionic acid, 60% for (*R*)-2-methyl-3-phenylpropionic acid, and 61% for (*S*)-3-phenylbutanoic acid. Later on, Valentine et al. [4] succeeded in hydrogenation of 3,7-dimethyl-2, 6-octadienoic (geranic) acid to optically active (*R*)-3,7-dimethyl-6-octenoic (citronellic) acid under mild conditions on the dimeric complex $[\text{Rh}(\text{COD})\text{Cl}]_2$ and (+)-nMDPP in the presence of MeONa in 65-70% optical yield after 3 days. Less than moderate activity of the catalyst was observed for hydrogenation of α -(acetylamino)-6-methylindol-3-acrylic acid: the conversion after 7 days in the presence of triethylamine and with ratio substrate:Rh = 100 was as low as 29%. Neither optical yield nor configuration was determined.

PP-22

Table 2. Hydrogenation of IA and AACA on complex (1) in the presence of nMDPP (C₆H₆:MeOH = 3:7; C_{Rh} = 2 mmol/L, 5-24 h)

Entry	nMDPP:Rh	P _{H₂} , atm	t, °C	Substrate (substrate:Rh)	Chemical yield, %	Optical yield, %
1	1	1	20	IA (25)	34.6	62.2 (<i>R</i>)
2	1.2	1	60	IA (25)	100.0	48.3 (<i>R</i>)
3	1.9	1	20	IA (25)	8.3	74.3 (<i>R</i>)
4	2	1	60	IA (25)	21.2	65.3 (<i>R</i>)
5	1	1	60	AACA (50)	7.0*	
6	1	20	20	AACA (50)	25.0	32.7 (<i>S</i>)
7	–	35	20	AACA (40)	100	20.3 (<i>S</i>)

* – catalysate contained 73% of AACA and 20% of its methyl ester.

Indeed, as can be seen, addition of nMDPP to complex 1 gives rise to a decrease of activity of the catalyst and an increase of optical yield (up to 62-74% for IA) with retention of the direction of stereoselection. These optical yields exceed those obtained on complex 1 in the presence of achiral phosphine Ph₃P [1] as well as those obtained on rhodium complex with nMDPP (Table 1). This is true both for mild conditions and hydrogenation under high pressure of hydrogen. Consequently, we do observe a consistent action of the two chiral ligands in the coordination sphere, which may be considered as manifestation of 'matched' effect.

Transformations of rhodium(+1) complexes in the catalytic system

In spite of good results obtained for hydrogenation on rhodium complexes with nMDPP [2-4] their spectral characteristics were not studied. We made an attempt to fill in this gap by the use of ¹H and ³¹P NMR spectroscopy. Addition of two equivalents of 3 to brick-red solution of complex [Rh(COD)₂]⁺ TfO⁻ in acetone-*d*₆ changes the color to yellow-orange. Along with the singlet at -14.1 ppm belonging to 3, a doublet at 26.42 ppm with ¹J_{P-Rh} 141.3 Hz appears in the ³¹P NMR spectrum, and signals of free COD (5.50 and 2.32 ppm) appear in the proton spectrum. This testifies coordination of 3 to rhodium and formation of complex 4 (see the Scheme below).

Addition of one equivalent of (*S, S*)-DIODMA with respect to rhodium results in changing the ratio of the signals of the coordinated and free nMDPP in favor of the latter. Simultaneous downfield shift of the signals of DIODMA ($\Delta\delta_{\text{CH}}$ 0.14, $\Delta\delta_{\text{CH}_A}$ 0.22, $\Delta\delta_{\text{CH}_B}$ 0.27, $\Delta\delta_{\text{CH}_3\text{N}}$ 0.20, $\Delta\delta_{\text{CH}_3\text{C}}$ 0.03) gives an indication of its coordination to rhodium with formation of complex 5. On

the contrary, on addition of phosphine **3** to complex **1** no signals of free DIODMA are observed, so nMDPP is unable to replace diamine from the rhodium coordination sphere.

Further treatment of complex **5** with molecular hydrogen during 20 min gives rise to disappearance of complex **4** and appearance of two new doublets in the ^{31}P NMR spectrum at 55.15 ppm ($^1J_{\text{P-Rh}}$ 204.2 Hz) (complex **6**) and 78.45 ppm ($^1J_{\text{P-Rh}}$ 190.4 Hz) (complex **7**) of similar intensity. Signals of DIODMA suffer further downfield shift in the ^1H NMR spectrum and approach the values characteristic of the ligand in complex **1**. Chemical shifts of DIODMA and COD in various complexes are given in Table 3.

Table 3. Chemical shifts of DIODMA and COD in rhodium(+1) complexes

Complex	CH	CH _A in CH ₂	CH _B in CH ₂	N-CH ₃	C-CH ₃
DIODMA					
(<i>S,S</i>)-DIODMA	3.80	2.52	2.37	2.21	1.29
Complex 1	4.06	2.97	2.89	2.61	1.36
4 + (<i>S,S</i>)-DIODMA (complex 5)	3.94	2.74	2.63	2.41	1.32
4 + (<i>S,S</i>)-DIODMA + H ₂	4.05	2.94	2.86	2.60	1.35
Rh(DIODMA)(IA) ⁺ TfO ⁻ (complex 8)	4.21	3.37	3.02	2.79	1.38
COD					
Rh(COD) ₂ ⁺ TfO ⁻	4.15	2.50	1.77		
Rh(COD)(PPh ₃) ₂ ⁺ TfO ⁻	4.70	2.58	2.28		
Complex 4	5.12 br	2.50 m	2.50 m		
4 + (<i>S,S</i>)-DIODMA (complex 5)	4.18 br	*	*		

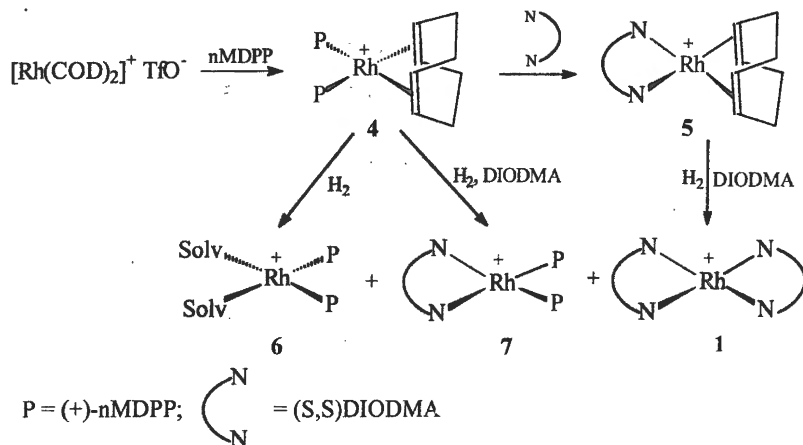
* overlapped with signals of DIODMA.

Based on the literature data we assign complexes **6** and **7** the structure of the solvate and diamine complexes $[\text{Rh}(\text{solv})_2\{(+)\text{nMDPP}\}_2]^+ \text{OTf}^-$ (**6**) [5] and $[\text{Rh}(\text{DIODMA})\{(+)\text{nMDPP}\}_2]^+ \text{OTf}^-$ (**7**) [6].

Thus, the results of NMR monitoring of the catalytic system allow us to conclude that:

1. Ligand **3** does not replace DIODMA in complex **1**, whereas substrate (IA) replaces one molecule of DIODMA to form olefin-diamine rhodium complex **8** [1].
2. Complex **4** reacts with DIODMA to afford the diamino-diene rhodium complex **5** which after treatment with molecular hydrogen liberates cyclooctane and is transformed to complex **1**.
3. Complex **4** after treatment with molecular hydrogen also affords cyclooctane and complexes **6** and **7** possessing chiral phosphine **3**.

With all this taken into account the following tentative scheme can be suggested:



Therefore, at least three complexes possessing chiral ligands in different combinations are formed in the catalytic system during hydrogenation, the concentration of complexes 1, 6, and 7 depending on the reaction conditions. Complex 1 with two bidentate diamine ligands reacts with IA to afford rather stable complex 8 which then slowly reacts with hydrogen [1]. According to Brown et al. [5], cationic complexes $[(\text{PR}_1\text{R}_2\text{R}_3)_2\text{Rh}(\text{NBD})]^+\text{BF}_4^-$, where NBD stands for bicyclo-[2,2,1]-heptadiene form two types of complexes when treated with molecular hydrogen: bis-solvate rhodium rhodium(+1) complexes like 6 and dihydrido-bis-phosphine rhodium(+3) complexes with *trans* arrangement of the phosphine ligands, their ratio being very sensitive to the nature of a tertiary phosphine. In the present study we failed to detect the dihydride complex, apparently, due to its low stability at room temperature. Apparently, it is complex 7 and its precursor, complex 6, which are responsible for consistent action of chiral ligands in the catalytic system.

Catalytic hydrogenation is known to proceed via formation of an octahedral dihydrido-olefinic rhodium (+3) complex [7]. This requires six coordination sites for bidentate molecule of diamine, two hydrogen atoms, and a substrate (IA or AACA) coordinated to rhodium atom in bidentate mode. Hence, there is no free place for an additional ligand (in our case *n*MDPP). However, the results given in Table 2 unequivocally point to participation of phosphine 3 in the catalytic cycle, which is especially distinct for hydrogenation of IA where addition of two equivalents of phosphine 3 (cf. entries 1 vs. 3, and 2 vs. 4) gives rise to a sharp decrease of activity of the catalyst. Probably, coordination of chiral phosphine 3 is accompanied by monodentate coordination of the bidentate *N,N*-ligand to transition metal in the stage responsible for stereodifferentiation.

References

1. L.O.Nindakova, B.A.Shainyan, A.I.Albanov, Russ. Chem. Bull, 50 (2001) 1860.
2. J.D. Morrison, W.F. Master, J. Org. Chem., 39 (1974) 270.
3. A.M. Aguar, C.J. Morrow, J.D. Morrison, R.E. Burnett, W.F. Masler, N.S. Bhacca, J. Org. Chem., 41 (1976) 1545.
4. J.D. Valentine, K.K. Jonson, W. Priester, R.S. Sun, K. Toth, G. Saucy, J. Org. Chem., 45 (1980) 3698.
5. J.M. Brown, P.A. Chaloner, P.N. Nicholson, Chem.Comm., (1978) 646.
6. S. Inoue, H. Takaya, K. Tani, S. Otsuka, T. Sato, R. Noyory, J. Amer. Chem. Soc., 112 (1990) 4897.
7. A.S.C. Chan, J. Halpern, J. Amer. Chem. Soc., 102 (1980) 838.

CATALYTIC WET PEROXIDE OXIDATION OF PHENOL OVER METAL-OXIDE AND CARBON CATALYSTS

O.P. Pestunova, O.L. Ogorodnikova, V.N. Parmon

Boreskov Institute of Catalysis SB RAS, 630090 Novosibirsk, Russia

Fax: +7 3832 34-32-69; E-mail: oxanap@catalysis.nsk.su

Aqueous effluents from some industries such as chemical, petrochemical, pharmaceutical etc. contain toxic organic pollutants in concentration too high to be treated through biological oxidation. Catalytic wet oxidation (CWO) employing oxygen (CWAO), ozone or hydrogen peroxide appears to be more effective and more economical, because it allows to reduce significantly the temperature and pressure [1].

Homogeneous catalysts such as transition metal's cations and complexes (Fe and Cu are usually used) are very effective catalysts in processes of CWAO and CWPO [2,3]. However the heterogeneous catalysts allow to avoid the processes of the catalyst regeneration. There are two groups of the heterogeneous catalysts. The first group consists of oxides and mixed oxides of transition metals (usually Cu, Fe, Mn, Co) or oxides supported on oxide carriers [3,4]. These catalysts are sufficiently effective, but they have essential imperfection. Active component can be leached under reaction conditions. Second group is noble metals supported either oxides or carbon [4]. In contrast from oxide catalysts, these catalyst are usually stable, but much more expensive.

In our study we are comparing activity and stability of wide range of oxide catalysts and graphite like catalyst Sibunit in model reaction of phenol oxidation with the hydrogen peroxide.

We have tested following catalysts Cu, Fe and Mn-oxides supported on such stable carriers as α - Al_2O_3 , TiO_2 и CeO_2 , mixed oxide $\text{MnO}_2/\text{CeO}_2$ prepared via co-precipitation and porous graphite-like carbon sibunit.

The phenol oxidation was carried out in a batch reactor with a reflux condenser at atmospheric pressure and a temperature 368 K. Concentration of phenol and hydrogen peroxide was 0.01 mol/l and 0.1 mol/l, respectively.

Concentrations of phenol and some products of its oxidation were detected by HPLC. Concentration of hydrogen peroxide was determined by UV-Vis spectroscopy via reaction with Ti.

Metals leaches were detected with atomic absorptive analyzer.

Conversion of phenol and hydrogen peroxide after 30 minutes and 3 hours of reaction and TOC abatement after 3 hour are shown in the Table. The same Table presents amounts of active metals found in solution after reaction and pH of the solution.

Blank experiment (No.1) showed that phenol can be oxidized with hydrogen peroxide at 368 K without catalysts, but conversion after 3 hours was only 44% and TOC abatement 12%. The solution after reaction has dark brown color.

Table 1. Catalytic behavior of the different catalysts in the phenol oxidation by hydrogen peroxide

No	Catalyst	Phenol conversion, %		H ₂ O ₂ conversion, %		TOC abatement, % 3 hours	Active metal leaching, %	Final pH
		0.5 hour	3 hours	0.5 hour	3 hours			
1	none	5	44	15	33	12	-	3.7
2	2%Fe/CeO ₂	0	0	100	100	0	0.3	4.0
3	2%Fe/ α -Al ₂ O ₃	46	100	15	100	26	21	2.9
4	1%Cu/ α -Al ₂ O ₃	100	100	100	100	48	65	3.0
5	1%Cu/TiO ₂	100	100	100	100	39	80	3.0
6	1%Cu/CeO ₂	5	6	100	100	0	27	4.0
7	2%Mn/ α -Al ₂ O ₃	41	81	31	59	14	60	3.5
8	2%Mn/CeO ₂	0	0	100	100	0	39	5.1
9	MnO ₂ /CeO ₂	14	35	100	100	41	6.2	5.5
10	Sibunit	50	86	21	76	50	-	2.7

The catalysts containing ceric dioxide (Nos. 2, 6, 8, 9) and manganese dioxide (Nos. 8, 9) (except of the 2%Mn/ α -Al₂O₃) were found to be very active in hydrogen peroxide decomposition but inactive in phenol oxidation. Cu-containing catalysts (Nos. 4-6) and 2%Mn/ α -Al₂O₃ (No. 7) are extremely unstable under reaction conditions. The most part of copper and manganese leaches into solution, and, it seems to act like a homogeneous catalyst. The sample 2%Fe/ α -Al₂O₃ (No. 3) was found to be the most stable under reaction conditions and sufficiently active in phenol oxidation. Moreover, it was much more stable at the second use. (Only 4% of iron was leached and 90% of phenol was oxidized.)

However the most interesting result is the graphite-like carbon Sibunit turn out to be very active in phenol oxidation. The conversion of phenol was 86% and TOC abatement was 40%. The contents of iron did not exceed 0.02 weight %.

Hydroquinone and pyrocatechol were found to be the intermediate products in all cases. However, the final solution was colored in deep brown without a catalyst. That could be explained as formation of polymeric products from hydroquinone and pyrocatechol. More complete oxidation occurs when the Sibunit is used as a catalyst. The solutions have not a color in this case.

Acknowledgement

The authors gratefully acknowledged INTAS (grant 00-129) for financial support.

Reference

- 1 F.Luck, Chem.Biochem. Q., 1996,27,195.
- 2 V.S.Mishra, V.V.Mahajani, J.B.Joshi, Ind.Eng.Chem.Res., 1995, 34, 2.
- 3 J.Barrault, M.Abdellaoui, C.Bouchoule, et al., Appl. Cat. B., 2000, 27, 225.
- 4 Yu.I.Matatov-Meytal, M.Sheintuch, Ind.Eng.Chem.Res., 1998, 37, 309.

SOME APPLICATIONS OF PLASMA SPRAYING TECHNIQUE FOR THE PREPARATION OF SUPPORTED CATALYSTS

O.Yu.Podyacheva^{a*}, N.V. Shikina^a, Z.R. Ismagilov^a, V.A. Ushakov^a, A.I. Boronin^a,
N.A. Rudina^a, I.A. Ovsyannikova^a, S.A. Yashnik^a,
O.P. Solonenko^b, A.A. Michal'chenko^b and H. Veringa^c

^a *Boreskov Institute of Catalysis SB RAS, Pr. Acad. Lavrentiev 5, 630090 Novosibirsk, Russia*

^b *Institute of Theoretical and Applied Mechanics, Institutskaya st. 4/1, 630090 Novosibirsk, Russia*

^c *ECN, P.O.Box 1, 1755 ZG Petten, The Netherlands*

Introduction

Last years works on the synthesis of catalysts with substantially improved or new unique properties by the use of plasma techniques have been intensively carried out. Although most of the papers are devoted to the preparation of bulk catalysts, some efforts are undertaken to manufacture supported catalysts for different applications, i.e. selective hydrogenation, combustion processes, etc.

This paper focuses on the development of supported catalysts by the use of plasma spraying technique. Direct current plasma torch [1] with interelectrode insert and diffusive attachment of arc on anode surface was used for synthesis of Mn-containing catalysts supported on alumina as well as alumina coatings on metal surfaces of different geometry (plates, foams) with subsequent deposition of combustion catalysts.

Experimental

Powders of pure γ -alumina or γ -alumina impregnated by $\text{Mn}(\text{NO}_3)_2$ were injected into the plasma jet outflow and quenched in water. Influence of powder size (90-1000 μm), regime of plasma jet outflow (laminar or turbulent) and Mn content (5 wt.% or 17 wt.%) on the properties of catalysts synthesized in a plasma jet outflow (plasma catalysts) was studied. Reference catalysts having identical chemical composition were prepared using standard conventional route, i.e. the calcination of γ -alumina impregnated by $\text{Mn}(\text{NO}_3)_2$ at 550°C for 4 hours.

Alumina powders differing in phase composition and particle size (α - Al_2O_3 20-80 and γ - Al_2O_3 90-500 μm) were used to spray an intermediate (gradient) layer on titanium plates

* Corresponding author. Tel.: +7-3832-397357; fax: +7-3832-397352; E-mail address: pod@catalysis.nsk.su (O.Yu.Podyacheva)

PP-24

and Ni, Ni-Cr foam materials under laminar, transient and turbulent regimes of the plasma jet outflow [2]. Various combustion catalysts (LaCoO_3 , Pt, Pd, $\text{LaMnAl}_{11}\text{O}_{19}$) were deposited on Ni-Cr foams covered by plasma sprayed α -alumina layer by means of impregnation or suspension techniques [3,4].

Phase composition of the catalysts was studied by XRD analysis, specific surface area of the samples was measured by BET method, pore volume of the sprayed layers was calculated using water capacity technique. The morphology of the catalysts was studied by SEM. Active component distribution in alumina was defined by X-ray microprobe analysis, whereas catalyst surface was examined by XPS. Catalysts were tested in methane oxidation reaction in a flow set-up; the reaction mixture was 1% CH_4 in air with a space velocity 1000 h^{-1} .

Results

$\gamma\text{-Al}_2\text{O}_3$

Study of the influence of the regimes of jet outflow on the properties of alumina powders treated in plasma and quenched in water has been performed. The results for $\gamma\text{-Al}_2\text{O}_3$ powder are presented in Table 1.

Table 1. Properties of $\gamma\text{-Al}_2\text{O}_3$ after plasma treatment and quenching in water.

Particle size, μm	Flow rate g s^{-1}	Regime	Specific surface area, m^2g^{-1}	Phase composition	I_α/I_γ^*
90-200	0.5	laminar	2.2	$\alpha\text{-Al}_2\text{O}_3$, $\gamma\text{-Al}_2\text{O}_3$	30
90-200	1.0	transient	22	$\alpha\text{-Al}_2\text{O}_3$, $\gamma\text{-Al}_2\text{O}_3$	13
200-300	0.5	laminar	19	$\alpha\text{-Al}_2\text{O}_3$, $\gamma\text{-Al}_2\text{O}_3$	25
200-300	1.0	transient	76	$\alpha\text{-Al}_2\text{O}_3$, $\gamma\text{-Al}_2\text{O}_3$	11
300-400	0.5	laminar	67	$\alpha\text{-Al}_2\text{O}_3$, $\gamma\text{-Al}_2\text{O}_3$	8
300-400	1.0	transient	104	$\alpha\text{-Al}_2\text{O}_3$, $\gamma\text{-Al}_2\text{O}_3$	6
400-500	0.5	laminar	119	$\alpha\text{-Al}_2\text{O}_3$, $\gamma\text{-Al}_2\text{O}_3$	

* I_α/I_γ - ratio of intensities of line $d/n=2.085$ ($\alpha\text{-Al}_2\text{O}_3$) and $d/n=1.990$ ($\gamma\text{-Al}_2\text{O}_3$)

A comparison of cross section views of initial and plasma treated particles of $\gamma\text{-Al}_2\text{O}_3$ showed that in the latter case the pellet consists of a core and a shell (Fig. 1). Densities of these two basic areas are different. Analysis of scanning electron micrograph and XRD data

(Table 1) allows the assumption that the particle core consists of γ - Al_2O_3 phase, while the particle shell is formed by α - Al_2O_3 . It seems that the use of large particles for spraying and high quenching velocities lead to the formation of a cold core and a hot melted shell.

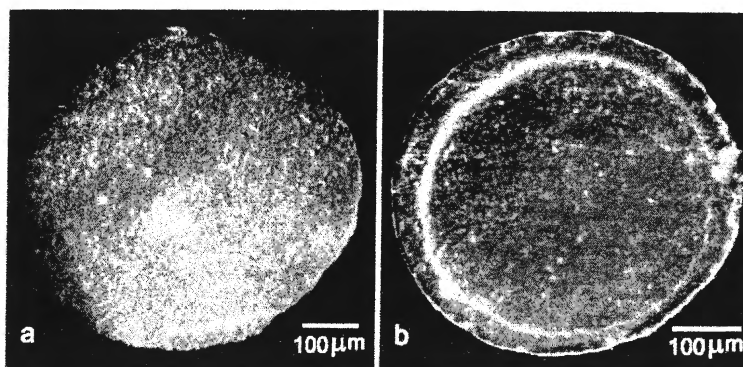


Fig. 1. Micrographs of a cross-section view of (a) initial and (b) plasma-treated γ - Al_2O_3 particles.

Mn- γ - Al_2O_3

XRD analysis showed the presence of β - Mn_2O_3 and γ - Al_2O_3 phases in all Mn-containing reference catalysts, independent on the content of Mn and particle size of the samples. Phase composition of the plasma catalysts is more complicated. It depends on the Mn content, particle size as well as the regime of plasma jet outflow. The Mn-containing phases are registered in plasma catalysts with particle size equal to 100-200 μm . It was found that Mn is present in solid solutions of Mn-Al-O composition based on spinel structure and having different cell sizes ($a=7.940$ - 8.242 Å).

X-ray microprobe analysis revealed that the active component in reference catalysts is uniformly distributed inside the particle, Fig. 2A. Discrepancy between $K_{\alpha}\text{Mn}$ and $K_{\alpha}\text{Al}$ profiles is observed. This fact correlates with XRD data showing the formation of crystalline β - Mn_2O_3 phase in reference catalysts. Analysis of $K_{\alpha}\text{Mn}$ and $K_{\alpha}\text{Al}$ profiles of plasma catalyst allows us to conclude that Mn is transferred to the catalyst surface, Fig. 2B. XPS confirmed that Mn concentration on the surface of the plasma catalyst exceeds the ones of the reference catalyst by 50%. The XPS spectra of plasma and reference catalysts present one O1s photoline at 531 eV corresponding to the lattice oxygen of alumina. Meantime, the chemical states of manganese in plasma and reference catalysts are different: binding energy of $\text{Mn}2p_{3/2}$ photoline of plasma catalysts is 641.6 eV, whereas that of reference catalysts is 640 eV.

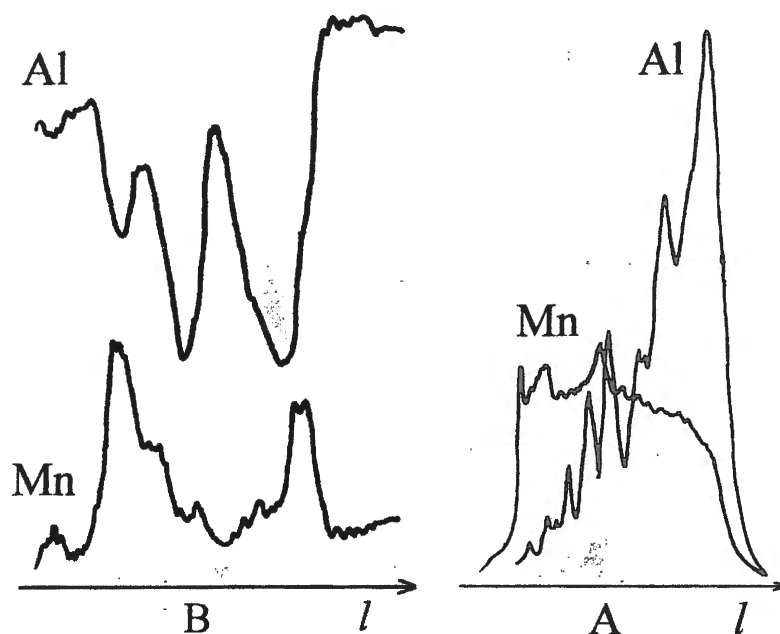


Fig. 2. X-ray microprobe spectra (K_{α} Mn, K_{α} Al) of cross section of particles of catalyst 17%Mn₂O₃/γ-Al₂O₃, 100-200 μm : A - reference catalyst, B - plasma catalyst (laminar regime of plasma jet outflow).

Plasma catalysts demonstrate superior activity in methane oxidation reaction, Fig. 3. Temperature of 50% methane conversion for plasma catalyst with the content of active component 5 wt.% is lower than the temperature of 50% methane conversion for reference catalyst by 90°C, whereas for catalysts with content of active component 17 wt.% by 120°C. This fact can be probably explained by increased concentration of manganese on the surface of plasma catalyst as well as by formation of active Mn-containing surface phases invisible for XRD analysis.

Thus, plasma technique allows the synthesis of Mn-containing catalysts deposited on γ-Al₂O₃ with substantially improved properties compared with those of reference catalysts prepared via conventional route.

Alumina-metal supports

Experiments on the plasma spraying of alumina of different phase composition and particle size on titanium plates have shown that the properties of plasma sprayed layers are quite similar and do not depend on the jet outflow regime used (Table 2).

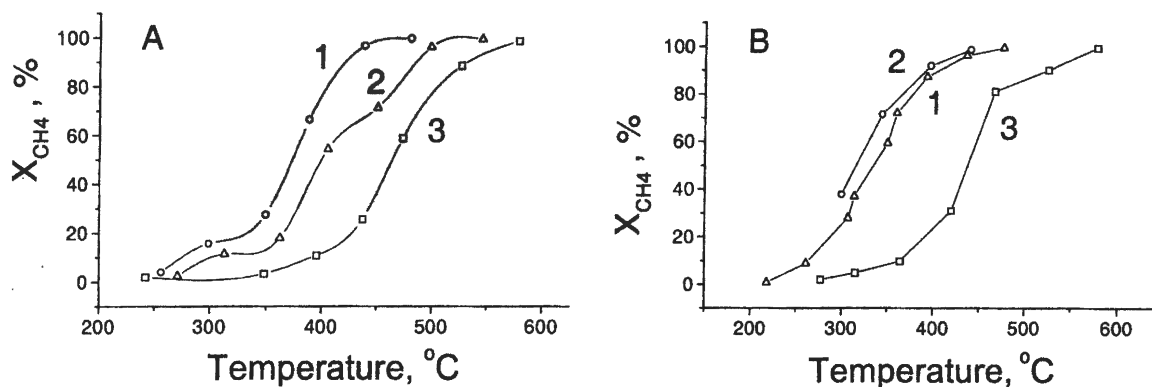


Fig. 3. Temperature dependencies of methane conversion ($1\%CH_4$ in air, $1000h^{-1}$) on catalysts: A - $5\%Mn_2O_3/\gamma-Al_2O_3$ and B - $17\%Mn_2O_3/\gamma-Al_2O_3$ synthesized using 1-turbulent or 2-laminar regime of jet outflow and 3-conventional route.

Table 2. Properties of alumina sprayed on titanium plates.

Particle size, μm	Type of alumina sprayed	Flow rate, $g s^{-1}$	Regime of plasma jet outflow	Specific surface area, $m^2 g^{-1}$	Phase composition	Pore volume, $cm^3 g^{-1}$
40	$\alpha-Al_2O_3$	0.75	Laminar-Transient	0.2	$\alpha-Al_2O_3$	0.052
40	$\alpha-Al_2O_3$	1.25	Transient	0.2	$\alpha-Al_2O_3$	0.065
40	$\alpha-Al_2O_3$	1.75	Turbulent	0.2	$\alpha-Al_2O_3$	0.167
90-200	$\gamma-Al_2O_3$	0.5	Laminar	0.2	$\alpha,\theta-Al_2O_3$	0.068
90-200	$\gamma-Al_2O_3$	0.75	Laminar-Transient	0.4	$\alpha,\theta-Al_2O_3$	0.075
90-200	$\gamma-Al_2O_3$	1.0	Transient	0.6	$\alpha,\theta-Al_2O_3$	0.166

When $\alpha-Al_2O_3$ is sprayed on titanium plates, the coatings are characterized by a low specific surface area and their pore volume increases when the spraying regime is changed from a laminar to a turbulent one. It has been established that the dependence of the regime on the coating properties is the same when $\gamma-Al_2O_3$ is sprayed. Moreover, in the latter case the spraying regime influences the quantitative proportions of $\alpha-Al_2O_3$ and $\theta-Al_2O_3$ phases of the coatings and their specific surface area. The maximum porosity and minimum $\alpha-Al_2O_3$ phase content were found when a transient jet outflow regime was used.

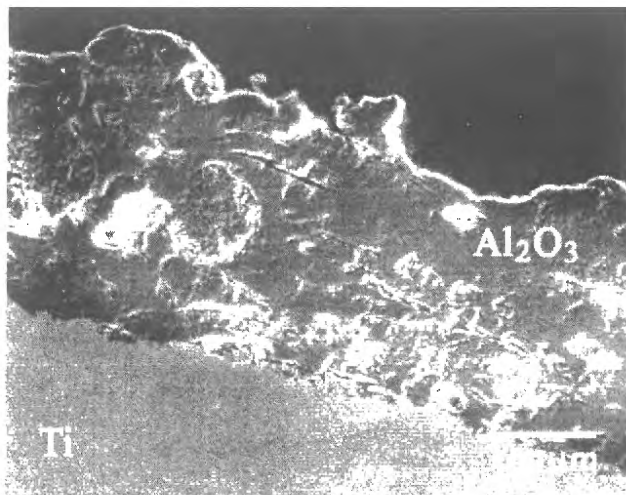


Fig. 4. Micrograph of cross section view of Al_2O_3 plasma sprayed on metal surface.

The formation of dense layers when $\gamma\text{-Al}_2\text{O}_3$ was sprayed on titanium plates was shown by scanning electron microscopy (Fig. 4). It is obvious that the contact between alumina and the metal surface is rather strong and uniform. The sprayed layer has a complicated structure consisting of dense areas and macropores of different forms and sizes.

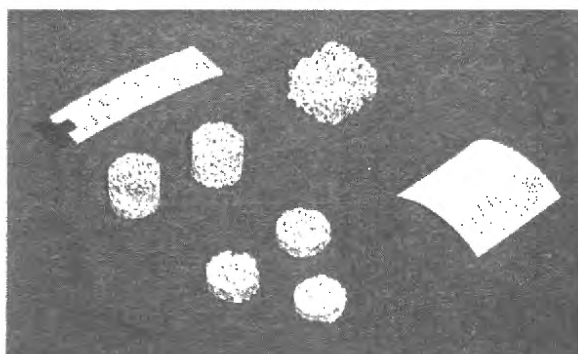


Fig. 5. Plasma sprayed samples of different surface geometry.

Taking into account that phase composition and BET area of plasma sprayed alumina do not depend significantly on the properties of alumina powders used for spraying, $\alpha\text{-alumina}$ with particle size $40\ \mu\text{m}$ was sprayed on metal supports of different geometry, Fig. 5.

Combustion catalysts on metal foams

It was shown in [3] that the genesis of an active component in the combustion catalyst is not affected by the presence of the plasma sprayed $\alpha\text{-alumina}$ on the metal foam. Meanwhile, the experiments on thermal cycling have revealed that the presence of the plasma sprayed alumina layer on the metal surface allows to improve the adhesive properties of the active

layer (Fig. 6). It was found that in the catalyst prepared by a pure chemical method the substantial destruction of the active layer continuously proceeds during each of 10 thermocycles performed, whereas in the catalyst with the plasma sprayed alumina the loss of the active layer is observed only after the first thermocycle.

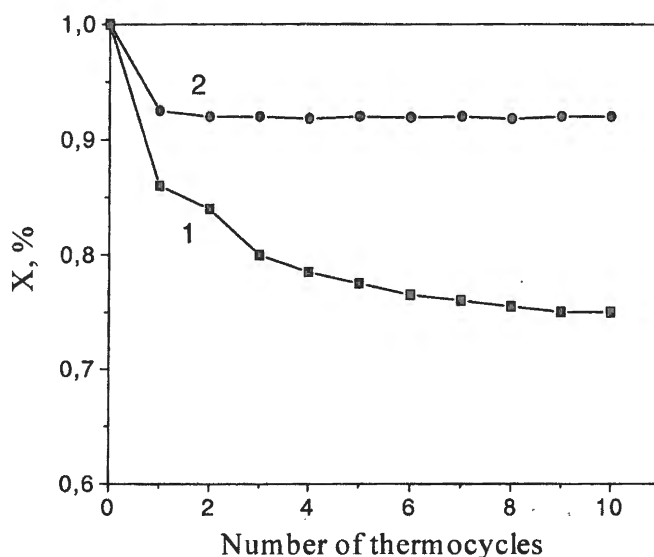


Fig. 6. Dependence of the catalyst weight loss on number of thermocycles, $X(\%) = m_n/m_0$ (m_0 -initial weight, m_n -weight after n thermocycles): 1-LaCoO₃/La- γ -Al₂O₃/Ni-Cr foam; 2-LaCoO₃/La- γ -Al₂O₃/ α -Al₂O₃/Ni-Cr, plasma sprayed α -Al₂O₃ layer.

Different types of combustion catalysts were synthesized on Ni-Cr foam supports covered by dense α -alumina gradient layer using plasma spraying technique. Comparative analysis of the initial activity of metal foamed catalysts calcined at 1000°C and having different types of active components allowed finding the best compositions for methane combustion at high temperatures: Pd/CeO₂- γ -Al₂O₃ > LaMnAl₁₁O₁₉/La-Al₂O₃ ~ Pd-LaCoO₃ > LaCoO₃/La- γ -Al₂O₃. Thermal stability of these catalysts was studied during long time catalyst operation at the following conditions: 8.6% CH₄ in air, GHSV=10000 h⁻¹, T=1000°C. The activity of catalysts was measured after 3, 6, 10, 20 and 50 hours of operation. The catalysts tested for 50 hours can be arranged into the following sequence according to their activity: LaMnAl₁₁O₁₉/La-Al₂O₃ > Pd/CeO₂- γ -Al₂O₃ >> Pd-LaCoO₃ > LaCoO₃/La- γ -Al₂O₃.

Thus, gradient alumina layer sprayed on the surface of a metal support successfully serves as a washcoat on which active component can be deposited and improves thermal stability of the catalysts.

HEX reactors

A catalytic heat-exchanging (HEX) tubular reactor for combining exothermic combustion and endothermic methane steam reforming has been developed [3,4]. The

PP-24

methane combustion and steam reforming catalysts were synthesized on the heat-conducting metal foam support materials by application of preliminary plasma spraying in order to increase adhesive properties of the active layer. The HEX reactor with perovskite or Pt supported catalyst on Ni-Cr foam material on the external surface of the HEX tube and with Ni containing reforming catalyst on the internal Ni foam was successfully tested in methane combustion reaction combined with methane steam reforming, Fig. 7.

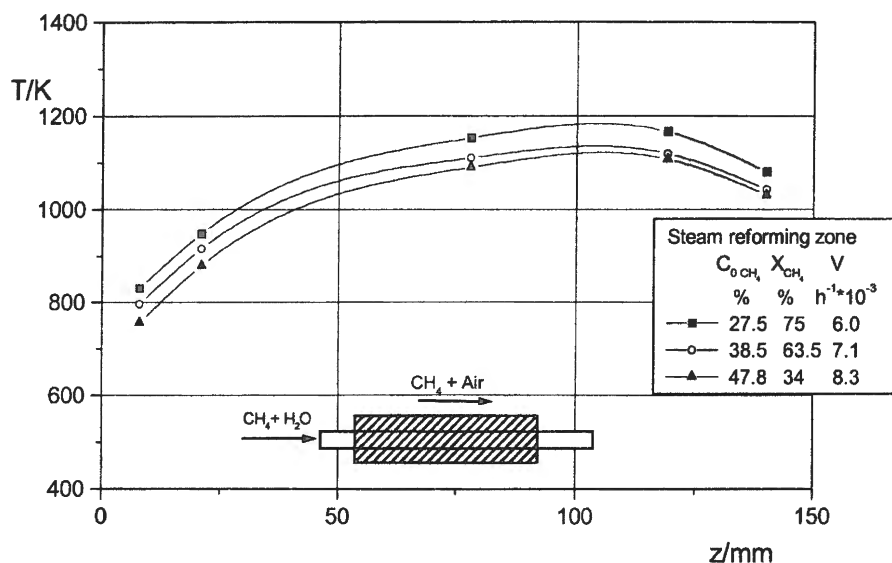


Fig. 7. Temperature profile in the combustion catalyst bed. Combustion of methane-hydrogen mixture with simultaneous steam reforming in heat-exchanging reactor.

Conclusions

Some prospects of application of plasma spraying technique for the synthesis of supported catalysts are demonstrated. Plasma spraying technique successfully allows to synthesise the supported catalysts with enhanced catalytic activity properties and to improve the performance characteristics of combustion catalysts on metal supports during long term operation at high temperatures.

Acknowledgements

This work was supported by the grant of the Siberian Division of the Russian Academy of Sciences in the frame of the Integrated Program 2000-2002; NWO grant in 1997-1999, The Netherlands and INTAS grant 99-1044.

References

1. Kuz'min V.I., Solonenko O.P., Zhukov M.F., Proc. 14th Int. Thermal Spray Conf., 25-28 May 1995, Kobe, Japan, p.1091-1096.
2. Z.R. Ismagilov, O.P. Solonenko, O.Yu. Podyacheva et al., Proc. 13th Int. Symp. on Plasma Chemistry, Beijing, China, 1997, V.4, p.1880-1885.
3. Z.R. Ismagilov, O.Yu. Podyacheva, O.P. Solonenko et al., Catalysis Today, 1999, V.51, p.411-417.
4. Z.R. Ismagilov, O.Yu. Podyacheva, V.V. Pushkarev et al., Studies in Surface Science and Catalysis, 2000, V.130, p.2759-2764.

THE INFLUENCE OF POROUS STRUCTURE AND ACID-BASE PROPERTIES OF
SURFACE OF CATALYST ON ITS ACTIVITY IN REACTION OF
DEHYDRATATION OF α -PHENYLETHANOL

R.G.Romanova, A.A.Lamberov, I.G.Shmelev

*Kazan State Technological University, 420015, Kazan, K.Marx str., 68, Russia
e-mail: rrg@kstu.ru*

The catalytic dehydration of aromatic alcohols is the main mode to produce unsaturated hydrocarbons, including styrene. In present time there is no common opinion on the mechanism of dehydration of aromatic alcohols on the surface of solid catalyst, in spite of the fact that reaction is known for more than 100 years. The aim of this work is investigation of influence of structural and acid-base properties of the surface of aluminum oxide on the selectivity and activity in reaction of dehydration of α -phenylethanol.

The results of investigation of the structure and catalytic activity for a number of standards of γ -Al₂O₃, obtained by traditional aluminately-nitrating and electrochemical modes are presented. The influence of structural characteristics of aluminum oxide, such as specific surface area, pore volume, pore size distribution, on degree of conversion and selectivity in reaction of dehydration of α -phenylethanol is revealed. It has been shown, that dependence of the degree of conversion of α -phenylethanol on pore size of catalyst has the extreme character. The catalyst, having the maximum of pore size distribution in the region of 150-165 Å, is optimal for process.

The influence of strength and number of acid-base centers on the surface of the catalyst on its selectivity to styrene and degree of conversion of α -phenylethanol is considered.

Genesis of porous structure and acid-base centers of catalysts surface in the course of process of dehydration is studied.

The possibility of modification of catalyst surface and of increase the efficiency of dehydration process by means of hydrothermal, thermal and electrochemical treatments is shown.

On the basis of carried out investigations it has been concluded that porous structure and acid-base properties of γ -Al₂O₃ determine its catalytic activity and duration of nonregenerative period of work of catalyst.

*The work was carried out at the financial supporter of Russian Foundation for Basic Research (project № 01-03-32857).

PROMOTED IRON CATALYSTS OF LOW-TEMPERATURE METHANE DECOMPOSITION

T.V. Reshetenko, L.B. Avdeeva, Z.R. Ismagilov,
V.A. Ushakov, A.L. Chuvilin, Yu. T. Pavlyukhin*

Boreskov Institute of Catalysis SB RAS, Pr. Akad. Lavrentieva, 5, Novosibirsk, 630090, Russia
**Institute of Solid State Chemistry and Mechanochemistry, Kutateladze, 18,
Novosibirsk, 630128, Russia*

Abstract

Iron-containing catalysts promoted by nickel or cobalt were tested in methane decomposition reaction at low temperature (600-650°C) and pressure 1 bar in order to study their catalytic properties and to produce catalytic filamentous carbon (CFC). Catalyst preparation method and composition of the catalysts were found to influence their properties. It was found, that introduction of cobalt or nickel in small amount (3-10 wt.%) results in the magnification of carbon yields 2-3 times in comparison with Fe-Al₂O₃. Investigations of Fe-Co-Al₂O₃ and Fe-Ni-Al₂O₃ catalysts genesis were performed by Mössbauer spectroscopy, XRD, TEM. It is established that Co or Ni additives render activating influence on Fe catalysts which become apparent in decrease of the methane decomposition temperature and the formation of multiwall carbon nanotubes (MWNTs).

1. Introduction

The increase of CO₂ concentration (a major greenhouse effect gas) in the atmosphere due to the use of fossil fuels such as petroleum, natural gas and coal leads to change in the planet's climate, so we have to develop a new energy production systems which decrease the CO₂ emission. From this point of view H₂ is a clean fuel that emits no CO₂ when it is burned or used in H₂-O₂ fuel cells. At present, many catalysts of methane transformation have been widely investigated because of their importance in the utilization of natural gas and production of H₂ [1]. Numerous studies of Ni, Fe, Co catalysts in steam reforming, hydrocarbon decomposition have shown that formation of filamentous carbon with graphitic structure – catalytic filamentous carbon (CFC) occurred [2-13]. Realistic way to produce hydrogen considers decomposition of methane, the main component of natural gas, into carbon and hydrogen without CO₂ emission. The hydrogen is used as a clean energy (or a fuel for fuel-cells) and the carbon should be used for synthesis of useful chemicals through synthesis-

gas production by water gas reaction. The carbon can be also used as the functional material such as composites, electrodes, catalyst supports, adsorbents and etc.

It was shown, that Ni and Co catalysts exhibit essential efficiency in CFC accumulation and methane conversion is close to equilibrium at temperatures 500-550°C. We found that a large amounts of filamentous carbon can be produced using coprecipitated catalysts: the 90 wt.% Ni-Al₂O₃ yields 110 g/g_{Ni}, 75 wt.% Co-Al₂O₃-60 g/g_{Co}. The CFC is usually formed as the granules of chaotically interlaced filaments or fibers. One carbon filament grows from one catalytic particle, the latter being located on its top. Carbon filament consists from graphitic planes which are coaxially arranged as cones. Average diameter of the carbon filament for Ni-based CFC is 50 nm, for Co-based - 20 nm. The nature of catalyst influences the microstructure of filament, that becomes apparent in the angle between graphitic planes and the filament axis, which varies from 45° for Ni catalyst [10] to 15° for Co catalyst [11]. The copper addition into Ni catalyst changes the crystallographic orientation of the catalyst particles and as a consequence changes microstructural and textural properties of formed CFC. As a result, the thermal stability and carbon capacity (which can reach 700 g/g_{Ni}) of Ni-Cu increase [12]. Earlier the methane decomposition over iron-contained catalysts was investigated at temperatures above 800°C with the purpose of deriving hydrogen [14] or carbon fibers [15]. However the developed iron catalysts were soon deactivated. Recently it was shown that CFCs were formed at methane decomposition over 85 wt.% Fe-SiO₂ catalyst at temperature not lower than 680°C [16]. It has been established that Co additives render activating influence on Fe catalysts which become apparent in decrease of the methane decomposition temperature and the formation of multiwall carbon nanotubes (MWNTs) [17,18].

The main purpose of the given work is development of the long-living promoted by Ni and Co iron-containing catalysts of methane decomposition and carbon accumulation at low temperatures. In this paper we investigate the activity of coprecipitated Fe-Al₂O₃, Fe-Ni-Al₂O₃ and Fe-Co-Al₂O₃ catalysts, as well as the structure and texture of the formed CFC.

2. Experimental part

Fe-Al₂O₃, Fe-Ni-Al₂O₃ and Fe-Co-Al₂O₃ catalysts were prepared by a coprecipitation method from a solution of metal nitrates using different precipitants. The coprecipitated samples were carefully washed with distilled water, dried at 110°C, and calcined in a flow of air at 450°C for 3 hours. The catalysts were reduced in a flow of pure hydrogen at 580°C for 5 hours, then the samples were in situ passivated in ethanol and dried at room temperature.

PP-26

Catalytic activity of the reduced samples was measured in a vibrating flow quartz reactor 30 cm³ in volume. Methane was supplied at a rate of 45 l/g_{cat}·h. Concentration of methane was measured by gas chromatography, and methane conversion was calculated. To determine the amount of carbon deposited, sample was weighted after the reaction, which was performed until complete catalyst deactivation.

The samples of catalysts and CFC were investigated by TEM, Mössbauer spectroscopy, XRD and adsorption methods. The XRD studies were performed in a Siemens URD-63 diffractometer using CuK_α radiation and a graphite crystal monochromator. Crystallite sizes were calculated from the line width of diffraction peaks (110) for α-Fe, (440) for Fe-Co-Al spinel and (002) for graphite following the Scherrer equation. Mössbauer spectra were obtained by using constant-acceleration NZ-640 (Hungary) spectrometer with a ⁵⁷Co in Rh source. Isomer shifts were reported relative to α-Fe at room temperature. TEM and HRTEM pictures were obtained with JEM-100CX and JEM-2010 microscopes respectively. The adsorption measurements were carried out using an ASAP-2400 apparatus to provide adsorption of N₂ at 77 K.

3. Results and discussion

In order to compare the carbon formation efficiency of prepared catalysts, we use the following parameters of the methane decomposition reaction: methane conversion, carbon accumulation until complete deactivation of the catalysts (the so called carbon capacity G, calculated as gram of carbon per gram of a catalyst) and lifetime of the catalysts.

3.1. Effect of catalyst preparation method

Earlier we have shown, that for high-loading catalysts the method of coprecipitation from aqueous solution of the salts is more favorable. Moreover, studying the Ni-Al₂O₃ and Co-Al₂O₃ systems we have found, that the best catalytic performance was observed with the catalysts prepared using sodium hydroxide as a precipitant [10, 11]. In order to study an effect of the preparation method for Fe catalysts we vary a precipitant (NH₄OH, NH₄HCO₃, NaOH, Na₂CO₃) which, in principle, can lead to the different Fe precursors. Data are summarized in Table 1.

Table 1. Catalytic properties of Fe-based catalysts for methane decomposition, demonstrating the influence of preparation methods ($T=625^{\circ}\text{C}$, methane space velocity = $45 \text{ l/g}_{\text{cat}}\cdot\text{h}$, $P_{\text{CH}_4}=1 \text{ bar}$, X_{CH_4} – methane conversion during 1 hour).

Catalysts	Precipitant	X_{CH_4} , %	Lifetime, hour	G, g/g _{cat.}	Co or Ni, wt. % chemical analysis
50wt% Fe- Al_2O_3	NH_4OH	4	23	26.5	-
50wt% Fe- Al_2O_3	NaOH	6	6	3.3	-
50wt% Fe- Al_2O_3	Na_2CO_3	4	6	2.3	-
90wt% Fe- Al_2O_3	NH_4OH	5.2	7	5.5	-
85Fe-5Co- Al_2O_3	NH_4OH	8	16.5	16.0	4.86
85Fe-5Co- Al_2O_3	NH_4HCO_3	7.7	16	16.0	4.89
85Fe-5Ni- Al_2O_3	NH_4OH	10	16.5	13.5	-
85Fe-5Ni- Al_2O_3	NH_4HCO_3	6	16	12.9	3.66
85Fe-10Ni- Al_2O_3	NH_4OH	10.3	15	17.6	3.03
85Fe-10Ni- Al_2O_3	NH_4HCO_3	7	16	14.9	6.63
85Fe-10Ni- Al_2O_3	NaOH	10	11	11.9	8.22
85Fe-10Ni- Al_2O_3	Na_2CO_3	8	9	7.2	5.82

In contrast to Ni and Co catalysts, from Table 1 one can see that the greatest carbon capacity of Fe- Al_2O_3 and Fe-Co- Al_2O_3 catalysts is observed for samples prepared by coprecipitation using aqueous solution of ammonia as a precipitant. In case of the Fe-Ni- Al_2O_3 catalysts ammoniac complexes of nickel are formed at coprecipitation by NH_4OH that results in incomplete precipitation of the components. We concluded that the best method of Fe-Ni- Al_2O_3 catalysts preparation is coprecipitation by NH_4HCO_3 solution and our studies were realized with catalysts prepared by the appropriate method.

3.2. Effect of the catalyst composition and temperature

Since the maximum carbon capacity during methane decomposition was observed for catalysts with the high metal loading (90 wt.% Ni and 60-75 wt.% Co), the iron content in coprecipitated Fe- Al_2O_3 catalysts has been varied from 20 to 90 wt.%. The obtained values of carbon capacity are plotted in Fig. 1a as a function of nominal bulk Fe concentration. Data show that carbon capacity reaches maximum (20-28 g/g_{cat.}) on the catalysts with 50-80 wt.% Fe. It is known, that Co or Ni additives (5-10 wt. %) render activating influence on iron catalysts [19], therefore we have investigated the influence of Co and Ni on Fe- Al_2O_3 catalysts of methane decomposition at 625°C . Table 2 and Fig. 1b show that introduction of Co or Ni in small amounts (3-10 wt.%) results in the magnification of carbon yields 2-3 times.

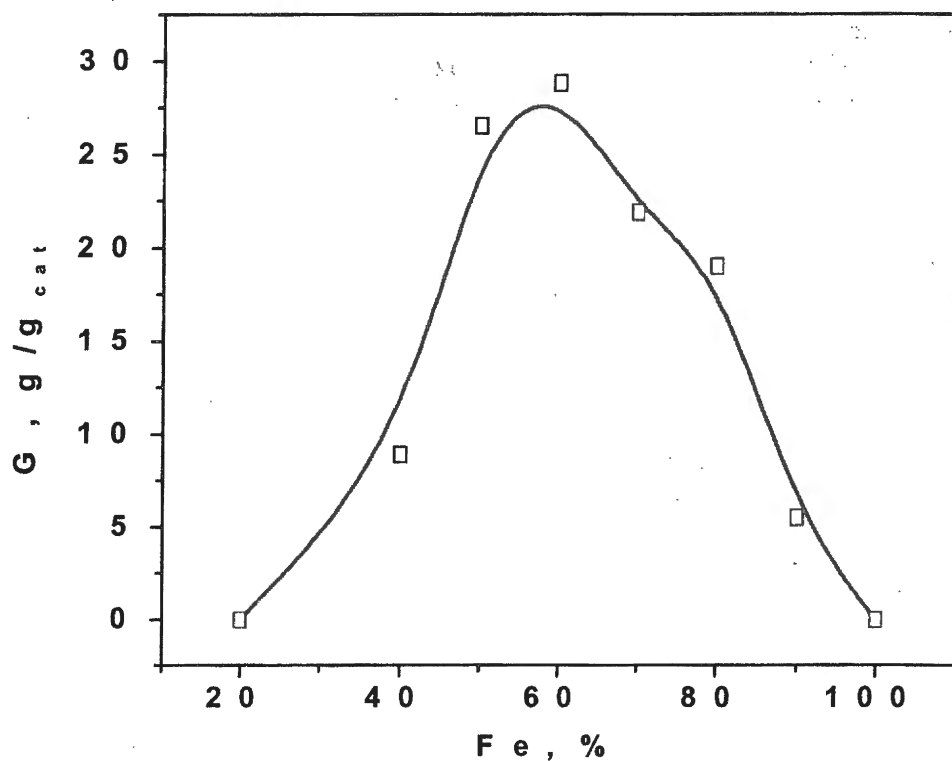


Fig. 1a. The relationship between carbon capacity and metal loading in the coprecipitated Fe-Al₂O₃ catalysts, prepared using NH₄OH as precipitant (methane decomposition reaction at 625°C, P_{CH₄} = 1 bar, methane space velocity = 45 l/g_{cat}·h).

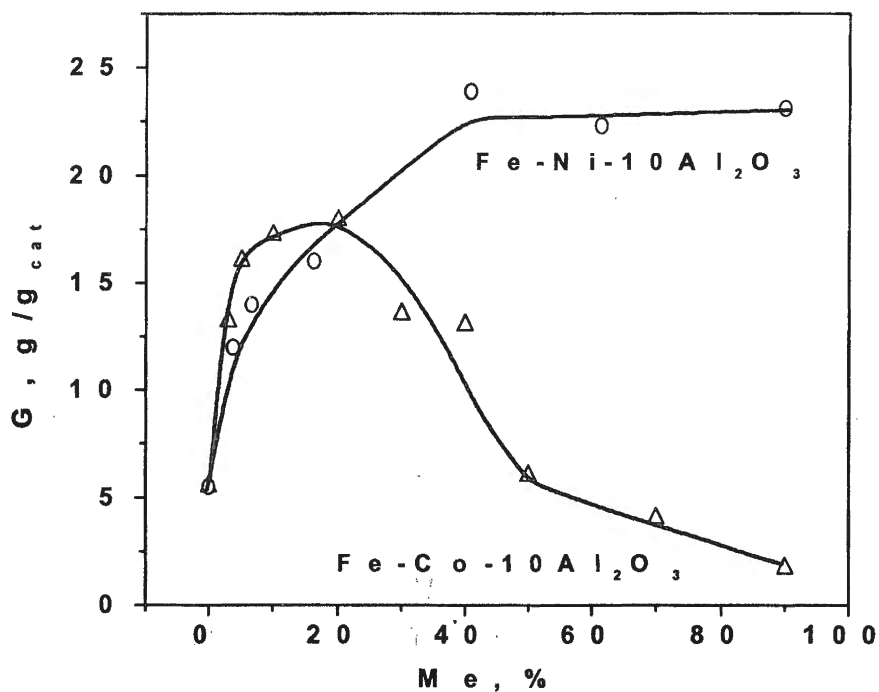
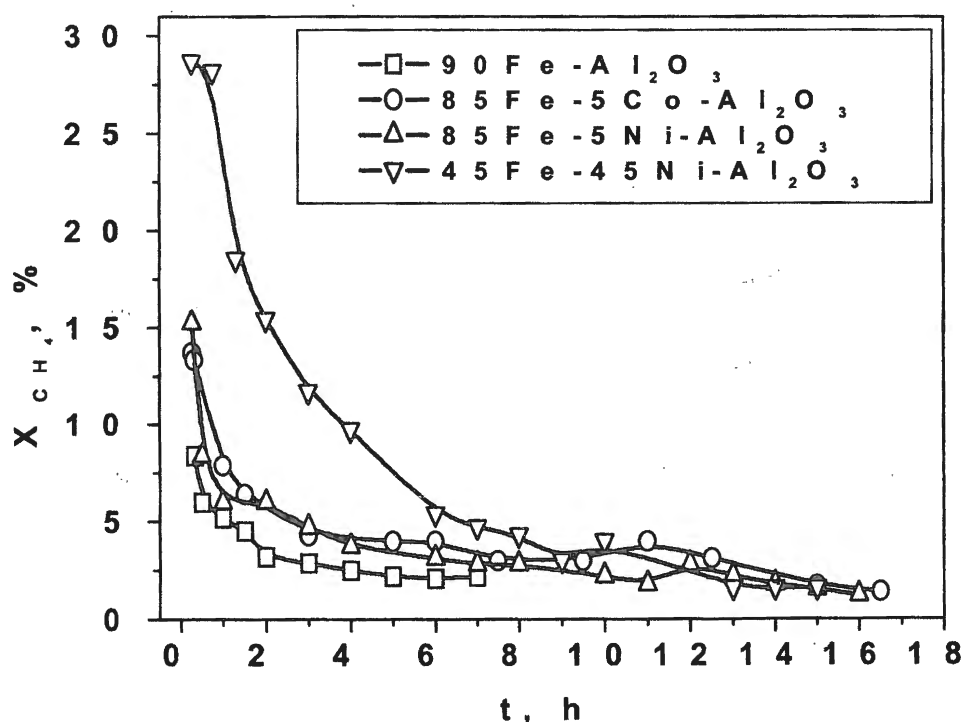


Fig. 1b. The relationship between carbon capacity and second metal content in the Fe-Me-10 wt. % Al₂O₃, (Me - Co or Ni)

Table 2. Catalytic properties of Fe-containing catalysts in the methane decomposition ($T=625^{\circ}\text{C}$, methane space velocity = $45 \text{ l/g}_{\text{cat}} \cdot \text{h}$, $P_{\text{CH}_4} = 1 \text{ bar}$).

Catalysts	Fe:Me:Al ₂ O ₃ , wt. %	Co or Ni, wt. % chemical analysis	Lifetime, hour	X _{CH₄} , %	G, g/g _{cat} .
90Fe-Al ₂ O ₃	90:-:10	-	7	5.2	5.5
85Fe-5Co-Al ₂ O ₃	85:5:10	4.86	16.5	7.9	16
60Fe-30Co-Al ₂ O ₃	60:30:10	-	15	7.3	12.4
50Fe-Al ₂ O ₃	50:-:50	-	23	4	26.5
50Fe-6Co-Al ₂ O ₃	50:6:44	4.0	40	8	52.4
85Fe-5Ni-Al ₂ O ₃	85:5:10	3.66	16	6	12.9
80Fe-10Ni-Al ₂ O ₃	80:10:10	6.5	16	7	14.9
20Fe-70Ni-Al ₂ O ₃	20:70:10	61.4	4	33.9	22.3
90Ni-Al ₂ O ₃	0:90:10	-	4	34.8	23.1

So, carbon capacity on the catalyst 50Fe6Co-Al₂O₃ achieves 52.4 g/g_{cat}. An increase of nickel amount up to 45 wt.% and above in the series of catalysts leads to the formation of catalysts with properties close to the properties of 90 wt.% Ni-Al₂O₃. Apparently, the presence of Co or Ni increases the number of the carbon growth centers of the Fe-Al₂O₃ catalyst. The studies of temperature dependence of methane decomposition over 85Fe5Co-Al₂O₃ catalyst have shown, that carbon capacity reaches its maximum at 625-650°C (Table 3). The methane conversion at 650°C reaches $\approx 13\%$. Fig. 2 shows methane conversion versus reaction time for the Fe-containing catalysts at 625°C.

**Fig. 2.** The global kinetics of methane decomposition on the Fe-Al₂O₃, Fe-Co-Al₂O₃ and Fe-Ni-Al₂O₃ catalysts at 625°C.

PP-26

Table 3. Temperature dependence of catalytic properties of 85Fe-5Co-Al₂O₃ catalyst (methane space velocity = 45 l/g_{cat}·h, P_{CH₄} = 1 bar).

T, °C	X _{CH₄} , %	Lifetime, hour	G, g/g _{cat}
550	3.0	13	5.1
600	5.1	8.5	6.7
625	8.0	16.5	16
650	12.9	13	15
675	10.9	8	13.2

3.3. Structure of catalysts

We performed XRD, Mössbauer spectroscopy and TEM studies of the calcined and fresh reduced Fe-Al₂O₃ and Fe-Co-Al₂O₃ catalysts, as well as of samples after their exposition to reaction mixture. According to the XRD data calcined samples of Fe-Al₂O₃ and Fe-Co-Al₂O₃ are X-ray amorphous that testifies to formation of highly dispersed phase. The Mössbauer spectrum of the calcined 85Fe-5Co-Al₂O₃ catalyst represents a composition of a quadrupole doublet and six-line pattern (Table 4).

Table 4. Mössbauer parameter for 85Fe-5Co-Al₂O₃ catalyst (Isomer shift - δ (mm/s), Quadrupole splitting - ϵ (mm/s), Magnetic field - H (T)).

Sample	Spectrum	Phase	δ , mm/s	ϵ , mm/s	H, T	Rel area
85Fe-5Co-Al ₂ O ₃ calcined in air at 480°C	Doublet	Superpara mag-netic	0.34±0.01	0.86±0.02		0.92
	Six-line pattern	Fe ₂ O ₃ Fe ₂ O ₃	0.39±0.03	-0.12±0.02	51.2±0.07	0.08
85Fe-5Co-Al ₂ O ₃ reduced in H ₂ at 580°C	Six-line pattern	Fe-Co	0.01±0.01	0.00±0.02	34.2±0.02	1.00
85Fe-5Co-Al ₂ O ₃ after 20 min in CH ₄ decomposition at 625°C	Six-line pattern	Fe-Co Fe ₃ C	-0.01±0.01 0.20±0.03	0.01±0.01 0.01±0.03	34.5±0.02 20.6±0.05	0.77 0.23
	Six-line pattern					
85Fe-5Co-Al ₂ O ₃ post reacted in CH ₄ at 625°C	Six-line pattern	Fe-Co Fe ₃ C	0.03±0.01 0.20±0.04	0.00±0.01 0.01±0.04	34.7±0.02 20.5±0.08	0.94 0.06
	Six-line pattern					

The spectrum, according to the determined parameters, is characteristic for Fe⁺³, located in a high-spin state and octahedral surrounding of oxygen anions. Accounting for the chemical nature of the precursor and method of preparation of a Fe-Co oxide system it may be assumed that following the proposed method of synthesis the iron oxide is obtained. The

presence of the quadrupole doublet and large value of ϵ indicate that it is in highly dispersed, superparamagnetic condition, and the particle size is not more than 80 Å. The similar parameters of the spectra were observed for highly dispersed Fe_2O_3 in the work [20]. The six-line pattern (Table 4) corresponds to the admixture of the Fe_2O_3 with a rather large size of particles. The fraction of this state is estimated as about 8% based on the area under the lines.

It is known, that iron can exhibit several crystal structures. α -Fe having a body centered cubic lattice with symmetry $Im\bar{3}m$ exists at the temperatures below 769°C. α -Fe has ferromagnetic properties. It was established that a bulk $\alpha \rightarrow \beta$ phase transition occurs at 769°C. β -Fe has the same symmetry as α -Fe, but already exhibits paramagnetic properties. γ -Fe is formed at the temperatures above 917°C, and has face centered cubic lattice with $Fm\bar{3}m$ symmetry. Since we work at the temperatures below 700°C, we should expect formation of only α -Fe, that is confirmed by XRD.

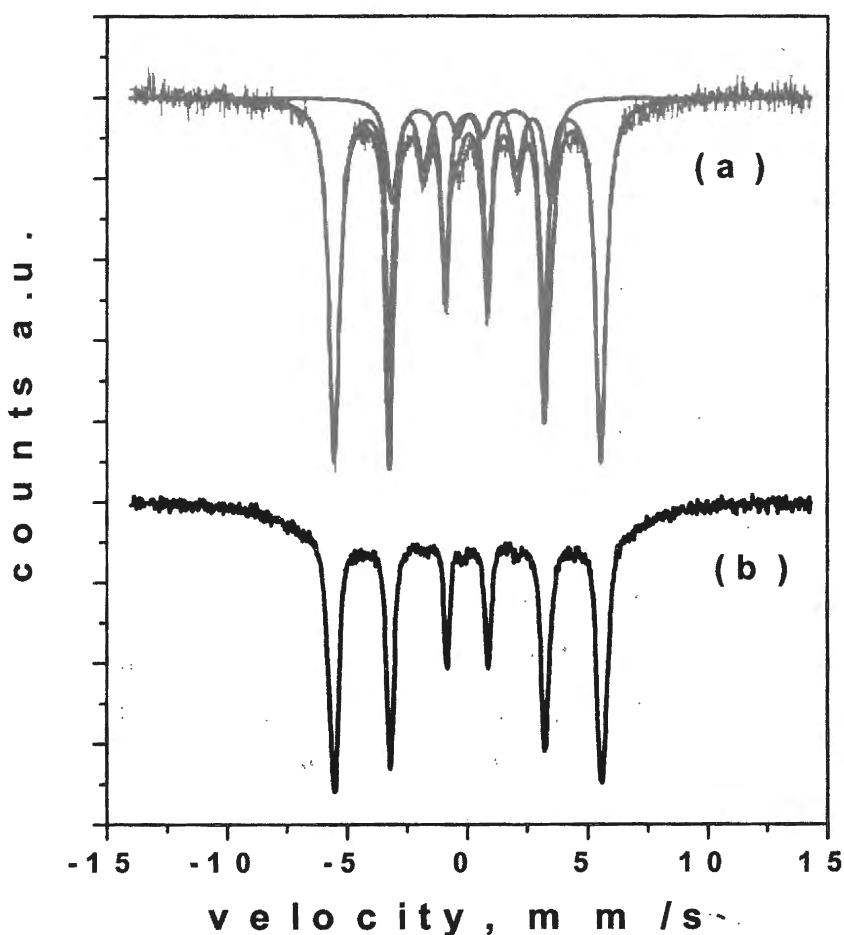


Fig. 3. Mössbauer spectra of ^{85}Fe -5Co- Al_2O_3 catalyst:

- (a) - after 20 min in methane decomposition reaction at 625°C,
- (b) - after 50 min in methane decomposition reaction at 625°C.

PP-26

XRD data (Table 5) of reduced catalysts show presence of α -Fe phase in the samples. The traces of Fe-Co-Al spinels are observed for the catalysts containing 10 wt.% Al_2O_3 . The Mössbauer spectrum of the reduced 85Fe-5Co- Al_2O_3 sample shows a six-line pattern characteristic of Fe-Co alloy plus a central doublet which can be attributed to the traces of superparamagnetic Fe_2O_3 . The reduced catalyst represents an alloy Fe-Co. The value of magnetic field exceeds the magnetic field for pure iron and corresponds to the alloy Fe-Co with 5 wt.% of Co (Table 4). According to the TEM data average particle size of the 85Fe-5Co- Al_2O_3 , 60Fe-30Co- Al_2O_3 , 50Fe-6Co- Al_2O_3 samples is 25-35 nm, for the 90Fe- Al_2O_3 – 35-55 nm, in case of the 50Fe- Al_2O_3 - 30-40 nm.

Table 5. X-ray diffraction and TEM data for the reduced Fe- Al_2O_3 and Fe-Co- Al_2O_3 catalysts.

Sample	d, Å	Phase	Particle size (TEM), nm
90Fe- Al_2O_3	2.867	α -Fe Fe-Al spinel (traces)	35-55
50Fe- Al_2O_3	2.867 8.242	α -Fe Fe-Al spinel	30-40
85Fe-5Co- Al_2O_3	2.866	α -Fe Fe-Co-Al spinel (traces)	25-35
60Fe-30Co- Al_2O_3	2.863	α -Fe Fe-Co-Al spinel (traces)	25-35
50Fe-6Co- Al_2O_3	2.865 8.261	α -Fe Fe-Co-Al spinel	25-35

The Mössbauer spectrum of the catalysts after 20 min in methane decomposition reaction (Fig. 3a) and after complete deactivation at 625°C consist of superposition two sextets which can be attributed to Fe-Co alloy and Fe_3C . It should be noted that the amount of observed Fe_3C in the deactivated catalyst is essentially less than in the sample after 20 min in methane decomposition. XRD data show also formation of Fe_3C phase.

In the case of the 85Fe-5Co- Al_2O_3 sample after 50 min exposition to reaction mixture the Mössbauer spectrum with complicated structure is observed (Fig. 3b). There is a “sagging” of the spectrum central part. Probably the formation of metastable [Fe-C] has resulted in appearance of such kind of the spectrum.

3.4. Morphology and texture of carbon

TEM images of CFC, formed upon low-temperature methane decomposition over 50Fe- Al_2O_3 , 85Fe-5Co- Al_2O_3 and 70Fe-20Ni- Al_2O_3 catalysts, are presented in Fig. 4.

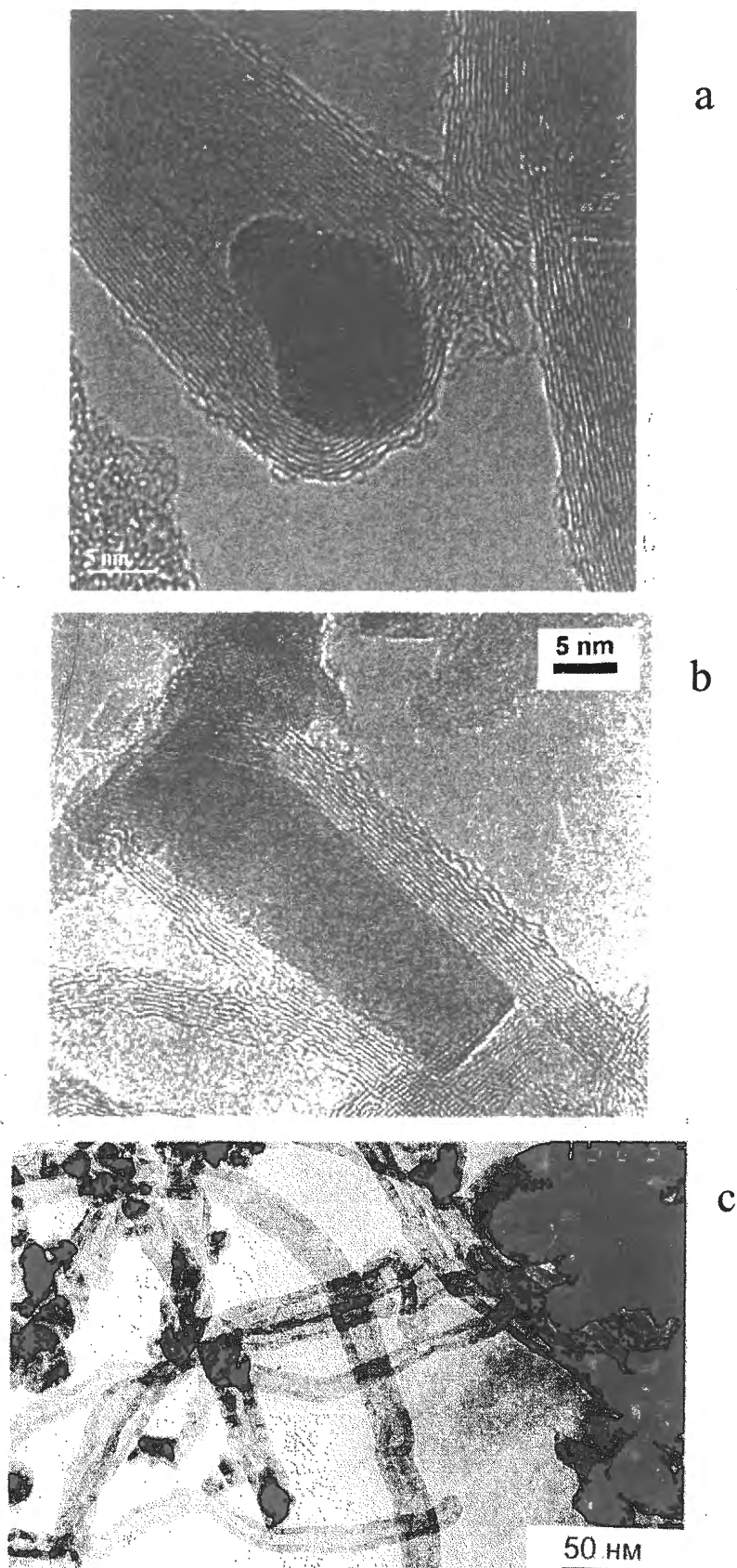


Fig. 4. TEM photographs of the catalysts: (a) - $50\text{Fe-Al}_2\text{O}_3$,
(b) - $85\text{Fe-5Co-Al}_2\text{O}_3$,
(c) - $70\text{Fe-20Ni-Al}_2\text{O}_3$
after 50 min in methane decomposition at 625°C , showing formation of the carbon nanotubes.

PP-26

The formed carbon has filamentary morphology and represents carbon nanotubes, consisting from the turbostratic carbon layers, which are parallel to the fiber axis and look as cylinders with growing diameters enclosed in each other. The turbostratic nature of the formed carbon is confirmed by XRD data (Table 6), indicating that the interplanar distance d_{002} is equal to 0.343 nm, i.e. a little higher than in a perfect graphite ($d_{002}=0.335$ nm), and also by HRTEM data (Fig. 4a, b). The diameter of carbon nanotubes varies at the range of 30-50 nm.

Table 6. Textural and structural properties of CFC formed in the methane decomposition at 625°C.

Sample	S_{BET} , m ² /g	V_{pore} , cm ³ /g	V_{μ} , cm ³ /g	D_{pore} , Å	d_{002} , nm	L_c , nm
CFC(85Fe-5Co-Al ₂ O ₃)	103.1	0.4417	0.0046	171	0.342	6.5
CFC(80Fe-10Co-Al ₂ O ₃)	118.2	0.3737	0.0057	126	-	-
CFC(60Fe-30Co-Al ₂ O ₃)	136.0	0.4744	0.0047	149	0.340	11.0
CFC(50Fe-Al ₂ O ₃)	151.5	0.5006	0.0068	132	0.343	8.7
CFC(50Fe-6Co-Al ₂ O ₃)	155	0.5582	0.0101	144	0.342	8.2
CFC(80Fe-10Ni-Al ₂ O ₃)	139.1	0.4871	0.0070	140	-	-
CFC(70Fe-20Ni-Al ₂ O ₃)	121.1	0.5481	0.0073	188.6	-	-

The analysis of TEM data allows to pick out two types of filamentous carbon:

- I. Nanotubes, consisting from 7-15 graphitic cylindrical layers, with outer diameter ranging between 25-30 nm and inner channel of 10 nm (Fig. 4b).
- II. Carbon fibers, which have internal caps formed by linkage of the inner carbon layers are observed. All of the internal caps are oriented perpendicularly to the fiber axis and along one direction only for the given fibers. Carbon fibers are observed predominantly in CFC (50Fe-Al₂O₃) and to a lesser extent in CFC (85Fe-5Co-Al₂O₃).

Nanotubes (type I) are formed mainly upon methane decomposition over 85Fe-5Co-Al₂O₃, however their yield does not exceed 20 g/g_{cat}. The carbon capacity is increased up to 52.4 g/g_{cat} with a diminution of the iron contents in the catalyst down to 50 wt.% (catalyst 50Fe6Co-Al₂O₃), however in this case carbon fibers (type II) are formed.

An increase of the Ni content in the Fe-Ni catalysts up to 70 wt.% formation of CFC characteristic for CFC (90 wt.% Ni-Al₂O₃) is observed. The catalytic particles have cubooctahedral shape, the carbon filament consists from graphitic planes which are coaxially arranged as cones at the angle 45° [10].

Textural properties of the tubular formed carbon were determined by nitrogen adsorption at 77 K (see Table 6). The magnitude of specific surface area (S_{BET}) varies in the range of 100-150 m²/g. The tubular CFC is more friable on the packing with a bulk density of 0.2 g/cm³, pore volume of 0.5 cm³/g and average pore diameter of 15 nm. Interplanar distance d_{002} and the average size of the coherent scattering area directed perpendicular to the graphite plane (002) (L_c) of CFC were determined from XRD data and represented in Table 6.

3.5. The nature of iron-containing catalyst promotion

It is known, that carbon deposition deactivates the catalyst in hydrocarbon decomposition reactions at high temperatures. However hydrocarbon decomposition under certain conditions, may result in the formation of filamentous carbon which does not poison the catalyst for a long time. Data presented above, show that it is possible to create long-living iron catalysts of methane decomposition if the conditions of filamentous carbon growth are ensured.

The properties of Fe-containing catalysts are found to be similar to the properties of Co-containing catalysts, and depend on the preparation method, amounts of the metal and temperature regimes [11]. Among the investigated catalysts, the best properties are exhibited by coprecipitated Fe-Al₂O₃ using aqueous solution of NH₄OH as a precipitant and containing not less than 50 wt.% of Fe (Table 1). Brown et. al. [21] had established, that introduction of Co at the stage of Fe and Al hydroxides formation results in the decrease of reducing temperature of iron oxides. Indeed, the known iron Fischer-Tropsch catalysts and catalysts for ammonia synthesis are reduced at the temperatures below 600°C. We have found, that the most effective Fe-Al₂O₃ catalysts of methane decomposition are formed after reduction at the temperature of 580°C, with subsequent passivation at room temperature in ethanol.

We have determined, that the maximum growth of filamentous carbon on Fe-Al₂O₃ catalysts occurs at 625°C. Thus, the temperature at which iron-containing catalysts show considerable efficiency in CFC deposition is much below than it was found in the works [15, 16]. It is known that the high-loaded metal catalysts have the greatest activity in low-temperature methane decomposition and CFC formation. However, the carbon capacity of pure iron catalysts was small, that can be explained by the low contents of iron metal, which is a center of carbon deposition, and the maximum carbon yield is observed for the sample with 50-80 wt.% Fe. Apparently the increase of high-to-reduce oxide admixture (Al₂O₃) in the catalyst results in the formation of the iron particles having appropriate size (\approx 25-35 nm) to growth of carbon filament.

We have shown, that introduction of the small amounts of cobalt (3-10 wt %) in Fe-Al₂O₃ catalysts at the stage of coprecipitation increases CFC yields 2-3 times (Table 2, Fig. 1b). The carbon capacities presented in Fig. 1b show that iron is less active than Fe-Co or Fe-Ni alloys. But the curves of the carbon capacity dependence for Fe-Co and Fe-Ni on the second metal loading (Co, Ni) differ from each other. The carbon capacity dependence for Fe-Co has a brightly expressed maximum at 10-20 wt. % Co, while for Fe-Ni extremum is not observed. There is, however, a significant decrease in the carbon yield for Fe-Co catalysts with increase of the Co content. This catalytic behavior is connected to the fact that pure cobalt is active in methane decomposition reaction at 500°C, and inactive at 625°C. Our results show that an increase in the Ni content of the Fe-Ni catalysts from 5 to 40 wt.% is accompanied by an

PP-26

increase in the amount of deposited carbon from 12 to 22 g/g_{cat}. Further addition of Ni appeared to exert very little impact on the carbon yield and catalyst properties become similar to that exhibited by 90 wt.% Ni-Al₂O₃ under the same condition, that is expressed in the increase of methane conversion and the modification of the CFC characteristics. The Fe-Co catalysts containing 5-10 wt.% of Co are some effective in nanotube formation than Fe-Ni alloys, i.e. the promotion influence of the small amount of Co is more expressed than in case of Ni.

Taylor et. al. [19] had established that some cobalt (5 wt.%) or nickel (5-15 wt.%) has a beneficial influence on iron for nitrogen adsorption, synthesis of ammonia and isotope exchange ¹⁴N₂-¹⁵N₂. They assumed [19], that the small amounts of Co or Ni affect the crystallisation of iron such that a greater proportion of the surface area exists as (111) faces, which are particularly active in the synthesis of ammonia and adsorption of N₂ [22], and these faces are necessary for the deposition of graphitic carbon upon hydrocarbon decomposition.

The typical global kinetics of the methane decomposition over Fe-Al₂O₃ is illustrated in Fig. 2. There is no induction period for Fe-Al₂O₃ catalysts, which is characteristic for Ni-Al₂O₃. Previously we have assigned the induction period to the sintering of carbon-saturated Ni particles from 17 nm to 50 nm within the first minutes of reaction [10]. The Fe-Al₂O₃ (Fe-Co-Al₂O₃) active particle size is 20-35 nm, which seems to be large enough for filamentous carbon growth. Based on the kinetics of methane conversion, it is possible to explain gradual fall of catalyst activity due to a covering of the active centers by constantly generating carbon nanotubes, so-called encapsulation of the active centers.

Fig. 4a-c demonstrate the active centers of iron-containing catalysts of methane decomposition. On the basis of the TEM data it can be assumed that the formation of graphite phase at initial stage of methane decomposition reaction leads to generation of faceted catalyst crystallites - the carbon nanotube growth centers apparently only at addition of the second metal (Co or Ni). Conventional model of methane decomposition includes the following stages: decomposition of CH₄ on the metal (100) and (110) planes involving the formation of surface carbon; carbon diffusion through a metal particle, and graphite precipitation on the metal (111) planes [8].

The Co addition is likely to cause the formation of catalyst particles with allocation of (100) planes where methane decomposition occurs, and planes (111) where carbon deposition can take place. Due to the certain orientation of the catalyst particle when the plane (100) is located perpendicularly to the carbon fiber growth direction the formation of carbon nanotubes with hollow internal channel is provided. Thus iron catalyst promotion by Co or Ni changes the shape of the active particles and the mechanism of the carbon deposition.

Conclusions

Fe-Al₂O₃, Fe-Co-Al₂O₃ and Fe-Ni-Al₂O₃ catalysts have sufficient efficiency in filamentous carbon formation and in a methane decomposition at moderate temperature (625°C). It has been established, that the properties of Fe-containing catalysts depend on a preparation method. The best method is a coprecipitation of components from solutions of appropriate metal nitrates by a solution of ammonia (Fe-Co-Al₂O₃) or ammonia bicarbonate (Fe-Ni-Al₂O₃). Carbon capacity of Fe-Al₂O₃ catalysts is increased in the presence of Co or Ni and reaches 52.4 g/g_{cat.} (104 g/g_{Fe}). TEM data have shown, that the carbon nanotubes are observed upon methane decomposition on the Fe-Co(Ni)-Al₂O₃ catalyst. Application of the developed catalysts allows to obtain CFC with a new microstructure (carbon nanotubes), which now have scientific and practical interest.

Acknowledgements

We are grateful to Professor V.B. Fenelonov for the adsorption data. The research described in this publication was possible owing to, Award No. REC-008 from the U.S. Civilian Research and Development Foundation for the Independent States of the Former Soviet Union (CRDF) and NWO-2001.

References

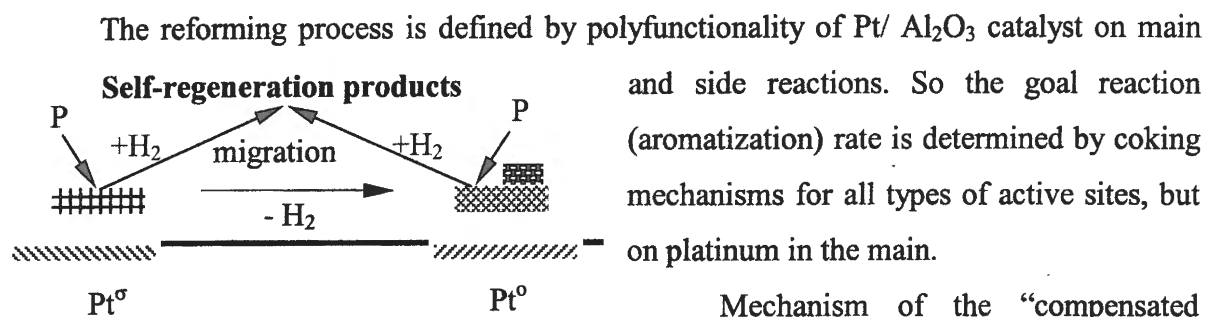
- [1] L. Guzzi, R.A. Van Santen, K.V. Sarma, *Catal. Rev.-Sci. Eng.* 38 (1996) 249.
- [2] L. Bonnetain, P. Gadelle, M. Audier, in J.L. Figuieredo, C.A. Bernardo, R.T.K. Baker and K.J. Huttinger (Ed.), *Carbon Fiber Filaments and Composites*, Kluwer Acad. Publ. Dordct, Boston/London, 1990, p. 507.
- [3] N. M. Rodriguez, M. S. Kim, M.S. Downs, R. T. K. Baker, in J.L. Figuieredo, C.A. Bernardo, R.T.K. Baker and K.J. Huttinger (Ed.), *Carbon Fiber Filaments and Composites*, Kluwer Acad. Publ. Dordct, Boston/London, 1990, p. 541.
- [4] C.A. Bernardo, I. Alstrup, J.R. Rostrup-Nielsen, *J. Catal.* 96 (1985) 517.
- [5] P.K. De Bokx, A.J.H.M. Kock, E. Boellaard, W. Klop, J.W. Geus, *J. Catal.* 96 (1985) 454.
- [6] C. Park, R.T.K. Baker, *J. Catal.* 179 (1998) 361
- [7] K.P. de Jong, J.W. Geus, *Catal. Rev.-Sci. Eng.*, 42 (2000) 481.
- [8] R.T. Yang, J.P. Chen, *J. Catal.* 115 (1989) 52.
- [9] Sh. K. Shaikhutdinov, L. B. Avdeeva, O. V. Goncharova, D. I. Kochubey, B. N. Novgorodov, L. M. Plyasova, *Appl. Catal. A*, 126 (1995) 125.
- [10] L. B. Avdeeva, O. V. Goncharova, D. I. Kochubey, V. I. Zaikovskii, L. M. Plyasova, B. N. Novgorodov, Sh. K. Shaikhutdinov, *Appl. Catal. A*, 141 (1996) 117.
- [11] L. B. Avdeeva, D. I. Kochubey, Sh. K. Shaikhutdinov, *Appl. Catal. A*, 177 (1999) 43.
- [12] T.V. Reshetenko, L.B. Avdeeva, Z.R. Ismagilov, A.L. Chuvilin, V.A. Likholobov, *Eurasian ChemTech Journal* 2 (2000) 237.
- [13] V.V. Chesnokov, R.A. Buyanov. *Russ. Chem. Rev.* 69 (2000) 623.
- [14] V.V. Veselov, T.A. Levanyuk, P.S. Pilinenko, N.T. Meshenko, in V.V. Veselov (Ed.), *Scientific basics of hydrocarbon catalytic conversion*, Kiev, Naukova dumka, 1977, p. 84 (in Russian).
- [15] G. Tibbetts, M. Devour, E. Rodda, *Carbon* 25 (1987) 357.
- [16] M.A. Ermakova, D.Yu. Ermakov, A.L. Chuvilin, G.G. Kuvshinov, *J. Catal.* 201 (2001) 183.
- [17] L. B. Avdeeva, V. A. Likholobov, The patent of Russian Federation № 2146648 (2000).
- [18] L. B. Avdeeva, T. V. Reshetenko, Z. R. Ismagilov, V. A. Likholobov. *Appl. Catal. A* 228 (2002) 53.
- [19] D.W. Taylor, P.J. Smith, D.A. Dowden, G. Kembal, D.A. Whan, *Appl. Catal.* 3 (1982) 161.
- [20] J.W. Niemanisverdriet, A.M. van der Kraan, W.N. Deglass, M.A. Vannice, *J. Phys. Chem.* 89 (1985) 67.
- [21] R. Brown, M.E. Cooper, D.A. Whan, *Appl. Catal.* 3 (1982) 177.
- [22] F. Zaera, A.J. Gellman, G.A. Somorjai, *Acc. Chem. Res.* 19 (1986) 24.

**“COMPENSATED DISINTEGRATION OF HYDROCARBONS” MODEL –
THE KEY TO UNDERSTANDING OF REFORMING REACTOR BEHAVIOR**

O.A.Reutova

Chemistry Department, Omsk State University,

55-a, Pr. Mira, Omsk, Russia, 644077 E-mail: reutova@univer.omsk.su



The temperature regime for reforming process is near 770 K, so the formation of densely packed coke on metal Pt component begins after 40-50 days start-up of reactor. As it was shown by derivatography for waste industrial catalyst (R-56 UOP, Sibneft – Omsk NPZ) the exothermic peak exists about 740°C (1100 K). It corresponds to the burning down of densely packed coke, which dramatically influences reforming reaction activity. So the catalyst doesn't reduce its activity during self-regeneration in hydrogen-content atmosphere or under oxygen (air) regeneration near 600°C.

In view of above-mentioned mechanism the kinetic model was used for monitoring of industrial catalytic reforming unit (Sibneft – Omsk NPZ). The temperature and concentration profiles are an important characteristic data because they reflect kinetics on the each process stage. These profiles show that the catalyst deactivation staggers in the reactor beds. For the aromatics and naphthenes concentration curves shift upwards and downwards. During deactivation the temperature decreases in the first reactor and increases in the following ones.

The work was supported by Federal Program “Integration – 2000” (Russia).

METHANE SELECTIVE OXIDATION INTO SYNGAS AT SHORT CONTACT TIMES: DESIGN OF MONOLITH CATALYSTS AND THEIR PERFORMANCE

Sadykov V.A., Pavlova S.N., Bunina R.V., Kuznetsova T.G., Zolotarskii I.A., Kuzmin V.A., Vostrikov Z.Y., Simakov A.V., Sazonova N.N., Veniaminov S.A., Parmon V.N., Paukshtis E.A., Rogov V.A., Bulgakov N.N., Lunin V.V.*, Kemnitz, E.**

Boreskov Institute of Catalysis SB RAS,

pr. Lavrentieva, 5, Novosibirsk, Russia, 630090. E-mail: sadykov@catalysis.nsk.su

**Chemical Department of Lomonosov Moscow State University, Moscow, Russia*

***Institute for Chemistry, Humboldt -Univ., Berlin, Germany*

The catalytic partial oxidation of methane (POM) to syngas at short times is an alternative process to the conventional steam reforming of methane. This work presents the results on design of efficient robust and non-expensive monolithic catalysts for this process.

Monolithic supports with square or triangular cells of 1-3 mm typical size and wall thickness in the range of 0.2-0.3 mm were obtained by the extrusion of plastic pastes comprised of highly dispersed corundum precursors and a binder, followed by their drying and calcination (up to 1300°C) in thoroughly controlled conditions.

Ceria-zirconia oxide solution with a fluorite-like structure modified by incorporation of calcium and fluorine into the lattice were synthesized via polymerized complex precursor approach (Pechini route), which was found to ensure a homogeneous spatial distribution of components. The chemical composition and methods of those systems preparation were optimized to ensure their phase homogeneity, high rates of the surface and bulk oxygen diffusion along with a reasonably low surface coverage by weakly bound oxygen forms responsible for methane deep oxidation. Both isothermal samples reduction by CO and methane and temperature-programmed reduction by hydrogen were used to characterize the bulk and surface oxygen mobility and reactivity. The real structure of those oxide solid solutions was studied and model explaining the reactivity and mobility of oxygen was suggested. The surface coordinatively unsaturated sites capable to retain CO and molecular forms of oxygen was elucidated using FTIRS spectroscopy.

The active components based upon platinum, nickel, and their combinations including perovskite-like lanthanum-containing mixed oxidic precursors were supported onto mixed modified ceria-zirconia secondary supports. Their reactivity was respect to interaction with methane and its mixture with oxygen at temperatures up to 900°C was characterized in the steady-state and unsteady-state kinetic experiments using both diluted and concentrated reaction mixtures. The effects of the active components on the oxygen mobility and oxygen storage capacity of fluorite-like mixed oxide support was elucidated as well.

The performance of the monolithic catalysts in the methane selective oxidation into syngas at short contact times was tested in the autothermal mode for feeds with stoichiometric content of methane in air (methane/O₂ ratio = 2:1) as well as in mixtures with addition of water and CO₂. The catalytic layer design was optimized for ensuring the highest yield of syngas at short contact times. It includes variation of the active component composition along the layer as well as the specific surface area of corundum monolithic support. Catalysts activity and selectivity (syngas yield exceeding 90%) were even improved due to presence of up to 100 ppm SO₂ in the feed.

Acknowledgements. This work is in part supported by RFBR-INTAS grant No 97-03-71046/IR-97-402

A.G. Sarmurzina, O.E. Lebedeva, A.A. Taltenov¹, S.V. Efremova, O.N. Kuznetsova

al-Faraby Kazakh National University, Karasai batira, 95a, Almaty, 480012, Republic of Kazakhstan, e-mail: olga@lorton.com

¹S. Toraigiro Pavlodar State University, Pavlodar, Republic of Kazakhstan

Catalytic refining and processing of petroleum feedstocks are of great ecological importance. Although conventional catalysts are quite active and stable, new catalysts are still being sought. Particularly new variants of supports are desirable in order to adapt the catalysts to different types of feeds. Generally the supports should possess high specific surface area, thermostability, reasonable price and availability of raw materials, environmentally friendly production. For decades the two latter requirements were not essential but nowadays they become crucial. For this reason new raw materials attract attention: natural minerals and industrial wastes.

Several non-traditional materials for support preparation were studied: clays, silicate industrial slags, mineral residue of shungite – unique carbon-containing mineral. Original materials as well as the materials after additional pretreatment were used.

Phosphorus slag is an essential and cheap source for a production of aluminosilicate porous materials. Leaching of the slag with nitric, phosphoric or hydrochloric acids leads to a formation of materials with high specific surface area. Pore size distribution depends on the leaching time and acid concentration. The formation of porous glasses from slag is presumably a result of phase separation in the slag and different resistance of the two phases towards acidic treatment. Moderate leaching causes formation of acidic sites.

Both clays and shungite mineral residue are other readily available sources of aluminosilicate materials, and their acidity as well can be regulated by acidic treatment.

Supported copper, platinum, cobalt-molybdenum, chromium catalysts were prepared. Copper-slag catalysts are active and selective in cyclohexanol dehydrogenation at 280°C; cobalt-molybdenum-slag catalysts are able to eliminate up to 90% of sulfur at 390°C. Other catalysts were tested in alkane isomerization and were shown to be effective.

The catalysts resulted have a versatile ecological effect because during their preparation useless industrial wastes are converted into useful products contributing to cleaner fuels production.

CO-FREE METHYL FORMATE FROM METHANOL: THE CONTROL OF SELECTIVITY OF THE PROCESS ON Cu-BASED CATALYSTS

N.V. Shtertser, I.I. Simentsova, L.P. Davydova, A.V. Khasin, T.P. Minyukova, T.M. Yurieva

*Boreskov Institute of Catalysis SB RAS, 5, Prosp. Lavrentieva, 630090 Novosibirsk, Russia
Tel.: 7 (3832) 34-41-09, Fax: 7 (3832) 34-30-56; e-mail: min@catalysis.nsk.su*

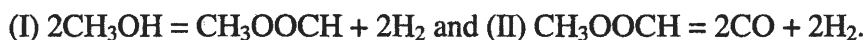
The direct dehydrogenation of methanol to methyl formate has the advantage over methanol carbonylation. The latter is the main method of methyl formate production in industry nowadays and it demands keeping and using carbon monoxide. The aim of present work is to study the active surface formation in copper-containing catalysts for direct synthesis of methyl formate from methanol.

The work is dealing with investigation of structure and composition of oxide-(hydroxo)-precursor and later of support effect as well as effect of pretreatment conditions on activity and selectivity in respect to methyl formate and sorption properties of copper-containing catalysts.

The catalytic properties in methanol dehydrogenation of copper metal formed as a result of reduction by hydrogen of copper-containing oxides with different structure: copper hydroxysilicate (Chrysocolla), copper-zinc hydroxysilicate (Zincsilite), copper chromite (tetragonally distorted spinel) have been studied. It should be noted that copper chromite was reduced at two different temperatures that led to obtaining of the samples with different structure: acid copper (Cu^{1+}) chromite with the structure of spinel and chromia.

The properties of catalysts in the respect to hydrogen adsorption were investigated by means of TPD. Two catalysts preserving the structures of their precursor-oxide after reduction (CuZnSi and CuCr) and having strong bonding of metal particles with the surface was found to have high temperature form of hydrogen adsorption (543 K and 723 K). This form is not observed for usual porous metal copper and for other two catalysts CuSi and $\text{Cu/Cr}_2\text{O}_3$.

Process of methanol dehydrogenation proceeds via successive reactions:



The methylformate selectivity for the catalysts studied was close to 1.0 at low methanol conversion, $X \leq 0.1$, where dehydrogenation process is represented by reaction (I), occurring far from its equilibrium. At $0.2 \leq X \leq 0.55$, the selectivity decreases with increasing conversion, and the ratio of the activities in successive reactions may serve as catalysts comparative characteristic. At high conversions, when reaction (I) is close to its equilibrium, selectivity is independent on the properties of studied catalysts and depends on the methanol conversion.

The catalyst activity in reaction (II) greatly depends on the state of metal copper in the catalysts. It was assumed that the catalyst activity in methylformate conversion to CO and H_2 and, hence, the selectivity of methanol dehydrogenation in respect to methylformate in the region of moderate methanol conversion depends on the character of interaction between metal copper particles and catalyst oxide surface, which is determined by the composition and structure of oxide-precursor.

OSCILLATIONS IN CONVERSION OF METHANE TO SYNGAS IN THE PRESENCE OF OXYGEN OVER SUPPORTED MIXED OXIDES PROMOTED WITH Pt

A.V. Simakov, S.N. Pavlova^{*}, N.N. Sazonova, V.A. Sadykov, O.I. Snegurenko, V.A. Rogov, V.N. Parmon, I.A. Zolotarskii, V.A. Kuzmin, E.M. Moroz

Boreshkov Institute of Catalysis, Siberian Branch of the Russian Academy of Sciences, pr. Lavrentieva, 5, 630090, Novosibirsk, Russia, e-mail: pavlova@catalysis.nsk.su

INTRODUCTION

The catalytic partial oxidation of methane (POM) to syngas at short contact times is an alternative process to the conventional steam reforming of natural gas [1-2]. The testing of the catalysts under atmospheric pressure revealed a good syngas selectivity and yields in the case of precious metal (first of all, Rh-containing) monolithic catalysts [3]. However, at high pressures syngas yield drops due to thermodynamic limitations and the impact of radical gas-phase reactions [4]. To minimize the impact of the gas-phase reactions the process is to be carried out under kinetic not thermodynamic control. To obtain a high conversion of methane at short contact times, the rate of methane conversion via the pyrolysis-oxidation route is to be very fast. To ensure kinetically controlled high yields of syngas at high pressures the catalysts providing the high rate of methane conversion through the route including methane pyrolysis - selective carbon oxidation into CO are to be designed. The problem includes design of the metal active component ensuring efficient methane decomposition and selection of the oxide support having a high bulk and surface oxygen mobility [6-7].

Supported lanthanum nickelates and cobaltites of the perovskite type promoted by small amounts of precious metals were shown to be more active and stable catalysts in this process than supported precious metals [8]. A high oxygen mobility in fluorite-like $\text{CeO}_2\text{-ZrO}_2$ solid solutions helps to ensure an efficient performance of Pt supported on monolithic corundum in POM [9]. The catalysts in those experiments were tested under non-isothermal conditions due to a high methane concentration used, monolithic shape of catalysts etc. In order to develop highly effective POM catalysts favoring direct methane conversion into syngas, it is necessary to obtain data characterising the intrinsic activity of active components under conditions as close as possible to industrially relevant ones (high temperatures, short contact times).

In this work the activity in POM of Ni, Pt, lanthanum nickelate with and without Pt supported on corundum carrier either pure or promoted with $\text{CeO}_2\text{-ZrO}_2$ was studied under conditions providing acquisition of intrinsic kinetic data (high temperature, short contact time, highly diluted gas mixture, small catalyst grains). The phase composition and reducibility of catalysts were also characterized with XRD and TPR.

EXPERIMENTAL

The catalysts containing Pt, Ni and LaNiO₃ either pure or promoted by Pt were prepared by incipient wetness impregnation of microspheric α -Al₂O₃ (100 μ m diameter) with required salt solutions (Table 1). First Ce-Zr oxide was deposited on α -Al₂O₃ from the solution of Ce(NO₃)₃ and ZrOCl₂. After the impregnation, samples were dried and calcined at 900°C in air. Active components were then supported using solutions of La and Ni nitrates, H₂PtCl₆, and samples thus obtained were dried and calcined once more.

XRD spectra of catalysts were recorded on an HZG-4C diffractometer Freiburger Präzisionmechanik with monochromatic Cu K α irradiation. The mean crystallite sizes of Ce-Zr mixed oxide, LaNiO₃, NiO and Pt were determined from XRD line broadening measurements using Scherrer equation. The reflexes at $d = 1.9065$ and 1.7027 Å corresponding to (202), (211) LaNiO₃ faces (No. 34-1181, JCPDS-ICDD) were used for estimation of LaNiO₃ lattice parameters and the average crystallite sizes. The lattice parameters and the average crystallite size of Ce-Zr mixed oxide were determined from the reflexes at $d = 1.83094$ Å corresponding to (202) CeZr solid solution face.

Before TPR experiments, the samples were heated in oxygen at 500°C for 30 min and cooled in oxygen to room temperature. Then oxygen was successively changed for argon and the feed containing 10 vol.% H₂ in Ar. The feed flow rate was 40 ml min⁻¹. The rate of heating from room temperature to 900°C was 10°C min⁻¹. During the experiment H₂O was frozen out at -80°C. The hydrogen concentration was determined using the thermal conductivity detector.

The catalysts were tested in the POM at atmospheric pressure in a continuous flow quartz reactor with 10 mm inner diameter. 0,01 g of the catalyst diluted with quartz powder (0,25-0,5 mm) was placed between two disks of "Buran" foam silica. The temperature of the catalytic bed was measured by a thermocouple placed outside the reactor. Before testing the catalysts were activated by using two procedures. In the first one, the samples were oxidized for 1 h at 900°C in the oxygen flow. In the second one, the catalysts were oxidized for 1 h at 700°C in the oxygen flow, then it was switched to He followed by the feed 30% H₂ in He. Simultaneously, the temperature was raised to 900°C so that the catalysts were reduced for 30 minutes. The catalysts were tested then at 900°C and contact times equal to $2 \cdot 10^{-3}$ and $30 \cdot 10^{-3}$ s. The methane content in the feed gases was 1 vol.%. The oxygen content was varied within 0.01 – 0.5 vol.% range (helium balance). The reaction products were analyzed by the GC. The

PP-31

conversion of methane and product selectivities were calculated on the basis of carbon numbers of the methane reacted. Carbon balances were closed to within $\pm 5\%$.

RESULTS AND DISCUSSION

XRD data

Some catalysts characteristics are presented in Table 1. The $\text{CeO}_2\text{-ZrO}_2$ oxide supported onto corundum is a solid solution of the cubic structure. For all samples, its lattice

Table 1. XRD data

Catalyst	Chemical composition	Phase composition	Lattice parameters (Å)		Crystal size (Å)
			a	c	
ZC-A	$\text{Zr}_{0.8}\text{Ce}_{0.2}/\alpha\text{-Al}_2\text{O}_3$	Cubic $\text{CeO}_2\text{-ZrO}_2$ solid solution	5.182		125
P-ZCA	0.4%Pt/ $\text{Zr}_{0.8}\text{Ce}_{0.2}/\alpha\text{-Al}_2\text{O}_3$	Cubic $\text{CeO}_2\text{-ZrO}_2$ solid solution Pt	5.179		105 250
LN-A	$\text{LaNiO}_3/\alpha\text{-Al}_2\text{O}_3$	LaNiO_3 NiO	5.366	6.579	220
LN-ZCA	$\text{LaNiO}_3/\text{Zr}_{0.8}\text{Ce}_{0.2}/\alpha\text{-Al}_2\text{O}_3$	Cubic $\text{CeO}_2\text{-ZrO}_2$ solid solution LaNiO_3 NiO	5.182 5.371	6.592	120 170 <50
LNP-A	0.2%Pt+ $\text{LaNiO}_3/\alpha\text{-Al}_2\text{O}_3$	LaNiO_3	5.382	6.629	175
LNP-ZCA	0.2%Pt+ $\text{LaNiO}_3/\text{Zr}_{0.8}\text{Ce}_{0.2}/\alpha\text{-Al}_2\text{O}_3$	Cubic $\text{CeO}_2\text{-ZrO}_2$ solid solution LaNiO_3 NiO	5.188 5.383	6.625	90 100
N-ZCA	1.3%Ni/ $\text{Zr}_{0.8}\text{Ce}_{0.2}/\alpha\text{-Al}_2\text{O}_3$	Cubic $\text{CeO}_2\text{-ZrO}_2$ solid solution NiO	5.179		110 50

parameter is nearly constant whereas the average crystallite size is reduced for samples containing Pt. Supported lanthanum nickelate phase either pure or containing Pt corresponds to perovskite of the hexagonal structure which predominates in all catalysts. The broad lines of a low intensity corresponding to NiO are observed in XRD patterns of LN-A and LNP-ZCA samples testifying the presence of some amount of small NiO particles. The diffraction lines of Pt were not observed for LNP-A and LNP-ZCA samples probably as a result of both Pt low concentration and its incorporation into the perovskite structure.

The lattice parameters of supported LaNiO_3 (Table 1) are different from those of a bulk perovskite (No. 34-1181, JCPDS-ICDD), thus evidencing that the structure of supported

perovskite is distorted due to its interaction with the support. The Pt addition results in the increase of perovskite lattice parameters and the decrease of the average perovskite crystal size. These alterations can be due to Pt incorporation into the perovskite lattice. For catalysts supported on Ce-Zr oxide promoted corundum, the variation of the perovskite lattice parameters is more pronounced depending on the presence of Pt as well. The parameter “*c*” of pure supported LaNiO_3 phase is bigger for LN-ZCA sample as compared with that for LN-A, whereas perovskite lattice parameters of LNP-ZCA and LNP-A samples containing Pt are the same. Corundum modification by Ce-Zr oxide favours a higher perovskite dispersion (Table 1), both for pure (LN-ZCA) or Pt containing system (LNP-ZCA).

Temperature-programmed reduction

The TPR data are presented in Fig. 1. Supported $\text{Ce}_{0.2}\text{Zr}_{0.8}\text{O}_2$ has three peaks of hydrogen consumption at 312, 440 and 530°C. The peaks are relatively small indicating a low total hydrogen uptake. In the spectrum of P-ZC-A the high intensive peak at 325°C appears evidencing that Pt facilitates the reduction of Ce-Zr oxide. For N-ZC-A three peaks at 235, 470 and 840°C are observed. For LaNiO_3 supported on pure corundum (LN-A), a small peak at ~350°C and two high intensity peaks at 530 and 890°C are observed. The spectrum of LN-ZCA also shows three peaks shifted to lower temperatures. In addition, the shoulder at 420 and 670°C appear. Thus, $\text{Ce}_{0.2}\text{Zr}_{0.8}\text{O}_2$ facilitates the reduction of LaNiO_3 . Such different behavior of LaNiO_3 perovskite supported on $\text{Ce}_{0.2}\text{Zr}_{0.8}\text{O}_2/\alpha\text{-Al}_2\text{O}_3$ correlates with the increase of the lattice parameter “*c*” indicating the influence of $\text{Ce}_{0.2}\text{Zr}_{0.8}\text{O}_2$ on the perovskite structure.

Addition of Pt strongly affects the TPR profiles of LNP-A and LNP-ZC-A samples. The most pronounced changes are observed at temperatures below 700°C. For LNP-A, an intensive peak at 650°C and the peak at 450°C appear, while the high temperature peak is shifted by 70°C to low temperatures as compared with that for LN-A sample. For LNP-ZCA, the spectrum is more complicated as compared with that for LNP-A: three peaks are observed at temperatures below 550°C, whereas

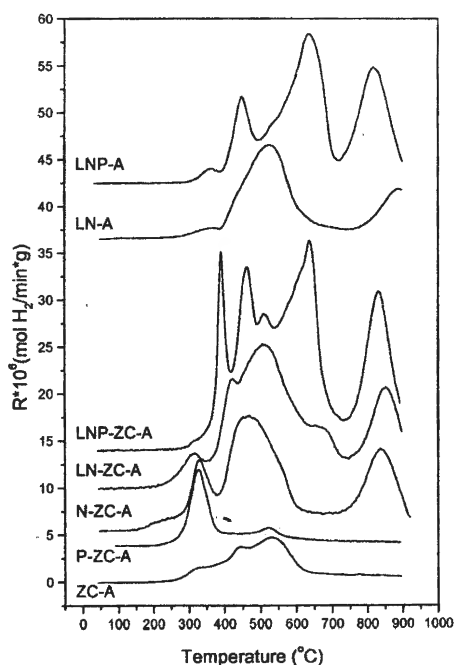


Fig. 1. TPR profiles of the catalysts.

PP-31

the position of the high temperature peaks at 650 and 820-850°C is unchanged. In the case of Pt containing catalysts, Ce-Zr oxide favours their reduction at temperature below 600°C.

Catalytic activity

The activity of catalysts depends on both the catalysts composition and the procedures of samples pretreatment before the kinetic study.

The initial activity of oxidized catalysts decreases in the order:

N-ZC-A > LNP-ZC-A > P-ZC-A > LN-ZC-A.

However, N-ZC-A having the highest initial activity is the least stable (Fig. 2).

The methane conversion substantially decreases with time whereas selectivity to syngas drops to zero after 6 h on stream (Fig. 2). The catalyst LNP-ZC-A is more stable (Fig. 3), though its activity decreases with the time-on-stream as well.

Simultaneously, the H_2/CO ratio changes from 2 to 1 with time. Some oscillations of reagents conversion and selectivities to CO and CO_2 appear after 4 hours on stream (note,

H_2/CO ratio decreases to 1) (Fig. 3). These oscillations take place only for both oxidized LNP-ZCA catalyst and P-

ZCA catalyst being similar to those found in [11] for $Rh/\gamma-Al_2O_3$ catalyst. This type of oscillations found here seems to be related with the formation of carbon deposit over the catalyst surface in the course of the methane conversion. It is important that these oscillations are not observed over the catalyst without Ce-Zr-O secondary layer.

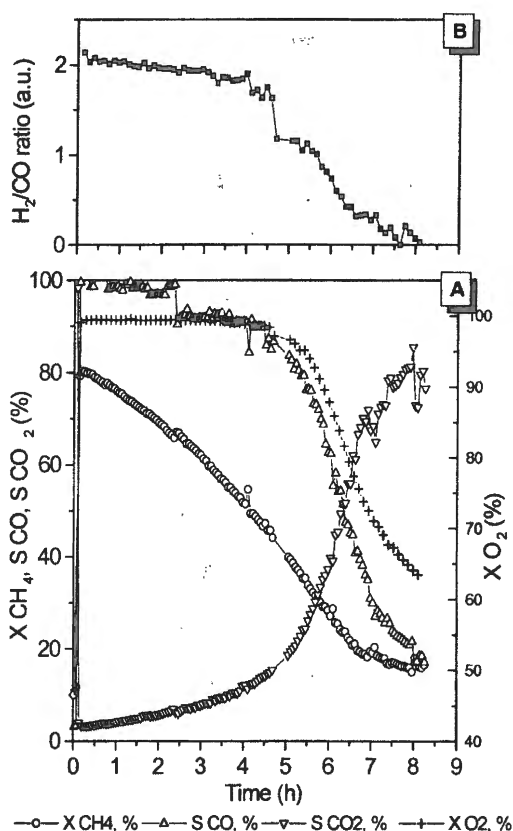


Fig. 2. Conversion of methane and oxygen, selectivities to CO and CO_2 (A); H_2/CO ratio (B) in the reaction products versus time-on-stream for preoxidized N-ZC-A catalyst.

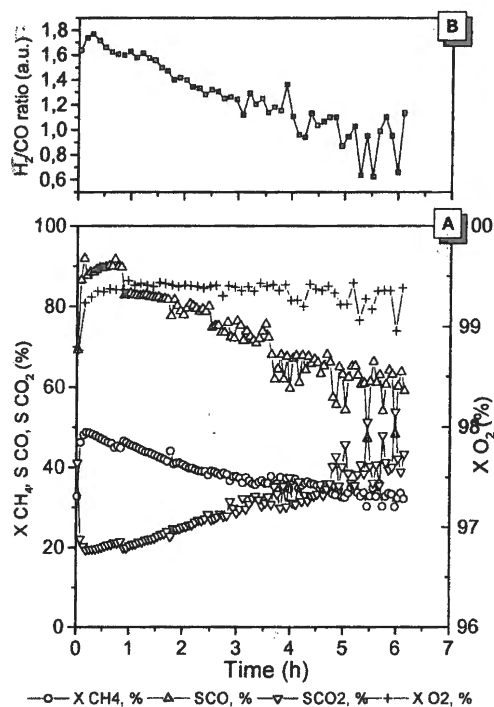


Fig. 3. Conversion of methane and oxygen, selectivities to CO and CO₂ (A); H₂/CO ratio (B) in the reaction products versus time-on-stream for preoxidized LNP-ZC-A catalyst.

For all catalysts, complete gas phase oxygen consumption is observed indicating strong catalyst reduction in the reaction conditions. So, it was very interesting to test the catalytic activity of pre-reduced catalysts. Kinetic data obtained over pre-reduced catalysts at the first few seconds and after 3 hours in stream are represented in Table 2. Initially, LN-ZCA catalyst is most active in syngas formation, but its activity decreases significantly after 3 hours in stream. The addition of Pt leads to the increase of perovskite stability in the syngas production. The state of pre-reduced catalysts changes with time-on-stream as in the case of oxidized samples. These changes are manifested in the decrease of the catalytic activity, the gas phase oxygen consumption and

Table 2. The conversion of methane, oxygen and selectivity to CO and CO₂ (initial values and after 3 hours of testing) over the catalysts studied

Catalyst	Conversion*(%)				Selectivity*(%)			
	CH ₄		O ₂		CO		CO ₂	
	1	2	1	2	1	2	1	2
P-ZCA	28	30	95	92	24	13	76	87
N-ZCA	44	15	99,7	52	65	10	35	90
LN-ZCA	56,5	17	99,7	52	84	29	16	71
LNP-ZCA	28	25	76	67	61	40	39	60

*- 1 – the initial activity, 2 – after 3 hours.

Temperature 900°C, time contact 2×10^{-3} s, reaction gas mixture: CH₄/O₂=2/1. Before activity testing the catalysts were reduced in hydrogen flow as described above.

H₂/CO ratio in the reaction products. In the case of pre-reduced LNP-ZCA stable oscillations in methane, oxygen (Fig. 4A) and products concentration (Fig. 4B) are observed as well. Note, that oscillations appear at the H₂/CO ratio closed to 1 as in case of oxidized LNP-ZCA catalyst. In contrast to the oxidized catalyst these oscillations are characterized with higher amplitude and

PP-31

lower frequency (Fig. 3, 5). Period of oscillations is rather long (about 40-50 min). The amplitude of these “low frequency” oscillations

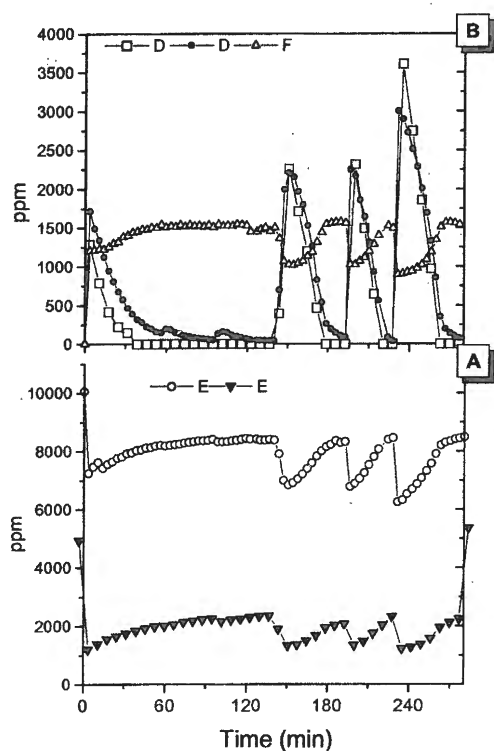


Fig. 4. Oscillations of the reagents (A) and products (B) concentrations over prerduced LNP-ZCA catalyst. $\text{CH}_4/\text{O}_2=2/1$, time contact 2×10^{-3} s.

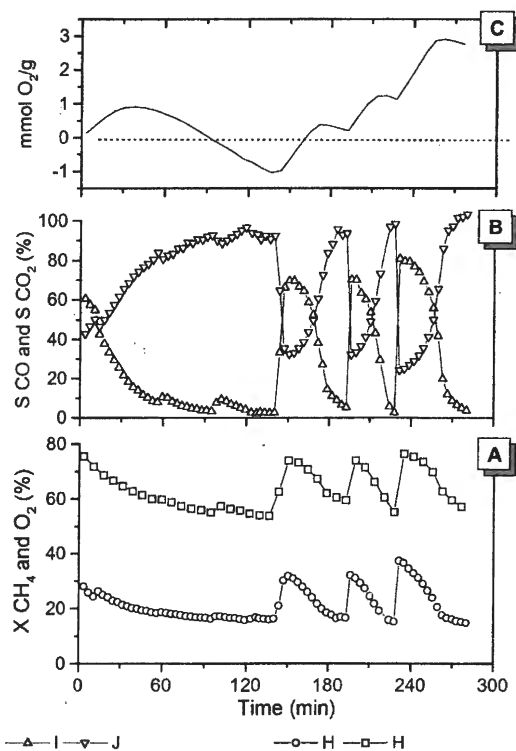


Fig. 5. Oscillations of conversions (A) and selectivities (B) over prerduced LNP-ZCA catalyst. $\text{CH}_4/\text{O}_2=2/1$, time contact 2×10^{-3} s. (C) – amount of oxygen consumed by the catalyst.

increases with time on stream. Some remarks concerning the cause of oscillations could be made on the bases of oxygen uptake in the system “catalyst-gas phase (reagents and products)”. The consumption of oxygen by the catalyst is presented in Fig. 5C by solid line. After about one hour of the experiment the concentrations of CO and hydrogen are practically close to zero (Fig. 4A). At that time, CO_2 is the main reaction product, the amount of oxygen consumed by the catalyst is close to 1 mmol O_2 per g of catalyst (Fig. 5C). Then oxygen consumption by catalyst was stopped. Just in that moment the first oscillation arises (Fig. 5). The subsequent oscillations proceed at moments when the catalyst releases or adsorbs about 1 mmol of molecular oxygen. According to TPR data, the oxygen capacity of Ce-Zr-O solid solution is comparable with that value. Note, that “low frequency” oscillations are observed only in the case of catalysts containing Ce-Zr-O secondary support. The coincidence of these values and the latter fact permit us to suggest that “low frequency oscillations” observed are caused by the changes in the catalysts state associated with the oxygen transport through the Ce-Zr-O secondary layer during the reaction.

CONCLUSIONS

The partial oxidation of methane to synthesis gas over supported mixed oxides (La, Ni) with Pt has been studied in isothermal conditions at millisecond contact times. In all catalysts supported lanthanum nickelate phase either pure or containing Pt predominates and corresponds to perovskite of the hexagonal structure with modified lattice parameters. The redox properties of catalysts depend on the presence of Pt and CeO₂-ZrO₂ solid solution.

The initial intrinsic activity of catalysts depends on both the catalysts composition and the procedures of samples pretreatment before the kinetic study. The addition of Pt and Ce-Zr oxide leads to the increase of the catalysts stability.

There are two types of self-sustained oscillations of the reaction rate and selectivity. The oscillations observed for preoxidized Pt-LaNiO₃/Ce-Zr-O/Al₂O₃ and Pt/ Ce-Zr-O/Al₂O₃ catalysts could be caused by changes of the catalyst state due to carbon deposit. The "low frequency" oscillations observed only for prereduced Pt-LaNiO₃/Ce-Zr-O/Al₂O₃ seem to be related with the oxygen transportation in Ce-Zr-O secondary layer.

REFERENCES

1. S. C. Tsang, J. B. Claridge, and M. L. Green, *Catal. Today*, **23** (1995) 3.
2. R. Burch and S. C. Tsang. *Current Opinion in Solid State & Materials Science*, **2** (1997) 90.
3. L. D. Schmidt and D. A. Hickman, *Science* **259**, (1993) 343.
4. L. D. Schmidt, *Stud. Surf. Sci. Catal.*, NGC V, **119** (1998) 685.
5. J. C. Slaat, R.J. Berger, and G.B. Marin, *Catal. Lett.*, **43**, (1997) 63.
6. H. Y. Wang and E. Ruckenstein, *J. Phys. Chem. B* **103**, (1999) 11327.
7. J.H. Bitter, K. Seshan, and J. A. Lercher, *J. Catal.* **176** (1998) 93.
8. S. N. Pavlova, V. A. Sadykov, N. F. Saputina, V. I. Zaikovskii, A.V. Kalinkin, G. N. Kustova, S. V. Tsybulya, I. A. Zolotarskii, R. V. Bunina, and S. F. Tikhov. *CHISA-98, Summaries*, **2**, P7.24, 72.
9. S. N. Pavlova, V. A. Sadykov, V. N. Parmon, I. I. Bobrova, I. A. Zolotarskii, V. A. Kuzmin, A. N. Salanov, R. V. Bunina, N. F. Saputina, O. I. Snegurenko, Z. Yu. Vostrikov, *EUROPACAT*, September, 2001, Abstracts, Book 4, 5-0-04.
10. J.R.H. Ross, A. N. J. van Keulin, M. E. S. Hegarty, and K. Seshan, *Catal. Today*, **30** (1996) 193.
11. Z.Tian, O. Dewaele and G.B.Marin, *Catal.Lett.*,**57**, (1999) 9.

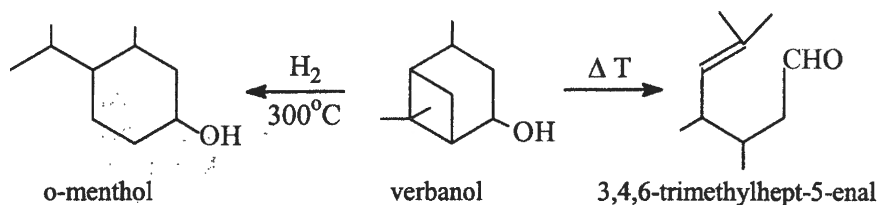
I. L. Simakova, V. A. Semikolenov

Boriskov Institute of Catalysis, Prospekt Ak. Lavrentieva 5, Novosibirsk 630090, Russia

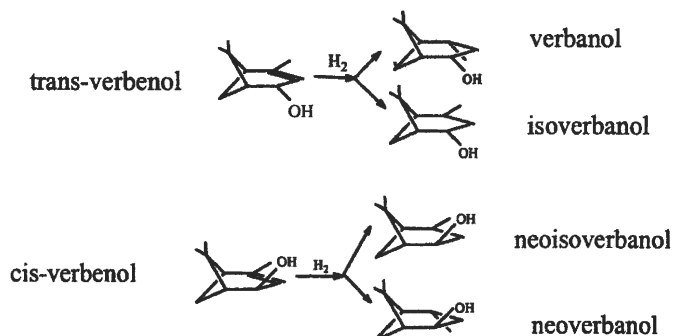
Tel.: +7(3832) 341222 Fax: +7(3832) 343056 E-mail: *simakova@catalysis.nsk.su*

INTRODUCTION

The perspective consumption of α -pinene (the main component of cheap large-tonnage product turpentine) is synthesis of medicines, fragrances and vitamins. The catalytic (Ni, Pd, Pt) hydrogenation of verbenol prepared by α -pinene oxidation gives saturated alcohol verbanol that is used in the fragrance syntheses. So verbanol can be converted in fragrance 3,4,6-trimethylhept-5-enal with strong lemon aroma. Hydrogenolysis of verbanol results in o-menthol that has a mild sweet odor somewhat suggestive of cloves and in this respect is unlike ordinary menthol. Because of its pleasant odor, it is useful in scenting soaps, cosmetic bases and in other perfumery applications. When converted to its salicylic ester it is useful as sun screening compound having optimum ultra violet filter properties, while other aromatic and aliphatic esters, preferably the higher ones, are useful as plasticizers, lubricants, cosmetics and the like [1].



Although verbanol is theoretically capable of existing in twelve possible forms (eight optically active and four racemic) only a few of these have been isolated in pure form. Thus, hydrogenation of *cis*- and *trans*-verbenol is known to result in stereoisomers with different reactivities: [1,2,3]:



According to [4] hydrogenation of *cis*-verbenol leads to *cis*-verbanol whereas hydrogenation of *trans*-verbenol gives *trans*-verbanol, but their structures are not drawn. The comparison of parameters of verbanol isomers patterns with ones of verbanol isomers obtained permit authors to conclude that *cis*-verbanol is neoisoverbanol and *trans*-verbanol is isoverbanol [2]. Authors [3] report that isomers content depends on catalyst employed. Thus, *trans*-verbenol hydrogenation over platinum oxide leads to isoverbanol (91%) and verbanol (9%) formations whereas hydrogenation of *trans*-verbenol over Pd/C gives isoverbanol (55%) and verbanol (45%). Catalytic hydrogenation of *cis*-verbenol yields neoisoverbanol [3]. However the reasons causing definite isomer formation as well as kinetics of verbenol hydrogenation haven't been yet considered in literature.

Earlier it has been found that the stereoselectivity of α -pinene hydrogenation over Pd/C into *cis*- and *trans*-pinane isomers is determined by hydrogen pressure and reaction temperature. Thus, *cis*-pinane content increased with hydrogen pressure growing and temperature decreasing [5].

The aim of this work is to study the general peculiarities of verbanol isomers synthesis by verbenol hydrogenation over Pd/C.

EXPERIMENTAL

Verbenol (*cis*-/*trans*-isomer mixture) was obtained by α -pinene air oxidation followed by vacuum distillation of α -pinene excess and borate ester rectification from verbenon [6]. Solution of verbenol (0.02 mol) in *n*-butanol (10 cc) was hydrogenated over 4% Pd on carbon support Sibunit (5-50 μ m) in stainless steel autoclave (150 ml) supplied with electromagnetic stirrer.

Reaction mixture was separated from the catalyst and products were analysed chromatographically using 7 m \times 3 mm column, Silicone SE 30/ Chromaton N-AW.

The reaction products were identified by VG-7070 GC/MS using a 25 m \times 0.2 quartz capillary column (Silicone SE-30).

RESULTS AND DISCUSSION

Routes of verbanol isomers formation

According to the GLC analysis there are two products of verbenol isomers hydrogenation over Pd/C in the course of reaction. The side products of the cycle opening are not observed. The quantity of hydrogen absorbed corresponds to the verbenol hydrogenated

PP-32

during the reaction. So the time dependence of hydrogen uptake is converted into time dependence of verbenol concentration expressed in relative units as ratio between current total products concentration (C) and initial (C₀) concentration of verbenol isomers mixture. Two linear parts on the kinetic curves of verbenol hydrogenation

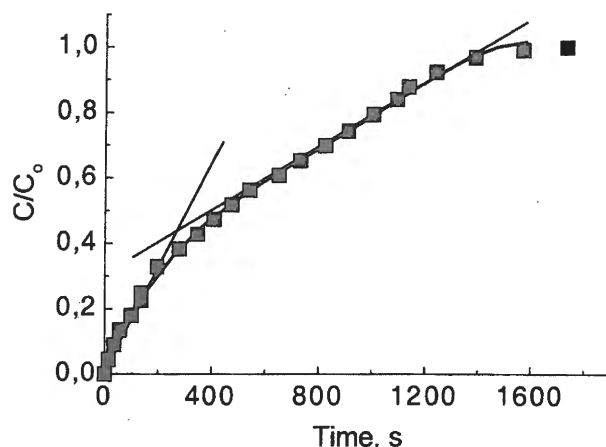


Fig. 1. Kinetic curve of product mixture formation. Reaction conditions: verbenol – 0.154 mol/l, P_{H₂}=11 bar, T=50°C, 0,2 g 4%Pd/C.

have been found: sharper at the beginning and slower at the end (Fig. 1). It indicates that reactivities of *cis*- and *trans*-verbenols presenting in the initial mixture differ substantially.

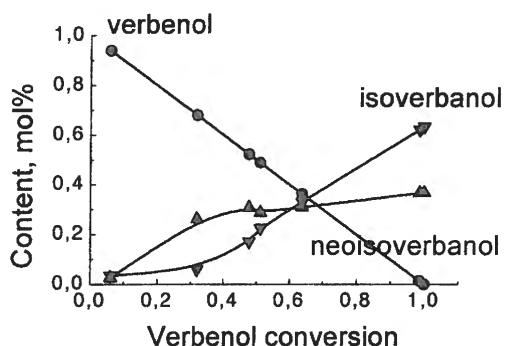
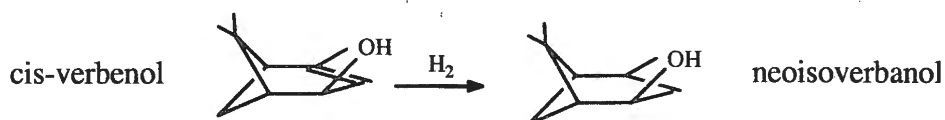


Fig. 2. Effect of verbenol conversion on verbanol isomers content.

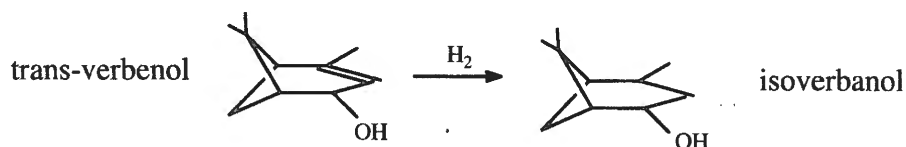
Reaction conditions: verbenol – 0.154 mol/l, 0,4 g 4%Pd/C, T=40°C, P_{H₂}=11 bar.

According to the GLC analysis (Fig. 2) *neoisoverbanol* formation occurs preferably at the initial verbenol conversion range and *isoverbanol*

starts to form at verbenol conversion more than 30% (Fig 2). It permits to suppose that in the beginning of verbenol conversion (up to 40%) the hydrogen uptake corresponds to *cis*-verbenol hydrogenation to form *neoisoverbanol*



and at higher verbenol conversion the rate of hydrogen uptake corresponds to the rate of *trans*-verbenol into *isoverbanol* hydrogenation:



Some increase of *neoisoverbanol* content (at verbenol conversion more than 30%) may be caused by isomerization of *trans*-verbenol into *cis*-verbenol over catalyst surface:



The linear character of kinetic curve (Fig. 1) indicates that verbenol isomers hydrogenation rates have the order on corresponding isomer concentration close to 0. Verbenol is seemed to adsorb strongly over the Pd surface and the limited step may be the interaction of it with hydrogen adsorbed.

Cis/trans verbenols hydrogenation rate constants ratio is calculated: $k_{cis}/k_{trans} = 2,7$ at 40°C. Higher reactivity of *cis*-verbenol seems to be explained by favorable mutual orientation of -OH and -CH₃ functional groups in this molecule.

Kinetic peculiarities

Effect of catalyst concentration

Dependence of initial hydrogenation rate (W_0) upon catalyst concentration is linear in the range of explored temperatures and hydrogen pressures. It demonstrates the absence of hydrogen mass transfer limitation during experiments.

Effect of P_{H_2}

Dependence of initial hydrogenation rate (W_0) upon hydrogen pressure is of linear character. It indicates that hydrogenation rate has the first order on hydrogen pressure.

The hydrogen pressure increase favors the isoverbanol formation (Fig. 3a). The decreasing of P_{H_2} causes the hydrogen adsorbed concentration diminution. The lack of hydrogen on the catalyst surface at low P_{H_2} seems to intensify the process of *trans*-verbenol isomerization into *cis*-verbenol.

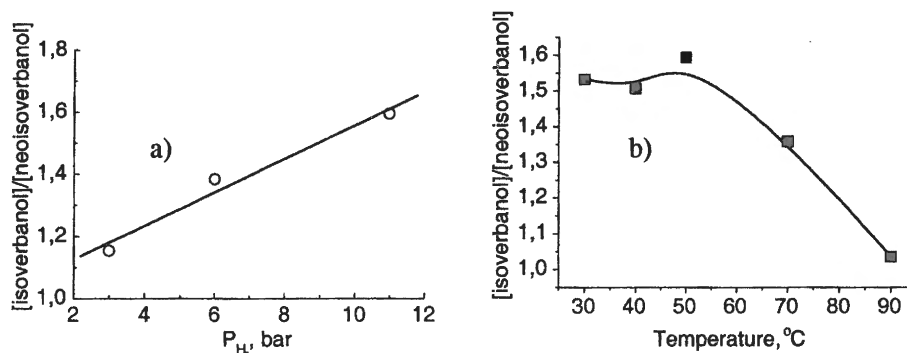


Fig. 3. Effect of P_{H_2} (a) and temperature (b) on the isoverbanol/ neoisoverbanol ratio. Reaction conditions: verbenol – 0.154 mol/l, 4% Pd/C – 0,2 g, a) $T=50$ °C, b) $P_{H_2}=11$ bar.

Effect of the temperature

The observed verbenol hydrogenation rate has been found to increase as the reaction temperature grows. Activation energies of verbenol hydrogenation were estimated to be 45.8 kJ/mol at the low temperature range (up to 60°C) and 8.8 kJ/mol at higher one.

PP-32

Note that the ratio of isoverbanol/neoisoverbanol doesn't change up to 60°C but declines at higher temperature (Fig. 3b). The rise of temperature seems to lead to the decrease of hydrogen adsorbed concentration on the catalyst surface and to the *cis*-verbenol into *trans*-verbenol isomerization.

CONCLUSION

The general peculiarities of verbanol synthesis by verbenol hydrogenation over Pd/C in mild conditions have been studied. The routes of verbanol isomers formation including the isomerization of verbenol isomers have been proposed. The main factors that force the hydrogenation process to turn to the definite verbanol isomer production were found to be hydrogen pressure and reaction temperature. Thus, isoverbanol/neoisoverbanol ratio increases with hydrogen pressure growth and temperature decrease (down to 60°C) in the course of hydrogenation over the Pd/C catalyst. Macrokinetic data of verbenol isomers hydrogenation have been obtained.

REFERENCES

1. Pat. 2,972,635 USA.
2. Bose A. K. *J. Org. Chem.* 1955, **20**, 1010-1015.
3. Regan A. F. *Tetrahedron.* 1969, **25**, 3801-3805.
4. Bull. Soc. Chim. Fr. 4 Ser, 1933, N 11, 1167.
5. Semikolenov V. A., Ilyna I. I., Simakova I. L. *Appl. Catal. A: Gen.* 2001, **211**, 91-107.
6. Harry Schmidt. *Bericht der Schimmel & Co. Aktiengesellschaft.* 1940, 38-52.

COMBUSTION AND PROCESSING OF RICE HUSK IN THE VIBROFLUIDIZED BED OF CATALYST OR INERT MATERIAL

A.D. Simonov,* T.I. Mishenko, N.A. Yazykov, V.N. Parmon

Boriskov Institute of Catalysis SB RAS, Pr. Acad. Lavrentieva, 5, Novosibirsk 630090, Russia

Abstract

In the present work, some data on catalytic combustion of one of the most widespread vegetative remainders - rice husk are adduced. The rice husk is used not only as a fuel, but also as a source of silicon for semiconductor industry, the synthesis of silicon carbides and silicon nitrides, etc. We studied the rice husk oxidation in the vibrofluidized bed of either a catalyst or an inert material in conditions allowing to reproduce with an adequate accuracy the data on scraps combustion in the dense and unloaded phase of the fluidized bed.

It is found, that the process of the rice husk combustion is localized completely in the bed of the catalyst. In the bed of an inert material the process occurs in a space above the bed; consequently, exhausts contain a fair quantity of CO. Studies on solid products of the rice husk combustion has shown that their texture is determined mainly by silicon, which is contained in rice husk as amorphous silicon $\text{SiO}_2 \cdot n\text{H}_2\text{O}$. The adsorption ability of these solid products in respect to methylene blue (MB) is investigated. With increasing of the process temperature, the value of limiting MB adsorption by the solid products passes through a maximum at the process temperature 600°C . It is found, that the values of the limiting MB adsorption for the solid combustion products in the bed of the catalyst exceed those for solid products obtained in the bed of an inert material.

Under discussion are also some distinctions of the process of rice husk processing in the vibrofluidized beds of either catalyst or inert material.

Introduction

Biomass is the most ancient source of energy for humans. Till now wood fuel remains the main energy source in many countries of the world [1]. Important sources of biomass are now also vegetative remainders (wheat and corn straw, chaff, rice and oat husk, etc.). The traditional combustion of biomass in a torch furnace at $1200\text{-}1600^\circ\text{C}$ for power purposes has an essential disadvantage due to high emission of toxic substances with exhaust gases (CO, nitrogen and sulfur oxides, benzpyrenes, and other).

PP-33

In the fluidized bed of inert particles, the process of solid organics combustion is essentially intensified in comparison with combustion of those in a fuel-bed furnace due to more vigorous transport of air oxygen to solid fuel particles [2]. A capability to burn the pulverized solid fuel in the fluidized bed makes this process similar to the torch burning with an advantage, that it is possible to regulate the residence time of the fuel particles in the bed and to achieve a high burn-off of the fuel at rather low temperatures of the bed 850-1000°C. However, in this case the concentration of the toxic substances in the exhaust gases also remains high enough.

A technology of the fuel combustion in the fluidized bed of catalyst, which was developed by the Boreskov Institute of Catalysis of SB RAS on an industrial scale [3,4], avoids many disadvantages of the conventional high temperature combustion of the fuel. The technology is based on a combination of four principles: use of heterogeneous catalysts for the complete oxidation of combustibles; combustion of fuels in the fluidized bed of the catalyst particles; combustion of the fuel without a significant excess of air; coupling the processes of heat generation and removal within the same fluidized bed.

The catalytic combustion differs essentially from the burning in traditional understanding, since the fuel is oxidized on the surface of solid catalysts without a flame formation [5]. The catalyst action during the complete oxidation (or heterogeneous burning) of the fuel-air mixes is based on the interaction of fuel components with superficial oxygen of the catalyst with the sequential regeneration of the restored surface of the catalyst by oxygen from the gas phase. Depending on the catalyst activity, the process of complete oxidation of many combustibles can proceed even at 250-300°C. Compared with the known combustion methods, the catalytic combustion allows:

- to decrease the temperature of organic fuel combustion from 1200-1600°C to 300-700°C;
- to mitigate requirements for thermochemical stability of furnace construction materials and reduce an erosion of apparatus;
- to diminish heat losses through the apparatus wall;
- to improve explosion safety of the heat generating installations;
- to reach high (up to $5 \cdot 10^8$ kJ/m³hr) values of the power loading during the fuel oxidation with a significant decrease of the size, weight and metal consumption of the installations;
- to exclude secondary endothermic reactions which form toxic products.

Basing on the new technology a variety of apparatuses has been designed for the heating and evaporation of liquids, materials drying and heating, detoxification of industrial gaseous, liquid, and solid wastes, and so on.

In this work, we present some experimental data on the catalytic combustion of one of the most widespread vegetative remainders - rice husk (RH). The RH is widely available in many southern countries and used now not only as a fuel, but also as a source of silicon for semiconductor industry, the synthesis of silicon carbide and silicon nitride, etc. [6]. We studied the RH oxidation in the vibrofluidized bed of both a catalyst and an inert material in conditions allowing to reproduce with an adequate accuracy the data on scraps combustion in the bubble and emulsion phase of the fluidized bed.

Experimental

In this work we used the rice husk from Vietnam. Table 1 shows the chemical composition of RH under investigation.

Table 1. Some chemical characteristics of the rice husk under investigation

General analysis, %*	
Volatile substances	70.2
Fixed carbon	14.1
Ash	15.7
Elemental analysis, %*	
C	43.5
H	5.5
O	35.2
N	0.05
S	0.02
	0.01
Ash	15.7

* - % wt. on dry substance

The scheme of the laboratory-scale plant for the RH combustion in the vibrofluidized bed of the catalyst or an inert material is presented in Fig. 1. The reactor (1) was a stainless steel cylinder 23 mm in diameter and 100 mm in height. The bottom of the reactor was made of a stainless steel net with sell of 0,5 mm. The reactor was loaded either by an inert material (river sand) or catalyst (16.6 cm³ each) with the particles of 1.5-2.0 mm in diameter. Then one turned on an electric heater (2) and vibrator (5). The frequency of the reactor oscillations was equal to 50 Hz, the vibrational amplitude was equal to 1 mm. The temperature in the reactor

PP-33

was controlled with a thermocouple. As the temperature in the reactor achieves the operation level, the crushed RH particles (0.2-0.4 mm) were fed with the supply rate 4.6 g/hr. The total supply of air into the reactor and to a husk feeder (8) made up 55 L/hr. The outlet gas mixture was cooled in a heat exchanger (4). Further, the solid combustion products were separated in a cyclone (6) and collected in a bunker (7).

The concentrations of CO, CO₂, CH₄, H₂, SO₂, O₂ in the flue gas were determined with gas chromatography.

A commercial CuCr₂O₄/γ-Al₂O₃ (IC-12-70) catalyst with 15% wt. of the active component was used for the experiments.

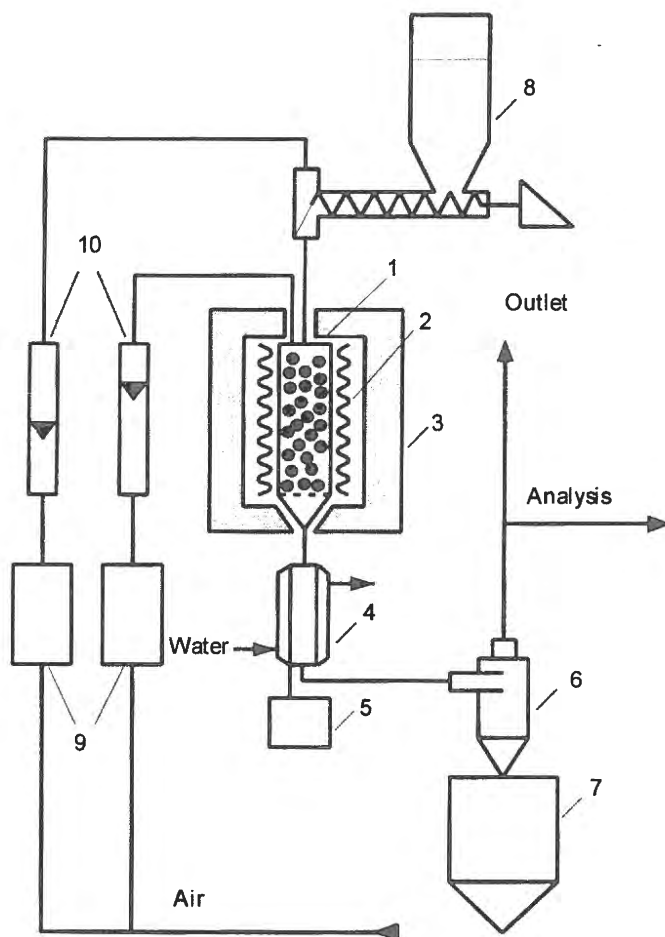


Fig. 1. The scheme of the laboratory-scale plant for the RH combustion in the vibrofluidized bed of the catalyst or an inert material

- | | |
|--------------------|---------------------------|
| 1. Reactor | 6. Cyclone |
| 2. Electric heater | 7. Tank for ash |
| 3. Heat isolation | 8. Screw feeder with tank |
| 4. Heat exchanger | 9. Air flow regulators |
| 5. Vibrator | 10. Rotameters |

The initial RH humidity was determined by weighting the samples after their drying at 120°C for 4 hours. The quantity of volatile substances in the RH was determined by weighting the dried samples after their heating 850°C for 7 minutes. The content of ash, organic part in initial RH and products of the RH combustion was determined by the weighting of the samples after their calcination at 800°C in air for 2 hours. The burn-off of the RH was calculated with the formula:

$$\beta = A_S - A_0/A_S (1 - A_0),$$

where A_0 is the ash fraction in the initial dried RH sample, while A_S is the ash fraction in the solid combustion products.

The composition of the mineral part of the initial RH was determined by an VRA-20 X-ray fluorimeter (Germany) with a fluorescent analyzer.

The morphological analysis of the initial RH and products of the RH combustion was determined with auto-emission high-vacuum raster electronic microscope BS-350 (Czechoslovakia).

The «bleaching» adsorption from water ability of the RH processing products was determined with the methylene blue (MB) adsorption [7]. A commercial activated birch coal was used for comparison.

Results and discussion

Combustion of rice husk

The RH under investigation contained 15.7% of ash, 14.1% of the fixed carbon and 70.0% of volatile substances (Table 1). The RH ash consisted of 94% of silica and also 2.5% of potassium, 0.6% of calcium, 0.4% of magnesium and 0.2% of manganese. The content of sodium, aluminium, iron, phosphorus and sulfur in the ash was less than 0.1% wt. content of another elements in the ash was less than 0.01% wt.

Fig. 2 shows a change of the RH burn-off in dependence on the vibrofluidized bed temperature. The RH burn-off increases by 5-10% with the rise in the temperature from 500°C to 700°C both in the bed of the catalyst, and in the bed of sand. It is seen that the difference in the RH burn-out values for the catalyst and sand beds is insignificant.

Much more significant is change of the CO and CO₂ concentration in the flue gas (see also Fig. 2). CO in flue gas after the catalyst bed is practically absent in the all temperature interval 500-700°C, i.e. the process of the combustion of both volatile compounds and CO is

PP-33

completely localized in the bed of the catalyst. On the contrary, in the bed of the sand, the process of the combustion appears to be not finished and the flue gas contains fair quantity of CO, the CO concentration exceeding 0,5% vol. even at 700°C.

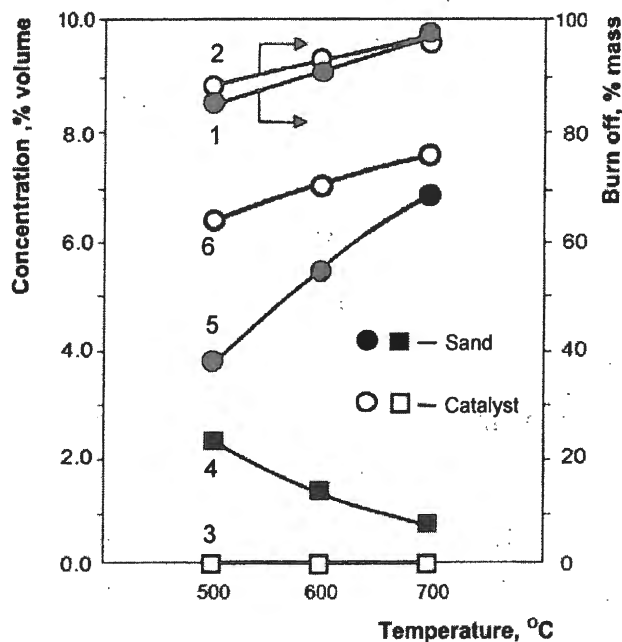


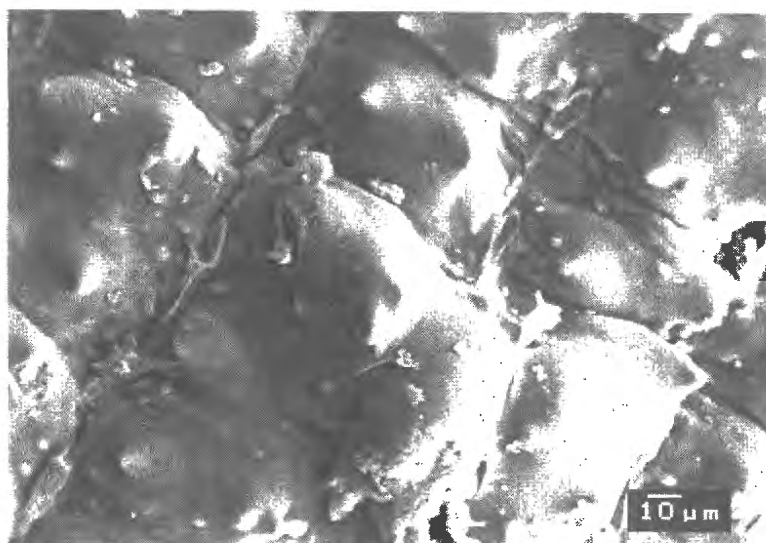
Fig. 2. The RH burn off (1), (2) and concentrations of CO (3), (4) and CO₂ (5), (6) in the flue gas vs. the temperature of the rise husk combustion in the vibrofluidized beds of the catalyst and inert material (sand), respectively.

Structural, textural and adsorption characteristics of solid products of the RH combustion

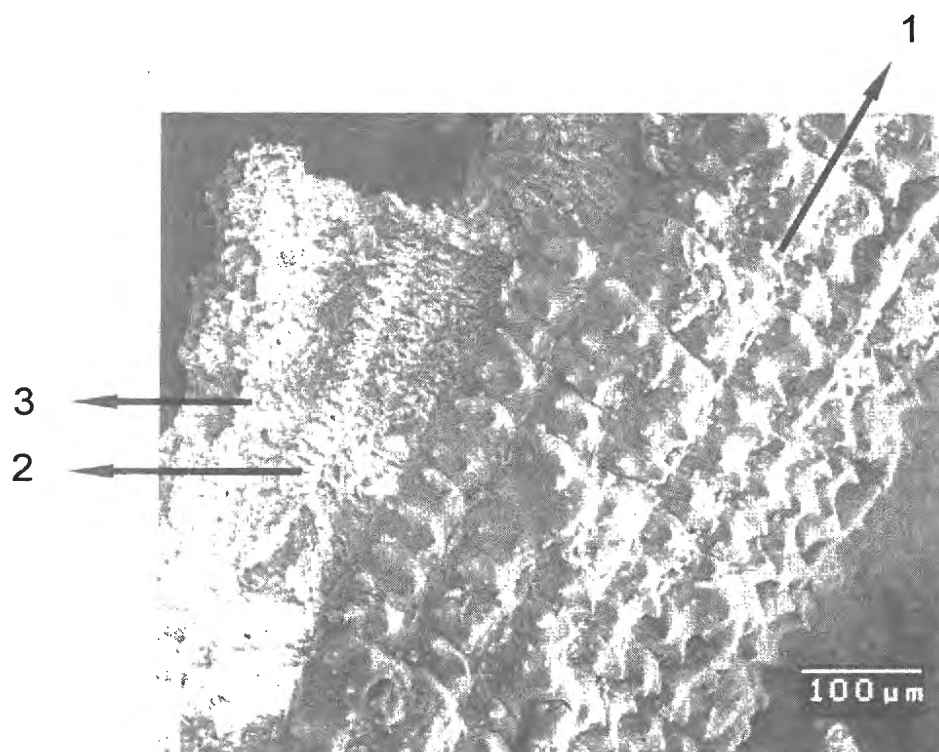
Of a top practical interest seem to be characteristics of the ash (i.e. solid products) of the RH combustion.

A typical texture of the RH ash external surface according SEM is shown in Fig. 3a. The solid products of the RH combustion in the vibrofluidized catalyst or sand bed at the temperature of 500-700°C have similar texture due to high contents of silica in the RH external epidermis [6]. A lateral chip of an ash particle, obtained at the RH combustion in the vibrofluidized bed of the catalyst at 700°C, is shown in Fig. 3b. Together with the well saved structure of the external epidermis (1), the structure of the RH internal layers (tubular (2) and spongy (3) parenchyma), which contain small quantity of silica, is also kept safe.

The X-ray diffraction analysis showed, that both initial RH and the solid RH combustion products in the catalyst bed at 500-700°C have no crystalline phases. The solid products, obtained at the RH combustion in the sand bed at 500°C, have no crystalline phases too. However, in the solid products, obtained at the RH combustion in the sand bed at 600-700°C, α -tridymite and α -cristobalite crystalline phases of silica are detected.



A



B

Fig. 3. Scanning electron micrographs (SEM) of the rise husk after its treatment in the in the vibrofluidized bed of either the catalyst or sand at 700°C:

A - outer surface of rise husk ash;

B - lateral chip of the ash particle (1 - epidermis; 2 - tubular parenchyma; 3 - spongy parenchyma)

PP-33

Some texture and adsorption characteristics of solid products, obtained at different temperatures of the RH combustion, are given in Table 2. With the process temperature rise from 500 to 700°C, the specific surface of the solid products, which are obtained in the catalyst bed, increases in value. In the case of the sand bed, the temperature rise from 500 to 600°C leads to an increase of the specific surface, while at 700°C its value sharply decreases. The total pore volume of the solid products (Table 2) varies in the same way. The values of the specific surface and total pore volume of the solid products, obtained at the RH combustion in the catalyst bed, exceed considerably the corresponding values for the products, obtained in the bed of the sand.

Table 2 shows also the adsorption ability of the solid products of the RH combustion in respect to methylene blue (MB). With increasing of the RH process combustion temperature, the value of the limiting MB adsorption passes through a maximum at the process temperature 600°C in both cases. However, the values of the MB adsorption for the solid products, obtained in the catalyst bed, exceed those for the products, obtained in the bed of the sand, by a factor of 1.5-2.0. Note, that this value is only in 2.5 times less, than the value of the MB adsorption for an industrial activated coal (Table 3).

Table 2. Some texture and adsorption characteristics of the solid products of the rice husk combustion and a commercial activated coal

Temperature, °C	Specific surface, m ² /g		Pore volume, cm ³ /g		Adsorption of MB, mg/g	
	Sand	IC-12-70	Sand	IC-12-70	Sand	IC-12-70
120*	1.1		0.005		—	
500	126	160	0.13	0.15	20.0	42.5
600	156	189	0.15	0.17	42.5	52.5
700	124	207	0.15	0.18	25.0	47.5
900**	730		0.49		137.5	

* - initial rice husk after drying

** - a commercial birch activated coal

Table 3. The experimentally measured temperature of particles of active sludge during their combustion in the beds of a catalyst and sand (according to [13,14])

Temperature of the bed, °C	Temperature of particles of active sludge, °C	
	Catalyst	Sand
500	500	540
600	600	750
700	730	900

Discussion

An important feature of free fluidized bed of solid particles is its non-uniformity in the volume and time. Inside the bed, one can distinguish two phases, which are subsequently replacing each other: there are gas bubbles and clusters of the bed particles (or the so called emulsion phase). The mass transfer between the emulsion phase and bubble occurs through the external boundary of the bubble. The main quantity of the gas, which exceeds quantity necessary for the fluidization, passes through the bed as the bubbles [8]. However, the filtration of the gas through the emulsion phase is also significant. In the case of the fluidization of large particles with more than 1.5 mm in diameter, the value of the filtration flow achieves 45% over the quantity of the gas necessary for the fluidization [2].

The particles of solid fuel with the size being equal to or exceeding the size of inert particles of the fluidized bed, burn out predominantly in the emulsion phase. The small-size particles burn out in the emulsion phase as well as in the bubbles. The porosity of the vibrofluidized bed depends on the vibration conditions. At the top-to-down filtration of the mixture of air and solid fuel small-size particles, the vibrofluidized bed remains homogeneous. Therefore, the data obtained in present work for the RH combustion in the vibrofluidized bed of an inert material or catalyst reproduce precisely enough the process of the RH combustion in the fluidized bed of the same material.

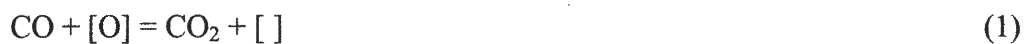
Generally, in the vibrofluidized or fluidized bed of inert particles the combustion of solid fuels, proceeds in three stages [9]: (1) initial heating of the fuel particles, which stimulated the emission of volatile substances and the coke formation; (2) combustion of these volatile substances in the gas phase; (3) combustion of the coke. At the combustion of large fuel particles the emission of the volatile substances occurs mainly before the ignition of the coke and the substances burn out in the gas phase, with heating and activating the particles of the coke. The heated particles of the coke promote the combustion of volatile substances. On the other hand, the emission of the volatile substances retards transport of oxygen to the coke surface. Therefore, the coke combustion proceeds only after the burning-out of the volatile substances, with the temperature of burning particles being by 100-300°C higher, than the temperature of the fluidized bed of an inert material [9-11].

In the case of the combustion of small-size particles of RH, the coke ignition occurs before the completing emission of the volatile substances, and thus the burning of the coke and volatile substances proceeds in the same time. The burning-out of volatile substances is not completed in the bed of inert material; for this reason the exhaust gases contain a

PP-33

significant quantity of CO (Fig. 2). However, in this case a flame shell around the RH particles is also formed. Burning of CO and volatile substances in the flame shell leads to decreasing the oxygen transport to the particles surface. As a result, the temperature of the burning RH particles exceeds considerably the temperature of the vibrofluidized bed bulk. It is easy confirmed by visual observations as well as by the presence of α -tridymite and α -cristobalite crystalline phases in the solid products of the RH combustion at temperature 600-700°C, since the formation of α -tridymite and α -cristobalite crystalline phases is possible only at temperatures above 900-1000°C [12].

The replacement of inert particles in the vibrofluidized bed by the catalyst particles does not change the general scheme of the RH combustion. However, in this case, the evolving volatile substances are oxidized mainly on the catalyst surface, for example, according to scheme:



where [] stands for an oxygen vacancy on the catalyst surface; [O] is surface oxygen of the catalyst.

The catalytic CO and volatile substances oxidation results in an increase of the oxygen concentration near the RH particles and increase the burn-off of those. At the same time, the temperature of the oxidized RH particles does not exceeds the temperature of the vibrofluidized catalyst bed, and thus a flame shell round the burning particles is not formed. It is also confirmed by visual observations and by the absence of any silica crystalline phases in the ash. Earlier, the same phenomenon was observed at the combustion of active sludge in the fluidized catalyst bed [13,14], where the flame shell is not formed and the temperature of the sludge particle practically was equals to the temperature of the bed (Table 3). This experiment was carried out with placing the active sludge globules of 5-8 mm in diameter in the fluidized bed of the sand or catalyst, a thermocouple being set in each granule. The temperature was fixed during the burning-out of granule.

At 500°C, the burn-off of RH achieves 85-90% in the bed of the catalyst as well as in the bed of an inert material (Fig. 2). It means that practically all volatile substances as well as main part of fixed carbon (Table 1) burn-out at 500°C. At the consequent increase of the combustion temperature up to 700°C, the burn-off is increased only by 5-10% (Fig. 2). It is known [2,8-11], that a heterogeneous combustion of the coke carbon is the most long stage

which limits the overall process of the solid organic substances combustion. The interaction of carbon and oxygen is determined by summary reactions:



The last reaction (6) in the absence of water proceeds with a noticeable speed at temperatures above 700°C. In the presence of water, CO is oxidized according to a free radical mechanism under lower temperatures. The oxidation of carbon with carbon dioxide, according to thermodynamic equilibrium of reaction (5), is possible only at temperatures above 600°C [15].

The rate of the coke combustion depends on the both kinetic factors of the interaction of carbon with O₂ and CO₂ and the transport of oxygen to the carbon surface through a boundary gas layer around the burning particle [16].

It is widely accepted that the process of the coke combustion in the fluidized bed of inert material is restricted by the diffusion of oxygen to the coke surface [2,8-11]. In the low temperature region (below 800-900°C), the combustion proceeds according to reactions (3) and (4). CO forms in reaction (4), is oxidized in the coke boundary layer and also reduces the concentration of oxygen at the coke surface. In addition, the particles of the inert material in the emulsion phase of the fluidized bed enclose coke particles. This enclosing leads to slowing down of the oxygen transport to the carbon surface. The ash shell, which is formed around the coke particles during the carbon burning, also leads to slowing down of oxygen supply to the carbon [17].

As it was already mentioned above, in the fluidized bed of inert material, the temperature of the burning carbon particles is by 100-300°C higher, than the temperature of the bed bulk. Consequently, if the temperature of the bed equals to 600-700°C, the carbon particles are heating up to 900-1000°C, and the combustion of carbon according to the reaction (5) is possible. It results in an increase of the CO concentration in the boundary layer near the coke particles and a decrease in the oxygen concentration on the coke surface at the CO oxidation according to the reaction (6).

At the presence of the catalyst, the coke combustion in the temperature interval 500-700°C proceeds via the reactions (3) and (4). However, in this case, the catalyst makes a significant

PP-33

contribution to the reaction (5) as provided by the schemes (1) and (2). That results in an increase of the oxygen concentration in the boundary gas layer around the coke particles. Though the temperature of coke particles in the vibrofluidized bed of an inert material is neighbour to those for the catalyst bed (Table 3), the coke burn-off in the catalyst bed appears to be a little bit greater or equal to the coke burn-off for the inert material bed. This seems to be a result of increasing the oxygen concentration in the boundary layer around the burning coke in the catalyst presence (Fig. 2).

Conclusion

Thus, the presence of the catalyst allows to achieve a sufficiently high burn-off of the RH at the same temperature of the vibrofluidized bed and particles of the RH. This process appears to be environmentally benign, since in the flue gas after such the combustion there are no products of partial oxidation of organics like CO even at rather low bed temperature 500°C. Of importance is also that the process enables to obtain in one stage, i.e. without additional stage of the coke activation, some valuable solid products with a high specific surface and good adsorption properties. Indeed, such solid product can be of large practical interest for the rise growing countries.

References

1. S.S. Sofer, O.R. Zaborsky. Biomass conversion process for energy and fuels. Plenum press, New York-London, 1981.
2. J.G. Yates. Fundamentals of fluidized-bed chemical processes. Butterworths, London, 1983.
3. A.D. Simonov, N.A. Yazykov, P.I. Vedyakin, G.A. Lavrov, V.N. Parmon. Catalysis today, 60 (2000) 139-145.
4. Russian Patent 826,798 (1983).
5. G.K. Boreskov. Heterogeneous catalysis. Nauka, Moscow, 1986 (in Russian).
6. D.F. Houston. Rice and it quality. Kolos, Moscow, 1976, p. 271-304 (in Russian).
7. D.A. Kolyshkin, K.K. Michailova Active coals. Kchimiya, Leningrad, 1972 (in Russian)
8. J.F. Davidson, D. Harrison. Academic Press, Fluidization. London, 1971.
9. V.A. Borodulya, L.M. Vinogradov. Combustion of solid fuel in fluidized bed. Science and Engineering, Minsk, 1980, 50 (in Russian).
10. I. B. Ross, M.S. Patel, J.F. Davidson. Trans. I. Chem. Engrs. 59 (1981) 83.
11. M. Radovanovich. Combustion of fuel in fluidized bed. Energoatomizdat, Moscow, 1990 (in Russian).
12. N.M. Bobkova. Physical chemistry of silicates, Vysshaya Shkola, Minsk, 1977 (in Russian).
13. A.D. Simonov, N.A. Yazykov, E.I. Yepifantseva, I.V. Wolf, Y.M. Chernoberezhsky. Chemistry for Sustainable Development, 1 (1993) 289.
14. A.D. Simonov, N.A. Yazykov. Chemical Industry, 3 (1996) 47.
15. P.D. Woker, F Rusinko, L.G. Austin. Advances in Catalysis, 11 (1959) 133.
16. B.V. Kantorovich. Fundamentals of the theory of combustion and gasification of solid fuel. Akademiya Nauk SSSR, Moscow, 1958 (in Russian).
17. V.V. Pomerantsev, K.M. Aref'ev, D.B. Achmedov, etc. Fundamentals of the practical combustion theory. Leningrad, Energoatomizdat, 1986 (Russian).

RADIAL HEAT TRANSFER IN PACKED BEDS OF SHAPED PARTICLES

E.I. Smirnov, A.V. Muzykantov, V.A. Kuzmin, I.A. Zolotarskii,

G.W. Koning^a, A.E. Kronberg^a

Boreskov Institute of Catalysis SB RAS, pr. Akad. Lavrentieva, 5, 630090 Novosibirsk, Russia

^a *Faculty of Mechanical Engineering, Twente University of Technology, P.O. Box 217, 7500*

AE Enschede, The Netherlands

Tel.: +7-3832-341278; fax: +7-3832-341878. E-mail address: esmirnov@catalysis.nsk.su

Abstract

Experimental data on the effective radial thermal conductivities and wall heat transfer coefficients of cylindrical beds formed of 4-hole and 52-hole cylindrical pellets, 6-spoke wheels and 3-hole trilobed particles are presented. A model with a linear variation of the radial thermal conductivity in the vicinity of the wall is proposed for description of the radial heat transfer in the packed bed. The model allows simple correlation between the wall Nusselt number and the bed core effective radial thermal conductivity. The model does not require any additional empirical parameters for the description of heat transfer in packed beds of different shaped particles.

1. Introduction

In order to develop tubular packed bed heat exchangers, adsorbers and chemical reactors reliable prediction of heat transfer from the tube wall to the packed bed is very important. A quasi-homogeneous, two-dimensional model is usually used for interpretation of the primary experimental results (temperature distribution in packed beds with fluid flow). Uniformity of flow velocity and radial thermal conductivity in the packed bed is assumed, the axial dispersion of heat is neglected and a boundary condition of the third kind is used at the tube wall [1]. Following many authors let call this model the "Standard Dispersion Model" (SDM). This model has two parameters for description of the radial heat transport: the wall heat transfer coefficient α_w and the effective radial thermal conductivity λ_{er} .

The main disadvantage of the SDM is the prediction of unrealistic fluid temperature near the wall because of the artificial boundary condition of the third kind at the tube wall (the concept of temperature jump at the wall). As a result the reaction rates in packed bed reactors can be predicted incorrectly. To avoid this problem another assumptions on the heat transport mechanism close to the wall are necessary.

PP-34

The concept based on locally varying radial thermal conductivity $\lambda_{er}(r)$ due to the near-wall porosity and velocity changes has gained ground in the last time. Such models are called $\lambda_{er}(r)$ -models and used the natural boundary condition of the first kind at the wall (condition of constant wall temperature). For example, Botterill and Denloye [2] separated the packed bed into a core and a wall region of $d_p/2$ thickness (d_p – the diameter of equivalent-volume sphere) with two different radial dispersion coefficients. Cheng and Vortmeyer [3] published a functional relation between radial thermal conductivity and local values of porosity and flow. The thickness of a wall region was assumed to equal to $2.5 d_p$. Tsotsas and Schlunder [4] obtained the distribution function of radial thermal conductivity of the packed bed on the ratio between the thermal conductivity of the particles and that of the fluid. Characteristic thickness of the wall region with varying radial thermal conductivity can be estimated from calculations of Tsotsas and Schlunder as about $1.5 d_p$, then the radial thermal conductivity practically does not depend on the radial position. Winterberg et al. [5] and Winterberg and Tsotsas [6] recommended a two-region model with radial dispersion coefficients depending on the near-wall channelling effects. The convective part of the radial thermal conductivity in the wall region was modelled as a quadratic function of the radial coordinate. Winterberg and co-workers concluded that a constant value of wall region thickness could be used to describe the experimental data with satisfactory results. For packed beds of spheres the thickness of the wall region was found about $0.44 d_p$ [5]. In beds packed with cylindrical particles the thickness of the wall region – about $0.4 d_p$ [6].

At present work a two-region model with a linear variation of λ_{er} in the vicinity of the wall is proposed for description of heat transfer experiments in packed beds of shaped particles.

$$\lambda_{er}(r) = \begin{cases} \lambda_{er,core} & \text{for } 0 \leq r \leq R - \delta \\ \lambda_{er,\delta}(r) & \text{for } R - \delta \leq r < R \end{cases} \quad (1)$$

In the packed bed core the effective radial thermal conductivity $\lambda_{er,core}$ does not depend on radial position r . In the wall region of δ thickness $\lambda_{er,\delta}(r)$ changes linearly from the fluid thermal conductivity λ_f at the wall ($r = R$) to the effective radial thermal conductivity $\lambda_{er,core}$ in the bed core:

$$\lambda_{er,\delta}(r) = \lambda_f + \frac{\lambda_{er,core} - \lambda_f}{\delta} \cdot (R - r) \quad \text{for } R - \delta \leq r < R \quad (2)$$

This model successfully describes experimental data for beds packed with spheres, cylinders and Rashig rings (Smirnov et al. [7]). One of the virtues of the model is possibility to

calculate the thickness of the wall region by one formula for particles of different form. The equivalent hydraulic diameter of the packed bed

$$d_{eqv} = \frac{4 \cdot \varepsilon_{bed}}{a_0 \cdot (1 - \varepsilon_{bed})} \quad (3)$$

is used as the characteristic thickness δ of the wall region. Here ε_{bed} – bed porosity without account of porosity of grains; a_0 – the specific surface of one solid particle.

2. Experimental

Measurements of temperature fields in packed beds were performed in steady state experiments without chemical reaction in the tube with inner diameter equal to 84 mm. Test section 650 mm high was cooled from outside by water with flow rate about 25 litres per minute, that guaranteed constant temperature at the inner wall of the tube T_w . Hot air was cooled while passing the tested bed and its temperature was measured in 144 points directly over the layer. Temperature fields were measured at several heights of the layer. Superficial velocities of the air were varied in the range 0.2÷2.0 m/s. Bed porosities were measured by a weighting method. Physical properties of the air were considered to be constant in the whole test section.

The effective radial thermal conductivity $\lambda_{er,core}$ and the wall heat transfer coefficient α_w in the packed bed were determined by fitting the SDM-solution to the measured temperature field using the method of least squares. In this work the experimental heat transport parameters were determined using only the temperatures measured in the bed core or at the distance larger than $\delta = d_{eqv}$ from the wall.

Thereby we assume that the heat transport within the core region is characterised in the same manner as the one-region SDM, the fluid temperature at the tube wall is T_w , and the temperature jump (from boundary condition of the third kind for SDM) takes place within the wall region. Obtained from the SDM value of α_w defines the heat flux from the packed bed to the wall and can be used as a criterion for experimental verification of a chosen model (see the following chapter).

3. Correlation between Nu_w and $\lambda_{er,core}$

Proposed two-region model allows correlation between experimentally determined SDM-parameters. It results in a simple correlation between the wall Nusselt number and the bed core effective radial thermal conductivity.

The wall heat transfer coefficient is defined as:

$$\alpha_w = \frac{q_R}{T_{r=R}^{SDM} - T_w} \quad (4)$$

where $T_{r=R}^{SDM}$ is the gas temperature at the tube wall calculated from the SDM, q_R – the heat flux to the wall.

Let us assume that the heat flux in the wall region does not depend on radial position. In this case the temperature jump $T_{r=R}^{SDM} - T_w$ predicted by the SDM can be calculated.

According to the SDM

$$q_R = -\lambda_{er,core} \frac{\partial T}{\partial r}, \quad R - \delta \leq r \leq R \quad (5)$$

and

$$T_{r=R}^{SDM} - T_{r=R-\delta} = -q_R \frac{\delta}{\lambda_{er,core}} \quad (6)$$

According to the two-region $\lambda_{er}(r)$ -model

$$q_R = -\lambda_{er,\delta}(r) \frac{\partial T}{\partial r}, \quad R - \delta \leq r \leq R \quad (7)$$

and

$$T_w - T_{r=R-\delta} = -q_R \int_{R-\delta}^R \frac{dr}{\lambda_{er,\delta}(r)} \quad (8)$$

From Eqs. (6) and (8) it follows:

$$T_{r=R}^{SDM} - T_w = q_R \cdot \int_{R-\delta}^R \frac{dr}{\lambda_{er,\delta}(r)} - q_R \frac{\delta}{\lambda_{er,core}} \quad (9)$$

Substituting Eq. (9) into Eq. (4) we find the relation between α_w and $\lambda_{er,core}$:

$$\alpha_w = \frac{1}{\int_{R-\delta}^R \frac{dr}{\lambda_{er,\delta}(r)} - \frac{\delta}{\lambda_{er,core}}} \approx \frac{\lambda_{er,core}}{\delta \cdot \left[\ln \left(\frac{\lambda_{er,core}}{\lambda_f} \right) - 1 \right]} \quad (10)$$

The wall Nusselt number (defined through the wall region thickness δ) is:

$$Nu_w = \frac{\alpha_w \delta}{\lambda_f} = \frac{\lambda_{er,core}^*}{\ln \lambda_{er,core}^* - 1} \quad (11)$$

where $\lambda_{er,core}^* = \lambda_{er,core} / \lambda_f$.

4. Results

The general correlation for the effective radial thermal conductivity of the packed bed is commonly written in the form:

$$\lambda_{er,core}^* = \lambda_{bed}^* + K \cdot RePr \quad (12)$$

where $\lambda_{bed}^* = \lambda_{bed} / \lambda_f$, and K – the convective heat transport parameter.

Table 1 presents the values of $K_{experimental}$, which satisfy the Eq. (12) for experimental dependences of SDM-parameter $\lambda_{er,core}^*$ on Reynolds number. It was estimated that $\lambda_{bed}^* = 10$ for all studied ceramic particles (Prandtl number was accepted $Pr = 0.71$ for the air.). The accuracy of the experimental determination of $K_{experimental}$ was about 15%.

Table 1. Convective heat transport parameter $K_{experimental}$ for packed beds of shaped particles

№	Grain	ε_{bed}	$K_{experimental}$
1	Ceramic 4-hole pellet: outer diameter 14mm, length 17mm, hole diameter 4mm	0.40	0.20
2	Ceramic 52-hole pellet: outer diameter 19mm, length 17mm, square holes 1.5×1.5mm	0.48	0.14
3	Ceramic 6-spoke wheel: outer diameter 18mm, length 16mm, wall thickness 2mm	0.42	0.17
4	Ceramic 3-hole trilobed particle: outer diameter of each lobe 7.5mm, length 11mm, hole diameter 3.5mm	0.38	0.24

Figures 1 and 2 present Nu_w as a function of Re for shaped particles. Theoretical values of Nu_w were calculated by using Eq. (11). In that case $\lambda_{er,core}^*$ was calculated from Eq. (12) using determined values of λ_{bed}^* and $K_{experimental}$. Experimental points of Nu_w were calculated from values of SDM-parameter α_w . The Reynolds number is based on the equivalent particle diameter d_p (the hole volume was included in the particle volume).

The obtained correlation (11) for the wall Nusselt number is in a good agreement with the experimental data.

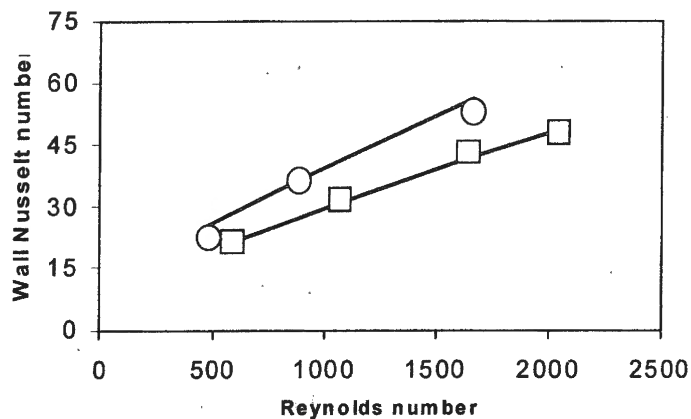


Fig. 1. Dependences of wall Nusselt number on Reynolds number for beds of 4-hole and 52-hole cylindrical pellets.

Open circles – ceramic 4-hole pellets, diameter 14mm, length 17mm, holes diameter 4mm

Open squares – ceramic 52-hole pellets, diameter 19mm, length 17mm, holes 1.5×1.5mm

Lines – Eq. (11)

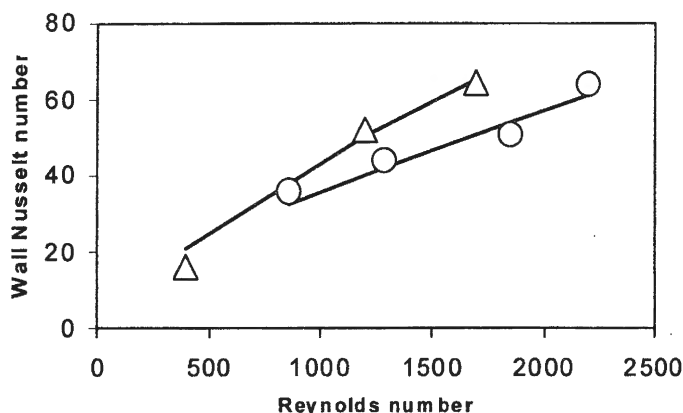


Fig. 2. Dependences of wall Nusselt number on Reynolds number for beds of 6-spoke wheels and 3-hole trilobed particles.

Open circles – ceramic 6-spoke wheels, diameter 18mm, length 16mm, wall thickness 2mm

Open triangles – ceramic 3-hole trilobed particles, diameter of each lobe 7.5mm, length 11mm, hole diameter 3.5mm

Lines – Eq. (11)

5. Conclusions

The two-region $\lambda_{er}(r)$ -model was proposed for description of the radial heat transfer in the packed bed. The model allows simple correlation between the wall Nusselt number and the bed core effective radial thermal conductivity. The obtained correlation stands comparison with the experimental data.

The model with a linear variation of λ_{er} in the vicinity of the wall does not require any additional empirical parameters for the description of heat transfer in packed beds of shaped

particles. The characteristic thickness of the wall region $\delta = d_{eqv}$ is defined by means of the bed porosity and the specific surface of the single particle.

Thus the model with a linear variation of λ_{er} in the vicinity of the wall was verified for beds of 4-hole and 52-hole cylindrical pellets, 6-spoke wheels and 3-hole trilobed particles.

Acknowledgements

The authors would like to thank NATO's Scientific Affairs Division for the support (grant SfP-972557).

References

1. D. Vortmeyer and E. Haidegger, Chem. Eng. Sci., 46 (1991) 2651.
2. J.S.M. Botterill and A.O.O. Denloye, Chem. Eng. Sci., 33 (1978) 509.
3. P. Cheng and D. Vortmeyer, Chem. Eng. Sci., 43 (1988) 2523.
4. E. Tsotsas and E.U. Schlunder, Chem. Eng. Sci., 45 (1990) 819.
5. M. Winterberg, E. Tsotsas, A. Krischke and D. Vortmeyer, Chem. Eng. Sci., 55 (2000) 967.
6. M. Winterberg and E. Tsotsas, Chem. Eng. Sci., 55 (2000) 5937.
7. E.I. Smirnov, A.V. Muzykantov, V.A. Kuzmin, A.E. Kronberg and I.A. Zolotarskii, "Radial heat transfer in packed beds of spheres, cylinders and Rashig rings. Verification of model with a linear variation of λ_{er} in the vicinity of the wall", Chem. Eng. Journal, to be published.

MONOMETALLIC AND BIMETALLIC Pt-AND Ru-BASED CATALYSTS FOR SELECTIVE OXIDATION OF CO IN EXCESS HYDROGEN

P.V. Snytnikov, V.A. Sobyenin, V.D. Belyaev, D.A. Shlyapin*

Borisev Institute of Catalysis SB RAS, 5, Academician Lavrentiev ave, 630090 Novosibirsk, Russia

**) Omsk Branch of the Borisev Institute of Catalysis SB RAS, 54, Neftezhavodskaya st.,
644040, Omsk, Russia*

Fax: +7-(383-2)-343056, E-mail: pvsnyt@catalysis.nsk.su

Abstract

Selective oxidation of CO in excess hydrogen and in the presence of CO₂ and H₂O has been studied over monometallic Pt, Ru and bimetallic Pt-Ru supported on porous carbonaceous material catalysts. The catalysts provided CO conversion $\geq 98\%$ and seem to be promising for efficient single-step removal of CO from hydrogen-rich streams containing CO₂ and H₂O.

Introduction

Hydrogen fuelled polymer electrolyte membrane fuel cells (PEMFC) have been recognized as a promising energy source for replacement of internal combustion engines in automobiles and other transportation systems. However, problematic storing of H₂ onboard a vehicle and a lack of hydrogen refueling infrastructure put forward an idea to combine PEMFC with onboard catalytic reformer that converts a common hydrocarbon fuel into hydrogen-rich gas [1-3].

Such reformer approach for PEMFC vehicles is currently based on steam reforming or autothermal reforming of hydrocarbon fuels and water-gas shift reaction processes. The product stream from the reformer typically contains 40-75 vol.% H₂, 20-25 vol.% CO₂, a few vol.% H₂O, N₂ (if air is an oxidant) and 0.5-2 vol.% CO. However, PEMFCs are intolerant to such streams, because CO easily poisons PEMFC anode. Thus, before PEMFC feeding, the content of carbon monoxide in the stream (reformed gas) must be reduced to 10-100 ppm. Selective or preferential oxidation of CO with oxygen (air) is considered now as the primary choice for the removal of carbon monoxide from hydrogen-rich streams.

Reported catalysts for this reaction are based predominantly on alumina-supported noble metals (Pt, Ru, Rh, Pd) [4-8] and zeolite-supported platinum [7,9,10]. It has been shown [4-6, 10] that Pt- and Ru-based catalysts are the most active towards selective oxidation of CO

and successfully operate in the temperature range of 150-200°C. Besides, in ref. [10] mordenite-supported bimetallic Pt-Ru (2:1 weight ratio) catalyst has been proposed for selective oxidation of CO. This catalyst, composed of bimetallic Pt-Ru particles, appeared to be more active than mordenite-supported monometallic Pt and Ru catalysts.

In this work the catalytic properties of Ru, Pt and Pt-Ru supported on Sibunit (a special hydrophobic porous carbonaceous material [11]) towards selective oxidation of CO in excess hydrogen have been studied as a function of temperature and composition of Pt-Ru bimetallic catalysts. The reaction was examined using a simulated reformed gas (containing H₂, CO, CO₂ and H₂O steam) at atmospheric pressure. The catalytic performance of monometallic Pt and Ru catalysts for selective CO oxidation has been compared to that of bimetallic Pt-Ru catalysts.

2. Experimental

2.1. Catalysts

Monometallic Pt, Ru, and bimetallic Pt-Ru catalysts (hereinafter Pt/C, Ru/C, Pt-Ru/C) were prepared using Sibunit as a support. Sibunit consisted of spherical granules of size ~1-2 mm and had pore volume 0.3 cm³/g and the BET surface area (S_{BET}) 300 m²/g.

The Pt/C catalyst was prepared by adsorbing cluster [Pt₃(CO)₆]₅²⁻ on Sibunit from water-acetone solution [12]. The sample obtained was dried at 120°C in air. The Pt content was 0.5 wt.%.

The Ru/C catalyst was prepared using RuOHCl₃ as the metal precursor. Sibunit granules were poured with hot acidified aqueous solutions of RuOHCl₃ and heated under agitation on water bath until complete evaporation of the solvent. The sample obtained was dried at 100°C in air and then reduced by hydrogen at 400°C. The Ru content was 0.5 wt.%.

XPS studies of Pt/C and Ru/C catalysts proved the presence of metallic Pt and Ru on Sibunit surface. According to TEM, the catalysts contained metal particles of size 20-30 Å.

Bimetallic Pt-Ru/C catalysts were prepared by the following procedure. First, the Pt/C catalysts containing 0.4, 0.3, 0.2 and 0.1 wt.% Pt were prepared as described previously. Then the samples obtained were poured with hot acidified aqueous solution of RuOHCl₃, heated under agitation on water bath until complete evaporation of the solvent, dried at 100°C in air and then reduced by hydrogen at 400°C. The procedure resulted in Pt-Ru/C catalysts with total content of noble metals equal to 0.5 wt. % and the following content of individual metals expressed as wt.%: Pt(0.4)-Ru(0.1); Pt(0.3)-Ru(0.2); Pt(0.2)-Ru(0.3); Pt(0.1)-Ru(0.4)

PP-35

All prepared catalysts consisted of spherical granules of size 1-2 mm, contained 0.5 wt.% of noble metals and had the same pore volume and S_{BET} as the initial Sibunit support.

2.2. Catalytic activity measurements

The reaction of selective oxidation of CO in excess hydrogen was carried out in a fixed-bed continuous-flow quartz reactor (i.d. 8 mm) at temperatures of 25-200°C under atmospheric pressure. The bed was made of 0.6 g of a catalyst mixed with 2 g of inert quartz powder and fixed by quartz wool. No catalyst pretreatment was applied.

The catalyst activities in the reaction of selective oxidation of CO in excess hydrogen were measured using reaction mixture of composition: 1 vol.% CO + 1.5 vol.% O₂ + 20 vol.% CO₂ + 3 vol.% H₂O + H₂ (balance). The total flow rate of the reaction mixture (WHSV) in all experiments was equal to 0.3 g·s/cm³.

The inlet and outlet gas mixtures were analyzed on-line by two gas chromatographs "Tsvet-530" (Russia) using Molecular Sieves and Porapak columns. Detection limit of CO, CO₂ and CH₄ was $\sim 10^{-4}$ vol.% (or ~ 1 ppm); detection limit of O₂, H₂O was not worse than $2 \cdot 10^{-3}$ vol.%.

The conversions of CO (X_{CO}) and O₂ (X_{O_2}) as well as the selectivity (S_{CO}) of CO oxidation in excess hydrogen were calculated by equations:

$$X_{\text{CO}}(\%) = \frac{[\text{CO}]_0 - [\text{CO}]}{[\text{CO}]_0} \cdot 100$$

$$X_{\text{O}_2}(\%) = \frac{[\text{O}_2]_0 - [\text{O}_2]}{[\text{O}_2]_0} \cdot 100$$

$$S_{\text{CO}}(\%) = \frac{0.5([\text{CO}]_0 - [\text{CO}])}{[\text{O}_2]_0 - [\text{O}_2]} \cdot 100$$

where $[\text{CO}]_0$ and $[\text{O}_2]_0$ are the inlet concentrations, $[\text{CO}]$ and $[\text{O}_2]$ are the outlet concentrations.

3. Results and discussion

3.1. CO oxidation on monometallic Ru/C and Pt/C catalysts

Fig. 1 presents the temperature dependencies of CO conversion and CO selectivity at selective CO oxidation in excess hydrogen over 0.5wt.% Pt/C and 0.5wt.% Ru/C. Note that in contrast to Pt/C, the products of selective CO oxidation over Ru/C contained ≤ 30 ppm of CH₄ (not shown in Fig. 1).

The principal observations with respect to CO removal from hydrogen-rich stream were as follows. For both catalysts, the CO conversion first increased and then slightly decreased with increasing temperature. The O₂ conversion increased with increasing temperature and attained 100%. Compared to Pt/C, the temperature dependencies of the CO and O₂ conversions for Ru/C demonstrated a 30-40°C shift towards the lower temperature region. The CO selectivity monotonically decreased from 60-65% to ~33% with increasing temperature for both catalysts.

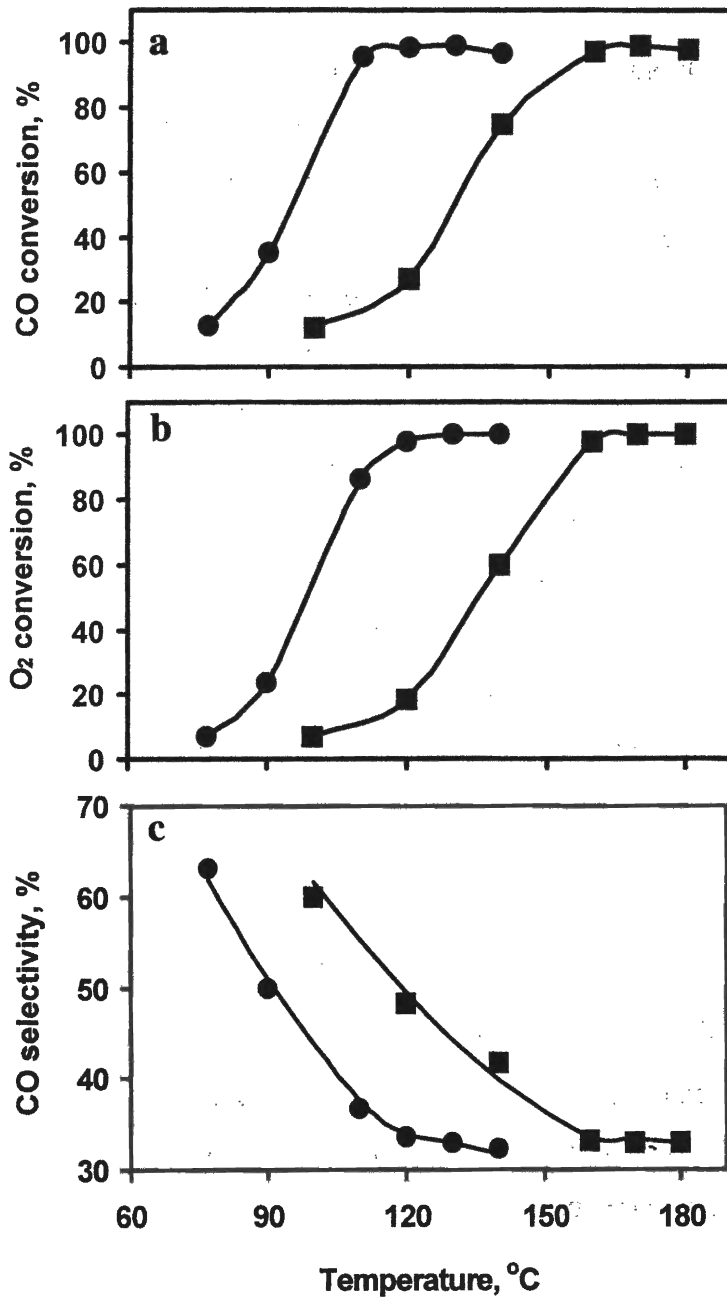


Fig. 1. Effect of temperature on CO conversion (a), O₂ conversion (b) and CO selectivity (c) at selective CO oxidation over 0.5wt.% Ru/C (●) and 0.5wt.% Pt/C (■)

PP-35

For Pt/C, the maximum CO conversion equal 98,5% was attained at 170°C. For Ru/C, the maximum CO conversion equal 98,3% was attained at 120°C. Respective outlet CO concentrations ranged within 150-170 ppm. It should be noted that the outlet CO concentrations could be decreased two-three-fold by means of a 10-20% increase of the inlet O₂ concentration (i.e., by increasing O₂/CO ratio from 1.5 to 1.65-1.8).

Analysis of the above data suggests a conclusion that, compared to Pt/C, Ru/C is more active for selective oxidation of CO in excess hydrogen. Similar trend has been reported previously for alumina- and mordenite-supported Pt and Ru catalysts [4,5,10].

3.2. CO oxidation on bimetallic Pt-Ru/C catalysts

The reaction of selective CO oxidation in excess hydrogen was studied over the following bimetallic catalysts: (0.1 Pt - 0.4 Ru)/C; (0.2 Pt - 0.3 Ru)/C; (0.3 Pt - 0.2 Ru)/C; (0.4 Pt - 0.1 Ru)/C. The maximum CO conversion for these catalysts was equal to $\geq 98\%$. For (0.1 Pt - 0.4 Ru)/C and (0.2 Pt - 0.3 Ru)/C, the reaction products contained ~10-20 ppm of CH₄, while in experiments with (0.3 Pt - 0.2 Ru)/C and (0.4 Pt - 0.1 Ru)/C no CH₄ was observed. The temperature dependencies of CO and O₂ conversions, and of CO selectivity at selective CO oxidation over all bimetallic catalysts were similar to each other and to respective dependencies for monometallic Pt and Ru catalysts (Fig. 1). The results obtained suggest a conclusion that the activity of bimetallic catalysts decreases with decreasing Ru content.

As an example, Fig. 2 demonstrates the temperature dependencies of X_{CO}, X_{O₂} and S_{CO} at selective CO oxidation over (0.2 Pt - 0.3 Ru)/C and (0.4 Pt - 0.1 Ru)/C. It is seen that the CO conversion increased with increasing temperature and attained 98.5% at 125°C for (0.2 Pt - 0.3 Ru)/C and 98,3% at 150°C for (0.4 Pt - 0.1 Ru)/C. At higher temperatures, the CO conversion slowly decreased for both catalysts. The O₂ conversion increased with increasing temperature and attained 100%. For both catalysts, the CO selectivity monotonically decreased from 50-55% to ~33% with increasing temperature. Compared to (0.4 Pt - 0.1 Ru)/C, the temperature dependencies of X_{CO} and X_{O₂} for (0.2 Pt - 0.3 Ru)/C demonstrated a 15-20°C shift towards the lower temperature region. This means that, compared to (0.4 Pt - 0.1 Ru)/C, (0.2 Pt - 0.3 Ru)/C is more active for selective CO oxidation in excess hydrogen.

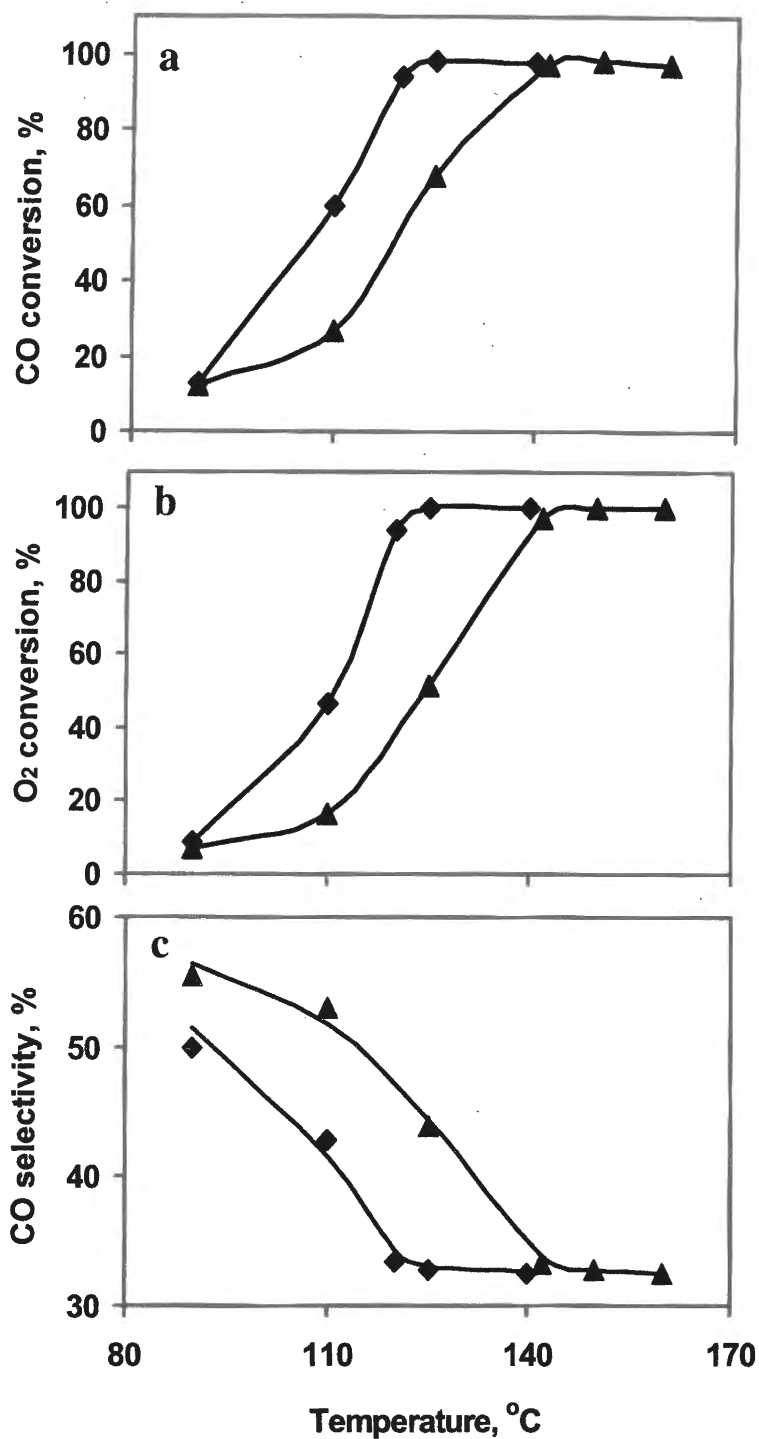


Fig. 2. Effect of temperature on CO conversion (a), O₂ conversion (b) and CO selectivity (c) at selective CO oxidation over (0.3wt.% Ru-0.2wt.%Pt)/C (▲) and (0.1wt.% Ru-0.4wt.%Pt)/C (◆).

3.3. Comparison of CO oxidation activity of monometallic and bimetallic catalysts

It has been shown in ref. [10] that mordenite-supported bimetallic Pt-Ru catalysts demonstrated higher activity towards selective oxidation of CO than both monometallic Pt

PP-35

and Ru mordenite-supported catalysts. The authors attributed this fact to the formation of bimetallic Pt-Ru particles (or alloy) in mordenite cages.

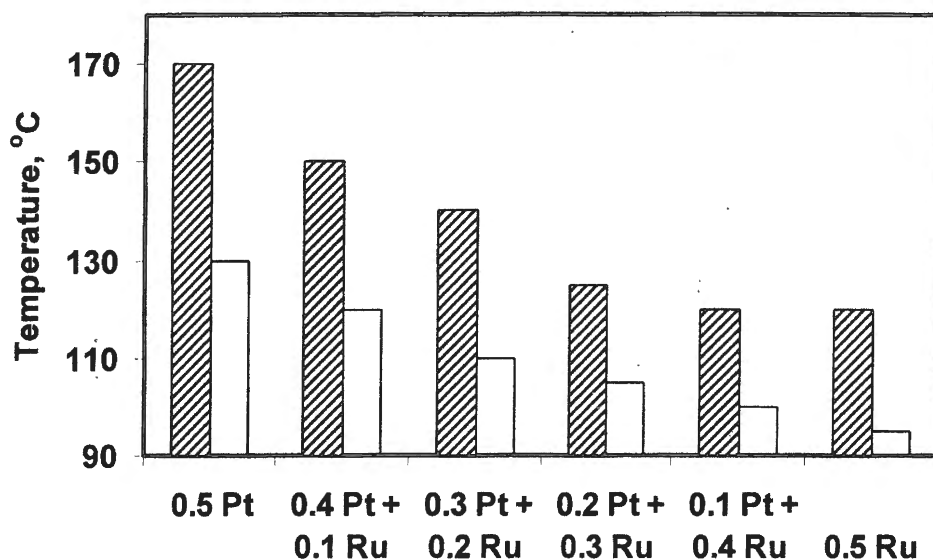


Fig. 3. Temperatures at which CO conversions of 50 % (□) and 98% (▨) were attained at selective CO oxidation in hydrogen excess over Pt-Ru/C catalysts

Fig. 3 compares catalytic activities of Pt/C, Ru/C and Pt-Ru/C in the reaction of selective CO oxidation in hydrogen excess. As a measure of the catalyst's activity, we selected the temperatures T_{50} and T_{98} at which CO conversions of 50% and 98% were attained. It is seen that both T_{50} and T_{98} monotonically decreased with increasing Ru content in the catalysts. Moreover, the maximum T_{50} and T_{98} were observed for Pt/C catalyst, the minimum – for Ru/C. That is, Pt/C showed the lowest catalytic activity, while Ru/C – the highest activity. Bimetallic Pt-Ru/C catalysts were more active than Pt/C and less active than Ru/C; their activity monotonically increased with increasing Ru content. The most likely explanation for these results is that the used procedure to prepare Pt-Ru/C catalysts (see Section 2.1) led to the formation of separate monometallic Pt and Ru particles. In particular, the formation of monometallic Pt and Ru particles was observed also in the case of Pt-Ru/SiO₂ catalysts when they were prepared by impregnating Pt/SiO₂ with aqueous solution containing [Ru(NH₃)₆]Cl₃ or RuCl₃ [13].

It should be stressed finally problematic comparison of the performance of Pt/C, Ru/C and Pt-Ru/C catalysts towards selective CO oxidation with other noble-metal based catalysts reported in literature owing to various reaction conditions used in different works. Nevertheless, under the used experimental conditions Pt/C, Ru/C and Pt-Ru/C provided

CO conversion $\geq 98\%$ and therefore seem to be promising catalysts for efficient single-step removal of CO from hydrogen-rich streams containing CO₂ and H₂O.

Acknowledgements

P.V. Snytnikov highly appreciates the support granted by the Zamarayev International Charitable Scientific Foundation. The authors are grateful to partial support provided by Award № REC-008, U.S. Civilian Research & Development Foundation.

References

1. J. C. Amphlett, R. F. Mann, B. A. Peppley, *Int. J. Hydrogen Energy* 21, 8 (1996) 673.
2. J. V. Ogden, M. M. Steinbugler, T. G. Kreutz, *Journal of Power Sources* 79 (1999) 143.
3. L. J. Pettersson, R. Westerholm, *Int. J. Hydrogen Energy* 26 (2001) 243.
4. M. L. Brown, A. W. Green, G. Cohn, H. C. Andersen, *Ind. Eng. Chem.* 52, 10 (1960) 841.
5. S. H. Oh, R. M. Sinkevitch, *J. Catal.* 142 (1993) 254.
6. M. J. Kahlich, H. A. Gasteiger, R. J. Behm, *J. Catal.* 171 (1997) 93.
7. H. Igarashi, H. Uchida, M. Suzuki, Y. Sasaki, M. Watanabe, *Applied Catal. A: General*, 159 (1997) 159.
8. O. Korotkikh, R. Farrauto, *Catal. Today* 62 (2000) 249.
9. M. Watanabe, H. Uchida, H. Igarashi, M. Suzuki, *Chem. Lett.* (1995) 21.
10. H. Igarashi, H. Uchida, M. Watanabe, *Chem. Lett.* (2000) 1262.
11. US Patent 4978649, B01G20/20.
12. N.B. Shitova, L.Ya. Alt, I.G. Perelevskaya, *Zh. Neorg. Khimii* 48 (1998) 800 (in Russ.).
13. R.D. Gonzalez, H.Miura, *Catal. Rev. – Sci.Eng.* 36(1) (1994) 145.

**FORMATION OF α -SITES UPON THERMAL ACTIVATION
OF Fe-CONTAINING ZEOLITES**

E.V. Starokon^a, K.A. Dubkov^a, N.S. Ovanesyan^b, A.A. Shteinman^b, G.I. Panov^a

^a*Borshkov Institute of Catalysis SB RAS, Novosibirsk 630090, Russia*

^b*Institute of Problems of Chemical Physics, Chernogolovka, Moscow region, 142432, Russia*

fax: (007) 3832 343056/3766/4687, e-mail: dubkov@catalysis.nsk.su

Zeolites are unique matrices allowing stabilization of small metal complexes, which often show unusual catalytic properties. One of prominent examples is iron complexes stabilized in the ZSM-5 matrix, called α -sites [1]. According to Mössbauer data [2], iron atoms composing α -sites are in bivalent state having special affinity to nitrous oxide.

In the present work, Mössbauer spectroscopy in situ was used to study the effect of high-temperature activation on the evolution of iron introduced into ZSM-5 zeolite by various methods. Activation process (calcination in air, in vacuum, or in the presence of water vapor) was shown to cause an intensive reduction of iron yielding two types of dinuclear Fe^{2+} complexes, which may comprise more than 60% of total metal content. Reduced ions Fe^{2+} are stable in the presence of O_2 , but are reversibly oxidized to Fe^{3+} by nitrous oxide, generating active α -oxygen species, which provide unique oxidation properties for the zeolite.

After coordinative saturation by adsorbed water molecules, both iron complexes show identical Mössbauer spectra, which are close to the spectra of dinuclear iron sites in MMO enzyme. A quantitative comparison between the number of α -oxygen atoms and the number of Fe atoms, involved in redox transition, shows that α -sites are dinuclear complexes in which both Fe atoms are capable of α -oxygen generation.

References

1. G.I. Panov, A.S. Kharitonov, V.I. Sobolev, *Appl. Catal.* 98, 1 (1993).
2. N.S. Ovanesyan, A.A. Steinman, V.I. Sobolev, K.A. Dubkov, G.I. Panov, *Kinet. Katal.* 39, 863 (1998).

MECHANISM OF HYDROGEN INTERACTION WITH α -OXYGEN OVER FeZSM-5 ZEOLITE

E.V. Starokon, K.A. Dubkov, E.A. Paukshtis, A.M. Volodin, G.I. Panov

*Boriskov Institute of Catalysis SB RAS, Novosibirsk, 630090, Russia
fax: (007) 3832 343056/3766/4687, e-mail: dubkov@catalysis.nsk.su*

Formation of active oxygen species on the catalyst surface, their reactivity and participation in the catalytic oxidation is a subject of numerous studies. Iron containing ZSM-5 zeolites are effective catalysts for benzene to phenol oxidation by nitrous oxide (N_2O) [1]. Their catalytic properties are due to the presence of iron-containing active sites. Upon N_2O decomposition these sites, called α -sites, are capable to form an active oxygen species (α -oxygen)



exhibiting some remarkable features. High concentration of α -oxygen on the zeolite surface provides a good opportunity to identify its participation in the room temperature oxidation of different hydrocarbons, including methane. In all cases the reaction results in a selective formation of hydroxylated products [2].

In the present work, mechanism of model reaction between hydrogen and α -oxygen on FeZSM-5 was studied. The kinetics study in the temperature range from $+20^{\circ}C$ to $-70^{\circ}C$ indicates that the reaction rate is described by the first-order equation on H_2 with very low activation energy (3.2 kcal/mol).

Using IR diffuse reflectance spectroscopy and isotope methods we have shown that α -oxygen interaction with hydrogen is accompanied by H_2 dissociation yielding $(HO)_{\alpha}$ -groups (bands at 3635 and 3673 cm^{-1}) on the catalyst surface. An experiment with α -oxygen substituted for ^{18}O isotope demonstrates that α -oxygen atoms enter the composition of these groups. The total reaction equation may be presented as follows:



The dissociative type of mechanism is additionally supported by stoichiometric ratio of H_2 to α -oxygen ($H_2:O_{\alpha}$), which is close to 1:2. Kinetic isotope effect measurements reported here reveal that similar to methane [3], the dissociation of H_2 molecule to occur at the limiting step of reaction. In case of hydrogen k_H/k_D value varies from 4.6 to 23 as the temperature decreases from $+20^{\circ}C$ to $-70^{\circ}C$.

References

1. G.I.Panov, A.S.Kharitonov, V.I.Sobolev, Appl. Catal. A, 98 (1993) 1.
2. M.A. Rodkin, V.I. Sobolev, K.A. Dubkov, N.H. Watkins, G.I. Panov, Proc. 12th Int. Congr. on Catalysis, Stud. Surf. Sci. Catal., 130 (2000) 875 – 880.
3. K.A. Dubkov, V.I. Sobolev, E.P. Talsi, M.A. Rodkin, N.H. Watkins, A.A. Shteinman, G.I. Panov, J. Molec. Catal., 123 (1997) 155-161.

THE CATALYTIC SYSTEMS FOR AMMONIA OXIDATION BASED ON THE PLATINUM GROUP METALS

N.I. Timofeev, V.I. Bogdanov, V.A. Dmitriev, G.M. Guschin, L.D. Gorbatova

JSC "Ekaterinburg Non-Ferrous Metals Processing Plant", Ekaterinburg, Russia

One of the most important activities of JSC "Ekaterinburg Non-Ferrous Metals Processing Plant" is the production of catalyst gauzes for nitrogen industry. The system of quality providing corresponds to ISO 9002 requirements (it is supported by the TUF-certificate, that was received in 1992.)

We have worked out the technology and have organized the production of knitted gauzes of alloys on the base of Pt. According to the results of commercial exploitation, the main performance of knitted catalyst gauzes exceeds the performance of woven gauzes. For example, for knitted gauzes the irrevocable losses and the capital expenditure are less and the gauze wear is more uniform along the stack height.

At the same time our Plant continues the manufacturing of woven gauzes of any alloy on the base of Pt and Pd from the wire with the diameter from 0.06 to 0.16 mm with the density from 64 to 1800 mesh/cm².

Presently accepted at our Plant method of electrochemical activation allows to produce the catalyst gauzes with cleaned surface and increased up to 10 times specific surface area. The gauzes produced by this method don't require an additional processing before installation in the device and having high activity they provide the maximum conversion in 8-10 hours after installation instead of 6-8 days for the ordinary gauzes.

To reduce the platinum group metals (pgm) losses our Plant have worked out the trapping stack of gauzes of the palladium alloys. The trapping stacks installed into the AK-72 devices have already worked for 7 years. The catching extent of platinum is about 80-90%. The weight of Pt in the stack is 17.6 - 18.5 kg. The usage of trapping stacks allows to decrease the platinum quantity by 40% (4 gauzes are installed instead of 7 gauzes) and to cut pgm losses to 50 mg per every ton of manufactured acid.

The trapping stack containing 5.6-6.0 kg of Pd is installed after 8 platinum gauzes weighting 16-17 kg on the UKL-7 device. During the exploitation period (2800-3000 hours) the stack catches about 3 kg of Pt; it is equal to 60-70% of total platinum losses from the catalyst. The total direct losses fall to 110 mg per ton of acid.

Our Plant is able to organize the clearing of ammonia oxidation aggregates. Also we have an opportunity to process slams and spent catalysts containing the pressure metals and to extract pure metals and to produce trapping and catalyst gauzes from them.

FTIR STUDY OF SURFACE ACIDITY OF ALUMINAS AND THEIR ACTIVITY IN H₂S OXIDATION

S.A.Yashnik, V.V.Kuznetsov, Z.R.Ismagilov, J.A.Moulijn*, I.V.Babich*

Boreskov Institute of Catalysis SB RAS, Prosp. Akad. Lavrentieva, 5, Novosibirsk 630090, Russia

Phone: +7 3832 341219, Fax: +7 3832 397352, E-mail: zri@catalysis.nsk.su

** Delft University of Technology, 136 Julianalaan 2628 BL Delft, The Netherlands*

Phone: 31 15 2785008, Fax: 31 15 2785006, E-mail: J.A.Moulijn@tnw.tudelft.nl

Abstract

The influence of acidic properties of alumina of different modifications on the catalytic activity in the reaction of direct hydrogen sulfide oxidation has been studied.

Acidic properties of α -Al₂O₃, γ -Al₂O₃, and γ - χ -Al₂O₃ were studied using IR spectroscopy of adsorbed CO.

Hydrogen sulfide interacts with all modifications of alumina (α -, γ -, and γ - χ -) to yield surface SO_x compounds (absorption bands at 1100 cm⁻¹) and inorganic sulfates (a.b. at 1232 and 1349 cm⁻¹). On the surface of α - and γ -Al₂O₃ samples, characterized by strong LAS, additional types of inorganic sulfates are formed having absorption bands at 1265 and 1330 cm⁻¹.

A comparison of the catalytic activity and selectivity of alumina samples and IR spectroscopy data suggests that the H₂S adsorption proceeds predominantly on the LAS of intermediate strength. Alumina containing χ -phase and/or a modifying ion Mg²⁺, is characterized by high concentration of LAS of intermediate strength and exhibit high catalytic activity.

Introduction

Direct catalytic oxidation of hydrogen sulfide into elemental sulfur [1-3] relies on the one-step heterogeneous catalytic oxidation reaction as $\text{H}_2\text{S} + \frac{1}{2} \text{O}_2 \rightarrow \text{S}_n + \text{H}_2\text{O}$. This reaction provides a selective removal of hydrogen sulfide from natural gas without a noticeable conversion of the hydrocarbon part of natural gas at "mild" operation conditions (T = 220-280°C). Though the number of publications devoted to the catalytic oxidation of hydrogen sulfide is rather large, the number of catalytic systems used in the process is limited. Thus, activated carbon [4-6] and zeolites [7,8] are usually used in the process. However, the individual oxides of transition metals or mixtures of these oxides are more promising [9-11].

The catalysts for direct heterogeneous catalytic oxidation of hydrogen sulfide should meet the following requirements: high activity and selectivity with respect to elemental sulfur at a wide range of the initial concentration of hydrogen sulfide and space velocity; high stability in the presence of hydrocarbons and steam. In the case of supported catalysts these parameters are partially provided by the nature of a support. Granulated and monolith aluminas are widely used as support material for this process [11-14]. However the ability of alumina to accelerate both the direct and reverse Claus processes [14] should be taken into account at the development of new catalysts for the direct hydrogen sulfide oxidation.

In the catalytic reactions of oxidation and high-temperature decomposition of hydrogen sulfide [15], the initial adsorption of hydrogen sulfide on the catalyst surface and its

PP-39

subsequent transformation to sulfide or sulfate-sulfite complexes are proposed as the necessary steps for hydrogen sulfide activation [16].

In this work the adsorption and interaction of hydrogen sulfide over a number of alumina supports with different phase compositions have been studied by FTIR. Identification of active sites of hydrogen sulfide adsorption on alumina using FTIR of the adsorbed CO as a probe molecule and characterization of the surface acidic properties of alumina are adopted to explain catalyst activity in the direct hydrogen sulfide oxidation.

Experimental

Preparation of Al_2O_3

We used five spherical alumina samples: $\gamma-Al_2O_3$, γ -+15% $\chi-Al_2O_3$, γ -+35% $\chi-Al_2O_3$, MgO/ γ -+15% $\chi-Al_2O_3$, and $\alpha-Al_2O_3$ prepared by hydrocarbon-ammonia moulding [17,18].

The sample of spherical $\gamma-Al_2O_3$ was prepared from aluminum hydroxide of the pseudoboehmite structure as in ref. [17].

The samples containing 15 and 35% of $\chi-Al_2O_3$ were prepared from pseudoboehmite aluminum hydroxide resulting from the thermal decomposition of gibbsite in a catalytic heat generator [18,19]. The calcination temperature of the above samples was 550°C.

Introduction of magnesium ion into the spherical granules of aluminum hydroxide, its subsequent drying at 110°C and heat treatment at 550°C were performed according to the method described elsewhere [12]. The concentration of MgO in the samples was 3.2 wt%. To prepare spherical samples of $\alpha-Al_2O_3$, the $\gamma-Al_2O_3$ was calcined at 1200°C for 6 h.

A sample of the sulfur modified $\gamma-Al_2O_3$ was prepared by wet impregnating of the spherical $\gamma-Al_2O_3$ containing 15% $\chi-Al_2O_3$ with a 2M sulfuric acid solution, drying at 110°C and calcination at 500°C for 4 h. The sulfur content was 10 wt% of SO_4^{2-} .

The chlorine modified $\chi-Al_2O_3$ sample was prepared by wet impregnation of spherical $\gamma-Al_2O_3$ containing 15% $\chi-Al_2O_3$ with a 0.5 M hydrochloric acid solution, drying at 110°C and calcination at 500°C for 4 h. The chlorine concentration was 1 wt.% of Cl.

The physicochemical properties of the samples are given in Table 1.

Table 1. Physicochemical properties of alumina samples

No	Sample	T_{calc} , °C	S_{sp} , m ² /g	Pore Volume, V_{Σ} , cm ³ /g	XRD phase composition
1	$\gamma-Al_2O_3$	550	214	0.46	$\gamma-Al_2O_3$
2	γ -+15% $\chi-Al_2O_3$	550	167	0.55	75% $\gamma-Al_2O_3$ +15% $\chi-Al_2O_3$
3	γ -+35% $\chi-Al_2O_3$	550	160	0.58	65% $\gamma-Al_2O_3$ +35% $\chi-Al_2O_3$
4	MgO/ γ -+15% $\chi-Al_2O_3$ (MgO~3.2 wt.%)	550	160	0.52	$\gamma^*-Al_2O_3$, (a~7.952Å)
5	$\alpha-Al_2O_3$	1200	9.3	0.37	$\alpha-Al_2O_3$
6	SO_4^{2-} / γ -+15% $\chi-Al_2O_3$ (SO_4^{2-} - 10 wt.%)	500	245	0.58	75% $\gamma-Al_2O_3$ +15% $\chi-Al_2O_3$
7	Cl/ γ -+15% $\chi-Al_2O_3$ (Cl ⁻ - 3.5 wt.%)	500	225	0.58	75% $\gamma-Al_2O_3$ +15% $\chi-Al_2O_3$

$\gamma^*-Al_2O_3$ – solid solution Mg^{2+} in $\gamma-Al_2O_3$

Activity test in the reaction of hydrogen sulfide oxidation

Catalytic activity of the samples was measured in a fixed-bed catalytic flow setup at the stoichiometric ratio of reagents ($\text{H}_2\text{S}/\text{O}_2 = 2/1$). The concentration of hydrogen sulfide in the initial reaction mixture was 0.6 vol.%. In all runs, a 1 cm^3 of a catalyst sample was placed into the quartz reactor. The space velocity of the reaction mixture was $100\text{ cm}^3/\text{min}$ and GHSV was 6000 h^{-1} . The reaction was studied in a temperature range of $200\text{--}400^\circ\text{C}$.

Gas mixtures were analyzed using a "Tsvet-500M" gas chromatograph equipped with a TCD and Teflon column (length 3 m, i.d. 3 mm) with a "Hayesep C" sorbent modified by 0.5% H_3PO_4 . The space velocity of the carrier gas (helium) was $30\text{ ml}/\text{min}$, the operation temperature of the column was 150°C .

FTIR experiments

A "BOMEM MB102" FTIR spectrometer was used for spectroscopic studies. Adsorption of carbon monoxide was studied in a low-temperature spectroscopic cell equipped with CaF_2 glasses. A high-temperature spectroscopic cell was used to study the adsorption of hydrogen sulfide.

The powdered samples were pressed into pellets of $10\text{--}20\text{ mg}/\text{cm}^2$ thick. A catalyst pellet was placed into the spectroscopic cell and pretreated under vacuum at 400°C for 3 h.

Pure carbon monoxide was introduced into the cell at 1-2 Torr. FTIR spectra were recorded at room temperature. Then the sample was cooled to -196°C with liquid nitrogen. Spectra were recorded at -196°C . A series of spectra were recorded as the temperature increased from -196°C to room temperature during liquid nitrogen evaporation. This procedure allowed registration of IR spectra of adsorbed CO during continuous decrease of CO coverage of the surface of the sample in one run.

The strength and amount of Lewis acid sites (LAS) were determined using the method described elsewhere [20].

The adsorption of hydrogen sulfide was studied at 20, 100, 200, and 300°C , the pressure of hydrogen sulfide introduced into the cell was 30 Torr.

Results and Discussion

Testing of catalytic activity

Data on the catalytic activity and selectivity of aluminas are shown in Fig. 1. It was found that the phase composition of the initial Al_2O_3 significantly affects its catalytic activity. The catalytic activity calculated as the total hydrogen sulfide conversion increases in a series: $\alpha\text{-Al}_2\text{O}_3 < \gamma\text{-Al}_2\text{O}_3 < \gamma\text{-}+15\%\chi\text{-Al}_2\text{O}_3 < \text{MgO}/\gamma\text{-}+15\%\chi\text{-Al}_2\text{O}_3 < \gamma\text{-}+35\%\chi\text{-Al}_2\text{O}_3$. The maximal conversion is $\sim 90\%$ on the $\text{MgO}/\gamma\text{-}+15\%\chi\text{-Al}_2\text{O}_3$ sample and $\sim 80\%$ on the $\gamma\text{-}+15\text{--}35\%\chi\text{-Al}_2\text{O}_3$ samples. For all alumina samples, the selectivity with respect to sulfur is $\sim 100\%$ at 200°C . As temperature increases, the selectivity decreases to 95% on the $\text{MgO}/\gamma\text{-}+15\%\chi\text{-Al}_2\text{O}_3$ sample and to 90% on the $\gamma\text{-Al}_2\text{O}_3$ sample due to the reaction of complete oxidation: $\text{H}_2\text{S} + 3/2\text{O}_2 \rightarrow \text{H}_2\text{O} + \text{SO}_2$ and reverse Claus reaction $3\text{S} + 2\text{H}_2\text{O} \leftrightarrow 2\text{H}_2\text{S} + \text{SO}_2$.

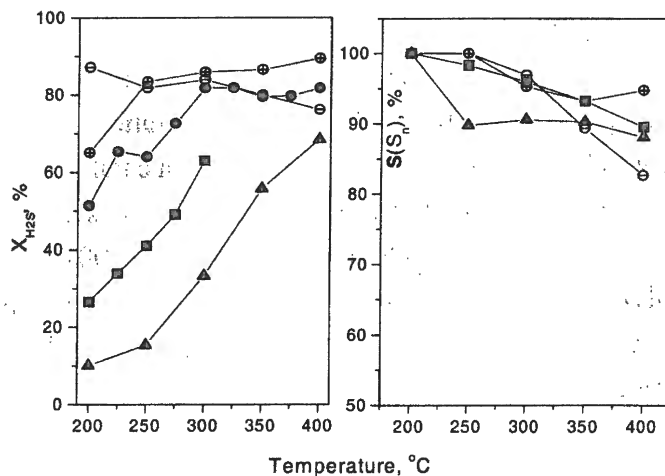


Fig. 1. Total H₂S conversion and sulfur selectivity in H₂S oxidation on aluminas:

- - γ+35%χ-Al₂O₃, ◻ - MgO/γ+15%χ-Al₂O₃, ● - γ+15%χ-Al₂O₃,
 ■ - γ-Al₂O₃, ▲ - α-Al₂O₃.

Study of Acidic properties of Al₂O₃

To study acidic properties of fresh alumina samples with different phase compositions, we used FTIR spectroscopy of adsorbed CO as a molecular probe on the Lewis and Bronsted acid sites.

The spectrum of CO adsorbed on γ-Al₂O₃ [10] contains two groups of adsorption bands: at 2147, 2154 cm⁻¹, and 2186, 2194, 2210 and 2216 cm⁻¹, which belong to CO adsorbed on the Bronsted and Lewis acid sites (BAS and LAS), respectively [10,20].

Figure 2 shows the spectra of CO adsorbed on alumina samples with different phase compositions, the temperature ranges from -196 to +20°C. The spectrum exhibits a range of CO stretching vibrations. According to the reference data [10], for all studied samples, the spectra of adsorbed CO exhibit the presence of acidic site groups corresponding to CO adsorbed on the Bronsted acid sites (a.b. at 2140-2160 cm⁻¹) and CO adsorbed on the Lewis acid sites as Al³⁺ (a.b. at 2180-2220 cm⁻¹).

As Fig. 2 suggests, the CO adsorption on γ-Al₂O₃ and α-Al₂O₃ results in the appearance of absorption bands belonging to CO adsorbed on LAS of intermediate strength (a.b. to 2200 cm⁻¹) and high-frequency absorption bands at 2210, 2216 cm⁻¹ for γ-Al₂O₃ and at 2212 cm⁻¹ for α-Al₂O₃, which correspond to CO adsorbed on LAS of Al³⁺, the adsorption heat is higher than 40 kJ/mole [20].

For the samples containing different amounts of alumina χ-phase, we have observed only LAS with an intermediate strength: absorption bands at 2187 and 2197 cm⁻¹ for γ+15%χ-Al₂O₃ and at 2186 and 2195 cm⁻¹ for γ+35%χ-Al₂O₃.

The definition of strength and concentration of BAS from CO adsorption presents difficulties because of the absence of the reference data on the integral absorption factor of CO bands adsorbed on the hydroxyl groups of catalysts. Table 2 presents the values of strength and concentration of the LAS observed on the surface of the considered samples.

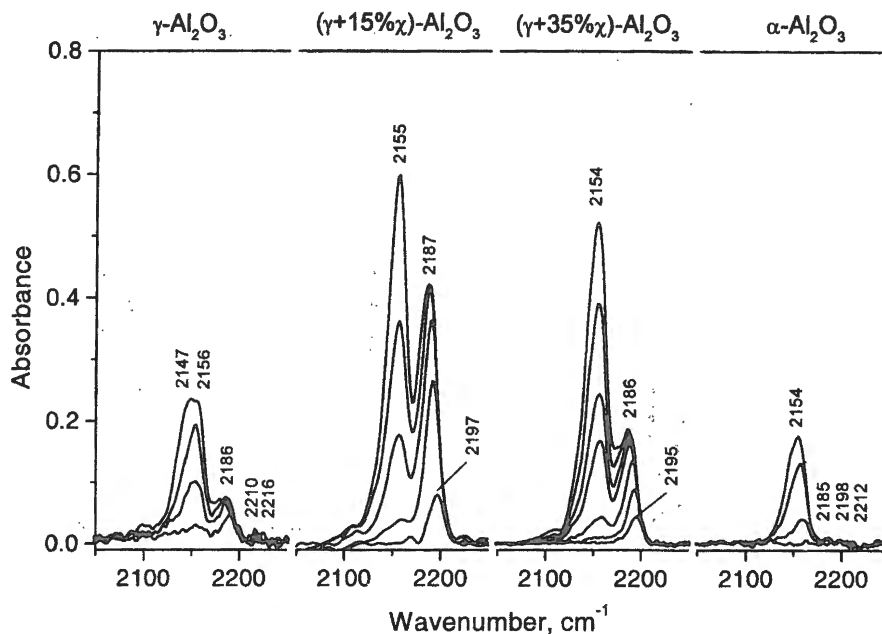


Fig. 2. Spectra of adsorbed CO on aluminas with different phase compositions at different coverage of the surface with CO. The upper spectra were recorded at temperature -196°C and lower spectra at increasing temperature up to ambient.

Fig. 3 shows spectra of CO adsorbed on the surface of $\gamma+15\%\chi\text{-Al}_2\text{O}_3$ modified by MgO , SO_4^{2-} , and Cl^- . As follows from the figure, the CO adsorption on the sample modified by MgO results in absorption bands at 2154 cm^{-1} , which correspond to vibrations of CO adsorbed on BAS, and in absorption bands at 2181 and 2193 cm^{-1} belonging to the vibrations of CO adsorbed on LAS of Al^{3+} . The CO adsorption on $\text{SO}_4^{2-}/\gamma+15\%\chi\text{-Al}_2\text{O}_3$ results in the appearance of absorption bands at 2210 , 2199 , and 2168 cm^{-1} , belonging to the CO adsorbed on the strong LAS (2210 cm^{-1}), cations Al^{3+} of intermediate strength (2199 cm^{-1}), and hydroxyl groups of the catalyst (2168 cm^{-1}). The CO adsorption on $\text{Cl}^-/\gamma+15\%\chi\text{-Al}_2\text{O}_3$ shows the presence of two types of LAS on the catalyst surface which correspond to the absorption bands of CO at 2198 and 2191 cm^{-1} . The values of strength and concentration of the acidic sites on the surface of modified samples are given in Table 2.

A comparison of the data on the CO adsorption suggests that aluminas with different phase composition significantly differ by acidity of their surface. The surface of $\gamma\text{-Al}_2\text{O}_3$ and $\alpha\text{-Al}_2\text{O}_3$ exhibit the presence of strong LAS (stretching vibrations of CO are higher than 2000 cm^{-1}) with the adsorption heat of CO exceeding 40 kJ/mole . However, the number of such sites is less than that of the sites whose CO adsorption heat is lower than 40 kJ/mole . The total amount of LAS on the $\gamma\text{-Al}_2\text{O}_3$ and $\alpha\text{-Al}_2\text{O}_3$ related to 1 m^2 surface is comparable. An introduction of $\chi\text{-Al}_2\text{O}_3$ into $\gamma\text{-Al}_2\text{O}_3$ results in the appearance of LAS with an intermediate strength (adsorption heat is $< 40\text{ kJ/mole}$) and an increase in the total number of LAS compared to γ - and $\alpha\text{-Al}_2\text{O}_3$. A comparison of the data obtained for samples containing 15 and 35% $\chi\text{-Al}_2\text{O}_3$ suggests that an increase in the number of the disordered $\chi\text{-Al}_2\text{O}_3$ phase provides a decrease in the concentration of LAS of Al^{3+} .

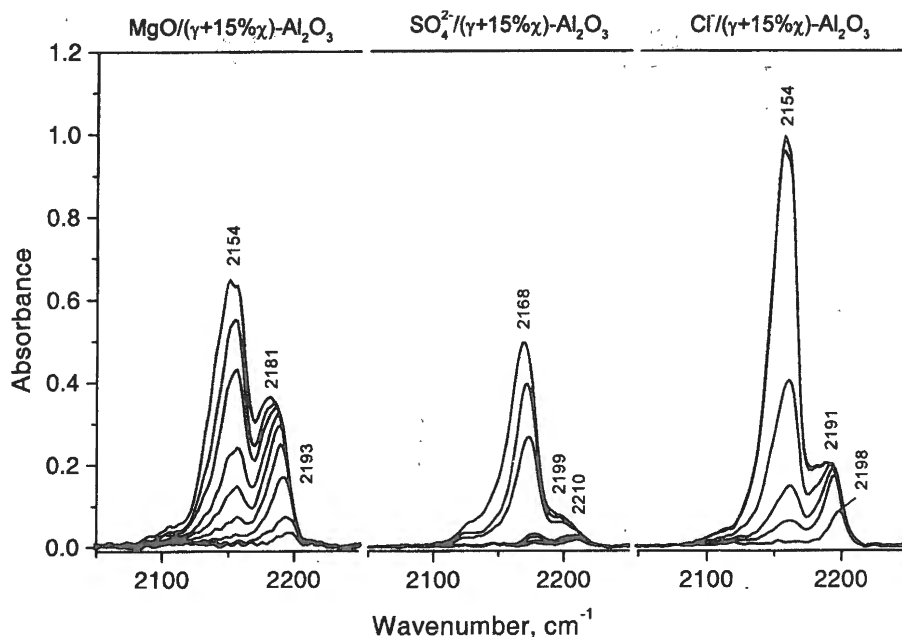


Fig. 3. Spectra of adsorbed CO on $\gamma+15\%\chi\text{-Al}_2\text{O}_3$ samples modified by MgO, SO_4^{2-} and Cl at different coverage of the surface with CO. The upper spectra were recorded at temperature -196°C and lower spectra at increasing temperature up to ambient.

Introducing the modifying agents of different nature it is possible to significantly change the acidity of alumina. An introduction of MgO into $\gamma+15\%\chi\text{-Al}_2\text{O}_3$ decreases the strength of LAS, which manifests itself as a shift of absorption bands to the low-frequency spectrum region, however, this is accompanied by an increase in the concentration of LAS.

Table 2. The values of strength and concentration of the acidic sites on the surface of alumina with different phase compositions

Sample	$\nu_{\text{CO}}, \text{cm}^{-1}$	$C_s, \mu\text{mole/g}$	$C_s, \mu\text{mole/m}^2$	$Q_{\text{CO}}, \text{kJ/mole}$
$\gamma\text{-Al}_2\text{O}_3$	2216	5.2	0.05	47
	2210	4.1	0.02	44
	2186	72	0.36	32
$\gamma+15\%\chi\text{-Al}_2\text{O}_3$	2197	33	0.18	38
	2187	370	2.1	33
$\gamma+35\%\chi\text{-Al}_2\text{O}_3$	2195	22	0.14	37
	2186	180	1.1	32
$\alpha\text{-Al}_2\text{O}_3$	2212	0.09	0.007	45
	2198	0.07	0.005	38
	2185	4.6	0.35	32
MgO/ $\gamma+15\%\chi\text{-Al}_2\text{O}_3$	2193	45	0.25	36
	2181	580	3.2	30
$\text{SO}_4^{2-}/\gamma+15\%\chi\text{-Al}_2\text{O}_3$	2210	16	0.066	44
	2199	22	0.091	39
Cl/ $\gamma+15\%\chi\text{-Al}_2\text{O}_3$	2198	46	0.20	38
	2191	210	0.95	35

When the support is treated with a solution of sulfuric acid, strong LAS appear. Modifying the sample with a hydrochloric acid solution, it is possible to stabilize the LAS of intermediate strength and considerably reduce their number compared to the non-modified sample.

Study of hydrogen sulfide adsorption

As is known, the process of hydrogen sulfide adsorption involves different sites of the catalyst surface. The process was studied in detail for the γ - Al_2O_3 sample [16,21-23]. H_2S can adsorb as a molecular form on BAS of γ - Al_2O_3 [16,22]. It adsorbs dissociatively on the basic sites, in particular on the surface oxygen [22,24]. For strong LAS, it adsorbs both dissociatively and in the molecular state. On the surface of oxide catalysts, the physical adsorption of hydrogen sulfide can be accompanied by oxidation of hydrogen sulfide to different surface sulfite-sulfate complexes at the expense of either bridged lattice oxygen of the catalyst or surface-adsorbed oxygen [25]. However, for Al_2O_3 , the process is hindered by low mobility of the surface oxygen.

Figure 4 presents IR spectra of H_2S adsorbed on the surface of γ - Al_2O_3 . When the adsorption proceeds at room temperature, the spectrum exhibits an absorption band at 1332 cm^{-1} , which corresponds to bending vibrations of the physically adsorbed hydrogen sulfide [23,25]. In addition, the spectrum shows absorption bands at 1180, 1262, and 1349 cm^{-1} , which correspond to vibrations of the surface sulfate-sulfite complexes. The absorption bands at 1180 cm^{-1} can be attributed to the vibrations of S-O bonds in a sulfate ion [10,26]. The bands at 1262 and 1349 cm^{-1} can be attributed to vibrations of surface inorganic sulfates [26], possessing free SO_2 unperturbed by hydrogen bonds. As the sample temperature increases to 100°C , the band at 1332 cm^{-1} vanishes, which may be associated with the oxidation of physically adsorbed hydrogen sulfide and formation of sulfur and water via reaction $\text{H}_2\text{S} + [\text{O}] \rightarrow \text{S}_n + \text{H}_2\text{O}$.

A temperature increase to 200°C results in a new band at 1232 cm^{-1} that can be attributed to symmetric stretching vibrations of inorganic sulfates [26] whose antisymmetric component may be situated in the region about 1350 cm^{-1} as evidenced by antisymmetric shape of absorption band at 1349 cm^{-1} .

As temperature increases to 300°C , there are no significant changes in the spectrum. At room temperature, the spectrum exhibits appearance of a broad absorption band at 1650 cm^{-1} (the spectrum is not shown) which corresponds to bending vibrations of the physically adsorbed water. Absorption bands at 1232 and 1262 cm^{-1} indicate that two types of inorganic sulfates form on the different surface sites of the sample.

In the adsorption of hydrogen sulfide on γ -+15% χ - Al_2O_3 , γ -+35% χ - Al_2O_3 and MgO/γ -+15% χ - Al_2O_3 , there are no significant differences in the spectra. For this reason, we used γ -+15% χ - Al_2O_3 to study the processes occurring on the surface of the above catalysts during hydrogen sulfide adsorption. At room temperature (Fig. 5), the adsorption of hydrogen sulfide on the surface of γ -+15% χ - Al_2O_3 results in an absorption band at 1331 cm^{-1} which corresponds to bending vibrations of the physically adsorbed hydrogen sulfide [23]. As temperature increases to 100°C , this band vanishes. The spectrum shows new bands at 1121,

PP-39

1166, 1229, and 1407 cm^{-1} . Two high-frequency bands at 1229 and 1407 cm^{-1} can be attributed to symmetric and antisymmetric stretching vibrations of the inorganic sulfates [26].

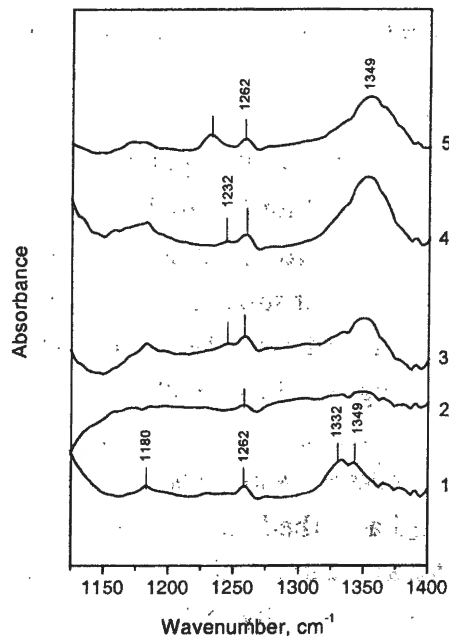


Fig. 4. IR spectra of sample $\gamma\text{-Al}_2\text{O}_3$ after interaction with hydrogen sulfide. 1: adsorption of hydrogen sulfide evacuated at 30 torr at room temperature; 2: 100°C; 3: 200°C; 4: 300°C; 5: evacuation to 10^{-3} torr, room temperature.

Absorption bands at 1121 and 1166 cm^{-1} are most likely associated with vibrations of the surface SO_x compounds [26]. A further rise of temperature to 300°C does not result in significant changes in the IR spectrum. When the temperature is decreased to room temperature and the sample is evacuated, the absorption band at 1121 cm^{-1} vanishes and a new broad band appears at 1646 cm^{-1} which belongs to deformation vibrations of the water physically adsorbed on the catalyst surface.

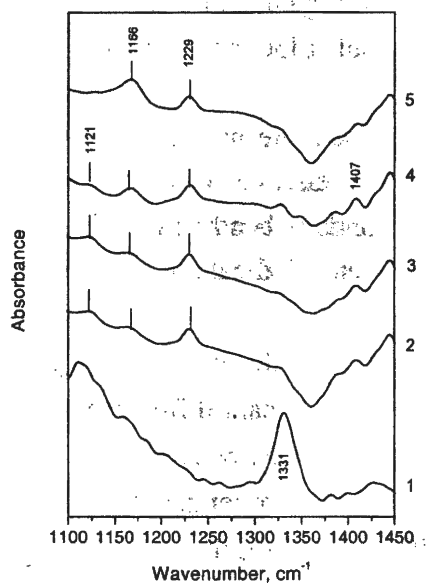


Fig. 5. IR spectra of sample $\gamma+15\%\chi\text{-Al}_2\text{O}_3$ after interaction with hydrogen sulfide. 1: adsorption of hydrogen sulfide evacuated at 30 torr at room temperature; 2: 100°C; 3: 200°C; 4: 300°C; 5: evacuation to 10^{-3} torr, room temperature.

The adsorption of hydrogen sulfide on $\alpha\text{-Al}_2\text{O}_3$ at room temperature (Fig. 6) results in the formation of an absorption band at 1368 cm^{-1} and a broad band at 2588 cm^{-1} (not shown in the spectrum), which correspond to the bending and stretching vibrations of the physically adsorbed hydrogen sulfide, respectively. The presence of a band at 2588 cm^{-1} indicates that the band at 1368 cm^{-1} really belongs to vibrations of the physically adsorbed hydrogen sulfide. As temperature rises to 100°C , the bands at 1368 and 2588 cm^{-1} vanish. The spectrum exhibits intensive absorption bands at 1155 , 1180 , 1237 , 1265 , and 1314 cm^{-1} and a broad band at 1361 cm^{-1} . The bands at 1155 and 1180 cm^{-1} correspond to vibrations of the surface SO_x compounds. The couples of bands at $1237\text{-}1361\text{ cm}^{-1}$ and $1265\text{-}1314\text{ cm}^{-1}$ can be attributed to vibrations of two types of inorganic sulfates, which are located on different sites of the sample surface [26].

As temperature rises to 300°C , the spectrum does not exhibit any significant changes.

A decrease to room temperature with following evacuation of the sample shift the vibration frequencies of surface SO_x compounds to 1159 and 1171 cm^{-1} . The vibration frequencies of inorganic sulfate compounds also shift to 1244 and 1260 cm^{-1} , which can be caused by water adsorption, resulting from a temperature decrease.

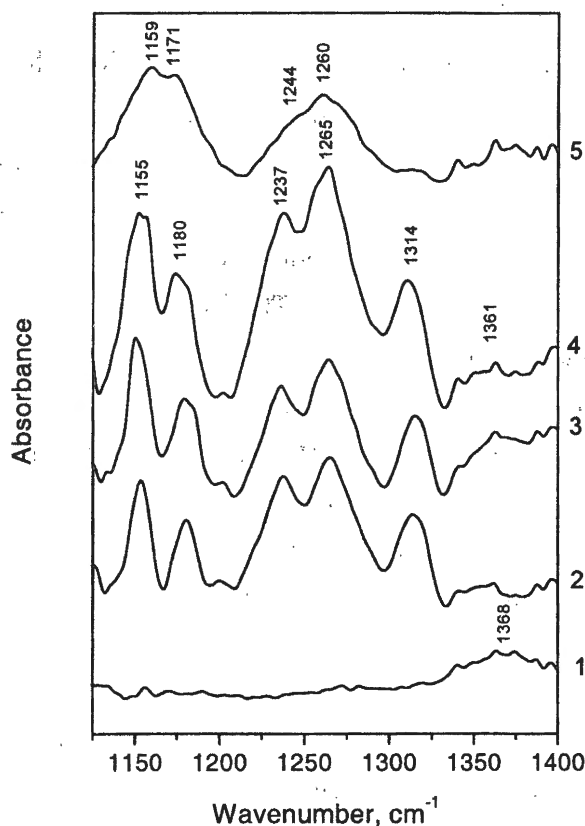


Fig. 6. IR spectra of sample $\alpha\text{-Al}_2\text{O}_3$ after interaction with hydrogen sulfide. 1: adsorption of hydrogen sulfide evacuated at 30 torr at room temperature; 2: 100°C ; 3: 200°C ; 4: 300°C ; 5: evacuation to 10^{-3} torr, room temperature.

Thus, the interaction of hydrogen sulfide with the support surface at elevated temperatures ($>100^\circ\text{C}$) results in the formation of surface SO_x compounds and inorganic sulfates. For sample $\gamma\text{-Al}_2\text{O}_3$, the oxidation of hydrogen sulfide involving formation of surface SO_x

PP-39

compounds begins at room temperature. One may suggest that the physically adsorbed hydrogen sulfide is oxidized at the expense of the catalyst surface oxygen [25].

On γ - Al_2O_3 and α - Al_2O_3 , the above interaction results in two types of surface inorganic sulfates, which can be attributed to the presence of two types of LAS on their surfaces. For samples γ -+15% χ - Al_2O_3 , γ -+35% χ - Al_2O_3 , and MgO/γ -+15% χ - Al_2O_3 , the IR spectra do not differ. Because of the absence of strong LAS on the catalyst surface, the hydrogen sulfide adsorption provides formation of inorganic sulfates of one type.

Knowing that different alumina modifications are widely used as supports of selective hydrogen sulfide oxidation catalysts [11,13,14], it is interesting to elucidate a contribution of different alumina supports into activity and selectivity of the discussed process. Data on the activity of different alumina supports in the reaction of hydrogen sulfide oxidation indicate that γ - Al_2O_3 , containing ~ 35% χ - Al_2O_3 , exhibits the highest activity. Pure γ - Al_2O_3 and the sample modified with χ - Al_2O_3 , characterized by high specific surface area (~180-220 m^2/g), exhibit similar selectivity at temperatures below 300°C. The difference in selectivity observed at temperatures higher than 350°C can be attributed both to textural (pore volume, pore size distribution) and surface acid-base properties of the support. The effect of textural properties on the process selectivity is more pronounced for α - Al_2O_3 . For this sample, the selectivity decreases from 100 to 90% even at 250°C. It is known, the effect of porous catalyst structure on the selectivity of hydrogen sulfide oxidation [27-29] is associated with a possible capillary condensation of sulfur vapor in the narrow pores, which catalyzes oxidation of hydrogen sulfide to predominantly yield elemental sulfur. The capillary condensation was observed on the zeolites and activated carbon [30].

Taking into account the known literature fact that the interaction of H_2S involving BAS does not significantly activate a molecule [16] and the interaction with LAS and base sites significantly activates a molecule of hydrogen sulfide and provide its decomposition to SH and H groups [16], we shall consider a correlation between the catalytic activity of alumina and the number of observed LAS. Since LAS with an adsorption heat of 32-35 kJ/mole (absorption band at 2186 cm^{-1} in the IR spectrum of adsorbed CO) prevail, Fig. 7 shows the hydrogen sulfide conversion in the reaction of direct oxidation as the function of the number of the above sites and reaction temperature. As the figure suggests, the acid-base properties of the alumina surface unambiguously affect the activity in the reaction of hydrogen sulfide oxidation at different temperatures. At 200-250°C, the activity has its maximum when the content of LAS is ~180 $\mu\text{mol}/\text{g}$. An increase in the concentration of LAS, typical for a pure and modified by MgO samples of γ -15% χ - Al_2O_3 , results in a decrease in the activity of the hydrogen sulfide oxidation at 200°C. The activity reaches its maximum (~85%) when the content of LAS is ~ 180 $\mu\text{mole}/\text{g}$ at 300°C. The dependencies observed at different temperatures suggest either an effect of different types of acid-base sites of alumina supports that participate in the adsorption of hydrogen sulfide and/or oxygen or a difference in the mechanism of hydrogen sulfide oxidation.

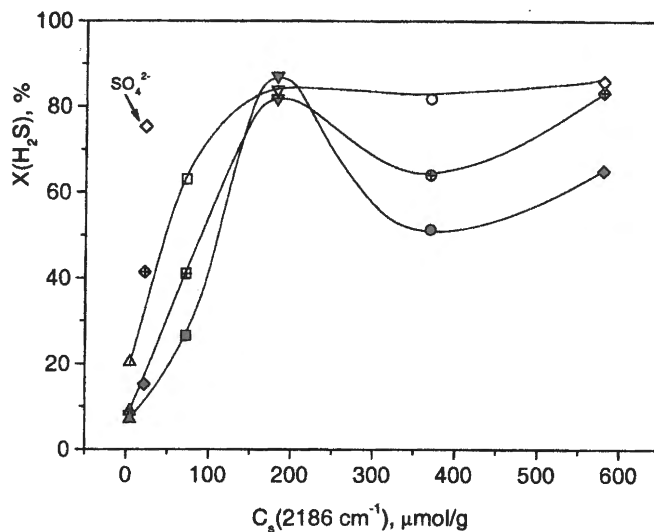


Fig. 7. H₂S conversion on the aluminas supports vs. content of LAS of intermediate strength (a.b. 2186 cm⁻¹). Temperature 200°C – solid dots, 250°C – cross dots, 300°C – opened dots.

At 200-300°C, there are initial curve parts where the hydrogen sulfide conversion linearly increases with an increase in the number of LAS, the heat of CO adsorption is about 32-35 kJ/mole. Modifying the surface of γ -15% χ -Al₂O₃ with a sulfate ion (~10 mass.%), it is possible to completely suppress the LAS of intermediate strength (see IR spectra). A decrease in the concentration of LAS reduces the activity of the sulfated sample as compared to the initial sample at temperatures below 250°C. When the temperature is higher than 300°C, the effect of a sulfate ion on the hydrogen sulfide conversion and the process selectivity becomes less pronounced.

An introduction of Cl⁻ (to 3.5 wt.%) significantly deactivates the catalyst (the maximal conversion does not exceed 35%). According to IR spectroscopic data on the CO adsorption, acidic properties of the surface change, namely, the number of LAS with an adsorption heat of 32-35 kJ/mole decreases by almost a factor of 2. However, a significant decrease in the activity is most probably caused by a negative effect of ion Cl⁻ on the catalyst activity as in the number of catalytic reactions.

Thus, the experimental data suggest that the LAS of intermediate strength contribute to catalytic activity of different alumina modifications, moreover, this contribution depends strongly on temperature (the highest effect is at temperatures below 300°C). Consequently, requirements on the acid-base properties of alumina change regarding the temperature of catalytic hydrogen sulfide oxidation performance. When the temperature is below 300°C, one may recommend γ -Al₂O₃ containing a disordered χ -Al₂O₃ phase or MgO with a high concentration of LAS of intermediate strength.

Conclusions

Phase composition of the initial alumina samples (α -, γ -, and γ + χ -Al₂O₃) strongly influences its activity in the reaction of hydrogen sulfide oxidation. In the presence of χ -Al₂O₃ phase, the catalytic activity of γ -Al₂O₃, including the sample modified with Mg²⁺, tends to increase.

Using IR spectroscopy, the acidic properties of the surface of α -Al₂O₃, γ -Al₂O₃, and γ + χ -Al₂O₃ samples were studied by CO adsorption. For α - and γ -Al₂O₃ samples, the spectra exhibit both

PP-39

2200 cm^{-1} and is 2186 cm^{-1} , respectively). On the γ - χ - Al_2O_3 sample, there are only the LAS of intermediate strength (2186 cm^{-1}). Introducing MgO into γ - Al_2O_3 containing 15% χ - Al_2O_3 reduces the strength of LAS (2181 cm^{-1}) and significantly increases the number of LAS.

The interaction of hydrogen sulfide with all modifications of Al_2O_3 (α -, γ -, and γ - χ -) results in the appearance of surface SO_x compounds (a.b. at 1100 cm^{-1}) and inorganic sulfates characterized by high-frequency absorption bands at 1232 and 1349 cm^{-1} . For α - Al_2O_3 and γ - Al_2O_3 (possessing strong LAS), additional types of inorganic sulfates form (a.b. at 1265 and 1330 cm^{-1}).

A comparison of the catalytic activity and selectivity of alumina samples and IR spectroscopy data allow to suggest that hydrogen sulfide is predominantly adsorbed on the LAS of intermediate strength. The alumina sample, containing χ -phase and/or modifying ion Mg^{2+} , is characterized by a high concentration of LAS of intermediate strength and exhibits high catalytic activity.

Acknowledgement. This work is supported by INCO-COPERNICUS EU Contract No ICA2-CT-1999-10028. The authors wish to thank N.V.Shikina for the preparation of catalysts.

Reference

1. G.K.Boreskov, E.A.Levitsky and Z.R.Ismagilov, *Zh. Vses. Khim. Ob. im. Mendeleeva*, 29 (1984) 379 (in Russian).
2. Z.R.Ismagilov and M.A.Kerzhentsev, *Catal. Rev. Sci. Eng.*, 32 (1990) 51.
3. Z.R.Ismagilov, N.M.Dobrynkin, S.R.Khairulin and F.R.Ismagilov, *Oil&Gas J.*, 7 (1994) 81.
4. B.W.Gamson and R.H.Elkins, *Chemical Engineering Progress*, 49 (1953) 203.
5. J.Klein and K.-D.Henning, *Fuel*, 63 (1984) 1064.
6. P.Zhenglu, Shan Weng Hung, Hau-yn Feng and J.M.Smith, *AIChE Journal*, 30 (1984) 1021.
7. A.Swinarski and A.Zytowicz, *Rev. Roum. Chim.*, 19 (1974) 1877.
8. Japan Patent No 51-16386, MKI³ C 01 B 17/04. A Method for Producing Sulfur from Hydrogen Sulfide. 1976.
9. V.I.Marshneva and V.V. Mokrinskii, *Kinet. Katal.*, 29 (1988) 989.
10. Z.R.Ismagilov, M.A.Kerzhentsev, S.R.Khairulin and V.V.Kuznetsov, *Chem. for Sustainable Development*, 7 (1999) 375.
11. M.V.Batygina, N.M.Dobrynkin, O.A.Kirichenko, S.R.Khairulin and Z.R.Ismagilov, *React. Kinet. Catal. Lett.*, 48 (1992) 55.
12. N.A.Koryabkina, Z.R.Ismagilov, R.A.Shkrabina et.al., *Appl. Catal.*, 91 (1991) 63.
13. T.G.Alhazov and A.A.Vartanov, *Oil&Gas J.*, 3 (1981) 45.
14. P.J. van den Brink, *Ph.D Thesis University of Utrecht*, 1992, The Netherlands.
15. T.V.Reshetenko, S.R.Khairulin, Z.R.Ismagilov and V.V.Kuznetsov, *Intern. J. Hydrogen Energy*, 27 (2002) 387.
16. A.V.Mashkina, *Heterogeneous Catalysis in Chemistry of Organic Sulfur Compounds*, Nayka, Novosibirsk, 1977 (in Russian).
17. M.N.Shepeleva, R.A.Shkrabina and Z.R.Ismagilov, *Technol. Today*, 3 (1990) 150.
18. Z.R.Ismagilov, R.A.Shkrabina and N.A.Koryabkina, *Catal. Today*, 47 (1999) 51.
19. R.A.Shkrabina, Z.R.Ismagilov, M.N.Shepeleva et.al., In Proc. 10th National Symp. "Recent Developments in Catalysis", New Delhi, Madrid, 1990, Part II, p.30.
20. E.A.Paukshtis, *Infrared Spectroscopy in Heterogeneous Acid-Base Catalysis*, Nauka, Novosibirsk, 1992 (in Russian).
21. A.V.Mashkina, E.A.Paukshtis and V.N.Yakovleva, *Kinet. Katal.*, 29 (1988) 596.
22. I.V.Desyatov, E.A.Paukshtis and A.V.Mashkina, *React. Kinet. Catal. Lett.*, 41 (1990) 161.
23. O.Saur, T.Chevreau, J.Lamotte, J.Travert and J.-C.Lavalley, *J. Chem. Soc. Faraday Trans. I*, 77 (1981) 427.
24. C.L.Liu, T.T.Chuang and I.G. Dalla Lana, *J. Catal.*, 26 (1972) 474.
25. A.V.Deo, I.G. Dalla Lana and H.W. Habgood, *J. Catal.*, 21 (1971) 270.
26. T.Yamaguchi and T.Jin, K.Tanabe, *J. Phys. Chem.*, 90 (1986) 3148.
27. G.C.Bond, In P.W.Atkins et, al. (Eds.), *Heterogeneous Catalysis, Principles and Applications*, Oxford Science Publ., Oxford, 1987.
28. C.N.Satterfield, *Mass Transfer in Heterogeneous Catalysis*, M.I.T Press, Cambridge, 1970.
29. A.Wheeler, In *Adv.Catal.*, Acad.Press, New York, 1951, p.313.
30. M.Steijns and P.Mars, *Ind. Chem. Prod. Res.Dev.*, 16 (1977) 35.

MONOLITH WASHCOATED Cu-ZSM-5 CATALYSTS FOR CONTROL OF DIESEL VEHICLE EMISSION

S.A. Yashnik, L.T. Tsykoza, Z.R. Ismagilov, V.A. Sazonov, N.V. Shikina,

V.V. Kuznetsov, I.A. Ovsyannikova, N.M. Danchenko*, S.P. Denisov* and H.J. Veringa**

Boreskov Institute of Catalysis SB RAS, Prosp. Akad. Lavrentieva, 5, Novosibirsk 630090, Russia

**Ural Electrochemical Plant, Novoural'sk, Russia*

***ECN, Westerduinweg 3, 1755 ZG Petten, the Netherlands*

Abstract

The composition of modified monolith zeolite catalysts containing the basic components in the washcoating layer is suggested. When the washcoating layer contains 80% zeolite, 10% TiO₂, and 10% Al₂O₃, the catalyst exhibits both activity and adhesion strength. The titanium catalyst is stable to sulfur poisoning (H₂S) at 500°C; a small decrease in the catalyst activity at 400°C is no longer observed after regeneration. Introducing 4 wt.% Ce (calculated for respect to the washcoating) into the ready catalyst, one can preserve the catalyst activity and provide its stable operation in the presence of water vapor both at 400 and 500°C. Activity of the titanium-cerium- modified monolith catalyst is stable in the presence of water vapor and sulfur compounds in the gas mixture at a time.

Introduction

Data on the preparation and investigation of bulk Cu-ZSM-5 catalysts [1,2] permitted us to choose the optimal ion exchange conditions, providing both high activity and stability of the catalysts. In the present work we use our earlier data [1,2] to synthesize and study the monolith catalysts containing copper-substituted zeolites in the washcoating and their operation on the selective catalytic reduction of nitrogen oxides (SCR NO_x) with propane in the presence of water vapor and sulfur compounds.

As is known, the Cu-substituted zeolites exhibit high activity on SCR NO_x with hydrocarbons and lose their activity in excess of oxygen [3-5], water vapor and/or SO₂ [3,6]. The catalyst activity can be partially reduced by regeneration, the degree of regeneration depends on the concentration of poisons in the reaction mixture. Thus, when the concentration of water is low (2 vol.% [6] or 3.9 vol.% [3] for 90 min [3]), the catalyst deactivation is a reversible process and the catalyst activity is completely reduced by regeneration. A treatment of the zeolite catalyst in wet air (to 14 vol.% water) in a temperature range of 200-600°C [7,8] results in a sharp decay in the Cu-ZSM-5 activity. A partial reduction of the activity after regeneration was attributed to [7,8] dealuminizing of the zeolite.

When waste gas contains sulfur compounds (SO₂ concentration is to 20 ppm) and the degree of NO conversion is high, the activity of Cu-ZSM-5 catalysts slightly decreases on SCR NO_x with hydrocarbons. The catalyst activity is completely restored by termination of SO₂ feeding into the reaction mixture [3,9]. Because of the presence of SO₂ (220-300 ppm) in the gas

PP-40

mixture, Cu-ZSM-5 partially loses its activity on SCR NO_x with hydrocarbons [3,10] and becomes completely deactivated in the reaction of direct NO_x decomposition [10]. In the latter case, the activity of Cu-ZSM-5 is partially restored after its training in a helium flow at 700°C.

When the reaction of SCR NO_x with hydrocarbons is promoted by oxygen (the concentration of oxygen in the reaction mixture is 10 vol.%), the activity of Cu-ZSM-5 is 60 times higher than in the absence of oxygen [4]. On the other hand, the dependence of activity of Cu-substituted zeolites on the oxygen concentration in the reaction mixture is maximum at oxygen concentrations ranging from 2 to 3 vol.%, the degree of conversion slowly decreases as the concentration of oxygen rises. Interestingly, oxygen-containing hydrocarbons can restore NO under highly oxidizing conditions [5].

Though zeolite catalysts have high initial activity, their application in the actual purification processes as cleaning of vehicle waste gases is limited because of their susceptibility to deactivation in the presence of water vapor and sulfur.

The number of publications devoted to the improvement of catalysts for the selective reduction of NO_x in the presence of SO₂ and water vapor is not large. It is well known that the catalytic systems containing titanium, cerium and aluminum oxides are more stable to poisoning with water vapor and sulfur compounds during the SCR NO_x with ammonia. On studying the stability of Cu, V, and Cu-V-O catalysts supported on the alumina and titania or their mixture on the SCR NO_x with ammonia in the presence of SO₂ [11], it was shown that catalysts based on TiO₂ are more stable to sulfur poisoning. Note that as the concentration of TiO₂ in the support increases, the catalyst activity holds at a higher level. In addition, the resistance of vanadium catalysts to sulfur poisoning increases if a support contains both TiO₂ and ~20% Al₂O₃. A comparison of the V and Cu-V catalysts supported on the same carrier shows that the copper catalyst is less stable to SO₂ poisoning, though it effectively removes SO₂ as a sorbent/catalyst. The authors attribute the loss of stability of the copper catalyst to its high capacity with respect to SO₂ and to formation of complex copper-aluminum sulfates. Studying the selective reduction of NO with decane on Cu-ZSM-5, CuO/Al₂O₃, CuO/ZrO₂, and CuO/TiO₂ in the presence of SO₂ [12], the authors attributed a lesser decrease in the activity of the latter two systems to the presence of strong Lewis sites in both catalysts.

According to refs. [13,14], the CuO/TiO₂ catalysts, pre-sulfated in gas mixture SO₂+O₂ at temperatures above 400°C or prepared from copper sulfate [13-15] are highly active in the reaction of SCR NO_x with ammonia and stable with respect to SO₂. Activity of Cu-Ti-O catalysts in the reaction is primarily determined by redox properties of copper. An introduction of sulfate ions into the Cu-Ti-O systems hinders the reduction of Cu(II) [12,15,16] and increases the activity of the system at temperatures above 400°C because of sulfation of titania and formation of copper sulfate [15].

Modifying the copper-substituted zeolite catalyst with cations as Cr, Ce or Sr [17,18], one increases their thermal and hydrothermal stability in the presence of water vapor and SO₂. This phenomenon is probably caused by prevention or inhibition of the processes of sintering of the active copper-containing structures in the zeolite and dealumination of the zeolite itself.

Based on the few reference data, in our work the monolith catalysts were prepared using titania and cerium oxide as modifying agents in order to increase their resistance to water and sulfur poisoning.

Experimental

Alumosilicate or cordierite monolith fragments (10x10x20 mm in size) were used as monolith supports (Table 1).

Table 1. Properties of monolith supports

Support	Channel size, mm	Wall thickness, mm	Phase composition	S_{sp} , m^2/g	Pore volume (with respect to water), cm^3/g
Alumosilicate	2.2x2.2	0.45	$SiO_2 \cdot Al_2O_3$	0.45	0.20
Cordierite	1.0x1.0	0.10	$Mg_2Al_4Si_5O_{18}$	0.30	0.12

The samples of H-ZSM-5 zeolite [1,2,19] were used to prepare the catalysts, the zeolite module (atomic ratio Si/Al) was 34 and 73. The washcoated monolith catalysts were synthesized via the below steps:

- preparation of a suspension, containing 80% zeolite and 20% binding agent (calculated for Al_2O_3), from aluminum hydroxide with a pseudoboehmite structure as in ref. [2,19];
- deposition of a washcoat on the monolith support by its submerging into the suspension, drying and heating at 550°C;
- performance of ion exchange from solutions of copper acetate (pH ~ 6) or ammonia copper acetate (pH ~ 10), the concentration of copper is 5-10 mg/ml [1,2]. Then the washcoated monolith catalyst is washed, dried and calcined at 500°C.

For titania modifying, we introduced a disperse powder of 10% TiO_2 (anatase modification) instead of 10% Al_2O_3 at the step of suspension preparation. The prepared catalyst was modified with cerium oxide via incipient wetness technique, the given concentration of cerium (2 and 4 wt.%) in the coating. Then the catalyst was dried and calcined at 500°C.

As in earlier works [1,2], activity of the modified catalysts was tested on the NO reduction with propane, the space velocity of gas flow was 42 000h⁻¹, temperature ranged from 200 to 500°C, the gas mixture had the following composition: NO 300 ppm, C_3H_8 0.15 vol.%, O_2 3.5 vol.%, N_2 balance. Activity of the catalysts at standard conditions was characterized by the degree of NO conversion (X_o , %) at the preset temperature.

After determination of NO conversion (X_o) at standard conditions, we introduced hydrogen sulfide (~300 ppm) and/or water vapor (~6 vol.%) into the reaction mixture at the preset temperature (400 or 500°C). The catalysts were poisoned with the above admixtures during 30 min (one cycle), then the feeding of H_2S and/or water vapor was stopped and the degree of NO conversion was determined in the standard reaction mixture (X_k , %) at the same temperature. Stability of the catalysts to poisoning with sulfur and water vapor was determined from parameter $\Delta X/X_o$ (determined as $(X_o - X_k)/X_o$ and expressed in %).

To determine stability of the catalysts in the presence of hydrogen sulfide and/or water vapor, poisoning lasted for 20 h, activity was measured every 2-4 h at standard conditions.

PP-40

The catalysts were regenerated at 500°C for 0.5-2 h in a flow of air. Activity was determined after regeneration of catalysts at standard conditions (X_{reg} , %).

In order to study the effect of concentration of oxygen and NO on the catalyst activity, the concentration of O₂ varied from 3 to 12 vol.% and of NO from 300 to 900 ppm. Studies were performed on the cordierite based monolith catalysts with an optimal composition of the zeolite coating.

The catalysts were subjected to DIESEL tests at the Electrochemical Plant (Novouralsk, Russia), the space velocity was 50 000 h⁻¹, the temperature was 400°C, and the gas mixture contained: O₂ 14.5 vol.%, NO 300 ppm, CO 1900 ppm, C₃H₆ 200 ppm, C₃H₈ 300 ppm, CO₂ 2500 ppm, H₂O 2.5 vol.%, nitrogen being the balance. Testing was performed on the cordierite based monoliths 25 mm in diameter and 75 mm in length, the composition of the zeolite-containing washcoat was optimal.

Morphology of the catalysts was characterized using the scanning electron microscopy method on a REM-100U electron microscope.

XRD was performed using a HZG-4 diffractometer supplied with Cu K_α radiation. Phase composition was determined from diffraction patterns registered at 1°/min and 2θ = 4-40°.

Formation of sulfur compounds on the catalyst surface subjected to poisoning with hydrogen sulfide was studied using a MAP-3 microanalyzer. The probe diameter was 1-2 mm, the working voltage was 25 kW, K_αAl, K_αTi, K_αCu, and K_αS were analytical lines.

Results and discussion

1. *Initial activity of the monolith catalysts*

In this work we studied the monolith catalysts whose washcoating have the below compositions: (1) Cu [80% ZSM-5 + 20% γ-Al₂O₃]

(2) Cu [80% ZSM-5 + 10% TiO₂ + 10% γ-Al₂O₃]

(3) Ce{Cu[80% ZSM-5 + 20% γ-Al₂O₃]}

(4) Ce{Cu[80% ZSM-5 + 10% TiO₂ + 10% γ-Al₂O₃]}

In all synthesized monolith catalysts, the washcoat was 10-13 wt.%. The concentration of both copper and cerium in the washcoating was 1-4 wt.%. According to the scanning electron microscopy (Fig. 1), the support surface is densely covered with a homogeneous (without defects) washcoating layer. To provide uniform and strong coverage of cordierite and aluminosilicate based supports, the optimal thickness of the washcoat should be 15-20 and 20-50 mkm, respectively.

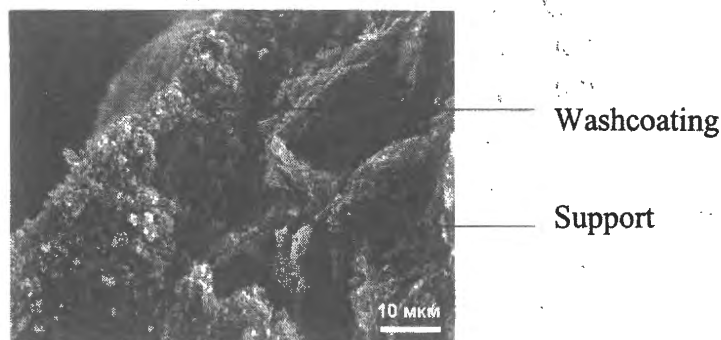


Fig. 1. Micrographs of surface of the washcoated support.

Table 2 presents data on the activity of monolith catalysts with a zeolite washcoat, the supports have different geometries, the experimental conditions are standard (without poisoning admixtures). For comparison, the table presents the activity of bulk Cu-ZSM-5 catalysts [1] which differ by copper concentration (1.1 and 3.5 wt.%) and zeolite module (Si/Al =34 and 73). It was shown [1] that irrespective of the zeolite module, the activity of bulk Cu-ZSM-5 catalysts reaches its maximum (the absolute maximal activity is 94-97% at $T = 400-500^{\circ}\text{C}$) when the level of ion exchange ($2 \times 100x \text{ Cu/Al}$, % [20]) is close to 100%. This maximum activity maintains as the degree of exchange increases to 430%. According to [2], an introduction of 20 wt.% Al_2O_3 or 10 wt.% $\text{TiO}_2 + 10 \text{ wt.} \% \text{ Al}_2\text{O}_3$ results in a small decrease in the activity of the bulk zeolite-containing composition.

At 400°C , the activity of the monolith catalysts with a washcoating supported on the aluminosilicate or cordierite is 30-47 rel.% lower than that of the bulk catalysts of similar composition (compare samples 3 and 7,12; 5 and 9,13; 6 and 8 in Table 2). The difference between activity of the bulk and washcoat monolith catalysts reduces to 17-24 rel.% as temperature rises to 500°C .

Table 2. Properties of the synthesized bulk and washcoat monolith catalysts

№	Washcoat composition	NO conversion, %, at $T^{\circ}\text{C}$		
		400	450	500
1	3.5%Cu- ZSM-5(bulk), Si/Al=73, [1]	94	99	97
2	1.1%Cu- ZSM-5(bulk), Si/Al=34, [1]	94	97	96
3	0.9%Cu[80%ZSM-5 + 20% Al_2O_3], (bulk), Si/Al=73, [2]	85	92	93
4	0.9%Cu[80%ZSM-5 + 20% Al_2O_3], (bulk), Si/Al=34, [2]	77	86	90
5	1.6%Cu[80% ZSM-5 + 10% TiO_2 +10% Al_2O_3], (bulk), Si/Al=34, [19]	84	87	87
6	4%Ce{1.2%Cu[80%ZSM-5 + 20% Al_2O_3]}, (bulk), Si/Al=34, [19]	64	77	84
7	Cu[80%ZSM-5 + 20% Al_2O_3]/aluminosilicate, Si/Al=73, [19]	45	65	70
8	Ce{Cu[80%ZSM-5 + 20% Al_2O_3]}/aluminosilicate, Si/Al=73, [19]	43	62	69
9	Cu[80% ZSM-5 + 10% TiO_2 + 10% Al_2O_3]/aluminosilicate, Si/Al=34, [19]	55	64	72
10	4%Ce{Cu[80%ZSM-5 + 10% TiO_2 + 10% Al_2O_3]}/aluminosilicate, Si/Al=34, [19]	48	60	64
11	4%Ce{Cu[80%ZSM-5 + 10% TiO_2 + 10% Al_2O_3]}/aluminosilicate, Si/Al=73, [19]	48	59	65
12	Cu[80%ZSM-5 + 20% Al_2O_3]/cordierite, Si/Al=34	60	70	73
13	Cu[80% ZSM-5 + 10% TiO_2 + 10% Al_2O_3]/cordierite, Si/Al=34	58	67	72
14	2%Ce{Cu[80%ZSM-5 + 10% TiO_2 + 10% Al_2O_3]}/cordierite, Si/Al=34	45	59	64
15	4%Ce{Cu[80%ZSM-5 + 10% TiO_2 + 10% Al_2O_3]}/cordierite, Si/Al=34	37	56	61
16	Co-ZSM-5, [21]*	89	96	95
17	[Cu-ZSM-5 + Co-ZSM-5], [21]*	89	90	89

*) the space velocity is $12\,000 \text{ h}^{-1}$, C_2H_4 is a reducing agent.

PP-40

When the conditions of ion exchange provide the exchange degree close to 100% (the concentration of copper acetate solution is not lower than 5 mg CuO/ml [1,2]), the zeolite module does not affect the activity of monolith catalysts based aluminosilicate (compare samples 10 and 11 in Table 2) as in the case of bulk CuZSM-5 catalysts [1]. In case of the catalysts containing copper-substituted zeolite and 20% Al₂O₃ in the washcoat, introduction of 10% TiO₂ instead of 10% Al₂O₃ into the washcoat does not change the catalysts activity (compare samples 12 and 13).

As cerium dioxide is introduced in the washcoated monolith catalysts, the activity decreases (compare samples 4 and 6, 9 and 10, 13,14, and 15 in Table 2). When the concentration of cerium dioxide is 2-4 wt.%, the activity decreases by 40-60 rel.% at 300-400°C and by 10-20 rel.% at 450-500°C. It should be noted that an introduction of both 2 and 4 wt.% CeO₂ changes less the activity of catalysts prepared by ion exchange from solutions containing 5 mg CuO/ml than those prepared from the solutions containing 10 mg CuO/ml.

For comparison, Table 2 presents literary data on the activity of monolith catalysts with a washcoat containing Co or (Co-Cu)-substituted zeolite [21]. Taking into account the fact that nitrogen oxide was reduced with ethylene [21] and the time of contact was 3.5 times longer than in our work, one can conclude that the activity of the samples is comparable.

As the concentration of NO in the reaction mixture is raised from 300 to 900 ppm and the concentrations of C₃H₈ and O₂ are ~ 1200 ppm and 4.2 vol.% respectively, the degree of NO conversion on the cordierite based catalyst modified with titania and cerium oxide preserves constant and is 18-22% at 400°C and 39-42% at 500°C.

2. Activity of the monolith catalysts after poisoning with H₂S and/or H₂O

Actual diesel vehicle emission gases contain large amounts of oxygen (~ 5-12 vol.%), water vapor (~ 10 vol.%), and SO₂ (~ 20 ppm) [3,5,7], for this reason it is important to elucidate their effect on the activity of copper-substituted zeolite catalysts.

In our recent work [19] we have shown that H₂S completely converts into SO₂ at temperatures higher than 250°C on both bulk and monolith CuZSM-5 catalysts. Changes in the catalyst activity (sample 9 in Table 2) and concentration of SO₂ at the reactor outlet were studied during one cycle of poisoning with H₂S at 400 and 500°C. At the instant H₂S is introduced into the gas mixture at 400°C, the degree of NO conversion decays rapidly and the outlet concentration of SO₂ increases at a time. Then both parameters become stable. As H₂S feeding is cut off, the catalyst activity lightly increases at 400°C, but the initial activity is recovered only after the catalyst regeneration. At 500°C, the catalyst activity decreases from 65 to 60% during H₂S feeding into the gas mixture and regains its initial value as H₂S supply is cut off. Note that SO₂ emission was not observed when the catalyst was regenerated at 550°C.

Deactivation of the catalyst observed during one poisoning cycle at 400 and 500°C, partial reduction of the catalyst activity after removal of H₂S and SO₂ from the gas mixture and the possibility of almost complete catalyst regeneration at 550°C during 30 min indicate that the interaction of SO₂ with the catalyst surface is of the adsorption nature. The observation that the catalyst stability to sulfur poisoning sharply increases as temperature raises from 300 to 500°C also confirms the adsorption nature of SO₂ interaction with the catalyst surface. In the

presence of water vapor in the reaction gas mixture, the dynamics of a decrease in the activity of the above catalyst is similar.

Based on the testing results one can suggest that the degree of catalyst deactivation during poisoning with water or sulfur and consequently their stability to these poisons is determined by the catalyst composition and reaction temperature and can be estimated using $\Delta X/X_0$. Data on the catalyst stability to poisoning with water vapor and sulfur are given in Table 3.

A comparison of $\Delta X/X_0$ for samples 1,2, and 3 (Table 3) shows that it is possible to increase the catalyst stability to hydrogen sulfide both at 400 and 500°C by modifying the washcoat with titanium dioxide. Regenerating (500°C, 30 min, air flow) the catalysts containing 10% TiO₂ in the washcoat, one can completely restore their initial activity. When the catalyst sample is not doped with TiO₂, its activity restores only partially.

Introduction of ~ 4 wt.% cerium into the washcoat provides the catalyst stability at 400-500°C in the presence of water vapor (compare $\Delta X/X_0$ for samples 5 and 6 in Table 3).

Table 3. Activity of monolith catalysts after one cycle of poisoning with water or/and hydrogen sulfide

№	Washcoat composition	T, °C	NO conversion					
			X ₀ %	Poisoning		X _k %	$\Delta X/X_0$ %	X _{реген} %
				H ₂ O	H ₂ S			
1	Cu[80%ZSM-5 + 20%Al ₂ O ₃] (Sample 7, Table 2)	400	45	-	+	10	78	29
		500	70			41	44	52
2	Cu[80%ZSM-5 + 10%TiO ₂ + 10%Al ₂ O ₃] (Sample 9, Table 2)	400	56	-	+	40	29	55
		500	65			64	2	64
3	Ce{Cu[80%ZSM-5+ 10%TiO ₂ + 10%Al ₂ O ₃]} (Sample 10, Table 2)	400	42	-	+	26	38	42
		500	54			54	0	54
4	Cu[80%ZSM-5 + 20%Al ₂ O ₃] (Sample 7, Table 2)	400	45	+	-	8	82	42
5	Cu[80%ZSM-5 + 10%TiO ₂ + 10%Al ₂ O ₃] (Sample 9, Table 2)	400	55	+	-	10	82	53
6	Ce{Cu[80%ZSM-5+ 10%TiO ₂ + 10%Al ₂ O ₃]} (Sample 10, Table 2)	400	41	+	-	41	0	41
		500	54			54	0	54
7	Ce{Cu[80%ZSM-5+ 10%TiO ₂ + 10%Al ₂ O ₃]} (Sample 10, Table 2)	400	44	+	+	26	40	44
		500	56			56	0	56

When the catalyst modified with titania and cerium oxide (sample 10 in Table 2) is treated with water vapor and sulfur compounds, it behaves as in the case of poisoning with hydrogen sulfide alone (compare samples 3 and 7). After regeneration, the catalyst activity restores completely.

Stability of the titanium-cerium modified catalyst supported on the aluminosilicate monolith (sample 10 in Table 2) was studied during long-term tests both in the presence and in the absence of poisons at a temperature of 400°C when maximal changes in the catalyst activity are observed during short-term poisoning of catalysts. The results are given in Table 4.

Activity of the catalyst subjected to poisoning with hydrogen sulfide for 20 h at 400°C changes as in the case of short-term poisoning [19]. The catalyst activity decreases and $\Delta X/X_0$ is 54 rel. % after 20 hours of catalyst deactivation. Regeneration at 500°C for 30 min results in a partial restoration of the catalyst activity and a four-hour regeneration recovers almost

PP-40

completely the initial catalyst activity. According to X-ray microanalysis (Fig. 2), about 0.8% of sulfur compounds (compare to 1.1% sulfur immediately after sulfur poisoning) remain in the washcoat after long regeneration and complete restoration of the initial catalyst activity. Since line $K_{\alpha}S$ behaves similar to line $K_{\alpha}Cu$ and partially follows line $K_{\beta}Ti$, one can suggest that sulfur is bonded with copper and titanium, but the bond with copper is more pronounced.

Table 4. Activity of monolith catalysts subjected to long poisoning (20 h) with water vapor and /or hydrogen sulfide

№	Washcoat composition	T, °C	NO conversion					
			X_0 %	Poisoning		X_K %	$\Delta X/X_0$ %	$X_{\text{перен}}$ %
				H ₂ O	H ₂ S			
1	Ce{Cu[80%ZSM-5+ 10%TiO ₂ + 10%Al ₂ O ₃] } (analogue of Sample 10, Table 2)	400	41	-	-	39	5	-
2	Ce{Cu[80%ZSM-5+ 10%TiO ₂ + 10%Al ₂ O ₃] } (analogue of Sample 10, Table 2)	400	39	+	-	27	31	36
3	Ce{Cu[80%ZSM-5+ 10%TiO ₂ + 10%Al ₂ O ₃] } (analogue of Sample 10, Table 2)	400	39	-	+	18	54	23
4	Ce{Cu[80%ZSM-5+ 10%TiO ₂ + 10%Al ₂ O ₃] } (analogue of Sample 10, Table 2)	400	37	+	+	28	24	36

Testing of the catalyst (sample 10 in Table 2) in the presence of water vapor at 400°C for 20 h results in a significant decrease in the catalyst activity (note that this decrease is not observed for a short-term poisoning of this catalyst). After regeneration at 500°C for 30 min in air, the catalyst activity restores almost completely. A comparison of the diffraction patterns of the Cu-ZSM-5 catalyst (Si/Al = 34 and 3.1% Cu) before and after its testing for 20 h in the presence and absence of water vapor does not reveal changes in the initial structure of Cu-ZSM-5: the diffraction patterns of the samples are similar to those of zeolite H-ZSM-5. In the presence of both water vapor and hydrogen sulfide in the gas mixture at 400°C for 20 h, the catalyst activity decreases by 24 rel.% and restores completely after regeneration at 500°C for 30 min.

For the catalyst with a washcoat supported on the cordierite and promoted with both titanium and cerium oxides (sample 15 in Table 2), the dynamics of changes in the activity in the presence of water vapor and/or sulfur is similar. The catalyst loses its activity after the introduction of water vapor (~ 6 vol.%) into the reaction mixture during the initial 15-20 min (Fig. 3). During the next 20 h the activity holds at a level of 20-22%. However, the catalyst restores its activity after regeneration at 500°C for 30 min.

3. Effect of the concentration of oxygen and water vapor on the NO conversion

As water vapor (~ 2.5 vol.%) is introduced into the reaction mixture and the concentration of oxygen is raised from 3.5 to 12 vol.% at a time, the catalyst activity significantly decreases over the entire temperature range. For the catalysts modified with titanium and cerium oxides, the maximal degree of NO conversion is 30-32% at 500°C, which corresponds to a two-fold dip in the catalyst activity as compared to the NO conversion in the dry mixture, containing ~ 3.5 vol.% oxygen ($X_{NO} \sim 61-64\%$).

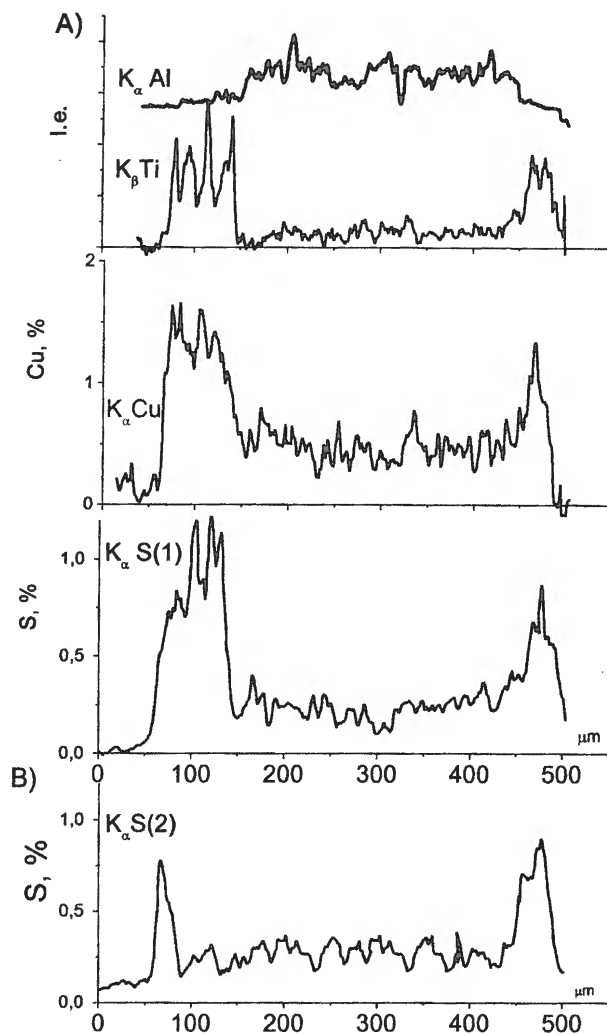


Fig. 2. Intensity of $K_{\alpha} Al \times 2 \times 10^4$, $K_{\beta} Ti \times 200$, $K_{\alpha} Cu \times 200$, $K_{\alpha} S(1) \times 200$ lines for the washcoated catalyst after long poisoning with hydrogen sulfide (a) and spectrum $K_{\alpha} S \times 200$ (2) after catalyst regeneration at $500^{\circ}C$ for 4 h (b)

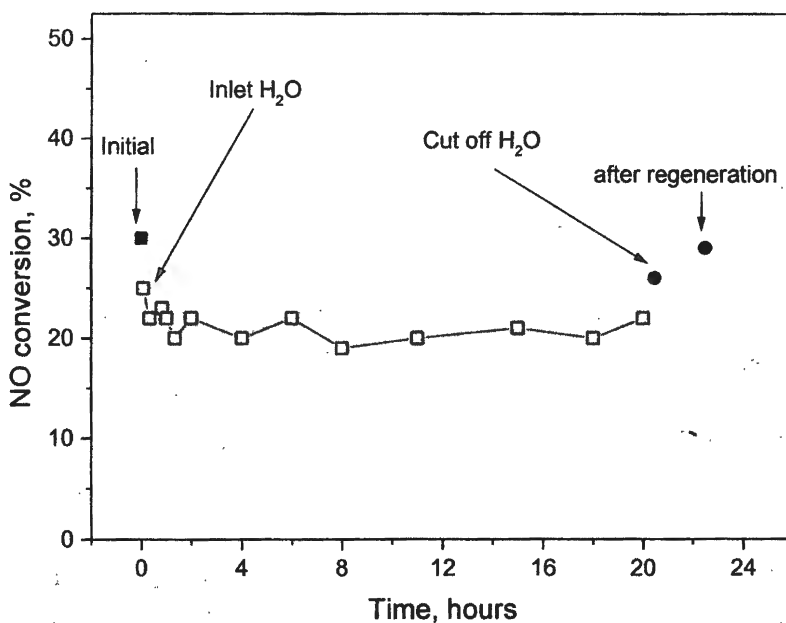


Fig. 3. Changes in the NO conversion on sample 15 (Table 2) in the presence of water vapor (6 vol.%) at $400^{\circ}C$

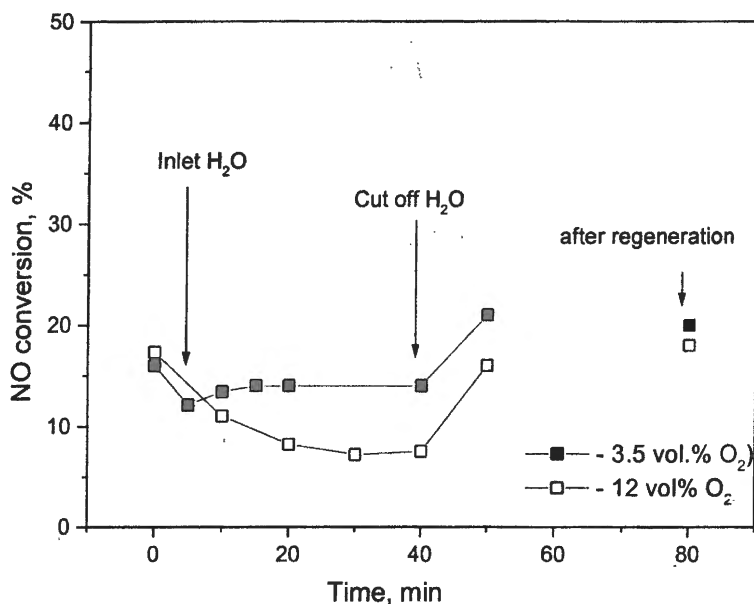


Fig. 4. Stability of sample 15 (Table 2) in the presence of water vapor (2.5 vol.%) at varying concentration of oxygen at 400°C

Figure 4 shows the dynamics of changes in the activity of the above catalyst in the presence of water vapor (2.5 vol.%) and at varying concentrations of oxygen in the reaction mixture. The figure suggests that the degree of NO conversion is the same at 400°C and reaches 16-18% when the concentration of oxygen in the dry reaction mixture is 3.5 and 12 vol.%. As water vapor is introduced in the above reaction mixtures, the catalyst activity decays. When the reaction mixture contains ~3.5 vol.% O₂, an introduction of water vapor decreases the catalyst activity up to 15%. After termination of water vapor feeding into the reaction mixture, the catalyst activity restores to its initial value. When water vapor is introduced into the mixture containing ~12 vol.% O₂, the catalyst activity decays by a factor of 2 and restores completely after termination of water feeding and regeneration of the catalyst at 500°C for 30 min (Fig. 4). Therefore, the monolith catalyst with a modified Cu-ZSM-5 washcoat layer undergoes significant deactivation by small amounts of water vapor (~2.5 vol.%) in the presence of large amounts of oxygen (~12 vol.%).

4. DIESEL tests of the catalyst modified with titanium and cerium oxide admixtures

The cordierite based catalyst, containing 4% Ce/1% Cu(80% ZSM-5 + 10% TiO₂ + 10% Al₂O₃) in the washcoat layer, was subjected to DIESEL tests. Three samples were aged in the moist air atmosphere during 4 h at 500, 600, and 800°C, respectively. The catalyst preliminary aged at 500°C for 4 h in moist air was additionally aged at ~800°C for 7 h in dry air. The catalyst activity was characterized by a temperature at which 50% conversion of hydrocarbons (HC) and carbon monoxide CO was obtained and by the degree of conversion of HC, CO, and NO at 400°C. The results of testing of the fresh catalyst samples and the samples aged at different conditions are given in Table 5.

According to DIESEL test, simulating the lean-burn operation conditions, the monolith catalyst containing Cu-ZSM-5 and titanium and cerium modifying agents in the washcoat exhibits rather low activity. At 400°C, the degree of conversion of hydrocarbons, CO, and NO

is 70.7, 85.6, and 8.8%, respectively. When the catalyst is aged in moist air, the degree of CO conversion tends to decrease as the aging temperature rises from 500 to 600°C. Note that the catalyst aging at the above conditions does not affect its activity with respect to HC and NO. As the temperature of aging in the moist air atmosphere increases to 800°C, the catalyst completely loses its activity, the degree of conversion of HC, CO, and NO decreases by a factor of 4, 9, and 3, respectively. When the catalyst was preliminary aged at 500°C in the presence of water vapor and then additionally aged at 800°C in dry air, the catalyst activity decreases by a factor of 1.3, 5.3, and 2 with respect to HC, CO, and NO, respectively. Thus, the DIESEL test suggests that the catalyst is significantly deactivated at 800°C. Note that water vapor enlarges the degree of catalyst deactivation.

It should be noted that thermal aging at 800°C in the atmosphere of dry gas mixtures as 5% H₂/N₂ and 5% O₂/N₂ and hydrothermal aging at 500-600°C in the presence of water vapor (to 10 vol.%) were observed for the bulk [22,23] and monolith [24] Cu-ZSM-5 catalysts. Thus, the activity of the monolith Cu-ZSM-5 catalyst [24] decayed from 60 to 17% during 70h at 485°C in the reaction mixture simulating the lean-burn gases at a flow rate of 30000 h⁻¹.

Table 5. DIESEL testing of the cordierite based catalyst containing 4% Ce/1% Cu (80% ZSM-5 + 10%TiO₂ + 10% Al₂O₃) in the washcoat

	Conversion temperature (T _{50%}), °C		Conversion (%) degree at 400°C		
	HC	CO	HC	CO	NO
Fresh catalyst samples					
1	323	357	70	86	8
2	318	358	71	87	9
3	321	362	71	83	10
Samples aged in moist air					
500°C/4hrs	330	379	70	74	9
600°C/4hrs	335	393	70	63	8
800°C/4hrs	-	-	16	9	3
800°C/7hrs, dry air	396	-	55	16	5

Discussion

The literature data [4,25] permit one to suggest that isolated ions Cu²⁺ in Cu-ZSM-5 catalysts are responsible for reduction of NO_x with hydrocarbons. In the presence of water vapor, the zeolite is dealuminated [7,18,22] and the state of copper changes irreversibly [18,26], which may result in following action of copper with Al₂O₃ [22,23,27,28] formed upon dealumination. However, XRD data of this work and ref. [22] do not show changes in the crystallinity of ZSM-5. On long storage in air [1], Cu-ZSM-5 can undergo aging resulting in formation of the clustered copper as inactive CuO.

A stabilizing effect of cerium ions on the activity of Cu-ZSM-5 in the presence of water vapor can be attributed to the suppression of both formation of clusters CuO and dealumination of

PP-40

the zeolite. After removal of water vapor from the gas phase at temperatures below 500°C, the initial activity of the cerium modified Cu-ZSM-5 catalyst [18] partially reduces. According to ref. [19] and our data, the catalyst activity restores completely. Note that as the concentration of cerium increases, its stabilizing effect in the presence of water vapor improves [18]. Increasing the concentration of copper in Cu-ZSM-5, it is also possible to slightly increase its stability [18]. Cerium doping of Cu-ZSM-5 probably hinders migration of Cu^{2+} to the zeolite surface and formation of CuO. A slowing down in the formation of surface clusters CuO was confirmed by the absence of changes in the atomic ratio Cu/Si, which was observed by XPS of the modified Cu-ZSM-5 catalysts subjected to different treatments [18,29].

On the other hand, water vapor (the reaction temperature is ~400°C) is responsible for a decrease in the number of aluminum tetrahedrally coordinated cations at the expense of dealumination of the zeolite [3,7,18]. In this case, the zeolite crystal structure does not practically change. Ion Ce^{3+} partly situated on the ion-exchange positions interacts with ion Al^{3+} in its tetrahedral positions to hinder diffusion of aluminum from these positions into the octahedral positions as in the case of stabilization of low-temperature $\gamma\text{-Al}_2\text{O}_3$ [30]. In addition, the ion-exchanged cerium may lower the zeolite dealumination, caused by hydrolysis in the presence of water vapor, owing to the decrease in the number of positions occupied by ion-exchanged copper, where protonation would take place easier. Similar effect of a decrease in the dealumination degree was observed in the case Cu-ZSM-5 in the presence of 2% H_2O , compared to H-ZSM-5 [23].

Stability of the cerium modified zeolite catalyst in the presence of water vapor is apparently provided by two facts: occupation of the ion-exchange positions with cerium cations, which hinders the catalyst dealumination, and presence of the surface CeO_2 phase, which hinders formation of clusters CuO.

The titania modified zeolite catalysts are more resistant to sulfur poisoning, which is probably associated with the fact that sulfation of the high disperse anatase is similar to that of copper and aluminum oxide yielding titanyl sulfate. We suggest that a presence of titanium oxide in the catalyst results in a decrease in the portion of sulfur interacting with copper cations in the zeolite. For this reason, the titanium modified zeolite catalysts are only partially stabilized in the presence of hydrogen sulfide. In contrast to TiO_2 , the titanium oxide modified with a sulfate ion [32] exhibits a rather high activity on the selective reduction of NO with propane especially at a temperature range of 400-600°C. This observation was attributed to a change in the oxidation ability of TiO_2 with respect to hydrocarbons. Thus an increase in the stability of titania modified zeolite catalysts to sulfur poisoning can be also caused by formation of sulfated TiO_2 contributing to the total catalyst activity on SCR NOx with propane.

So, the composition of the modified monolith zeolite catalysts, synthesized by the ion exchange method described elsewhere [1,2], provides their stable operation in the presence of water vapor and sulfur when the conditions of the reaction performance and catalyst treatment are properly chosen.

Acknowledgement

This work was supported by the NWO and INTAS 1044 grants. We are grateful to

Dr. N.A. Rudina for electron microscopy studies of the samples and to V.A. Ushakov for XRD studies of the samples.

References

1. Z.R.Ismagilov, R.A.Shkrabina, L.T.Tsykoza et al., *Kinet. Katal.*, 42 (2001) 928.
2. Z.R.Ismagilov, R.A.Shkrabina, L.T.Tsykoza et al., *Kinet. Katal.*, 42 (2001) 935.
3. A.P.Walker, *Catal.Today*, 26 (1995) 107.
4. M.Iwamoto, H.Hamada, *Catal. Today*, 10 (1991) 57.
5. C.N.Montreuil, M.Shelef, *Appl.Catal.B; Environ.*, 1 (1992) L1.
6. J.N.Armor, *Catal.Today*, 26 (1995) 99.
7. R.A.Grinsted, H.-W.Jen, C.N.Montreuil et al., *Zeolites*, 13 (1993) 602.
8. R.Gopalakrishnan, P.R.Stafford, J.E.Davidson et al., *Appl. Catal. B: Environ.*, 2 (1993) 165.
9. K.C.C.Kharas, *Appl. Catal. B: Environ.*, 2 (1993) 207.
10. M.Iwamoto, H.Yahiro, S. Shundo et al., *Appl.Catal.*, 69 (1991) L15.
11. G.Centi, S.Perathoner, B. Kartheuser et al., *Appl. Catal. B: Environ.*, 1 (1992) 129.
12. F.Figueros, B.Coq, G.Mobilon et al., in *Proc. 11th ICC*, Baltimore, M.D., USA, June 30-July 5, 1996, Part A, P. 621.
13. G.Centi, S.Perathoner, B.Kartheuser, B.K.Hodnett, *Catal. Today*, 17 (1993) 103.
14. J.H.A.Kiel, W.Prins, W.P.M.Swaaij, *Appl. Catal. B: Environ.*, 1 (1992) 13.
15. O.V.Komova. Ph.D Thesis. Novosibirsk. 2000.
16. G.Delahay, B.Coq, E.Ensugue, F. Figueras, *Catal. Lett.*, 39 (1996) 105.
17. K. Rahkamaa, R.L.Keiski, T.Maunula et.al, *Proc. 8-th Intern. Symp. Heterogen. Catal.*, Varna, Bulgaria, 5-9 Oct. 1996, P. 365.
18. Y.Zhang, A.F.Sarofim, M.Flytzoni-Stephanopoulos, 1st World Congress Environ. Catal., Pisa, Italy, May 1-5, 1995, P.271.
19. Z.R.Ismagilov, R.A.Shkrabina, L.T.Tsykoza et. al., *Topics in Catalysis*, 16/17 (2001) 307.
20. P.Ciambelli, P.Corbo, M.Yambino, F. Migliani, *Proc. CAPOC4*, Brussels, Belgium, April. 1997. V.1. P. 109.
21. Z.S.Rak and H.J.Veringa, *React. Kinet. Catal. Lett.*, 60 (1997) 303.
22. J.Y.Yan, G.-D.Lei, W.M.H.Sachtler, H.H.Kung, *J. Catal.*, 161 (1996) 43.
23. J.N.Armor, T.S.Farris, *Appl. Catal. B: Environ.*, 4 (1994) L11.
24. G.P.Ansell, S.E.Golunski, J.W.Hayes et al., *Proc. CAPOC-3*, Amsterdam, 1994, V. 1, p.255.
25. W.Grunert, N.W.Hayes, R.W.Joyner et.al., *J.Phys. Chem.*, 98 (1994) 10832.
26. K.C.C.Kharas, H.J.Robota, D.J. Liu, *Appl. Catal. B: Environ.*, 2 (1993) 225.
27. K.Suzuki, T.Sano, H.Shoji, T.Murakami, *Chem. Lett.*, (1987) 1507.
28. S.Matsumoto, K.Yokata, H.DoI et al., *Catal. Today*, 22 (1994) 127.
29. E.S.Shpiro, W.Gruner, R.W.Joyner, G.N. Baeva, *Catal. Lett.*, 24 (1994) 159.
30. Z.R.Ismagilov, R.A.Shkrabina, N.A.Koryabkina, *Catal. Today*, 47 (1999) 51.
31. V.R.Grinwald. *Production of Gas Sulfur*, Khimiya, Moskva 1992.
32. H.Hamada, Y.Kintaichi, M.Tabata et. al., *Chem. Lett.*, (1991) 2179.

**FUEL COMBUSTION IN THE FLUIDIZED BED OF AN INERT MATERIAL
EQUIPPED WITH AN UNMOVABLE CATALYTIC SMALL-VOLUME PACKAGE****N.A. Yazykov, A.D. Simonov, T.I. Mishenko, A.S. Aflyatunov, C.V. Smolin, V.N. Parmon**

*Boreshkov Institute of Catalysis SB RAS, Novosibirsk 630090, Russian Federation
Fax: +7(383-2) 34-32-69, e-mail: A.D. Simonov@catalysis.nsk.su*

Abstract

The capability of combustion of solid fuels (such as the brown coal of the Kansk-Achinsk coal deposit) in the fluidized bed of an inert material in the presence of unmovable catalytic packages is investigated. This arrangement of the catalytic process is shown to allow the achievement of the same parameters of the fuel burn-off and the content of toxic substances in the flue gas as in the case of fuel combustion in the fluidized bed of catalyst grains. The new arrangement of catalytic processes can be recommended for the accomplishing of some other exothermic catalytic reactions which require the maintenance of isothermal conditions.

Introduction

Today, the use of fluidized bed of catalyst to conduct some exothermic catalytic reactions is a common approach of chemical industry [1,2]. An important advantage of such arrangement of catalytic processes is the possibility to maintain their isothermity, and as result, there is possibility to eliminate heat directly from the bed at the maintenance of the predetermined temperature.

One of directions of the use of fluidized bed of catalyst is the low-temperature combustion of fuels [3,4]. Indeed, the presence of a catalyst allows to decrease the temperature of the organic fuels combustion from 1000-1200°C (the temperature of a torch combustion) to 300-700°C, with high rates of the fuel combustion being saved and the complete fuel combustion being provided without excess of air. In comparison with known conventional ways, fuel combustion in the fluidized bed of catalyst allows: to reduce the requirements to thermochemical stability of constructional materials of the combustion apparatus and to diminish their erosive wear; to reduce losses of heat through the walls of the apparatus; to reduce the explosion risk of the combustion devices; to achieve high (up to $5 \cdot 10^8$ kJ/m³hr) values of the calorific intensity of the furnace volume and, therefore, to reduce considerably the overall sizes, weight and power-to-weight ratio of the combustion devices; to eliminate the secondary endothermic reactions which are accompanied by producing the toxic products. On the base of the fuel combustion in the fluidized bed of catalyst, a set of apparatuses for heating and evaporation of liquids, drying and heat treatment of solid materials, neutralization of industrial gaseous, liquid and solid emissions as well as for number of other processes [5-9] were created.

At the same time the fluidized bed of catalyst has two essential disadvantages.

(1) The attrition of the catalyst achieves 0.3-0.5 wt.% per day, that requires a permanent additional loading of the catalyst in the reactor during its operation. Under condition of the catalyst high selling value (up to \$15,000 per ton), there are certain financial difficulties during the operation of existing plants as well as at the creation of new installations.

(2) The fluidized bed is usually characterized by the presence of gas bubbles, within those the running of the fuel burning process via the conventional flame mechanism is possible, that leads to the formation of toxic compounds (CO, NO_x, SO₂, etc.). To exclude the phenomenon of the bubbles formation, it is needed to regulate the fluidized bed with a small volume package which is able to break the gas bubbles. But the package presence results in an increase of the catalyst attrition.

Previously we have shown [10], that the both disadvantages can be avoided with the use of the fluidized bed of an inert material (for example, sand) regulated with an unmovable small volume catalytic package. The rings from the pressed nickel-chrome wire or blocks from the metal-ceramic plate were used as the packages in these experiments. Catalytic active components (palladium, copper chromite, and other) were deposited on the packages.

However, the technology of the manufacturing the indicated above packages is indeed rather laborious. In addition, the increase of the surface of the catalytic packages requires precoating the packages with a porous carrier.

In the present work, the possibility of an application of the unmovable catalytic packages on the base of the shaped porous alumina with the developed specific surface to carry out the solid fuel combustion in the fluidized bed of inert material is considered.

Methods

The study of the solid fuel combustion in the fluidized bed of an inert material with catalytic packages was conducted with the laboratory installation, the scheme of which is shown in Fig. 1. A stainless steel reactor (1) had 40 mm in diameter, 1000 mm in height and 1260 cm³ in volume. The bottom of the reactor was provided with a gas-distribution grid (2) made as a stainless steel plate with thickness 1.5 mm and holes of 0.5 mm. The upper part of the reactor was provided with a water heat exchanger (3) for cooling the powder-gas mixture.

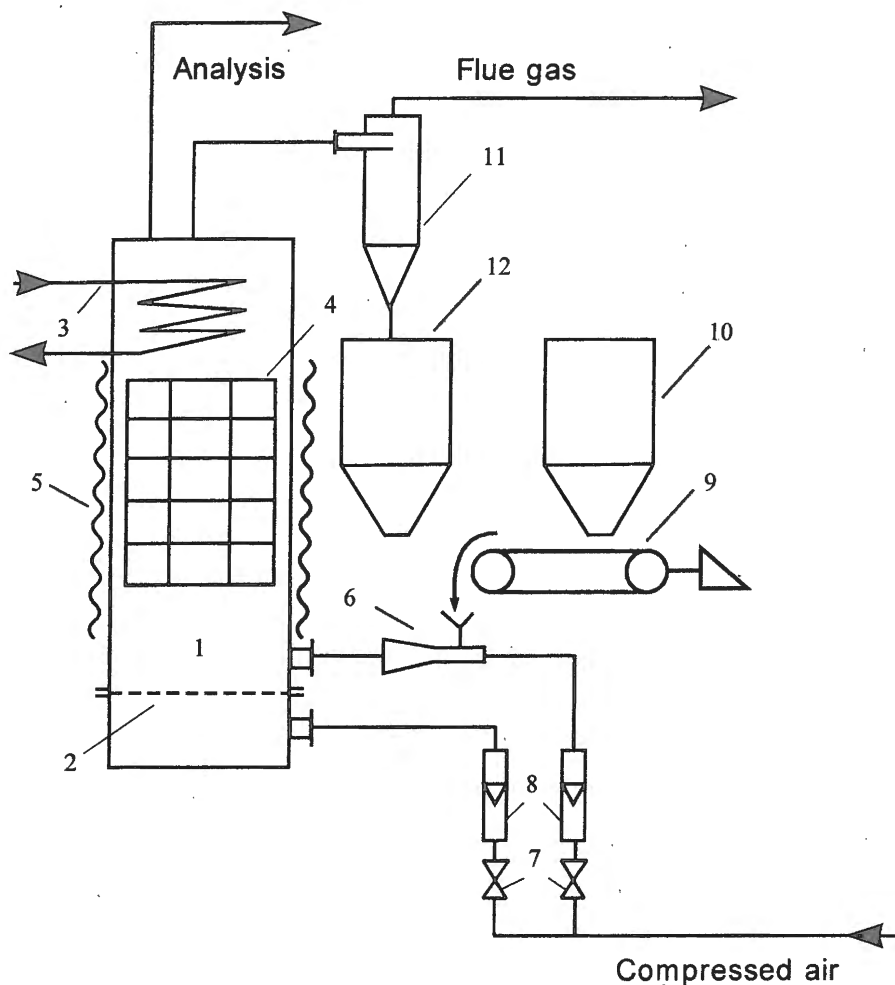


Fig. 1. A scheme of the laboratory set up for testing the unmovable catalytic packages at the solid fuel combustion in the fluidized bed of an inert material:

1 - reactor; 2 - gas-distribution grid; 3 - water heat-exchanger; 4 - unmovable catalytic package; 5 - electric heater; 6 - ejector; 7 - rotameters; 8 - valves; 9 - transporter-feeder; 10 - bunker for solid fuel; 11 - cyclon; 12 - bunker for ash.

The procedure of the experiments was the following. A catalytic package (4) with overall height 850 mm was placed in the reactor (1), and then an inert material (a river sand) with the particles size of 0.63-1.25 mm in quantity 0-400 cm³ is loaded. The bed of this inert material in the fixed state is heated up to the operating temperature with an external electric heater (5). The temperature control in the reactor is carried out with thermocouples. Then, the necessary air supply to an ejector (6) and to the bottom of the reactor under the gas-distribution grid (2) is fixed with the use of valves (7) equipped with rotameters (8). The total air supply to the reactor makes up 3.5 m³/hr. After supplying the air in the reactor and fluidizing the sand bed, the mover of a transporter-feeder (9) is turned on to doze a solid fuel. The fuel supply to the reactor is regulated by the size of a gap between bunker (10) and the transport tape and makes up 105 g/hr. The powder-gas mixture formed in the reactor goes to a cyclone (11), where the ash particles are separated from the gas. Then, the ash particles are transported to a bunker (12).

Chromatograph LCM-80 (USSR) and a Quintox (Kane International Ltd.) equipment were used for the flue gas analysis.

A brown coal of the Kansk-Achinsk deposit with wetness of 13.0%, ash content of 29.0% and the particles size less than 0.2 mm was used as the solid fuel.

The burn-off, β , of the coal was determined with the data on the ash content in the solid products as:

$$\beta(\%) = 10000 (A_t - A_o) / (A_t (100 - A_o)),$$

where A_o is the initial ash content in the coal, %; A_t is the ash content in the solid products after the coal combustion, %.

Porous ceramic rings of 18-20 mm in height, 10-11 mm in internal diameter, 18-20 mm in external diameter were used as elements for the preparation of the packages. The rings were prepared by the extrusion of a mixture of plasticized aluminium hydrate and powder-like alumina with the following drying and calcination at 600°C. The specific surface area of the rings was 150 m²/g. The rings were impregnated by the 30% copper bichromate solution. The solution amount for the impregnation was corresponded to the pore volume of the rings. Then the rings were dried at 120°C during four hours and calcinated at 700°C during two hours. Two types of packages (*A* and *B*) both 850 mm in the overall height with a different disposition of the rings were produced (Fig. 2). In package *B*, the distance between the layers composed of three rings was equal to the height of one ring. In package *A*, one additional catalytic ring was placed between such layers of the rings. The volume part of package *B* in the reactor made up 22.0%, while the volume part of package *A* in the reactor made up 28.0%.

A commercial catalyst IC-12-73, produced by AO "catalizator" (Novosibirsk) and consisting of aluminium, copper, magnesium and chromium oxides, with the particles 2 mm in diameter was used for providing some comparative experiments with the fluidized bed of catalyst. In this case, the fluidized bed of the catalyst was regulated with a small volume package made of a stainless steel with sells 15x15x15 mm in size.



Fig. 2. The tested arrangement of the unmovable catalytic packages on the base of the Raschig rings.

PP-41

Results and discussion

It is well known [11], that in the cylindric reactors of a small diameter, particles fluidization occurs in a plug mode. In this connection, the effect of the discussed catalytic packages on the character of the fluidization of sand with the particles size of 0.63-1.25 mm was studied preliminary with a "cold" model of the reactor. This model reactor has shape of a glass tube of 40 mm in diameter, the range of the air flow velocity varied from 0.88 m/s to 3.3 m/s. The bottom of the glass tube was provided with the same gas-distribution grid as the experimental reactor for the coal combustion. The packages were placed above the gas-distribution grid of the glass tube, and the distance between the bottom of the packages and the gas-distribution grid made up 100 mm. It turned out, that in the presence of catalytic packages *A* or *B*, the character of the sand fluidization along the packages becomes uniform. That provides an intensive circulation of the sand particles between the bottom and upper part of the bed. The plug mode of the sand fluidization is observed only under the packages at the bottom of the bed, which is used for the mixing of the sand and solid fuel particles. The plug mode of the sand fluidization disappears at placing, in the bottom of the reactor, of a small volume metal regulating package with sells 15x15x15 mm in size. Such arrangement of the catalytic and regulating packages was used in the stainless still reactor too for conducting the coal combustion in the fluidized bed of the sand.

The combustion of the brown coal in the fluidized bed of the sand in the presence of the catalytic packages and comparative experiments with the fluidized bed of catalyst IC-12-73 were conducted at the air supply 3.5 m³/hr and the bed temperature 700-800°C. In these conditions, the operating velocity of the gas flow makes up 2.8-3.0 m/s. At the same time, the coal particles with the size less then 0.2 mm pass through the fluidized sand bed as well as the catalyst bed in the regime of the pneumatic transport.

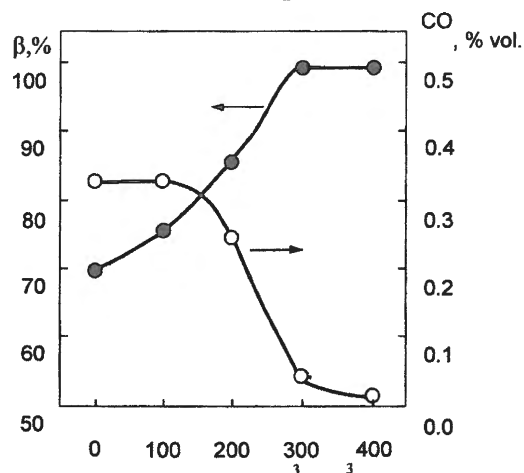


Fig. 3. Dependence of the brown coal burn-off (β), and CO concentration in the flue gas at the brown coal combustion in the fluidized bed of the river sand in the presence of unmovable catalytic package *B* at 750°C on the load of the sand.

Fig. 3 shows the influence of the sand quantity loaded in the reactor on both the burn-off of the brown coal and the CO concentration in the flue gas at the coal combustion temperature 750°C in the presence of package *B*. It is obvious, that in the absence of the sand, the burn-off of the brown coal achieves only 70.4%, and the CO concentration makes up 0.32% vol. Gradual increasing of the sand load leads to an essential increase in the burn-off of the brown coal particles and decrease in the CO concentration in the flue gas. The maximal burn-off of the brown coal at the predetermined temperature was reached at the sand load 300 cm³; accordingly, the CO concentration falls to 0.03% vol. At the further increasing of the sand load from 300 cm³ up to 400 cm³, the burn-off of coal practically does not change, however, the CO concentration in the flue gas falls from 0.03% vol. to 0.01% vol. The amount of the loaded sand influences also the temperature regime of the coal combustion. For example, at the combustion of the brown coal with package *B* in the absence of the sand, the temperature of the bottom of the reactor (under the package) makes up 550-600°C, while in the upper part of the reactor the temperature makes up 750°C. The temperature gradient between the bottom and upper part of the reactor keeps the same value, when 100 cm³ of the sand is loaded in the reactor. The equilibration of temperatures in the bottom and upper part of the reactor occurs only at increasing the sand load from 100 cm³ to 400 cm³; in this situation the unmovable catalytic package *B* completely locates completely inside the fluidized bed of the sand.

Thus, the combustion of dusted brown coal in the mixture with air in the presence of catalytic package *B* without a load of sand does not provide the required coal burn-off, and the flue gas contains a significant amount of CO. At the same time, the gradient of temperatures along the reactor achieves 200°C. A high burn-off of the brown coal under isothermal conditions is achieved when the catalytic package locates completely inside the fluidized bed of sand.

The data on the influence of temperature on the burn-off of the brown coal and the CO concentration in the flue gas at the coal combustion in the presence of unmovable catalytic package *B* with the sand load 400 cm³ are listed in Table 1. It is evident, that with rising the temperature from 700°C to 800°C, the burn-off of the coal increases from 89.8% to 97.6%. While the CO concentration in the flue gas decreases from 0.06% vol. to less than 0.01% vol. It should be stressed, that at the temperature interval from 750°C to 800°C the change of the brown coal burn-off is negligible the same as the change of the CO concentration in the flue gas.

PP-41

Table 1. Influence of temperature in the reactor on the burn-off of the brown coal in the fluidized bed of the sand with catalytic package *B* (the load of the sand particles is 400 cm³)

Temperature, °C	CO concentration % vol.	Coal burn-off β , %
700	0.06	89.8
750	0.01	93.7
800	< 0.01	96.6

Table 2. Comparison of the brown coal burn-off at its combustion in the fluidized bed of the sand in the presence of different unmovable catalytic packages and in the regulated fluidized bed of catalyst IC-12-73, the temperature in all cases is 750°C

Catalyst	CO concentration, % vol.	Coal burn-off β , %
Package <i>B</i> and 400 cm ³ of the sand	0.01	93.7
Package <i>A</i> and 400 cm ³ of the sand	< 0.01	98.0
400 cm ³ of IC-12-73	< 0.01	97.6

The use of unmovable catalytic package *A* allows to achieve a higher, in comparison with the package *B*, burn-off of the brown coal (98.0%) already at 750°C. And the CO concentration in the flue gas also makes up less than 0.01% vol. (Table 2). The experimental data on the brown coal combustion in the regulated fluidized bed of catalyst IC-12-73 are listed also in Table 2. One can see, that locating the unmovable catalytic package of type *A* in the fluidized bed of the sand allows to achieve the same parameters of the brown coal combustion as at the use of the fluidized bed of the catalyst. This is confirmed also by close values of the concentrations of toxic compounds in the flue gas in both cases (Table 3).

Thus, unmovable catalytic package *A* appears to be more efficient, in comparison with package *B*, for the combustion of the dusted brown coal in the fluidized bed of the sand. Furthermore, the combustion of the dusted brown coal in the fluidized bed of the sand in the presence of unmovable catalytic package *A* provides the same burn-off of the coal as well as low concentrations of toxic compounds in the flue gas as at the combustion of this coal in the fluidized bed of the catalyst.

Today, the selling price of spherical catalyst IC-12-73 makes up \$15,000 per ton. The selling price of catalytically active Raschig rings, from which the catalytic package can be produced, makes up \$7,000 per ton. A commercial catalytic heat supply unit (CHSU) with useful heat power 1 Gcal/hr needs 1 ton of catalyst IC-12-73 for loading the reactor. The necessary quantity of the Raschig rings for CHSU with the same power would make up 0.3 ton. A warranty assurance of catalyst IC-12-73 equals to 6 months of the continuous operation; accordingly, the annual operating cost of the catalyst will make up \$30,000. If the life time of the unmovable catalytic package equals even to 1 year (the expected life time is 3 years), the annual operating cost of the catalyst like the above Raschig rings would be equal only to \$2,100.

Table 3. Concentration of harmful substances in the flue gas at the brown coal combustion in the fluidized bed of the sand with catalytic package A and in the fluidized bed of catalyst IC-12-73 at 750°C (the data are obtained with the Quintox device)

Catalyst	Concentration in the flue gas, ppm			
	NO	NO ₂	SO ₂	CO
IC -12-73	76	1	16	41
Package A	92	1	23	70

Conclusion

Catalytic combustion of solid fuels in the fluidized bed of inert material in the presence of an unmovable catalytic package allows to achieve the same parameters of the process as in the case of the fuel combustion in the regulated uniform fluidized bed of catalyst. At the same time, in the second case, the operating cost of the catalyst is reduced more than by the factor of 10. The suggested arrangement of catalytic processes can be recommended for accomplishing also some other exothermic catalytic reactions which require the maintenance of isothermal conditions.

Literature

1. D. Kunii, O. Levenshpil, Industrial Fluidization, Khimiya: Moscow, 1976 (in Russian).
2. I.P. Muhlyonov, V.N. Anohin, V.A. Proskuryakov, etc., Catalysis in Fluidized Bed, Khimiya: Leningrad, 1978 (in Russian).
3. G. K. Boreskov, Heterogeneous Catalysis, Nauka: Moscow, 1986 (in Russian).
4. Russian Patent 826,798 (1983).
5. V.N. Parmon, Z.R. Ismagilov, V.A. Kirillov, A.D. Simonov, Works of the Sixth Session of International School of Improvement of Professional Skill of the Experts in the field of Engineering Chemistry, 2 (2001) 50-72.
6. A.D. Siminov, N.A. Yazykov, P.I. Vedyakin, G.A. Lavrov, V.N. Parmon, Chemistry for Sustainable Development, 9 (2001) 97-104 (in Russian).
7. A.D. Siminov, N.A. Yazykov, P.I. Vedyakin, G.A. Lavrov, V.N. Parmon, Catalysis Today, 60 (2000) 139-145.
8. A.D. Simonov, Chemistry for Sustainable Development, 6 (1998) 277-292 (in Russian).
9. A.D. Simonov, N.A. Yazykov, Khimicheskaya Promyshlennost', 3 (1996) 47 (in Russian).
10. Russian Patent 2,064,831 (1997).
11. D. Eys, Fundamentals of Fluidized-Bed Chemical Processes, Butterworths: London, 1983.

NEW APPROACHES TO SYNTHESIS OF LOW TEMPERATURE CATALYSTS FOR METHANE DEEP OXIDATION

G.R.Kosmambetova, M.R.Kantserova, K.S.Gavrylenko, S.M.Orlyk, V.L.Struzhko

Pisarzhevsky Institute of Physical Chemistry of the NAS of Ukraine,

31, Pr.Nauki, Kyiv, 03039, Ukraine

e-mail: orlyk@ukrtel.com

A need for efficient use of carbon fuel is challenging more rigid requirements to catalysts for fuel deep oxidation in heat generators and combustion chambers. New generation's catalysts have to provide 100% conversion of methane into CO₂ at temperatures below 500°C with exhibiting high operation characteristics.

In order to obtain low-temperature catalysts for methane deep oxidation, a series of different type Mn-, Co- and Cr-containing catalysts has been synthesized, i.e. aluminoxide catalysts modified by rare-earth and alkaline-earth elements, including Pd-promoted samples; zirconium-containing oxides and binary systems of Me_xO_y/ZrO₂, Me_xO_y/(ZrO₂ – zeolite), Me_xO_y/(ZrO₂ + Al₂O₃), including those promoted by Rh and Pd; nano-sized ferrites with Me^{II}Fe^{III}₂O₄(Me-Mn, Co, Ni) spinel structure.

Applying the up-to-date techniques such as a method of support impregnation under non-equilibrium conditions, sol-gel method, a thermal decomposition method of hetero-metal organic complexes of transition metals allowed to get the best out of these catalytic systems potential. Testing the prepared catalysts in the reaction of 1 % methane-in-air deep oxidation with 0,6 sec. contacting time shows that the synthesized samples provide 80-100% conversion of methane at temperatures of 400-450°C. That is by 50-100°C lower compared to catalysts prepared by using conventional techniques of support impregnation and oxides stoichiometric mixture sintering .

The physico-chemical properties of the prepared catalysts were studied using by X-ray diffraction analysis and X-ray photo electron spectroscopy.

**DIRECT METHANE OXIDATIVE CARBONYLATION INTO ACETIC ACID ON
SUPPORTED RHODIUM CATALYSTS IN GAS PHASE**

**G.R. Kosmambetova¹, M.V. Pavlenko¹, V.I. Grytsenko¹,
I.N. Stepanenko², L.B. Kharkova², V.I. Pekhnio²**

¹*L.V.Pisarzhevsky Institute of Physical Chemistry of the NAS of Ukraine*

31, Pr.Nauki, Kyiv, 03039, Ukraine, e-mail: kosmambetova@yahoo.co.uk

²*V.I.Vernadsky Institute of General and Inorganic Chemistry of the NAS of Ukraine*

32/34, Pr. Palladina, Kyiv, 03680, Ukraine

Natural gas-based direct one-step processes are the most attractive methods for preparing products and semiproducts of organic synthesis, e.g. obtaining of acetic acid and its derivatives via oxidative carbonylation of methane. This reaction was first carried out in 1993 in liquid phase at 80 atm pressure in the presence of RhCl₃-HCl-H₂ [1] and in gas phase in 1997 using nitrogen monoxide as oxidant on Rh/FePO₄ catalyst [2].

For preparing acetic acid through methane oxidative carbonylation by molecular oxygen in gas phase, a number of rhodium-containing (0.5-2.0% Rh) catalysts (oxides, chlorides, chalcogen chlorides) on carriers of different types (SiO₂, Al₂O₃, activated carbon) have been tested. These experiments were conducted at atmospheric pressure by widely varying CH₄:CO:O₂ gas mixture (from stoichiometric to reducing one, containing 7% oxidant) and space velocity 50000-180000 h⁻¹. It was found that in the case of the catalysts prepared through impregnation by rhodium chloride, irrespective of the reaction conditions and support type, the main reactions products were carbon oxides (CO and CO₂) formed both directly from CO and CH₄ and as a result of further oxidation of partial oxidation products, formed on polynuclear particles of rhodium oxide. The catalysts containing rhodium chalcogen chlorides on support have been prepared by mixing mechanically activated mixtures of thermally stable compounds (Rh₄Cl₃Se₅, Rh₄Cl₂SeS₃, Rh₄Cl₇S), synthesized for the first time, and silica gel followed by treatment in air at 500°C. It has been shown that it is possible in principle to synthesize acetic acid directly from methane on applied rhodium chalcogen chlorides.

1. M.Lin, A.Sen, *Nature*, 1994, v.368, 613
2. Y.Wang, M.Katagari, K.Otsuka. *Chemical Communications*, 1997, 1187

KINETIC OSCILLATIONS IN CO OXIDATION OVER PLATINUM CATALYSTS: MONTE CARLO SIMULATIONS

E. S. Kurkina, N. L. Semendyaeva

Faculty of Computational Mathematics and Cybernetics, Moscow State University, Moscow, 19899, Russia; E-mail: NatalyS@cs.msu.su

Investigations of the origin and the detailed driving mechanism for oscillations of the rate of CO+O₂ reaction over platinum catalyts have been carried out. A well-known model using an alternate slow oxidation and CO reduction of the metal surface (TSM mechanism) has been used. Two mathematical models of different spatial scales have been developed: the imitation model using dynamic Monte Carlo type algorithms with correct time dependence and the deterministic model using the ideal adsorbed layer approximation.

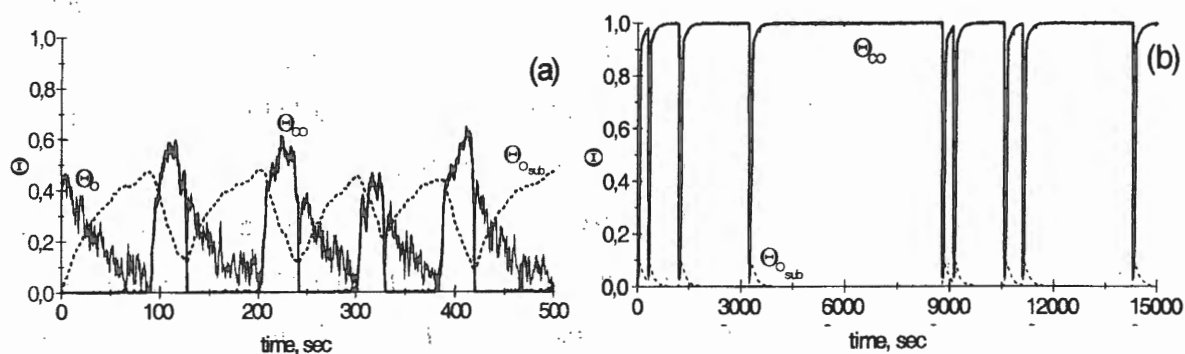


Fig. 1. The coverages of CO, O and O_{sub} as functions of time; MC data. The deterministic model under the same conditions has one stable stationary state in the case (a) or two stable stationary states (b)

Both models are based on the same kinetic scheme. Nevertheless they describe the qualitatively different behavior of the CO+O₂ reaction. While the deterministic model has one steady state or multiple steady states and displays hysteresis, the imitation model demonstrates oscillations in the rate of the CO+O₂ reaction and concentrations of adsorbed particles in the wide range of CO pressure under the same conditions (the realistic values for the kinetic rate constants, temperatures and partial pressures in the gas phase).

The detailed qualitative analysis of the results of simulations removes all contradictions and shows that the kinetic oscillations predicted by MC technique depend on spatial fluctuations in adsorbate concentrations and the excitable dynamics of the models.

This research was supported by the Russian Foundation of for Basic Research (Grant № 00-01-000587).

**TUNING OF THE ELECTRONIC STATE OF THE SUPPORTED METAL BY
VARYING ACID-BASE PROPERTIES OF Al₂O₃**

**A.Yu. Stakheev, G.N. Baeva, A.V. Ivanov, N.S. Telegina, D.C. Koningsberger*,
B.L. Mojet*, L.M. Kustov**

*119991, Zelinsky Institute of Organic Chemistry, Leninsky Pr., 47, Moscow, Russia
*3584 CA, Department of Inorganic Chemistry and Catalysis, Utrecht University,
Sorbonnelaan 16, Utrecht, Netherlands*

It is well known that the catalytic properties of supported metal clusters are dramatically affected by their electronic state (electron-deficient vs electron-rich), which, in turn, is a function of the support acid-base properties. The main focuses of this study were: 1) the development of a flexible method for variation of acid-base properties of alumina; 2) a systematic study of the effect of Al₂O₃ acid-base properties on the electronic state of supported Pt and Pd clusters.

Acid-base properties of the support were tuned using the sol-gel method for Al₂O₃ preparation. Different basic (K, Rb, Cs) and acidic (F, W, Si) additives were introduced in the alumina sol followed by alumina gel formation, drying, and calcination. XPS data indicate that additives are uniformly distributed, without pronounced enrichment/depletion of the surface layer. The specific surface area of the resulted materials was measured by low-temperature N₂ adsorption. Acidic properties were evaluated by FTIR spectroscopy of adsorbed CO and from the spectra in the OH-group region. Basic properties were evaluated by FTIR spectroscopy of adsorbed C₂H₂ and CH₃CN. It was found that the use of sol-gel method allows systematic variation of Al₂O₃ acid-base properties. The resulted samples can be ranked according to their acidity:

Si-Al₂O₃ > W-Al₂O₃ > F-Al₂O₃ > Cl-Al₂O₃ ≈ Al₂O₃ >> K-Al₂O₃ > Rb-Al₂O₃ > Cs-Al₂O₃

The series of aluminas thus prepared was used as supports for preparation of Pt/Al₂O₃ and Pd/Al₂O₃ catalysts. The Pt particle size in selected samples was calculated on the basis of EXAFS data. It was found that the Pt cluster size is within the range of 15-20 atoms.

The electronic state of Pt and Pd clusters was evaluated by FTIR spectroscopy of adsorbed CO and XPS, respectively. The electronic state was determined from the position of the XPS line, the shift of the stretching vibration frequency of adsorbed CO, and variation of the linealy/bridged adsorbed CO ratio.

It was found that the electronic state of both metals is a function of the support acidity-basicity. An increase in the support acidity results in the corresponding increase in the metal clusters electron deficiency. On the contrary, a systematic increase in the support basicity leads to a gradual increase of the negative charge on the metal particles.

List of participants

Igor E. Abroskin

Novosibirsk Plant of Chemical Concentrates

B. Khmel'nitskii str., 94
630110 Novosibirsk

Russia

Tel.: +7 383 2 74 84 75

Fax: +7 383 2 76 33 02

E-mail: abroskin@online.sinor.ru

Vladimir N. Antsifirov

Republican Engineering Center "Powder Metallurgy"

Politehnicheskii proezd, 6
614000 Perm

Russia

Tel.: +7 342 2 39 11 19

Fax: +7 342 2 39 11 22

E-mail: patent@pm.pstu.ac.ru

Igor V. Babich

Twente University

Faculty of Chemical Engineering
Postbus 217

7500 AE Enschede

The Netherlands

Tel.: +31 53 489 3536

Fax: +31-53 489 4683

E-mail: i.v.babych@ct.utwente.nl

Johannes H. Bitter

Utrecht University

Department of Inorganic
Chemistry and Catalysis

Sorbonnelaan 16

3584 CA Utrecht

The Netherlands

Tel.: +31 30 253 7400

Fax: +31 30 251 1027

E-mail: J.H.Bitter@chem.uu.nl

Vladimir I. Bogdanov

Ekaterinburg Non Ferrous Metals
Processing Plant

Lenin ave., 8

620014 Ekaterinburg

Russia

Tel.: +7 343 2 56 85 84

Fax: +7 343 2 56 85 96

E-mail: ocm@mail.ur.ru

Hans Bouma

NIOK, Utrecht University

Organische Synthese, Padualaan, 8
3584 CH Utrecht

The Netherlands

Tel.: +31 30 253 9445

Fax: +31 30 253 4019

E-mail: h.bouma@chem.uu.nl

Konstantin P. Bryliakov

Boreskov Institute of Catalysis SB RAS
pr. Akademika Lavrentieva, 5
630090 Novosibirsk

Russia

Tel.: +7 383 2 34 18 77

Fax: +7 383 2 34 37 66

E-mail: bryliako@catalysis.nsk.su

Tatyana N. Burdeynaya

Topchiev Institute of Petrochemical
Synthesis RAS

Leninskii pr., 29

119991 Moscow

Russia

Tel.: 095 955 4271

Fax: 095 230 2224

E-mail: Tretjak@ips.ac.ru

Alexander R. Cholach

Boreskov Institute of Catalysis SB RAS
pr. Akademika Lavrentieva, 5

630090 Novosibirsk

Russia

Fax: +7 3832 34 37 66

E-mail: cholach@catalysis.nsk.su

Hessel L. Castricum

University of Amsterdam

Chemical Engineering Department

Nieuwe Achtergrach, 166

1018 WV Amsterdam

The Netherlands

Tel.: +31 20 525 6493

Fax: +31 20 525 5788

E-mail: castric@science.uva.nl

Gennadii A. Chumakov

Sobolev Institute of Mathematics SB RAS

pr. Akademika Koptyuga, 4

630090 Novosibirsk

Russia

Tel.: +7 383 2 33 38 87

Fax: +7 383 2 33 25 98

E-mail: chumakov@math.nsc.ru

Menno Crajé

Delft University of Technology

Mekelweg, 15

2629 JB Delft

The Netherlands

Tel.: +31 15 278 4597

Fax: +31 15 278 8303

E-mail: m.w.j.craje@iri.tudelft.nl

Arthur de Jong
Eindhoven University of Technology
Department of Physics
PO Box 513
5600 MB Eindhoven
The Netherlands
Tel.: +31 40 247 4051
Fax: +31 40 243 8060
E-mail: a.m.de.jong@tue.nl

Konstantin A. Dubkov
Boreskov Institute of Catalysis SB RAS
pr. Akademika Lavrentieva, 5
630090 Novosibirsk
Russia
Tel.: +7 383 2 34 46 07
Fax: +7 383 2 34 30 56
E-mail: dubkov@catalysis.nsk.su

Vladimir I. Elokhin
Boreskov Institute of Catalysis SB RAS
pr. Akademika Lavrentieva, 5
630090 Novosibirsk
Russia
Tel.: +7 383 2 34 47 70
Fax: +7 383 2 34 30 56
E-mail: elokhin@catalysis.nsk.su

Stanislav I. Fadeev
Sobolev Institute of Mathematics SB RAS
pr. Akademika Koptyuga, 4
630090 Novosibirsk
Russia
Tel.: +7 383 2 33 33 87
Fax: +7 383 2 33 25 98
E-mail: fadeev@math.nsc.ru

Vladimir V. Galvita
Boreskov Institute of Catalysis SB RAS
pr. Akademika Lavrentieva, 5
630090 Novosibirsk
Russia
Tel.: +7 383 2 34 47 89
Fax: +7 383 2 34 30 56
E-mail: galvita@catalysis.nsk.su

Vladimir V. Gorodetskii
Boreskov Institute of Catalysis SB RAS
pr. Akademika Lavrentieva, 5
630090 Novosibirsk
Russia
Tel.: +7 383 2 39 73 15
Fax: +7 383 2 34 30 56
E-mail: gorodetsk@catalysis.nsk.su

Natalia E. Goryainova
Korolev Samara State Aerospace
University, Chemistry Department
Moskovskoe shosse, 34
443086 Samara
Russia
Tel.: +7 846 2 35 71 64
Fax: +7 846 2 34 87 56
E-mail: chem@ssau.ru

Emiel J.M. Hensen
Eindhoven University of Technology
Department of Chemical Engineering
PO Box 513
5600 MB Eindhoven
The Netherlands
Tel.: +31 40 247 2304
Fax: +31 40 245 5054
E-mail: e.j.m.hensen@tue.nl

Kazimira G. Ione
Scientific Engineering Center "Zeosit"
SB RAS
pr. Akademika Lavrentieva, 5
630090 Novosibirsk,
Russia
Tel.: 383 2 30 05 96
Fax: 383 2 39 62 51
E-mail: zeosit@batman.sm.nsc.ru

Ilias Z. Ismagilov
Boreskov Institute of Catalysis SB RAS
pr. Akademika Lavrentieva, 5
630090 Novosibirsk
Russia
Tel.: +7 383 2 34 26 70
Fax: +7 383 2 39 73 52
E-mail: iismagil@catalysis.nsk.su

Zinfer R. Ismagilov
Boreskov Institute of Catalysis SB RAS
pr. Akad. Lavrentieva, 5
630090 Novosibirsk
Russia
Tel.: +7 383 2 34 12 19
Fax: +7 383 2 39 73 52
E-mail: zri@catalysis.nsk.su

Lyubov A. Isupova
Boreskov Institute of Catalysis SB RAS
pr. Akad. Lavrentieva, 5
630090 Novosibirsk
Russia
Tel.: +7 383 2 34 37 63
Fax: +7 383 2 34 30 56
E-mail: isupova@catalysis.nsk.su

Sergey S. Ivanchev
St. Petersburg Department of the
Boreskov Institute of Catalysis SB RAS
pr. Dobrolubova, 14
197198 St. Petersburg
Russia
Tel.: +7 812 238 0890
Fax: +7 812 233 0002
E-mail: ivanchev@SM2270.spb.edu

Dmitri P. Ivanov
Boreskov Institute of Catalysis SB RAS
pr. Akad. Lavrentieva, 5
630090 Novosibirsk
Russia
Tel.: +7 383 2 34 46 07
Fax: +7 383 2 34 30 56
E-mail: divan@catalysis.nsk.su

Elena A. Ivanova
Institute of Chemistry and Chemical
Technology
K. Marx str., 42
660049 Krasnoyarsk
Russia
Tel.: +7 391 2 23 93 19
Fax: +7 391 2 23 86 58
E-mail: ei@krsk.infotel.ru

Amina Jumabaeva
Al-Farabi Kazakh State National University
Karasai batira, 95a
Almaty
Kazakhstan
Tel.: +7 327 2 92 70 26 ext 21 28
E-mail: olga@lorton.com

Vladimir B. Kazanskii
Zelinskii Institute of Organic
Chemistry RAS
Leninskii pr., 47
117913 Moscow
Russia
Tel.: +7 095 137 7400
Fax: +7 095 135 5328
E-mail: vbk@ioc.ac.ru

Mikhail A. Kerzhentsev
Boreskov Institute of Catalysis SB RAS
pr. Akad. Lavrentieva, 5
630090 Novosibirsk
Russia
Tel.: +7 383 2 34 21 54
Fax: +7 383 2 39 73 52
E-mail: ma_k@catalysis.nsk.su

Sergei R. Khairulin
Boreskov Institute of Catalysis SB RAS
pr. Akad. Lavrentieva, 5
630090 Novosibirsk
Russia
Tel.: +7 383 2 34 26 70
Fax: +7 383 2 39 73 52
E-mail: sergk@catalysis.nsk.su

Adrianus C. Kolen
Eindhoven University of Technology
Department of Chemical Engineering
PO Box 513
5600 MB Eindhoven
The Netherlands
Tel.: +31 40 247 5363
Fax: +31 40 245 5054
E-mail: a.kolen@tue.nl

Bert Koning
Twente University
Faculty of Chemical Technology
Postbus 217
7500 AE Enschede
The Netherlands
Tel.: +31 53 431 5057
Fax: +31 53 489 4738
E-mail: gwkoning@hetnet.nl

Diederik C. Koningsberger
Utrecht University
Department of Inorganic
Chemistry and Catalysis
Sorbonnelaan, 16
3584 CA Utrecht
The Netherlands
Tel.: +31 30 253 7400
Fax: +31 30 251 1027
E-mail: d.c.koningsberger@chem.uu.nl

Alina O. Koriabkina
Eindhoven University of Technology
PO Box 513
5600 MB Eindhoven
The Netherlands
Tel.: +31 40 247 2833
Fax: +31 40 245 5054
E-mail: a.koryabkina@TUE.NL

Gulnara Kosmambetova
Pisarzhevsky Institute of Physical
Chemistry of NAS of Ukraine
pr. Nauki, 31
03039 Kyiv
Ukraine
Tel.: 804 4265 6570
E-mail: kosmambetova@yahoo.co.uk

Galina A. Kovalenko
Boreskov Institute of Catalysis SB RAS
pr. Akademika Lavrentieva, 5
630090 Novosibirsk,
Russia
Tel.: +7 383 2 397359
Fax: +7 383 2 34 30 56
E-mail: galina@catalysis.nsk.su

Elena G. Kovalyova
Institute of Organic Synthesis of the
Ural Branch of RAS
S. Kovalevskoy str., 20
620219 Ekaterinburg
Russia
Tel.: +7 343 2 49 35 38
Fax: +7 343 2 74 11 89
E-mail: gek@mail.ur.ru

Roman A. Kozlovskiy
D. Mendeleev University of Chemical
Technology of Russia
Miuskaya sq., 9
125047 Moscow
Russia
Tel.: +7 095 978 9554
Fax: +7 095 978 9554
E-mail: kra@muctr.edu.ru

Vladimir N. Kruchinin
Boreskov Institute of Catalysis SB RAS
pr. Akademika Lavrentieva, 5
630090 Novosibirsk
Russia
Tel.: +7 383 2 34 26 70
Fax: +7 383 2 39 73 52
E-mail: kruch@catalysis.nsk.su

Lidya V. Krüpenya
Tomsk Polytechnical University
Lenin ave., 30
634034 Tomsk
Russia
Tel.: +7 382 2 41 54 43
Fax: +7 382 2 41 52 35
E-mail: a_crow@mail.ru

Gennady G. Kuvshinov
Boreskov Institute of Catalysis SB RAS
pr. Akademika Lavrentieva, 5
630090 Novosibirsk
Russia
Tel.: +7 383 2 33 16 18
Fax: +7 383 2 34 30 56
E-mail: ggk@catalysis.nsk.su

Vadim V. Kuznetsov
Boreskov Institute of Catalysis SB RAS
pr. Akad. Lavrentieva, 5
630090 Novosibirsk
Russia
Tel.: +7 383 2 34 16 81
Fax: +7 383 2 39 73 52
E-mail: vadimk@catalysis.nsk.su

Svetlana A. Kuznetsova
Institute of Chemistry and Chemical
Technology SB RAS
Akademgorodok
660036 Krasnoyarsk
Russia
Tel.: +7 391 2 49 54 81
E-mail: ksa@krsk.infotel.ru

Alexander A. Lamberov
Kazan State Technological University
K. Marks str., 68
420015 Kazan
Russia
Tel.: +7 843 2 72 03 24
Fax: +7 843 2 72 03 24
E-mail: segorova@rambler.ru

Yurii. V. Larichev
Boreskov Institute of Catalysis SB RAS
pr. Akademika Lavrentieva, 5
630090 Novosibirsk
Russia
Tel.: +7 383 2 34 17 71
Fax: +7 383 2 34 30 56
E-mail: vib@catalysis.nsk.su

Alexander V. Lavrenov
Omsk Department of Boreskov
Institute of Catalysis SB RAS
Neftezhavodskaya str., 54
644040 Omsk
Russia
Tel.: +7 381 2 66 43 14
Fax: +7 381 2 64 61 56
E-mail: lavr@incat.okno.ru

Martin Lok
Synetix
P.O.Box 1, Billingham
Cleveland, TS23 1LB
UK
Tel.: +44 1642 52 24 98
Fax: +44 1642 52 26 06
E-mail: lavr@incat.okno.ru

Anna A. Lysova
International Tomography Center SB RAS
Institutskaya str., 3a
630090 Novosibirsk
Russia
Tel.: +7 383 2 33 35 61
Fax: +7 383 2 34 32 69
E-mail: lysova@tomo.nsc.ru

Alexander M. Makarov
Institute of Solid State Chemistry
Ural Branch of Russian Academy of
Science
Genkel str., 4
614600 Perm
Russia
Tel.: +7 342 2 39 66 43
Fax: +7 342 2 33 27 38
E-mail: mak_perm@mail.ru

Alexander A. Makarov
Perm State Technical University
Komsomolsky pr., 29a, PSTU
614600 Perm
Russia
Tel.: +7 342 2 19 80 61
Fax: +7 342 2 19 80 61
E-mail: mak_perm@mail.ru

Michiel Makkee
Delft University of Technology
Faculty of Applied Science
Julianalaan 136
2628 BL Delft
The Netherlands
Tel.: +31 15 278 13 91
Fax: +31 15 278 44 52
E-mail: m.makkee@tnw.tudelft.nl

Gennadii D. Malchikov
Korolev Samara State Aerospace
University
Chemistry Department
Moskovskoe shosse, 34
443086 Samara
Russia
Tel.: +7 846 2 35 18 06
Fax: +7 846 2 34 87 56
E-mail: chem@ssau.ru

Zulhair A. Mansurov
Combustion Problems Institute
Al Farabi Kazakh State National University
Bogenbay Batyr str., 172,
480012 Almaty
Kazakhstan
Tel.: +7 327 2 92 43 46
Fax: +7 327 2 92 58 11
E-mail: mansurov@lorton.com

Ekaterina V. Matus
Boreskov Institute of Catalysis SB RAS
pr. Akad. Lavrentieva, 5
630090 Novosibirsk
Russia
Tel.: +7 383 2 34 26 70
Fax: +7 383 2 39 73 52

Andrey V. Matveev
Boreskov Institute of Catalysis SB RAS
pr. Akad. Lavrentieva, 5
630090 Novosibirsk
Russia
Tel.: +7 383 2 39 73 15
Fax: +7 383 2 34 30 56
E-mail: matveev@catalysis.nsk.su

Nadejda I. Maximova
Fritz Haber Institute
Berlin Faradayweg 4-6
14195 Berlin
Germany
Tel.: +49 30 84134 499
Fax: +49 30 84134 401
E-mail: nadya@fhi.berlin.mpg.de

Yurii V. Medvedev
JSC "Tomskgazprom"
Bolshaya Podgornaya str., 73
634009 Tomsk
Russia
Tel.: +7 382 2 27 55 29
Fax: +7 382 2 72 20 71
E-mail: medvedev@public.tsu.ru

Ilya I. Moiseev
Kurnakov Institute of General and
Inorganic Chemistry
Leninskii pr., 31
117907 Moscow
Russia
Tel.: +7 095 952 12 03
Fax: +7 095 954 12 79
E-mail: iimois@igic.ras.ru

Jacob A. Moulijn
Delft University of Technology
Faculty of Applied Science
Julianalaan 136
2628 BL Delft
The Netherlands
Tel.: +31 0 15 278 50 08
Fax: +32 0 15 278 44 52
E-mail: J.A.Moulijn@tnw.tudelft.nl

Anna V. Natrova
Boreskov Institute of Catalysis SB RAS
pr. Akad. Lavrentieva, 5
630090 Novosibirsk
Russia
Tel.: +7 383 2 34 17 71
Fax: +7 383 2 34 30 56
E-mail: vib@catalysis.nsk.su

Alexander P. Nemudry
Institute of Solid State Chemistry
and Mechanochemistry SB RAS
Kutateladze str., 18
6300128 Novosibirsk
Russia
Tel.: +7 383 2 36 38 32
Fax: +7 383 2 32 28 47
E-mail: nemudry@solid.nsk.su

Bernard E. Nieuwenhuys
Leiden University
Leiden Institute of Chemistry
PO Box 9502
2300 RA Leiden
Netherlands
Tel.: +31 71 527 4545
Fax: +31 71 527 4451
E-mail: b.nieuwe@chem.leidenuniv.nl

Lidiya O. Nindakova
A.E. Favorsky Irkutsk Institute of
Chemistry
1 Favorsky str.,
664033 Irkutsk
Russia
Tel.: 395 2 51 14 25
Fax: 395 2 39 60 46
E-mail: bagrat@irioc.irk.ru

Margarita D. Novikova
JSC "Kirovo-Chepetsk Chemical Plant"
Pozharnyi per., 7
613040 Kirovo-Chepetsk
Russia
Tel.: +7 83 361 947 00
Fax: +7 83 361 942 59

Arian R. Overweg
Delft University of Technology
Interfaculty Reactor Institute
Mekelweg 15
2629 JB Delft
The Netherlands
Tel.: +31 15 278 5545
Fax: +31 15 278 8303
E-mail: a.r.overweg@iri.tudelft.nl

Valentin N. Parmon
Boreskov Institute of Catalysis SB RAS
pr. Akad. Lavrentieva, 5
630090 Novosibirsk
Russia
Tel.: +7 383 2 34 32 69
Fax: +7 383 2 34 32 69
E-mail: parmon@catalysis.nsk.su

Svetlana N. Pavlova
Boreskov Institute of Catalysis SB RAS
pr. Akad. Lavrentieva, 5
630090 Novosibirsk
Russia
Tel.: +7 383 2 34 26 72
Fax: +7 383 2 34 30 56
E-mail: pavlova@catalysis.nsk.su

Oxana P. Pestunova
Boreskov Institute of Catalysis SB RAS
pr. Akad. Lavrentieva, 5
630090 Novosibirsk
Russia
Tel.: +7 383 2 34 25 63
Fax: +7 383 2 34 30 56
E-mail: oxanap@catalysis.nsk.su

Larisa V. Pirutko
Boreskov Institute of Catalysis SB RAS
pr. Akad. Lavrentieva, 5
630090 Novosibirsk
Russia
Tel.: +7 383 2 34 46 07
Fax: +7 383 2 34 30 56
E-mail: pirutko@catalysis.nsk.su

Yuri V. Plyuto
Institute of Surface Chemistry
National Academy of Sciences of Ukraine
General Naumov str., 17
03164 Kyiv
Ukraine
Tel.: +38 044 444 9653
Fax: +38 044 444 3567
E-mail: plyuto@mail.kar.net

Olga Yu. Podyacheva
Boreskov Institute of Catalysis SB RAS
pr. Akad. Lavrentieva, 5
630090 Novosibirsk
Russia
Fax: +7 3832 39 73 52
E-mail: pod@catalysis.nsk.su

Gennadii E. Remnev
JSC "Tomskgazprom"
Bolshaya Podgornaya str., 73
634009 Tomsk
Russia
Tel.: +7 382 2 41 91 58
Fax: +7 382 2 41 91 58
E-mail: remnev@ephc.tomsk.ru

Tatyana V. Reshетенko
Boreskov Institute of Catalysis SB RAS
pr. Akad. Lavrentieva, 5
630090 Novosibirsk
Russia
Tel.: +7 383 2 34 26 70
Fax: +7 383 2 39 73 52
E-mail: t_reshetenko@mail.ru

Olga A. Reutova
Omsk State University
Chemistry Department
pr. Mira, 55 A
644045 Omsk
Russia
Tel.: +7 381 2 64 24 85
Fax: +7 381 2 64 24 10
E-mail: reutova@univer.omsk.su

Raziy G. Romanova
Kazan State Technological University
K. Marks str., 68
420015 Kazan
Russia
Tel.: +7 843 2 19 42 66
Fax: +7 843 2 19 42 66
E-mail: rrg@kstu.ru

Vladislav A. Sadykov
Boreskov Institute of Catalysis SB RAS
pr. Akad. Lavrentieva, 5
630090 Novosibirsk
Russia
Tel.: +7 383 2 34 37 63
Fax: +7 383 2 34 30 56
E-mail: sadykov@catalysis.nsk.su

Alexey A. Saifulin
Tomsk Polytechnical University
Lenin ave., 30
634034 Tomsk
Russia
Tel.: +7 382 2 41 54 43
Fax: +7 382 2 41 52 35
E-mail: a_crow@mail.ru

Alexei N. Salanov
Boreskov Institute of Catalysis SB RAS
pr. Akad. Lavrentieva, 5
630090 Novosibirsk
Russia
Tel.: +7 383 2 34 42 55
Fax: +7 383 2 34 37 66
E-mail: salanov@catalysis.nsk.su

Alma G. Sarmurzina
Al-Farabi Kazakh State National University
Karasai batira, 95a
Almaty
Kazakhstan
Tel.: +7 327 2 92 70 26 ext 21 28
E-mail: olga@lorton.com

Elena R. Savinova
Technische Universitaet Muenchen
Physik Department E19
James Franck Str. 1
85748 Garching bei Muenchen
Germany
Tel.: +49 89 289 12538
Fax: +49 89 289 12536
E-mail: savinova@Physik.TU
Muenchen.DE

Nataliya L. Semendyaeva
Lomonosov Moscow State University
Lenynskie Gory
119899 Moscow
Russia
Tel.: +7 095 939 40 79
Fax: +7 095 939 25 96
E-mail: NatalyS@cs.msu.su

Nadezhda V. Shikina
Boreskov Institute of Catalysis SB RAS
pr. Akad. Lavrentieva, 5
630090 Novosibirsk
Russia
Tel.: +7 383 2 34 26 70
Fax: +7 383 2 39 73 52
E-mail: Yashnik@catalysis.nsk.su

Natalya V. Shtertser
Boreskov Institute of Catalysis SB RAS
pr. Akad. Lavrentieva, 5
630090 Novosibirsk
Russia
Tel.: +7 383 2 34 41 09
Fax: +7 383 2 34 30 56
E-mail: min@catalysis.nsk.su

Alexander A. Shubin
Boreskov Institute of Catalysis SB RAS
pr. Akad. Lavrentieva, 5
630090 Novosibirsk
Russia
Tel.: +7 383 2 34 10 64
Fax: +7 383 2 34 30 56
E-mail: A.A.Shubin@catalysis.nsk.su

Irina L. Simakova
Boreskov Institute of Catalysis SB RAS
pr. Akad. Lavrentieva, 5
630090 Novosibirsk
Russia
Fax: +7 383 2 34 30 56
E-mail: simakova@catalysis.nsk.su

Anatoliy G. Sipatrov
Boreskov Institute of Catalysis SB RAS
pr. Akad. Lavrentieva, 5
630090 Novosibirsk
Russia
Tel.: +7 383 2 34 41 09
Fax: +7 383 2 34 30 56
E-mail: los@catalysis.nsk.su

Marina M. Slinko
Institute of Chemical Physics RAS
Kosygina str., 4
117334 Moscow
Russia
Tel.: +7 095 939 75 04
Fax: +7 095 939 74 49
E-mail: Slinko@polymer.chph.ras.ru

Evgenii I. Smirnov
Boreskov Institute of Catalysis SB RAS
pr. Akad. Lavrentieva, 5
630090 Novosibirsk
Russia
Tel.: +7 383 2 34 12 78
Fax: +7 383 2 34 30 56
E-mail: esmirnov@catalysis.nsk.su

Pavel V. Snytnikov
Boreskov Institute of Catalysis SB RAS
pr. Akad. Lavrentieva, 5
630090 Novosibirsk
Russia
Tel.: +7 383 2 34 47 89
Fax: +7 383 2 34 30 56
E-mail: pvsnyt@catalysis.nsk.su

Vladimir I. Sobolev
Boreskov Institute of Catalysis SB RAS
pr. Akad. Lavrentieva, 5
630090 Novosibirsk
Russia
Tel.: +7 383 2 34 46 07
Fax: +7 383 2 34 30 56
E-mail: sobolev@catalysis.nsk.su

Vladimir A. Sobyandin
Boreskov Institute of Catalysis SB RAS
pr. Akad. Lavrentieva, 5
630090 Novosibirsk
Russia
Tel.: +7 383 2 34 43 06
Fax: +7 383 2 34 30 56
E-mail: sobyandin@catalysis.nsk.su

Evgenij V. Starokon
Boreskov Institute of Catalysis SB RAS
pr. Akad. Lavrentieva, 5
630090 Novosibirsk
Russia
Tel.: +7 383 2 34 46 07
Fax: +7 383 2 34 30 56
E-mail: starokon@catalysis.nsk.su

Evgenii P. Talsi
Boreskov Institute of Catalysis SB RAS
pr. Akad. Lavrentieva, 5
630090 Novosibirsk
Russia
Tel.: +7 383 2 34 18 77
Fax: +7 383 2 34 37 66
E-mail: talsi@catalysis.nsk.su

Nikolai I. Timofeev
Ekaterinburg Non Ferrous Metals
Processing Plant
Lenin ave., 8
620014 Ekaterinburg
Russia
Tel.: +7 343 2 56 85 48
Fax: +7 343 2 56 85 96
E-mail: ocm@mail.ur.ru

Valentin F. Tretjakov
Topchiev Institute of Petrochemical
Synthesis RAS
Leninskii pr., 29
119991 Moscow
Russia
Tel.: +7 095 955 42 71
Fax: +7 095 230 22 24
E-mail: Tretjak@ips.ac.ru

Lidiya T. Tsykoza
Boreskov Institute of Catalysis SB RAS
pr. Akad. Lavrentieva, 5
630090 Novosibirsk
Russia
Tel.: +7 383 2 34 26 70
Fax: +7 383 2 39 73 52

Marat I. Tulepov
Combustion Problems Institute
Al Farabi Kazakh State National University
Bogenbay Batyr str., 172
480012 Almaty
Kazakhstan
Tel.: +7 327 2 92 43 46
Fax: +7 327 2 92 58 11
E-mail: tulepov@rambler.ru

Herman van Bekkum
Delft University of Technology
Faculty of Applied Science
Julianalaan 136
2628 BL Delft
The Netherlands
Tel.: +31 15 278 26 03
Fax: +31 15 278 14 15
E-mail: H.vanBekkum@stm.tudelft.nl

Bas L. van Drooge
TO&MMA b.v.
Vliegdenweg, 15
1406 MX Bussum
The Netherlands
Tel.: +31 6 51 54 62 21
Fax: +31 35 692 24 26

Johannes C. van den Heuvel
University of Amsterdam
Chemical Engineering Department
Nieuwe Achtergrach, 166
1018 WV Amsterdam
The Netherlands
Tel.: +31 20 525 50 78
Fax: +31 20 525 56 04
E-mail: heuvel@science.uva.nl

Rutger A. van Santen
Eindhoven University of Technology
Rector's Office
P.O. Box 513
5600 MB Eindhoven
The Netherlands
Tel.: +31 402 47 22 60
Fax: +31 402 45 50 54
E-mail: r.a.v.santen@tue.nl

Sergei N. Vereshchagin
Institute of Chemistry and Chemical
Technology SB RAS
K.Marx str., 42
660049 Krasnoyarsk
Russia
Tel.: +7 391 2 43 94 31
Fax: +7 391 2 43 94 31
E-mail: snv@krsk.infotel.ru

Marina P. Vorobyeva
Zelinskii Institute of Organic Chemistry RAS
Leninskii pr., 47
117913 Moscow
Russia
Tel.: +7 095 137 6617
Fax: +7 095 137 29 35
E-mail: marina55@mail.ru

Timur V. Voskoboinikov
UOP LLC
50 East Algonquin Rd
60005 Des Plaines, IL
USA
Tel.: 1 847 391 2445
Fax: 1 847 391 3724
E-mail: tvoskob@uop.com

Dmitry G. Yakhvarov
Arbuzov Institute of Organic and
Physical Chemistry RAS
Arbuzov str., 8
420088 Kazan
Russia
Tel.: +7 843 2 75 23 92
Fax: +7 843 2 75 22 53
E-mail: yakhvar@iopc.knc.ru

Svetlana A. Yashnik
Borekov Institute of Catalysis SB RAS
pr. Akad. Lavrentieva, 5
630090 Novosibirsk
Russia
Tel.: +7 383 2 34 26 70
Fax: +7 383 2 39 73 52
E-mail: Yashnik@catalysis.nsk.su

Nikolay A. Yazykov
Borekov Institute of Catalysis SB RAS
pr. Akad. Lavrentieva, 5
630090 Novosibirsk
Russia
Tel.: +7 383 2 34 46 82
Fax: +7 383 2 34 30 56
E-mail: A.D.Simonov@catalysis.nsk.su

Olga M. Zakharova
JSC "Kirovo-Chepetsk Chemical Plant"
Pozharnyi per., 7
613040 Kirovo-Chepetsk
Russia
Tel.: +7 833 6 19 47 00
Fax: +7 833 6 19 42 59

Georgy M. Zhidomirov
Borekov Institute of Catalysis SB RAS
pr. Akad. Lavrentieva, 5
630090 Novosibirsk
Russia
Tel.: +7 383 2 34 10 64
Fax: +7 383 2 34 3056
E-mail: zhi@catalysis.nsk.su

Ilya A. Zolotarskii
Borekov Institute of Catalysis SB RAS
pr. Akad. Lavrentieva, 5
630090 Novosibirsk
Russia
Tel.: +7 383 2 34 44 91
Fax: +7 383 2 34 30 56
E-mail: zol@catalysis.nsk.su

AUTHOR INDEX*

Antsifirov Vladimir N.	189	Kruchinin Vladimir N.	272	Simakova Irina L.	354
Babich Igor V.	106, 149, 389	Krupenya Lidya V.	271	Sipatrov Anatoliy G.	110
Bitter Johannes H.	101	Kuvshinov Gennady G.	277	Slinko Marina M.	167, 193, 194
Bogdanov Vladimir I.	251, 294, 388	Kuznetsov Vadim V.	389, 401	Smirnov Evgenii I.	371
Bryliakov Konstantin P.	174, 237	Kuznetsova Svetlana A.	233	Snytnikov Pavel V.	378
Burdeynaya Tatyana N.	175, 235	Lamberov Alexander A.	282, 327	Sobolev Vladimir I.	104, 253
Cholach Alexander R.	38, 195	Larichev Yurii V.	283	Sobyanin Vladimir A.	105, 378
Castricum Hessel L.	186	Lavrenov Alexander V.	291	Starokon Evgenij V.	386, 387
Chumakov Gennadii A.	238	Lysova Anna A.	75	Talsi Evgenii P.	174, 237
Craje Menno	37, 87	Makarov Alexander M.	293	Timofeev Nikolai I.	294, 388
Danchenko Yurii V.	401	Makarov Alexander A.	292, 293	Tretyakov Valentin F.	175, 235
De Jong Arthur	259	Malchikov Gennadii D.	294	Tsykoza Lidiya T.	295, 401
Dubkov Konstantin A.	386, 387	Mansurov Zulkhair A.	145	Tulepov Marat I.	145
Elokhin Vladimir I.	206	Matus Ekaterina V.	295	Van Bekkum Herman	13
Fadeev Stanislav I.	194	Matveev Andrey V.	206, 212, 220	Van Santen Rutger A.	7, 14, 177, 259
Galvita Vladimir V.	105	Maximova Nadejda I.	298	Vereshchagin Sergei N.	122
Gorodetskii Vladimir V.	206, 212, 220	Moulijn Jacob A.	18, 149, 389	Yakhvarov Dmitry G.	245
Goryainova Natalia E.	294	Natrova Anna V.	299, 307	Yashnik Svetlana A.	149, 189, 389, 401
Hensen Ermiel J.M.	49, 177	Nemudry Alexander P.	145	Yazykov Nikolay A.	359, 414
Ione Kazimira G.	90	Nieuwenhuys Bernard E.	33, 38, 167, 220	Zhidomirov Georgy M.	14
Ismagilov Ilias Z.	164	Nindakova Lidiya O.	311	Zolotarskii Ilya A.	343, 371
Ismagilov Zinifer R.	29, 149, 164, 189, 272, 295, 307, 319, 328, 389, 401	Overweg Arian R.	37		
Isupova Lyubov A.	254	Parmon Valentin N.	10, 75, 110, 164, 317, 343, 359, 414		
Ivanchev Sergey S.	100	Pavlova Svetlana N.	343		
Ivanov Dmitri P.	104, 253	Pestunova Oxana P.	317		
Ivanova Elena A.	232	Pirutko Larisa V.	103		
Jumabaeva Amina	256	Podyacheva Olga Yu.	145, 189, 307, 319		
Kazanskii Vladimir B.	8, 14	Reshetenko Tatyana V.	328		
Kerzhentsev Mikhail A.	164, 272	Reutova Olga A.	342		
Khairulin Sergei R.	149, 307	Romanova Raziya G.	327		
Koning Bert	130, 371	Sadykov Vladislav A.	235, 343		
Koningsberger Diederik C.	9, 101, 435	Saifulin Alexey A.	270		
Koriabkina Alina O.	259	Salanov Alexei N.	88, 122		
Kosmambetova Gulnara	422, 423	Sarmurzina Alma G.	344		
Kovalenko Galina A.	262	Savinova Elena R.	62		
Kovalyova Elena G.	263	Semendyaeva Nataliya L.	424		
Kozlovskiy Roman A.	63	Shikina Nadezhda V.	149, 189, 319, 401		
		Shtertser Natalya V.	345		
		Shubin Alexander A.	14		

*Only authors of the papers who applied for the conference are included into this index.

Content

PLENARY LECTURES

PL-1 R.A. van Santen MOLECULAR MODELLING.....	7
PL-2 V.B. Kazanskii LOCALIZATION OF BIVALENT TRANSITION METAL IONS IN HIGH SILICA ZEOLITES PROBED BY LOW TEMPERATURE ADSORPTION OF MOLECULAR HYDROGEN	8
PL-3 D.C. Koningsberger ELECTRON DISTRIBUTION EFFECTS IN CATALYSIS.....	9
PL-4 V.N. Parmon CATALYTIC METHODS OF ENERGY PRODUCTION FROM RENEWABLE SOURCES AND MATERIALS	10
PL-5 H. van Bekkum, A.C. Besemer SELECTIVE OXIDATION OF CARBOHYDRATES WITH FOCUS ON TEMPO CATALYSIS..	13
PL-6 G.M. Zhidomirov, A.A. Shubin, V.B. Kazansky, V.N. Solkan, R.A. van Santen, A.L. Yakovlev, L.A.M.M. Barbosa STRUCTURAL STABILITY AND CATALYTIC REACTIVITY OF ZINC ION SPECIES IN ZEOLITES	14
PL-7 J.A. Moulijn, A. Stankiewicz, F. Kapteijn THE POTENTIAL OF STRUCTURED REACTORS IN PROCESS INTENSIFICATION.....	18
PL-8 Z.R. Ismagilov, O.Yu. Podyacheva, L.T. Tsykoza, V.N. Kruchinin, S.A. Yashnik, V.V. Kuznetsov, T.V. Reshetenko, H.J. Veringa DEVELOPMENT OF ADVANCED CATALYSTS FOR ENVIRONMENTAL PROTECTION	29
PL-9 C.J. Weststrate, A. Gluhoi, R.J.H. Grisel, B.E. Nieuwenhuys OXIDATION REACTIONS OVER MULTICOMPONENT CATALYSTS CONSISTING OF GOLD AND A TRANSITION/RARE EARTH METAL OXIDE	33

ORAL PRESENTATIONS

OP-1 A.R. Overweg, M.W.J. Crajé, A.M. van der Kraan, I.W.C.E. Arends THE CHARACTERIZATION OF FeZSM-5 BY ⁵⁷ Fe MÖSSBAUER SPECTROSCOPY	37
---	----

OP-2	
A.R. Cholach, V.M. Tapilin	
THE CONJUGATE ELECTRON EXCITATION IN A SUBSTRATE-ADSORBATE SYSTEM.....	38
OP-3	
E.J.M. Hensen, L. Coulier, A. Borgna, J.A.R. van Veen, J.W. Niemantsverdriet	
SILICON-WAFER BASED PLANAR MODELS FOR HYDROTREATING CATALYSTS	49
OP-4	
E.R. Savinova, U. Stimming	
CATALYSIS FOR DIRECT METHANOL FUEL CELLS	62
OP-5	
R.A. Kozlovskiy, V.F. Shvets, A.V. Koustov, L.E. Kitaev, V.V. Yushchenko, V.V. Kriventsov, D.I. Kochubey, M.V. Tsodikov	
RELATIONSHIP BETWEEN SURFACE PROPERTIES OF MODIFIED TITANOOXIDES AND THEIR CATALYTIC PROPERTIES IN REACTION OF ETHOXYLATION OF ETHYLENE OXIDE.....	63
OP-6	
A.A. Lysova, I.V. Koptuyug, A.V. Kulikov, V.A. Kirillov, V.N. Parmon, R.Z. Sagdeev	
THE INVESTIGATION OF THE HETEROGENEOUS CATALYTIC REACTIONS BY ¹ H NMR MICROIMAGING	75
OP-7	
M.W.J. Crajé, A.M. van der Kraan, J. van de Loosdrecht, P.J. van Berge	
THE APPLICATION OF MÖSSBAUER EMISSION SPECTROSCOPY TO INDUSTRIAL COBALT BASED FISCHER-TROPSCH CATALYSTS	87
OP-8	
A.N. Salanov, A.L. Titkov	
MECHANISMS OF CHEMISORPTION OF GASES ON METALS: MODERN TRENDS.....	88
OP-9	
K.G. Ione, V.M. Mysov	
APPLICATION OF POLYFUNCTIONAL CATALYSIS IN TRANSFORMATION OF CO ₂ AND BIOSILTS TO MOTOR FUELS AS A METHOD OF UTILIZATION OF ENVIRONMENTALLY DANGEROUS WASTES.....	90
OP-10	
S.S. Ivanchev, G.A. Tolstikov, V.K. Badaev, I.I. Oleinik, N.I. Ivancheva, D.G. Rogozin, I.V. Oleinik, M.V. Tikhonov	
NEW BIS-(ARYLIMINO)PYRIDYL AND BIS-(ARYLIMINO)ACENAPHTHYL COMPLEXES	100
OP-11	
J.H. Bitter, A.A. Battiston, S. van Donk, K.P. de Jong, D.C. Koningsberger	
ACCESSIBILITY OF THE IRON SPECIES IN OVEREXCHANGED Fe/ZSM5 PREPARED BY CHEMICAL VAPOR DEPOSITION OF FeCl ₃	101
OP-12	
L.V. Pirutko, V.S. Chernyavsky, A.K. Uriarte, G.I. Panov	
OXIDATION OF BENZENE TO PHENOL BY NITROUS OXIDE. ACTIVITY OF IRON IN ZEOLITE MATRICES OF VARIOUS COMPOSITION	103
OP-13	
V.I. Sobolev, D.P. Ivanov, G.I. Panov	
DIRECT HYDROXYLATION OF PHENOL TO DEHYDROXYBENZENES WITH N ₂ O.....	104

OP-14	
V.V. Galvita, A.V. Frumin, V.D. Belyaev, G.I. Semin, V.A. Sobyenin	
CONVERSION OF ETHANOL OR DIMETHYL ETHER TO HYDROGEN REACH-GAS.....	105
OP-15	
I. Babich, L. Leveles, K. Seshan, L. Lefferts	
OXIDATIVE DEHYDROGENATION AS A ROUTE FOR LIGHT OLEFINS.....	106
OP-16	
A.G. Sipatrov, A.A. Khassin, T.M. Yurieva, V.A. Kirillov, V.N. Parmon	
FISCHER-TROPSCH SYNTHESIS USING POROUS CATALYST PACKING	110
OP-17	
S.N. Vereshchagin, N.N. Anshits, A.N. Salanov*, O.M. Sharonova, T.A. Vereshchagina, A.G. Anshits	
MICROSPHERES OF FLY ASH AS A SOURCE FOR CATALYTIC SUPPORTS, ADSORBENTS AND CATALYSTS	122
OP-18	
G.W. Koning, A.E. Kronberg, W.P.M. van Swaaij	
MODELING OF HEAT AND MASS TRANSPORT IN WALL-COOLED TUBULAR REACTORS	130
12.00	
OP-19	
Z.A. Mansurov, Y.A. Ryabikin, M.I. Tulepov, O.V. Zashkvara	
INVESTIGATION OF PARAMAGNETIC PROPERTIES OF CATALYSTS ON THE BASIS OF $\text{Ca}_{1-x}\text{Sr}_x\text{FeO}_{2.5+y}$ BY EPR METHOD	145
OP-20	
Z.R. Ismagilov, S.A. Yashnik, N.V. Shikina, I.P. Andrievskaya, S.R. Khairulin, V.A. Ushakov, J.A. Moulijn, I.V. Babich	
MANGANESE OXIDE MONOLITH CATALYSTS MODIFIED BY Fe AND Cu FOR HIGH-TEMPERATURE AMMONIA DECOMPOSITION AND H_2S REMOVAL.....	149
OP-21	
I.Z. Ismagilov, M.A. Kerzhentsev, Z.R. Ismagilov, V.N. Parmon, , V.N. Eryomin, L.N. Rolin, V.A. Shandakov, G.V. Sakovich, F. Garin, H.J. Veringa	
CATALYTIC OXIDATION OF UNSYMMETRICAL DIMETHYLHYDRAZINE AS THE METHOD FOR NEUTRALIZATION OF HAZARDOUS LIQUID ROCKET FUELS: TECHNOLOGY DEVELOPMENT BASED ON THE LABORATORY AND PILOT PLANT STUDIES.....	164
OP-22	
N.V. Peskov, M.M. Slinko, S.A. C. Carabineiro, B.E. Nieuwenhuys	
MATHEMATICAL MODELING OF OSCILLATORY BEHAVIOUR DURING $\text{N}_2\text{O}+\text{H}_2$ REACTION OVER Ir (110).....	167
OP-23	
K.P. Bryliakov, N.V. Semikolenova, V.A. Zakharov, E.P. Talsi	
^{13}C NMR STUDY OF Ti(IV) SPECIES FORMED VIA ACTIVATION OF Cp^*TiCl_3 WITH METHYLALUMINOXANE (MAO).....	174
OP-24	
V.F. Tretyakov, T.N. Burdeynaya, V.A. Matyshak	
ENVIRONMENTAL CATALYSIS: SELECTIVE REDUCTION OF NO BY ALKANES	175
OP-25	
E.J.M. Hensen, Q. Zhu, P.C.M.M. Magusin, R.A. van Santen	
IRON CLUSTERS OCCLUDED IN ZEOLITE ZSM5 MICROPORES	177

OP-26

H.L. Castricum, V.V. Malakhov, T.M. Yurieva, H. Bakker, E.K. Poels MECHANOCHEMICAL PREPARATION OF Cu/ZnO CATALYSTS	186
--	-----

INTAS SESSION

IN-1 Z.R. Ismagilov, S.A. Yashnik, O.Yu. Podyacheva, N.V. Shikina, L.M. Kustov, Yu.V. Danchenko, P.G. Tsyrunnikov, A. Kalugin, P. Siffert, R. Keiski, J. Herguido CATALYTIC MATERIALS.....	189
IN-2 N.V. Peskov, M.M. Slinko, N.I. Jaeger PARTICLE SIZE EFFECT OF REACTION RATE OSCILLATIONS DURING CO OXIDATION OVER ZEOLITE SUPPORTED Pd CATALYSTS	193
IN-3 N.V. Peskov, M.M. Slinko, I.A. Gainova, S.I. Fadeev THE STUDY OF ONE MODEL OF CO OXIDATION OVER Pd CATALYSTS	194
IN-4 A.R. Cholach, N.N. Bulgakov, B.E. Nieuwenhuys ON THE MECHANISM OF OSCILLATION PHENOMENA IN THE NO+H ₂ REACTION	195
IN-5 A.V. Matveev, E.I. Latkin, V.I. Elokhin, V.V. Gorodetskii ANISOTROPIC EFFECT OF ADSORBED CO DIFFUSION ON THE OSCILLATORY BEHAVIOR DURING CO OXIDATION OVER Pd(110) - MONTE-CARLO MODEL.....	206
IN-6 A.V. Matveev A.A. Sametova, N.N. Bulgakov, V.V. Gorodetskii OXYGEN-INDUCED RECONSTRUCTION AND SURFACE EXPLOSION PHENOMENA IN THE NO+CO/Pd(110) SYSTEM: THEORETICAL AND EXPERIMENTAL STUDIES.....	212
IN-7 V.V. Gorodetskii, A.V. Matveev, A.V. Kalinkin, B.E. Nieuwenhuys CO, O ₂ COADSORPTION and CO + O ₂ OSCILLATORY REACTION ON Pd TIP AND Pd(110) SURFACES: FEM, TPR, XPS STUDIES	220
IN-8 E.A. Ivanova, V.A. Nasluzov, A.I. Rubaylo, N. Rösch THEORETICAL INVESTIGATION OF THE MECHANISM OF METHANOL CARBONYLATION CATALYZED BY DICARBONYLDIIDDORHODIUM COMPLEX.....	232
IN-9 S.A. Kuznetsova, V.G. Danilov, O.V. Yatsenkova, N.B. Alexandrova, V.K. Shambasov, B.N. Kuznetsov ENVIRONMENTALLY FRIENDLY PRODUCING OF CELLULOSE BY ABIES-WOOD ORGANOSOLVENT PULPING IN THE PRESENCE OF CATALYSTS.....	233
IN-10 V.A. Sadykov, V.P. Doronin, T.P. Sorokina, T.G. Kuznetsova, G.M. Alikina, R.V. Bunina, D.I. Kochubei, B.N. Novgorodov, E.A. Paukshtis, V.B. Fenelonov, A.Yu. Derevyankin, V.I. Zaikovskii, V.N. Kolomiichuk, V.F. Anufrienko, A.Ya. Rozovskii, V.F. Tretyakov, T.N. Burdeynaya, V.A. Matyshak, G.A. Konin, J.R.H. Ross NANOSTRUCTURED CATALYSTS OF NO _x SELECTIVE REDUCTION BY HYDROCARBONS BASED UPON ZIRCONIA-PILLARED CLAYS: SYNTHESIS AND PROPERTIES.....	235

IN-11 K.P. Bryliakov, E.P. Talsi THE REACTIVE INTERMEDIATES IN ASYMMETRIC OXIDATIONS CATALYZED BY VANADIUM(V) COMPLEXES.....	237
IN-12 G.A. Chumakov, N.A. Chumakova DIFFERENT WAYS TO WEAKLY STABLE DYNAMICS IN A THREE-DIMENSIONAL KINETIC MODEL OF CATALYTIC HYDROGEN OXIDATION.....	238
IN-13 D.G. Yakhvarov, J. Heinicke, Yu.H. Budnikova, O.G. Sinyashin SYNTHESIS AND CATALYTICAL ACTIVITY OF TERTIARY <i>RTHO</i> -PHOSPHINOPHENOLS AND THEIR DERIVATIVES	245

POSTER PRESENTATIONS

PP-1 V.I. Bogdanov, L.D. Gorbatova, A.A. Lavrov, S.Yu. Chelnakov PLATINUM AND RHENIUM EXTRACTION FROM DEACTIVATED CATALYST OF THE PETROLEUM-CHEMICAL INDUSTRY.....	251
PP-2 D.P. Ivanov, V.I. Sobolev, G.I. Panov OXIDATION OF BENZENE TO PHENOL BY NITROUS OXIDE: THE MECHANISM OF DEACTIVATION AND REGENERATION OF FeZSM-5 ZEOLITE CATALYSTS.....	253
PP-3 L.A. Isupova, V.A. Sadykov DEVELOPMENT OF Fe ₂ O ₃ - BASED CATALYSTS OF DIFFERENT GEOMETRIES FOR ENVIRONMENTAL CATALYSIS.....	254
PP-4 A.I. Jumabayeva, A.N. Sartaeva, K.A. Zhubanov ALUMINUM-CHROMIUM CATALYSTS FOR SO ₂ OXIDATION.....	256
PP-5 A.O. Koriabkina, D. Schuring, A.M. de Jong, R.A. van Santen DIFFUSION OF HEXANES IN SILICALITE: CONCENTRATION DEPENDENCE.....	259
PP-6 G.A. Kovalenko, I.B. Ivshina, E.V. Kuznetsova, I.S. Andreeva, A.V. Simakov BIOEPOXIDATION OF PROPENE BY NON-GROWING CELLS OF <i>RHODOCOCCUS</i> sp.	262
PP-7 E.G. Kovalyova, A.B. Shishmakov, V.G. Kharchuk, L.A. Petrov, O.V. Kuznetsova, O.V. Koryakova, M.Yu. Yanchenko, L.A. Petrov, L.S. Molochnikov THE ROLE OF ELEMENTS DIOXIDES HYDROGELS AND THEIR SURFACE COPPER STRUCTURES IN HYDROXYARENES CATALYTIC OXIDATIVE TRANSFORMATION.....	263
PP-8 A.V. Kravtsov, A.A. Novikov, A.A. Saifulin, V.V. Samoilenko FORECASTING OF THE EFFICIENCY OF MODIFIED CATALYSTS IN METHANOL SYNTHESIS.....	270
PP-9 A.V. Kravtsov, E. D. Ivanchina, L.V. Krupenya, S.A. Galushin REDUCTION OF COKE FORMATION ON Pt-Re REFORMING CATALYSTS OF GASOLINES.....	271

PP-10 V.N. Kruchinin, M.A. Kerzhentsev, Z.R. Ismagilov, V.N. Korotkih, G.M. Zabortsev, Yu.M. Ostrovskii, H.J. Veringa THE INVESTIGATION OF PROCESSES OF BIOMASS PYROLYSIS AND GASIFICATION IN FLUIDIZED BED REACTORS	272
PP-11 G.G. Kuvshinov, D.G. Kuvshinov, A.M. Glushenkov THE INFLUENCE OF INERT IMPURITIES ON THE CATALYST LIFETIME AND PROPERTIES OF NANOFIBROUS CARBON PRODUCED BY UTILIZATION OF DILUTED HYDROCARBON GASES	277
PP-12 A.A. Lamberov, R.G. Romanova, E.Yu. Sitnikova, Kh.Kh. Gil'manov, S.R. Egorova THE INFLUENCE OF STRUCTURE AND CHARACTER OF DISTRIBUTION OF PALLADIUM ON SURFACE OF CATALYST ON IT ACTIVITY IN REACTION OF HYDROGENATION OF DIENES	282
PP-13 Y.V. Larichev, B.L. Moroz, I.P. Prosvirin, V.I. Bukhtiyarov, V.A. Likholobov XPS STUDY OF THE METAL-SUPPORT INTERACTION IN Ru/MgO CATALYST FOR LOW-TEMPERATURE AMMONIA SYNTHESIS	283
PP-14 A.V. Lavrenov, E.A. Paukshtis, V.K. Duplyakin, B.S. Bal'zhinimaev STUDIES OF SULFATED ZIRCONIA CATALYSTS DEACTIVATED IN ALKYLATION OF ISOBUTANE WITH BUTANES.....	291
PP-15 A.A. Makarov, A.M. Khanov, A. Tzschatzsch 3D SIMULATION OF DIESEL ENGINE EXHAUST GASES CATALYTIC CONVERTER.....	292
PP-16 A.M. Makarov, A.A. Makarov, A. Tzschatzsch REDOX NO _x ON SOOT PARTICULE TRAP	293
PP-17 G.D. Malchikov, N.I. Timofeev, V.I. Bogdanov, E.N. Tunikova, N.E. Goryanova OXIDATION CATALYST FOR GAS OXYGEN SENSORS.....	294
PP-18 E.V. Matus, L.T. Tsykoza, Z.R. Ismagilov STUDY OF Mo PRECURSOR SPECIES IN IMPREGNATION SOLUTION OF AMMONIUM HEPTAMOLYBDATE.....	295
PP-19 N.I. Maximova, V.V. Kuznetsov, Yu.V. Butenko, G. Mestl, R. Schloegl SOME ASPECTS OF THE REACTION MECHANISM OF OXIDATIVE DEHYDROGENATION OF ETHYLBENZENE TO STYRENE	298
PP-20 A.V. Nartova, R.I. Kvon STM and XPS STUDY OF THE MODEL SUPPORTED SILVER CATALYSTS.....	299
PP-21 A.P. Nemudry, O.Yu. Podyacheva, Z.R. Ismagilov, V.A. Ushakov, S.R. Khairulin SYNTHESIS AND STUDY OF MICRODOMAIN TEXTURED PEROVSKITE CATALYSTS	307

PP-22	
L.O. Nindakova, O.V. Gamzikova, B.A. Shainyan, F.K. Schmidt	
DOUBLE STEREOSELECTION IN HYDROGENATION OF PROCHIRAL DEHYDROCARBOXYLIC ACIDS ON $\text{Rh}(\text{S,S-DIODMA})_2 + \text{TfO}^-$ COMPLEX IN THE PRESENCE OF (+)-NEOMENTHYLDIPHENYLPHOSPHINE	311
PP-23	
O.P. Pestunova, O.L. Ogorodnikova, V.N. Parmon	
CATALYTIC WET PEROXIDE OXIDATION OF PHENOL OVER METAL-OXIDE AND CARBON CATALYSTS	317
PP-24	
O.Yu. Podyacheva, N.V. Shikina, Z.R. Ismagilov, V.A. Ushakov, A.I. Boronin, N.A. Rudina, I.A. Ovsyannikova, S.A. Yashnik, O.P. Solonenko, A.A. Michal'chenko, H. Veringa	
SOME APPLICATIONS OF PLASMA SPRAYING TECHNIQUE FOR THE PREPARATION OF SUPPORTED CATALYSTS	319
PP-25	
R.G. Romanova, A.A. Lamberov, I.G. Shmelev	
THE INFLUENCE OF POROUS STRUCTURE AND ACID-BASE PROPERTIES OF SURFACE OF CATALYST ON ITS ACTIVITY IN REACTION OF DEHYDRATATION OF α-PHENYLETHANOL	327
PP-26	
T.V. Reshetenko, L.B. Avdeeva, Z.R. Ismagilov, V.A. Ushakov, A.L. Chuvilin, Yu.T. Pavlyukhin	
PROMOTED IRON CATALYSTS OF LOW-TEMPERATURE METHANE DECOMPOSITION	328
PP-27	
O. Reutova	
"COMPENSATED DISINTEGRATION OF HYDROCARBONS" MODEL	342
PP-28	
V.A. Sadykov, S.N. Pavlova, R.V. Bunina, T.G. Kuznetsova, I.A. Zolotarskii, V.A. Kuzmin, Z.Y. Vostrikov, A.V. Simakov, N.N. Sazonova, S.A. Veniaminov, V.N. Parmon, E.A. Paukshtis, V.A. Rogov, N.N. Bulgakov, V.V. Lunin, E. Kemnitz	
METHANE SELECTIVE OXIDATION INTO SYNGAS AT SHORT CONTACT TIMES: DESIGN OF MONOLITH CATALYSTS AND THEIR PERFORMANCE	343
PP-29	
A.G. Sarmurzina, O.E. Lebedeva, A.A. Taltenov, S.V. Efremova, O.N. Kuznetsova	
NON-TRADITIONAL SOURCES FOR CATALYST SUPPORTS	344
PP-30	
N.V. Shtertser, T.P. Minyukova, I.I. Simentsova, A.V. Khasin, T.M. Yurieva	
CO-FREE METHYLFORMATE FROM METHANOL: THE CONTROL OF SELECTIVITY OF THE PROCESS ON Cu-BASED CATALYSTS	345
PP-31	
A.V. Simakov, S.N. Pavlova, N.N. Sazonova, V.A. Sadykov, O.I. Snegurenko, V.A. Rogov, V.N. Parmon, I.A. Zolotarskii, V.A. Kuzmin, E.M. Moroz	
OSCILLATIONS IN CONVERSION OF METHANE TO SYNGAS IN THE PRESENCE OF OXYGEN OVER SUPPORTED MIXED OXIDES PROMOTED WITH Pt	346
PP-32	
I.L. Simakova, V.A. Semikolenov	
CATALYTIC SYNTHESIS OF VERBANOL FROM α-PINENE DERIVATIVE	354

PP-33	A.D. Simonov, T.I. Mishenko, N.A. Yazykov, V.N. Parmon COMPARATIVE FEATURES OF COMBUSTION AND PROCESSING OF RICE HUSK IN THE VIBROFLUIDIZED BEDS OF CATALYST AND INERT MATERIAL	359
PP-34	E.I. Smirnov, A.V. Muzykantov[†], V.A. Kuzmin, I.A. Zolotarskii, G.W. Koning, A.E. Kronberg RADIAL HEAT TRANSFER IN PACKED BEDS OF SHAPED PARTICLES	371
PP-35	P.V. Snytnikov, V.A. Sobyenin, V.D. Belyaev, D.A. Shlyapin CATALYSTS FOR H ₂ PURIFICATION BY SELECTIVE CO OXIDATION	378
PP-36	E.V. Starokon, K.A. Dubkov, E.A. Paukshtis, A.M. Volodin, G.I. Panov MECHANISM OF HYDROGEN INTERACTION WITH α -OXYGEN OVER FeZSM-5 ZEOLITE	386
PP-37	E.V. Starokon, K.A. Dubkov, N.S. Ovanesyian, A.A. Shteinman, G.I. Panov FORMATION OF α -SITES UPON THERMAL ACTIVATION OF Fe-CONTAINING ZEOLITES	387
PP-38	N.I. Timofeev, V.I. Bogdanov, V.A. Dmitriev, G.M. Guschin, L.D. Gorbatova THE CATALYTIC SYSTEMS FOR AMMONIA OXIDATION BASED ON THE PLATINUM GROUP METALS	388
PP-39	S.A. Yashnik, V.V. Kuznetsov, Z.R. Ismagilov, J.A. Moulijn, I.V. Babich FTIR STUDY OF SURFACE ACIDITY OF ALUMINAS AND THEIR ACTIVITY IN H ₂ S OXIDATION	389
PP-40	S.A. Yashnik, L.T. Tsikoza, Z.R. Ismagilov, V.A. Sazonov, N.V. Shikina, V.V. Kuznetsov, I.A. Ovsyannikova, N.M. Danchenko, S.P. Denisov, H.J. Veringa THE Cu-ZSM-5 CATALYSTS WASHCOATED ON MONOLITH FOR DIESEL VEHICLE EMISSION CONTROL	401
PP-41	N.A. Yazykov, A.D. Simonov, T.I. Mishenko, A.S. Aflyatunov, C.V. Smolin, V.N. Parmon FUEL COMBUSTION IN THE FLUIDIZED BED OF AN INERT MATERIAL WITH AN UNMOVABLE CATALYTIC SMALL-VOLUME PACKAGE	414
PP-42	G.R. Kosmambetova, M.R. Kantserova, K.S. Gavrylenko, S.M. Orlyk, V.L. Struzhko NEW APPROACHES TO SYNTHESIS OF LOW TEMPERATURE CATALYSTS FOR METHANE DEEP OXIDATION	422
PP-43	G.R. Kosmambetova, M.V. Pavlenko[†], V.I. Grytsenko, I.N. Stepanenko, L.B. Kharkova, V.I. Pekhnio DIRECT METHANE OXIDATIVE CARBONYLATION INTO ACETIC-ACID ON SUPPORTED RHODIUM CATALYSTS IN GAS PHASE	423
PP-44	E.S. Kurkina, N.L. Semendyaeva KINETIC OSCILLATIONS IN CO OXIDATION OVER PLATINUM CATALYSTS: MONTE CARLO SIMULATIONS	424

PP-45

A.Yu. Stakheev, G.N. Baeva, A.V. Ivanov, N.S. Telegina, D.C. Koningsberger, B.L. Mojet, L.M. Kustov

TUNING OF THE ELECTRONIC STATE OF THE SUPPORTED METAL BY VARYING ACID-BASE PROPERTIES OF Al_2O_3 425

LIST OF PARTICIPANTS 427

AUTHOR INDEX..... 435

CONTENT 436

